

Novel expansion mechanisms for space creation and organ retraction during laparoscopic surgery

SHAH, Dignesh

Available from the Sheffield Hallam University Research Archive (SHURA) at:

<http://shura.shu.ac.uk/21653/>

A Sheffield Hallam University thesis

This thesis is protected by copyright which belongs to the author.

The content must not be changed in any way or sold commercially in any format or medium without the formal permission of the author.

When referring to this work, full bibliographic details including the author, title, awarding institution and date of the thesis must be given.

Please visit <http://shura.shu.ac.uk/21653/> and <http://shura.shu.ac.uk/information.html> for further details about copyright and re-use permissions.

**NOVEL EXPANSION MECHANISMS FOR
SPACE CREATION AND ORGAN RETRACTION
DURING LAPAROSCOPIC SURGERY**

Dignesh Shah

**A thesis submitted in partial fulfilment of the
requirements of Sheffield Hallam University for the
degree of Doctor of Philosophy.**

January 2018

Collaborating Organisations

TrusTECH and Manchester University NHS Foundation Trust

© Copyright 2018

by

Dignesh Shah

CONTENTS

NOVEL EXPANSION MECHANISMS FOR SPACE CREATION AND ORGAN RETRACTION DURING LAPAROSCOPIC SURGERY.....	i
CONTENTS	iii
LIST OF TABLES	ix
LIST OF FIGURES	xii
ABSTRACT	xxxix
ACKNOWLEDGEMENT	xxxix
ABBREVIATION.....	xxxix
CONFLICT OF INTERESTS.....	xxxv
LIST OF PUBLICATIONS	xxxvi
1 Introduction	1
1.1 Motivation	1
1.2 Aim and objectives.....	2
1.3 Layout of chapters	3
2 Literature review - Human abdomen, abdominal surgery and the LaparOsphere™	5
2.1 The human abdominal environment - key organs and biomechanical properties.....	5
2.1.1 Human abdomen and abdominal wall	5
2.1.2 Solid organs	7
2.1.3 Hollow organs	23
2.1.4 Summary.....	31
2.2 Abdominal surgery and the LaparOsphere™ concept	33
2.2.1 Open and laparoscopic abdominal surgery	33
2.2.2 Disadvantages of use of CO ₂ insufflation	38
2.2.3 Existing space creation and/or organ retraction devices	39
2.2.4 The LaparOsphere™ concept and expansion mechanisms	42

2.3	Surface pressure application during abdominal surgery	45
2.4	Summary	45
3	Literature Review of Elasticity Theory, Beam Theory, and Cellular Structures	47
3.1	Elasticity theory	47
3.1.1	Hooke's law and Poisson's ratio	48
3.1.2	Generalised (anisotropic) Hooke's law	50
3.1.3	Orthotropic materials	52
3.1.4	Isotropic materials	53
3.1.5	Saint-Venant's principle	54
3.2	Beam theory	57
3.2.1	Bending of beam	57
3.2.2	Buckling of pinned-end columns	57
3.2.3	Negative stiffness	61
3.3	Cellular materials and structures	63
3.3.1	Introduction to cellular structures	63
3.3.2	Analytical expressions for the mechanical properties of honeycombs	64
3.4	Auxetic materials	70
3.4.1	Introduction	70
3.4.2	Types of auxetic materials	70
3.4.3	Properties	72
3.4.4	Auxetic structure-mechanism combinations	75
3.4.5	Biomedical applications	82
3.5	Summary	86
4	Materials and Methodology 1: Abdominal simulator and in-vivo measurement of organ surface pressures and retraction distances	87
4.1	Selection of simulant organ materials	87
4.1.1	Solid organ simulant materials	87
4.1.2	Hollow organ simulant materials	91
4.2	Fabrication of the simulant organs	92
4.2.1	Solid organ simulants	92

4.2.2	Hollow organ simulants	102
4.3	Assessment of biomechanical properties of simulant organs	103
4.3.1	Evaluation of simulant organ density	103
4.3.2	Evaluation of solid simulant and pig organ elasticity	103
4.3.3	Survey of biomechanical properties of simulant organs	105
4.4	In-house abdominal simulator	106
4.5	In-vivo measurement of surface pressures	109
4.5.1	Ethics committee approvals of in-vivo pilot study	109
4.5.2	Description of pressure sensor	111
4.5.3	Set up within the operating theatre	113
4.5.4	Methodology of measurement of surface pressures	115
4.5.5	Methodology of calculation of organ retraction distances	116
4.5.6	Data analysis	117
4.6	Summary	118
5	Materials and Methodology 2: Finite element (FE) modelling of a solid wall cylinder	120
5.1	Finite Element methods and Computer Aided Design	120
5.1.1	Finite Element methods	120
5.1.2	Computer Aided Design (CAD)	120
5.1.3	Summary	121
5.2	Rationale	121
5.3	Study set up	122
5.3.1	Dimensions of cylinder and types of end pieces	122
5.3.2	Coordinate systems	123
5.3.3	Material properties	123
5.3.4	Boundary conditions	133
5.3.5	Meshing	135
5.3.6	Solutions	139
5.4	FE modelling of uniform material properties	139
5.4.1	Isotropic material properties	140
5.4.2	Orthotropic material properties	140
5.5	Summary	141

6	Materials and Methodology 3: Mesh Cylinders.....	142
6.1	Cellular mesh derivation methodology	142
6.1.1	‘Bottom-up’ approach	142
6.1.2	‘Top-down’ approach.....	146
6.1.3	Combined ‘Bottom-up’ and ‘Top-down’ approach	148
6.2	Cellular mesh models	150
6.2.1	CAD models for validation of outputs of FE modelling of solid wall cylinder.....	152
6.2.2	CAD models for fabrication of expansion mechanisms	155
6.3	Fabrication of cellular mesh cylinders	158
6.4	Mechanical characterisations of cellular mesh cylinders	160
6.5	In-vitro assessments of cellular mesh cylinders.....	160
6.6	In-vivo and in-vitro assessments of Doughnut shape inflatable prototypes.....	163
6.7	Summary	165
7	Results 1: Abdominal simulator and in-vivo measurement of organ surface pressures and retraction distances.....	166
7.1	Fabrication of simulants organs	166
7.1.1	Solid organ simulants	166
7.1.2	Hollow organ simulants	169
7.2	Assessment of biomechanical properties.....	170
7.2.1	Density of simulant organs	170
7.2.2	Elasticity of solid simulants.....	172
7.2.3	Survey of biomechanical properties of simulant organs	185
7.3	In-house abdominal simulator.....	186
7.4	In-vivo measurement of surface pressures	189
7.4.1	Open abdominal surgery	190
7.4.2	Hand assisted laparoscopic surgery.....	194
7.4.3	Data analysis.....	202
7.5	Calculation of organ retraction distances	207
7.5.1	Open abdominal surgery	207
7.5.2	Hand assisted laparoscopic surgery.....	212

7.5.3	Degree of organ retraction distance	218
7.6	Comparison of in-vivo and in-vitro surface pressures	218
7.7	Summary	220
8	Results 2 - Finite element (FE) modelling of a solid wall cylinder	222
8.1	Isotropic material properties.....	222
8.2	Orthotropic material properties	224
8.2.1	Parametric study 1 of solid wall cylinder with end pieces	224
8.2.2	Parametric study 2 of solid wall cylinder with end pieces	252
8.2.3	Parametric study 2 of solid wall cylinder without end pieces ..	255
8.3	Summary	274
9	Results 3 - Cellular mesh cylinders, Fabrication, Characterisation, and in-vitro and in-vivo assessments of prototypes	276
9.1	Cellular mesh cylinders.....	276
9.1.1	Validation of outputs of FE modelling of a solid wall cylinder .	276
9.1.2	FE predictions of laser cut and 3D printed cellular mesh cylinders	286
9.1.3	Relationships between global, RVE and cellular mesh parameters	288
9.2	Fabrication of cellular mesh cylinders.....	296
9.3	Characterisation of experimental expansion mechanisms	300
9.3.1	Mechanical characterisation.....	300
9.3.2	Calculation of equatorial deformations	304
9.3.3	Comparison of Experimentations and FE predictions.....	312
9.4	In-vitro assessments of expansion mechanisms.....	313
9.4.1	Assessments using foam blocks	314
9.4.2	Assessments using simulant organs	317
9.4.3	Experimentations vs FE predictions	340
9.4.4	Surface pressure for the retraction of human and simulant abdominal organs.....	342
9.4.5	Summary of in-vitro assessment of expansion mechanisms..	349
9.5	In-vivo and in-vitro assessments of Doughnut shape inflatable prototypes.....	350

9.6	Novel expansion mechanisms	354
9.7	Summary	358
10	Discussion.....	359
10.1	Development of in-house abdominal simulator.....	359
10.1.1	Fabrications and assessment of simulant organs	359
10.1.2	In-house abdominal simulator (in-vitro test rig)	363
10.2	In-vivo measurement of organ surface pressures and retraction distances	363
10.3	FE modelling of a solid wall cylinder.....	367
10.4	Designing cellular mesh cylinders	372
10.4.1	Validation of outputs of FE modeling of a solid wall cylinder.....	372
10.4.2	FE predictions of cellular mesh cylinders	374
10.5	Fabrication of expansion mechanisms	376
10.6	Characterisation of experimental cylinders	377
10.7	In-vitro assessment of expansion mechanisms	379
10.8	Summary	384
11	Conclusion, Novelties and Recommendations for Future work	385
11.1	Conclusion.....	385
11.2	Novelties.....	386
11.3	Recommendations for future works	390
12	References.....	393
Appendix A.....		A-1
Appendix B.....		B-4
Appendix C.....		C-26
Appendix D.....		D-34

LIST OF TABLES

Table 2.1: Biomechanical properties of human abdomen and abdominal wall.	6
Table 2.2: Physical dimensions of human liver.	9
Table 2.3: Human liver volume.	11
Table 2.4: Human liver weight.....	12
Table 2.5: Human liver Density.	12
Table 2.6: Human liver tissue elasticity.	13
Table 2.7: Elastic modulus of liver by mechanical indentation method.	13
Table 2.8: Physical dimensions of human kidney.	15
Table 2.9: Human kidney volume.....	16
Table 2.10: Human kidney weight.....	17
Table 2.11: Elastic modulus of human and pig kidney	18
Table 2.12: Physical dimensions of human spleen.	20
Table 2.13: Human spleen volume.	20
Table 2.14: Human spleen weight.....	21
Table 2.15: Human spleen density.....	22
Table 2.16: Elasticity of human spleen.	23
Table 2.17: Human stomach volume.	24
Table 2.18: Human stomach weight.....	25
Table 2.19: Elasticity of human stomach.	27
Table 2.20: Physical dimensions of human large intestine.	28
Table 2.21: Elasticity of human bowel.....	29
Table 2.22: Physical dimensions of human small intestine.	30
Table 2.23: Elasticity of human small intestine.	31
Table 2.24: Summary of biomechanical properties for key abdominal organs.	32
Table 3.1: End constraint factors for elastic buckling of honeycomb.....	68
Table 3.2: Auxetic structures and their mechanisms 1.....	76
Table 3.3: Auxetic structures and their mechanisms 2.....	77
Table 3.4: Auxetic structures and their mechanisms 3.....	78
Table 3.5: Auxetic structures and their mechanisms 4.....	79
Table 3.6: Auxetic structures and their mechanisms 5.....	80

Table 3.7: Auxetic structures and their mechanisms 6.....	81
Table 4.1: Physical properties of materials evaluated for the solid organ simulants.	89
Table 4.2: Score table for each material assessed for solid organ simulants.	90
Table 4.3: Fabrication of solid organ simulants using the Pro Gel 10 system.	99
Table 5.1: Isotropic material properties of structural steel.....	125
Table 5.2: Elastic constants of the orthotropic material properties.....	126
Table 5.3: Orthotropic material properties for positive definite matrix in the cylindrical coordinate system.....	129
Table 5.4: Orthotropic material properties for positive definite matrix in the cylindrical coordinate system.....	133
Table 5.5: Finite and Infinite BCs.....	135
Table 5.6: Mesh statistics for the relevance of mesh.	136
Table 5.7: Mesh metrics for fine mesh generated for cylinder without end pieces.	138
Table 5.8: Mesh metrics for coarse mesh generated for cylinder without end pieces.	139
Table 6.1: Cylinder and RVE geometrical parameters.	146
Table 6.2: Input parameters for graphical method.	148
Table 6.3: Selective pairs of N_c and N_v (RVEs) for negative in-plane Poisson's ratio to achieve a target value of $N_c/N_v = 1.68$	149
Table 6.4: Cellular mesh parameters obtained by the combined approach with input parameters specified in Table 6.2.	150
Table 6.5: Honeycomb cylinders simulated for the validation of outputs of FE modelling of a solid wall cylinder.	154
Table 6.6: Cellular cylinders designed for fabrication.....	157
Table 7.1: Average density of solid simulants.....	171
Table 7.2: Thickness of real and simulant pig liver samples.	173
Table 7.3: Thickness of pig kidney samples and equivalent simulants.	181
Table 7.4: Opinions of surgeons for solid simulant organs.	185
Table 7.5: Opinions of five surgeons for hollow simulant organs.	186

Table 7.6: In-vivo measurement of surface pressures applied to abdominal organs.	203
Table 7.7: Retraction distances extracted from video footage for the second liver retraction event for patient 3.	210
Table 8.1: Maximum axial compressive force applied during parametric study of geometrical parameters (parametric study 1 of cylinder with pronged cone end pieces and negative in-plane Poisson's ratio).....	237
Table 8.2: 'Shape change' properties for parametric study 1 of solid wall cylinder with pronged cone end pieces.	241
Table 8.3: Calculation of orthotropic constants corresponding to the change in E_θ during parametric study 2 of cylinder with pronged cone end pieces (in-plane negative Poisson's ratio).....	253
Table 8.4: 'Shape change' properties to carry out parametric study of cylinder with pronged cone end pieces.	255
Table 8.5: Calculation of orthotropic constants corresponding to the parametric study of E_θ (parametric study 2 of cylinder without end pieces and with in-plane positive Poisson's ratio).....	256
Table 8.6: 'Shape change' properties for parametric study 2 of solid wall cylinder without end pieces and with in-plane positive Poisson's ratio.	260
Table 8.7: Calculation of orthotropic constants corresponding to the change in E_θ during parametric study 2 of cylinder without end pieces (in-plane negative Poisson's ratio).	266
Table 8.8: 'Shape change' properties to carry out parametric study 2 of solid wall cylinder without end pieces and with in-plane negative Poisson's ratio.	269
Table 9.1: Segments of auxetic honeycombs from CAD models and length of end pieces.	277
Table 9.2: Segments of conventional honeycombs from CAD models and length of end pieces.	278

LIST OF FIGURES

Figure 2.1: Human abdominal environment and key organs.....	6
Figure 2.2: Human liver, gallbladder situated underneath of liver and pancreas.....	7
Figure 2.3: A schematic diagram showing physical dimensions of human liver.....	8
Figure 2.4: Human kidney environment.	14
Figure 2.5: Human spleen environment.	19
Figure 2.6: Human stomach environment.	23
Figure 2.7: Human bowel environment.	28
Figure 2.8: Human small intestine environment.	30
Figure 2.9: Global coordinates, anatomical planes, and directions of organ retractions for the human body.....	33
Figure 2.10: A typical incision along the midline of the abdomen during open surgery.	34
Figure 2.11: Schematic representation of retraction of liver and stomach during an open abdominal procedure.	35
Figure 2.12: CO ₂ insufflation and port placement during laparoscopic cholecystectomy.....	36
Figure 2.13: A GelPort used for hand assisted laparoscopic surgery.	37
Figure 2.14: Space creation devices.....	40
Figure 2.15: PretzelFlex™ organ retraction device.	41
Figure 2.16: Retraction of liver using FreeHold Trio™.	42
Figure 2.17: LaparOsphere™ concept.....	43
Figure 2.18: LaparOsphere™ device with port and on/off valve for fluid/air control.....	44
Figure 3.1: Stress-strain diagrams.	48
Figure 3.2: Definition of Poisson's Ratio.	50
Figure 3.3: Stress distribution in a rectangular elastic plate showing Saint- Venant's principle.	55
Figure 3.4: Cantilever beam illustrating use of Saint-Venant's principle.	56
Figure 3.5: Pinned-end column.....	58
Figure 3.6: Relation between load and deflection for columns.....	59

Figure 3.7: Deformation of buckled beam.	62
Figure 3.8: Linear elastic compression of conventional honeycomb.	65
Figure 3.9: Curvatures of auxetic and conventional honeycombs.....	73
Figure 3.10 Folded sheet of paper showing an auxetic effect.	73
Figure 3.11: Origami cylinder to ball mechanism.	74
Figure 3.12 Semi-solid fold face deployable paper cylinder/ball.	75
Figure 3.13: Dilator device with an auxetic expansion member. ⁽¹⁸²⁾	82
Figure 3.14: Schematic of smart bandage concept.	83
Figure 4.1: Structure of silicone and silicone gel.....	91
Figure 4.2: Mould for fabrication of simulant of human kidney and spleen. .	93
Figure 4.3: CT scan images showing anatomy of human liver.....	94
Figure 4.4: Calibration of CT scan slice.	94
Figure 4.5: CT scan slice showing 2D coordinates of human liver.....	95
Figure 4.6: 3D printed liver from ABS material.....	95
Figure 4.7: Assembly for making 2-part silicone rubber mould.	97
Figure 4.8: Two-part silicone rubber mould.....	98
Figure 4.9: One part of the 2-parts Plaster of Paris pig liver mould.....	102
Figure 4.10: Pig liver, pig kidney, and simulant kidney mounted on Instron machine.....	104
Figure 4.11: Right angle assembly (first test-rig) for the in-house simulator.	107
Figure 4.12: Second test-rig mounted on the Instron machine.	109
Figure 4.13: Pressure sensor system and ultrasound probe cover.	112
Figure 4.14: 'Laparoscopy' software for surface pressure data logging.	113
Figure 4.15: Representation of pressure measurements carried out in the surgical theatre.....	114
Figure 4.16: Origin (0, 0) and Local co-ordinate system (x_1 - x_2) for plane of image.....	117
Figure 4.17: Properties extracted for data analysis of 'clean' retraction event.	118
Figure 5.1: Types of end pieces.....	122

Figure 5.2: (a) Cylindrical coordinate system and (b) global coordinate system with corresponding mapping of the cylindrical axes (in parentheses) of an unfolded cylinder.	123
Figure 5.3: Effect of angle of diagonal rib of honeycomb on Poisson's ratio.	128
Figure 5.4: Negative definite matrix in the Ansys software.	131
Figure 5.5: Effect of angle of diagonal rib of honeycomb on Poisson's ratio.	132
Figure 5.6: Boundary conditions with respect to cylindrical coordinate systems. (a) 'Load' applied on top face (negative sign indicates axial compressive load), (b) 'Displacements' at top face, and (c) 'Displacements' at bottom face.....	134
Figure 5.7: Solid186 element. (a) Homogeneous and (b) Layered structural solid, showing node locations, element coordinate system and shape options (Version 17.1 and 18.1 ANSYS Inc.).....	137
Figure 5.8: FE modelling of isotropic material properties.	140
Figure 6.1: Cellular mesh parameters h/l (a), t/l (b) and E_z (c) as functions of honeycomb angle α for a hexagonal honeycomb cylinder with $\nu_{z\theta} = -10$, $G_{\theta z} = 1.0 \times 10^7$ Pa and $E_s = 2 \times 10^{11}$ Pa.....	145
Figure 6.2: The cylinder, RVE and cellular parameters of a conventional and auxetic hexagonal honeycomb cylinder.....	147
Figure 6.3: Target α for designing of cellular cylinders.	151
Figure 6.4: Target $\nu_{z\theta}$ for designing of cellular cylinders.....	151
Figure 6.5: Cylinders mounted on rotary attachment of the Speedy 100™ laser cutter.....	159
Figure 6.6: Study set up for in-vitro assessments of prototype structures..	161
Figure 6.7: Inflatable doughnut shape prototypes.	163
Figure 6.8: Inflation of the doughnut shape prototype within the pig abdomen.	164
Figure 6.9: In-vitro study set up to assess expansion capabilities of doughnut shape prototypes within the test rig.	165
Figure 7.1: Human kidney simulants.....	167
Figure 7.2: Human spleen simulants.....	168

Figure 7.3: Human liver simulants.....	168
Figure 7.4: Pig liver simulant (50% v/v of Pro Gel softener).....	169
Figure 7.5: Stomach simulant. (a) Empty (b) Full (mixture of water and air).	169
Figure 7.6: Bowel simulants (5% and 7.5% w/v concentration of wallpaper paste).	170
Figure 7.7: Average density of solid simulants compared with the actual densities of the human kidney, spleen and liver.	171
Figure 7.8: Force vs Displacement curves for the right and left lobe of pig liver A.	172
Figure 7.9: Stress vs strain curves for area 4 of the right and area 1 of the left lobe of pig liver A.....	173
Figure 7.10: Fourth order polynomial fit to the stress vs strain curve for the right lobe (area 4) of pig liver A.	174
Figure 7.11: Tangent modulus vs strain for area 4 of the right lobe of pig liver A.....	175
Figure 7.12: Average stresses for the right and left lobe of pig liver A.	175
Figure 7.13: Average tangent modulus of pig liver A compared with the average tangent modulus of the right and left lobes of pig liver A.	176
Figure 7.14: Average tangent modulus of four pig livers compared with the individual pig liver average responses.....	177
Figure 7.15: Average Force vs Displacement curves for the right and left lobe of the pig liver simulants.	178
Figure 7.16: Average stress-strain responses for pig liver simulants.	178
Figure 7.17: Average tangent modulus of pig liver simulants.....	179
Figure 7.18: Average tangent modulus of actual pig liver and equivalent pig liver silicone simulants.....	180
Figure 7.19: Average force vs displacement for pig kidney samples.	181
Figure 7.20: Average stress vs strain for pig kidney samples.	182
Figure 7.21: Average tangent modulus vs strain for pig kidney samples. ...	182
Figure 7.22: Average force vs displacement for pig kidney simulants.....	183
Figure 7.23: Average stress vs strain for pig kidney simulants.	184

Figure 7.24: Average tangent modulus vs strain for actual pig kidney and pig kidney simulants.....	184
Figure 7.25: Moving and squashing of pig liver inside the test-rig.....	187
Figure 7.26: Lifting of pig liver inside the test-rig.....	187
Figure 7.27: Lifting of simulant human liver inside the test-rig.	188
Figure 7.28: Moving and squashing of simulant human bowel pieces inside the test-rig.	189
Figure 7.29: Retraction events for the liver for patient 3 undergoing open abdominal surgery.....	190
Figure 7.30: Clean retraction event for the liver for patient 3 undergoing open abdominal surgery (second event of Figure 7.29).	191
Figure 7.31: Retraction events for the bowel for patient 3 undergoing open abdominal surgery.....	192
Figure 7.32: Retraction of the bowel using a metal retractor for patient 3..	193
Figure 7.33: Retraction events for the stomach for patient 10 undergoing open abdominal surgery.....	194
Figure 7.34: Unclean retraction event of liver for patient 4 during HALS. Selected stills from the video footage are included.	195
Figure 7.35: Clean retraction event of liver for patient 8 during HALS.	195
Figure 7.36: Retraction of the liver using a PretzelFlex™ retractor for patient 4. Selected stills from the video footage are included.	196
Figure 7.37: Retraction of the liver using a laparoscopic grasper for patient 5. Selected stills from the video footage are included.	197
Figure 7.38: Retraction event for the bowel (patient 5) undergoing HALS.	198
Figure 7.39: Retraction event for the kidney (patient 7) undergoing HALS.	199
Figure 7.40: Retraction event for the kidney (patient 6) undergoing HALS. Selected stills from the video footage are included.	199
Figure 7.41: Retraction event for the spleen (patient 5) undergoing HALS. Selected stills from the video footage are included.	200
Figure 7.42: Retraction event for the stomach (patient 5) undergoing HALS. Properties extracted for data analysis and selected stills from the video footage are included.....	201

Figure 7.43: Retraction events for the abdominal aorta and omentum for patient 7 and IVC and duodenum for patient 8.	202
Figure 7.44: Average root mean square and maximum surface pressure ('clean' events), and average maximum surface pressure (all events) applied to key abdominal organs.	204
Figure 7.45: Average hold time for pressure applied to key abdominal organs ('clean' events).	204
Figure 7.46: Surface pressure relaxation: $[\Delta P/T_{\text{Hold}}]/P_{\text{max}}$ vs T_{Hold} for the Liver-OC. OC = Open Cholecystectomy.	206
Figure 7.47: Surface pressure relaxation: $[\Delta P/T_{\text{Hold}}]/P_{\text{max}}$ vs T_{Hold} for the liver (OC – empty squares), bowel (OC – empty triangles), bowel (HALS – filled diamonds, and kidney (HALS – filled circles). OC = Open Cholecystectomy. HALS = Hand Assisted Laparoscopic Surgery.	206
Figure 7.48: Coordinate axes, known distance of retractor (7 cm), stationary points (1-4) and identifying marks (spot 5 and 6) for Image at 1 sec.	207
Figure 7.49: Sequence of images extracted from the video footage of the second liver retraction event for patient 3.	208
Figure 7.50: Retraction distances (ΔX_1 and ΔX_2) compared against applied surface pressure in the second liver retraction event for patient 3.	211
Figure 7.51: Correlation between surface pressure and retraction distance (ΔX) in the plane of the image for the second retraction event of the liver for patient 3 during OC.	212
Figure 7.52: Coordinate axes, known width of thumb of surgeon (2 cm), stationary points (1-4) and identifying marks (spot 5 and 6) for Image at 9 secs for retraction of bowel for patient 5.	213
Figure 7.53: Coordinate axes, known width of fingertips of surgeon (2 cm), stationary points (1-4) and identifying marks (spot 5 and 6) for Image at 0 sec for retraction of kidney for patient 6.	213
Figure 7.54: Coordinate axes, known width of fingertips of surgeon (2 cm), stationary points (1-4) and identifying marks (spot 5 and 6) for Image at 0 sec for retraction of stomach for patient 5.	214

Figure 7.55: Coordinate axes, known width of thumb of surgeon (2 cm), stationary points (1-4) and identifying marks (spot 5 and 6) for Image at 29 secs for retraction of spleen for patient 5.....	214
Figure 7.56: Correlation between surface pressure and retraction distance for the second retraction event of the bowel for patient 5 during HALS....	215
Figure 7.57: Correlation between surface pressure and retraction distance for the kidney for patient 6 during HALS.....	216
Figure 7.58: Correlation between surface pressure and retraction distance for the stomach for patient 5 during HALS.....	216
Figure 7.59: Correlation between surface pressure and retraction distance for the spleen for patient 5 during HALS.....	217
Figure 7.60: Retraction distances of key abdominal organs.	218
Figure 7.61: Surface pressures applied to retract pig (in-vitro), simulant human liver (in-vitro), and human liver (in-vivo).....	219
Figure 7.62: Surface pressures applied to retract pig (in-vitro), simulant human liver (in-vitro), and human liver (in-vivo).....	220
Figure 8.1: Equatorial radial deformation vs axial deformation of a solid wall cylinder with isotropic material properties employing finite and infinite BCs.	222
Figure 8.2: Equatorial radial deformation vs axial deformation of a cylinder with isotropic material properties and end pieces under uniaxial compressive force.	223
Figure 8.3: ERD vs AD for parametric study of E_r (parametric study 1 of cylinder with pronged cone end pieces and in-plane negative Poisson's ratio).	225
Figure 8.4: ERD vs compressive axial force for parametric study of E_r (parametric study 1 of cylinder with pronged cone end pieces and in-plane negative Poisson's ratio).....	226
Figure 8.5: ERD vs AD for parametric study of E_θ (parametric study 1 of cylinder with pronged cone end pieces and in-plane negative Poisson's ratio).	226

Figure 8.6: ERD vs compressive axial force for parametric study of E_θ (parametric study 1 of cylinder with pronged cone end pieces and in- plane negative Poisson's ratio).....	227
Figure 8.7: ERD vs axial strain for parametric study of E_θ (parametric study 1 of cylinder with pronged cone end pieces and in-plane negative Poisson's ratio).	227
Figure 8.8: ERD vs AD for parametric study of E_z (parametric study 1 of cylinder with pronged cone end pieces and in-plane negative Poisson's ratio).	228
Figure 8.9: ERD vs compressive axial force for parametric study of E_z (parametric study 1 of cylinder with pronged cone end pieces and in- plane negative Poisson's ratio).....	229
Figure 8.10: ERD vs AD for parametric study of $G_{r\theta}$ (parametric study 1 of cylinder with pronged cone end pieces and in-plane negative Poisson's ratio).	230
Figure 8.11: ERD vs compressive axial force for parametric study of $G_{r\theta}$ (parametric study 1 of cylinder with pronged cone end pieces and in- plane negative Poisson's ratio).....	231
Figure 8.12: ERD vs AD for parametric study of $G_{\theta z}$ (parametric study 1 of cylinder with pronged cone end pieces and in-plane negative Poisson's ratio).	232
Figure 8.13: ERD vs compressive axial force for parametric study of $G_{\theta z}$ (parametric study 1 of cylinder with pronged cone end pieces and in- plane negative Poisson's ratio).....	233
Figure 8.14: ERD vs AD for parametric study of G_{rz} (parametric study 1 of cylinder with pronged cone end pieces and in-plane negative Poisson's ratio).	234
Figure 8.15: ERD vs compressive axial force for parametric study of G_{rz} (parametric study 1 of cylinder with pronged cone end pieces and in- plane negative Poisson's ratio).....	234
Figure 8.16: ERD vs AD for parametric study of in-plane Poisson's ratios (parametric study 1 of cylinder with pronged cone end pieces and in- plane negative Poisson's ratio).....	235

Figure 8.17: ERD vs compressive axial force for parametric study of in-plane Poisson's ratios (parametric study 1 of cylinder with pronged cone end pieces and in-plane negative Poisson's ratio).	236
Figure 8.18: Parametric study of outer diameter of cylinder using 'standard' properties (parametric study 1 of cylinder with pronged cone end pieces and in-plane negative Poisson's ratio).	238
Figure 8.19: Parametric study of length of cylinder using 'standard' properties (parametric study 1 of cylinder with pronged cone end pieces and in-plane negative Poisson's ratio).	238
Figure 8.20: Parametric study of wall thickness of cylinder using 'standard' properties (parametric study 1 of cylinder with pronged cone end pieces and with in-plane negative Poisson's ratio).	239
Figure 8.21: Parametric study of Young's modulus of pronged cone end pieces using 'standard' properties (parametric study 1 of cylinder with pronged cone end pieces and with in-plane negative Poisson's ratio).	239
Figure 8.22: Parametric study of different types of end pieces using 'standard' properties (parametric study 1 of cylinder with pronged cone end pieces and with in-plane negative Poisson's ratio).	240
Figure 8.23: ERD vs AD for parametric study of in-plane Poisson's ratios using 'shape change' properties (parametric study 1 of cylinder with pronged cone end pieces and in-plane negative Poisson's ratio).	242
Figure 8.24: ERD vs axial compressive force for parametric study of in-plane Poisson's ratios using 'shape change' properties (parametric study 1 of cylinder with pronged cone end pieces and in-plane negative Poisson's ratio).	243
Figure 8.25: Parametric study of outer diameter of cylinder using 'shape change' properties (ERD vs AD) (parametric study 1 of cylinder with pronged cone end pieces and in-plane negative Poisson's ratio).	244
Figure 8.26: Parametric study of outer diameter of cylinder using 'shape change' properties (ERD vs axial compressive force) (parametric study 1 of cylinder with pronged cone end pieces and in-plane negative Poisson's ratio).	245

Figure 8.27: Parametric study of outer diameter of cylinder using 'shape change' properties (ERD vs axial strain) (parametric study 1 of cylinder with pronged cone end pieces and in-plane negative Poisson's ratio).	245
Figure 8.28: Parametric study of length of cylinder using 'shape change' properties (ERD vs AD) (parametric study 1 of cylinder with pronged cone end pieces and in-plane negative Poisson's ratio).....	246
Figure 8.29: Parametric study of length of cylinder using 'shape change' properties (ERD vs axial compressive force) (parametric study 1 of cylinder with pronged cone end pieces and in-plane negative Poisson's ratio).	247
Figure 8.30: Parametric study of length of cylinder using 'shape change' properties (ERD vs axial strain) (parametric study 1 of cylinder with pronged cone end pieces and in-plane negative Poisson's ratio).....	247
Figure 8.31: Parametric study of wall thickness of cylinder using 'shape change' properties (ERD vs AD) (parametric study 1 of cylinder with pronged cone end pieces and in-plane negative Poisson's ratio).....	248
Figure 8.32: Parametric study of wall thickness of cylinder using 'shape change' properties (ERD vs axial compressive force) (parametric study 1 of cylinder with pronged cone end pieces and in-plane negative Poisson's ratio).....	249
Figure 8.33: Parametric study of wall thickness of cylinder using 'shape change' properties (ERD vs axial strain) (parametric study 1 of cylinder with pronged cone end pieces and in-plane negative Poisson's ratio).	249
Figure 8.34: Parametric study of Young's modulus of pronged cone end pieces using 'shape change' properties (ERD vs AD) (parametric study 1 of cylinder with pronged cone end pieces and in-plane negative Poisson's ratio).....	250
Figure 8.35: Parametric study of Young's modulus of pronged cone end pieces using 'shape change' properties (ERD vs axial compressive force) (parametric study 1 of cylinder with pronged cone end pieces and in-plane negative Poisson's ratio).....	251
Figure 8.36: Parametric study of Young's modulus of pronged cone end pieces using 'shape change' properties (ERD vs axial strain) (parametric	

study 1 of cylinder with pronged cone end pieces and in-plane negative Poisson's ratio).	251
Figure 8.37: ERD vs compressive axial deformation for parametric study of E_θ (parametric study 2 of cylinder with pronged cone end pieces and in-plane negative Poisson's ratio).	253
Figure 8.38: ERD vs axial strain for parametric study of E_θ (parametric study 2 of cylinder with pronged cone end pieces and in-plane negative Poisson's ratio).	254
Figure 8.39: ERD vs AD for parametric study of E_θ (parametric study 2 of cylinder without end pieces and with in-plane positive Poisson's ratio).	257
Figure 8.40: ERD vs axial compressive force for parametric study of E_θ (parametric study 2 of cylinder without end pieces and with in-plane positive Poisson's ratio).	258
Figure 8.41: ERD vs axial strain for parametric study of E_θ (parametric study 2 of cylinder without end pieces and with in-plane positive Poisson's ratio).	259
Figure 8.42: Parametric study of outer diameter of cylinder for uniaxial compression mechanism (ERD vs compressive axial deformation) (parametric study 2 of cylinder without end pieces and with in-plane positive Poisson's ratio).	261
Figure 8.43: Parametric study of outer diameter of cylinder for uniaxial compression mechanism (ERD vs axial compressive force) (parametric study 2 of cylinder without end pieces and with in-plane positive Poisson's ratio).	261
Figure 8.44: Parametric study of outer diameter of cylinder for uniaxial compression mechanism (ERD vs axial strain) (parametric study 2 of cylinder without end pieces and with in-plane positive Poisson's ratio).	262
Figure 8.45: Parametric study of length of cylinder for uniaxial compression mechanism (ERD vs compressive axial deformation) (parametric study 2 of cylinder without end pieces and with in-plane positive Poisson's ratio).	262

Figure 8.46: Parametric study of length of cylinder for uniaxial compression mechanism (ERD vs axial compressive force) (parametric study 2 of cylinder without end pieces and with in-plane positive Poisson's ratio).	263
Figure 8.47: Parametric study of length of cylinder for uniaxial compression mechanism (ERD vs axial strain) (parametric study 2 of cylinder without end pieces and with in-plane positive Poisson's ratio).	263
Figure 8.48: Parametric study of wall thickness of cylinder for uniaxial compression mechanism (ERD vs AD) (parametric study 2 of cylinder without end pieces and with in-plane positive Poisson's ratio).	264
Figure 8.49: Parametric study of wall thickness of cylinder for uniaxial compression mechanism (ERD vs axial compressive force) (parametric study 2 of cylinder without end pieces and with in-plane positive Poisson's ratio).	264
Figure 8.50: Parametric study of wall thickness of cylinder for uniaxial compression mechanism (ERD vs axial strain) (parametric study 2 of cylinder without end pieces and with in-plane positive Poisson's ratio).	265
Figure 8.51: ERD vs AD for parametric study of E_{θ} (parametric study 2 of cylinder without end pieces and with in-plane negative Poisson's ratio).	267
Figure 8.52: ERD vs axial tensile force for parametric study of E_{θ} (parametric study 2 of cylinder without end pieces and with in-plane negative Poisson's ratio).	267
Figure 8.53: ERD vs axial strain for parametric study of E_{θ} (parametric study 2 of cylinder without end pieces and with in-plane negative Poisson's ratio).	268
Figure 8.54: Parametric study of outer diameter of cylinder for uniaxial tension mechanism (ERD vs AD) (parametric study 2 of cylinder without end pieces and with in-plane negative Poisson's ratio).	270
Figure 8.55: Parametric study of outer diameter of cylinder for uniaxial tension mechanism (ERD vs axial tensile force) (parametric study 2 of	

cylinder without end pieces and with in-plane negative Poisson's ratio).	270
Figure 8.56: Parametric study of outer diameter of cylinder for uniaxial tension mechanism (ERD vs axial strain) (parametric study 2 of cylinder without end pieces and with in-plane negative Poisson's ratio).	271
Figure 8.57: Parametric study of length of cylinder for uniaxial tension mechanism (ERD vs AD) (parametric study 2 of cylinder without end pieces and with in-plane negative Poisson's ratio).	271
Figure 8.58: Parametric study of length of cylinder for uniaxial tension mechanism (ERD vs axial tension force) (parametric study 2 of cylinder without end pieces and with in-plane negative Poisson's ratio).	272
Figure 8.59: Parametric study of length of cylinder for uniaxial tension mechanism (ERD vs axial strain) (parametric study 2 of cylinder without end pieces and with in-plane negative Poisson's ratio).	272
Figure 8.60: Parametric study of wall thickness of cylinder for uniaxial tension mechanism (ERD vs AD) (parametric study 2 of cylinder without end pieces and with in-plane negative Poisson's ratio).	273
Figure 8.61: Parametric study of wall thickness of cylinder for uniaxial tension mechanism (ERD vs tensile axial force) (parametric study 2 of cylinder without end pieces and with in-plane negative Poisson's ratio).	273
Figure 8.62: Parametric study of wall thickness of cylinder for uniaxial tension mechanism (ERD vs axial strain) (parametric study 2 of cylinder without end pieces and with in-plane negative Poisson's ratio).	274
Figure 9.1: FE predictions of auxetic honeycomb mesh models (ERD vs Tensile axial deformation).	279
Figure 9.2: FE predictions of conventional honeycomb mesh models (ERD vs Compressive axial deformation).	280
Figure 9.3: FE predictions of auxetic honeycomb mesh models (ERD vs Axial tension force).	281
Figure 9.4: FE predictions of conventional honeycomb mesh models (ERD vs axial compressive force).	281
Figure 9.5: FE predictions of auxetic honeycomb mesh models (ERD vs Tensile axial strain).	282

Figure 9.6: FE predictions of conventional honeycomb mesh models (ERD vs Compressive axial strain).	283
Figure 9.7: FE predictions of auxetic honeycomb mesh models with pronged cone end pieces (ERD vs Compressive axial deformation).	284
Figure 9.8: FE predictions of auxetic honeycomb mesh models with pronged cone end pieces (ERD vs Axial compressive force).	284
Figure 9.9: FE predictions of auxetic honeycomb mesh models with pronged cone end pieces (ERD vs Compressive axial strain).	285
Figure 9.10: FE predictions of laser cut and 3D printed auxetic and conventional honeycomb mesh models (ERD vs AD).	286
Figure 9.11: FE predictions of laser cut and 3D printed auxetic and conventional honeycomb mesh models (ERD vs Axial force).	287
Figure 9.12: FE predictions of laser cut and 3D printed auxetic and conventional honeycomb mesh models (ERD vs Axial strain).	288
Figure 9.13: Relationship of the mechanical properties (E_z/E_θ and $\nu_{z\theta}$) with the cellular mesh parameter (α) for the different aspect ratios (h/l) of auxetic honeycombs.	289
Figure 9.14: Relationship of the mechanical property ($\nu_{z\theta}$) and RVE (N_c/N_v) with the cellular mesh parameter (α) for the different aspect ratios (h/l) of auxetic honeycombs and outer diameters of the cylinder.	290
Figure 9.15: Relationship of RVE (N_c/N_v) with the cellular mesh parameter (W) for the different aspect ratios (h/l) of auxetic honeycombs and outer diameters of the cylinder.	291
Figure 9.16: Relationship of RVE (N_c/N_v) with the cellular mesh parameter (t/l) for the different aspect ratios (h/l) of auxetic honeycombs and outer diameters of the cylinder.	292
Figure 9.17: Relationship of the mechanical properties (E_z/E_θ and $\nu_{z\theta}$) with the cellular mesh parameter (α) for the different aspect ratios (h/l) of conventional honeycombs.	293
Figure 9.18: Relationship of the mechanical property ($\nu_{z\theta}$) and RVE (N_c/N_v) with the cellular mesh parameter (α) for the different aspect ratios (h/l) of conventional honeycombs and outer diameters of the cylinder.	295

Figure 9.19: Relationship of RVE (N_c/N_v) with the cellular mesh parameter (t_l/l) for the different aspect ratios (h/l) and t_l of conventional honeycombs.	296
Figure 9.20: Laser cut PVC cellular mesh tubes.	297
Figure 9.21: Laser cut PP cellular mesh tube.	298
Figure 9.22: Laser cut PP cylinders consisting of beams/strips.	299
Figure 9.23: 3D printed cellular mesh cylinder.	299
Figure 9.24: Axial force vs axial displacement curves of the expansion mechanisms.	301
Figure 9.25: Tangent stiffness vs axial displacement curve of the Conventional 8 model characterised in the absence of a surrounding material.	302
Figure 9.26: Tangent stiffness vs axial displacement curves of the expansion mechanisms.	303
Figure 9.27: Stress vs strain curves of the expansion mechanisms.	304
Figure 9.28: Image analysis of selected stills extracted from the video footage of the mechanical characterization of the Conventional 8 cylinder.	305
Figure 9.29: Equatorial radial deformation vs axial deformation curve for the Conventional 8 cylinder.	306
Figure 9.30: Axial compressive force and total equatorial deformation vs axial deformation curves showing the expansion capability of the Conventional 8 cylinder.	307
Figure 9.31: Axial compressive force and total equatorial deformation vs axial deformation curves showing the expansion capability of the Conventional 6 cylinder.	308
Figure 9.32: Axial compressive force and total equatorial deformation vs axial deformation curves showing the expansion capability of the Conventional 7 cylinder.	309
Figure 9.33: Axial compressive force and total equatorial deformation vs axial deformation curves showing the expansion capability of the Conventional 9 cylinder.	310

Figure 9.34: Equatorial deformation vs axial deformation curve for the Beam 2 cylinder.	311
Figure 9.35: Axial compressive force and total equatorial deformation vs axial deformation curves showing the expansion capability of the Beam 2 cylinder.	311
Figure 9.36: Axial compressive force and total equatorial deformation vs axial deformation curves showing the expansion capability of the Beam 1 cylinder.	312
Figure 9.37: ERD vs AD curves obtained from experimental and FE approaches for the Conventional 8 cylinder.	313
Figure 9.38: Surface pressure exerted by expansion mechanisms on surrounding foam blocks within the test rig during in-vitro assessment.	315
Figure 9.39: Retraction of surrounding foam blocks within the test rig mounted on the Instron machine by the Conventional 8 cylinder.	316
Figure 9.40: Axial force vs axial deformation data for the expansion mechanisms surrounded by foam blocks within the test rig.	317
Figure 9.41: Surface pressure exerted on simulant organs by the Conventional 8 cylinder within the test rig vs time.	318
Figure 9.42: Axial compressive force vs axial deformation curves of the Conventional 8 cylinder surrounded by individual and combinations of simulant organs.	320
Figure 9.43: Tangent stiffness vs axial displacement curves of the Conventional 8 cylinder surrounded by a combination of (Liver)-(Bowel & Kidney) simulants.	321
Figure 9.44: Tangent stiffness vs axial displacement curves of the Conventional 8 cylinder surrounded by individual and combinations of simulant organs.	322
Figure 9.45: Axial compressive stress vs axial strain curves of the Conventional 8 cylinder surrounded by individual and combinations of simulant organs.	323

Figure 9.46: Image analysis of selected stills extracted from the video footage recorded during the retraction of the combination of (Liver)-(Bowel & Kidney) simulants by the Conventional 8 cylinder.	324
Figure 9.47: ERD vs AD curves obtained for retraction of individual and combinations of the simulant organs present within the test rig during in-vitro assessment of the Conventional 8 cylinder.	325
Figure 9.48: Surface pressure and total equatorial deformation vs time for retraction of the (Liver)-(Bowel & Kidney) simulant combination by the Conventional 8 cylinder.	326
Figure 9.49: Surface pressure and total equatorial deformation vs time for retraction of the (Stomach & Spleen)-(Bowel) simulant combination by the Conventional 8 cylinder.	327
Figure 9.50: Surface pressure and total equatorial deformation vs time for retraction of bowel simulants by the Conventional 8 cylinder.	327
Figure 9.51: Surface pressure and total equatorial deformation vs time for retraction of kidney simulants by the Conventional 8 cylinder.	328
Figure 9.52: Surface pressure and total equatorial deformation vs time for retraction of spleen simulants by the Conventional 8 cylinder.	328
Figure 9.53: Maximum surface pressure (P_{\max}) and root mean square surface pressure (P_{rms}) for the retraction of the simulant organs by the Conventional 8 cylinder.	330
Figure 9.54: Surface pressure exerted on the simulant organs by the Conventional 10 and Beam 2 cylinders within the test rig.	332
Figure 9.55: Axial compressive force vs axial deformation curves of the Conventional 10 and Beam 2 cylinders for the retraction of surrounding individual and combinations of simulant organs.	333
Figure 9.56: Tangent stiffness vs axial displacement curves of the Conventional 10 and Beam 2 cylinders for the retraction of surrounding combination and individual simulant organs.	334
Figure 9.57: Axial stress vs axial strain curves of the Conventional 10 and Beam 2 cylinders for the retraction of the individual and combinations of simulant organs.	335

Figure 9.58: ERD vs AD curves for the retractions of the individual and combinations of the simulant organs obtained during in-vitro assessment of the Conventional 10 and Beam 2 cylinders.	337
Figure 9.59: Surface pressure and total equatorial deformation vs time for retraction of bowel simulants by the Beam 2 cylinder.....	338
Figure 9.60: Surface pressure and total equatorial deformation vs time for retraction of kidney simulants by the Conventional 10 cylinder.	338
Figure 9.61: Surface pressure and total equatorial deformation vs time for retraction of spleen simulants by the Conventional 10 cylinder.	339
Figure 9.62: Surface pressure and total equatorial deformation vs time for retraction of the combination of (Stomach & Spleen)-(Bowel) simulants by the Conventional 10 cylinder.	339
Figure 9.63: Total equatorial deformation vs AD curves obtained from the FE modelling and experimental approaches for the Conventional 8 cylinder.	341
Figure 9.64: Total equatorial deformation vs AD curves obtained from the FE modelling and experimental approaches for the Conventional 10 cylinder.	341
Figure 9.65: Surface pressure applied (a) on the combination of Liver-BowelKidney simulants within the test rig (in-vitro) by the Conventional 8 cylinder and (b) on the human liver during OC and HALS (in-vivo) by the fingertips of the surgeon and metal retractors.	343
Figure 9.66: Surface pressure applied (a) on the bowel simulants within the test rig (in-vitro) by the Conventional 8 cylinder and (b) on the human bowel during OC and HALS (in-vivo) by the fingertips of the surgeon.	344
Figure 9.67: Surface pressure applied (a) on the kidney simulants within the test rig (in-vitro) by the Conventional 8 and 10 cylinders and (b) on the human kidney during HALS (in-vivo) by the fingertips of the surgeon.	345
Figure 9.68: Surface pressure applied (a) on the combination of StomachSpleen-Bowel simulants within the test rig (in-vitro) by the Conventional 8 and 10 cylinders and (b) on the human stomach during HALS (in-vivo) by the fingertips of surgeon.	347

Figure 9.69: Surface pressure applied (a) on the spleen simulants within the test rig (in-vitro) by the Conventional 8 and 10 cylinders and (b) on the human spleen during HALS (in-vivo) by the fingertips of the surgeon.	348
Figure 9.70: Retraction of pig liver and bowel by the doughnut shape inflatable prototypes.	351
Figure 9.71: Surface pressure exerted by the fingertips of the surgeon on the pig liver, bowel and abdominal wall.	352
Figure 9.72: Retraction of pig liver during the in-vitro assessment of the inflatable doughnut shape prototypes.....	353
Figure 9.73: Retraction of the bowel simulant during the in-vitro assessment of the inflatable doughnut shape prototypes.....	353
Figure 9.74: Retraction of the liver simulant during the in-vitro assessment of the inflatable doughnut shape prototypes.....	354
Figure 9.75: Ranking of the expansion mechanisms according to (a) axial deformation and (b) axial force predicted during FE modeling.	356
Figure 9.76: Ranking of the promising expansion mechanisms according to the experimental outputs.	357

ABSTRACT

Expansion mechanisms have been developed, which deploy from a cylinder to a sphere upon simple mechanical compression or tension along the cylinder axis, for use in organ retraction and space creation during laparoscopic surgery. An abdominal simulator consisting of simulant abdominal organs has also been developed to enable in-vitro evaluation of the space creation and organ retraction functions of prototype expanding structures. In-vivo retraction distances and surface pressures applied to key abdominal organs during open and hand-assisted laparoscopic abdominal procedures have been measured for 12 patients. The working space quantified in the in-vivo study was used as the target expansion in the fully deployed state of the proposed device during the design and development of prototype structures.

A Finite Element (FE) modelling parametric investigation has been undertaken to determine the influence of the mechanical properties (including negative and positive Poisson's ratios) of the cylinder wall on the expansion behaviour of solid wall cylinders with and without end pieces. Subsequently, cellular mesh cylinders were designed using computer-aided-design (CAD) and FE models with effective mechanical properties closely matching the mechanical properties of the optimal solid wall cylinders. Cylinders comprising of circumferential vertical strips or beams were additionally simulated as candidate expansion mechanisms.

Promising candidate polymeric mesh and strip prototypes have been fabricated via 3D printing and laser cutting and subsequently characterised using mechanical compression and tension tests to quantify the degree of expansion without surrounding materials. In-vitro measurements of surface pressures and retraction distances generated by promising expanding prototype structures when retracting simulant organs in the abdominal simulator mounted on a mechanical testing machine were then undertaken. The surface pressures generated in-vitro by the expansion mechanisms are in good agreement with the surface pressures generated in-vivo on key human abdominal organs by surgeons.

ACKNOWLEDGEMENT

I would like to acknowledge Engineering and Physical Science Research Council (EPSRC), TrusTECH (NorthWest NHS Innovation Service), and Manchester University Foundation Trust (MFT) [formerly known as Central Manchester University Hospitals NHS Foundation Trust (CMFT)] for funding my PhD. I would like to thank Mr Titus Augustine (Manchester Royal Infirmary, MFT), Dr James Corden (TrusTECH), and Prof Andrew Alderson (Sheffield Hallam University) for giving me an opportunity to develop novel prototypes of the LaparOsphere™ device.

I express my deepest gratitude to Prof Andrew Alderson (Director of Studies) for his unwavering support in achieving objectives of PhD, motivating me for the in-depth scientific investigations, imparting skills required to develop as next generation scientist and excellent inputs during writing of the thesis. I also extend my genuine gratitude to Dr James Corden, who acted as an industry supervisor and provided valuable inputs. I would also thank second supervisor Dr Ian Halliday (Sheffield Hallam University) and external advisor Prof Kim Alderson (University of Bolton). I am extremely grateful to Prof Tahir Shah for his supervisory role in absence of Prof Andrew Alderson at the University of Bolton.

I sincerely appreciate efforts of Mr Titus Augustine and Mr Thomas Satyadas for conducting in-vivo pilot study at the Manchester Royal Infirmary. I deeply appreciate the technical support provided at the University of Bolton and Sheffield Hallam University for the silicone moulding, CAD designing, and fabrication, mechanical characterisation, and assessment of prototype structures.

I am thankful to my fellow colleagues at the University of Bolton and Sheffield Hallam University for enthralling discussions on research topics. Lastly, I am indebted to my extremely supportive parents, beloved wife and in-laws for their continuous encouragements besides their financial and moral support.

DIGNESH GIRISH SHAH

ABBREVIATION

MIS – Minimally Invasive Surgery

MRI – Manchester Royal Infirmary

MFT – Manchester University NHS Foundation Trust

CMFT – Central Manchester University Hospitals NHS Foundation Trust

CT – Computerised Tomography

MRI – Magnetic Resonance Imaging

TE – Transient Elastography

MRE – Magnetic Resonance Elastography

ARFI – Acoustic Radiation Force Impulse

US – Ultrasound Sonography

SSI – Supersonic Shear wave Imaging

UE – Ultrasound Elastography

OC – Open cholecystectomy

HALS – Hand assisted laparoscopic surgery

ePTFE – Expanded Polytetrafluoroethylene

UHMWPE – Ultra-high molecular-weight polyethylene

PP – Polypropylene

CAD – Computer Aided Design

ABS – Acrylonitrile Butadiene Styrene

FEA – Finite Element Analysis

BCs – Boundary Conditions

OD – Outer Diameter

WT – Wall Thickness

ERD – Equatorial Radial Deformation

AD – Axial Deformation

RVE – Representative Volume Element

E – Young's modulus

ν – Poisson's ratio

G – Shear modulus

σ – Normal stress

ε – Normal strain

CONFLICT OF INTERESTS

Funding:

This work was financially supported by the Engineering and Physical Sciences Research Council [grant number EP/J501839/1], TrusTECH and the Manchester University NHS Foundation Trust (MFT).

Competing Interests:

The data reported in this thesis is integrally linked to the development of the LaparOsphere™, a conceptual laparoscopic instrument for the organ retraction and space creation functions.

Three patents applications have been filed for the LaparOsphere™ by the industry sponsors (TrusTECH and MFT) of this project. Titus Augustine is named inventor for an inflatable version of the LaparOsphere™ (WO2011128622 (A1) - SURGICAL DEVICE AND METHODS) whilst Dr James Corden and Titus Augustine are named inventors for an auxetic version of the LaparOsphere™ (WO2013054093 (A1) and GB2495522 - SURGICAL DEVICE AND METHODS). ***UK Intellectual Property Office has granted patent for GB2495522 - SURGICAL DEVICE AND METHODS on 21 December 2016.***

Andrew Alderson and Mohammad Sanami are named inventors on the UK patent application (GB2496167 – DEPLOYABLE DEVICES).

LIST OF PUBLICATIONS

- 1) **Dignesh Shah**, Andrew Alderson, James Corden, Thomas Satyadas, Titus Augustine, "In-vivo Measurement of Surface Pressures and Retraction Distances Applied on Abdominal Organs During Surgery", Surgical Innovation, December 2017.
DOI:10.1177/1553350617745952.

1 Introduction

1.1 Motivation

Laparoscopic surgery, also known as Minimally Invasive Surgery (MIS), is the modern surgical procedure of operating within body cavities through small incisions. It has been preferred over open abdominal surgery (large incision performed along midline to get access to the major abdominal organs) in the last two decades since it offers reduced post-operative pain, faster recovery, reduced length of stay, reduced morbidity, and more cost effective outcomes.⁽¹⁾ The most common laparoscopic procedures include laparoscopic cholecystectomy, laparoscopic nephrectomy, laparoscopic appendectomy and laparoscopic hernia repair.^(2,3) Laparoscopic surgery is increasingly being used in complex abdominal procedures including hepatic resections and even surgery on major vascular structures including the aorta.

Briefly, the technique involves making several small incisions in the abdominal wall to enable the insertion of a camera and surgical instruments. CO₂ insufflation is currently used to inflate abdominal wall and create space for the surgeon to operate during abdominal laparoscopic procedures. There are several clinical issues associated with CO₂ insufflation, providing impetus for the development of an alternative means of creating space during MIS.

During both open and laparoscopic abdominal surgery, access to, and visibility of the surgical field is reduced due to the presence of surrounding organs and tissues. It is necessary for the surgeon to constantly retract (move) surrounding organs and tissues from the surgical field. For example, during a routine laparoscopic cholecystectomy it can be necessary for the operating surgeon to lift the liver many times to gain access to the gall bladder which often requires an assistant surgeon, is distracting and can be time consuming. The need to constantly handle surrounding organs increases the potential of inadvertent damage or injury to these structures.

Mr Titus Augustine, a consultant transplant and endocrine surgeon at the Manchester University NHS Foundation Trust (formerly known as Central Manchester University Hospitals NHS Foundation Trust), has proposed that

the clinical drawbacks associated with CO₂ insufflation, organ retraction and space creation within the abdomen can be overcome by using a generic inflatable, hollow and transparent structure (the LaparOsphere™) to create space within the abdomen and retract abdominal organs.⁽⁴⁾ The LaparOsphere™ is an expanding device that is initially inserted into the abdominal cavity in its unexpanded state. Upon inflation it takes the shape of a truncated hollow sphere with many access holes for surgical instruments. It creates space within the abdomen by retracting surrounding organs and tissues away from the surgical field. The surgeon operates within the space inside the sphere. The laparoscope and other laparoscopic instruments are inserted through holes/apertures within the surface of the sphere without affecting the inflation or structural integrity of the sphere. Surrounding organs and tissues remain outside the sphere and are retracted and protected from the surgical field.

In this PhD project, co-sponsored by TrusTECH and MFT, it is proposed that the expansion of the LaparOsphere™ can be achieved with use of cellular structures in response to mechanical deployment, as an alternative (or additional) to the introduction of air/fluid into the current inflatable double-walled device (i.e. inflatable doughnuts) to enable space creation and organs retraction during surgery. Auxetic flat plates are known to undergo double (synclastic) curvature under pure bending.⁽⁵⁾ Here, the ability of an auxetic structure in cylindrical or tubular form to deploy in to a sphere on application of an external force has been investigated.⁽⁶⁾ In particular honeycomb/mesh structures have been considered to take advantage of the cellular nature to allow access for instruments. The expansion and retraction responses of conventional honeycomb cylinders, inflatable doughnuts, and cylindrical arrangements of beams have also been investigated.

1.2 Aim and objectives

The overall aim was to design, develop, fabricate and characterise deployable expansion mechanisms for improved space creation and organ retraction during laparoscopic surgery.

The objectives to achieve the overall aim are enlisted below:

- To determine the biomechanical properties of the human abdomen and key abdominal organs.
- To develop an in-house abdominal simulator composed of artificial simulants mimicking the biomechanical properties of human abdominal organs which can be used as an in-vitro test rig to evaluate the space creation and organ retraction functions of prototype expanding structures.
- To quantify the degree of organ retraction required during abdominal open and laparoscopic procedures and the typical surface pressures applied to the key abdominal organs to achieve the required degree of organ retraction.
- To simulate expansion properties of a range of auxetic and other non-auxetic expansion mechanisms.
- To design promising prototype structures.
- To fabricate candidate expanding structures.
- To characterise promising expansion mechanisms without surrounding materials.
- To undertake in-vitro assessment of the expansion mechanisms using the in-house abdominal simulator.

1.3 Layout of chapters

Appropriate literature is reviewed in Chapter 2 and Chapter 3 for issues related to open and keyhole abdominal surgery, existing space creation and/or organ retraction devices, surface pressures applied during surgical procedures, biomechanical properties of key human abdominal organs, classical elasticity theory, the fundamentals of auxetic structures, properties and deformation mechanisms, and the applications of auxetic materials in the healthcare sector.

Chapters 4 describes the methodologies used for the development of an in-house abdominal simulator, the in-vivo measurement of the surface pressures applied on key abdominal organs during abdominal surgery, and

the determination of in-vivo organ retraction distances. The Finite Element (FE) modelling methodologies used for simulation of cylinder expansion properties as a function of the mechanical properties of the cylinder wall are elucidated in Chapter 5. Design, fabrication, characterisation, and in-vitro assessment methods for the expansion mechanisms of prototype auxetic and non-auxetic honeycomb and beam cylindrical structures are explained in Chapter 6.

The Results chapters begin with the results of the design and development of the in-house simulator and the quantification of surface pressures and organ retraction distances during surgical procedures in Chapter 7. A parametric investigation into the expansion properties from FE simulations of auxetic and non-auxetic cylinders described in Chapter 8. Results from computer aided design models, fabrication, mechanical characterisation, and in-vitro assessment of candidate structures are narrated in Chapter 9. The results presented in Chapters 7, 8 and 9 are discussed in Chapter 10. The overarching conclusions and future work related to the further development of prototypes are subsequently described in Chapter 11.

2 Literature review - Human abdomen, abdominal surgery and the LaparOsphere™

2.1 The human abdominal environment - key organs and biomechanical properties

To evaluate space creation and organ retraction functions of prototype expansion mechanisms an in-house abdominal simulator has been designed and fabricated from consideration of the biomechanical properties of key abdominal organs. The main biomechanical and physical properties of abdominal organs are weight, dimensions, volume, density, and elasticity.

2.1.1 Human abdomen and abdominal wall

The human abdomen is the largest cavity or space in the body, characterised by an oval (adult male) and ovoid (adult female) shape which varies in form and extent with age and sex. The abdomen begins from the thorax (chest) and terminates at the pelvis. The abdomen contains all the digestive organs, including the stomach, small and large intestines, pancreas, liver, kidney, spleen, and gallbladder. These organs are held together loosely by connecting tissues (mesentery) that allow them to expand and to slide against each other. In the front, the abdomen is protected by a thin, tough layer of tissue called fascia. In front of the fascia are the abdominal muscles and skin. In the rear of the abdomen are the back muscles.⁽⁷⁾

The biomechanical properties of the human abdomen and abdominal wall are summarised in Table 2.1. Song et al⁽⁸⁾ measured the average wall thickness prior to the operation with an ultrasound scanner using a 7.5MHz probe (SSD-2200, UST-995, Aloka, Japan) from six standardised measuring points on the outer surface of the abdomen.⁽⁸⁾ The mean Young's modulus was calculated from the constitutive stress-strain relationship of the abdominal wall which was derived from the measured inflation pressure and abdominal wall motion.⁽⁸⁾ The abdominal cavity volume was measured using the Computerised Tomography (CT) scan reconstruction technique in two steps. Firstly, multi-slice (slice thickness 0.75 cm) helical CT scans were carried out and 3D reconstruction was then done. The liver, spleen, greater

omentum, gastrointestinal tract, and uterus were included in the abdominal cavity.⁽⁹⁾

Table 2.1: Biomechanical properties of human abdomen and abdominal wall. N/R = Not reported.

Dimensions	Mean Value	Standard deviation	Sample size (n)	Reference
Abdominal wall thickness (mm)	30	N/R	18	(8)
Young's modulus of abdominal wall (kPa)	27 (M), 21 (F)	5 (M), 4 (F)	18	(8)
Abdominal cavity volume (ml)	9760	600	7	(9)

The human abdominal organs are shown in Figure 2.1. The liver, kidney, and spleen are solid and compressible abdominal organs while the stomach and bowel are also compressible but hollow.⁽¹⁰⁾

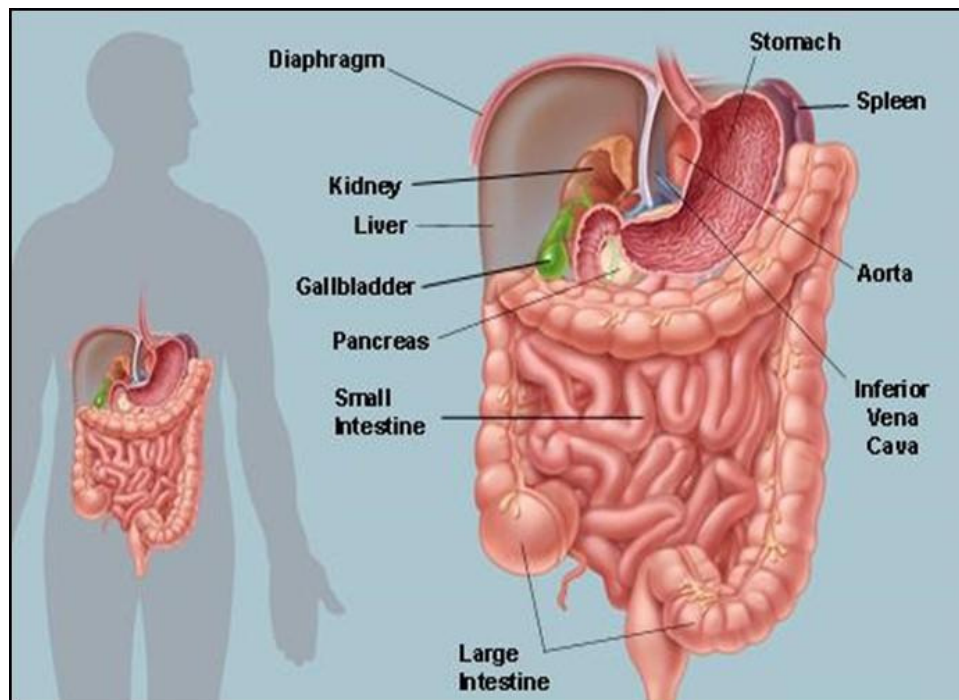


Figure 2.1: Human abdominal environment and key organs. '©2016, WebMD, LLC. All rights reserved'.⁽¹⁰⁾

Soft organ tissues exhibit complex non-linear, anisotropic, and inhomogeneous behaviour. Fung has revealed that a non-linear stress–strain

relationship is common for soft tissues but the degrees are different for different organs.⁽¹¹⁾ Currently, mechanical indenters, rotational rheometers, and medical imaging techniques are used to collect dynamic material properties of soft tissues.⁽¹²⁾ Ex-vivo (autopsy), in-vivo (medical imaging), and in-vitro techniques for the evaluation of biomechanical properties of abdominal organs are present in the literature.^(13–19)

The weight, volume, density, and elasticity of the key abdominal organs have been reviewed and are briefly summarized in the Sections 2.1.2 and 2.1.3.

2.1.2 Solid organs

2.1.2.1 Liver

The human liver is a pinkish-brown colour and is the largest internal organ in the human body. It is in the right upper quadrant of the abdominal cavity, resting just below the diaphragm. The liver lies to the right of the stomach and overlies the gallbladder (Figure 2.2).⁽¹⁰⁾

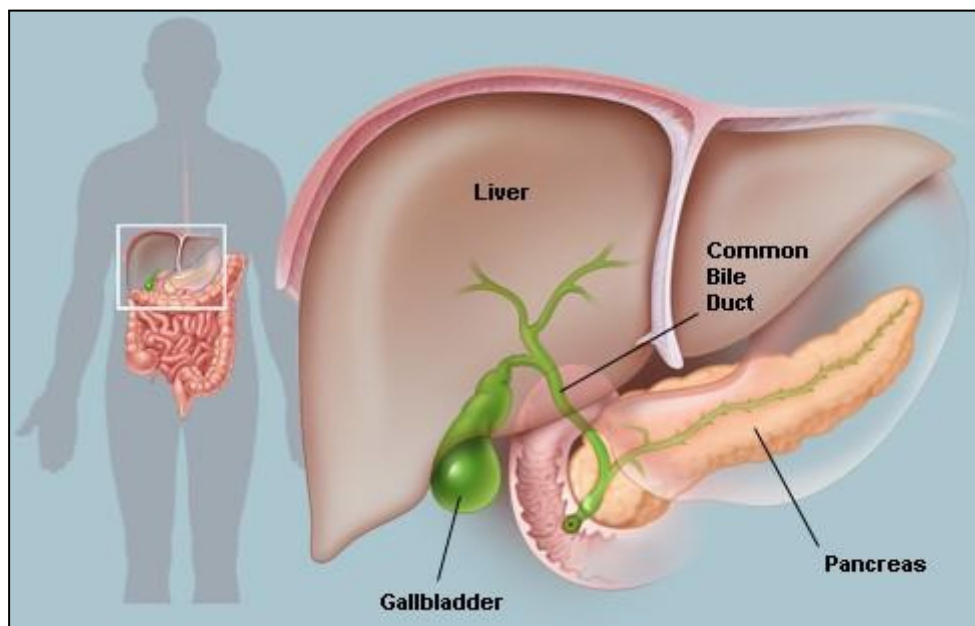


Figure 2.2: Human liver, gallbladder situated underneath of liver and pancreas. '©2016, WebMD, LLC. All rights reserved'.⁽¹⁰⁾

Physical dimensions:

Gupta et al⁽²⁰⁾ measured the physical dimensions (Figure 2.3) of fifty human cadaveric livers by Vernier Calliper (Mitotoyo, Japan) (Figure 2.3)⁽²⁰⁾ and are summarised in Table 2.2.

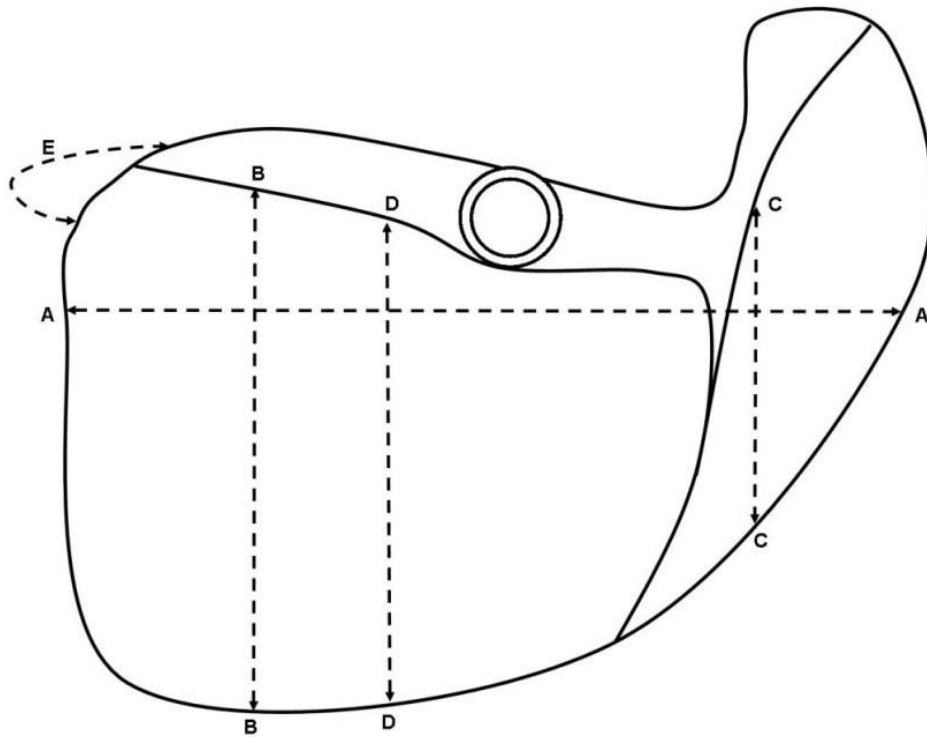


Figure 2.3: A schematic diagram showing physical dimensions of human liver. AA = Maximum transverse diameter, BB = Maximum vertical diameter, CC = Vertical diameter at falciform ligament, DD = Vertical diameter at centre of fossa for gall bladder, E = Maximum anteroposterior diameter.⁽²⁰⁾

Table 2.2: Physical dimensions of human liver.⁽²⁰⁾

Physical Dimensions	Mean Value (cm)
Transverse diameter (Length) (AA)	20 ± 2.5
Vertical diameter (Width) (BB)	15 ± 2
Vertical diameter at falciform ligament (CC)	10 ± 1
Vertical diameter at centre of fossa for gall bladder (DD)	13 ± 2
Anteroposterior diameter (Thickness) (E)	8.5 ± 2

Liver volume

CT scanning and Magnetic Resonance Imaging (MRI) based liver volumetry are presently used as methods to assess liver volume for liver transplant surgeries (Table 2.3). In addition, autopsy examination was identified as a method of choice for the measurement of liver volume. In the latter case, liver volume was measured using Archimedes' principle during post-mortem examination.⁽²¹⁾

Discrepancies in the values of mean liver volume obtained by CT scan, MRI, and autopsy methods have been explained by factors such as sample size, age distribution within sample size, and anatomy and physiology of liver sample.^(21–27) The mean liver volume measured by MRI tends to overestimate the values of mean liver volume obtained by CT scanning for the following reasons⁽²²⁾:

- MRI examinations require long acquisition times. If the patients can't hold their breath properly; the liver may be virtually enlarged due to breathing artefacts
- Inclusion of non-liver tissue in the volumetric measurements

- Blurring artefacts at the liver border can lead to overestimation of liver volume.

The autopsy method is an ex-vivo method and liver volume measurement include the anatomically attached gall bladder and ligaments. Hence, the autopsy method is not deemed in the literature to be as accurate as in-vivo methods of liver volumetry (CT scan & MRI).

Table 2.3: Human liver volume. N/A = Not applicable, N/R = Not reported.

Method of Measurement	Mean Value (ml)	Standard Deviation	Sample Size (n)	Reference
Magnetic Resonance Image (MRI)	2020	680	30	(22)
CT scan	1470	130	10	(23)
	1710 (M)	290	41	(24)
	1410 (F)	270	36	
	1500	230	11	(25)
	1930	500	30	(22)
	1230 (M)	120	31	(26)
	1050 (F)	110		
Average value of CT scan	1475	230	N/A	N/A
Autopsy/Post mortem	1660	370	652	(21)
	1862	N/R	33	(27)
Average value of Autopsy	1761	N/A	N/A	N/A

In conclusion, the CT scan method has distinct advantages over both autopsy and MRI methods. Liver volume obtained by the CT scan method has, therefore, been considered as the benchmark in the development of a liver simulant for the in-house abdominal simulator.

Liver weight

The weight of the human liver has been measured using cadaver livers obtained through post mortem procedures (Table 2.4). The small degree of discrepancy in mean weight reported in the two studies can be explained by different ethnic groups considered for study (Korean and Caucasian), sample size, age distribution, and anthropometric data such as body weight, body size, and body surface area.

Table 2.4: Human liver weight. N/A = Not applicable, N/R = Not reported.

Source of Liver	Mean Value (g)	Standard Deviation	Sample Size (n)	Reference
Post mortem (Autopsy/Cadaver)	1730	370	652	(21)
	1724	N/R	33	(27)
Average value	1727	N/A	N/A	N/A

Liver density

The density of human cadaveric livers obtained via post mortem^(27,28) has been calculated from liver volume (measured using the water displacement method) and weight (Table 2.5).

Table 2.5: Human liver Density. N/A = Not applicable, N/R = Not reported.

Source of Liver	Mean Value (Kg/L)	Standard Deviation or Range	Sample Size (n)	Reference
Post mortem/Autopsy	1.04	0.07	652	(28)
	1.08	N/R	33	(27)
Average value	1.06	N/A	N/A	N/A

Liver elasticity

Transient Elastography (TE), a medical imaging in-vivo non-invasive ultrasonography method, has been used to measure liver tissue elasticity by measuring the shear wave velocity of ultrasound propagated through the liver (Table 2.6).^(29–33) Magnetic Resonance Elastography (MRE) and Acoustic Radiation Force Impulse (ARFI) imaging⁽³⁰⁾ have also been used to

measure liver tissue elasticity.⁽³⁴⁾ The small degree of disagreement in tissue elasticity measured by TE, ARFI imaging, and MRE may be due to sample size variation, gender distribution within sample, age, body mass index (BMI), metabolic syndrome, and ethnicity.^(29–33)

Table 2.6: Human liver tissue elasticity. N/A = Not applicable.

Method of Measurement	Mean Value (kPa)	Standard Deviation	Sample Size (n)	Reference
TE	4.64	1.18	42	(29)
ARFI with Ultrasound	4.68	0.12	42	(30)
TE	5.36	1.51	370	(31)
TE	5.10	1.10	445	(32)
MRE	4.23	0.69	24	(33)
Average value	4.80	0.53	N/A	N/A

The elastic modulus of healthy human liver has also been measured in-vivo during minor open surgery using a hand-held compliance probe with 4.5 mm round tip, and ex-vivo for pig liver using a static compliance probe with 30 mm flat tip interchangeable with 4.5 mm round tip (Table 2.7).⁽³⁵⁾ A displacement rate of 1 ± 0.02 mm/s to a displacement of 10 mm was employed.

Table 2.7: Elastic modulus of liver by mechanical indentation method. N/R = Not reported.

Source of Liver	Mean Value (kPa)	Standard Deviation	Sample Size (n)	Reference
Human	270	N/R	N/R	(35)
Pig	400	N/R	6	

The significant degree of disagreement amongst values of elastic modulus outlined is due to measurement methods (in-vivo against in-vitro), testing conditions, and source of liver (pig against human liver).^(14,35)

2.1.2.2 Kidney

The anatomical locations of kidneys (pair of organs) in the human body are in the back of the abdominal cavity in the retro peritoneum. The kidney has a bean-shaped structure (Figure 2.4). The superior border of the right kidney is adjacent to the liver; while the top surface of left kidney is closest to the spleen. Therefore, both move down on inhalation, as does the liver.

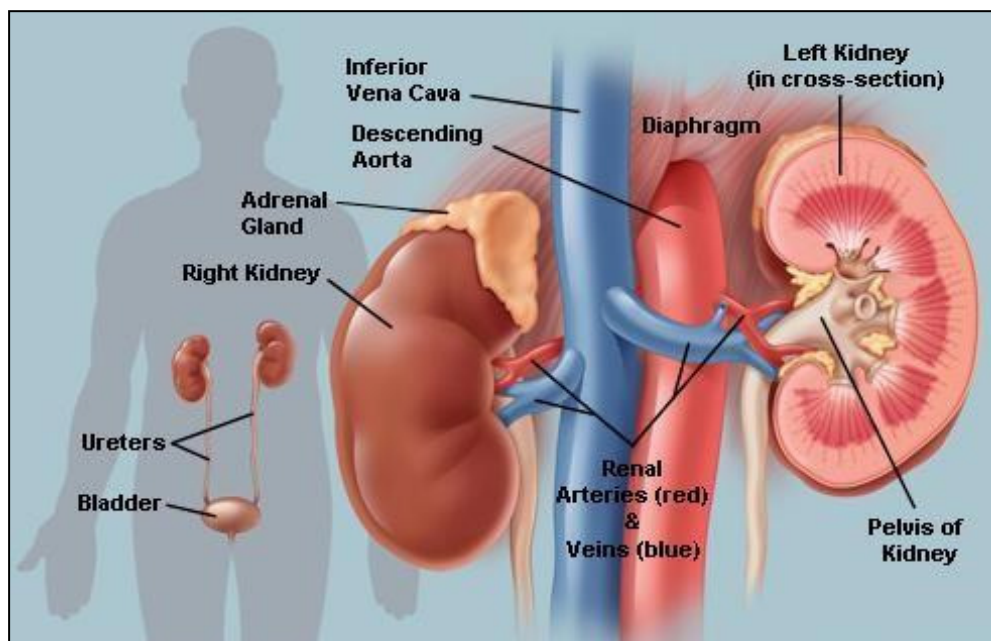


Figure 2.4: Human kidney environment. '©2016, WebMD, LLC. All rights reserved'.⁽¹⁰⁾

Physical dimensions

The physical dimensions of the human kidney such as length, width, and thickness are described in Table 2.8. They were measured by normal sonography and abdominal CT methods.^(36–38)

Table 2.8: Physical dimensions of human kidney. N/R = Not reported.

Dimensions	Mean Value (cm)	Standard Deviation	Sample Size (n)	Reference
Length	11	0.7	113	(38)
	11	N/R	665	(37)
	11	1	125	(36)
Width	6	N/R	665	(37)
	6	0.67	125	(36)
Thickness	5	0.6	125	(36)
	2	1.6	10	(37)

Kidney volume

CT scanning, Ultrasound Sonography (US), and MRI based kidney volumetry are presently used as methods to assess kidney volume for kidney transplant surgeries (Table 2.9). Discrepancies in the values of mean kidney volume obtained by such methods could be explained by factors such as sample size, age distribution within sample size, diseased organ, and anatomy and physiology of kidney samples. Discrepancies were also observed between two techniques (Ellipsoid formula and Voxel count method) employed for the measurement of volume during MRI and US methods.⁽³⁹⁾

Table 2.9: Human kidney volume. N/A = Not applicable. N/R = Not reported.

Method of Measurement	Mean Value (ml)	Range (ml)	Sample Size (n)	Reference
US (Ellipsoid Formula)	135	90 – 210	20	(39)
MRI (Ellipsoid Formula)	145	105 – 170	20	
MRI (Voxel Count Method)	180	140 – 200	20	
MRI (Voxel Count Method)	130	20 – 255	50	(40)
US	150	N/R	665	(41)
CT scanning	160	N/R	125	(36)
CT scanning	210	140 – 360	113	(38)
Average Value	160 ± 30	N/A	N/A	N/A

Kidney weight

In medical textbooks, the range of kidney weight is typically 120 – 160 g.⁽⁴²⁾ The weight of the human kidney has been measured using abdominal CT scan and autopsy (post mortem) methods (Table 2.10). Small degree of discrepancy in mean weight measured by autopsy can be explained by different ethnic groups considered for study (Indian and Caucasian), sample

size, age distribution within sample size, and participant body mass index (BMIs). The higher discrepancy in mean weight is observed between CT scanning and autopsy methods owing to in-vivo and in-vitro nature of study, respectively.

Table 2.10: Human kidney weight. N/A = Not applicable.

Method of measurement	Mean Value (g)	Standard Deviation or Range	Sample Size (n)	Reference
Abdominal CT scan	200	40	125	(36)
Autopsy	130 (M)	25	457 (M)	(43)
	130 (F)	35	204 (F)	
	160 (M)	40	355 (M)	(44)
	140 (F)	35	329 (F)	
Average Value	152 ± 30	N/A	N/A	N/A

Kidney density

In medical textbooks, the density of kidney is typically reported to be 1.05 kg/L.⁽⁴⁵⁾

Elastic modulus of kidney

The elastic modulus of human kidney has been measured by in-vivo techniques such as Supersonic Shear wave Imaging (SSI), ARFI, and Ultrasound Elastography (UE) (Table 2.11). In-vivo imaging techniques are non-invasive which provide a real-time measurement and quantitative assessment of renal stiffness particularly to assess the renal fibrosis for pre- and post-kidney transplantation. The small degree of discrepancy in mean elastic modulus of cortex of kidney measured by these techniques can be explained by different sample size and age distribution within sample size.

The cortical and medullary elasticity (i.e. renal tissue stiffness) of six pig kidneys were evaluated in-vivo using the MRE technique and are reported in Table 2.11.⁽⁴⁶⁾

Table 2.11: Elastic modulus of human and pig kidney

Method of Measurement	Mean Value (kPa)	Standard Deviation	Sample Size (n)	Reference
SSI Technique (cortex, outer portion)	11	2	49	(47)
ARFI	4.83	0.1	66	(30)
UE (cortex, outer portion)	15	3	Small sample	(48,49)
MRE	7.4 (Cortical), 7.8 (Medulla)	0.3 (Cortical), 0.5 (Medulla)	6	(46)

2.1.2.3 Spleen

The spleen is situated in the upper far left quadrant of the abdomen, to the left of the stomach (Figure 2.5). It lies precisely between the 9th and 11th ribs on the left-hand side. The spleen varies in size and shape between humans and is generally purple in colour. Because the spleen is protected by the rib cage, one can't easily feel it unless it abnormally enlarges.

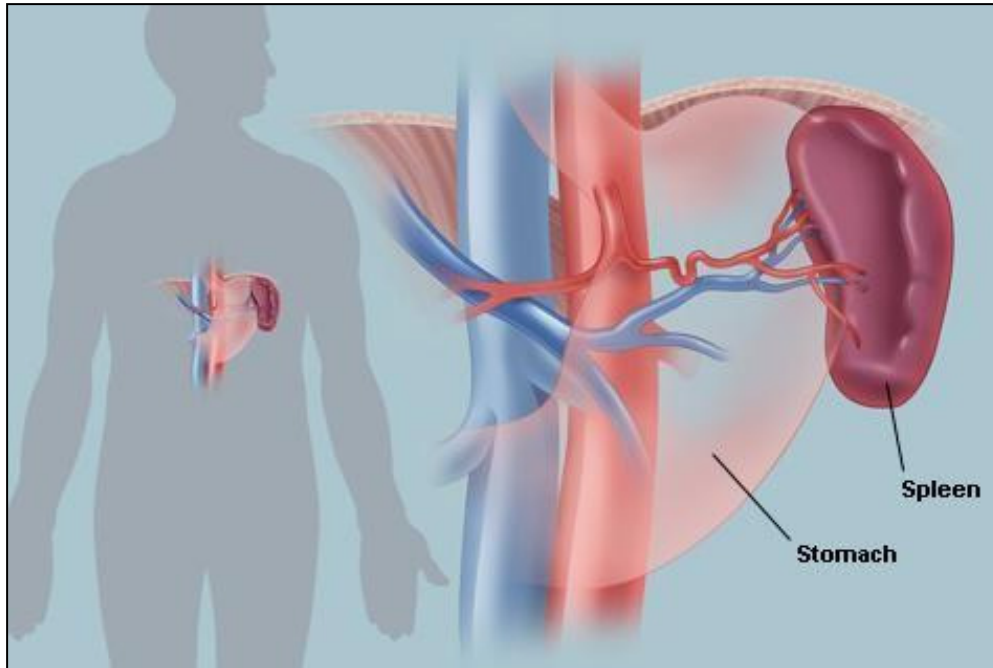


Figure 2.5: Human spleen environment. '©2016, WebMD, LLC. All rights reserved'.⁽¹⁰⁾

Physical dimensions

The physical dimensions of the human spleen are reported in Table 2.12. The shape of the spleen is influenced by the presence of adjacent organs such as stomach, left kidney, colon, pancreatic tail, and diaphragm.⁽⁵⁰⁾

Table 2.12: Physical dimensions of human spleen. N/R = Not reported.

Method of Measurement	Length (cm) × Width (cm) × Thickness (cm)	Sample Size (n)	Reference
Abdominal CT scan (In-vivo)	15 × 10 × 6 (Reported maximum value)	N/R	(51) cited by (50)
Ultrasonography	11.1 × 7.9 × 2.9	N/A	(52) cited by (53)
Ultrasonography	11.1 × 7.9 × 4.4	200	(54)
Ultrasonography	10.7±1.6 × 5.2±1.2 × N/R	631	(55)

Spleen volume

The abdominal CT scan method has been employed to measure the mean volume of the spleen and is summarised in Table 2.13. The discrepancy in the mean volumes reported in Table 2.13 can be attributed to different ethnic groups considered for study (Asian and European), sample size, age distribution within sample size, gender, anthropometric parameters and participants' body mass indexes (BMIs).

Table 2.13: Human spleen volume. N/A = Not applicable.

Method of Measurement	Mean Value (ml)	Standard Deviation or Range (ml)	Sample Size (n)	Reference
Abdominal CT Scan	215	110 – 340	140	(56)
	130	60 (22 – 417)	230	(57)
	112	32 – 209	150	(58)
Average	152 ± 55	N/A	N/A	N/A

Spleen weight

Spleen weight was measured during post-mortem (autopsy) and in-vivo and is summarised in Table 2.14. The small degree of discrepancy amongst mean weights reported in Table 2.14 can be interpreted due to different ethnic groups considered for study (Indian and Thai), sample size, age distribution within sample size, anthropometric parameters, and participant's body mass indexes (BMIs).

Table 2.14: Human spleen weight. N/R = Not retracted, N/A = Not applicable.

Method of Measurement	Mean Value (kg)	Standard Deviation or Range (kg)	Sample Size (n)	Reference
Autopsy	N/R	0.088 – 0.202	102	(59)
Autopsy	N/R	0.15 – 0.2	N/R	(60)
Autopsy	0.15	0.1 - 0.25	140	(56)
Autopsy	0.139	0.043 - 0.344	232	(17)
Autopsy	0.131	0.105 - 0.164	N/R	(61)
Average (Autopsy)	0.14 ± 0.01	N/A	N/A	N/A
In-vivo	0.225	0.112 - 359	140	(56)

Spleen density

The spleen density was measured during autopsy and in-vivo (Table 2.15). The density was measured by obtaining spleen volume [in a laboratory glass cylinder by calculating amount of water displaced by spleen] and weighing spleen.⁽⁶²⁾

Table 2.15: Human spleen density. N/A = Not applicable.

Method of Measurement	Mean Value (kg/L)	Standard Deviation or Range	Sample Size (n)	Reference
Autopsy	1.04	0.12 (0.85-1.25)	12	(62)
In-vivo	1.05	N/A	N/A	(63) cited in (56)

The spleen density has also been measured by abdominal radiographs and CT scanning methods. Pixels in an image obtained by CT scanning are displayed in terms of relative radio density. The pixel value is displayed according to the mean attenuation of X-rays through the tissue that it corresponds to from -1024 to +3071 on the Hounsfield scale. Water has an attenuation of 0 Hounsfield units (HU) while air is -1000 HU. On non-contrast-enhanced CT images, the healthy spleen density was reported at approximately 45 HU.⁽⁶⁴⁾

Elasticity of spleen

The elastic modulus of pig spleen has been measured ex-vivo (Table 2.16). A 4.5mm diameter round-ended static compliance probe was used to carry out ten indentation tests on pig spleen at a constant rate of $1 \pm 0.02 \text{ mm s}^{-1}$. The round tip probe was interchangeable with one having a 30mm flat tip.⁽³⁵⁾ In contrast to the ex-vivo method, the spleen tissue stiffness was measured in-vivo using the MRE method (human) and is reported in Table 2.16.^(65,66) The significant degree of difference in the elasticity values reported in Table 2.16 is due to the different methods (ex-vivo against in-vivo) employed and source (pig and human) of the spleen.

Table 2.16: Elasticity of human spleen. N/A = Not applicable.

Method of Measurement	Mean Value (kPa)	Standard Deviation	Sample Size (n)	Reference
Ex-vivo (Elastic modulus)	110	30	6	(35)
MRE (Shear modulus)	3.6	0.6	16	(65)
MRE (Shear modulus)	4.7	0.7	11	(66)
Average (MRE)	4.2	0.7	N/A	N/A

2.1.3 Hollow organs

2.1.3.1 Stomach

The stomach is a muscular, hollow and dilated part of the digestion system which lies between the oesophagus (food pipe) and the small intestine. It is situated on the left upper part of the abdominal cavity (Figure 2.6). The top of the stomach lies against the diaphragm.

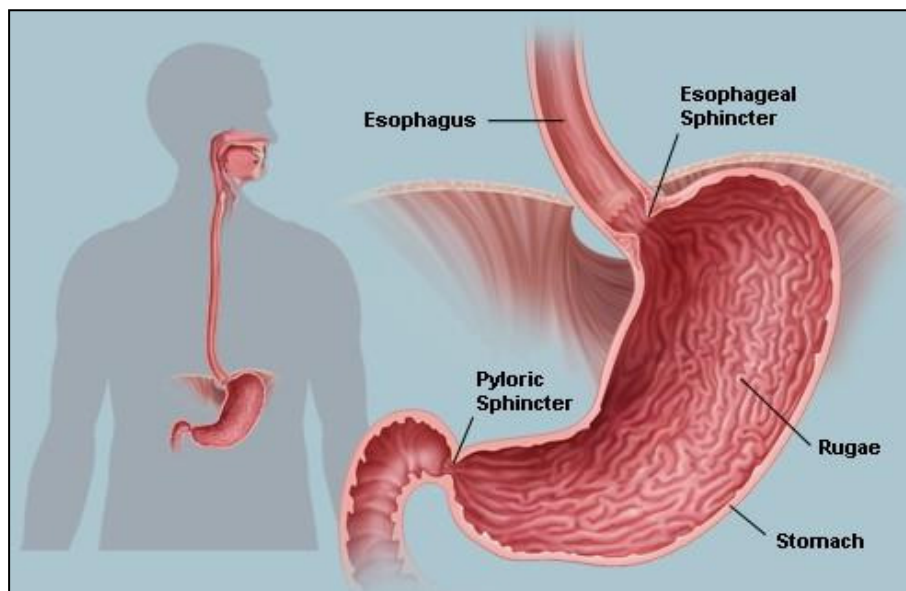


Figure 2.6: Human stomach environment. '©2016, WebMD, LLC. All rights reserved'.⁽¹⁰⁾

Physical dimensions

The human stomach is somewhat J-shaped and so the physical dimensions such as length and width are not clearly defined in the scientific literature and medical textbooks.

Stomach volume

Empty and full stomach volumes have been measured in-vivo and during human autopsy (Table 2.17).

Table 2.17: Human stomach volume. N/R = Not reported.

Method of Measurement	Mean Value (L)	Standard Deviation or Range (Empty – full)	Sample Size	Reference
In-vivo (Maximum gastric capacity)	0.8	0.1	9	(67)
Autopsy	N/R	1 – 2	N/R	(68) cited in (16)
Autopsy	N/R	1.6 – 1.7	N/R	(69) cited in (16)

Stomach weight

In-vitro and human autopsy methods have been employed for the measurement of empty stomach weight (Table 2.18). The mean weight (0.163 Kg) and true standard deviation (0.003 Kg) were calculated from the values reported in Table 2.18. The minor discrepancy for stomach weight between in-vitro and autopsy methods can be explained by differences in sample size.

Table 2.18: Human stomach weight. N/R = Not retracted.

Method of Measurement	Mean Value (kg)	Standard Deviation or Range (Empty stomach)	Sample Size (n)	Reference
Autopsy	0.165 (male), 0.150 (female)	N/R	126	(16)
Autopsy	N/R	0.125 – 0.175	N/R	(68) cited in (16)
Autopsy	N/R	0.113 – 0.141	N/R	(69) cited in (16)
In-vitro	0.160	0.029	165	(70)

Stomach density

The empty stomach density was measured during autopsy and found to be in the range 0.07 – 0.08 kg/L.⁽⁶⁹⁾

Elasticity of the stomach

A modification of the Kolsky bar technique was used to measure the bulk modulus of cadaveric stomach under dynamic compressive load.⁽¹⁸⁾ Stomach specimens were taken from the stomach body just below the cardiac notch and preserved until Kolsky bar tests were performed at high impact velocity (1–50 m/s) to measure the dynamic bulk modulus at an effective nominal strain rate (defined by final strain over rise time) of $\sim 10 \text{ s}^{-1}$ (Table 2.19).⁽¹⁸⁾

The tensile stress of healthy middle parts of surgically removed and of cadaveric stomach was measured by ex-vivo method.⁽¹⁵⁾ The longitudinal and transversal specimens in rectangular shape (6–6.5cm long and 10mm

wide) were cut from the front wall of stomach (i.e. gastric wall) and examined using Instron 1122 tensiometer at constant strain rate of $2\lambda/\text{min}$ (loading velocity $50\text{mm}/\text{min}$).⁽¹⁵⁾ Egorov et al.⁽¹⁵⁾ have also employed this methodology to obtain bowel and small intestine specimens (anterior and posterior walls) and tensile stresses are reviewed in Section 2.1.3.2 (Table 2.21) and Section 2.1.3.3 (Table 2.23), respectively.

There was a minor discrepancy for the maximum tensile stresses between surgically removed and cadaveric stomach specimens that can be explained by difference in the sample size (Table 2.19).

The elastic modulus of fresh cadaveric stomach was measured ex-vivo using an in situ indentation tool⁽⁷¹⁾. An indenter (1.5mm radius), connected to a force transducer, was driven to various depths (1–8 mm) at various velocities (1–8 mm/s) and was held at each depth for 60 s ('ramp-and-hold' tests). Tissue relaxation was ensured by a 3-min interval after each of the five trials. The value of elastic modulus reported in Table 2.19 is for 8mm indentation depth at various velocities (1-8mm/s) and held at each depth for 60s.

Table 2.19: Elasticity of human stomach. N/R = Not reported.

Method of Measurement	Elasticity Value (kPa)	Standard Deviation	Sample Size (n)	Reference
Ex-vivo (Cadaveric)	480,000 (Mean bulk modulus)	N/R	N/R	(18)
Ex-vivo (Surgically removed)	670 (longitudinal), 500 (transverse) (Maximum tensile stresses)	190 (longitudinal), 120 (transverse)	60 (30 each longitudinal and transverse)	(15)
Ex-vivo (Cadaveric)	650 (longitudinal), 520 (transverse) (maximum tensile stresses)	210 (longitudinal), 160 (transverse)	100 (50 each longitudinal and transverse)	(15)
Ex-vivo (Cadaveric)	3.0 (Elastic modulus)	1.3	10	(71)

2.1.3.2 Bowel (Large intestine)

The bowel, also known as the large intestine, is a long, hollow and continuous tube that absorbs water from wastes, creating stool.⁽⁷²⁾ The large intestine extends from the end of the ileum to the anus coiling the small intestine and it is divided into the cecum, colon, rectum, and anal canal. Colon is made up of cecum, the ascending colon, transverse colon, descending colon, and sigmoid colon (Figure 2.7).⁽⁷⁾

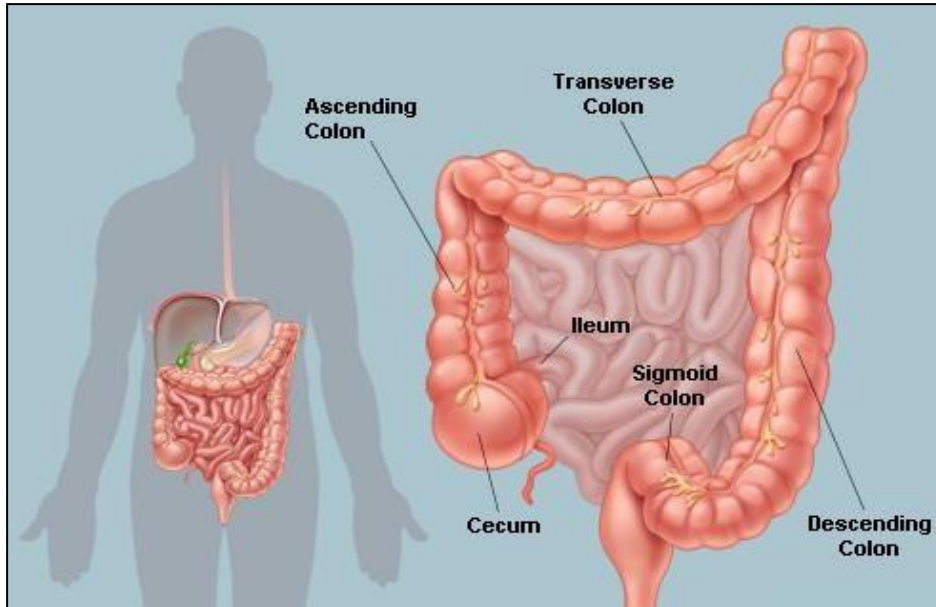


Figure 2.7: Human bowel environment. '©2016, WebMD, LLC. All rights reserved'.⁽¹⁰⁾

Physical dimensions

The physical dimensions such as length and diameter of the large intestine are summarised in Table 2.20.

Table 2.20: Physical dimensions of human large intestine. N/R = Not retracted. N/A = Not applicable.

Physical dimensions	Value (cm)	Standard deviation or Range	Sample Size (n)	Reference
Length	154	113 - 207	N/R	(73) cited in (72)
	150	N/R	N/R	(7)
	150	N/R	N/R	(74)
	160.5	33 (80 - 313)	200	(74)
Average (Length)	153.6	5.0	N/A	N/A
Diameter	N/R	5 - 7.5	N/R	(7)
Diameter	6	N/R	N/R	(75)

Bowel volume

The volume was measured by the volumetric method and was reported to be 3 – 8 L.⁽⁷⁾

Bowel weight

Human bowel weight was measured in-vivo for 46 samples and found to have an empty to full range of 0.06 – 0.9 kg and a mean value of 0.22 kg.⁽⁷³⁾
(cited in (72))

Elasticity of Bowel

The tensile stress (explained in Section 2.1.3.1) is shown in Table 2.21.

Table 2.21: Elasticity of human bowel.

Method of Measurement	Elasticity Value (kPa)	Standard Deviation	Sample Size (n)	Reference
Ex-vivo (Cadaveric)	1190 (longitudinal), 645 (transverse) (first maximum tensile stress)	300 (longitudinal), 165 (transverse)	150 (100 longitudinal and 50 transverse)	(15)

2.1.3.3 Small intestine

The small intestine, also known as the gut, is the longest part in the human abdomen which connects the stomach to the large intestine (or colon) and folds many times to fit inside the abdomen (Figure 2.8). It is divided into duodenum, jejunum and ileum.

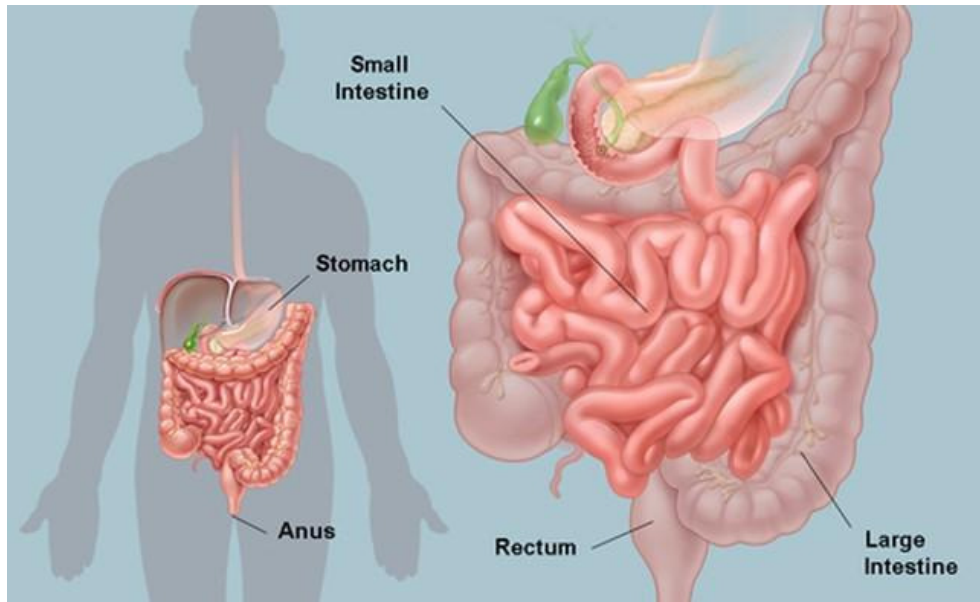


Figure 2.8: Human small intestine environment. '©2016, WebMD, LLC. All rights reserved'.⁽¹⁰⁾

Physical dimensions

The length and diameter of the small intestine are summarised in Table 2.22.

Table 2.22: Physical dimensions of human small intestine. N/R = Not reported.

Physical Dimensions	Value (cm)	Standard Deviation or Range	Sample Size (n)	Reference
Length	610	N/R	N/R	(10)
	700	N/R	N/R	(7)
Diameter	2.5	N/R	N/R	(10)
	4	N/R	N/R	(7)

Small intestine weight and density

The volume, weight, and density of small intestine are not reported in the scientific literature and medical textbooks.

Elasticity of the small intestine

The tensile stress measured by ex-vivo method (explained in Section 2.1.3.1) is shown in Table 2.23. The human small intestinal stiffness

(Young's modulus) was measured ex-vivo using a microelastometer (Microelastometer, Artann Laboratories, West Trenton, NJ, USA).⁽⁷⁶⁾ Force was applied three times on 1cm×1cm regions of intestinal tissue using a small piston. The Young's modulus was obtained from stress-strain curves (Table 2.23).

Table 2.23: Elasticity of human small intestine. N/R = Not reported.

Method of Measurement	Elasticity Value (kPa)	Standard Deviation	Sample Size (n)	Reference
Ex-vivo (Surgically removed)	1370 (longitudinal), 920 (transversal) (Maximum tensile stress)	510 (longitudinal), 480 (transverse)	98 (51 longitudinal and 47 transverse)	(15)
Ex-vivo (Cadaveric)	1470 (longitudinal), 830 (transverse) (Maximum tensile stress)	500 (longitudinal), 280 (transverse)	363 (181 longitudinal and 182 transverse)	(15)
Ex-vivo (Cadaveric)	2.9 (Young's modulus)	N/R	N/R	(76)

2.1.4 Summary

The biomechanical properties of the key human abdominal organs have been reviewed and average values or range of each biomechanical properties of liver, kidney, spleen, bowel and stomach [for example, average liver volume reported in Table 2.3 for CT scan method is 1.475 ± 0.230

(rounded to one decimal point to 1.5 ± 0.3)] are summarised in the Table 2.24. Elasticity of liver, kidney and spleen reported in Table 2.6, Table 2.11 and Table 2.16, respectively can be compared due to similar method of measurement (i.e. in-vivo non-invasive) employed in literature. Elasticity of bowel (Section 2.1.3.2) and stomach (Table 2.19) were measured by ex-vivo methods and hence, can't be compared with elasticity of liver, kidney and spleen. The biomechanical properties have provided useful benchmarks for the subsequent fabrication of simulant organs in the design and development of the in-house abdominal simulator.

Table 2.24: Summary of biomechanical properties for key abdominal organs.

N/A = Not applicable, N/R = Not reported.

Key Biomechanical Properties	Name of Organ				
	Liver	Kidney	Spleen	Stomach	Bowel
Volume (L)	1.5 ± 0.2 (Table 2.3)	0.16 ± 0.3 (Table 2.9)	0.15 ± 0.6 (Table 2.13)	0.8 ± 0.1 (Table 2.17)	3-8
Weight (kg)	1.73 (Table 2.4)	0.15 ± 0.3 (Table 2.10)	0.14 ± 0.01 (Table 2.14)	0.160 ± 0.03 (Table 2.18)	0.06 – 9 (Empty-Full)
Density (kg/L)	1.06 (Table 2.5)	1.05	1.04 ± 0.12 (Table 2.15)	0.07-0.08	N/R
Modulus of elasticity (kPa)	4.8 ± 0.5 (Table 2.6)	13 ± 2 (Table 2.11)	4.2 ± 0.7 (Table 2.16)	3 ± 1.3 (Table 2.19)	N/A
Tensile Stress (kPa)	N/A	N/A	N/A	650 ± 210 (Table 2.19)	1190 ± 300
Bulk Modulus (kPa)	N/A	N/A	N/A	480,000	N/A

2.2 Abdominal surgery and the LaparOsphere™ concept

Open and keyhole abdominal surgical procedures are briefly described, and current clinical and economical drawbacks reviewed in this section. Existing organ retraction and space creation devices are assessed thereafter. The LaparOsphere™ concept is introduced and the potential clinical benefits are explained.

2.2.1 Open and laparoscopic abdominal surgery

The global coordinate system, anatomical planes and directions to describe the human anatomy and retraction of abdominal organs during surgical procedures are shown in Figure 2.9.

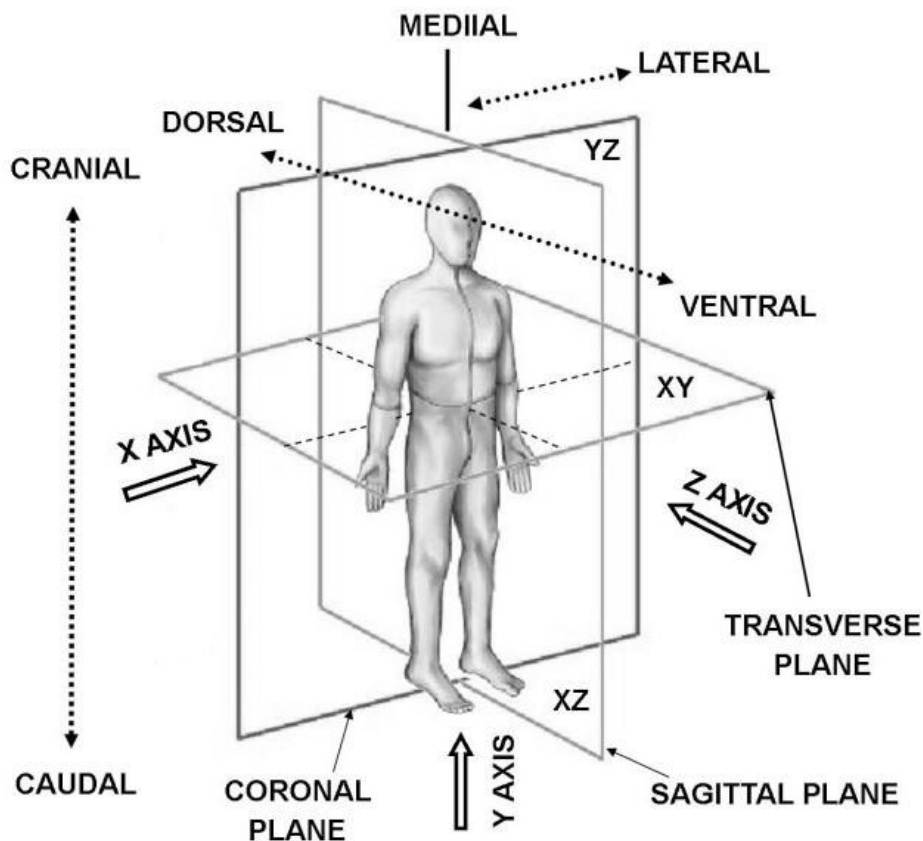


Figure 2.9: Global coordinates, anatomical planes, and directions of organ retractions for the human body.

Open abdominal surgery

In open abdominal surgery, an incision is made along the midline of the abdomen. The muscle and fascia are retracted using steel retractors to expose the main abdominal organs (Figure 2.10).

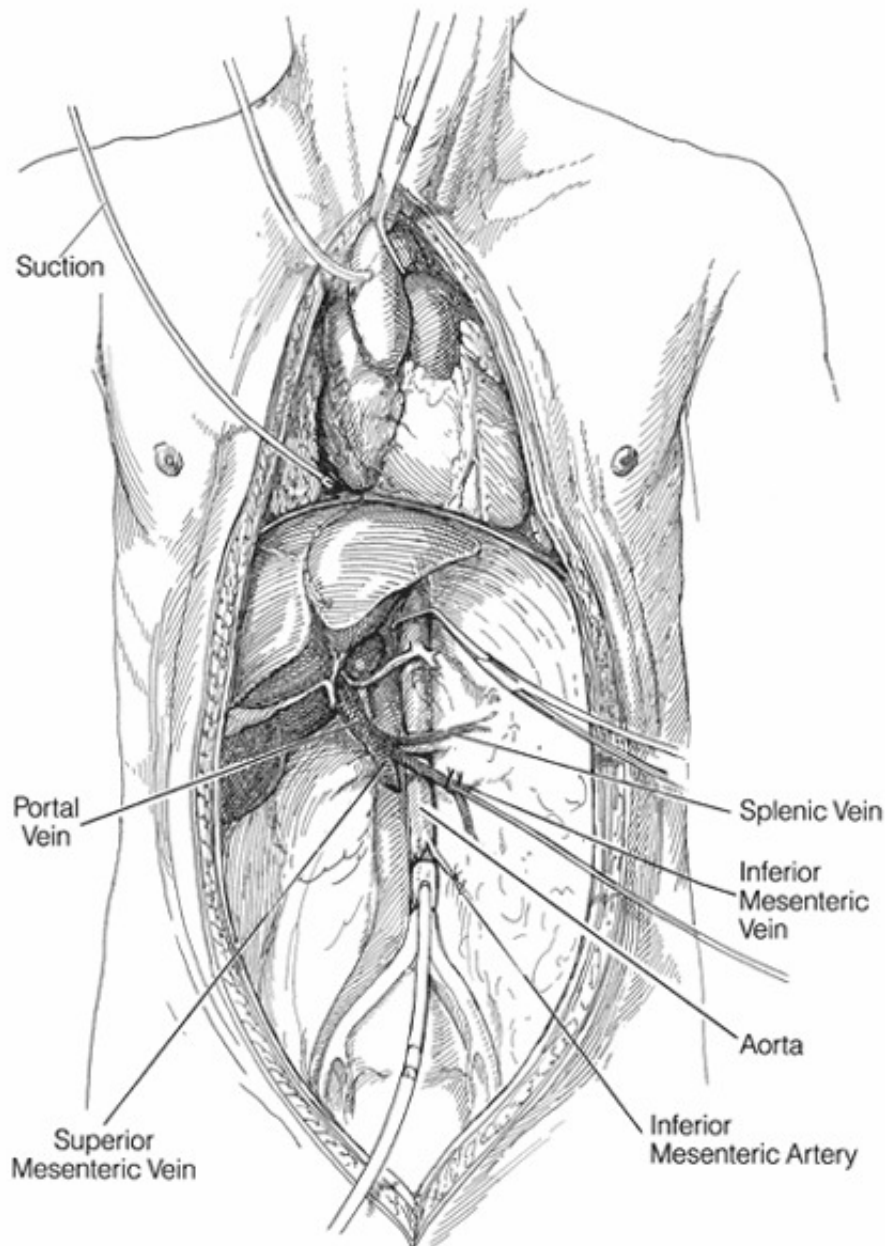


Figure 2.10: A typical incision along the midline of the abdomen during open surgery. 'ACS Surgery 2003. © 2003 WebMD Inc. All rights reserved'.⁽⁷⁷⁾

A common open abdominal procedure is removal of the gall bladder (open cholecystectomy - OC). The gall bladder is located below the left lobe of the liver. In order to obtain deeper access to the gall bladder, surgeons lift the

liver in the cranial direction, move the stomach in left lateral directions, and large bowel in the caudal direction several times during surgery (Figure 2.11).



Figure 2.11: Schematic representation of retraction of liver and stomach during an open abdominal procedure. 'ACS Surgery 2003. © 2003 WebMD Inc. All rights reserved'.⁽⁷⁷⁾

Laparoscopic (keyhole) abdominal surgery

Laparoscopic surgery, also recognised as MIS and Keyhole surgery, is the surgical technique of operating within body cavities through small incisions. Surgeons perform abdominal laparoscopic operations by making small incisions of 1-1.5 inch in the patient's abdomen. The surgeon inserts an insufflation device via a laparoscopic port to inflate the abdominal cavity with a supply of medical grade carbon dioxide gas (Figure 2.12), to create a pneumoperitoneum, which enables the insertion of a laparoscope (a high resolution video camera) and surgical instruments.⁽⁷⁸⁾ A laparoscope transmits live images of the abdominal area of the patient during the surgery to a computer screen and, accordingly, surgeons can carry out the surgery.^(2,3,79)



Figure 2.12: CO₂ insufflation and port placement during laparoscopic cholecystectomy.⁽⁷⁸⁾

Hand assisted laparoscopic surgery (HALS) is a half-way house between open and laparoscopic procedures. A larger incision of 3 to 5cm is also made in the abdomen to enable the surgeon to insert their hand into the abdomen to facilitate advanced retraction of the abdominal organs. CO₂ insufflation is used in this procedure and to prevent CO₂ leakage a “GelPort® Laparoscopic System” (Applied Medical) is used to seal round the surgeon’s

hand and the incision in the abdomen (Figure 2.13). HALS is typically used during more advanced laparoscopic procedures such as laparoscopic donor nephrectomy which involves retraction of the bowel and spleen to gain access to the kidney.



Figure 2.13: A GelPort used for hand assisted laparoscopic surgery.⁽⁸⁰⁾

Key clinical advantages of laparoscopic procedures over open abdominal surgery are: limited exposure of internal organs to possible external contaminants (thereby minimizing the risk of acquiring infections), reduced hemorrhaging (reducing the need for blood transfusion), reduced pain, quicker recovery, reduced length of stay, and reduced overall healthcare costs to the patient and healthcare provider.⁽⁸¹⁾

Cholecystectomy is considered as the gold standard therapy for the treatment of symptomatic gall stone developed in the gall bladder. It is one of the major gastrointestinal operations performed in the United Kingdom (UK) and United States of America (USA) where more than 60,000⁽⁸²⁾ and 500,000 gall bladder removal surgeries are, respectively, carried out annually.⁽⁸³⁾ Although this disease has a low mortality rate, its economic and health impact is significant due to its high morbidity. Open Cholecystectomy (OC)

and hand assisted donor nephrectomy are considered as the primary surgical procedures for this research project.

2.2.2 Disadvantages of use of CO₂ insufflation

The surgical drawbacks associated with the use of CO₂ insufflation, thereby limiting the scope of laparoscopic procedures, are^(84–86):

1. Increased risk of hypothermia and peritoneal trauma because of increased exposure to cold, dry CO₂ gas during inflation of the abdomen.
2. Surgeons must insert more CO₂ gas into the abdominal cavity to avoid deflation due to suction of blood.
3. Raised abdominal pressure resulting in reduced heart and lung function.
4. Electrosurgical and laser based cutting and sealing devices generate smoke impeding the visibility in the surgical space created inside the abdomen. This then requires use of suction device to improve visibility but at the cost of reduced CO₂ peritoneum.
5. Increased intra-abdominal pressure due to the pneumoperitoneum can cause hemodynamic and metabolic effects such as an increase in CO₂ absorption.
6. The requirement to assemble several different components to introduce the CO₂ and the availability of medical grade CO₂ in some less developed markets are setbacks with the use of CO₂.
7. The time taken by the surgeon to identify and eliminate CO₂ leakage increases surgery time and, therefore, can affect the overall cost of surgery.

Additionally, any abdominal laparoscopic procedure carries the risk of unintentional injuries in the form of puncture and perforation to organs (e.g.

stomach, bowel and liver).^(87–89) This is due to continuous moving and lifting of vital abdominal organs and tissues to expose the surgical field and inadequate haptic feedback resulting in excessive force applied on the abdominal organs and tissues.⁽⁸⁷⁾

Consequently, the next part of the review focuses on devices used to create space and/or retract organs to overcome the issues associated with CO₂ insufflation and retraction of organs.

2.2.3 Existing space creation and/or organ retraction devices

Existing space creation and organ retraction devices are briefly reviewed here.

Space creation devices

In order to create space within the abdomen during laparoscopic surgery, an abdominal wall lifter can also be employed as an alternative to CO₂ insufflation (i.e. gasless laparoscopic technique).⁽⁹⁰⁾ This is a mechanical device that fits under the abdominal wall and is lifted vertically by an external crane. This causes a high amount of stress on the abdominal wall tissues and can cause cosmetic damage to skin. It tends to create further trauma to the patient and does not involve retraction of organs.⁽⁹⁰⁾ For example, the LaparoLift System (LaparoLift, Origin Medsystem, Inc.) has been used for Laparoscopic gastrostomy (Figure 2.14).^(84,91) It does not create a dome-shaped abdominal cavity produced by a pneumoperitoneum but creates only a partially extended tent-like shape.⁽⁸⁴⁾

Similarly, the AbdoLift⁽⁹²⁾ and VarioLift systems^(93–95) have also been employed to improve the gasless laparoscopic technique (Figure 2.14). AbdoLift offers advantages over LaparoLift such as reusability and spreading evenly to lift the abdominal wall due to the presence of three retractors. However, AbdoLift is complex to handle due to its 19 components and does not offer the improved visibility of a pneumoperitoneum. The VarioLift system^(93–95) is made up of seven parts, is reusable and unfolds in the upper

abdomen after insertion allowing inspection of the liver as in the case of pneumoperitoneum.

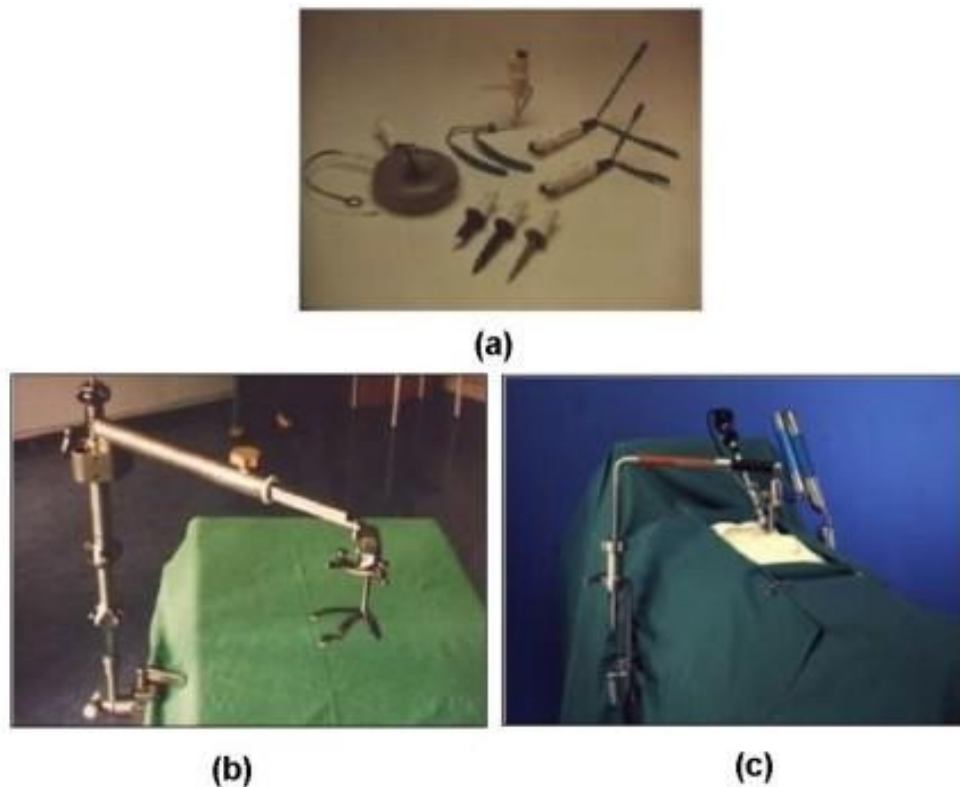


Figure 2.14: Space creation devices. (a) LaparoLift (b) AbdoLift and (c) VarioLift for gasless laparoscopy.^(84,92)

Organ retraction devices

Existing organ retraction devices such as the PretzelFlex™ retractor, a reusable surgical retraction system, are inserted into the human abdomen during keyhole surgery for the sole purpose of retracting large organs (for example, liver) and tissues (Figure 2.15).⁽⁹⁶⁾ The PretzelFlex™ is the advanced version of the Endoflex™ retractor and is currently used by laparoscopic surgeons at the MFT, co-sponsor of this PhD project. When it is inserted through laparoscopic port, it is converted into a pretzel shape inside the abdomen by dominant hand of operating surgeon to then elevate/retract the liver to get access to gall bladder. (I have viewed the hand assisted

donor nephrectomy carried out by Titus Augustine, inventor of LaparOsphere™ to understand the use of existing organ retraction devices and associated drawbacks.)

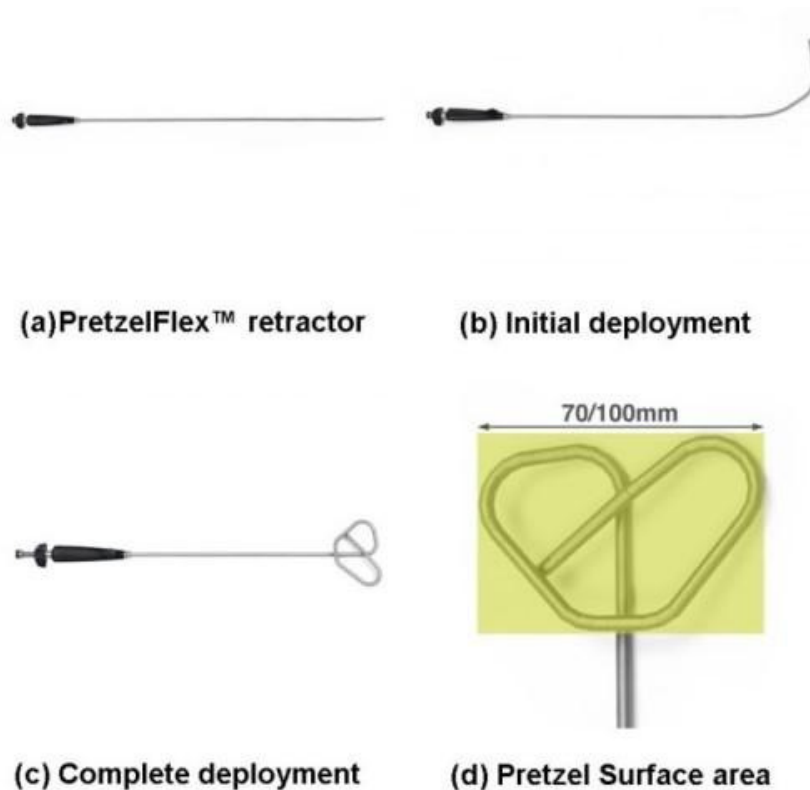


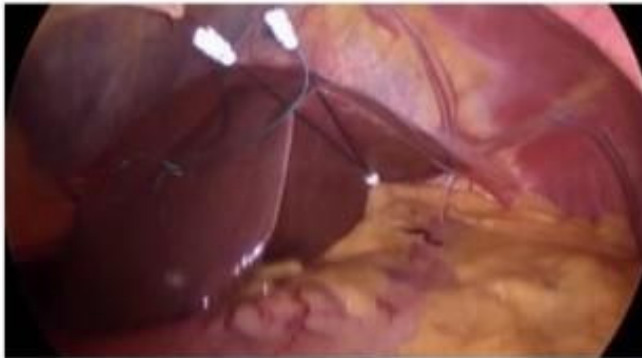
Figure 2.15: PretzelFlex™ organ retraction device. Images are obtained from Surgical Innovations website. "©Copyright - Surgical Innovations".⁽⁹⁶⁾

The Cinch organ retraction system is developed for single incision laparoscopic surgery and it retracts the liver during gall bladder removal surgery.^(97,98) It is used to retract liver during laparoscopic cholecystectomy in four steps: (a) clip set-up in the application forcep and inserted into abdomen through 12mm trocar; (b) clip application on to gall bladder fundus and application forcep is removed from abdomen; (c) Needle fixation – laparoscopic needle holder is brought into the abdomen to grasp, pull, and secured needle on the parietal peritoneum thus retracting liver; and (d) clip removal by laparoscopic needle holder.

FreeHold Duo™ and FreeHold Trio™ retractors optimize the visualisation inside human abdomen by lifting/retracting the liver (Figure 2.16) and, hence, enable surgeon autonomy and reduce the need of additional retractors.⁽⁹⁹⁾



(a) Inserted through trocar



(b) Deployed to retract liver

Figure 2.16: Retraction of liver using FreeHold Trio™. Images are extracted from video footage available on FreeHold Surgical website. "© 2016 FreeHold Surgical, Inc. All rights reserved".⁽⁹⁹⁾

Since these devices are reliant on the CO₂ insufflation technique to create space, there is scope for a medical device which can not only create space in the abdomen but can simultaneously also retract the abdominal organs.

2.2.4 The LaparOsphere™ concept and expansion mechanisms

The LaparOsphere™ uses a generic expanding, hollow and transparent structure to create space within the abdomen and retract abdominal organs (Figure 2.17).⁽⁴⁾ This original idea has been developed by Mr Titus Augustine (Consultant Transplant, Endocrine and General Surgeon at the MFT).

The device should be approximately 200mm in diameter when deployed. It should create space within the abdomen for surgeons to accommodate the free movement of laparoscopes and associated surgical instruments and also swiftly move the organs away from the operation site to avoid any organ injuries (Figure 2.18).⁽⁴⁾

Multiple holes should enable access of various instruments to the surgical field (Figures 2.17 and 2.18). After dissection of the gall bladder during gall bladder removal surgery, it can be enclosed within the LaparOsphere™ and its retrieval can be made possible upon collapse of the LaparOsphere™.⁽⁴⁾

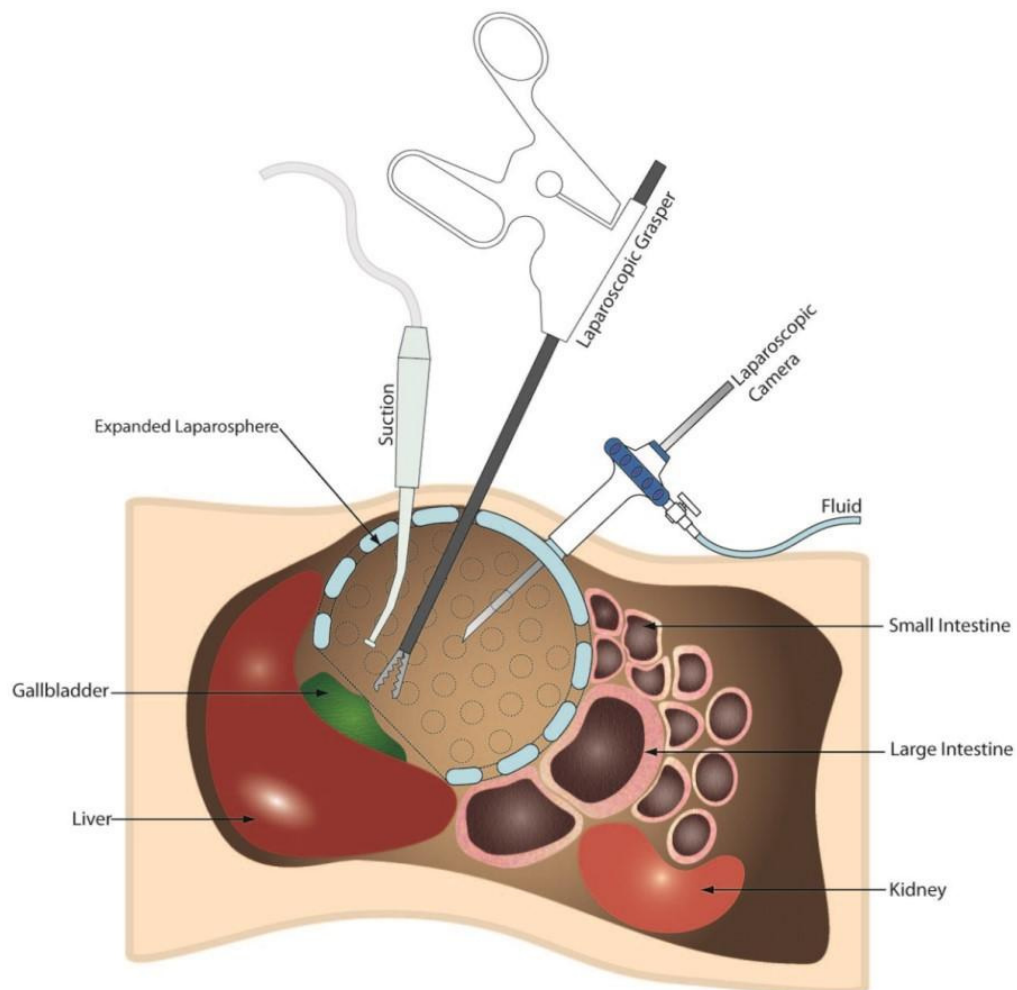


Figure 2.17: LaparOsphere™ concept. "2017 Copyright MFT, all rights reserved".^(4,100)

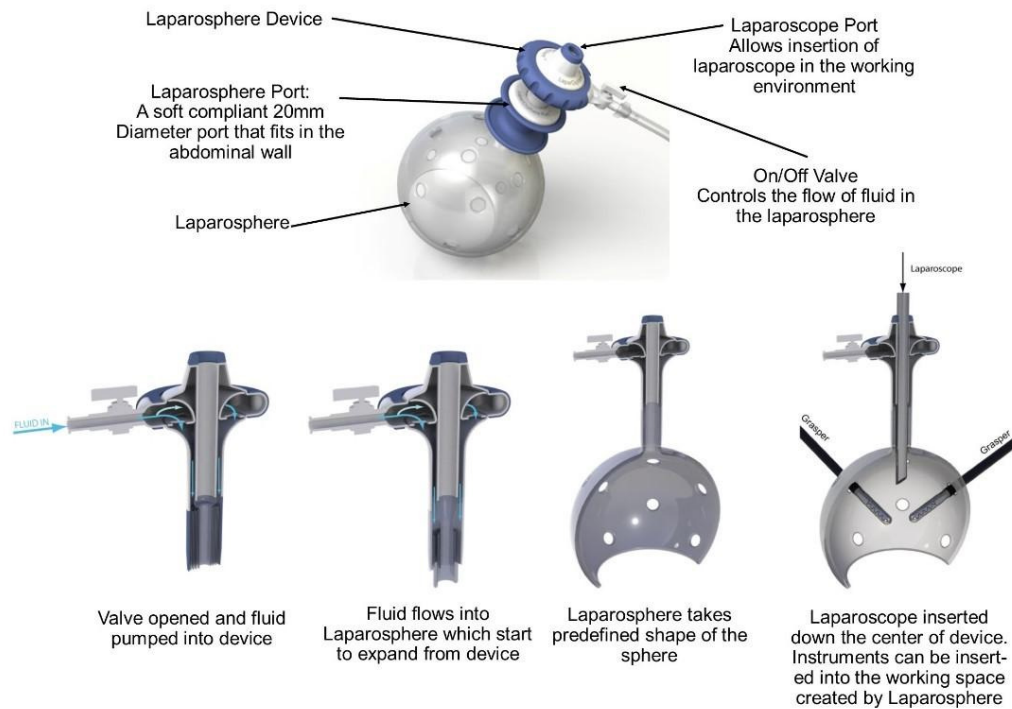


Figure 2.18: LaparOsphere™ device with port and on/off valve for fluid/air control. “2017 Copyright MFT, all rights reserved”.^(4,100)

An inflatable double-walled structure was initially envisaged for the expansion mechanism of the LaparOsphere™. The potential advantages of the inflatable LaparOsphere™ proposed over CO₂ insufflation include: space creation, organ retraction, use of suction without compromising space created, protection of surrounding organs and tissues, eliminates need for assistant surgeon, single device replaces multiple devices and CO₂ insufflation system, and makes laparoscopic surgery simpler and easier to learn. It was developed by TrusTECH (co-sponsor of this PhD project) in parallel to this PhD project. Doughnut shape double-walled structures in different diameters were fabricated from polyurethane (PU) film using the radio frequency (RF) welding technique. They were inflated by using pressurised air. They do not have cellular structures and hence, do not permit insertion of surgical instruments. In this PhD project, they have been assessed in-vivo and in-vitro within pig abdomen and in-house simulator, respectively.

In this project, replacing the inflatable double-walled expansion mechanism of the LaparOsphere™ by cellular or lattice semi-rigid structures responding

to mechanical deployment is investigated. The cellular mechanisms considered include non-auxetic and auxetic structures. The design and development of cylindrical prototype structures approximately 300mm long with diameter in the range of 20-40mm in the undeployed configuration has been carried out.

2.3 Surface pressure application during abdominal surgery

The design and development of expandable prototype structures require an understanding of the surface pressures applied by surgeons to retract organs and tissues in the abdominal region during open and laparoscopic abdominal procedures. To the author's knowledge no studies have been undertaken to accurately quantify the surface pressures applied to human intraabdominal organs undergoing typical retraction forces during abdominal surgical procedures. This is despite the fact that such procedures for example, laparoscopic cholecystectomy are carried out in large numbers in the UK & USA (60,000 and 500,000, respectively)^(82,83) and globally.

Several studies have been carried out for robotic-assisted surgery and MIS where force sensing capability has been introduced.^(101–103) In-vivo mechanical properties of soft tissues and organs have also been measured and analysed to diagnose, define and localize tumours.⁽¹⁰⁴⁾ Force feedback information has been collected for incorporation in computer-based surgical simulators.⁽³⁵⁾ The mechanical properties of human liver have been reported from in-vivo indentation tests during MIS⁽³⁵⁾ and open abdominal surgery⁽¹⁰⁵⁾. Grasping forces have been measured during retraction of major abdominal organs in an in-vivo porcine model using a fenestrated grasper.⁽¹⁰⁶⁾

In this project, an in-vivo pilot study involving human participants has then been devised and undertaken to measure the surface pressures applied to human intraabdominal organs undergoing typical retraction movements during abdominal surgical procedures.

2.4 Summary

The biomechanical properties of human abdominal organs, abdominal surgical procedures and existing space creating devices, and in-vivo force

measurements for the retraction of abdominal organs have been reviewed in this Chapter. The LaparOsphere™ concept was then explained and the initial expansion mechanism reviewed. This project has considered cellular and lattice-type structures as alternative expansion mechanisms. Chapter 3 will, then, review relevant elasticity theory, theory related to buckled beams and cellular solids, and auxetic structures and their biomedical applications.

3 Literature Review of Elasticity Theory, Beam Theory, and Cellular Structures

The relevant elasticity theory, theory related to buckled beams and cellular solids, and auxetic structures are reviewed to understand the mechanics of the cellular structures proposed in this project for the design and development of expansion mechanisms.

3.1 Elasticity theory

Elasticity theory is described to understand the mechanical properties associated with the design of expansion mechanisms, and the mechanical properties of living tissues described briefly in Chapter 2 for key abdominal organs. The review of elasticity theory considers linear elastic materials and incorporates anisotropic, orthotropic and isotropic cases, which can all be features of cellular or biological materials. However, consideration of non-linear elasticity and viscoelasticity, which can also be features of cellular solids and soft tissues, are not presented here.

Solid mechanics:

"*Solid mechanics*" is a physical science that describes the behaviour and conditions of solid bodies at rest when force is applied. It is also known as "mechanics of materials" and "mechanics of deformable bodies".⁽¹⁰⁷⁾ The deformable body can also be defined as a solid that changes size and/or shape in response to an applied load.

Classical Elasticity Theory:

The mechanics of solids is concerned with the relationships of external forces to internal stresses and strains and is described by two approaches known as elementary theory and the theory of elasticity. The theory of elasticity uses mathematical analysis to determine the precise stress and strain distributions in a loaded body. The objectives of elasticity theory are the examination of the load-carrying capacity of a solid body and, hence, evaluation of strength, stiffness, and stability.^(107,108)

3.1.1 Hooke's law and Poisson's ratio

Most of engineering materials exhibit a linear stress-strain relationship at low stress levels. This is known as elastic behaviour of the material. An elastic material returns to its original (unloaded) shape upon the removal of applied forces, unlike plastically deformed solid materials which undergo permanent deformation and do not return to their original shape when load is removed. Consider the stress-strain curve showing the elastic range (Figure 3.1a) (OE) and plastic range (Figure 3.1c) (OAB). Elastic behaviour of material is considered when the load is removed exactly at point E or before (Figure 3.1b), and the material follows exactly the same curve back to the origin O when load is removed.

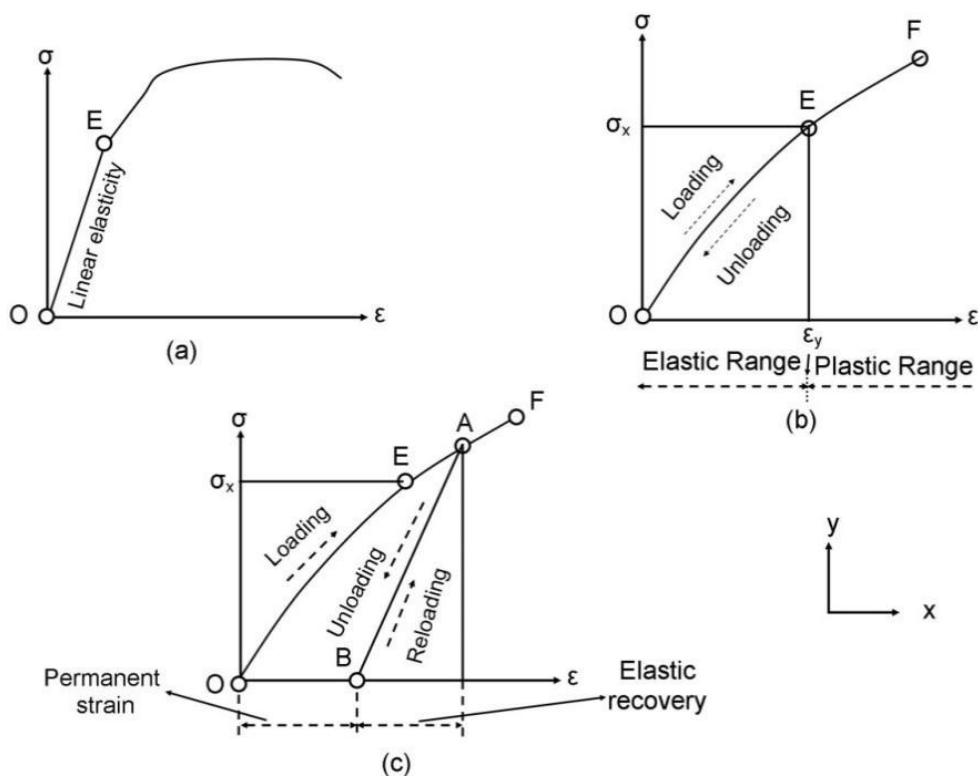


Figure 3.1: Stress-strain diagrams. (a) Linear elasticity, (b-c) Nonlinear elasticity.⁽¹⁰⁷⁾

The stress-strain curve from O to E in Figure 3.1a is a straight line and therefore the material is linearly elastic. In contrast, the strain-stress curves from O to E in Figure 3.1b and Figure 3.1c are not straight lines and, hence, the material is nonlinearly elastic. Plastic behaviour is observed when load is

removed beyond point E, for instance, at point A in Figure 3.1c. The material follows the line AB on the curve upon unloading and does not return to the origin O. This scenario leaves permanent or plastic deformation in the material.

For the OE portion in Figure 3.1a, stress is directly proportional to strain. If a normal stress is considered acting in the x direction,

$$\sigma_x = E_x \varepsilon_x \quad 3.1$$

The relationship in Equation 3.1 is known as Hooke's law. The constant E_x is called the modulus of elasticity, or Young's modulus, in the x direction and has units of σ (Pa or N/m²) since ε is a dimensionless quantity. Young's modulus is the slope of the stress-strain diagram in the linear elastic region (Figure 3.1a).

Axial loading usually induces a change in the cross-sectional area of the body. The change in transverse dimension relative to axial dimensional change is governed by the Poisson's ratio (ν) which is defined as the ratio of the transverse strain to the axial strain (Figure 3.2)

$$\nu_{xy} = - \frac{\varepsilon_y}{\varepsilon_x} \quad 3.2$$

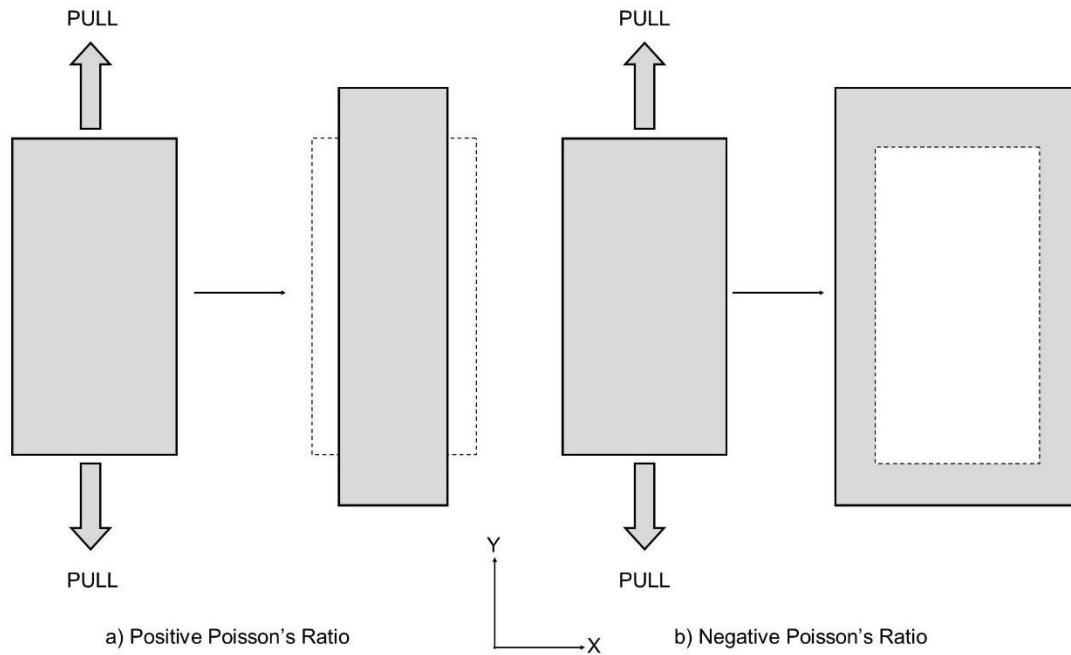


Figure 3.2: Definition of Poisson's Ratio.

The common engineering materials have a positive Poisson's ratio although, as will become clear, materials with negative values are also allowed within elasticity theory.

In the linear elastic region under pure shear loading, stress and strain are also related by Hooke's law in a 2-dimensional material by

$$\tau_{xy} = G_{xy} \gamma_{xy} \quad 3.3$$

In Equation 3.3, the proportionality constant G_{xy} is the shear modulus or modulus of rigidity.

3.1.2 Generalised (anisotropic) Hooke's law

Stress is proportional to strain in an elastic material according to Hooke's law (Equation 3.1). The generalised Hooke's law for any homogeneous elastic material in a 3-D state of stress relates each of the six stress components as a linear function to the six components of strain within the linear elastic range, i.e.

$$\begin{Bmatrix} \sigma_x \\ \sigma_y \\ \sigma_z \\ \tau_{xy} \\ \tau_{yz} \\ \tau_{xz} \end{Bmatrix} = \begin{bmatrix} C_{11} & C_{12} & C_{13} & C_{14} & C_{15} & C_{16} \\ C_{21} & C_{22} & C_{23} & C_{24} & C_{25} & C_{26} \\ C_{31} & C_{32} & C_{33} & C_{34} & C_{35} & C_{36} \\ C_{41} & C_{42} & C_{43} & C_{44} & C_{45} & C_{46} \\ C_{51} & C_{52} & C_{53} & C_{54} & C_{55} & C_{56} \\ C_{61} & C_{62} & C_{63} & C_{64} & C_{65} & C_{66} \end{bmatrix} \begin{Bmatrix} \varepsilon_x \\ \varepsilon_y \\ \varepsilon_z \\ \gamma_{xy} \\ \gamma_{yz} \\ \gamma_{xz} \end{Bmatrix} \quad 3.4$$

The coefficients C_{ij} ($i, j = 1, 2, 3, \dots, 6$) are the material-dependent stiffness constants.

The alternative form of Hooke's law for anisotropic materials relates the strain tensor to the stress tensor via the compliance matrix

$$\begin{Bmatrix} \varepsilon_x \\ \varepsilon_y \\ \varepsilon_z \\ \gamma_{xy} \\ \gamma_{yz} \\ \gamma_{xz} \end{Bmatrix} = \begin{bmatrix} S_{11} & S_{12} & S_{13} & S_{14} & S_{15} & S_{16} \\ S_{21} & S_{22} & S_{23} & S_{24} & S_{25} & S_{26} \\ S_{31} & S_{32} & S_{33} & S_{34} & S_{35} & S_{36} \\ S_{41} & S_{42} & S_{43} & S_{44} & S_{45} & S_{46} \\ S_{51} & S_{52} & S_{53} & S_{54} & S_{55} & S_{56} \\ S_{61} & S_{62} & S_{63} & S_{64} & S_{65} & S_{66} \end{bmatrix} \begin{Bmatrix} \sigma_x \\ \sigma_y \\ \sigma_z \\ \tau_{xy} \\ \tau_{yz} \\ \tau_{xz} \end{Bmatrix} \quad 3.5$$

Succinct representations of the stress-strain relationships (Equation 3.4 and 3.5) are shown in Equation 3.6 and Equation 3.7, respectively, where, S_{pq} = compliance coefficients, and C_{qp} = stiffness coefficients.

$$\sigma_p = C_{pq} \varepsilon_q \quad 3.6$$

$$\varepsilon_p = S_{pq} \sigma_q \quad 3.7$$

Strain energy considerations can be used to reduce the 36 elastic constants to 21 independent elastic constants for anisotropic materials. The strain energy consideration leads to a demonstration that the stiffness and compliance matrices are symmetric, i.e. $s_{ij} = s_{ji}$ and $c_{ij} = c_{ji}$, respectively.

The relationship between compliance coefficients and elastic constants are determined by employing specific loading conditions in Equation 3.5. For example, the Young's modulus and Poisson's ratio (in the x-y plane) for a uniaxial load applied along the x direction (i.e. $\sigma_x \neq 0$; $\sigma_y = \sigma_z = \tau_{xy} = \tau_{yz} = \tau_{xz} = 0$) are shown in Equation 3.8 and 3.9.

$$E_x = \frac{\sigma_x}{\varepsilon_x} = \frac{1}{S_{11}} \quad 3.8$$

$$\nu_{xy} = -\frac{\varepsilon_y}{\varepsilon_x} = -\frac{S_{21}\sigma_x}{S_{11}\sigma_x} = -\frac{S_{21}}{S_{11}} \quad 3.9$$

3.1.3 Orthotropic materials

A general orthotropic material has three planes of symmetry and three corresponding orthogonal axes called the orthotropic axes. Within each plane of symmetry, material properties may be different and independent of direction. For elastic orthotropic materials, the elastic coefficients C_{ij} remain invariant at a point under a rotation of 180° about any of the orthotropic axes. In an orthotropic material, there is no interaction between the normal stresses and the shear strains and so the generalized Hooke's law for the most general orthotropic elastic material is given by

$$\begin{Bmatrix} \varepsilon_x \\ \varepsilon_y \\ \varepsilon_z \\ \gamma_{xy} \\ \gamma_{yz} \\ \gamma_{xz} \end{Bmatrix} = \begin{bmatrix} S_{11} & S_{12} & S_{13} & 0 & 0 & 0 \\ S_{21} & S_{22} & S_{23} & 0 & 0 & 0 \\ S_{31} & S_{32} & S_{33} & 0 & 0 & 0 \\ 0 & 0 & 0 & S_{44} & 0 & 0 \\ 0 & 0 & 0 & 0 & S_{55} & 0 \\ 0 & 0 & 0 & 0 & 0 & S_{66} \end{bmatrix} \begin{Bmatrix} \sigma_x \\ \sigma_y \\ \sigma_z \\ \tau_{xy} \\ \tau_{yz} \\ \tau_{xz} \end{Bmatrix} \quad 3.10$$

The compliance coefficients of Equation 3.10 are replaced in Equation 3.11 by considering relationships of Young's modulus, Poisson's ratio and shear modulus in Equation 3.1-3.3 and Equations 3.4-3.5.

$$\begin{Bmatrix} \varepsilon_x \\ \varepsilon_y \\ \varepsilon_z \\ \gamma_{xy} \\ \gamma_{yz} \\ \gamma_{xz} \end{Bmatrix} = \begin{bmatrix} \frac{1}{E_x} & -\frac{\nu_{yx}}{E_y} & -\frac{\nu_{zx}}{E_z} & 0 & 0 & 0 \\ -\frac{\nu_{xy}}{E_y} & \frac{1}{E_y} & -\frac{\nu_{zy}}{E_z} & 0 & 0 & 0 \\ -\frac{\nu_{xz}}{E_x} & -\frac{\nu_{yz}}{E_y} & \frac{1}{E_z} & 0 & 0 & 0 \\ 0 & 0 & 0 & \frac{1}{G_{yz}} & 0 & 0 \\ 0 & 0 & 0 & 0 & \frac{1}{G_{zx}} & 0 \\ 0 & 0 & 0 & 0 & 0 & \frac{1}{G_{xy}} \end{bmatrix} \begin{Bmatrix} \sigma_x \\ \sigma_y \\ \sigma_z \\ \tau_{xy} \\ \tau_{yz} \\ \tau_{xz} \end{Bmatrix} \quad 3.11$$

The symmetric compliance matrix condition for the orthotropic material constants leads to relationships shown in Equation 3.12.

$$\begin{aligned} \frac{\nu_{xy}}{E_x} &= \frac{\nu_{yx}}{E_y} \\ \frac{\nu_{yz}}{E_y} &= \frac{\nu_{zy}}{E_z} \\ \frac{\nu_{xz}}{E_x} &= \frac{\nu_{zx}}{E_z} \end{aligned} \quad 3.12$$

3.1.4 Isotropic materials

An isotropic material has every plane as a plane of symmetry leading to the number of essential elastic constants reducing to two. Hooke's law for isotropic materials relating the strain tensor to the stress tensor via the compliance matrix is shown in Equation 3.13.

$$\begin{Bmatrix} \varepsilon_x \\ \varepsilon_y \\ \varepsilon_z \\ \gamma_{xy} \\ \gamma_{yz} \\ \gamma_{xz} \end{Bmatrix} = \frac{1}{E} \begin{bmatrix} 1 & -\nu & -\nu & 0 & 0 & 0 \\ -\nu & 1 & -\nu & 0 & 0 & 0 \\ -\nu & -\nu & 1 & 0 & 0 & 0 \\ 0 & 0 & 0 & 2(1+\nu) & 0 & 0 \\ 0 & 0 & 0 & 0 & 2(1+\nu) & 0 \\ 0 & 0 & 0 & 0 & 0 & 2(1+\nu) \end{bmatrix} \begin{Bmatrix} \sigma_x \\ \sigma_y \\ \sigma_z \\ \tau_{xy} \\ \tau_{yz} \\ \tau_{xz} \end{Bmatrix} \quad 3.13$$

The relationship between elastic constants E, ν and G according to Hooke's law for isotropic materials (Equation 3.14) is

$$G = \frac{E}{2(1 + \nu)} \quad 3.14$$

Similarly, the bulk modulus of elasticity (K) is related to E and ν by

$$K = \frac{E}{3(1 - 2\nu)} \quad 3.15$$

A positive definite strain energy requires $E > 0$, $G > 0$ and $K > 0$ and, hence, the allowable range for Poisson's ratio for isotropic materials according to Equations 3.14 and 3.15 ranges between $-1 < \nu < +0.5$.

When Poisson's ratio is 0.5, an isotropic material is incompressible (i.e. maintains volume due to an infinite bulk modulus – Equation 3.15) but can change shape easily (minimum value of shear modulus – Equation 3.14). Conversely, when $\nu = -1$ the isotropic material can undergo large volume change (minimum value of bulk modulus – Equation 3.15) but maintains shape (infinite shear modulus – Equation 3.14).

3.1.5 Saint-Venant's principle

Saint-Venant's principle suggests that the distribution of stress and strain across the body is altered only near the regions of load application. The expansion mechanisms proposed in this project will undergo uniaxial compression and tension loading during mechanical characterisations at the top end of cylinder. Hence, the maximum stress for real materials, advocated by Saint-Venant's principle, is higher at the top end of cylinder due to edge effects and loading constraints or boundary conditions.

Saint-Venant's principle is shown in Figure 3.3. It demonstrates the stress distribution across three sections of rectangular plate of width d when it is subjected to a concentrated load (F).

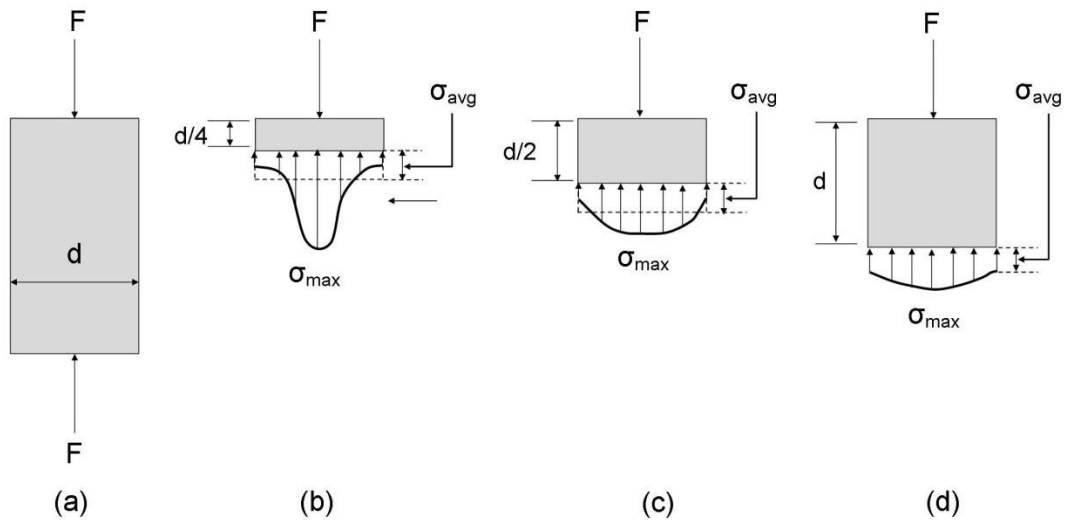


Figure 3.3: Stress distribution in a rectangular elastic plate showing Saint-Venant's principle. (a) Rectangular plate; (b-d) stress distribution across three sections of rectangular plate of width d .⁽¹⁰⁷⁾

The maximum stress (σ_{\max}) greatly exceeds the average stress (σ_{avg}) near the point of application of the load (Figure 3.3b) and diminishes along the vertical centre axis of the plate away from an end (Figure 3.3c). At a distance equal to the width of the plate, the stress is nearly uniform (Figure 3.3d). This phenomenon is valid for most stress concentrations and any type of loading.

If the region of interest is sufficiently away from the boundary conditions, then the stress variation near the boundary regions does not affect stress conditions in the area of interest. The complex distribution of force supplied by the wall to a cantilever beam, for example, can be replaced by vertical and horizontal forces and a moment for purposes of determining stresses acting at a distance from the wall equal to or greater than the depth h of the beam (Figure 3.4).

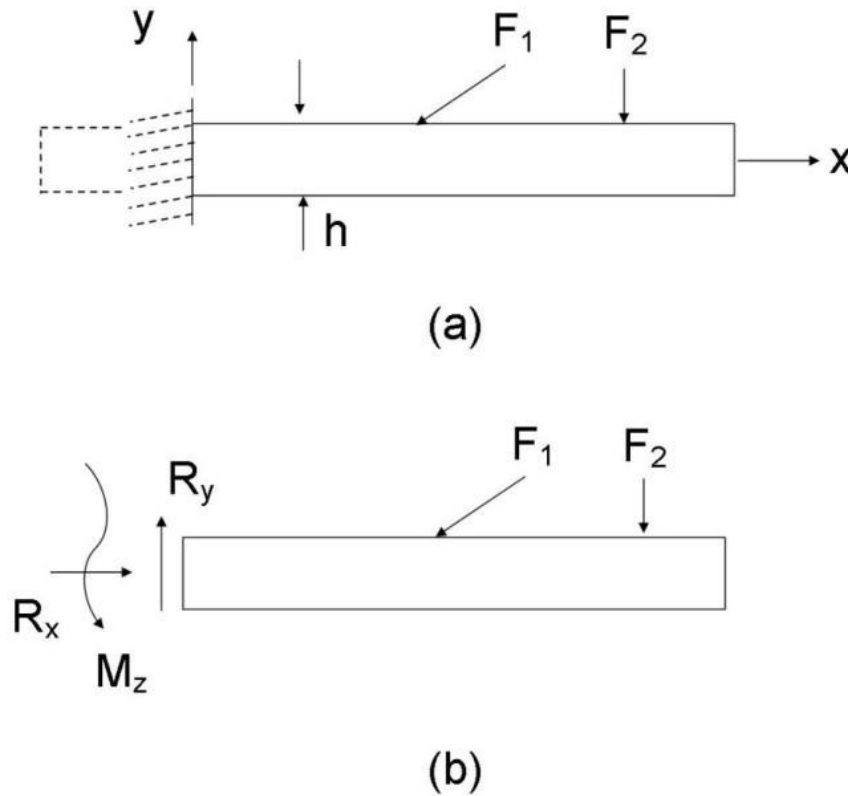


Figure 3.4: Cantilever beam illustrating use of Saint-Venant's principle. (a) Actual support; (b) Statically equivalent.⁽¹⁰⁷⁾

However, Sanami et al⁽¹⁰⁹⁾ have predicted slow decay of end stress for a cylinder with negative Poisson's ratio material which would be useful to consider for the expansion mechanisms designed and developed during this project using auxetic materials. Additionally, Horgan⁽¹¹⁰⁾ has reported that the high anisotropy can lead to a slower decay of Saint-Venant's end stresses.

Summary:

Elasticity theory has been described to understand the origin of mechanical properties of materials such as Young's modulus, Poisson's ratio and shear modulus. The theory is used to obtain approximate solutions through numerical analysis and exact solutions for simple loading of a beam. The buckling of beams is considered as one of the expansion mechanisms for the LaparOsphere™ device and, hence, beam theory is next described in Section 3.2.

3.2 Beam theory

The theory related to buckled beams is reviewed since it is considered as one of the expansion mechanism in this project.

3.2.1 Bending of beam

The elasticity of homogenous, straight and linearly elastic beams in pure bending has been studied.⁽¹⁰⁷⁾ In pure bending, each element of infinitesimal length experiences identical deformation resulting in uniform beam curvature. The deflected axis of the beam or the deflection curve of a beam can then be obtained using Equation 3.16.

$$\frac{d^2v}{dx^2} = -\frac{M}{EI} \quad 3.16$$

where,

v = deflection (small)

x = axial displacement

M = bending moment

EI = flexural rigidity (I = moment of inertia, E = modulus of elasticity)

The expression in Equation 3.16 relates the beam curvature to the bending moment which is known as the Bernoulli-Euler law of elementary bending theory. For a beam of constant flexural rigidity EI , Equation 3.16 can be written as

$$M = EIv'' \quad 3.17$$

3.2.2 Buckling of pinned-end columns

Buckling is defined by immediate lateral deflection of a structural member due to compressive stress and leads to a structural instability and failure. The buckling or elastic instability of beams and slender members subject to axial compression are reviewed for an ideal column (straight and homogenous) which follows Hooke's law of linear elasticity while under centric loading.

Ideal column:

The pin-ended ideal column (Figure 3.5a) can be held in a deformed configuration (Figure 3.5b) by a load P while remaining in the elastic range (the requisite axial motion is permitted by the movable end support). The collinear forces P acting at the centroid of the cross section is shown in assumed deflection (Figure 3.5c).

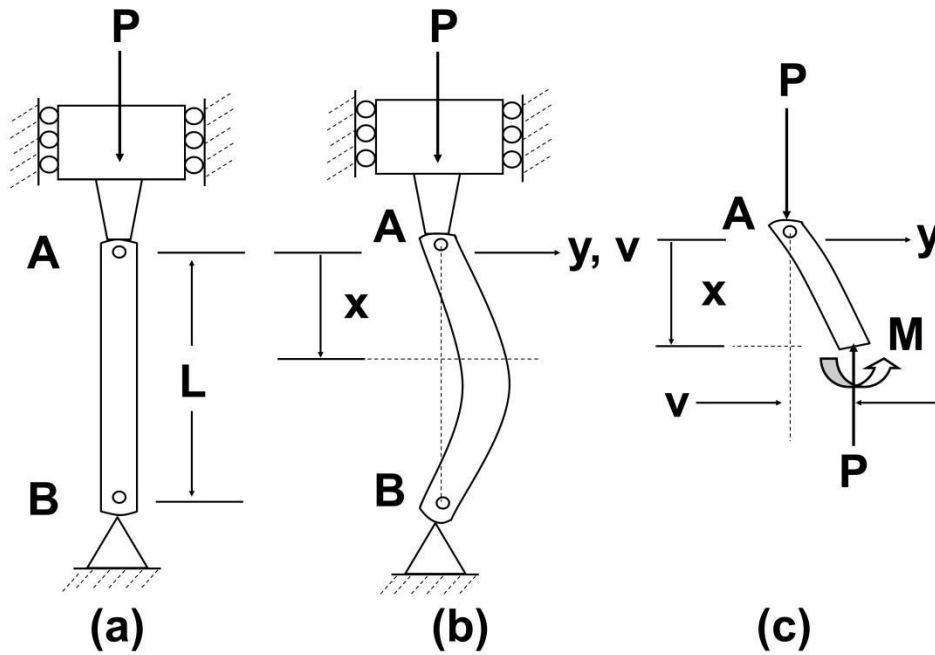


Figure 3.5: Pinned-end column.(a) Initial form; (b) buckled form; (c) free-body diagram of column segment.⁽¹⁰⁷⁾

The bending moment at any section is derived by

$$M = Pv \quad 3.18$$

Inserting equation 3.18 in to equation 3.16,

$$\left(EI \frac{d^2v}{dx^2} \right) - (Pv) = 0 \quad 3.19$$

The differential solution of Equation 3.19 leads to an infinite set of discrete values of load, defined as critical load $[(P^{cr})_n]$. It means that the column may be maintained in a deflected shape. The critical load is given by

$$(P^{cr})_n = \frac{n^2 \pi^2 EI}{L^2} \quad 3.20$$

where, L = original length of the column.

When $n = 1$, the lowest critical load or Euler buckling load of the pin-ended column is obtained using Equation 3.39.

$$P^{cr} = \frac{\pi^2 EI}{L^2} \quad 3.21$$

These solutions for many engineering problems are termed eigenvalues, and the corresponding deflections v are the Eigen functions.

Imperfect column:

The impact of imperfections on the elastic behaviour of a column is shown in Figure 3.6.

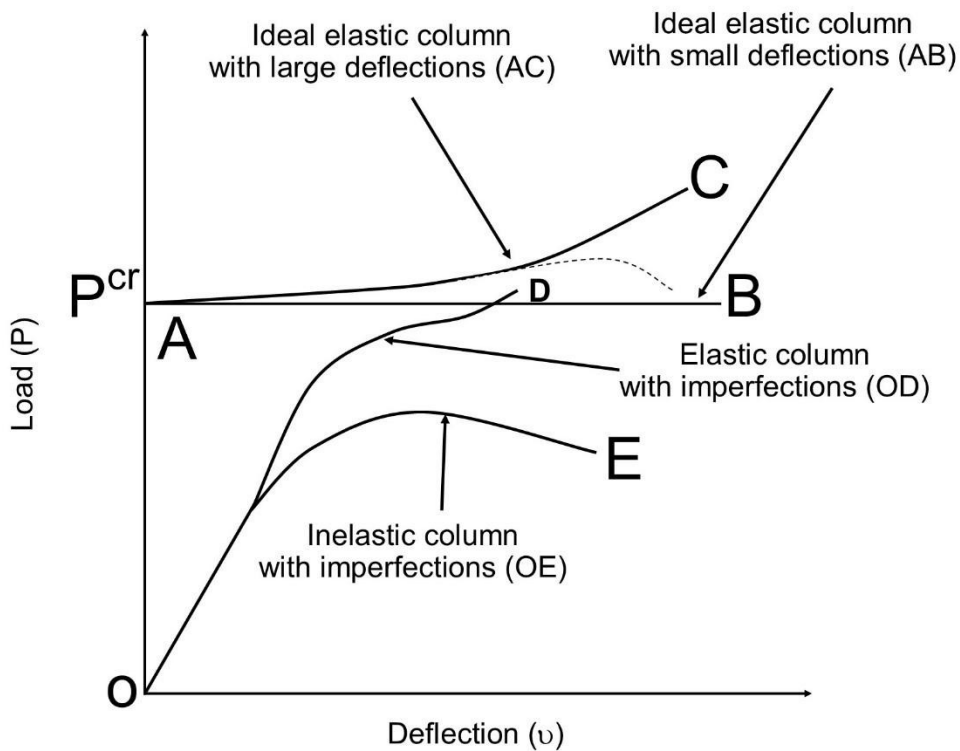


Figure 3.6: Relation between load and deflection for columns.⁽¹⁰⁷⁾

Curve AC represents the ideal elastic column with large deflections. When bending stresses accompanying large deflection carry the material into the inelastic regime, the buckling load diminishes. Hence, the load-deflection

curve AC drops (dashed lines in Figure 3.6) and the column fails either by excessive yielding or fracture. Consequently, P^{cr} is considered as the maximum load sustainable by a column.

When the column deviates from the ideal conditions assumed for an ideal column, it is considered as an imperfect column. An imperfection could be in the form of a misalignment of load or a small initial curvature which can impact load-carrying capacity and deformation under load. The specified form of curve such as an ideal elastic column with small deflections (line AB in Figure 3.6), imperfection in elastic column (curve OD in Figure 3.6), ideal elastic column with large deflections (curve AC in Figure 3.6), and elastic behaviour with imperfections (curve OE in Figure 3.6) depend upon the material properties and column dimensions. Additionally, curve OE in Figure 3.6 suggests an inelastic column (i.e. stresses exceed the proportional limit and the column material no longer follows Hooke's law) should exhibit plastic collapse and this phenomenon requires smaller and smaller loads to maintain larger deflections.

Slenderness ratio:

It is established that the critical load depends not on material strength but on the flexural rigidity (EI) for different end conditions. The moment of inertia (I) is given by

$$I = Ar^2 \quad 3.22$$

where,

r = radius of gyration

A = square cross-sectional area

The critical load (Equation 3.21) can then be rewritten using Equation 3.22 as

$$P^{cr} = \frac{\pi^2 EA}{\left(\frac{Le}{r}\right)^2} \quad 3.23$$

where,

L_e = effective column length

L_e/r = effective slenderness ratio

The second moment of area describes the resistance of a particular area distribution to bending about an intersecting axis, it is found by solving

$I_{xx} = \int y^2 dxdy$, where y is the height to area elements from the neutral surface. For a circular cross section this results in $I_{xx} = \frac{\pi d^4}{64}$. For complex structures such as the auxetic lattices this integral can be solved numerically if required and is found routinely in CAE software.

The effective slenderness ratio is an important parameter in the classification of a column under compression. The behaviour of an ideal column is often represented on a plot of average compressive stress (P/A) versus slenderness ratio (L_e/r). A large slenderness ratio allows elastic buckling at a stress which does not exceed the elastic limit of the material. Hence, Equation 3.23 can be rearranged for critical stress (σ^{cr}) as

$$\sigma^{cr} = \frac{P^{cr}}{A} = \frac{\pi^2 E}{\left(\frac{L_e}{r}\right)^2} \quad 3.24$$

The critical stress can be increased by using material of higher modulus of elasticity (E) or by increasing the radius of gyration (r). The range of L_e/r depends on the material under consideration. For instance, in the case of structural steel, when $L_e/r > 100$, $30 < L_e/r < 100$, and $L_e/r < 30$, the columns are considered as long, intermediate, and short struts, respectively.

3.2.3 Negative stiffness

Negative stiffness exists like positive stiffness but is unstable.⁽¹¹¹⁾ The force applied to a negative stiffness material is in the opposite direction to the displacement. It assists deformation due to internal stored energy and the system may not require additional force.^(111,112) This behaviour leads to

significantly larger system deformation than would be obtained for the same force applied to a positive stiffness system.⁽¹¹²⁾

Man-made composite materials⁽¹¹¹⁾, foams⁽¹¹³⁾, buckled beams⁽¹¹²⁾, carbon nanotubes⁽¹¹⁴⁾ and honeycomb structures⁽¹¹⁵⁾ have been reported to have negative stiffness properties. As an example of a negative stiffness system, a typical force vs displacement curve of a buckled beam is shown in Figure 3.7.

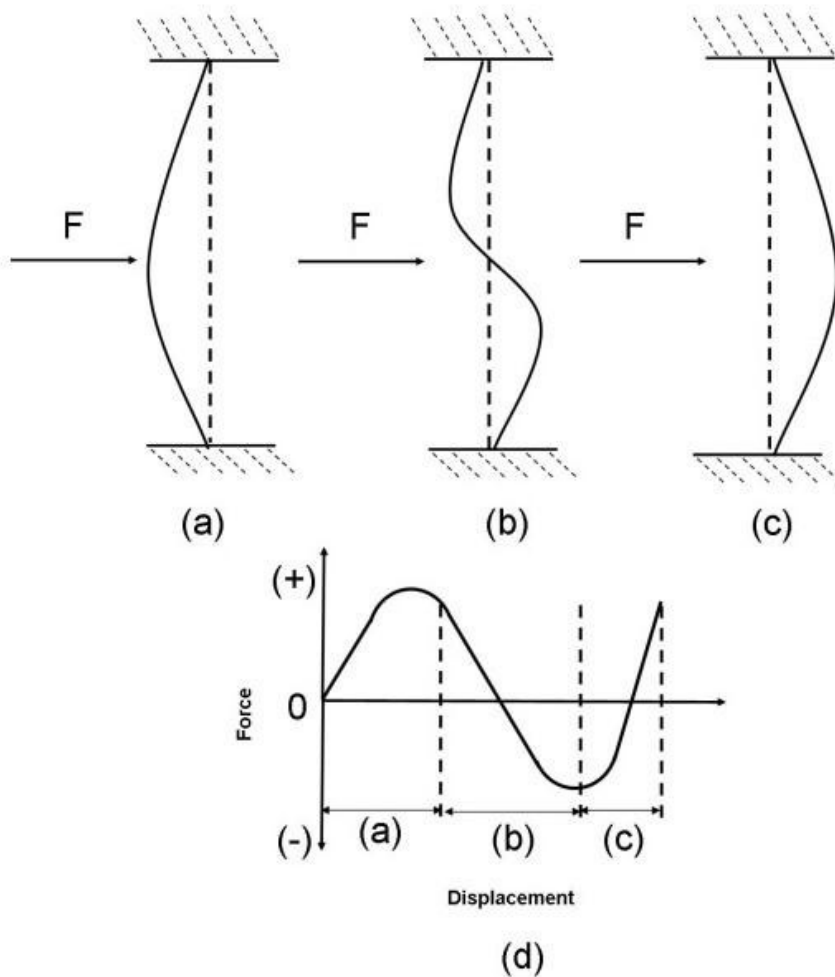


Figure 3.7: Deformation of buckled beam. (a) Initial stable phase, (b) transverse force leads to unstable phase, (c) second stable phase, and (d) force vs displacement curve showing negative stiffness effect.⁽¹¹²⁾

When a transverse force is applied to an initially stable buckled beam (Figure 3.7a), it resists deformation until a certain threshold is reached and the beam

snaps through to the second stable phase (Figure 3.7c) via the unstable phase (Figure 3.7b).⁽¹¹²⁾

Summary:

The theory related with the bending of straight beam is described to understand the mechanics when uniaxial compressive load applied. Negative stiffness phenomenon is also explained to demonstrate the unstable phase of the buckled beam when deformed.

3.3 Cellular materials and structures

Cellular structures are considered in the development of expansion mechanisms for the LaparOsphere™. Hence, the analytical expressions governing the mechanical properties of the most common of these structures (the hexagonal honeycomb) are reviewed.

3.3.1 Introduction to cellular structures

A cellular solid is one made up of an interconnected network of solid struts forming edges and faces of cells. Many natural materials are cellular such as the interior of bone, wood (axial section), and cork (radially). They are structured like a network of regular hexagons termed as honeycombs.⁽¹¹³⁾

Mechanics of honeycombs:

The elastic deformations of two and three dimensional honeycomb geometries under axial and biaxial loads have been studied.^(7, 11) Linear and nonlinear elastic and plastic mechanical properties of two and three dimensional cellular materials have been analysed and evaluated experimentally for bending, elastic buckling and plastic behaviours.

The mechanism of linear-elastic deformation of two dimensional cellular structures is primarily that of bending of the cell walls and edges, with small contributions from shear and axial deformations of the cell walls/edges. The collapse of flexible walls of cellular material can be due to elastic buckling of the cell wall, plastic bending of cell walls (via the formation of plastic hinges) or sometimes can be attributed to fracture.⁽¹¹³⁾

The mechanical properties of three dimensional cellular structures are similarly linked to the properties of the cell wall and to the cellular geometry.

3.3.2 Analytical expressions for the mechanical properties of honeycombs

Gibson and Ashby⁽¹¹³⁾ have considered in-plane and out-of-plane deformation mechanisms for honeycombs. The analytical expressions are reviewed for both in-plane and out-of-plane mechanical properties.

In-plane properties:

The in-plane properties of a conventional honeycomb undergoing linear elastic deformation in response to uniaxial loading (Figure 3.8) have been derived.⁽¹¹³⁾ Consider the honeycomb in Figure 3.8 loaded in the x_2 direction deforming by linear elastic cell wall bending. The key parameters of the honeycomb in Figure 3.8 are

- l = diagonal rib length of honeycomb
- h = vertical rib length of honeycomb
- α = angle of diagonal rib with the horizontal (x_1) axis¹
- t = in-plane thickness of vertical rib.

¹ Gibson and Ashby denote the honeycomb angle by the symbol θ . Here, the symbol α replaces θ to avoid ambiguity and confusion with the use of θ to denote the circumferential direction in cylindrical coordinates employed in the description of cylinder properties and directions elsewhere in the thesis.

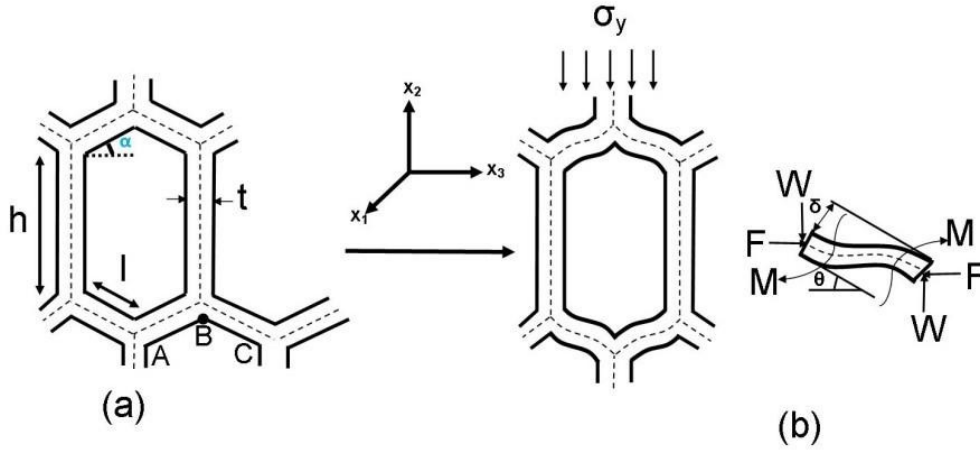


Figure 3.8: Linear elastic compression of conventional honeycomb.⁽¹¹³⁾

(a) Undeformed honeycomb, (b) bending caused by load in the x_2 direction and associated forces, moments, and displacements.

The in-plane linear elastic response is described by five moduli: two Young's moduli (E_1 and E_2 parallel to the x_1 and x_2 axes, respectively), a shear modulus in the x_1 - x_2 plane (G_{12}), and two Poisson's ratios (ν_{12} and ν_{21}). They are not independent and the reciprocal relationship (e.g. Equation 3.12) reduces the number of independent in-plane moduli to four.

Gibson and Ashby⁽¹¹³⁾ have used standard beam theory outlined by Roark and Young⁽¹¹⁸⁾ to derive expressions for the two in-plane Young's moduli in the x_2 and x_1 directions (assuming small cell wall deflections):

$$E_2 = E_s \left(\frac{t}{l} \right)^3 \frac{\left(\frac{h}{l} + \sin \alpha \right)}{\cos^3 \alpha} \quad 3.25$$

$$E_1 = E_s \left(\frac{t}{l} \right)^3 \frac{\cos \alpha}{\left(\frac{h}{l} + \sin \alpha \right) \sin^2 \alpha} \quad 3.26$$

where

E_s = Young's modulus of solid material

For regular honeycombs with $h/l = 1$, $\alpha = 30^\circ$ and uniform wall thickness, both Young's moduli reduce to the same value and the honeycomb is isotropic:

$$\frac{E_2}{E_s} = \frac{E_1}{E_s} = 2.3 \left(\frac{t}{l} \right)^3 \quad 3.27$$

The above analysis is valid for small t/l , where axial shortening of the diagonal ribs is negligible to the bending deflection.

The in-plane Poisson's ratios for loading in the x_2 and x_1 directions are

$$\nu_{21} = -\frac{\varepsilon_1}{\varepsilon_2} = \frac{\left(\frac{h}{l} + \sin\alpha \right) \sin\alpha}{\cos^2\alpha} \quad 3.28$$

$$\nu_{12} = -\frac{\varepsilon_2}{\varepsilon_1} = \frac{\cos^2\alpha}{\left(\frac{h}{l} + \sin\alpha \right) \sin\alpha} \quad 3.29$$

Note that the in-plane Poisson's ratios (Equations 3.28 and 3.29) obey a reciprocal relationship, further reducing the number of independent in-plane moduli for the hexagonal honeycomb to three. For the isotropic (regular, $h/l = 1$ and $\alpha = 30^\circ$) honeycomb, $\nu_{21} = \nu_{12} = 1$. When $\alpha < 0$, the diagonal ribs are inverted, and the Poisson's ratios become negative. This type of honeycomb is known as a re-entrant honeycomb and is included in the auxetic materials discussed in Section 3.4.

Gibson and Ashby⁽¹¹³⁾ also derived an analytical expression for the reciprocal theorem by substituting Equations 3.25, 3.26, 3.28 and 3.29 into Equation 3.12:

$$E_1 \nu_{21} = E_2 \nu_{12} = E_s \left(\frac{t}{l} \right)^3 \frac{1}{\sin\alpha \cos\alpha} \quad 3.30$$

The in-plane shear modulus, G_{12} , derived by Gibson and Ashby⁽¹¹³⁾ is

$$G_{12} = E_s \left(\frac{t}{l} \right)^3 \frac{\left(\frac{h}{l} + \sin\alpha \right)}{\left[\frac{h}{l} \right]^2 \left(2 \left[\frac{h}{l} \right] + 1 \right) \cos\alpha} \quad 3.31$$

Equation 3.31 reduces to Equation 3.50 for regular and uniform honeycombs, which obey the isotropic relation (Equation 3.14) of shear modulus with Young's modulus and Poisson's ratio.

$$G_{12} = 0.57E_s \left(\frac{t}{l}\right)^3 \quad 3.32$$

Non-linear elasticity was considered by Gibson and Ashby to occur when walls, treated like end-loaded columns, buckle as the load exceeds the Euler buckling load (Equation 3.21). The end constraint factor, n , describes the rotational stiffness of the node where three cell walls meet.⁽¹¹³⁾ The value of n depends on the degree of constraint to rotation at the node B caused by wall AB and BC (Figure 3.8). If rotation is freely allowed, $n=0.5$, and if there is no rotation, $n=2$. Gibson and Ashby⁽¹¹³⁾ developed a relationship between n and h/l (Table 3.1).

Table 3.1: End constraint factors for elastic buckling of honeycomb.⁽¹¹³⁾

h/l	n
1	0.686
1.5	0.760
2	0.806

Out-of-plane properties:

The out-of-plane properties of a hexagonal honeycomb during linear elastic deformation under uniaxial loading were also derived by Gibson and Ashby⁽¹¹³⁾. Five additional moduli describe out-of-plane mechanical properties. For normal loading in the x_3 direction (Figure 3.8), the Young's modulus is

$$E_3 = E_s \left(\frac{t}{l} \right) \frac{\left(\frac{h}{l} + 2 \right)}{2 \left(\frac{h}{l} + \sin \alpha \right) \cos \alpha} \quad 3.33$$

The two Poisson's ratios under out-of-plane loading are equal to the solid material Poisson's ratio:

$$\nu_{31} = \nu_{32} = \nu_s \quad 3.34$$

The Poisson's ratios ν_{13} and ν_{23} are then found using the reciprocal relationship (Equation 3.12), Equations 3.28 and 3.29, and the appropriate in-plane Young's modulus expression (Equation 3.25 and 3.26).

Upper and lower bounds of the two shear moduli were formulated by calculating strain energy.⁽¹¹⁹⁾ For loading in the x_1 direction, acting on the face normal to the x_3 direction, the upper and lower bounds of the shear modulus (G_{13}) are identical:

$$G_{13} = G_s \left(\frac{t}{l} \right) \frac{\cos \alpha}{\left(\frac{h}{l} + \sin \alpha \right)} \quad 3.35$$

For loading in the x_2 direction, acting on the face normal to the x_3 direction, the upper and lower bounds for G_{23} are not identical. The upper bound for G_{23} is

$$G_{23} \leq \frac{1}{2} G_s \left(\frac{t}{l} \right) \frac{\left(\frac{h}{l} + 2\sin^2\alpha \right)}{\left(\frac{h}{l} + \sin\alpha \right) \cos\alpha} \quad 3.36$$

The lower bound for G_{23} is

$$G_{23} \geq G_s \left(\frac{t}{l} \right) \frac{\left(\frac{h}{l} + \sin\alpha \right)}{\left(1 + \frac{2h}{l} \right) \cos\alpha} \quad 3.37$$

For the isotropic, regular hexagon case, the two out-of-plane shear moduli are

$$G_{13} = G_{23} = 0.577 G_s \left(\frac{t}{l} \right) \quad 3.38$$

The out-of-plane moduli (Equations 3.33 and 3.36-3.38) depend linearly on relative density (t/l) while the in-plane moduli (Equations 3.25, 3.26 and 3.31) scale as $(t/l)^3$. The out-of-plane moduli are therefore larger than the in-plane moduli by a factor $(l/t)^2$ or, for typical honeycombs, a factor of between 10 and 1000.⁽¹¹³⁾

A theoretical model has been developed to predict elastic constants of hexagonal honeycombs based on the deformation of cell walls by flexure, stretching and hinging.⁽¹¹⁷⁾ Analytical expressions for the Young's moduli, shear moduli and Poisson's ratios have been derived, and the off-axis properties were also considered using standard axis transformation equations.

The flexure model of Gibson and Ashby⁽⁵⁾ and the multiple-mechanism model of Masters and Evans⁽¹¹⁷⁾ both demonstrate that tailoring the geometry of the honeycomb cells can lead to isotropic or extremely anisotropic mechanical properties. The mathematical models have also demonstrated that Poisson's ratio in excess of +1 can be obtained by means of an open

cell structure for regular honeycombs. Negative Poisson's ratios for re-entrant hexagonal honeycomb structures can, similarly, be achieved with values much less than -1.

Summary:

Analytical expressions for in-plane and out-of-plane mechanical properties of hexagonal honeycombs deforming by flexure of the cell walls have been described. These expressions are valid for positive and negative values of honeycomb angle α , leading to positive and negative values, respectively, of in-plane Poisson's ratios. In the next section of this chapter, auxetic (negative Poisson's ratio) materials are reviewed.

3.4 Auxetic materials

3.4.1 Introduction

In 1944, Love⁽¹¹⁶⁾ reported regular pyrites (crystal) with a negative Poisson's ratio (-1/7). Referring to the definition of Poisson's ratio in Equation 3.20, the unique characteristic of a negative Poisson's ratio material is the ability to expand widthwise when stretched lengthwise. Similarly, when compressed in one particular direction a negative Poisson's ratio material contracts in at least one direction transverse to that direction.

In 1982, Gibson and Ashby⁽¹¹³⁾ reported the auxetic effect in the form of 2-D silicone rubber or aluminium honeycombs deforming by flexure of ribs^(120,121). A negative Poisson's ratio in foams was first published by Lakes in 1987⁽¹²²⁾. This was closely followed in 1989 by the report from Evans and Caddock of microporous expanded polytetrafluoroethylene (PTFE) possessing negative Poisson's ratio⁽¹²³⁾⁽¹²⁴⁾. The term "auxetic" to describe negative Poisson's ratio materials was coined in 1991 by Evans⁽¹²⁵⁾. The word auxetic is derived from the Greek word *auxetos* which means "that which tends to increase".

3.4.2 Types of auxetic materials

Auxetic materials and auxetic behaviour are reported in nature.⁽¹²⁶⁾ Soft biological tissues such as cat skin⁽¹²⁷⁾, cow teat skin⁽¹²⁸⁾, bovine common carotid arteries^(129,130), human achilles tendon⁽¹³¹⁾, the nuclei of human

embryonic stem cells^(132,133), early stage amphibian embryo tissues⁽¹³³⁾, load-bearing cancellous bone from human shins⁽¹³⁴⁾, and porcine adipose and skeletal muscle tissues⁽¹³⁵⁾ have shown auxetic behaviour either in uniform or gradient manner. The natural mineral α -cristobalite displays negative Poisson's ratios in certain single-crystal directions and also in polycrystalline aggregate (isotropic) form.^(136,137) In addition, other natural minerals such as pyrolytic graphite⁽¹³⁸⁾, iron pyrites (FeS_2)⁽¹¹⁶⁾, arsenic and bismuth⁽¹³⁹⁾, cadmium⁽¹⁴⁰⁾, phosphorous⁽¹⁴¹⁾, and several cubic and face-centred cubic rare gas solids along a specific crystallographic direction⁽¹⁴²⁾ have been reported to be auxetic. Crystalline cellulose⁽¹⁴³⁾ and mother-of-pearl (nacre)⁽¹⁴⁴⁾ are other examples of naturally occurring auxetic materials.

Artificial auxetic materials and structures and their mechanisms have been developed in the form of polymers, composites and textiles. Auxetic behaviour is attributed to geometries and mechanisms which are reviewed later in this chapter. A negative Poisson's ratio (NPR) of -0.7 was first reported in polyester foam by Lakes.⁽¹⁴⁵⁾ An expanded form of microporous polytetrafluoroethylene (PTFE) possessing large NPR (-12) was reported by Evans and Caddock^(123,124). Cylinders of auxetic ultra-high molecular-weight polyethylene (UHMWPE) were reported to achieve NPR down to -19 by compaction, sintering and extrusion of UHMWPE powder.⁽¹⁴⁶⁾

The 2D auxetic honeycombs, re-entrant anti-trichiral are fabricated by Alderson et al⁽¹⁴⁷⁾ possessing -0.77 in-plane Poisson's ratio. The gradient auxetic hexagonal honeycombs were fabricated using 3D printing technology.⁽¹⁴⁸⁾ Novel 2D kirigami (origami + cut patterns) honeycombs were designed, simulated, and fabricated for large deformations, morphing antenna, and deployability functions.⁽¹⁵⁰⁾

Polypropylene (PP) monofilament fibres displaying auxetic behaviour (-0.6) were first produced by extending the previous batch process for microporous polymer cylinder production to a fully continuous partial melt extrusion process⁽¹⁵¹⁾. 2-component double helix yarns have also been developed where the auxetic effect arises due to straightening of an (initially) helical thin wrap yarn causing helical fattening of an (initially) straight thick core yarn.⁽¹⁵²⁾

The design, fabrication, and characterisation of auxetic warp knit textile structures, having NPR of -0.22 ± 0.03 at $\pm 45^\circ$ to the warp direction, were reported.⁽¹⁵³⁾ Weft-knitted auxetic fabrics have also been developed.^(154,155) Carbon fibre/epoxy resin laminates with in-plane NPR (-0.245) was designed, fabricated and tested, and through-thickness NPR can also be designed by appropriate choice of stacking sequence and/or reinforcement.^(122,156)

3.4.3 Properties

Auxetic materials can have other enhanced mechanical properties by virtue of possessing a negative Poisson's ratio. These include, for example:

- Enhanced shear modulus⁽¹⁵⁷⁾
- Enhanced hardness⁽¹⁵⁸⁾
- Enhanced fracture toughness⁽¹⁵⁹⁾
- Enhanced energy absorption⁽¹⁶⁰⁾
- Synclastic (dome-shaped) curvature^(5,161)

Taking enhanced shear modulus as an example, when Poisson's ratio (ν) $\rightarrow -1$ in Equation 3.14, the shear modulus (resistance) increases significantly compared to the Young's modulus.

Similarly, for the final example of double-curvature when subject to out-of-plane bending, auxetic materials adopt a synclastic (dome-shaped) curved form (Figure 3.9). This is opposite to the anticlastic (saddle shape) curvature adopted by a material possessing positive Poisson's ratio under the same out-of-plane bending^(5,161). The relationship between the radii of curvature and Poisson's ratio for a moment applied along the sides of a plate parallel to the y axis is⁽⁵⁾

$$R_y = \frac{-R_z}{\nu_{zy}} \quad 3.39$$

In Equation 3.39, when the Poisson's ratio is negative, the radius of curvature R_y has the same sign as the radius of curvature R_x , leading to the double curvature effect. This mechanical property is considered further in this investigation to determine whether an auxetic sheet rolled into a cylinder and subjected to an axisymmetric bending load transforms into a sphere.

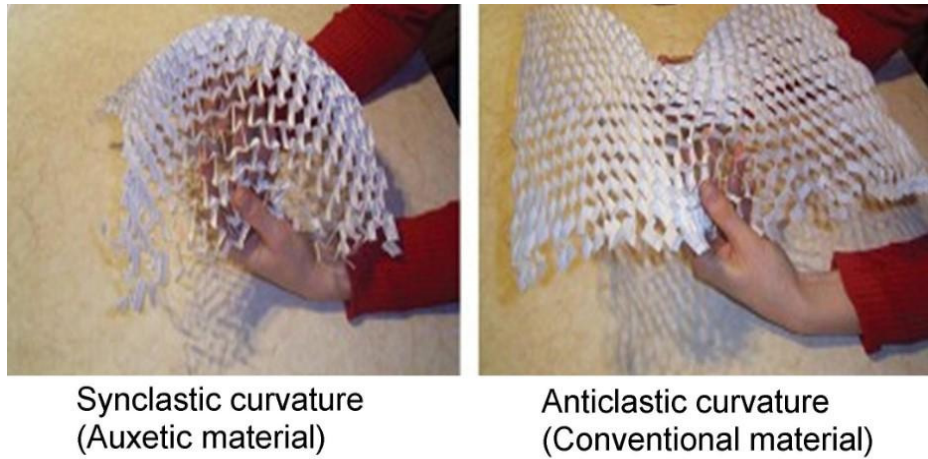


Figure 3.9: Curvatures of auxetic and conventional honeycombs.^(5,161,162)

The auxetic effect can be attributed to the macro, micro or nano structure of the material or structure. A simple example of the auxetic effect can be found from origami where a series of predetermined folds in a sheet of paper can produce a structure which expands transversely when stretched longitudinally (Figure 3.10).⁽¹⁶³⁾

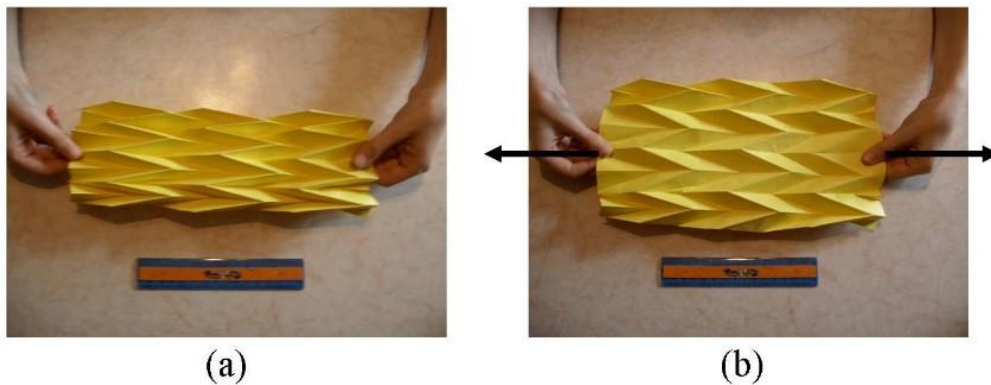


Figure 3.10 Folded sheet of paper showing an auxetic effect. Expansion from relaxed state (a) to stretched state (b).⁽¹⁶³⁾

It is also known that a cylinder comprised of folded paper which demonstrates auxetic behaviour in planar sheet form, deploys into a sphere when compressed along its length (Figure 3.12)⁽¹⁶⁴⁾. In the initial undeployed state, the folds at the ends of the cylinder are reversed with respect to the folds of the main body of the cylinder. Under axial compression the reverse-fold end pieces convert the axial load into a bending load. The bending load is responsible for the overall deformation of the wall to cause the change of shape from cylinder into sphere in the fully deployed state. The effects of end pieces are similarly considered during a systematic investigation into cylinder wall material properties in Chapter 5.

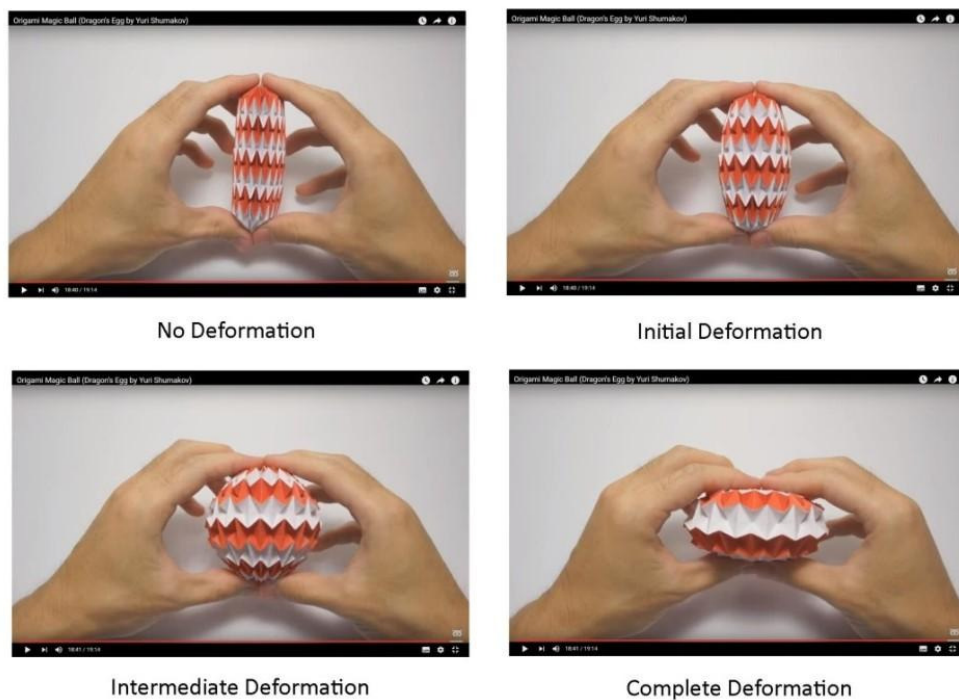


Figure 3.11: Origami cylinder to ball mechanism.⁽¹⁶⁴⁾

Preliminary work carried out at the University of Bolton has shown that it is possible to make deployable folded paper cylinder-to-sphere structures containing holes/apertures in the structure (Figure 3.11).⁽⁶⁾ This provided the impetus for the full investigation undertaken in this project.

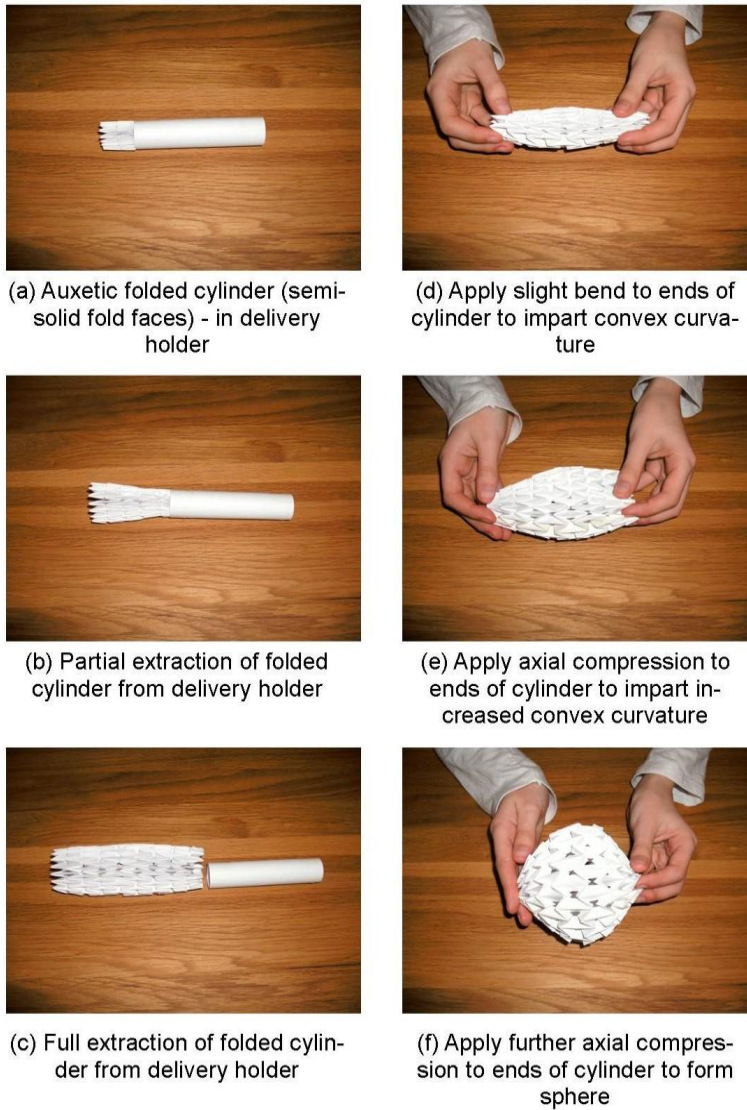


Figure 3.12 Semi-solid fold face deployable paper cylinder/ball.⁽⁶⁾

3.4.4 Auxetic structure-mechanism combinations

Auxetic behaviour is achieved through the appropriate combination of the geometry of the internal structure of the material and its deformation mechanism(s). The mechanical properties such as stiffness and Poisson's ratios can be tailor-made to an application at hand.

Several such auxetic structures and their mechanisms are outlined in Table 3.2 to Table 3.7.

Table 3.2: Auxetic structures and their mechanisms 1.

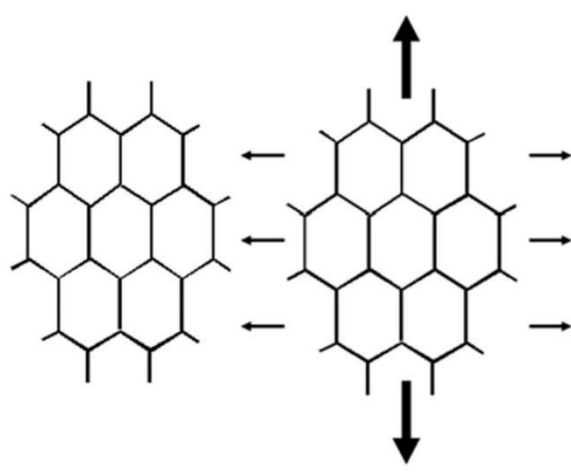
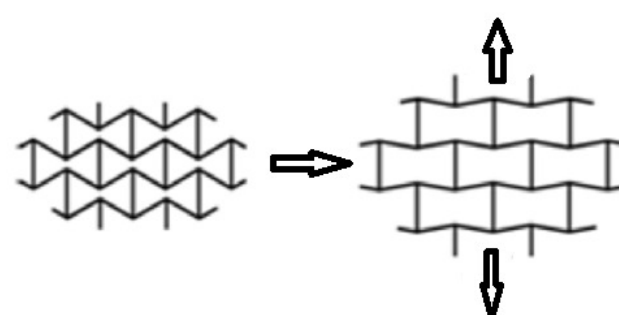
Geometry/ Structure	Mechanism (Auxetic Behaviour)	Diagram & Reference
2D Conventional honeycomb	Stretching of the ribs	 <p>Rib stretching = auxetic</p> <p>(117)</p>
2D Re-entrant honeycomb	Flexure and/or hinging of the diagonal ribs	 <p>UNDEFORMED</p> <p>DEFORMED</p> <p>(120,162,165)</p>

Table 3.3: Auxetic structures and their mechanisms 2.

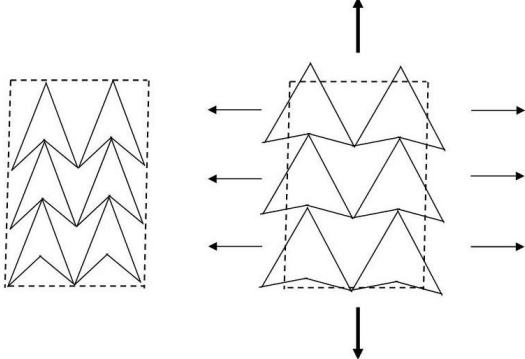
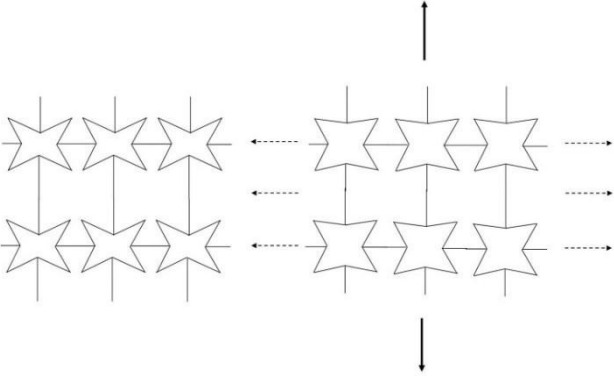
Geometry/ Structure	Mechanism (Auxetic Behaviour)	Diagram & Reference
Double arrow-head	Opening or closing of the arrowheads due to rib flexure and/or hinging	 <p>The diagram illustrates the mechanism of a double arrow-head auxetic structure. On the left, a unit cell is shown within a dashed rectangular boundary. On the right, the same unit cell is shown in an expanded state, with horizontal arrows pointing outwards from the sides and vertical arrows pointing outwards from the top and bottom, indicating lateral expansion during stretching. The reference (165,166) is noted below the diagram.</p> <p>(165,166)</p>
Star honeycomb	Opening or closing of the stars due to rib flexure and/or hinging	 <p>The diagram illustrates the mechanism of a star honeycomb auxetic structure. On the left, a unit cell is shown within a dashed rectangular boundary. On the right, the same unit cell is shown in an expanded state, with horizontal arrows pointing outwards from the sides and vertical arrows pointing outwards from the top and bottom, indicating lateral expansion during stretching. The reference (165–168) is noted below the diagram.</p> <p>(165–168)</p>

Table 3.4: Auxetic structures and their mechanisms 3.

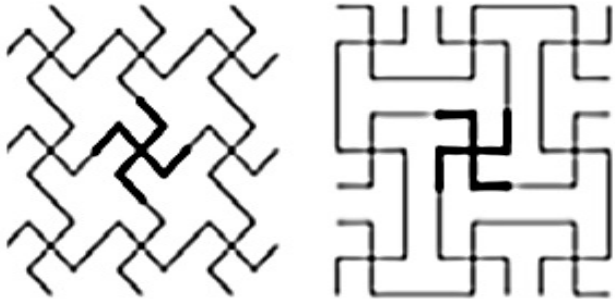
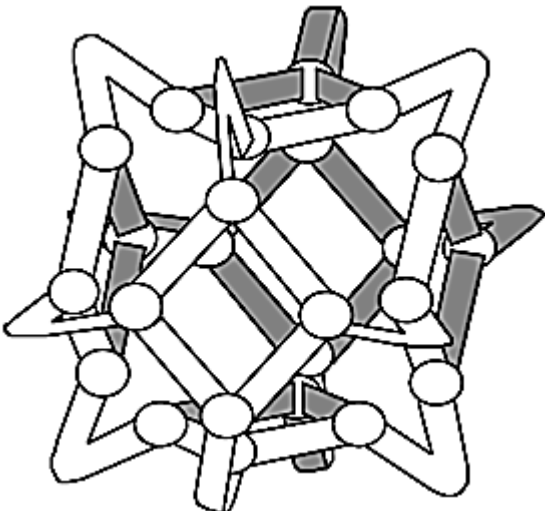
Geometry/ Structure	Mechanism (Auxetic Behaviour)	Diagram & Reference
Lozenge & square grids containing 'missing' ribs	Rotation of ribs	 <p>This schematic is not a before and after of the same geometry but represents two alternative missing rib model geometries.</p> <p>(165,169,170)</p>
3D re-entrant structures	Flexure or hinging of the ribs	 <p>(171,172)</p>

Table 3.5: Auxetic structures and their mechanisms 4.

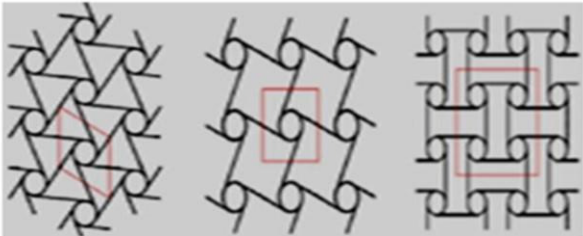
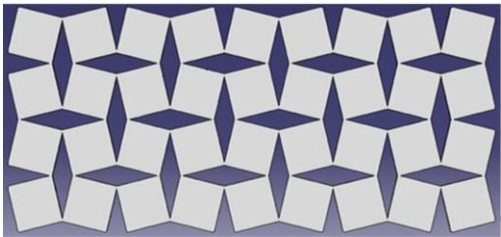
Geometry/ Structure	Mechanism (Auxetic Behaviour)	Diagram & Reference
Chiral honeycomb	Node rotation and ligament flexing	 <p>HEXACHIRAL TETRACHIRAL ANTI TETRACHIRAL</p> <p>(165,173–177)</p>
Rotating polygonal units – (a) Triangle units (b) Square units (c) Rectangle units (d) Tetrahedron units	Rotation or dilation of the polygonal units	 <p>Rotating Square Units</p> <p>(165,167)</p>

Table 3.6: Auxetic structures and their mechanisms 5.


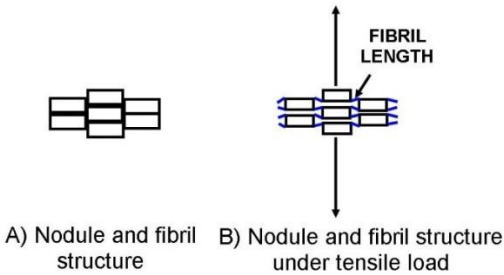
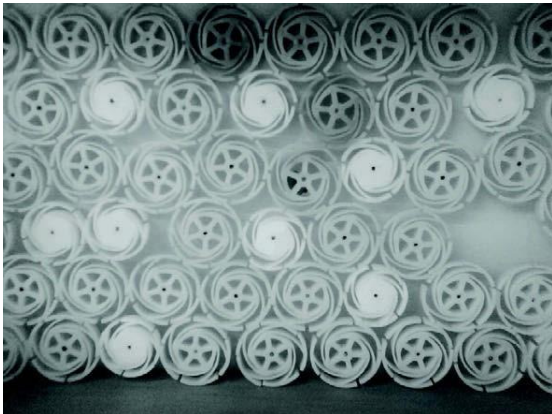
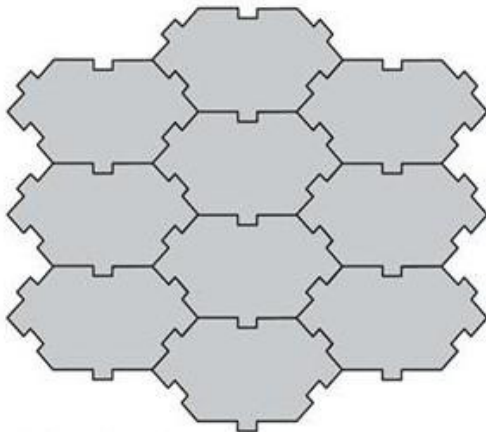
Geometry/ Structure	Mechanism (Auxetic Behaviour)	Diagram & Reference
Sinusoidal/ elliptical ligaments	Simultaneous rotation and expansion of ligaments	 (178)
Nodule-fibril structure which consists of nodules interconnected by fibrils	Lateral nodule translation through hinging of the fibrils on application of tensile load	 A) Nodule and fibril structure B) Nodule and fibril structure under tensile load (123)

Table 3.7: Auxetic structures and their mechanisms 6.

Geometry/ Structure	Mechanism (Auxetic Behaviour)	Diagram & Reference
2D granular material	Dilation of contacting particles	 <p>(179)</p>
2D 'Rough Particle' model consisting of interlocking hexagons	Deformation by particle translation along the interlocks	 <p>Full densified interlocking hexagonal structure</p> <p>(180)</p>

Some of the auxetic geometries and mechanisms identified above have been used for novel biomedical device applications and these are reviewed in the following section.

3.4.5 Biomedical applications

Auxetic materials have been employed or proposed in the design and development of medical devices with enhanced functionality or optimised capabilities and these are summarised below.

An auxetic arterial material (expanded polytetrafluoroethylene also known as ex-PTFE) in contrast to a blood vessel made of conventional material (fibrillar polyurethane) becomes thicker in response to a pulse of blood flowing through it, preventing rupture of the arterial wall.⁽¹⁸¹⁾

The lateral expansion of an auxetic PTFE sheath in a dilator to open the lumen of an artery occurs in response to axial expansion applied by movement of a central guide wire using a simple finger–thumb mechanism, similar in principle to operation of a hypodermic syringe (Figure 3.13).⁽¹⁸²⁾

The elimination of inflating a balloon, desirable control over radial expansion of the dilator device by the physician, and possibility of developing dilators of various diameters for patient-specific and/or controlled distention operation are the key benefits of deploying auxetic expansion members over conventional balloon catheters. Auxetic ultra-high molecular-weight polyethylene (UHMWPE) has been proposed as an alternative liner component.⁽¹⁸³⁾ UHMWPE is stronger than PTFE allowing a thinner lining to maximise the diameter of the inner lumen with respect of the outer profile of the catheter. UHMWPE offers superior mechanical properties for instance, high lubricity, flexibility, and abrasion resistance than PTFE.

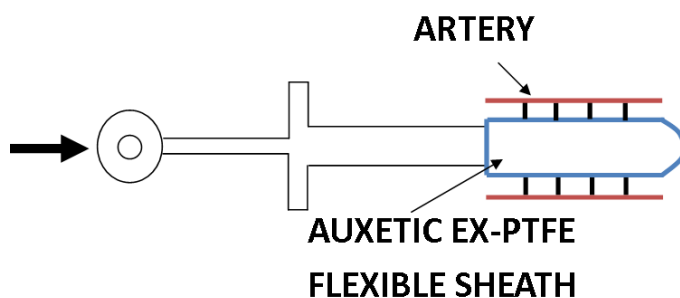


Figure 3.13: Dilator device with an auxetic expansion member.⁽¹⁸²⁾

An auxetic smart bandage concept envisages opening of auxetic fibre micropores, responding to fibre stretching due to wound swelling, to facilitate

the controlled release of guest active pharmaceutical ingredients (API) onto the wound (Figure 3.14).⁽¹⁸⁴⁾ Subsequent wound healing relaxes the fibres due to reduced swelling of tissues and switches off release of the API. Recent developments in the field of the auxetic knit fabrics^(41-43,75) and auxetic fabrics⁽¹⁸⁶⁾ (carefully arranged double helix yarns) have promoted further the idea of smart bandages. Moreover, the release of guest material from an auxetic host has been demonstrated in honeycomb and foam materials^(187,188) as well as in computer simulations of auxetic molecular sieves.⁽¹⁸⁹⁾

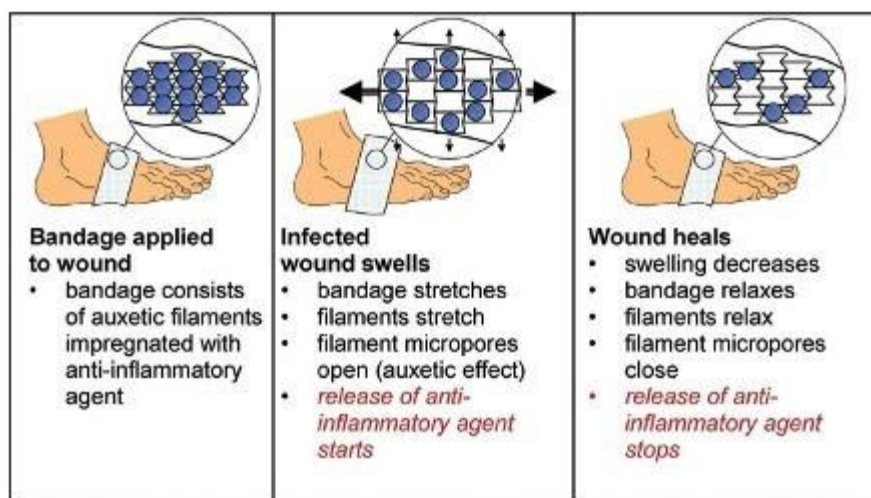


Figure 3.14: Schematic of smart bandage concept.⁽¹⁸⁴⁾

Auxetic copper foam and polypropylene (PP) monofilaments have been demonstrated to have superior anchoring and fixation properties^(190,191) with potential in medical devices such as bone anchors and sutures, for example.⁽¹⁶²⁾ The enhanced mechanical properties of auxetic materials reviewed in Section 3.4.3 present unique opportunities to develop novel adjustable and conformable lining materials for improved comfort and energy absorbing prosthetic limb sockets.⁽¹⁸¹⁾ Auxetic foam pads are expected to improve wearer acceptance and compliance in hip protector devices due to improved comfort/fit (double curvature), enhanced energy absorption (impact response) and lower device weight and/or volume.^(192,193)

Auxetic materials are expected to play an important role in implant devices. 3D auxetic cellular structures (hexagonal, octahedral and rhombic

dodecahedral) have been fabricated from biocompatible alloy (Ti-6Al-4V alloy) and suggested to augment bone in-growth and reduce implant stiffness in orthopaedic implants.⁽¹⁹⁴⁾ Auxetic UHMWPE possesses hardness up to a factor of two higher than conventional UHMWPE⁽¹⁹⁵⁾ and this enhanced indentation resistance property has been proposed for the lining of the femoral component of the hip replacement device during Total Hip Arthroplasty (THA).⁽¹⁸¹⁾ The honeycomb-like re-entrant auxetic structure has been proposed to be useful as a bone material substitute or as part of a bone implant.⁽¹⁹⁶⁾ A functionally graded auxetic (FGA) structure (gradient of conventional and re-entrant honeycombs) has been proposed to provide continuous contact between bone and stem, inter-connectivity and custom porosity which would not only be expected to match bone stiffness and architecture but also to enhance bone fixation and osseointegration.⁽¹⁹⁷⁾

An auxetic re-entrant honeycomb material has been proposed for use as an artificial intervertebral disc sheath material to reduce lower back pain by reducing disc bulge under compression.⁽⁸⁷⁾⁽¹⁹⁸⁾ Reduced disc bulging has been confirmed in a Finite Element Modelling investigation, although an increase in stress and a decrease in range of motion was also predicted as Poisson's ratio reduced from -0.3 to -0.999.⁽¹⁹⁹⁾ A two-piece artificial intervertebral disc implant incorporating 3D auxetic mesh structure has been developed, claiming enhanced shear modulus, indentation resistance, fracture toughness, energy absorption and disc bulge mitigation.⁽²⁰⁰⁾

Auxetic polyurethane (PU) foam has shown excellent shock absorbing properties and hence has been proposed as a superior material for the design of shoes for diabetic patients.^(201,202) The elastomeric monolith of an intra ocular lens (IOLs) fabricated with anisotropic auxetic material provides double curvature reactions by elastically engaging the lens capsule to optimise force transduction from zonular tensioning and de-tensioning forces.⁽²⁰³⁾ Tissue engineering scaffolds possessing negative Poisson's ratio have been proposed to be more ideal than positive Poisson's ratio scaffolds⁽²⁰⁴⁾ by mimicking the properties of native tissues and accommodating and transmitting forces to the native tissues^(129,205,206). An

NPR scaffold would expand biaxially in both the axial and transverse directions simultaneously. Fozdar⁽²⁰⁵⁾ and Sonam^(129,207) have fabricated single and multi-layered three-dimensional polyethylene glycol (PEG) scaffolds from arrays of re-entrant honeycomb with tuneable in-plane strain-dependent negative Poisson's ratios.

Auxetic stent:

Stents are tubular expanding structures that keep the blood vessels or any other tubular organ open. The prominent use of a stent is for the coronary artery to prevent clogging of blood vessels in patients with cardiac arrests. Other than a coronary stent, an auxetic oesophageal stent has been reported for the palliative treatment of oesophageal cancer.⁽²⁰⁸⁾ Auxetic geometries such as 2D re-entrant honeycomb (Table 3.2), rotating square (Table 3.4), and sinusoidal ligaments (Table 3.5) were considered for the development of the stent.^(209,210)

The ideal stent must possess a high degree of expandability, minimal foreshortening and dog-boning, and conformability under high strain⁽²¹¹⁾ to prevent clot formation, migration and collapse⁽²¹²⁾. This degree of clinical performance can only be achieved with optimal mechanical behaviour which in turn is governed by the design pattern or geometry and fabrication material. Mizzi et al⁽²⁰⁹⁾ have explored the mechanical behaviour of stent design using re-entrant (auxetic) honeycomb geometries. Several patents have also been filed highlighting the significance of auxetic geometries in improving design patterns⁽²¹³⁾, for optimizing expansion ratio⁽²¹⁴⁾, and alternatives to existing tubular liners⁽²¹⁵⁾. In addition, an auxetic drug-eluting stent⁽²¹⁶⁾ and an auxetic oesophageal stent for the prevention of dysphagia⁽²¹⁷⁾ have also been reported. The high circumferential strength in their expanded configuration and the low flexural rigidity in their crimped configuration, making the insertion procedure easier, are key attributes of auxetic stents responsible for the upward trend in research in this area.

Tuneable mechanical properties, including negative Poisson's ratio, of re-entrant 3D origami structures based on the Tachi-Miura polyhedron (TMP)

have been investigated and proposed for engineering applications⁽²¹⁸⁾. Kuribayashi et al have likewise developed novel deployable auxetic stents considering origami folded pattern design⁽²¹⁹⁾. The small volume of a folded crease structure is used to deliver the stent to the correct location. The creases disappear when the stent is deployed. There are a number of advantages of an auxetic origami stent to optimize the mechanical behaviour and clinical performance of the deployed stent over currently deployable stents comprising strut structure and cover components^(181,219). These include avoiding geometrical incompatibility between cover and stent, reduced manufacturing cost due to absence of cover-to-stent attachment, elimination of cover-sliding with respect to struts, and mitigation of uneven distribution of stresses, entanglement or rupture during expansion.

The expansion mechanism of auxetic stent to open the lumen of the coronary artery can be explored to develop expansion mechanisms in this project. Elasticity theory, beam theory, cellular structures and auxetic materials have, then, been reviewed in this chapter to understand the mechanical properties of materials and their role in investigating expansion mechanisms for space creation and organ retraction in keyhole surgery.

3.5 Summary

Elasticity and beam theories were reviewed to explain mechanical properties and the mechanics, respectively essential for the development of the cellular and non-cellular (beam/strips) semi-rigid expansion mechanisms. Analytical model for honeycombs (i.e. cellular structure) was reviewed and envisaged to utilise during finite element modelling and designing of expansion mechanisms. Auxetic materials and structures were especially reviewed for their unique mechanical properties owing to negative Poisson's ratio, structure-mechanism combinations, and applications in medical device design and development. Auxetic honeycomb structure-mechanism combinations is considered in this project as one of the expansion mechanism.

4 Materials and Methodology 1: Abdominal simulator and in-vivo measurement of organ surface pressures and retraction distances

The methodology for the fabrication and assessment of simulant organs, the development of in-house test rigs, and in-vivo measurement of surface pressures and retraction distances applied to key abdominal organs during surgery are described in this chapter.

4.1 Selection of simulant organ materials

An in-house abdominal simulator has been developed for the quantitative assessment of the space creation and organ retraction functions of prototype expanding structures. It is composed of equivalent simulant materials that mimic the biomechanical properties of the key human abdominal organs. The materials screened for the fabrication of such simulant organs are described in this section.

4.1.1 Solid organ simulant materials

The physical properties of materials evaluated for solid organ (liver, kidney and spleen) simulants are density, shore hardness, and thermal stability. Table 4.1 describes the physical properties of the materials from the technical data sheet of each material sourced for consideration.

The physical properties of nutrient gelatine were not provided in the technical data sheet. The shore hardness scale developed by Smooth-on, Inc. suggests that shore hardness of gel-like material ('gummi' jelly candy) is measured on Shore A00 scale.⁽²²⁰⁾ Gelatine is the preferred material to make 'gummi' jelly candy and hence, the shore hardness of jelly candy was considered as the shore hardness of the solid simulant (fabricated in round shape in 55mm diameter petri dish, 10mm thickness) made using nutrient gelatine. The volume of nutrient gelatine simulant was measured by the water displacement method. The volume was obtained by subtracting the final volume of water from the initial volume of water when the simulant was placed inside a 1L volumetric flask. The density of nutrient gelatine simulant was calculated after measuring the weight of the simulant on a weighing

scale. The thermal stability of nutrient gelatine simulant was assessed by observing the melting point at room temperature and during manual handling.

The sample material of silicone sponge provided by SPG Ltd was stable at room temperature and retained physical dimensions during manual handling. The density and shore hardness of silicone sponge was supplied in a technical data sheet. The physical properties of silicone sheet, silicone sealant, and silicone foam (extra firm) were given in the respective technical data sheet.

The volume of silicone gel simulant (fabricated in round shape in 55mm diameter petri dish, 10mm thickness) was measured by the water displacement method. The density was calculated after measuring the weight of the simulant on a weighing scale. The thermal stability was assessed by observing the melting point at room temperature and during manual handling.

Table 4.1: Physical properties of materials evaluated for the solid organ simulants.

Material or Product name	Supplier (Product number/code)	Density (kg/L)	Shore hardness scale	Thermally stable at room temperature (°C)
Nutrient Gelatine	Sigma Aldrich (70151)	1.00±0.01	00 ⁰ (shore A) ⁽²²⁰⁾	No
Expanded Silicone Sponge	SPG Ltd. (FT1 515)	0.26	45±5 ⁰ (shore 00)	Yes
Silicone Sheet	Polymax (FDA 60)	0.20	60±5 ⁰ (shore A)	Yes (-60 ⁰ - 200 ⁰)
Silicone Sealant	Momentive (RTV116)	1.09	20 ⁰ (shore A)	Yes (-60 ⁰ - 260 ⁰)
Silicone Foam (extra firm)	Stockwell Elastomerics (Bisco® HT-840)	0.45	10 - 70 ⁰ (shore 00)	Yes (-67 ⁰ - 392 ⁰)
Silicone Gel	PS Composites (PRO GEL 10)	1.04±0.04	57 ⁰ (shore 00)	Yes

To rank each material, the density, shore hardness and thermal stability were given a score of 0, 0.5 or 1, corresponding to poor, moderate and good assessment, respectively (Table 4.2). The density of the material should be as close as possible to the density of human liver (Table 2.5, Chapter 2), kidney (described in text in Chapter 2.1.2), and spleen (Table 2.15, Chapter 2, Chapter 2) reviewed in Chapter 2. The material must be able to retain the physical dimensions of the liver, kidney and spleen (Table 2.2, Table 2.8, and Table 2.12, Chapter 2, respectively) at room temperature to meet the thermal stability requirements.

Equation 4.1 was established to obtain the total score for each material outlined in Table 4.2, which places a higher weighting for density over shore hardness, and recognises that thermal stability is critical for any simulant material in practice. The total score was highest for silicone gel (Table 4.2) compared to the other materials. Hence, silicone gel was selected for the fabrication of solid simulants.

$$Total\ score = [2(Density) + Shore\ Hardness](Thermal\ stability) \quad 4.1$$

Table 4.2: Score table for each material assessed for solid organ simulants.

Types of Material	Physical Properties			
	Density	Shore Hardness	Thermal Stability	Total Score
Gelatine	1	1	0	0
Silicone sponge	0	1	1	1
Silicone sheet	0	0.5	1	1.5
Silicone sealant	1	0.5	1	2.5
Silicone foam	0	1	1	1
Silicone gel	1	1	1	3

Silicone gel:

Silicone forms a broad family of synthetic organosiloxane polymers containing a repeating silicon-oxygen backbone with organic side groups attached via carbon-silicon bonds. Depending on their structure, they are classified as liquids, gels or elastomers (Figure 4.1). Silicone gel has inherent physical properties such as wide operating temperature range -115 to 300°C, resistance to humidity and water, no or low toxicity, does not support microbial growth, and low chemical and thermal conductivity.(221)

Advanced prosthetic-grade silicone, Pro Gel 10, was purchased from PS composites, UK. It consists of Part A, Part B, and Pro Gel softener. The chemical names of Part A and Part B as well as Pro Gel softener were not disclosed by PS Composites. However, the combination of Part A and Part B are a two-part platinum silicone system with a mix ratio of 1:1. Pro Gel softener is mixed with the mixture of two-part (Part A and Part B) Pro Gel 10 system at a ratio of anywhere from 20-80% v/v to soften the silicone mixture. The Pro Gel 10 softener enables cross linking of Part A and Part B, with the resulting flexible and soft nature of the silicone gel simulant depending on softener concentration (% v/v).

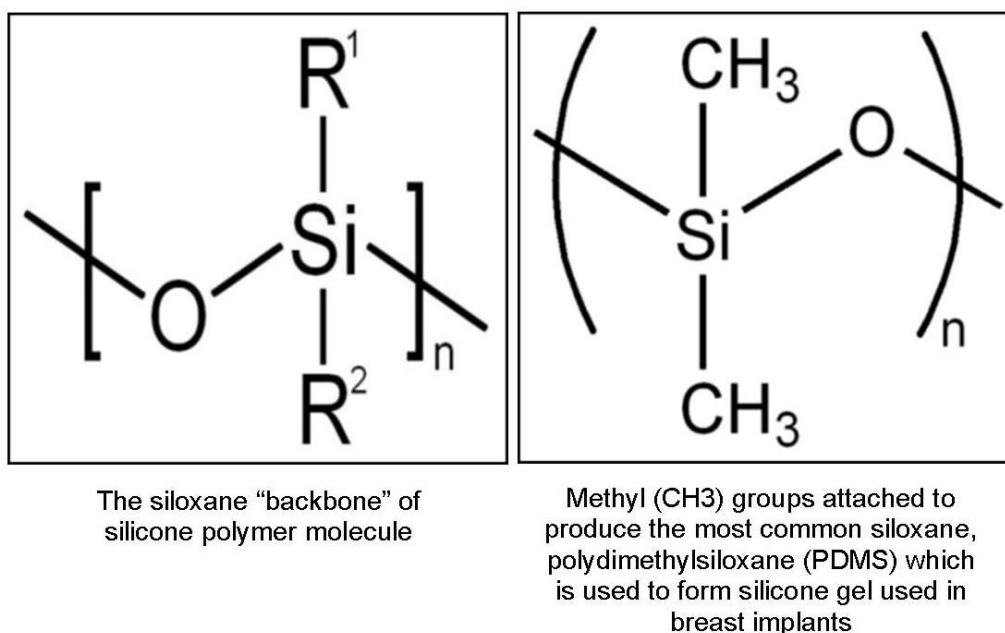


Figure 4.1: Structure of silicone and silicone gel.(221)

4.1.2 Hollow organ simulant materials

The hollow stomach simulant was built using thermoplastic polyurethane. This material was selected since it can be inflated by filling with a mixture of water and air to match the physical dimensions and the pliability of the human stomach.

The mechanical characteristics (especially elasticity) of latex rubber material (10000-100000 kPa)(222)(223) can be considered to achieve the elasticity of the human bowel (Table 2.23, Chapter 2). Hence, unlubricated condoms (Durex® Thin Feel), manufactured from the latex rubber material, were

considered as a choice of material for the hollow tube required for the development of simulant bowel. Durex® Thin Feel condom is a transparent latex material and has nominal width and length of 56mm and 200mm, respectively.(224) The hollow tubes were filled with different concentrations (% weight) of wallpaper paste (B & Q All Purpose Wallpaper Adhesive) since the bowel is generally filled with digested food and water.

4.2 Fabrication of the simulant organs

Solid simulant organs such as the liver, kidney and spleen were fabricated using the Pro Gel 10 system. Hollow simulant organs such as the bowel and stomach were fabricated from compliant and inflatable material to allow them to be filled with a mixture of water-wallpaper paste and a mixture of water-air, respectively.

4.2.1 Solid organ simulants

Fabrication of solid organ simulants was carried out in two steps. The first step was to prepare moulds which match the physical dimensions of the human kidney, spleen and liver outlined in Chapter 2. The second step was to mix the Pro Gel 10 system using predetermined consistencies of Pro Gel 10 softener to match the elasticity of solid organ simulants reviewed in Chapter 2.

Preparation of moulds:

Human kidney simulants were fabricated using a kidney bean shaped in-house rubber mould (Figure 4.2). The physical dimensions of the human spleen (Table 2.12, Chapter 2) closely match those of the human kidney (Table 2.8, Chapter 2) and, hence, simulants of the human spleen were fabricated from the same mould shown in Figure 4.2.



Figure 4.2: Mould for fabrication of simulant of human kidney and spleen.

The mould for the fabrication of human liver simulants was developed to achieve the complex contours of the human liver (Figure 2.3 and Table 2.2, Chapter 2). The steps are described below.

- The anonymised database of CT scan images of adult and healthy human abdomen-pelvic regions was obtained from the Radiology Department of (MRI), MFT in Manchester, UK. CT scan images showed the anatomy of the abdomen and pelvic organs in 333 slices. The liver anatomy was seen between the 5th and 134th slice (Figure 4.3).
- CT scan slice (number 25) was calibrated using the 'known dimension (abdominal region of 28 cm)' (Figure 4.4).

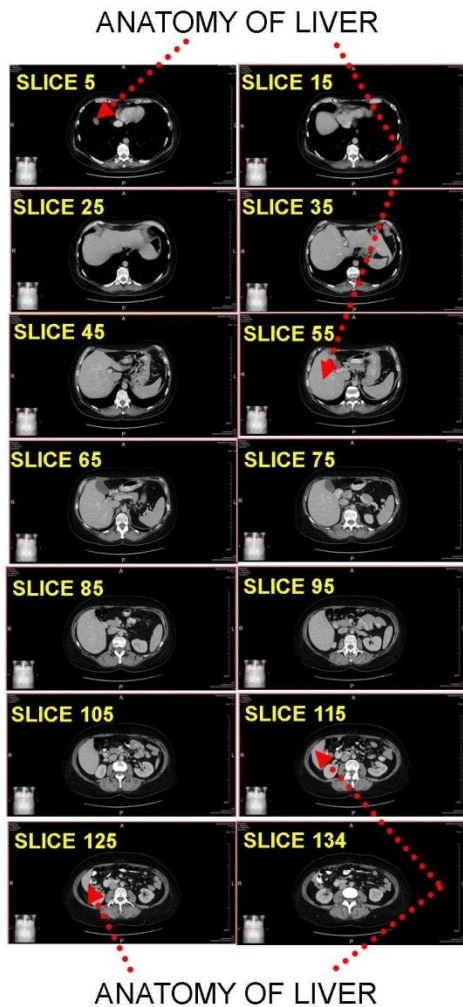


Figure 4.3: CT scan images showing anatomy of human liver.

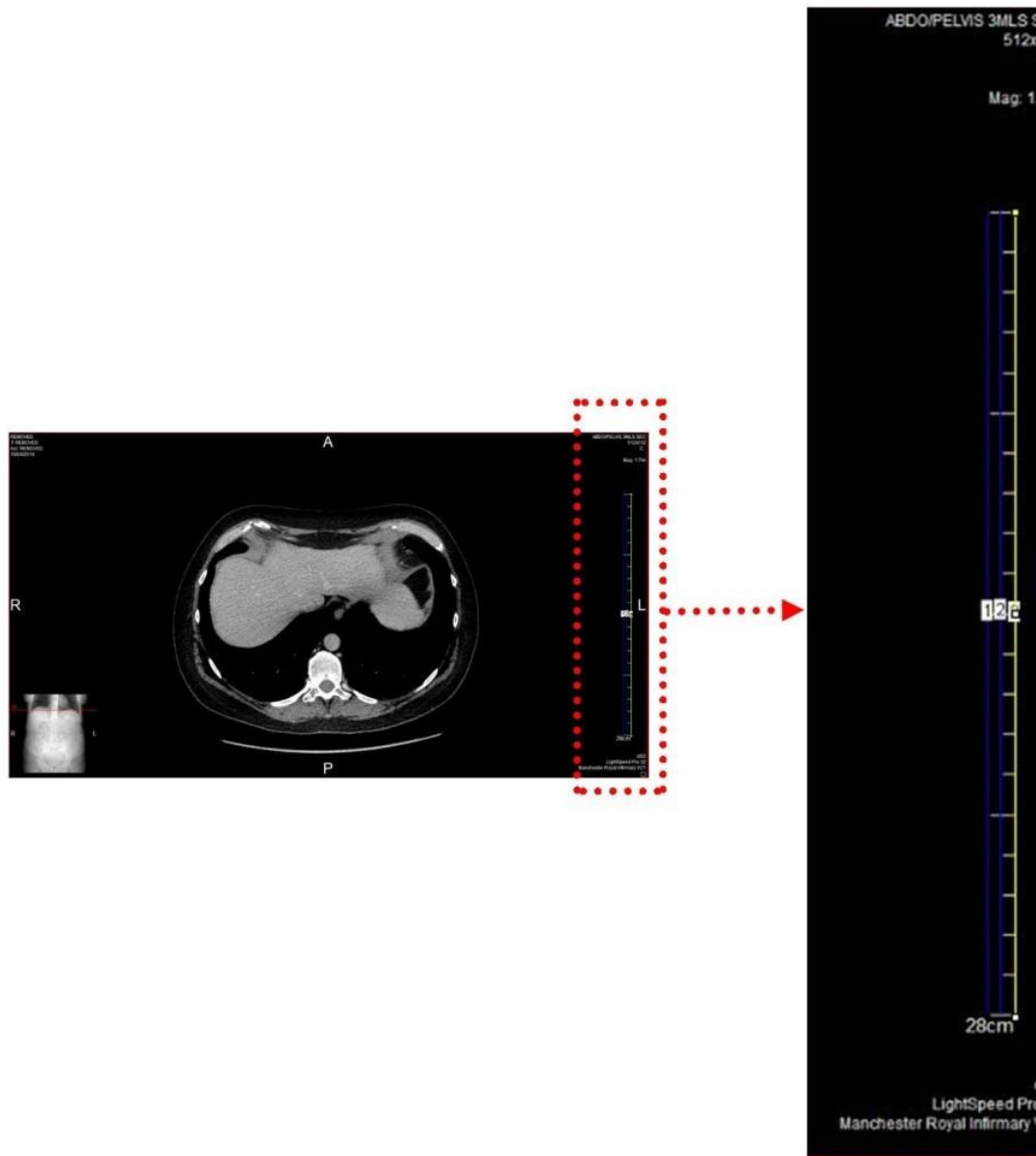


Figure 4.4: Calibration of CT scan slice.

- The dimensions of each CT scan slice extracted from the database were 1681×1051 (in pixels) and hence, calibration was carried out for only one slice.
- Every tenth slice from the 5th slice was assigned a series of points (yellow in colour in Figure 4.5) to obtain the coordinates of the liver surface in the plane of the slice using image analysis software – ImageJ (Version 1.48) (Figure 4.5).(225)

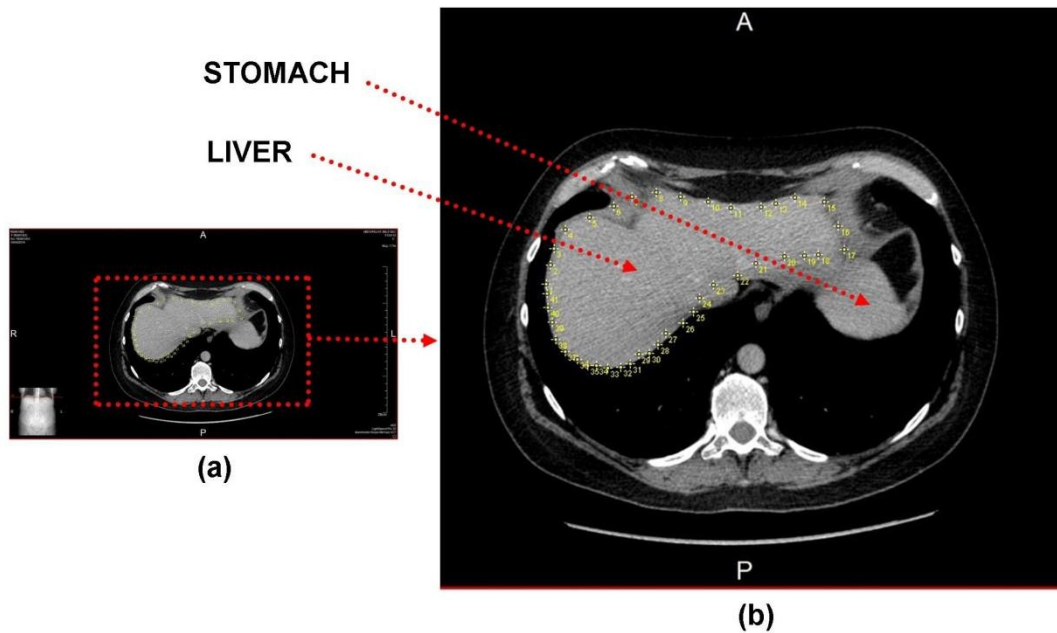


Figure 4.5: CT scan slice showing 2D coordinates of human liver. (a) Slice number 25, (b) Series of point (yellow in colour) to extract 2D coordinates of liver in the plane of the slice are shown in the enlarged image.

- Each slice taken by the CT scan instrument had a thickness of 1.3 mm which, combined with the number of the slice, was used to generate the 3rd coordinate for each point on the liver surface. The 3D coordinates (.txt file) were imported into the SolidWorks software (2014-15 version) to create the CAD part file using the 'ScanTo3D' process. The CAD file was thereafter imported into a 3D printer (Model: ABS P400; Make: Dimension SST 768). A 3D hollow but rigid liver model was fabricated from Acrylonitrile Butadiene Styrene (ABS) material (Figure 4.6).



Figure 4.6: 3D printed liver from ABS material.

- Process of making 2-parts silicone rubber mould:
 - Acrylic sheets were glued together to create a cube chamber five times the volume of the ABS liver model. An acrylic tube was clamped to the chamber and the bottom part was glued on to the top surface of the ABS liver model and positioned in the centre of the chamber (Figure 4.7).
 - A two-component silicone rubber (VTV 740, Renishaw plc) was mixed to make 4.5L (three times the volume of the liver). This mixture was then mixed with 1% catalyst, also known as vulcanising agent. The resultant mixture was blended and scraped from the sides and bottom of the container to ensure that there were no unmixed pockets of material. The final mixture was vacuumed to extract all excess air out of the mixed silicone.
 - The petroleum jelly was used as release agent and applied on the both surfaces of the ABS liver model. The deaerated mixture was subsequently poured into the chamber in a slow steady stream and allowed to flow freely around and over the model. The silicone rubber was allowed to cure for 24 hours at room temperature.
 - The chamber and acrylic tube were removed. The ABS liver model encapsulated inside the cured silicone rubber mould was removed by halving the mould by scalpel from the hole created due to presence of acrylic tube. This final step resulted in a two-part silicone rubber mould (Figure 4.8).

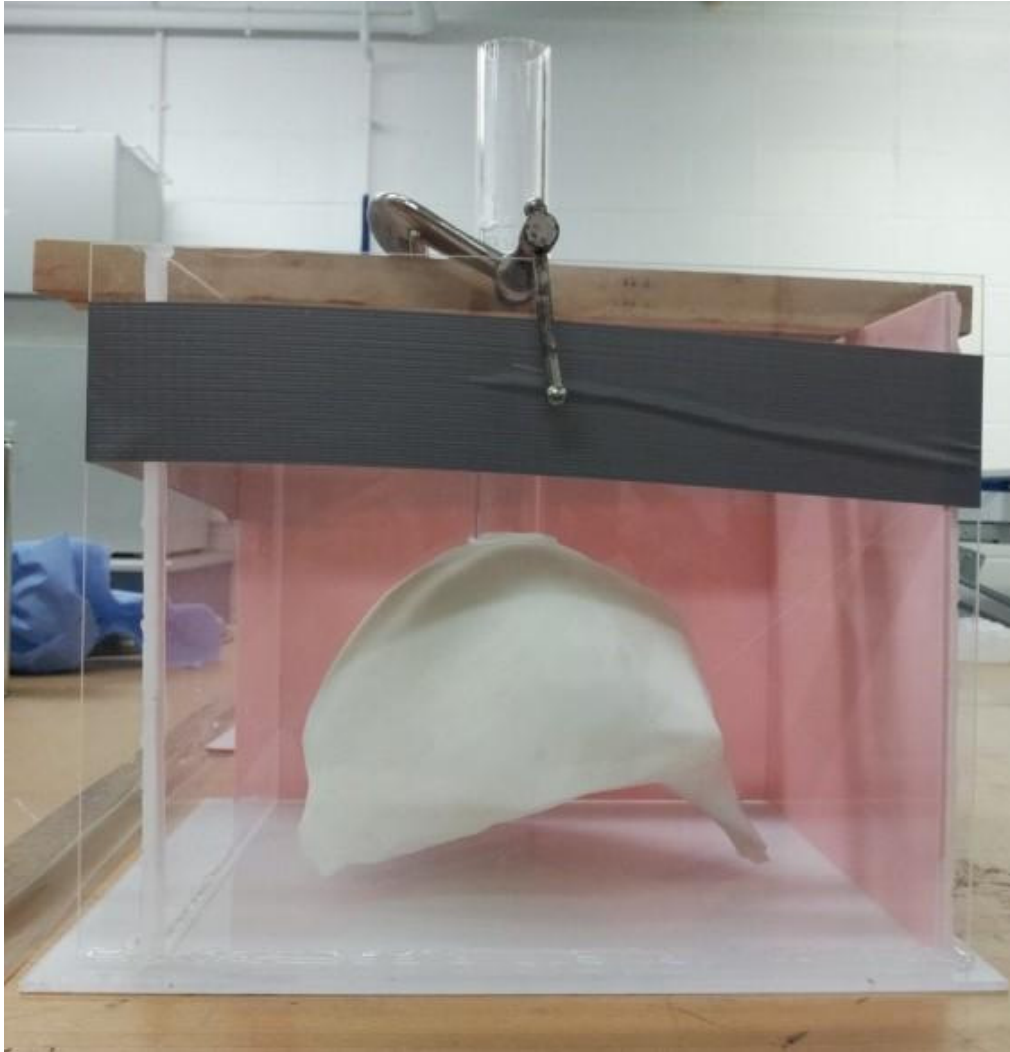


Figure 4.7: Assembly for making 2-part silicone rubber mould.



Figure 4.8: Two-part silicone rubber mould.

- The acrylic tube left a hole on the top surface of the 2-part silicone rubber mould. The hole was used to pour the mixture of Pro Gel 10 system to fabricate human liver simulants.

Fabrication of solid simulants of human organs:

Solid simulants were cured using different concentrations of Pro Gel 10 softener (20-70% of total volume weight of simulants). Table 4.3 shows the quantity of Part A, Part B, and Pro Gel softener of the Pro Gel system mixed to determine the density and elasticity of simulant organs most closely

matching the density and elasticity of human abdominal organs reported in Chapter 2.1.

Table 4.3: Fabrication of solid organ simulants using the Pro Gel 10 system.

Solid organ simulant	Final consistency (% v/v)	Target Volume (L)	Target Density (Kg/L)	Pro Gel 10 softener (L)	Part A (L)	Part B (L)
Kidney	20	0.16 ± 0.03 (Table 2.9)	1.09 (Chapter 2.1)	0.032	0.064	0.064
	30			0.048	0.056	0.056
	40			0.064	0.048	0.048
	50			0.080	0.040	0.040
	60			0.096	0.032	0.032
	70			0.112	0.024	0.024
Spleen	20	0.152 ± 0.055 (Table 2.13)	1.045 (Table 2.15)	0.304	0.608	0.608
	30			0.456	0.572	0.572
	50			0.76	0.42	0.42
Liver	20	1.475 ± 0.23 (Table 2.3)	1.06 (Table 2.5)	0.295	0.59	0.59
	30			0.442	0.516	0.516
	50			0.737	0.370	0.370

Part A and Part B of the Pro Gel 10 system were mixed in a clean dry container by stirring gently and manually with a stainless steel or wooden rod without forming any air bubbles. The resultant mixture was allowed to react for 10 – 15 minutes. A predetermined concentration of softener (% v/v) was subsequently mixed gradually and with constant manual stirring. For aesthetic appearance, food colours (Dr Oetker Gel Food Colour) were obtained from the local supermarket. The brown colour for the kidney, green colour for the spleen, and red colour for the liver were added in the proportion of 1% of the total volume of the simulant in the final mixture with continuous stirring. The final mixture was poured into the moulds of the

kidney, spleen and liver and left to cure at room temperature for 3-4 hrs. Simulants of the liver, kidney and spleen were taken out of their respective moulds when completely cured.

The kidney simulants were fabricated using 20-70% v/v range of the Pro Gel softener. There was an onset of stickiness in the kidney simulants when the Pro Gel 10 softener concentrations were greater than 50% v/v. This caused significant inconvenience in manual handling. Hence, the spleen and liver simulants were subsequently fabricated only with 20% v/v, 30% v/v and 50% v/v concentrations of Pro Gel 10 softener.

Fabrication of solid simulants of pig organs:

An assessment of the elasticity of simulant organs was evaluated against real organs in this project to assess the effect of the quantity of the Pro Gel softener concentration. There are obvious difficulties in measuring the mechanical properties of human organs in their natural state as well as in-vitro in this project. Hence, the elasticity of solid simulants was compared against the elasticity of pig simulants. Fabrication of solid simulants of pig liver and kidney were therefore carried out and is reported in this section. Pig liver and kidney were sourced from a local butcher to carry out in-vitro mechanical tests.

The physical dimensions of pig kidney (Chapter 2.1) closely match those of the human kidney (Table 2.8, Chapter 2) and, hence, simulants of human kidney were used as simulants of pig kidney during the in-vitro mechanical tests.

The physical dimensions of pig liver are not identical to human liver and, hence, a 2-part mould using modelling clay and Plaster of Paris (PoP) was developed for the pig liver (Figure 4.9). The steps of making the 2-part mould are outlined below.

- Making one side of the mould: A container 5cm larger than all sides of the pig liver was chosen. The container was filled with the clay to a depth that allowed the pig liver to be embedded to the half-way point

with approximately 2.5cm of clay beneath the pig liver. The clay surface was smoothed out to a flat even finish.

- Registration hole: It is required to fit the finished 2-part mould halves together. This was done by making a ~1.25cm circular indentation in one corner of the clay surface by fingertip. The indentation allowed plaster to subsequently flow into it, creating a raised bump. When the second half of the mould was poured, a reverse 'hole' matched the raised bumps of the first mould half.
- Create a pouring spout: A spout was created to enable pouring of plaster into the final 2-part mould by placing a length of rolled clay between the pig liver and the wall of the container. Petroleum jelly was applied as release agent to all surfaces of the container.
- Mixing and pouring the plaster: 4.5kg of PoP (three times the volume of pig liver) was mixed with 3L of water ($\frac{2}{3}$ rd the volume of the PoP) at room temperature in a large bucket able to accommodate the full amount of mixed plaster. When the plaster consistency was like a thick cream, it was poured into the mould from a corner so that it found its own way around the pig liver. The mixture was poured into the mould to at least a 2.5cm depth above the pig liver. The plaster was allowed to set for 3-4 hrs.
- Preparation for part two of the mould: Once the plaster mould was set, the container was flipped over to gently peel away the clay, except the clay of the pouring spout which was left in place. The embedded pig liver in plaster was removed by scraping around the edges of the pig liver with a wooden spatula to break the bond between the mould and pig liver.
- Making part two of the mould: The pig liver was placed back into the mould. A release agent was applied to the containers, plaster mould and pig liver and the process of mixing and pouring the plaster was repeated.
- Separating the two mould parts and releasing the pig liver: The entire mould from the container was released once the second half of the mould completely set. A wooden spatula was used to separate the

two parts of the mould. Although the two parts of the mould were separated, the pig liver was still embedded in one part and released by wooden spatula as described earlier.

- Cleaning of the 2-part mould: The 2 parts of the mould were thoroughly cleaned by cold water and soft brush to remove excess clay without damaging the details in the surfaces of the mould.



Figure 4.9: One part of the 2-parts Plaster of Paris pig liver mould.

The pig liver mould was then used to fabricate pig liver simulants as described above for human liver simulants using 20% v/v, 30% v/v, and 50% v/v of Pro Gel softener.

4.2.2 Hollow organ simulants

The stomach is a J-shaped abdominal organ (Chapter 2.1). A J-shaped sketch was drawn and extruded in the SolidWorks (2014-15 version). The CAD file was generated using SolidWorks software (2014-15 version) and used as the input file when the stomach simulant was fabricated by Radio Frequency (RF) welding (M & L Tooling Ltd of Burnley, UK) of polyurethane sheets. It has a capacity to accommodate approximately 1 litre of fluid (water-air mixture) through a tube incorporated during the RF welding process.

RF welding is the process by which electromagnetic energy is used to permanently, hermetically and cohesively bond together thermoplastic

materials such as polyurethane, polyvinyl chloride (PVC), nylon and other customized resins. The RF welding process uses radio frequency energy to produce molecular agitation in thermoplastic materials such that they melt and flow together, forming a bond that is as strong as the original material. During welding, the components were clamped under pressure between machined electrodes. A magnetic field was generated between the electrodes, passing through the components, fusing the material together.

Bowel simulants were fabricated by filling unlubricated condoms (Durex® Thin Feel) with different concentrations of wallpaper paste (0%, 2.5%, 5%, and 7.5 % w/v) to assess their match with the pliability of the human bowel.

4.3 Assessment of biomechanical properties of simulant organs

The density and elasticity of simulant organs were evaluated to identify the closest match with the density and elasticity of human and pig organs.

4.3.1 Evaluation of simulant organ density

Solid simulants were weighed three times to determine their average weight. Volume was measured by the water displacement method. Simulant organs were placed in an appropriate vessel (considering the volume of solid organ simulant) filled with water and the volume of water displaced by simulants was recorded. This was repeated three times to determine an average volume for each simulant organ. For example, the kidney simulant (average volume is 0.160L) was placed inside a 1L capacity volumetric flask filled with 0.5L of water. The volume of kidney was calculated by subtracting the final volume of water plus kidney from the starting volume of water. The density was calculated from the average values of weight and volume and compared with the density of solid organs reported in the literature review in Chapter 2.1.

4.3.2 Evaluation of solid simulant and pig organ elasticity

Simulant organs were evaluated for their elasticity to make an assessment of the effects of different concentrations of Pro Gel 10 softener. In-vitro

mechanical tests on solid simulants of pig liver and kidney, and actual pig kidney and pig liver were carried out to obtain the elastic tangent modulus following protocols like whole organ mechanical testing identified in the literature review (Chapter 2). In-vitro mechanical tests were performed via compression tests using an Instron 3369 Universal Testing Machine (Figure 4.10).

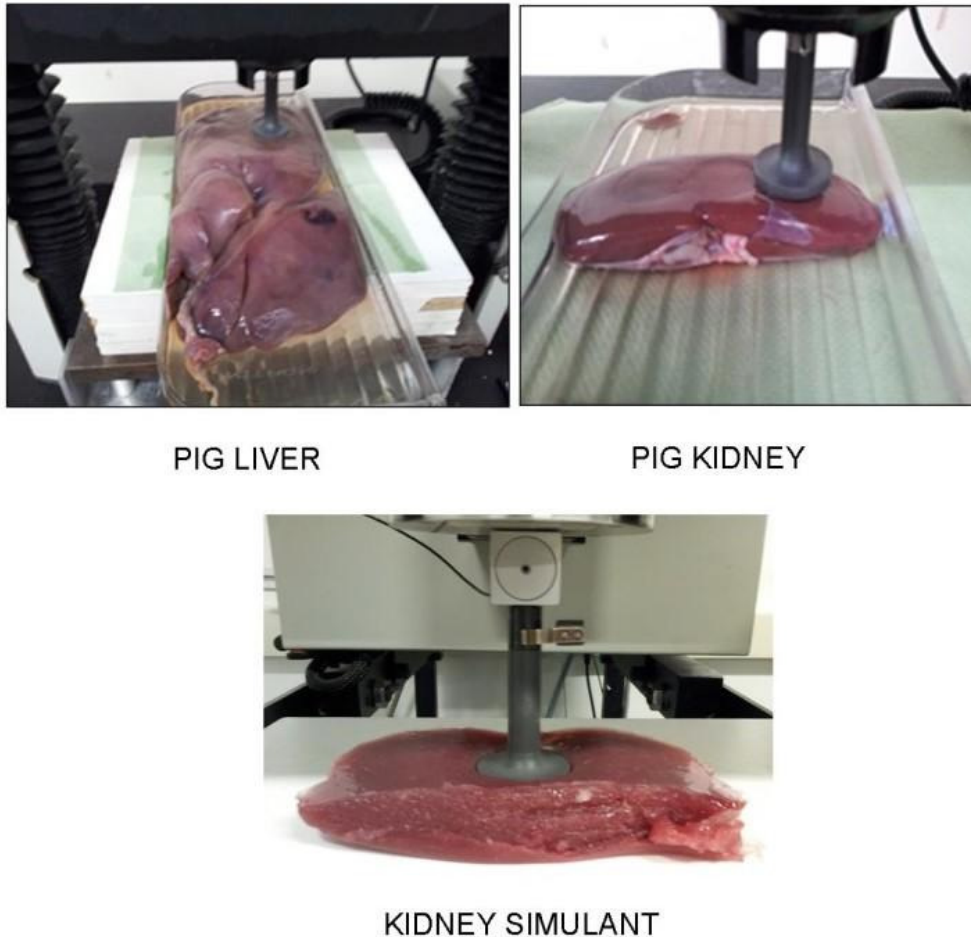


Figure 4.10: Pig liver, pig kidney, and simulant kidney mounted on Instron machine.

The load capacity of the Instron was 100 Newton (N). Compressions tests employing a circular indenter of diameter 35 mm, indentation speed 30 mm/min, to an indentation compression of 10 mm, were performed in a climate-controlled room and the temperature was kept constant at 25 °C during the tests. Preconditioning of the samples was not required during this study. New portions of pig liver and kidney and equivalent simulants were used for each test to ensure that the natural (unconditioned) state of the

sample was compressed. The organ/silicone simulant under study remained intact throughout the experiment, as is the case during abdominal surgery. Force against displacement curves for the right and left lobe of the pig liver, pig kidney, and equivalent simulants were obtained. Force and displacement were converted to stress (calculated by dividing the applied force with the area of indenter) and strain (calculated by dividing average thickness of sample with the displacement), and elastic tangent moduli were obtained from the slopes of the stress vs strain curves. The elastic tangent moduli of pig liver and pig kidney were compared with the elastic tangent moduli of the equivalent simulants of pig fabricated using different concentrations of Pro Gel 10 softener.

It was not possible to obtain samples of pig stomach and pieces of bowel from local butchers which would have allowed the assessment of their elastic tangent modulus, and in turn permitted comparison with stomach and bowel simulants in a similar way to that described earlier for solid simulants. As a result, the evaluation of the elastic properties of hollow simulants was undertaken as part of a survey of surgeons on the biomechanical properties (dimensions, pliability and density) of liver, kidney, spleen, stomach and bowel simulants.

4.3.3 Survey of biomechanical properties of simulant organs

Five surgeons with more than five years' experience of carrying out open and hand assisted laparoscopic abdominal surgery were invited to participate in a survey at the MRI. Titus Augustine was part of the research team and was also involved with the pilot clinical study. Hence, he was excluded from the survey.

The survey sheet for participating surgeons included the background to the project, introduction to simulant organs, and statement of request to participate in the survey. A separate data collection sheet was also provided to the participating surgeons requesting job title, number of years of experience in abdominal surgical procedures, and independent opinions on the overall dimensions, density, and pliability of simulant organs. The

consistencies of material used to fabricate simulant organs were anonymised from surgeons to prevent bias in their opinions.

The survey and data collection sheets are included in Appendix A.

4.4 In-house abdominal simulator

Two types of test-rig were developed as an in-house abdominal simulator. The first test-rig or in-house assembly was used initially to assess the surface pressures applied by the operator on pig and simulant organs. The second test-rig was fabricated to mount on the Instron machine to test the expansion capabilities of prototype structures.

The first assembly was designed as a 'right angled shape', and fabricated using 5 mm thick acrylic sheets. It has a separate adjustable acrylic sheet to vary the volume of the assembly and can be clamped to make it immovable (Figure 4.11). Horizontal and vertical rulers were fixed to gauge the degree of retraction (i.e. squashing, lifting and moving) of simulant organs (Figure 4.11). A digital camera (Nikon D3100) set up on a tripod at the front of the right-angled assembly, evident from Figure 4.11, to capture the movements of the pig and simulant organs within the assembly.

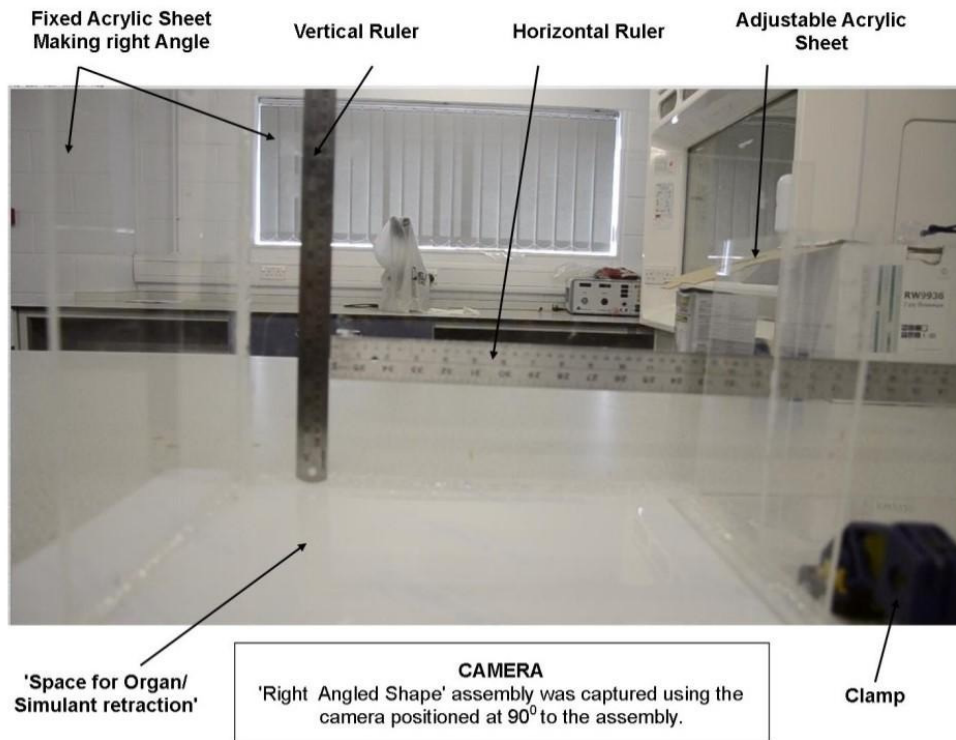


Figure 4.11: Right angle assembly (first test-rig) for the in-house simulator.

The first assembly was developed to evaluate the responses of each of the defined typical 'movements' (finalised following observation of several open and laparoscopic procedures and discussing with surgeons) for pig and simulant organs when surface pressures are applied by the operator. The defined typical 'movements' applied by the surgeon during actual surgical procedures are

- Moving (translation) occurs at the beginning of retraction of bowel for instance prior to the squashing,
- Squashing occurs when spleen for instance, is lifted, moved and then retracted/squashed against abdominal wall,
- Moving (translation) and squashing,
- Lifting generally requires for solid organs for example, liver is lifted and moved to get access to gall bladder and eventually it is fully retracted/squashed against diaphragm.

Pig liver, simulant human liver, and simulant human bowel pieces were placed inside the first assembly. They were evaluated for the defined typical

'movement' when surface pressure is applied by the fingertips of the operator. The thin film pressure sensor (Figure 4.13) was used to quantify the surface pressures applied by the operator.

The second assembly of the in-house abdominal simulator, utilised for the mechanical characterisation of prototype structures, was designed as a rectangular chamber by gluing 5mm thick acrylic sheets to mount on an Instron machine (Figure 4.12). The bottom acrylic sheet (15cm×40cm) had a hole of 68mm diameter exactly in the centre to allow prototype cylinder placement before the start of the test. The top surface of the chamber was open to facilitate the mechanical testing of prototype structures. The front and back sides of the chamber were also kept open in this study although the option is available for them to be closed if required. Two rigid acrylic sheets formed the left and right-hand sides by gluing them to the bottom acrylic sheet and encircling with wire reinforcement towards the top of the assembly.

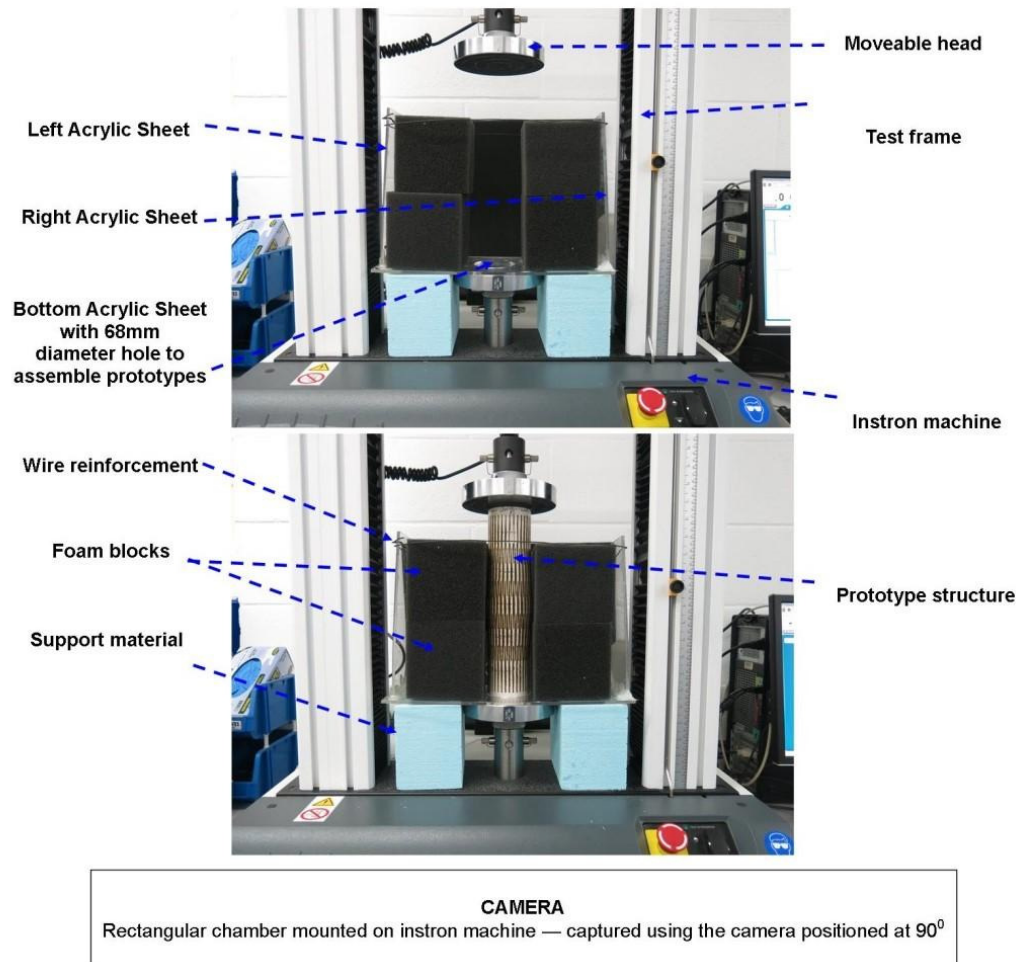


Figure 4.12: Second test-rig mounted on the Instron machine.

4.5 In-vivo measurement of surface pressures

Laparoscopic and open abdominal surgeries involve retraction of abdominal organs. The quantitative assessments of surface pressures applied to the abdominal organs and tissues, and the degree of organ retraction, during surgery are expected to be key inputs for the design and development of prototype expansion structures. Hence, an in-vivo pilot study was carried out to quantify surface pressures and organ retraction distances during open and keyhole abdominal surgeries.

4.5.1 Ethics committee approvals of in-vivo pilot study

The protocol for carrying out the in-vivo pilot study (Appendix B), the patient information sheet and patient consent form (Appendix C) were submitted to the ethics committees of the NHS and Sheffield Hallam University (SHU). Ethical approval for this pilot study was obtained from the North West

National Research Ethics Committee, study ref 13/NW/0258 and is included in Appendix D. The Faculty of ACES Research Ethics Committee (FREC) of Sheffield Hallam University also approved the pilot study.

The complete study protocol contains details on the following:

- description of background to surgical practises and the LaparOsphere™ concept
- rationale for the in-vivo pilot study
- the importance of the outcomes within the PhD research project and to the wider surgical practise
- names and details of participating surgeons as well as study co-ordinators,
- study sites, study procedures, surgical procedures and the setup within the operating theatre
- sterility issues and their remedies
- surface pressure measurement procedures after accessing the patient's abdomen
- inclusion and exclusion criteria
- study size
- confidentiality and data protection
- adverse event and mitigating steps
- data analysis after the completion of the in-vivo pilot study

The patient consent form and the patient information sheet were given to the patients attending for abdominal surgery at the MFT, Manchester, UK.

During pre-op assessment surgeon discussed the study with the patient and asked if they were prepared to take part and obtained signed consent form.

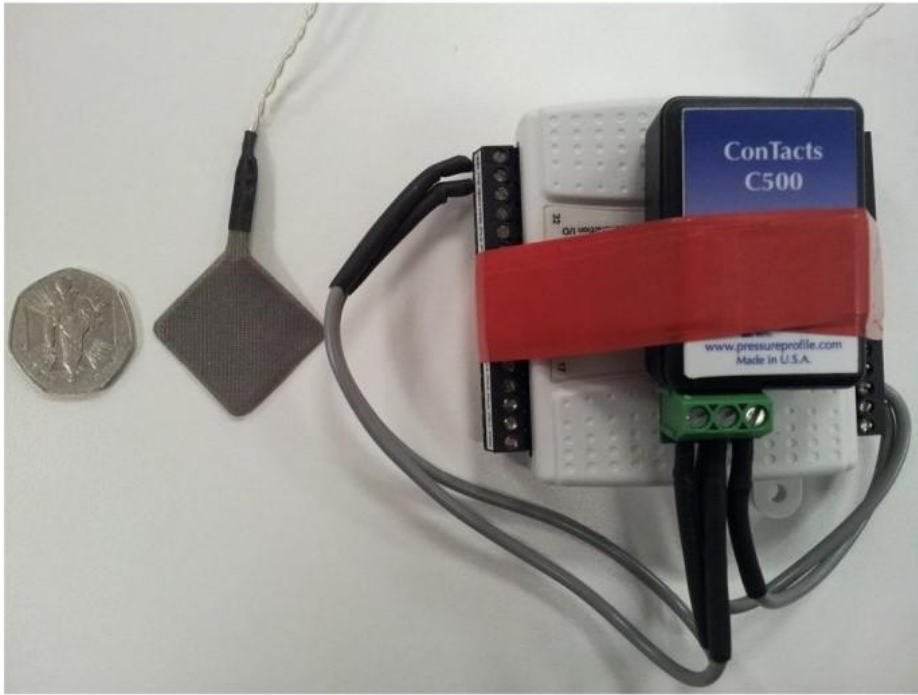
The patient information sheet covers detailed information on the following key points:

- an invitation to take part in a research study from the participating surgeons (Titus Augustine and Thomas Satyadas)
- name and contact details of the participating surgeons

- patient's role if consent is given to participate
- advantages study will bring to future surgical practises
- risk associated with the study
- impacts on the actual surgery if the patient does not give consent
- use of data collected during the study
- type of patients participating in the study
- declaration of commercial interests
- complaints procedure.

4.5.2 Description of pressure sensor

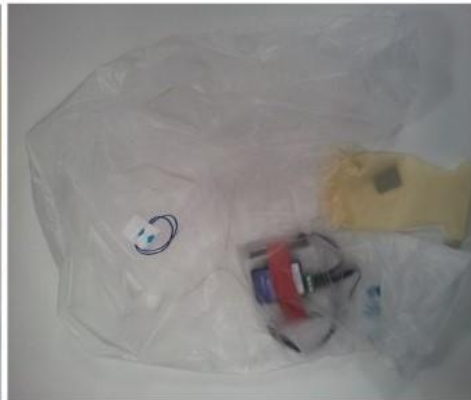
All pressure measurements were taken using a Pressure Profile C500 Tactile Sensor (Quadrtec Limited, UK), which consists of a thin film flexible capacitive sensor encapsulated within a fabric layer. The sensor had dimensions of 25mm x 25mm, and a thickness of ~ 1mm. A 1 metre length cable connects the sensor to an amplifier and signal conditioning unit (Figure 4.13a). The signal conditioning unit connects via a USB interface to a laptop with associated data logging software called 'Laparoscopy' (Figure 4.14). The 'Laparoscopy' software was calibrated by Quadrtec Limited to display applied surface pressure in kPa unit. The display panel has 'start', 'stop' and 'data logging' buttons to record the pressure measurement data.



(a)



(b)



(c)

Figure 4.13: Pressure sensor system and ultrasound probe cover.
 (a) Components of C500 Pressure Sensor System (b) Enclosure of the Pressure Sensor (c) Sterile Ultrasound Probe Cover encapsulating Pressure Sensor System.

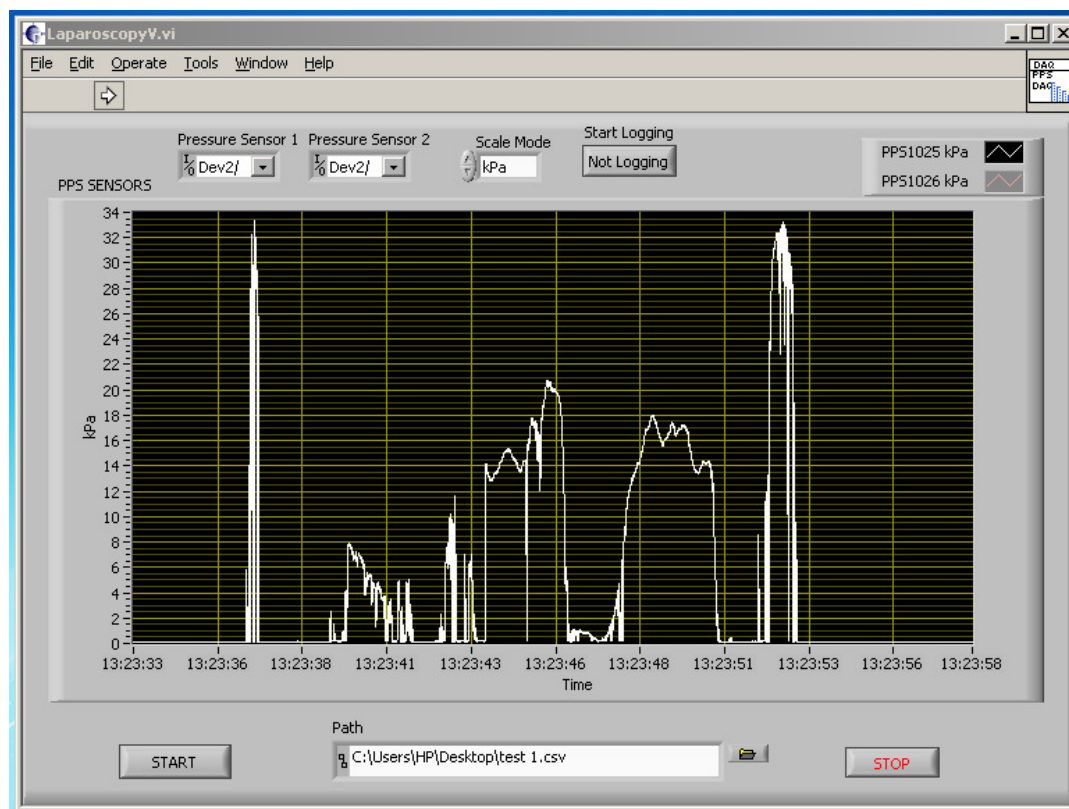


Figure 4.14: 'Laparoscopy' software for surface pressure data logging.

4.5.3 Set up within the operating theatre

The pressure sensor was placed in the terminal latex section of a sterile ultrasound probe cover (Figure 4.13b). The ultrasound probe cover encapsulated the entire sensor-cable-signal conditioning unit assembly (Figure 4.13c). The process of placing pressure sensor and the entire assembly was undertaken in the operating theatre using sterile procedures by the scrub nurse. The pressure sensor and cable assembly were located in the sterile operative field. The associated laptop was positioned in the non-sterile surgical field (Figure 4.15). Surface pressure measurements were collected during retraction of the liver, bowel, stomach, spleen and kidney for 6 patients undergoing open procedures and 6 patients undergoing laparoscopic procedures at the MRI of the MFT. A medical statistician has suggested 10-12 patients for this pilot study (Appendix B). Surface pressure measurements in theatre were undertaken by the participating surgeons - Titus Augustine during Hand Assisted Donor Nephrectomy and Thomas Satyadas during OC. Titus Augustine has over 25 years of surgical

experience (15 years of experience in laparoscopic surgery) and Thomas Satyadas has over 15 years of experience in open and laparoscopic abdominal procedures.

Surface pressure measurements were captured once access to the abdomen was established but prior to commencing the planned surgical procedure. Video footage of the organ being retracted was also recorded, to enable the surface pressure measurements to be correlated with organ retraction distance. It was not possible to locate a camera at a constant fixed location in respect of every patient on the operating table under anaesthesia due to logistical and infection control imperatives in the operating theatre. The camera (Samsung S2 GTI9100) was positioned facing the abdomen of the patient at $\sim 45^\circ$ to both the coronal and transverse planes of the body of the patient (Figure 4.9, Chapter 2) to the right or left of the operation table.

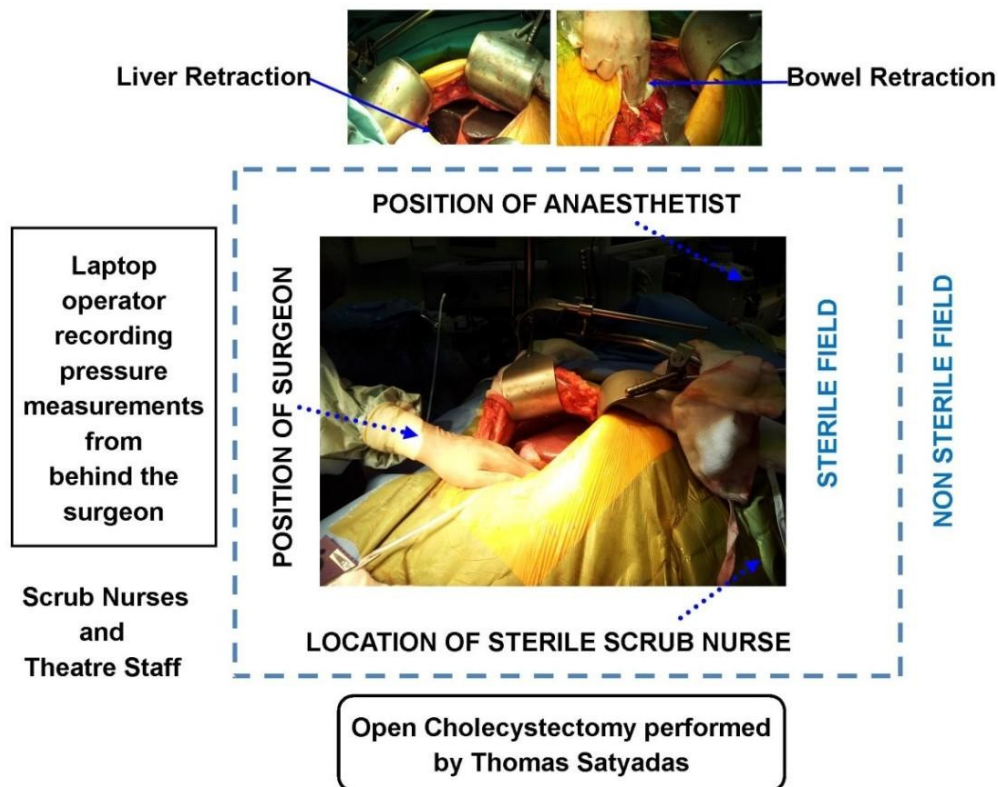


Figure 4.15: Representation of pressure measurements carried out in the surgical theatre.

4.5.4 Methodology of measurement of surface pressures

The entire surface area of the pressure sensor enveloped in the latex end of the sterile ultrasound probe cover (Figure 4.13b) was maintained in complete contact with two fingertips of the surgeon before the recording of each retraction event. During HALS, the entire surface area of the pressure sensor was also maintained in complete contact with the surgical retractors. Prior to the actual surgical procedures, the participating surgeons extensively carried out typical retraction movements keeping the pressure sensor between the two fingertips and key organ simulants of the liver, bowel, kidney, spleen and stomach fabricated for the in-house abdominal simulator.

Surface pressure vs time graphs were obtained from the pressure sensor software. Surface pressures were measured during several retraction events to key organs in each patient to confirm the repeatability and reproducibility of the measured surface pressure values. Across the 12 patients measurements were obtained during 35 typical liver retractions to access the gall bladder, 36 bowel retractions, 9 kidney retractions, 8 stomach retractions and 5 spleen retractions. It was, however, not practicable to undertake retraction of the spleen and kidney in patients undergoing open cholecystectomy due to their anatomical locations. Additionally, liver was retracted by metal retractor (PretzelFlex™ part of the Endoflex™ retractor) and laparoscopic grasper during HALS. Bowel was also retracted with metal retractor (part of Omnitract™ retractor system) during open abdominal surgery.

Surface pressures required for the supporting tissues as well as key blood vessels surrounding abdominal organs were also measured. Abdominal aorta (largest artery in the abdominal cavity) and omentum (layer of peritoneum that surrounds abdominal organs) were retracted twice during HALS for patient 7. Similarly, inferior vena cava (large retroperitoneal vein that lies posterior to the abdominal cavity) and duodenum (first section of the small intestine) were retracted during HALS for patient 8.

4.5.5 Methodology of calculation of organ retraction distances

Image processing and analysis open-source software, ImageJ (Version 1.48)(225), was utilised to calculate organ retraction distances from the video footage. Sequences of images were selected from the video footage to determine retraction distance based on three key considerations:

- presence of instruments or fingertips of surgeon of known dimension to enable calibration of the image using the image analysis software
- presence of four stationary points in the plane of the image for determination of relative movements of points of interest
- two distinctive identifying marks on the edge or surface of the organ as defined points of interest to track the retraction movements in the plane of the image relative to the four stationary points

To relate the measured surface pressures to retraction of an organ in specific directions a global x-y-z coordinate system was defined with respect to the human body (Figure 2.9, Chapter 2). The global x-y plane corresponded to the human coronal plane, the x-z plane to the transverse plane, and the y-z plane to the sagittal plane. Additionally, an x_1 - x_2 coordinate system was defined for the plane of the images extracted from the video footage (Figure 4.16). Figure 4.16 also shows calibration of an image carried out using known dimensions (width) of retractor used for open cholecystectomy, an example of 4 stationary points (points 1-4) and two identifying marks (points 5 and 6) used in the image analysis for retraction of the liver (patient 3).

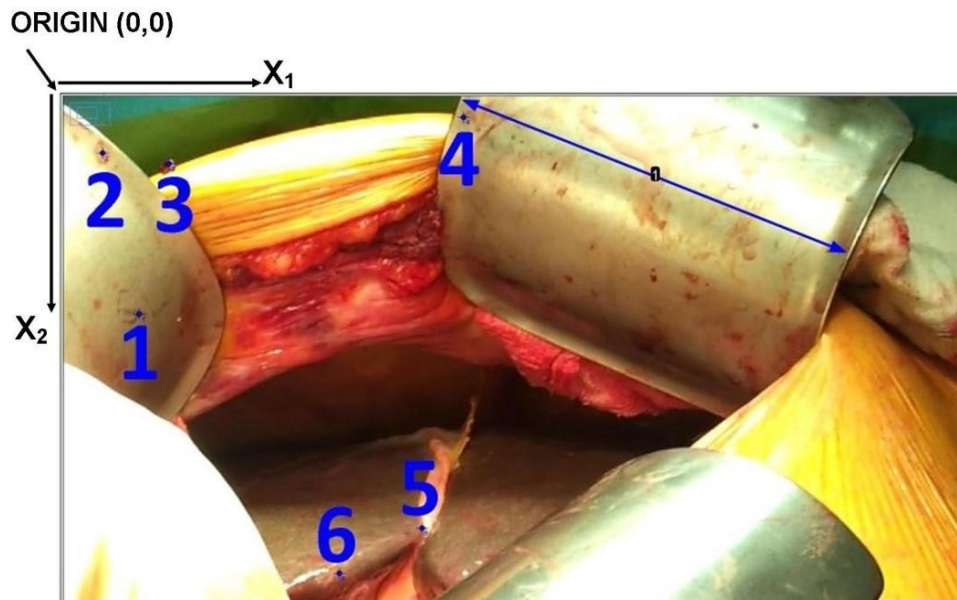


Figure 4.16: Origin (0, 0) and Local co-ordinate system (x_1 - x_2) for plane of image.

4.5.6 Data analysis

Typical surface pressure versus time data acquired during open abdominal surgery and hand assisted laparoscopic surgery were plotted for the liver, bowel, spleen, stomach, and kidney.

Clearly identifiable ('clean') peaks corresponding to retraction events were identified and plotted. These data typically showed decay in the applied surface pressure during the 'hold' period of the retraction event. The data were analysed to calculate the maximum surface pressure (P_{\max}), or pressures in the case of multiple peaks, applied by the fingertips of the surgeon. The length of time the organ was retracted during each retraction event (T_{hold}) was also determined, with the start of the retraction event defined by the maximum pressure and the end defined by the onset of a sudden decrease in pressure (P_{end}), or a sudden increase corresponding to a further retraction event. The root mean square surface pressure (P_{rms}) was calculated over the period of T_{hold} for each retraction event. Those data for individual retraction events which were less well defined in terms of a 'clean' peak, only the maximum surface pressure for each event was determined.

Properties extracted for data analysis are schematically presented in Figure 4.17.

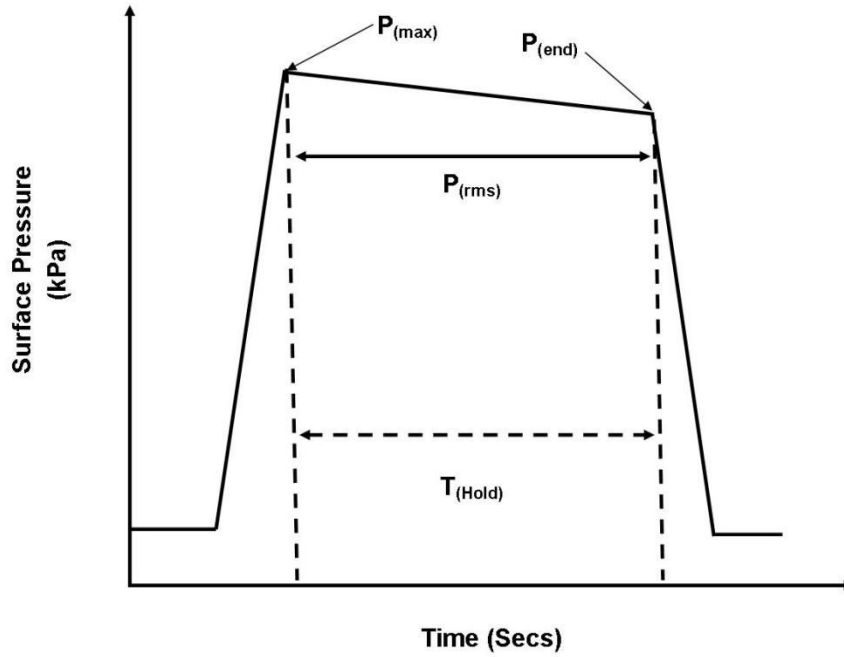


Figure 4.17: Properties extracted for data analysis of 'clean' retraction event.

For each identifying mark the movement ΔX_1 and ΔX_2 along the x_1 and x_2 axes, respectively, relative to the initial image location was measured in subsequent images. The overall retraction distance in the plane of the respective image was then calculated using $\Delta X = \sqrt{(\Delta X_1)^2 + (\Delta X_2)^2}$. The retraction distances (in the x_1 - x_2 image plane) vs time data extracted from the image analysis of the video footage showing retraction of liver, bowel, spleen, stomach and kidney were then also plotted.

4.6 Summary

The methodology for the fabrication and assessment of simulant organs, development of in-house test rigs, and in-vivo measurement of surface pressures and organ retraction distances during typical retraction movements of key abdominal organs during OC and HALS have been described in this Chapter.

5 Materials and Methodology 2: Finite element (FE) modelling of a solid wall cylinder

The methodology of the finite element modeling of solid wall of cylinder is described in this chapter. The uniform material properties are defined to carry out the parametric study of solid wall cylinder with and without end pieces.

5.1 Finite Element methods and Computer Aided Design

5.1.1 Finite Element methods

The Ansys software has been employed in this project to evaluate and solve the elastic deformation of three-dimensional cylindrical prototype structures.

5.1.2 Computer Aided Design (CAD)

Computer aided design (CAD) is a modern tool to develop complex three-dimensional geometries in space. It creates an interface between analytical modelling and laboratory experiments. A plethora of CAD software has been developed such as Autodesk, SolidWorks and Pro Engineer to design geometry files for input to manufacturing machines such as laser cutting and 3-D printing (additive manufacturing) equipment.

SolidWorks is the most widely used software package, not only in industry but also as a useful modelling tool in academic disciplines such as material physics and mechanical engineering, to design complex 3D objects. It allows the design of complex geometries, their assembly and creation of two-dimensional drawings. It possesses diverse features such as extrude boss/bass, revolved boss/bass, linear patterns, cut, pattern, wrap, shell and mirror, which can be useful for the design of the proposed cylinder prototype structures in the current project. Designs are saved as a part file and assembled when required. The assembly segment of SolidWorks has key features such as mates, linear pattern components and reference geometry. They were used in this project to assemble end pieces with the cylinder design during simulation of the expansion behaviour of prototypes. The part and assembly files can be saved in various file formats such as stl, iges,

asm, pdf and jpeg. The stl file format has been used for 3D printing of prototype structures. The engineering drawings of prototype structures were saved as pdf files for laser cutting of prototype structures.

5.1.3 Summary

CAD tools were used to generate solid wall cylinders of different diameter, length and wall thickness, and to design and assemble different types of end pieces onto a solid wall cylinder. The finite element method was used to study the impact of the mechanical properties of a solid wall cylinder and the effect of end pieces on the deformation of a solid wall cylinder in this Chapter.

5.2 Rationale

The large equatorial expansion for small axial strain displayed, for example, in the deployment of a folded paper cylinder into a sphere (Figures 3.15 and Figure 3.16, Chapter 3) can be attributed to factors such as in-plane and out-of-plane deformation of the cylinder wall under an applied load. This is in turn determined by the material properties (Young's modulus, Poisson's ratio and shear modulus), and the presence of end pieces or other loading conditions, or a combination of such factors.

The aim of the FE modelling in this chapter is to determine the required material properties and end pieces/loading conditions for the deployment of a solid wall cylinder (i.e. without cellular meshes or folded facets) into a sphere under an applied axial load. The end pieces are considered to convert a load applied along the direction of the longitudinal cylindrical axis into an axisymmetric out-of-plane bending load on the cylinder wall. The modelling of a solid wall cylinder in the first instance deliberately ignores the additional complexity introduced by considering honeycomb (or any other) wall structure. Once the required material properties have been identified, cylindrical honeycomb structures will then be developed in Chapter 6 having effective mechanical properties matching the identified properties of the solid wall models.

5.3 Study set up

5.3.1 Dimensions of cylinder and types of end pieces

The length, outer diameter and wall thickness of solid wall cylinder was 300mm, 40mm and 1mm for simulating isotropic material properties. The length (L), outer diameter (D) and wall thickness (T) of the cylinder were defined as 300mm, 40mm and 2.5mm, respectively to simulate orthotropic material properties. The types of end pieces considered in this study were cone, pronged cone, funnel and pronged funnel (Figure 5.1). They were designed and assembled at both ends of the solid wall cylinder in the SolidWorks CAD software (2014-15 and 2015-16 editions).

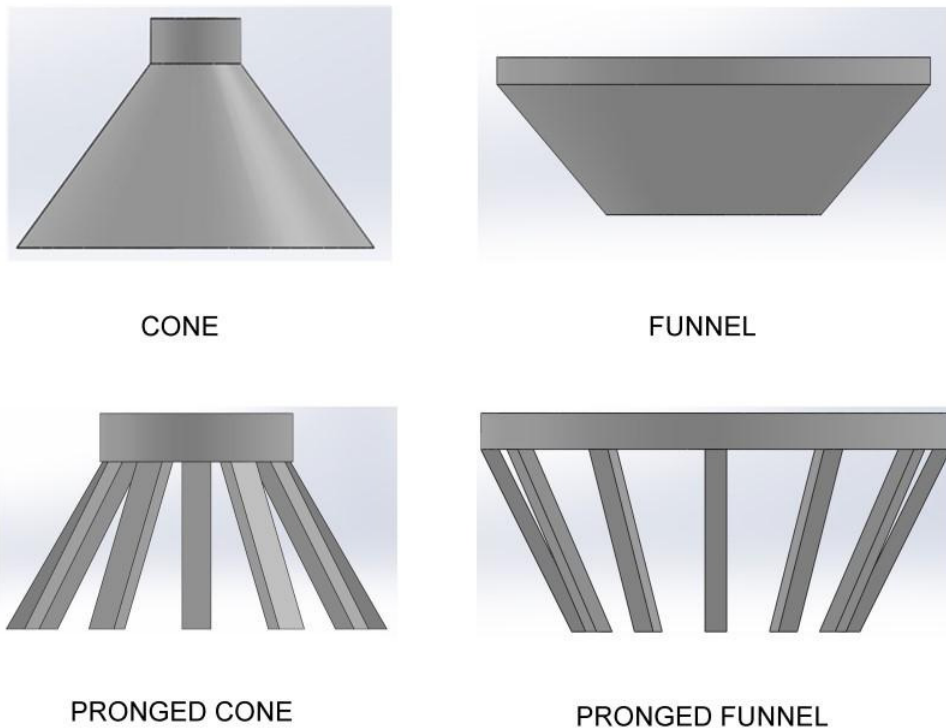


Figure 5.1: Types of end pieces.

The FE modelling was carried out using the Ansys Workbench software (version 16.1 and 17.1). A static structural analysis was used to simulate the effect of material properties and of end pieces on the solid wall cylinder.

5.3.2 Coordinate systems

Ansys employs a global Cartesian coordinate system and a cylindrical coordinate system, although unfortunately uses the same lettering notation (x , y , z) for both. In this thesis, the traditional r , θ , z notation is employed for the cylindrical coordinates and the relationship between these and the global coordinate system employed by Ansys is shown in Figure 5.2 by unrolling a cylinder into flat sheet form.

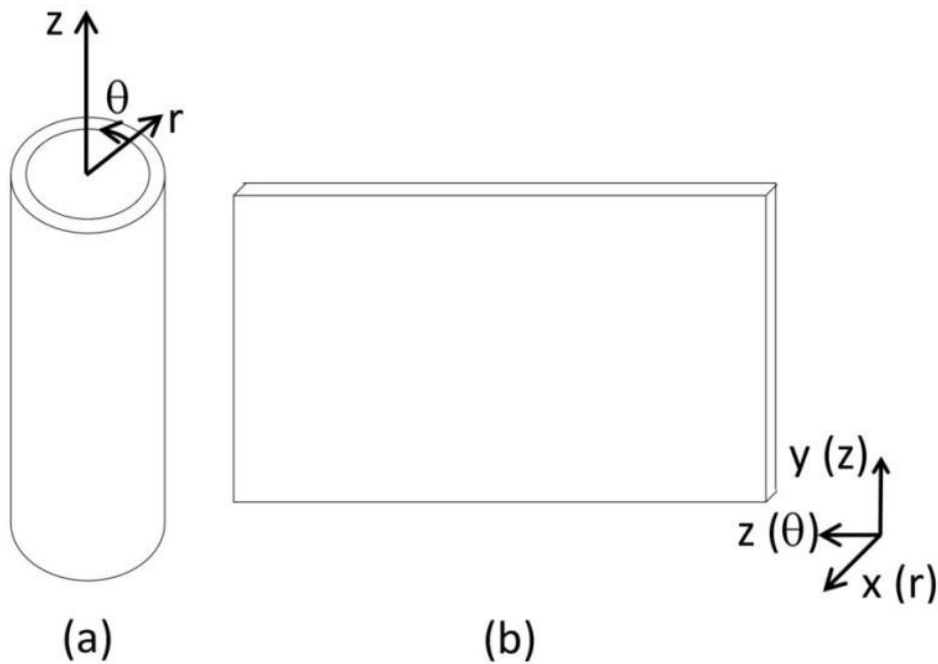


Figure 5.2: (a) Cylindrical coordinate system and (b) global coordinate system with corresponding mapping of the cylindrical axes (in parentheses) of an unfolded cylinder.

5.3.3 Material properties

Linear elastic material properties (isotropic and orthotropic) were assigned to the solid wall of the cylinder with and without end pieces. The large deflection effect in the 'Analysis Setting' was turned 'OFF' to simulate linear material properties. The large deflection effect in the 'Analysis Setting' was turned 'ON' to simulate nonlinear plastic behaviour of cellular cylinders.

5.3.3.1 Isotropic properties

Structural steel was selected from the 'Engineering Data' segment (an in-house library for material properties) of the Ansys workbench software (Table 5.1) to simulate isotropic material properties. The shear and bulk moduli in Table 5.1 were automatically derived from the Young's modulus and Poisson's ratio values in the software, according to the relationships between elastic constants for isotropic materials (Equations 3.32 and 3.33, Chapter 3).

Table 5.1: Isotropic material properties of structural steel.

Property	Value	Unit
Young's modulus	2×10^{11}	Pa
Poisson's ratio	0.3	-
Shear modulus	7.6923×10^{10}	Pa
Bulk modulus	1.6667×10^{11}	Pa

The FE modelling using isotropic material was carried out to check the solid wall cylinder expands under a uniaxial compressive load as expected for positive Poisson's ratio. The magnitude of expansion of the solid wall cylinder using isotropic material properties is not sufficient for the development of the expansion mechanism proposed in this project and hence, orthotropic material properties (as expected for a honeycomb) are considered for the solid wall cylinder in the next section of this chapter.

5.3.3.2 Orthotropic properties

Orthotropic material properties were defined in this study in addition to isotropic properties. As described in Chapter 3, the twelve elastic constants of orthotropic properties are 3 Young's moduli, 3 major Poisson's ratios, 3 minor Poisson's ratios, and 3 shear moduli. These are summarised in Table 5.2 for the cylindrical co-ordinate system. In this study, E_r is greater than E_z and hence, according to the symmetric compliance matrix requirement (Chapter 3, Equation 3.33), $\nu_{rz} > \nu_{zr}$. Therefore, ν_{rz} is referred to as the 'major Poisson's ratio' while ν_{zr} is considered as the 'minor Poisson's ratio'.

Table 5.2: Elastic constants of the orthotropic material properties.

Description of Elastic constants	Annotations
Elastic modulus (radial direction)	E_r
Elastic modulus (axial direction)	E_z
Elastic modulus (circumferential direction)	E_θ
Major radial-axial Poisson's ratio	ν_{rz}
Major axial-circumferential Poisson's ratio	$\nu_{z\theta}$
Major radial-circumferential Poisson's ratio	$\nu_{r\theta}$
Minor radial-axial Poisson's ratio	ν_{zr}
Minor axial-circumferential Poisson's ratio	$\nu_{\theta z}$
Minor radial-circumferential Poisson's ratio	$\nu_{\theta r}$
Radial-axial shear modulus	G_{rz}
Axial-circumferential shear modulus	$G_{z\theta}$
Radial-circumferential shear modulus	$G_{r\theta}$

Two parametric studies were carried out in this project and derivation of orthotropic constants for both the parametric studies are described below.

Parametric study 1:

The parametric study 1 varies each parameter in turn from the 'standard' conditions and, when varying Poisson's ratio or Young's modulus, it is necessary to vary two other parameters (one in each plane) in order to maintain a symmetric compliance matrix. This first study utilises a standard parameter set where certain values were halved from the ones calculated due to the rounding error in Ansys producing a negative stiffness matrix.

The twelve elastic constants of the solid wall cylinder orthotropic material for the parametric study 1 are derived below.

Young's moduli and Poisson's ratios:

The Young's moduli and Poisson's ratios of the orthotropic solid wall were determined to be in the ballpark of the likely effective properties of the honeycomb meshes to be developed after the solid wall cylinder model,

whilst simultaneously satisfying the requirement of positive definite strain energy. The hypothesis was that a large magnitude in-plane Poisson's ratio would facilitate the required large equatorial deformation for relatively small axial deformation (or strain). Hence, $\nu_{z\theta}$ was specified to +10 and -10 to simulate large positive and negative Poisson's ratios in the conventional and auxetic solid wall cylinders, respectively. The out-of-plane Poisson's ratios ν_{rz} and $\nu_{r\theta}$ were set to 0.3 (same as structural steel).

To be consistent with the previous isotropic cylinder wall model, the Young's modulus of structural steel (2×10^{11} Pa) was specified as the Young's modulus (E_r) of the orthotropic cylinder wall in the radial direction. From consideration of the flexure model of hexagonal honeycombs⁽¹¹³⁾, the Young's modulus in the axial direction (E_z) is likely to be less than E_r , but significantly larger than the Young's modulus in the circumferential direction (E_θ). E_z and E_θ were set to $E_r/5$ and $E_r/1000$, respectively (i.e. $E_z = 4 \times 10^{10}$ Pa and $E_\theta = 2 \times 10^8$ Pa).

$\nu_{\theta z}$ is derived from the symmetric compliance matrix for orthotropic material properties (Chapter 3, Equation 3.30):

$$\nu_{\theta z} = \frac{\nu_{z\theta} E_\theta}{E_z} \quad 5.1$$

Hence $\nu_{\theta z} = +0.05$ and -0.05 for the conventional and auxetic solid wall cylinders, respectively. Similarly, from the equivalent symmetric compliance matrix conditions, $\nu_{\theta r} = +0.0003$ and $\nu_{zr} = +0.06$.

Shear moduli:

The values of shear moduli were determined based on the expressions (Equation 3.48, 3.49, 3.53, 3.55, Chapter 3) for the effective shear moduli due to flexure of hexagonal honeycombs⁽¹¹³⁾.

The correspondence between cylindrical and Gibson & Ashby et al. coordinate systems are $G_{z\theta} = G_{21}$, $G_{rz} = G_{32}$, $G_{r\theta} = G_{31}$. The vertical-to-diagonal cell wall length ratio was set to $h/l=2$ which allows the cell wall angle to cover the full range of $-90^\circ \leq \alpha \leq 90^\circ$. According to the Gibson and Ashby

model, the in-plane Poisson's ratios are related to the geometrical parameters by Equation 3.46 and 3.47 in Chapter 3.

Values of α were obtained graphically for $v_{z\theta} = +10$ and -10 , specified above, and they were found to be $\alpha=60.1^\circ$ and -71.6° , respectively (Figure 5.3).

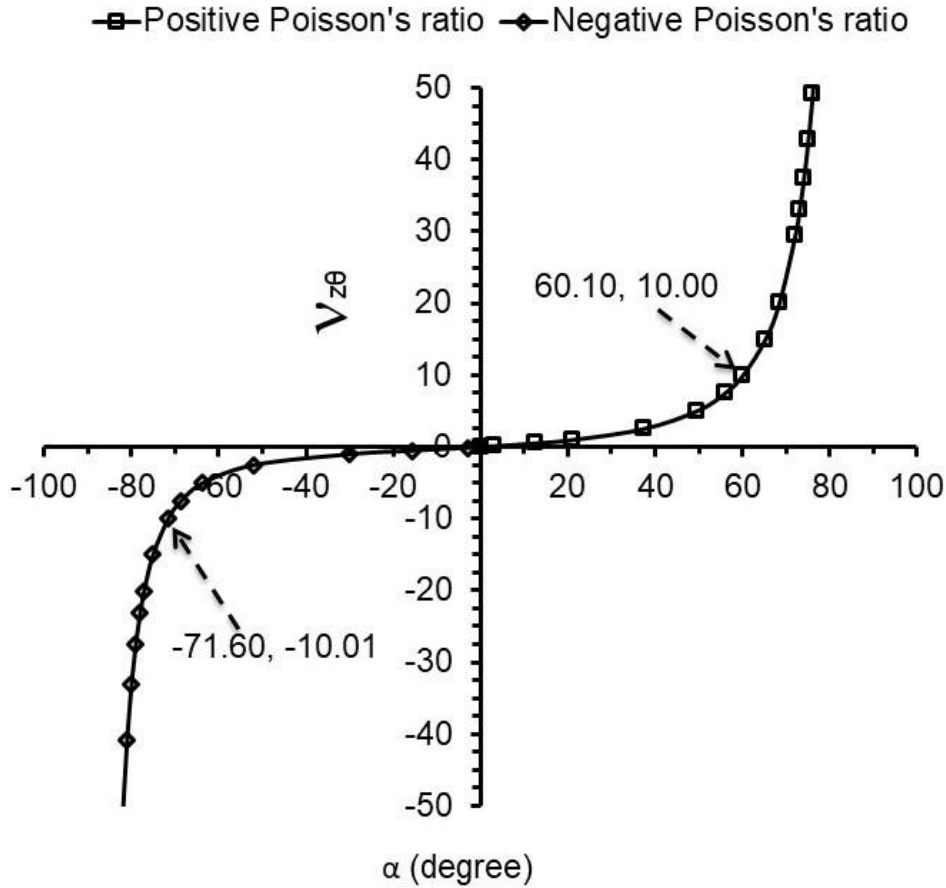


Figure 5.3: Effect of angle of diagonal rib of honeycomb on Poisson's ratio. These values of α were subsequently used to calculate values of t/l from Equation 3.48 described in Chapter 3 (reciprocal theorem) derived by Gibson and Ashby⁽¹¹³⁾.

For $\alpha=60.1^\circ$, $v_{z\theta} = +10$, $E_\theta = 2 \times 10^8$ Pa (specified above) and $E_s = 2 \times 10^{11}$ Pa (structural steel), Equation 3.48 described in Chapter 3 gives $t/l = 0.163$, which is the value used in Equations 3.49, 3.53, 3.55 to determine the values of the shear moduli to be employed in the positive Poisson's ratio solid wall cylinder model. Similarly, employing $\alpha=-71.6^\circ$, $v_{z\theta} = -10$, $E_\theta = 2 \times 10^8$ Pa and $E_s = 2 \times 10^{11}$ Pa in Equation 3.48 described in Chapter 3 gives $t/l = 0.144$,

which is the value used for the calculation of the shear moduli to be used in the negative Poisson's ratio solid wall cylinder model. The lower bound expression (Equation 3.55, Chapter 3) was chosen for the calculation of $G_{r\theta}$ in the solid wall cylinder.

The twelve elastic constants of the solid wall cylinder orthotropic material are summarised in Table 5.3.

Table 5.3: Orthotropic material properties for positive definite matrix in the cylindrical coordinate system.

Orthotropic properties	Cylindrical Coordinate System	
E_r (Pa)	2×10^{11}	2×10^{11}
E_θ (Pa)	2×10^8	2×10^8
E_z (Pa)	4×10^{10}	4×10^{10}
$\nu_{r\theta}$	0.3	0.3
$\nu_{\theta r}$	3×10^{-4}	3×10^{-4}
$\nu_{\theta z}$	+0.05	-0.05
$\nu_{z\theta}$	+10	-10
ν_{rz}	0.3	0.3
ν_{zr}	0.06	0.06
$G_{r\theta}$ (Pa)	2.2×10^9	3.3×10^9
$G_{\theta z}$ (Pa)	2.5×10^8	1.0×10^7
G_{rz} (Pa)	1.5×10^{10}	7.4×10^9

Parametric study 2:

The parametric study 2 varies a selected parameter (E_θ) based on the outcomes of the first study identifying this as a key parameter. In this study parameter variation is considered with more importance attached to the eventual cellular nature of the expansion mechanism. Hence, parameter variation is in accordance with the symmetric compliance matrix condition and the reciprocal Poisson's ratio relationship in hexagonal honeycombs deforming by flexure. The shear modulus is also recalculated in this second study, guided by the honeycomb theory expressions. So, this second study is

a half-way house between the solid wall study in parametric study 1 and the cellular mesh study described later. The additional constraints in the second parametric study mean that 7 parameters are varied simultaneously. The standard set in this study were very close to those determined from the honeycomb considerations, with only slight reduction in certain parameters to achieve the positive definite stiffness matrix.

The twelve elastic constants of the solid wall cylinder orthotropic material for the parametric study 2 are derived below.

Young's moduli and Poisson's ratios:

E_z and E_θ were set to $E_r/10$ and $E_r/1000$, respectively (i.e. $E_z = 2 \times 10^{10}$ Pa and $E_\theta = 2 \times 10^8$ Pa) for this parametric study. When nine orthotropic constants (method of derivation of the remaining two out-of-plane minor Poisson's ratios and three shear moduli are explained below) entered in the Ansys software, it gave negative definite matrix due to rounding off decimal point error (Figure 5.4). Hence, E_z and E_θ were set to $E_r/9.9$ and $E_r/999.9$, respectively (i.e. $E_z = 2.02 \times 10^{10}$ Pa and $E_\theta = 1.98 \times 10^8$ Pa) to get positive definite matrix and subsequently three minor Poisson's ratios and three shear moduli calculated. Hence, $\nu_{z\theta}$ become +10.11 and -10.12 for the conventional and auxetic solid wall cylinders, respectively. Please note that Ansys software changes the minor Poisson's ratios into the major Poisson's ratios during solution step and hence, values of three minor Poisson's ratios were substituted in the software.

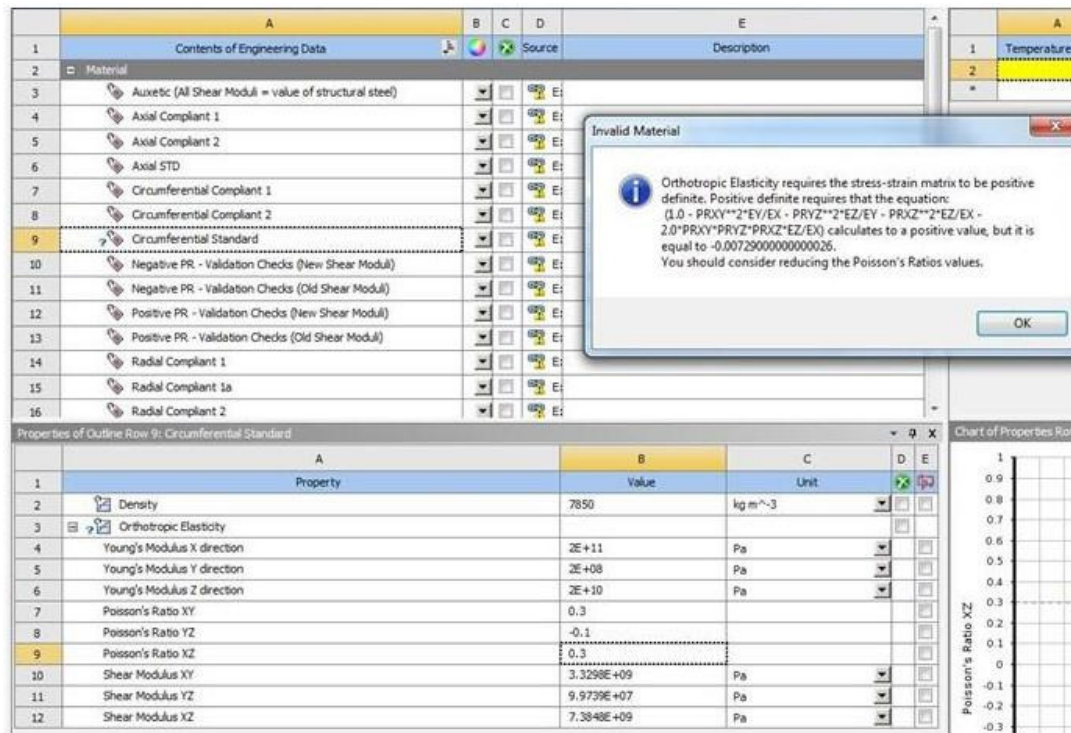


Figure 5.4: Negative definite matrix in the Ansys software.

$\nu_{\theta z}$ is derived from the symmetric compliance matrix for orthotropic material properties (Equation 5.1). Hence $\nu_{\theta z} = +0.09891$ and -0.09891 for the conventional and auxetic solid wall cylinders, respectively. Similarly, from the equivalent symmetric compliance matrix conditions, $\nu_{\theta r} = +0.0002967$ and $\nu_{zr} = +0.03033$

Shear moduli:

The values of shear moduli were determined according to method described for the parametric study 1.

Values of α were obtained graphically for $\nu_{z\theta} = +10.11$ and -10.12 , specified above, and they were found to be $\alpha = 60.3^\circ$ and -71.7° , respectively (Figure 5.5).

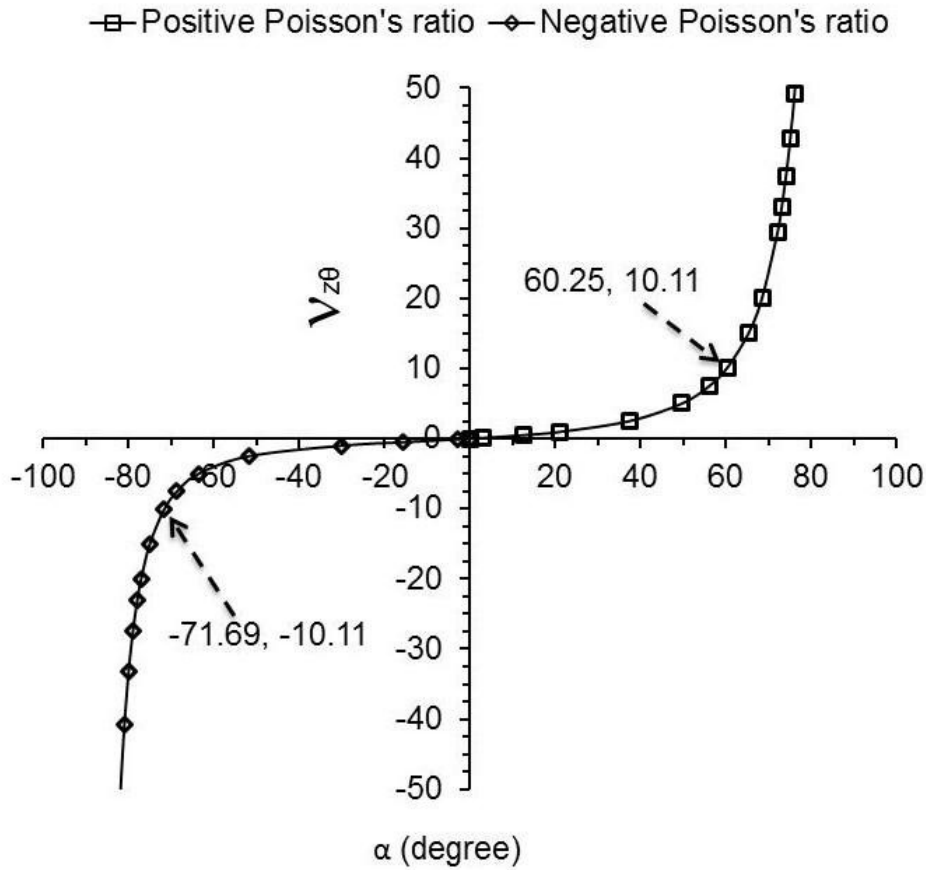


Figure 5.5: Effect of angle of diagonal rib of honeycomb on Poisson's ratio. These values of α were subsequently used to calculate values of t/l from Equation 3.48 described in Chapter 3 (reciprocal theorem) derived by Gibson and Ashby⁽¹¹³⁾.

For $\alpha=60.3^\circ$, $\nu_{z\theta} = +10.11$, $E_\theta = 1.98 \times 10^8$ Pa (specified above) and $E_s = 2 \times 10^{11}$ Pa (structural steel), Equation 3.48 described in Chapter 3 gives $t/l = 0.163$, which is the value used in Equations 3.49, 3.53, 3.55 to determine the values of the shear moduli to be employed in the positive Poisson's ratio solid wall cylinder model. Similarly, employing $\alpha=-71.7^\circ$, $\nu_{z\theta} = -10.12$, $E_\theta = 1.98 \times 10^8$ Pa and $E_s = 2.02 \times 10^{11}$ Pa in Equation 3.48 described in Chapter 3 gives $t/l = 0.144$ for the calculation of the shear moduli to be used in the negative Poisson's ratio solid wall cylinder model. The lower bound expression (Equation 3.55) was chosen for the calculation of $G_{r\theta}$ in the solid wall cylinder.

The twelve elastic constants of the solid wall cylinder orthotropic material are summarised in Table 5.4.

Table 5.4: Orthotropic material properties for positive definite matrix in the cylindrical coordinate system.

Orthotropic properties	Cylindrical Coordinate System	
E_r (Pa)	2×10^{11}	2×10^{11}
E_θ (Pa)	1.98×10^8	1.98×10^8
E_z (Pa)	2.02×10^{10}	2.02×10^{10}
$\nu_{r\theta}$	0.3	0.3
$\nu_{\theta r}$	2.967×10^{-4}	2.967×10^{-4}
$\nu_{\theta z}$	+0.09891	-0.09891
$\nu_{z\theta}$	+10	-10
ν_{rz}	0.3	0.3
ν_{zr}	0.03033	0.03033
$G_{r\theta}$ (Pa)	2.2×10^9	3.3×10^9
$G_{\theta z}$ (Pa)	2.5×10^8	1.0×10^7
G_{rz} (Pa)	1.5×10^{10}	7.4×10^9

5.3.4 Boundary conditions

Two sets of boundary conditions (BCs) were considered: Finite BCs and Infinite BCs.

5.3.4.1 Finite BCs

The Finite BCs were assigned to simulate the real life (mechanical testing) scenario in which the cylinder is fixed at the bottom end in all directions and axial load is applied on the top face of the cylinder. The Finite BCs were applied in the form of axial 'load' on the top surface (Figure 5.6a), with the top surface allowed to displace axially but constrained from displacement radially or circumferentially (Figure 5.6b). This simulates constraint against radial movement or torsion at the top edge due to the clamp attached to the moveable crosshead in the testing machine. The bottom surface of the

cylinder was constrained from displacing in all 3 directions (Figure 5.6c), equivalent to the fixed grip applied to the bottom edge in the testing machine.

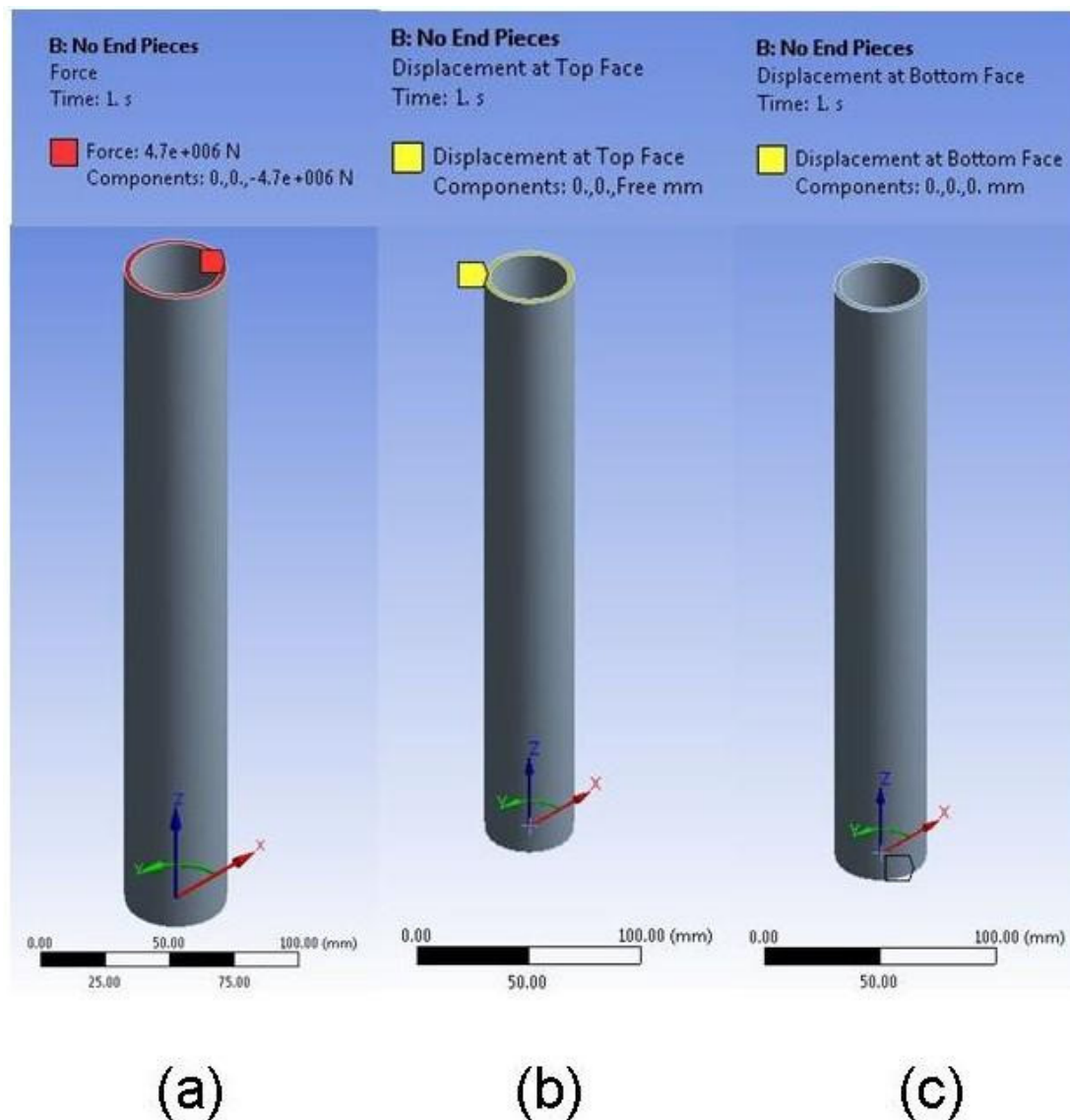


Figure 5.6: Boundary conditions with respect to cylindrical coordinate systems. (a) 'Load' applied on top face (negative sign indicates axial compressive load), (b) 'Displacements' at top face, and (c) 'Displacements' at bottom face.

5.3.4.2 Infinite BCs

The Infinite BCs were employed to check that the predicted cylinder response was as expected from the defined material properties and loading conditions, neglecting effects associated with edges.

In the Infinite BCs, the top and bottom surfaces were allowed to displace radially. This is exactly analogous to the infinite BCs applied to planar honeycombs where nodes were free to move in the transverse direction (perpendicular to the loading direction).⁽²²⁶⁾⁽²²⁷⁾ All other BCs were as for the Finite BCs. The Infinite and Finite BCs and loading conditions are summarised in Table 5.5.

Table 5.5: Finite and Infinite BCs. The negative and positive signs indicate axial compression and axial tension load, respectively. 'd' = value of force applied.

BCs	Finite BCs	Infinite BCs
Load at the top face of cylinder (N)	r axis = 0	r axis = 0
	θ axis = 0	θ axis = 0
	z axis = \pm 'd'	z axis = \pm 'd'
Displacement at the top face of cylinder	r axis = fixed	r axis = free
	θ axis = fixed	θ axis = fixed
	z axis = free	z axis = free
Displacement at the bottom face of cylinder	r axis = fixed	r axis = free
	θ axis = fixed	θ axis = fixed
	z axis = fixed	z axis = fixed

5.3.5 Meshing

5.3.5.1 Mesh size

The relevance is the most basic global mesh size control and it can be set as coarse, medium or fine. The mesh statistics are outlined in Table 5.6 for a cylinder with and without end pieces. The element size was set as default for all three relevance centres. The simulations took 2s, 15s and 30s for coarse, medium and fine meshes, respectively.

Table 5.6: Mesh statistics for the relevance of mesh.

End Pieces	Relevance of Mesh	Statistics	
		No. of Elements	No. of Nodes
No End Pieces	Coarse	2870	19025
	Medium	3870	29025
	Fine	6708	46438
Cone	Coarse	3748	18729
	Medium	5248	23126
	Fine	7304	42454
Pronged Cone	Coarse	4524	22169
	Medium	6396	25643
	Fine	9537	49227
Funnel	Coarse	3962	19323
	Medium	5620	24076
	Fine	8308	43759
Pronged Funnel	Coarse	3688	19349
	Medium	4830	23562
	Fine	7470	43063

5.3.5.2 Element type and shape

The default element type used during the solution step by Ansys Workbench was Solid186, which is a structural solid, higher order, 3-D and 20-node solid element. Nodes have three degrees of freedom per node (translations) in the nodal x, y, and z directions. It is available in homogeneous and layered structural solid forms during the FE modelling. The homogeneous form is used in this study (Figure 5.7).

It is generally used to model a physical system undergoing large deflection and large strain (Version 17.1 and 18.1 ANSYS Inc.). Solid186 supports plasticity, creep, stress stiffening, large deflection and large strain capabilities. It supports the use of anisotropic material properties and they are generally assigned to the element coordinate system.

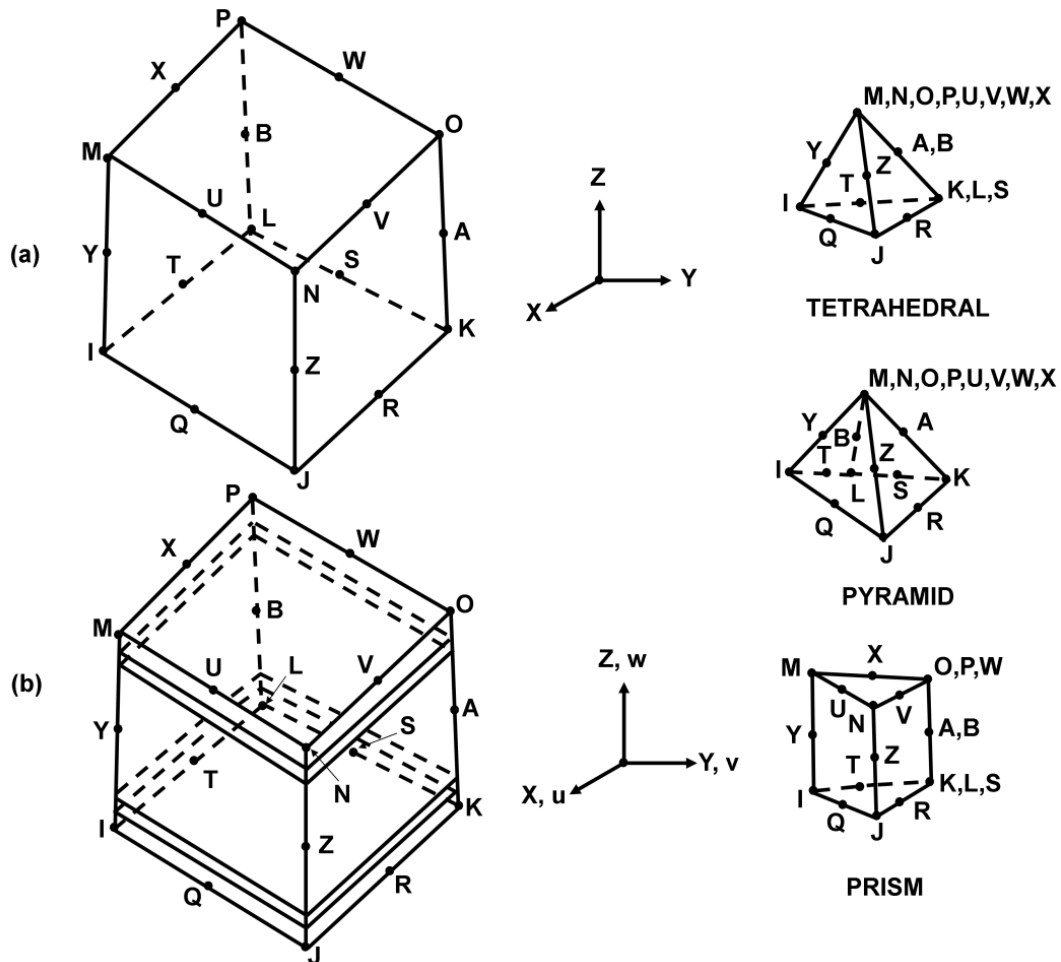


Figure 5.7: Solid186 element. (a) Homogeneous and (b) Layered structural solid, showing node locations, element coordinate system and shape options (Version 17.1 and 18.1 ANSYS Inc.).

Solid186 has brick, tetrahedral, prism and pyramid shapes (Figure 5.7). The geometry, node locations and the element coordinate system for this element are shown Figure 5.7. A prism-shaped element may be formed by defining the same node numbers for nodes K, L, and S; nodes A and B; and nodes O, P, and W. A tetrahedral-shaped element and a pyramid-shaped element may also be formed as shown in Figure 5.7.

The element shapes used during the solution of each model in this study were Hex20 (20 nodes nonlinear tetrahedron) and Wed15 (15 nodes nonlinear prism or wedge). These element shapes are typically used for modelling of large deflection and large strain.

The large deflection was turned OFF in the solver controls of 'analysis setting' in the Ansys Workbench to permit linear elastic deformation of the solid wall of the cylinder. If a nonlinear static structural analysis is required, then the large deflection should be turned ON. For this project, only linear elastic deformation was considered.

5.3.5.3 Mesh quality checks

A good quality mesh means that the mesh quality criteria are within the correct range for element quality, aspect ratio, Jacobean ratio, warping factor, parallel deviation, maximum corner angle, skewness and orthogonal quality. By way of example, the mesh metrics of a fine and coarse mesh metrics generated for a cylinder without end pieces are summarised in Table 5.7 and Table 5.8, respectively which confirms that the fine mesh should be used during FE modelling.

Table 5.7: Mesh metrics for fine mesh generated for cylinder without end pieces.

Mesh Metrics	Standard range (minimum-maximum)	Maximum value	Minimum value	Average & Standard Deviation
Element quality	0-1	0.99	0.69	0.9 ± 0.008
Aspect ratio	1-10	2.20	1.16	1.12 ± 0.28
Jacobean ratio	1-100	2.05	1.02	1.17 ± 0.30
Skewness	0-1	0.5	0.02	0.25 ± 0.13
Orthogonal quality	0-1	1	0.74	0.91 ± 0.07

Table 5.8: Mesh metrics for coarse mesh generated for cylinder without end pieces.

Mesh Metrics	Standard range (minimum-maximum)	Maximum value	Minimum value	Average & Standard Deviation
Element quality	0-1	0.98	0.48	0.78 ± 0.12
Aspect ratio	1-10	6.62	1.46	1.82 ± 0.92
Jacobean ratio	1-100	5.86	1.02	1.31 ± 0.84
Skewness	0-1	0.71	0.066	0.42 ± 0.20
Orthogonal quality	0-1	0.98	0.53	0.78 ± 0.14

5.3.6 Solutions

The directional deformations (radial, axial, and circumferential) of the solid wall cylinder were read from the legend bars. In some cases, nodes were selected in the equatorial plane to identify specific nodal deformations, stresses and strains. Node numbers were exported in Excel spreadsheet (.xlsx file) format from the Ansys Workbench software. These node numbers were then matched with the node numbers associated with deformations, stresses and strains (exported as .xlsx files).

5.4 FE modelling of uniform material properties

The FE modelling of a cylinder (with and without end pieces) displaying uniform linear elastic isotropic or orthotropic material properties is described in this section. Axial compression and tension loads were considered. The length, outer diameter (OD), and wall thickness (WT) of solid wall cylinder were specified as 300mm, 40mm, and 2.5mm, respectively. Static structural analysis was chosen from the 'Analysis Systems' of the Ansys software. Linear elastic (isotropic and orthotropic) material properties were created in the 'Engineering Data' segment of static structural analysis. The isotropic and

orthotropic material properties derived in Section 5.3.3 were then entered to carry out the parametric studies.

5.4.1 Isotropic material properties

Isotropic material properties (Table 5.1) were considered for positive Poisson's ratio wall material employing Finite and Infinite BCs (Figure 5.8). The properties were assigned as described in Section 5.3.4. Axial compression and tension loads were applied to evaluate the expansion behaviour of the solid wall cylinder. Cylinders with and without end pieces were considered in the simulations employing Finite BCs.

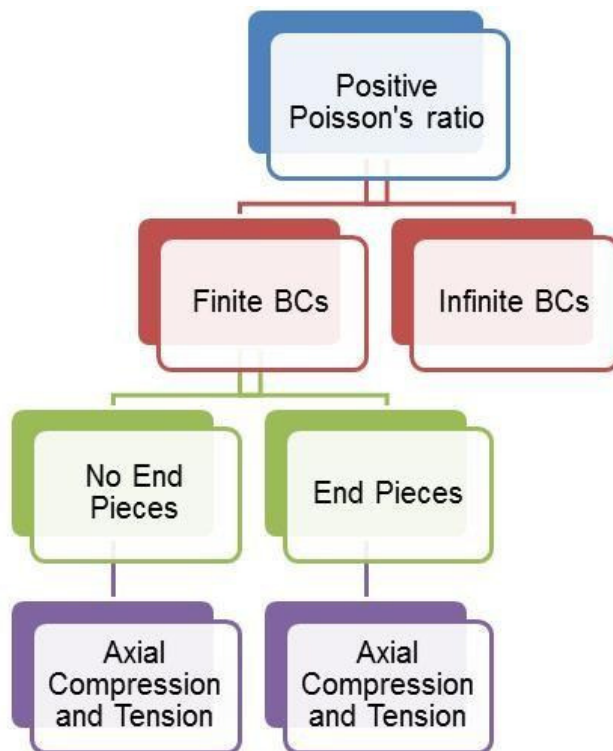


Figure 5.8: FE modelling of isotropic material properties.

5.4.2 Orthotropic material properties

Orthotropic material properties (Table 5.3 and 5.4) were taken as 'standard' parameter sets for positive and negative Poisson's ratio wall materials. The expansion behaviour of solid wall cylinders employing positive and negative Poisson's ratios walls were simulated with Finite BCs. Uniaxial compression and tension loads were used.

E_r , E_z , shear moduli, and out-of-plane Poisson's ratios ($\nu_{\theta r}$ and ν_{zr}) were however not varied during parametric study 2 to maintain the set of 'standard' properties outlined in Table 5.4. Rationales are outlined below.

- E_r and E_z require new set of orthotropic constants and linked with the in-plane Poisson's ratio due to the reciprocal relationship, respectively. For example, if E_r is changed from 2×10^{11} Pa (structural steel) to 2×10^9 Pa (Paper) or 4×10^9 Pa (Polymer) then the new set of orthotropic constants (Table 5.4) will be derived (Section 5.3.3.2).
- Similarly, shear moduli were derived for the specific in-plane Poisson's ratio (± 10).
- Out-of-plane Poisson's ratios were derived using reciprocal relationships (i.e. dependent on E_r , E_θ , E_z , and $\nu_{\theta z}$).

When varying the circumferential Young's modulus (E_θ), $\nu_{\theta z}$ was varied to maintain a symmetric compliance matrix (Equation 3.30, Chapter 3). Out-of-plane Poisson's ratios and three shear moduli were also updated.

The effects of pronged cone end pieces (Figure 5.1) were simulated for uniaxial compression loading. Compression and tension loading along the cylinder axis were considered for in-plane positive and negative Poisson's ratio, respectively during parametric study of a cylinder without end pieces.

5.4.3 Summary

The study set up for FE modelling of solid wall cylinder was explained in this chapter. The methodology to simulate uniform linear elastic (isotropic and orthotropic) material properties for solid wall cylinder was outlined.

6 Materials and Methodology 3: Mesh Cylinders

The methodology for the derivation of cellular meshes, fabrication methods, mechanical characterisation without surrounding materials and in-vitro assessments of promising expansion mechanisms are described in this chapter. Additionally, in-vivo and in-vitro assessment methodologies of doughnut shape inflatable prototypes, developed by industry sponsors of this project are outlined.

6.1 Cellular mesh derivation methodology

Cellular meshes for the expansion mechanisms were developed to achieve the essential features of the orthotropic material properties obtained from the FE modelling of a solid wall cylinder. Expressions for the effective mechanical properties of hexagonal honeycomb meshes assumed to deform by flexure of the honeycomb ribs, previously developed by Gibson and Ashby⁽¹¹³⁾, were employed to provide indicative geometries. Two scenarios were considered. In the first ('bottom-up') case, modified key target wall properties from the FE simulations were incorporated into the Gibson and Ashby expressions to realise ballpark honeycomb geometrical parameters. In the second ('top-down') approach, global cylinder dimensions were defined and related to the internal geometrical parameters enabling a parametric fit to be undertaken to achieve the desired FE model properties. Expansion mechanisms based on bending of initially straight parallel beams were additionally considered.

6.1.1 'Bottom-up' approach

Large equatorial radial expansions (~80mm) for small axial strains ($\leq 10\%$) in a solid wall cylinder under uniaxial compression and tension were identified in Chapter 5 as necessary for the development of expansion mechanisms. The range of Poisson's ratio for isotropic materials is insufficient to achieve the necessary expansion and so orthotropic material properties were considered in Chapter 5 and are summarised below.

- Orthotropic material properties – negative in-plane Poisson's ratio in combination with pronged cone end pieces under axial compression

- Orthotropic material properties – positive in-plane Poisson's ratio in combination with constrained ends (no end pieces) under axial compression
- Orthotropic material properties – negative in-plane Poisson's ratio in combination with constrained ends (no end pieces) under axial tension

The aim here is to design cellular meshes possessing effective properties matching the key aspects of the orthotropic material properties from the FE solid wall cylinder simulations.

6.1.1.1 Analytical expressions

The expressions developed by Gibson & Ashby⁽¹¹³⁾ to describe the effective mechanical properties of honeycomb structures were reviewed in Equations 3.43 to 3.56 of Chapter 3. The expansion of honeycomb cylinders is considered principally to be due to the (axial-circumferential) ‘in-plane’ flexure of the ribs forming the honeycomb mesh. Further, the requirement of large lateral expansion for small axial strain implies the in-plane Poisson’s ratio due to axial loading will have a large magnitude. Consequently, the expressions for in-plane Poisson’s ratio and Young’s modulus under axial loading, together with the in-plane shear modulus, are reproduced here using the cylindrical coordinates notation according to the convention defined in Chapter 5.

$$E_z = E_s \left(\frac{t}{l} \right)^3 \frac{\left(\frac{h}{l} + \sin \alpha \right)}{\cos^3 \alpha} \quad 6.1$$

$$\nu_{z\theta} = \frac{\left(\frac{h}{l} + \sin \alpha \right) \sin \alpha}{\cos^2 \alpha} \quad 6.2$$

$$G_{\theta z} = E_s \left(\frac{t}{l} \right)^3 \frac{\left(\frac{h}{l} + \sin \alpha \right)}{\left[\frac{h}{l} \right]^2 \left(2 \left[\frac{h}{l} \right] + 1 \right) \cos \alpha} \quad 6.3$$

where (Figure 3.12)

E_s = Young's modulus of solid rib material

l = length of diagonal rib of honeycomb

h = height of vertical rib of honeycomb

α = angle diagonal rib of honeycomb makes with the θ axis

t = in-plane thickness of vertical and diagonal ribs of honeycomb

6.1.1.2 Derivation of cellular mesh parameters (h/l , t/l , and α)

Conventional and auxetic (i.e. re-entrant) hexagonal honeycomb mesh parameters were derived graphically based on the mechanical properties obtained from the FE modelling of a solid wall cylinder and global parameters of cylinder as 'input parameters'.

There are three independent parameters: h/l , t/l and α , and three simultaneous equations: Equations (6.1), (6.2) and (6.3). The equation for h/l was derived by rearranging Equation (6.2):

$$\frac{h}{l} = \nu_{z\theta} \frac{\cos^2 \alpha}{\sin \alpha} - \sin \alpha \quad 6.4$$

The ratio h/l can then be plotted as a function of α for a specified value of $\nu_{z\theta}$ and is shown by way of example in Figure 6.1(a) for $\nu_{z\theta} = -10$. Note, in Figure 6.1(a), $h/l < 0$ when $0 < \alpha < 90^\circ$ (pink square symbols) which is unphysical. Hence, in this case only the range of $-90 < \alpha < 0^\circ$ (blue diamond symbols) need be considered.

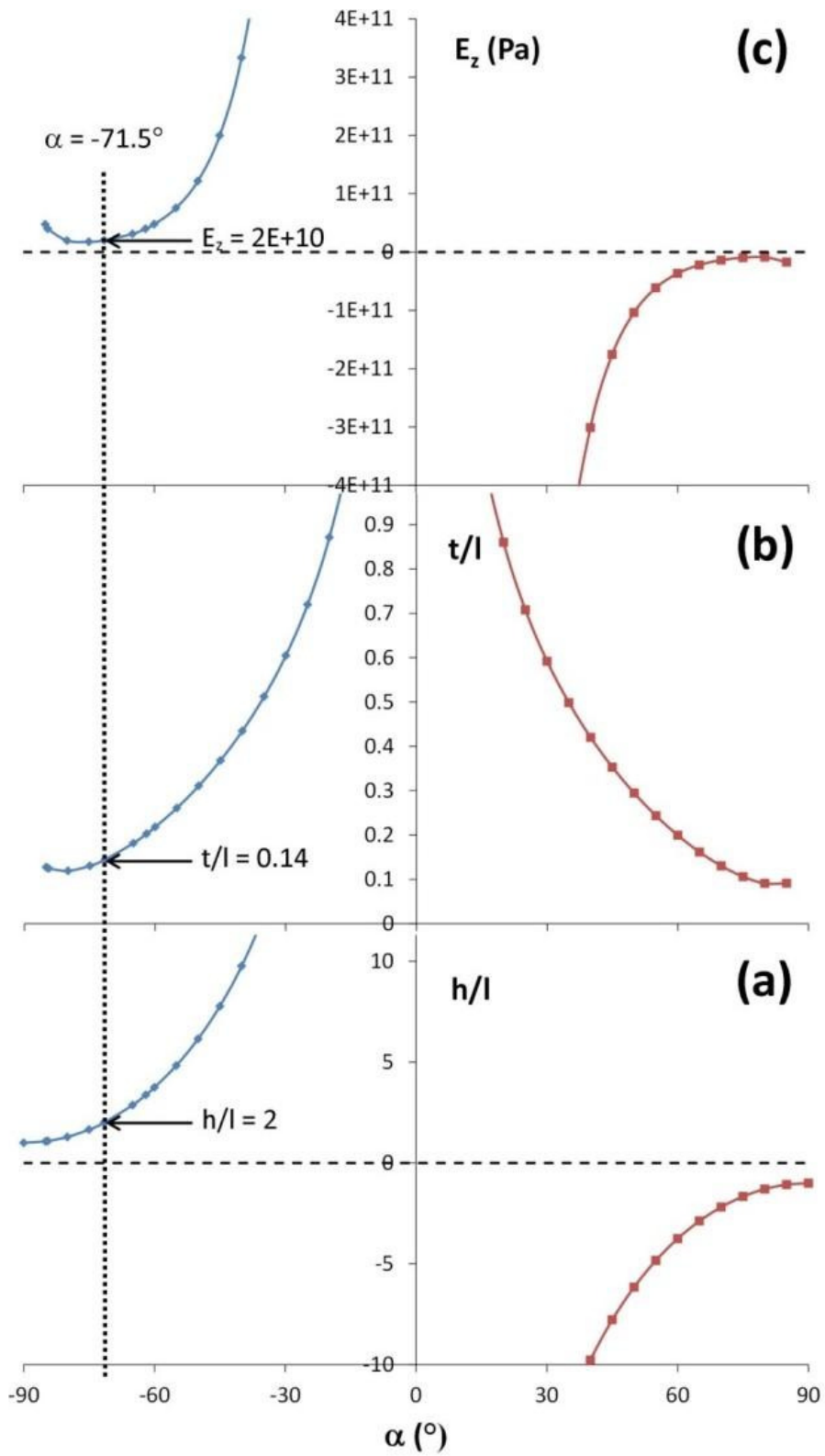


Figure 6.1: Cellular mesh parameters h/l (a), t/l (b) and E_z (c) as functions of honeycomb angle α for a hexagonal honeycomb cylinder with $v_{z\theta} = -10$, $G_{\theta z} = 1.0 \times 10^7$ Pa and $E_s = 2 \times 10^{11}$ Pa.

Next values of t/l were obtained by substituting $-90 < \alpha < +90^\circ$, the corresponding values of h/l obtained in the previous step, E_s and $G_{\theta z}$ into Equation (6.3). This is shown in Figure 6.1(b) for $E_s = 2 \times 10^{11}$ Pa and $G_{\theta z} = 1.0 \times 10^7$ Pa (Table 5.3). Finally, E_z was obtained as a function of α (Figure 6.1(c)) using Equation (6.1) with the corresponding values of h/l and t/l from the preceding steps. The target value of $E_z = 2.02 \times 10^{10}$ Pa is then determined from Figure 6.1 to correspond to values of $\alpha = -71.7^\circ$, $h/l = 2$ and $t/l = 0.14$.

A similar approach for the conventional case of $\nu_{z\theta} = +10.1$, $G_{\theta z} = 2.5 \times 10^8$ Pa (Table 5.3) and $E_s = 2 \times 10^{11}$ Pa, yielded $\alpha = +60.3^\circ$, $h/l = 2$ and $t/l = 0.16$ for a target value of $E_z = 2.02 \times 10^{10}$ Pa.

6.1.2 'Top-down' approach

In this section, the global cylinder parameters are related to the internal geometrical parameters of the mesh.

Relationships between global and internal geometrical parameters:

The global parameters of the cylinder and Representative Volume Element (RVE) are presented in Table 6.1.

Table 6.1: Cylinder and RVE geometrical parameters.

Type of Parameter	Symbol	Description
Cylinder	D	Outer diameter
	T	Wall thickness
	H	Length
	N_c	Number of circumferential RVEs
	N_v	Number of lengthwise RVEs
Representative volume element	M	Height of the RVE
	W	Planar width of the RVE

The cylinder (H , D , T , N_v and N_c), RVE (M and W) and cellular mesh (h , l , t_h , t_l and α) geometrical parameters of a conventional and auxetic hexagonal honeycomb cylinder are shown in Figure 6.2. CAD models designed for

validation of outputs of FE modelling of solid wall cylinder have equal t_h and t_l and denoted as 't'. CAD models designed for fabrication of expansion mechanisms have different in-plane thickness for vertical (t_h) and diagonal ribs (t_l).

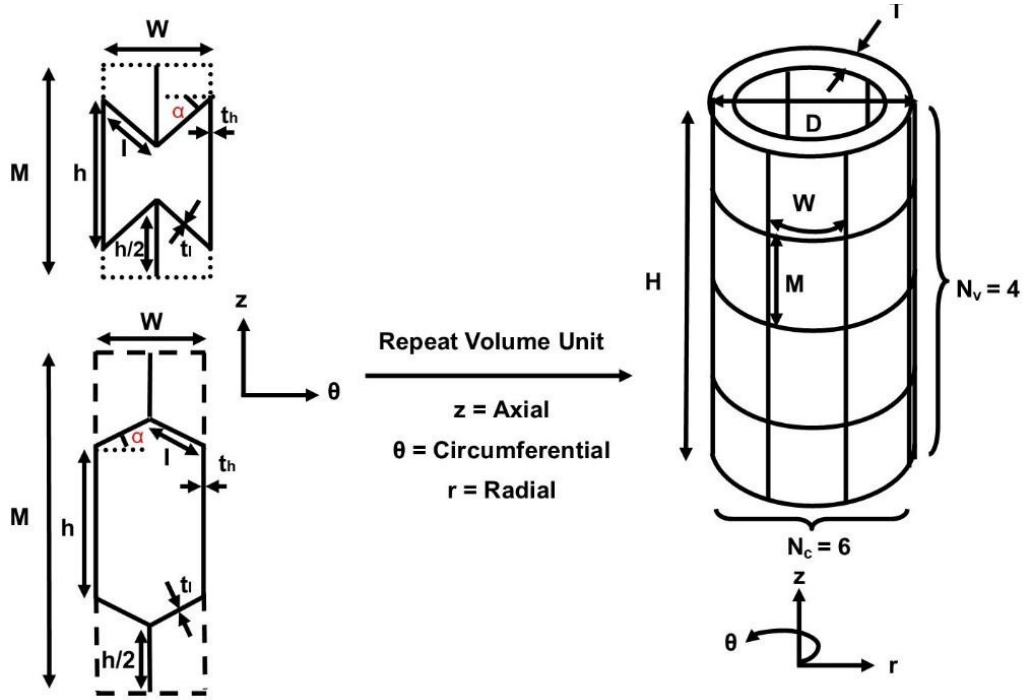


Figure 6.2: The cylinder, RVE and cellular parameters of a conventional and auxetic hexagonal honeycomb cylinder.

The relationships between the RVE and cellular mesh parameters are as follows

$$M = 2(h + l \sin \alpha) \quad 6.5$$

$$W = 2l \cos \alpha \quad 6.6$$

The relationships between the RVE and cylinder parameters are

$$M = \frac{H}{N_v} \quad 6.7$$

$$W = \frac{\pi D}{N_c} \quad 6.8$$

Equating Equations 6.5 and 6.6 with Equations 6.7 and 6.8, respectively, gives the relationship between the cylinder and cellular mesh parameters:

$$2(h + l\sin\alpha) = \frac{H}{N_V} \quad 6.9$$

$$2l\cos\alpha = \frac{\pi D}{N_c} \quad 6.10$$

6.1.3 Combined 'Bottom-up' and 'Top-down' approach

The global cylinder, RVE and cellular mesh parameters were utilised to design CAD models in SolidWorks. This section describes how the 'Bottom-up' and 'Top-down' approaches were combined to obtain values for the number of RVEs and the internal geometrical (i.e. cellular mesh) parameters α , h , l and t (as distinct from their ratios h/l and t/l in Section 6.1.1) for defined global cylinder parameters.

The in-plane mechanical properties (E_z , E_s , $\nu_{z\theta}$, and $G_{\theta z}$), taken from the FE simulations of a solid wall cylinder (Chapter 5, Table 5.3) and defined global cylinder parameters (D , H) were used as input parameters and they are shown in Table 6.2.

Table 6.2: Input parameters for graphical method.

Parameters (cylinder and in-plane mechanical properties from FE modelling)	Values
D	40mm
H	300mm (No end pieces) 25mm (End piece at top end) 25mm (End piece at bottom end)
E_s	2×10^{11} Pa
E_z	2.02×10^{10} Pa
$\nu_{z\theta}$	± 10.11
$G_{\theta z}$	1.0×10^7 Pa ($\nu_{z\theta} = -10$) 2.5×10^8 Pa ($\nu_{z\theta} = +10$)

In the combined method the values of h/l , t/l and α were obtained as described for the Bottom-up approach (Section 6.1.1). Equations (6.9) and (6.10) from the Top-up approach were combined to derive N_c/N_v :

$$\frac{N_c}{N_v} = \frac{\pi D \left(\frac{h}{l} + \sin \alpha \right)}{H \cos \alpha} \quad 6.11$$

Substituting the derived values of h/l and α with the specified values of D and H into Equation (6.11) gave the value of N_c/N_v .

The number of RVEs circumferentially must be an integer ($N_c = 1, 2, 3, \dots, n$) in the cylinder design. The presence of solid wall ends meant this exact requirement was not necessary for the lengthwise number of RVEs. RVE number pairs (N_c and N_v) were then obtained for the derived N_c/N_v ratio in the previous step, selecting those integer values of N_c for which N_v was within 0.1 of an integer value – with the value of N_v then rounded to the nearest whole integer. By way of example, selected RVE number pairs are depicted in Table 6.3 for the negative in-plane Poisson's ratio case, where the previous step defined a value of $N_c/N_v = 1.68$.

Table 6.3: Selective pairs of N_c and N_v (RVEs) for negative in-plane Poisson's ratio to achieve a target value of $N_c/N_v = 1.68$.

N_c	N_v	N_c/N_v
5	3	1.67
10	6	1.67
15	9	1.67
17	10	1.70
20	12	1.67
22	13	1.69

The value of l was obtained by substituting the determined values of N_c and α , and the specified value of D into Equation 6.10. The values of h and t were then obtained by substituting the value of l into the values for h/l and t/l determined in the previous steps. The RVE parameters (M and W) were obtained from Equations (6.7) and (6.8), respectively.

The α , h , l and t values and their corresponding RVE number pairs are shown in Table 6.4 for the negative and positive Poisson's ratio cellular meshes.

Table 6.4: Cellular mesh parameters obtained by the combined approach with input parameters specified in Table 6.2.

$\nu_{z\theta}$	N_c	N_v	α ($^\circ$)	h (mm)	l (mm)	t (mm)
-10.11	5	3	-71.7	79.6	39.6	5.7
	10	6	-71.7	39.8	19.8	2.9
	15	9	-71.7	26.5	13.2	1.9
	17	10	-71.7	23.4	11.6	1.7
	20	12	-71.7	19.9	9.9	1.4
	22	13	-71.7	18.1	9.0	1.3
+10.11	3	1	60.3	84.0	42.0	6.8
	6	2	60.3	42.0	21.0	3.4
	9	3	60.3	28.0	14.0	2.3
	17	6	60.3	14.8	7.4	1.2
	20	7	60.3	12.6	6.3	1.0
	23	8	60.3	11.0	5.5	0.9

6.2 Cellular mesh models

A large equatorial radial deformation of solid wall of cylinder without end pieces ($\sim 80\text{mm}$) for small axial strain ($<10\%$) was obtained from the FE parametric investigation when E_θ was $\leq 1.98 \times 10^7 \text{ Pa}$ (or $E_z/E_\theta \geq 1.02 \times 10^2$) as well as $\nu_{\theta z} \leq +0.0313$ ($\nu_{z\theta} \geq +31.6$) and $\nu_{\theta z} \geq -0.0313$ ($\nu_{z\theta} \leq -31.6$) for uniaxial compression and tension mechanisms, respectively (Chapter 8.1.2.3).

Similarly, cellular mesh cylinders with pronged cone end pieces were designed with effective properties corresponding to the solid wall 'shape' change mechanical properties shown in Table 8.4 (and Figure 8.37), Chapter 8. Additionally, cellular mesh cylinders were designed for high aspect ratio cells with long diagonal ribs by minimising the h/l ratio and/or $\alpha \rightarrow \pm 90^\circ$ for subsequent fabrication of expansion mechanisms.

Cellular meshes were derived for target α and $\nu_{z\theta}$ values (Figures 6.3 and 6.4) to achieve suitably high E_z/E_θ values for large equatorial radial deformation.

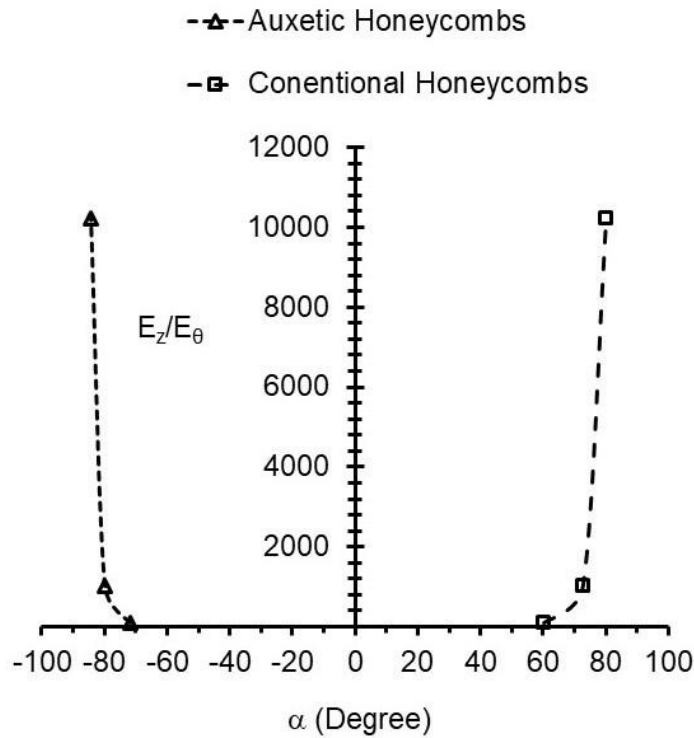


Figure 6.3: Target α for designing of cellular cylinders.

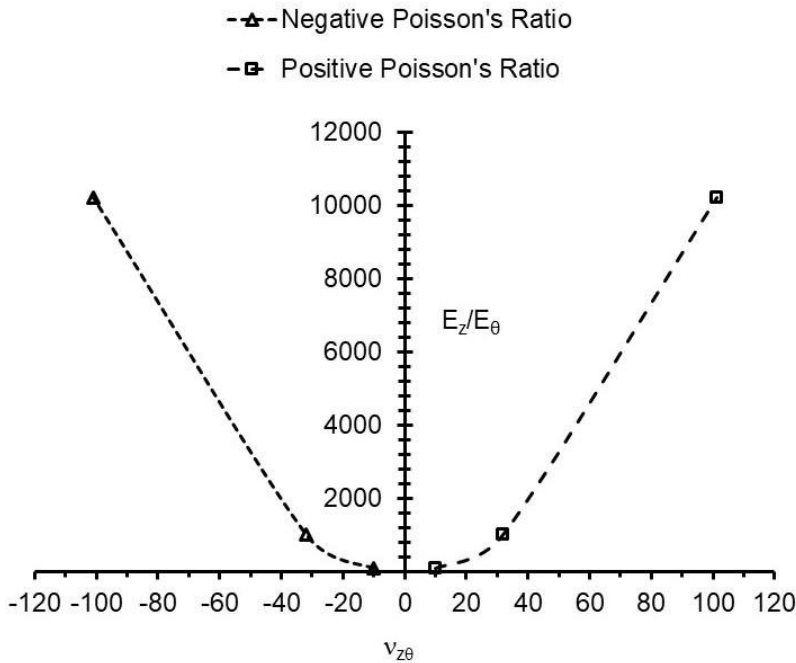


Figure 6.4: Target $\nu_{z\theta}$ for designing of cellular cylinders.

For the re-entrant hexagonal honeycomb, the minimum value of $h = 2l$ (the ends of the diagonal ribs overlap for $h/l < 2$). However, $h/l < 2$ is possible (indeed h/l can tend to zero) for the conventional honeycomb. Hence in this further extension of the use of the analytical flexure model, consideration is given to obtaining Poisson's ratios having larger magnitude than $|v_{z\theta}| = 10$ through reducing h/l for the conventional hexagonal honeycomb and also allowing $|\alpha| \rightarrow 90^\circ$ for both conventional and re-entrant hexagonal honeycombs.

Axial loading of honeycombs where $\alpha \rightarrow \pm 90^\circ$ will induce stretching or compression along the length of the ribs of length l , not accounted for in the Gibson and Ashby model. So, a range of honeycomb angles (typically $80 < |\alpha| < 88^\circ$) for fixed h/l ratios was considered in the FE modelling and experimental mesh designs.

CAD-FE-Experimental approach:

CAD models of the cellular meshes were created using the SolidWorks software (2015 version) and were then imported into the Ansys FE software package (Ansys Workbench 17.1 version). The methodology described in Chapter 5 for the FE modelling of the solid wall cylinder was employed to simulate the mesh cylinders. The forces applied and directional deformations (axial and radial) were output from the simulated FE models. Equatorial radial deformation (ERD) vs axial deformation (AD), ERD vs force, and ERD vs axial strain were subsequently plotted to determine the expansion capabilities of the cellular mesh models. These FE predictions can then be compared against experimental results to validate the cellular mesh models. The experimental part of the CAD-FE-Experimental approach is described in the 'Fabrication of cellular mesh cylinders' section of this Chapter.

6.2.1 CAD models for validation of outputs of FE modelling of solid wall cylinder

Auxetic and conventional honeycomb meshes can be derived for $v_{z\theta} \leq -10.1$ and $v_{z\theta} \geq +10.1$, respectively to achieve large equatorial radial deformation

for small axial strain (results of FE modelling of solid wall cylinder outlined in the Chapter 8). The mesh designs are presented in Table 6.6.

The global cylinder parameters considered during the FE modelling of the solid wall cylinder without end pieces (Chapter 5) were outer diameter (40mm), wall thickness (2.5mm) and length (300mm). The same global parameters were used for the expansion mechanism designs considered here. Moreover, cellular meshes were designed to assess the expansion capabilities for outer diameter of 20mm of cylinder (to ensure deployment of the expansion mechanism through various laparoscopic ports which are generally in the range of 15-25mm). For example, Auxetic 4 and Conventional 5 were designed for 20mm outer diameter of cylinder; however, wall thickness (2.5mm) and length (300mm) were not changed.

Auxetic honeycomb meshes (Auxetic 5-7) were designed (Table 6.5) and assembled with the pronged cone end pieces in SolidWorks software (version 2015). 'Auxetic 5-7' models were then simulated in Ansys to predict expansion capabilities of cellular meshes for the uniaxial compression mechanism.

Table 6.5: Honeycomb cylinders simulated for the validation of outputs of FE modelling of a solid wall cylinder.

Model name	$\nu_{z\theta}$	E_z/E_θ	α (degree)	Outer diameter (mm)	N_c	N_v	t (mm)	h (mm)	l (mm)	h/l	t/l
Auxetic 1	-10.5	1.02×10^2	-72.1	40	19	12	0.5	19.87	9.93	2	0.0503
Auxetic 2	-33.4	1.02×10^3	-80.0	40	31	12	0.5	20.52	10.26	2	0.0487
Auxetic 3	-100.8	1.02×10^4	-84.3	40	49	12	0.5	20.73	10.37	2	0.0482
Auxetic 4	-108.3	1.19×10^4	-84.5	20	18	8	0.5	31.11	15.55	2	0.0322
Auxetic 5	-10.5	1.02×10^2	-72.1	40	19	12	0.5	19.87	9.93	2	0.0503
Auxetic 6	-108.2	1.19×10^4	-84.5	40	18	4	1	62.22	31.11	2	0.0321
Auxetic 7	-216.2	4.76×10^4	-86.1	40	24	4	1	62.32	31.16	2	0.0322
Conventional 1	10.4	1.02×10^2	60.7	40	31	12	0.5	7.25	3.63	2	0.1379
Conventional 2	10.1	1.02×10^2	65.5	40	25	12	0.5	5.45	5.45	1	0.0917
Conventional 3	32.5	1.02×10^3	76.0	40	41	12	0.5	5.29	5.29	1	0.0946
Conventional 4	100.8	1.02×10^4	82.0	40	64	12	0.5	5.23	5.23	1	0.0955
Conventional 5	108.4	1.19×10^4	82.2	20	24	8	0.5	7.85	7.85	1	0.0637

Selective CAD models of cellular meshes were designed (Table 6.5) and simulated to predict expansion capabilities. Cellular cylinders without end pieces were pulled (auxetic honeycombs) and compressed (conventional honeycombs) axially (i.e. uniaxial tension and compression mechanism of deployment, respectively). Equatorial Radial Deformation (ERD) vs Axial Deformation (AD), ERD vs Force, and ERD vs strain were plotted.

The total numbers of circumferential and lengthwise RVEs were kept reasonably high to ensure sufficient cellular structures through the length of the cylinder. This should help to create a semi-rigid scaffold-like structure/device to support the retraction of simulant organs and maintain the surgical space/volume when fully deployed.

6.2.2 CAD models for fabrication of expansion mechanisms

Conventional honeycomb meshes were designed using high aspect ratios ($h/l=1, 0.33, \text{ and } 0.033$) and $\alpha \rightarrow 90^\circ$ (Table 6.6). Auxetic honeycomb meshes were designed for $h=2l$.

Cellular mesh cylinders outlined in the Table 6.6 were fabricated for 300mm length of cylinder. Fabrications of honeycomb meshes (Auxetic 8 and Auxetic 9, Conventional 6-9 models) were carried out using 68mm OD and 2.5mm wall thickness (Table 6.6). Conventional 10 and 11 as well as Beam 1 and 2 models were fabricated using 41mm OD and 2.5mm wall thickness cylinder (Table 6.6). Conventional 12 model was 3D printed for 40mm OD and 2.5mm of wall thickness (Table 6.6).

The top and bottom 25mm of the length of the cylinder were solid wall ends to protect the cellular meshes from damage during mechanical characterisation of the expansion response. Hence, the effective length of the cylinder having cellular structures (Table 6.6) was 250mm. However, the effective length of Conventional 10 and 11 models were 270mm to minimise the solid end pieces at both ends of cylinder.

The fillet feature of the SolidWorks software was used to reduce the sharp edges of the inverted ribs of the auxetic honeycombs during development of CAD models of auxetic cellular cylinders. The edges of beam strips were

rounded off by employing fillets to mitigate against high levels of stress concentration.

Auxetic 8 and Auxetic 9, Conventional 6-11, and Beam 1 and 2 models were fabricated using the laser cutting technique, while Conventional 12 model was fabricated using 3D printing technology. CAD models of cellular meshes outlined in Table 6.6 were designed and simulated using Ansys software (version 17.1) to predict expansion capabilities. Auxetic 8 and Conventional 12 cylinders were simulated using orthotropic material properties outlined in Table 5.5 albeit ensuring changes in the Poisson's ratios and shear moduli. Conventional 8 and 10 cylinders were simulated using orthotropic material properties for PVC polymer (Young's modulus = $3.83\text{E}+09$ Pa and Poisson's ratio = 0.4) consistent with PVC tube used during fabrication. Equatorial Radial Deformation (ERD) vs Axial Deformation (AD), ERD vs Force, and ERD vs strain were plotted.

Transient structural analysis was considered for simulating a nonlinear plastic behaviour of cellular cylinders (CAD-FE part of CAD-FE-Experimental approach). 'Isotropic Elasticity' and 'Multilinear Isotropic Hardening' components were selected from the database of material properties of the Ansys software to develop the 'Engineering Data'. Young's modulus (2×10^9 Pa) and Poisson's ratio (0.4) of PVC was added to 'Isotropic Elasticity' part of Engineering Data. True stress vs true strain curve obtained by stack compression tests for PVC sheets⁽²²⁸⁾ was utilised to extract data points and imported into the 'Engineering Data' to simulate 'Multilinear Isotropic Hardening' behaviour of cellular cylinders which would be laser cut from the PVC tube. As a way of example, a nonlinear plastic behaviour of Conventional 8 cylinder was simulated. Additionally, transient linear analysis was carried out for cellular cylinder to validate use of transient structural analysis instead of static structural analysis employed for solid wall cylinder.

Table 6.6: Cellular cylinders designed for fabrication. N/A=Not Applicable

Model name	$\nu_{Z\theta}$	E_z/E_θ	α (degree)	Outer Diameter (mm)	N_c	N_v	t_h (mm)	t_l (mm)	h (mm)	l (mm)	h/l	t_l/l
Auxetic 8	-39.1	1.56×10^3	-80.8	68	18	4	2	2	61.71	30.85	2	0.0648
Auxetic 9	-64.7	4.27×10^3	-82.9	68	22	4	2	2	62.02	31.01	2	0.0645
Conventional 6	689.9	9.45×10^5	87.8	68	30	3	4	2.5	1.35	40.35	0.033	0.0619
Conventional 7	1461.9	4.31×10^6	88.5	68	46	3	2.5	1.5	1.35	40.34	0.033	0.0372
Conventional 8	1392.1	1.96×10^6	88.2	68	36	3	4	2.25	10.42	31.26	0.33	0.0719
Conventional 9	504.6	2.58×10^5	86.4	68	38	3	3	2	20.85	20.85	1	0.0959
Conventional 10	211.1	4.51×10^4	84.4	41	16	3	4	2.5	20.88	20.88	1	0.1197
Conventional 11	317.3	1.53×10^5	86.3	41	16	3	4	2.5	10.43	31.29	0.33	0.0799
Beam 1	N/A	N/A	N/A	41	4	1	29.4	N/A	250	2	N/A	N/A
Beam 2	N/A	N/A	N/A	41	10	1	12.1	N/A	250	0.5	N/A	N/A
Conventional 12	45.0	2.03×10^3	78.0	40	24	6	1	1	10.53	10.53	1	0.0949

6.3 Fabrication of cellular mesh cylinders

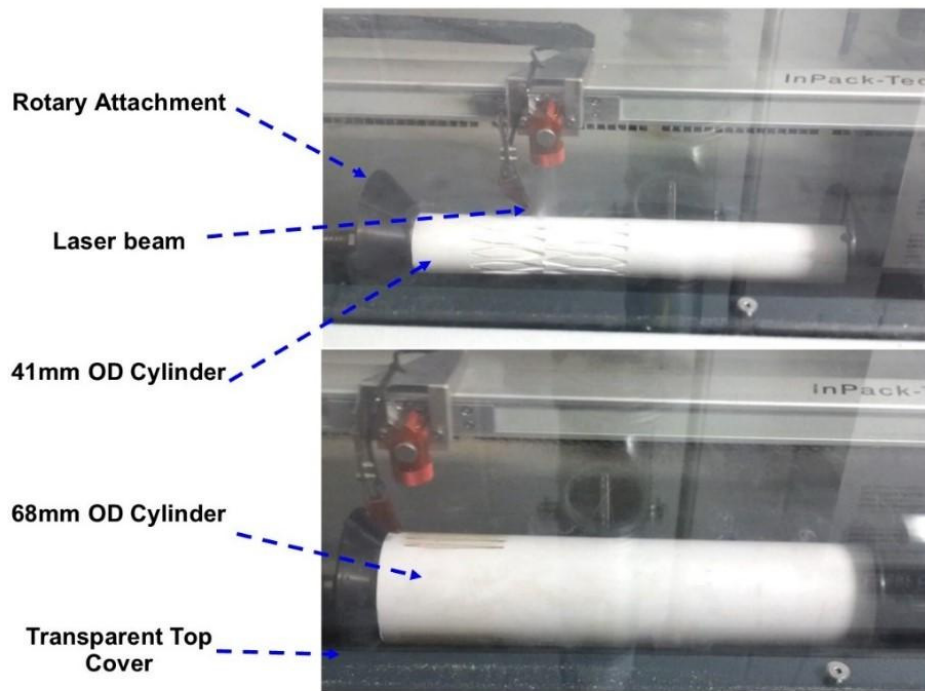
Cellular mesh cylinders were fabricated via 3D printing and laser cutting technology.

3D printing:

CAD models were 3D printed using Eden 350/350v™. DurusWhite™ RGD430, photopolymer of the PolyJet™ material family of Stratasys Ltd. was selected to simulate polypropylene-like behaviour for cellular mesh cylinders. DurusWhite™ imparts toughness, durability and flexibility to the 3D printed models. CAD models of cellular meshes were generated as a 3D part file (.stl format) for the 3D printing process. Eden 350/350v™ uses support material during the laying down process of successive layers of DurusWhite™ until the cylinder is printed. The support material of the 3D printed model was removed by spraying water with controlled force. The 3D printed cylinders were then dried at room temperature.

3D Laser cutting:

CAD models were laser cut using a Speedy 100™ Trotec laser cutter. It is a CO₂ based laser and has a 610×305mm working area (maximum height is 170mm) visible to the user due to the transparent design of the top cover. The Trotec laser software called JobControl® supports cutting jobs. Speedy 100™ comes with a rotary attachment used in this project to laser cut cellular mesh cylinders (Figure 6.5). When the rotary attachment is placed within the working area of the Speedy 100™, the movement of the axis in the y-direction is replaced by a rotary movement and is governed by InPack Technology™ for high quality cutting. The diameter of the laser beam is 0.2mm. The cylindrical tubes (FloPlast waste pipe) of 41mm and 68mm outer diameters were obtained from the local B & Q store and are made up of polypropylene (PP) and polyvinyl chloride (PVC), respectively. The wall thickness of both the PP and PVC cylinder is 2.5mm. They were cut to 300mm length prior to the laser cutting process.



Working Area of Speedy 100™

Figure 6.5: Cylinders mounted on rotary attachment of the Speedy 100™ laser cutter.

CAD models of cellular meshes were generated as 2D part files equivalent to the circumferences of 41mm and 68mm outer diameter cylinders. 2D drawings were imported and optimised using CorelDRAW® X4 and CorelDRAW® X7 software packages (version 17.1.0.572) in the PC associated with the Speedy 100™. A wooden rod of 30mm diameter was positioned inside the 41mm outer diameter cylinders using plastic rings at both ends to prevent the laser beam passing through the cylinder to affect the inner surface. The wooden rod was not used for the 68mm outer diameter cylinder since the laser beam did not penetrate through the cylinder. The height of the cylinder mounted on the rotary attachment was adjusted with in-built controls. The position of the laser beam was brought to the starting point by leaving the end pieces at both ends before initiating the laser cutting.

The power, speed and frequency of laser were kept at 95% (laser power range is 20-60 watts), 25% (maximum processing speed is 2.5 m/sec), and 5000 Hz, respectively, to laser cut the 41mm and 68mm outer diameter cylinders (Table 6.6 except prototypes fabricated via 3D printing). The laser cut cylinders were

unmounted from the rotary attachment and removed from the working area. Laser cut slots (i.e. cellular structures) of cylinders were removed by tapping with the hand and a scalpel. Prototypes were washed with warm and cold water to remove dark spots due to the laser cutting process.

6.4 Mechanical characterisations of cellular mesh cylinders

Mechanical characterisation of promising laser cut prototypes was carried out using an Instron E3367 machine. BlueHill 4.0 software associated with the Instron machine was used to record data. The load cell capacity was 5kN. Prototypes were compressed and pulled to a maximum of 50mm (i.e. end of test) through the length of cylinder at a rate of 10mm/min. Preload was 1N prior to the beginning of uniaxial compression and tension tests. A Nikon D3100 SLR camera mounted on standard tripod was used to record the degree of expansions of the range of prototypes.

Instron tests were carried out for cellular cylinders and prototypes consisting of beam strips shown in Table 6.6 except Conventional 12 (3D printed). Load vs displacement curves were plotted from the raw data extracted from the BlueHill software. Stress vs strain and tangent modulus vs strain were subsequently plotted. Stills images were extracted from the video footage to determine the degree of expansion of the prototypes.

6.5 In-vitro assessments of cellular mesh cylinders

In-vitro assessments of candidate prototypes were carried out to assess their organ retraction and space creation capabilities within the in-house test-rig.

Study set up:

The study set up is shown in Figure 6.6 and described below.

- The pressure sensor system (Figure 4.13a, Chapter 4) along with laptop consisting of data logging software was located next to the Instron machine mounted with the second test-rig (Figure 4.12, Chapter 4). The pressure sensor was attached to one of the struts in the equatorial region of the mounted prototype using double-sided tape (Figure 6.6). This is to measure the surface pressure exerted by promising prototypes on foam

blocks (PUR30 FR, density = 28-32 kg/m³) or simulant organs during assessment of the expansion mechanisms.

- A Nikon D3100 SLR camera mounted on standard tripod was set up in front of the Instron machine to record organ retraction and space creation functions of promising prototypes.
- The Instron tests were carried out using the set up described for the mechanical characterisation of promising prototypes without surrounding materials (Section 6.5).

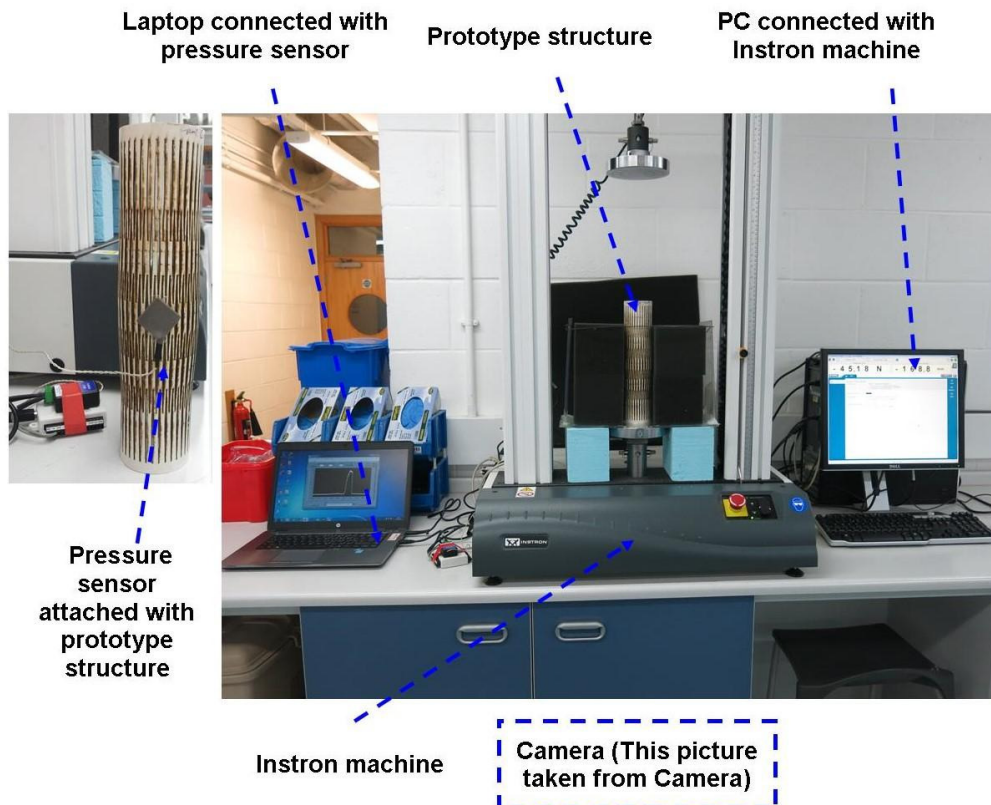


Figure 6.6: Study set up for in-vitro assessments of prototype structures.

Evaluation of expansion capabilities inside the test-rig:

The foam blocks and simulant organs were retracted inside the in-house test-rig mounted on the Instron machine by promising prototype expanding structures.

The Instron machine as shown in Figure 6.6 was used to apply uniaxial compressive and tension loads on to the prototypes. Surface pressure exerted on to the foam blocks and simulant organs due to expansion of prototypes was recorded using data logging software on the laptop. Video footage was collected during evaluation of expansion capabilities of prototypes. The

retraction events were simultaneously recorded and subsequently analysed to quantify the degree of retraction and space created inside the test-rig consisting of foam blocks and simulant organs.

The synchronisation of data collected during in-vitro assessments of prototypes expanding structures was attained by implementing following steps:

- Run the pressure sensor for flat line in the data logging software (there was ~1-2kPa pressure recorded at the beginning of each Instron test due to the presence of the sensor between the prototype and foam blocks/simulant organs).
- Turn camera ON to start recording of video footage
- Start the Instron test
- Complete the test cycle of the Instron test
- Continue recording surface pressure exerted by prototype in its deployed state and video footages for additional ~1 min 20 secs to capture any drop in surface pressure when the foam blocks and simulant organs are kept in the retracted state
- Stop the Instron test (i.e. release the load applied on prototypes)
- Turn the camera OFF
- Stop the pressure sensor to get flat line in the data logging software.

Data analysis:

Load vs displacement curves were plotted using the raw data extracted from the Instron machine. Stress vs strain, tangent stiffness vs axial compression, and tangent modulus vs strain were subsequently plotted to demonstrate the mechanical behaviour of the cellular prototypes within the test-rig consisting of foam blocks and simulant organs. Sequences of still images were extracted from the video footage and analysed using ImageJ(225) to calculate the ERD and AD. Pressure sensor vs time curves were plotted for the retraction of foam blocks and simulant organs.

The correlation was established between times recorded on the pressure sensor software and the video footage. Thereafter, total equatorial deformation was correlated with the surface pressure exerted by prototypes by plotting

surface pressure and total equatorial deformation against time. In addition, axial compressive force and total equatorial deformation were plotted against axial deformation to demonstrate the degree of compressive force required for the large equatorial radial expansion.

6.6 In-vivo and in-vitro assessments of Doughnut shape inflatable prototypes

The Doughnut shape inflatable prototype structures of different inner diameters (Figure 6.7) were fabricated from polyurethane (PU) film using the radio frequency (RF) welding technique by the industry sponsors of this project in parallel to the development of expansion mechanisms. The inner diameters are 100mm and 80mm. They are connected to the air speed regulator through the pneumatic tubes. It is plugged into the DC voltage and air speed regulator is turned on to pass the pressurised air inside the doughnut shape prototypes through the pneumatic tubing. Additionally, there is an on/off valve to control the degree of inflation and deflation of the doughnut shape prototypes.

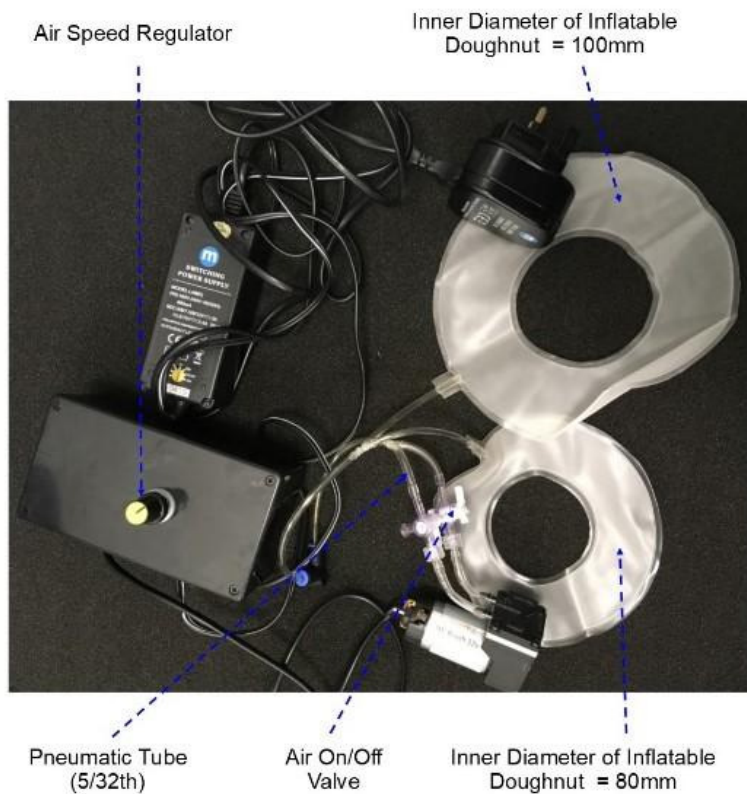


Figure 6.7: Inflatable doughnut shape prototypes.

They were assessed for their expansion capabilities within the pig abdomen (in-vivo) and inside the in-house test rig (in-vitro) using simulant organs.

In-vivo:

Ethics committee approvals were obtained from the Northwest NHS Research Ethics Committee and Faculty of ACES Research Ethics Committee (FREC) of Sheffield Hallam University. The in-vivo study was carried out at the Royal Veterinary College (RVC), London and led by Mr Titus Augustine (principle investigator). The doughnut shape prototypes were inflated to deploy within the pig abdomen (Figure 6.8). Stills were taken during the retraction of pig liver and bowel.

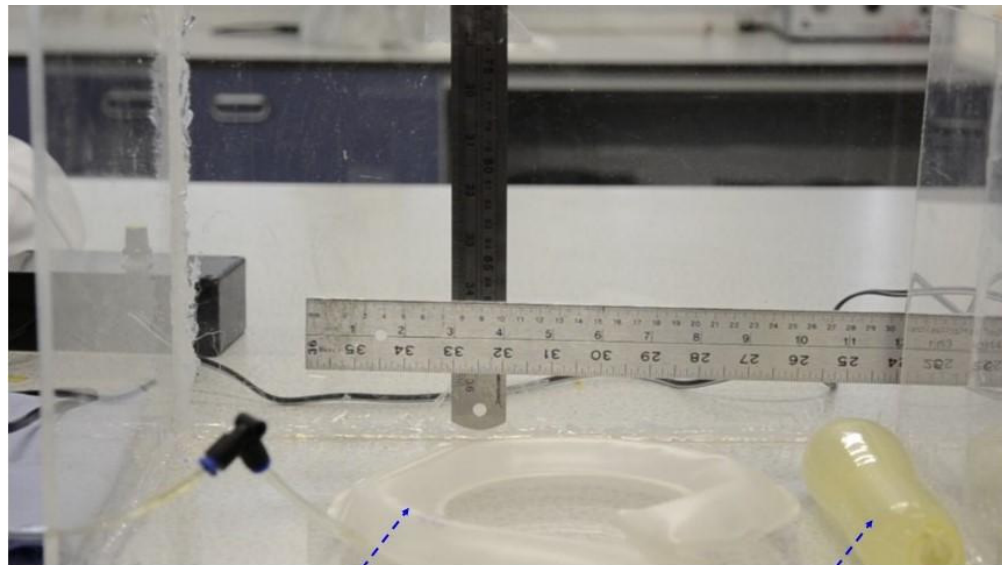
Additionally, surface pressure exerted by the fingertips of the principal investigator on the pig liver, bowel and abdomen were recorded using the pressure sensor (Figure 4.13). Surface pressure vs time curves for the retraction of pig liver, bowel and abdomen are plotted. Video footages were not recorded for the retraction of pig liver, bowel and abdomen.



Figure 6.8: Inflation of the doughnut shape prototype within the pig abdomen.

In-vitro:

The in-vitro study was carried out within the test rig developed in this project (Figure 4.11). The study set up is shown in Figure 6.9.



Doughnut shape inflatable prototype
placed within the test rig

Bowel Simulant

Figure 6.9: In-vitro study set up to assess expansion capabilities of doughnut shape prototypes within the test rig.

6.7 Summary

The methodology to derive cellular meshes using auxetic and conventional hexagonal honeycombs was outlined. Laser cutting and 3D printing techniques of fabrication, mechanical characterisation of candidate expansion mechanisms without surrounding materials, in-vitro set up to assess promising expansion mechanisms within the test rig and study set up for in-vivo and in-vitro assessment of doughnut shape inflatable prototypes were described in this chapter.

7 Results 1: Abdominal simulator and in-vivo measurement of organ surface pressures and retraction distances

The results of the fabrication and assessment of simulant organs, the use of in-house test rigs for in-vitro assessments of simulants and pig organs, and in-vivo measurement of surface pressures and retraction distances applied to key abdominal organs during abdominal surgery are described in this chapter.

7.1 Fabrication of simulant organs

Solid and hollow simulant organs were fabricated using materials screened and finalised in Chapter 4 and results are outlined below.

7.1.1 Solid organ simulants

Fabrication of solid simulants of human organs:

Solid organ simulants were made using the consistency (% v/v) of Pro Gel 10 softener shown in Table 4.3, Chapter 4. Kidney, spleen² and liver simulants are shown in Figure 7.1, Figure 7.2 and Figure 7.3, respectively. Different quantities of Dr Oetker food colour such as red, green and brown were used for kidney, spleen and liver simulants, respectively, to ensure that they can be easily differentiated after curing in addition to any difference in their elasticity.

² Human spleen simulants (20% and 30% v/v of Pro Gel 10 softener) reported in Figure 7.2 were fabricated using different mould than used for 50% v/v simulant (Chapter 4) and hence, they don't possess the physical dimensions of human spleen.

To solve this inconsistency, I have followed the methodology described for the fabrication of liver simulant in Chapter 4 and developed the 3D printed model to ensure the correct physical dimensions of spleen simulants. I have however not completed the final two steps – a) making two-parts mould and b) fabrication of the spleen simulants using 20%, 30% and 50% v/v of Pro Gel 10 softener within two-parts mould.



Figure 7.1: Human kidney simulants. The percentage values refer to the Pro Gel 10 softener concentration (% v/v) in each case.

Stickiness of kidney simulants fabricated from Pro Gel 10 softener concentration greater than 50% did create difficulty in manual handling and hence, they were preserved in plastic bags. Kidney simulants were made from 20-80 % v/v of Pro Gel 10 softener to check the impact of concentration of softener on the elastic modulus of cured simulants.



20%

30%

50%

Figure 7.2: Human spleen simulants. The percentage values refer to the Pro Gel 10 softener concentration (% v/v) in each case.



20%

30%

50%

Figure 7.3: Human liver simulants. The percentage values refer to the Pro Gel 10 softener concentration (% v/v) in each case.

Fabrication of solid simulants of pig organs:

Pig liver simulants were made from 20%, 30%, and 50% v/v of Pro Gel softener and 50% v/v simulant is shown by way of example in Figure 7.4.



Figure 7.4: Pig liver simulant (50% v/v of Pro Gel softener)

7.1.2 Hollow organ simulants

Stomach and bowel simulants (5 % and 7.5%) are shown in Figure 7.5 and Figure 7.6, respectively. The stomach simulant was filled with 50ml of water and inflated with pressurised air.

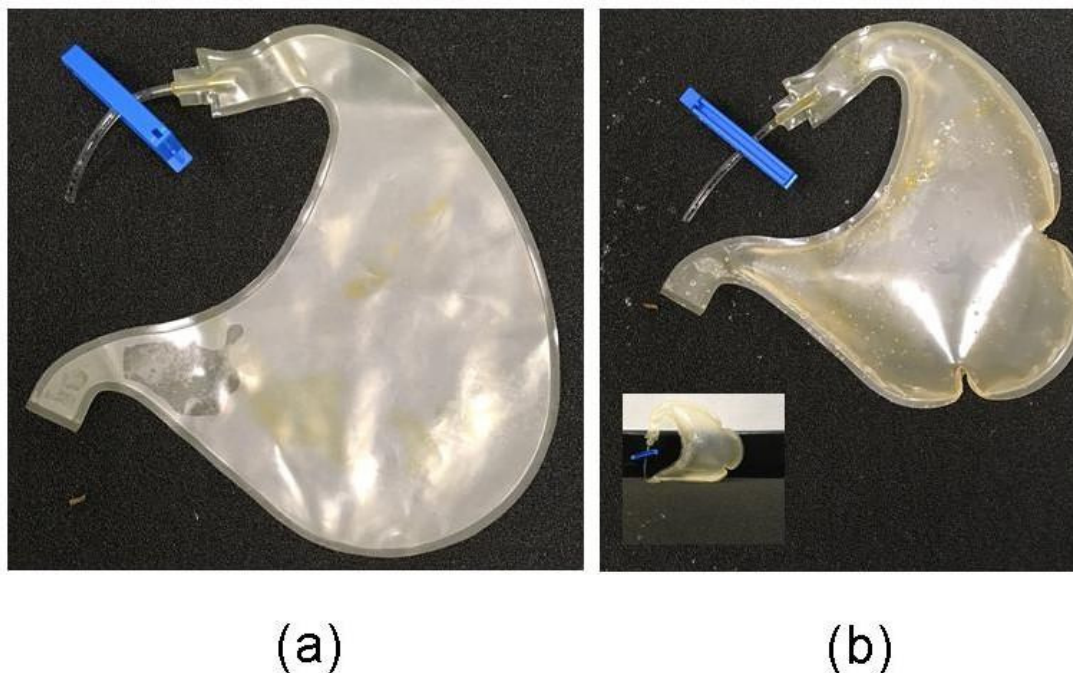


Figure 7.5: Stomach simulant. (a) Empty (b) Full (mixture of water and air). Inset picture in (b) shows stomach simulant filled with water and pressurised air in standing position.

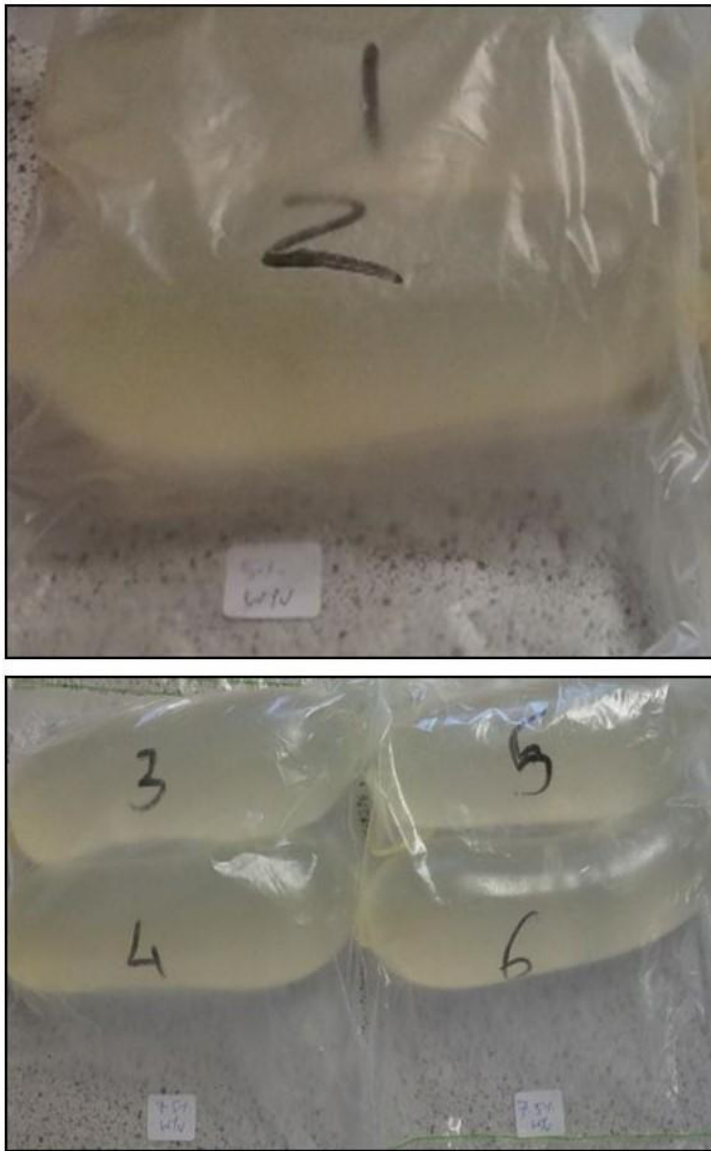


Figure 7.6: Bowel simulants (5% and 7.5% w/v concentration of wallpaper paste).

7.2 Assessment of biomechanical properties

Density and elasticity govern the quantity of force required to move, lift and deform the simulants and pig organs within the in-house abdominal simulator. These biomechanical properties have, therefore, been evaluated in the following sections.

7.2.1 Density of simulant organs

Average density values of simulants of the liver, spleen and kidney for different concentrations of Pro Gel 10 softener (% v/v) were calculated using weight and volume of solid simulants (Table 7.1) and plotted in Figure 7.7. Errors associated in the measurement of weight of solid simulants are also depicted in

Figure 7.7. The density of the solid simulants was similar to, but slightly lower than, the density of the human liver (Table 2.5, Chapter 2)^(27,28), kidney (described in text in Chapter 2.1.2)⁽⁴⁵⁾, and spleen (Table 2.15, Chapter 2)^(56,62,63), with the largest discrepancy occurring at 60 and 70 % v/v softener concentration (Figure 7.7).

Table 7.1: Average density of solid simulants.

Concentration of Pro Gel 10 softener (% v/v)	Average density (kg/L)
0	0.96±0.1
10	0.98±0.1
20	0.97±0.1
30	0.99±0.1
40	0.91±0.1
50	0.94±0.1
60	0.83±0.1
70	0.84±0.1
80	0.98±0.1

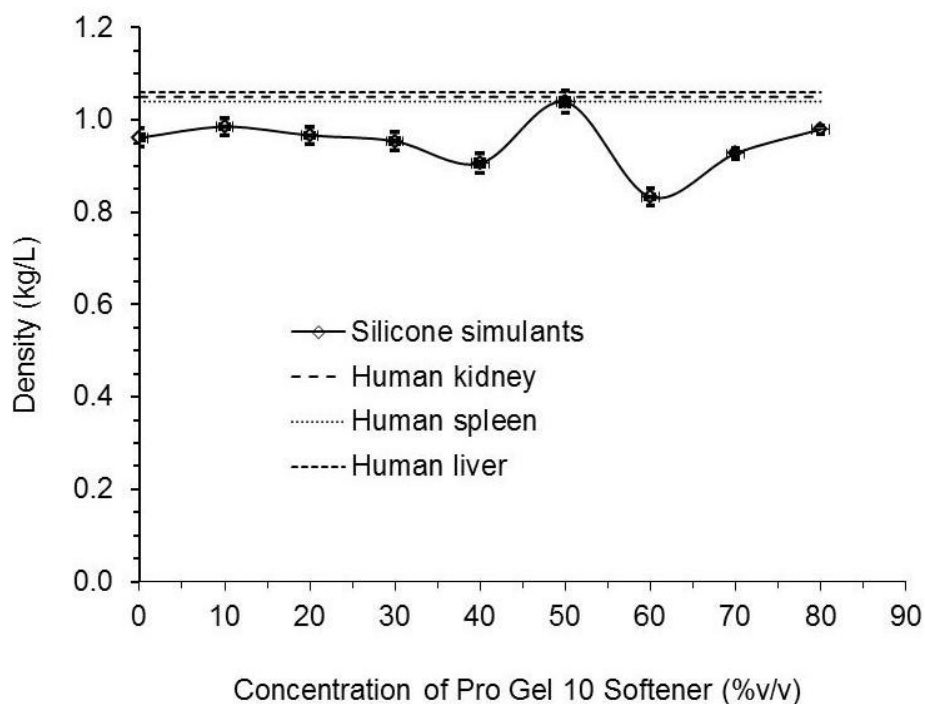


Figure 7.7: Average density of solid simulants compared with the actual densities of the human kidney, spleen and liver.

7.2.2 Elasticity of solid simulants

The results of the in-vitro mechanical tests on solid simulants of pig liver and kidney, and actual pig liver and pig kidney are reported in this section to evaluate the elasticity of the solid simulants.

Pig liver samples:

Typical force against displacement curves for the different areas of the right and left lobe were plotted for four pig livers (A-D). They are shown in Figure 7.8 for pig liver A.

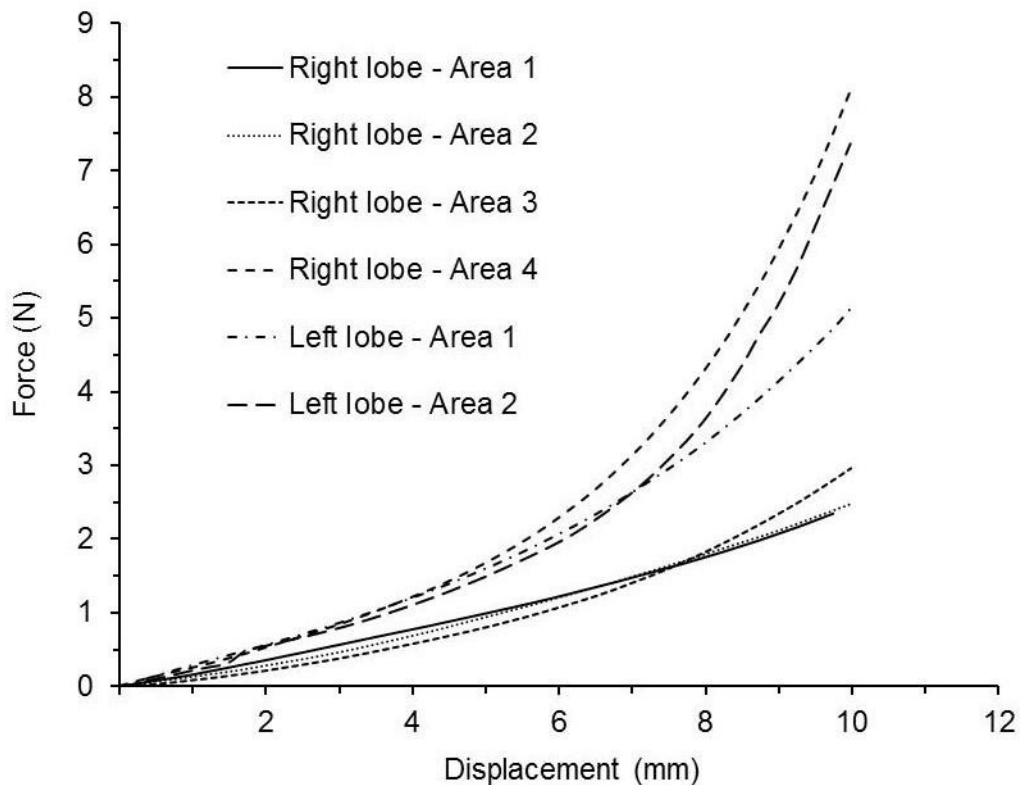


Figure 7.8: Force vs Displacement curves for the right and left lobe of pig liver A.

Force and displacement were converted to stress and strain, respectively, using Equations 3.1 and 3.6 (Chapter 3). In Equation 3.1, the area of the sample was taken as the area of the circular indenter in contact with the sample during the compression test. The difference in the deformed length and the original length in Equation 3.6 corresponds to the displacement or compression distance imposed by the Instron machine.

Initial thickness was measured (before Instron tests) three times using a standard scale for different locations of the (non-uniform) right and left lobes of each pig liver. The average thickness values of the right and left lobes of the four pig liver samples are shown in Table 7.2.

Table 7.2: Thickness of real and simulant pig liver samples.

Real pig liver			Pig liver simulant		
Pig liver sample	Thickness (mm)		Pro Gel 10 softener concentration (% v/v)	Thickness (mm)	
	Right lobe	left lobe		Right lobe	left lobe
A	20±1.3	16±1.2	20	20±1.3	16±1.2
B	30±0.8	20±0.5	30	20±1.3	16±1.2
C	20±1.2	16±0.2	50	20±1.3	16±1.2
D	30±1.1	20±0.6	-	-	-

Each of the force against displacement plots were converted into stress against strain curves for the four pig liver samples. Exemplar stress against strain curves for the right and left lobes of pig liver A are shown in Figure 7.9.

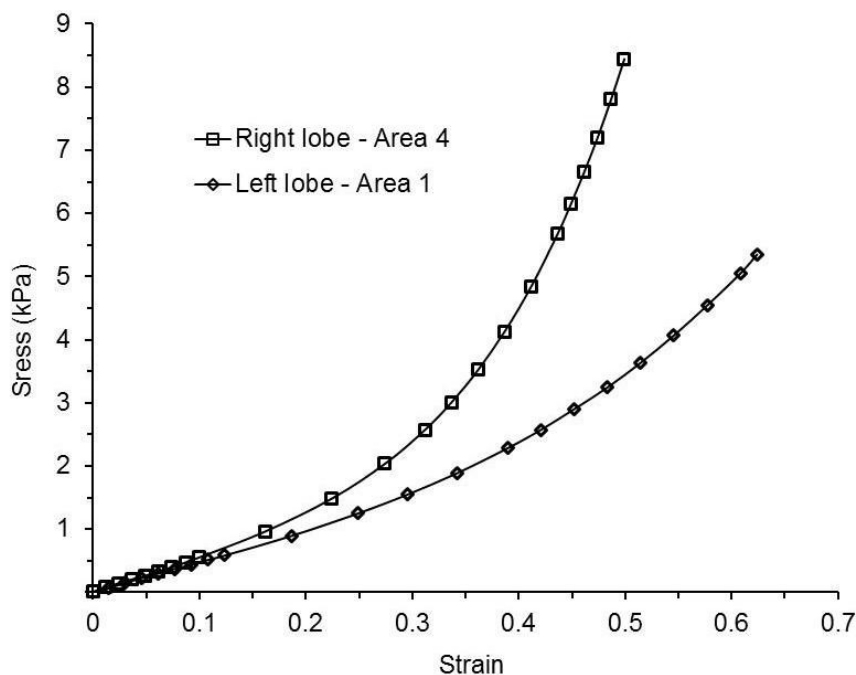


Figure 7.9: Stress vs strain curves for area 4 of the right and area 1 of the left lobe of pig liver A.

The stress-strain responses are non-linear and there is significant variation between regions of the same liver. Strain-dependent Young's modulus curves were, therefore, generated by differentiating the equations obtained from fitting fourth order polynomial curves to the data, corresponding to the tangent modulus. For example, the fourth order polynomial fitted curve to the stress-strain data for area 4 of the right lobe of pig liver A is shown in Figure 7.10. The corresponding Young's modulus vs strain data for the right lobe of pig liver A is shown in Figure 7.11. The fourth order polynomial fitted curves were similarly obtained for the remaining three areas (Area 1 to 3) of the right lobe and two areas (Area 1 and 2) of the left lobe (depicted in Figure 7.8) of pig liver A.

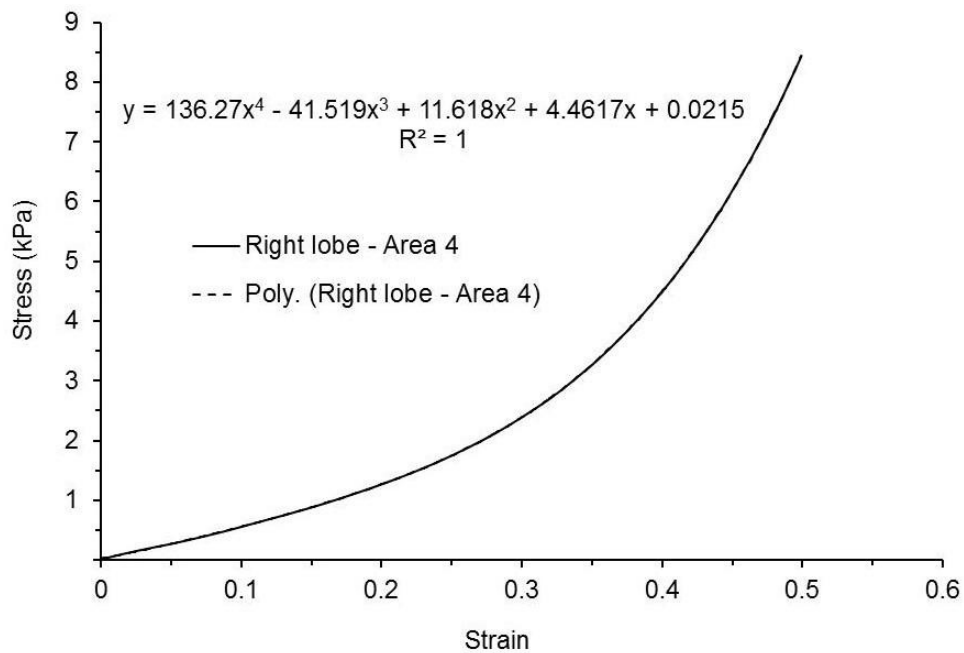


Figure 7.10: Fourth order polynomial fit to the stress vs strain curve for the right lobe (area 4) of pig liver A.

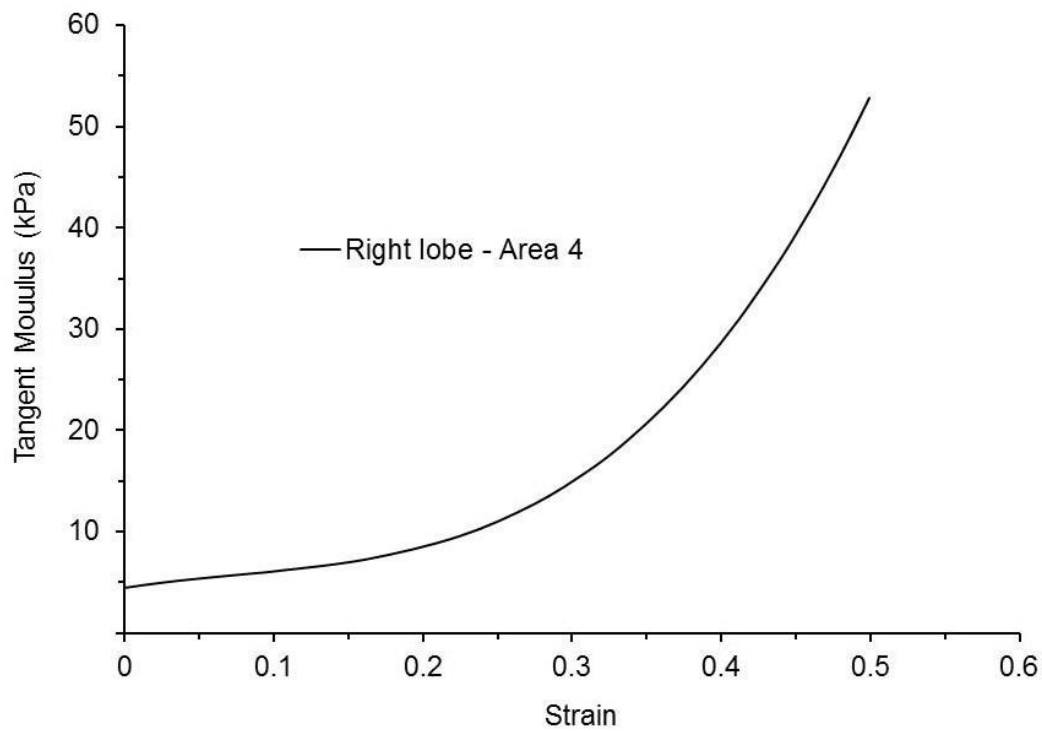


Figure 7.11: Tangent modulus vs strain for area 4 of the right lobe of pig liver A.

The average stress-strain curves were subsequently obtained from the individual responses for the right and left lobes and are plotted in Figure 7.12.

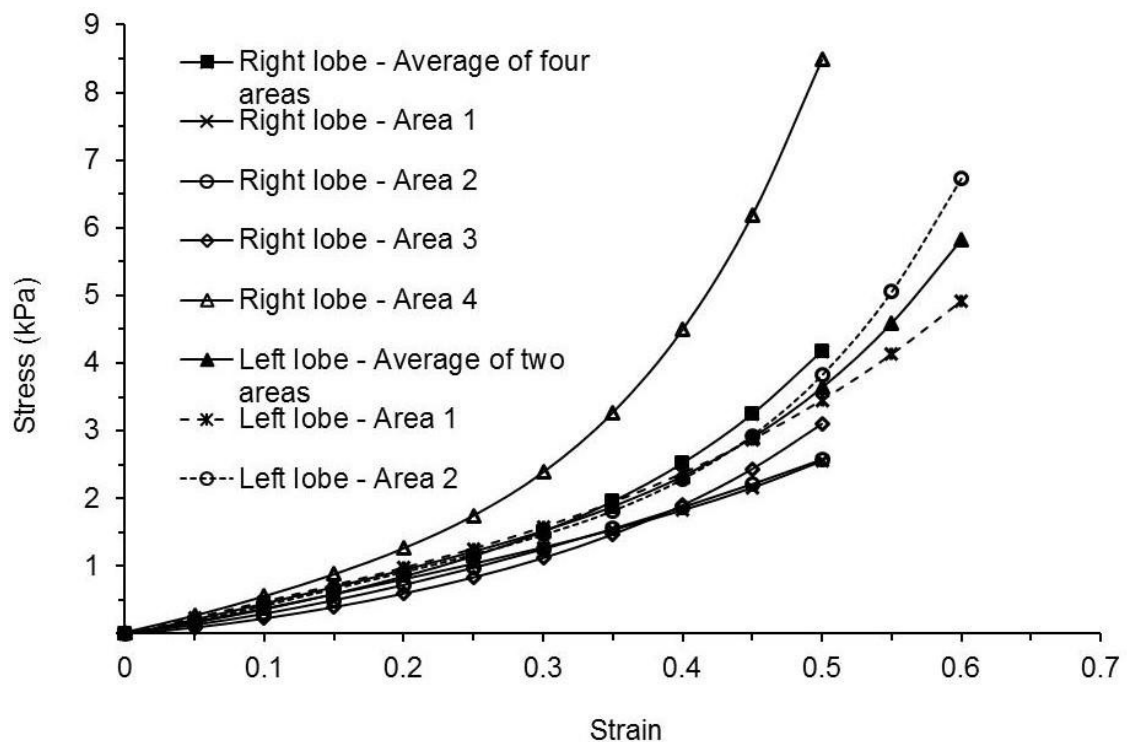


Figure 7.12: Average stresses for the right and left lobe of pig liver A.

The average tangent moduli were derived for the right and left lobe (Figure 7.13) using the fourth order polynomial equations obtained from the corresponding average stress-strain responses of the right and left lobes of pig liver A in Figure 7.12. The overall average stress-strain response for pig liver A was calculated using the average responses of the right and left lobe for the strain range of 0-0.5. The overall average tangent modulus for pig liver A was finally derived (Figure 7.13) using the fourth order polynomial equation obtained from the overall average stress vs strain plot for pig liver A.

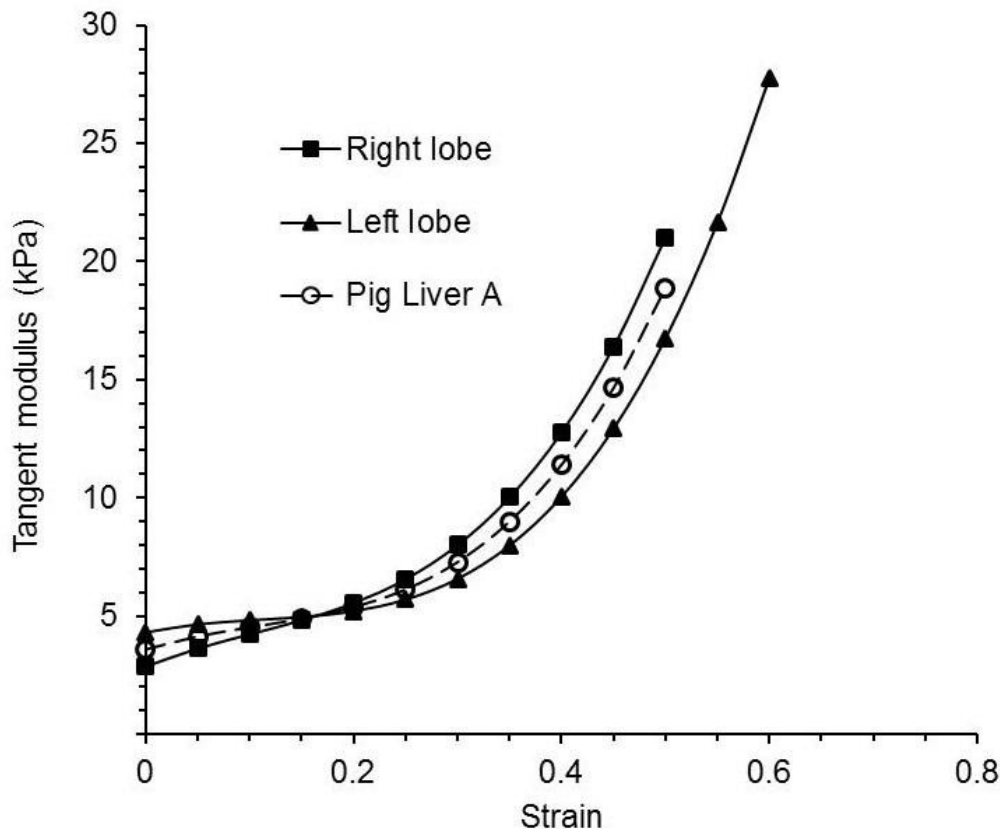


Figure 7.13: Average tangent modulus of pig liver A compared with the average tangent modulus of the right and left lobes of pig liver A.

Similarly, the average tangent modulus was obtained for the remaining three pig liver samples (pig liver B to D). The average tangent modulus of four pig livers is compared with the average tangent modulus of the individual pig liver samples in Figure 7.14. There is variability in the average tangent modulus responses between samples, but all follow the same generic trend of relatively low modulus at low strain, increasing in a non-linear manner as strain increases.

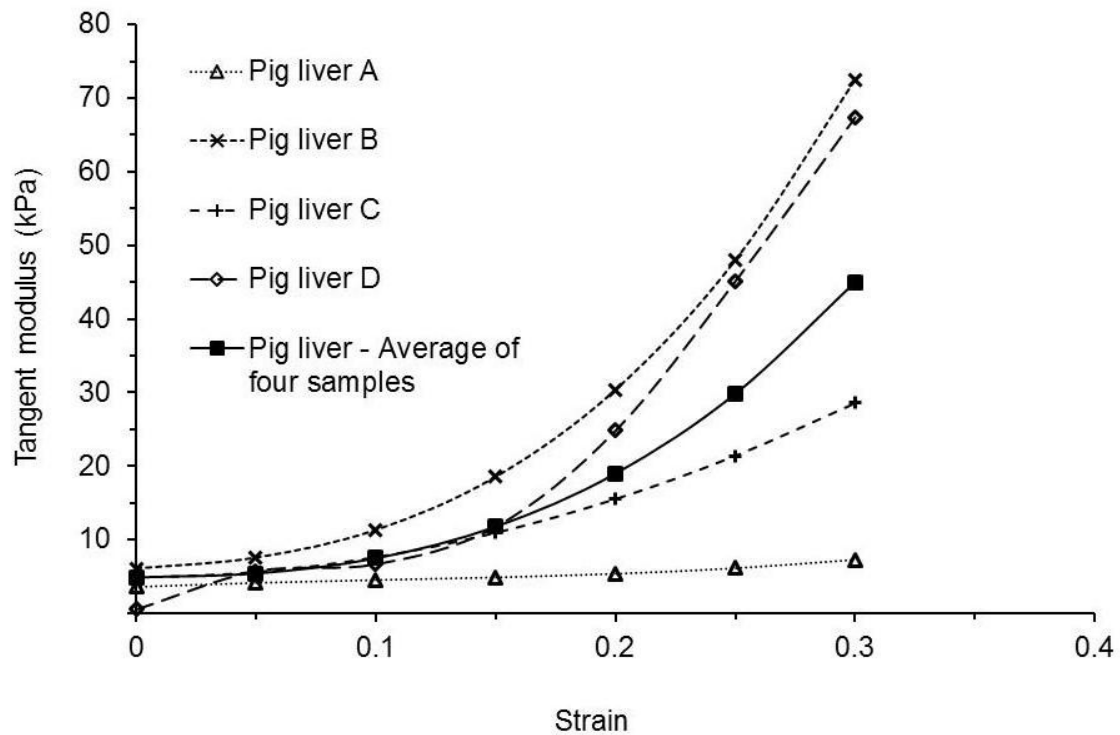


Figure 7.14: Average tangent modulus of four pig livers compared with the individual pig liver average responses.

Pig liver simulants:

The pig liver simulants were fabricated from 20% v/v, 30% v/v, and 50% v/v consistencies of the Pro Gel 10 softener (Chapter 4). In this chapter, these concentrations are referred in the abbreviated forms as 20%, 30%, and 50% for pig liver simulants (LS), for example, 'LS 30% Right lobe' in Figure 7.15.

Average force against displacement curves for the right lobe (four areas) and left lobe (two areas) were plotted for the pig liver simulants (Figure 7.15). Each of the force against displacement plots were converted into stress against strain curves for the pig liver simulants as explained for actual pig liver A. The average stresses were subsequently calculated for the pig liver simulants and plotted against strain in Figure 7.16. The fourth order polynomial fitted curve to the average stress-strain data of the 50% v/v softener concentration pig liver simulant is shown in Figure 7.16 by way of example. The average tangent modulus for each pig liver simulant was finally derived (Figure 7.17) using the fourth order polynomial equations obtained from the average stresses reported in Figure 7.16. The tangent modulus responses of the pig liver simulants (Figure

7.17) have the same general trend of increasing modulus with increasing strain as actual pig liver (Figure 7.14).

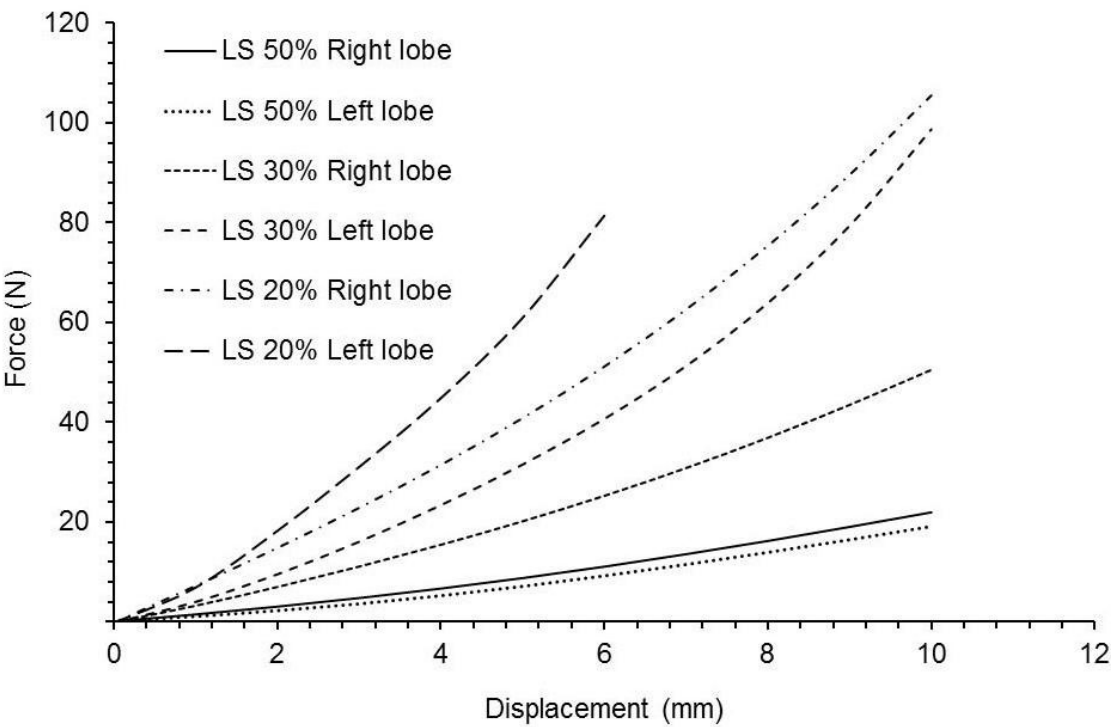


Figure 7.15: Average Force vs Displacement curves for the right and left lobe of the pig liver simulants.

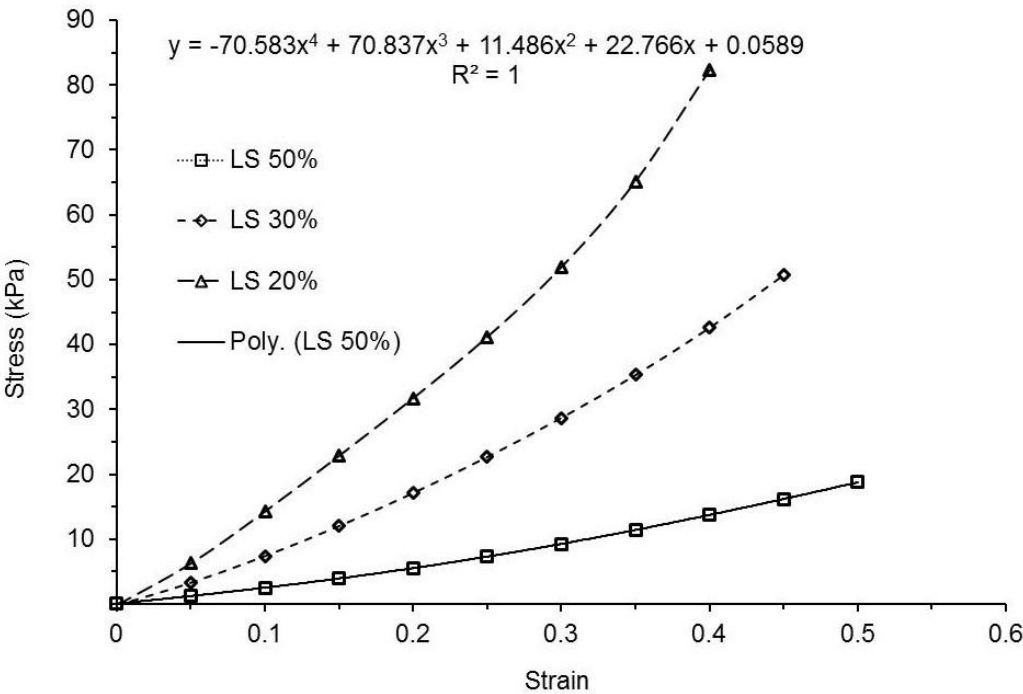


Figure 7.16: Average stress-strain responses for pig liver simulants.

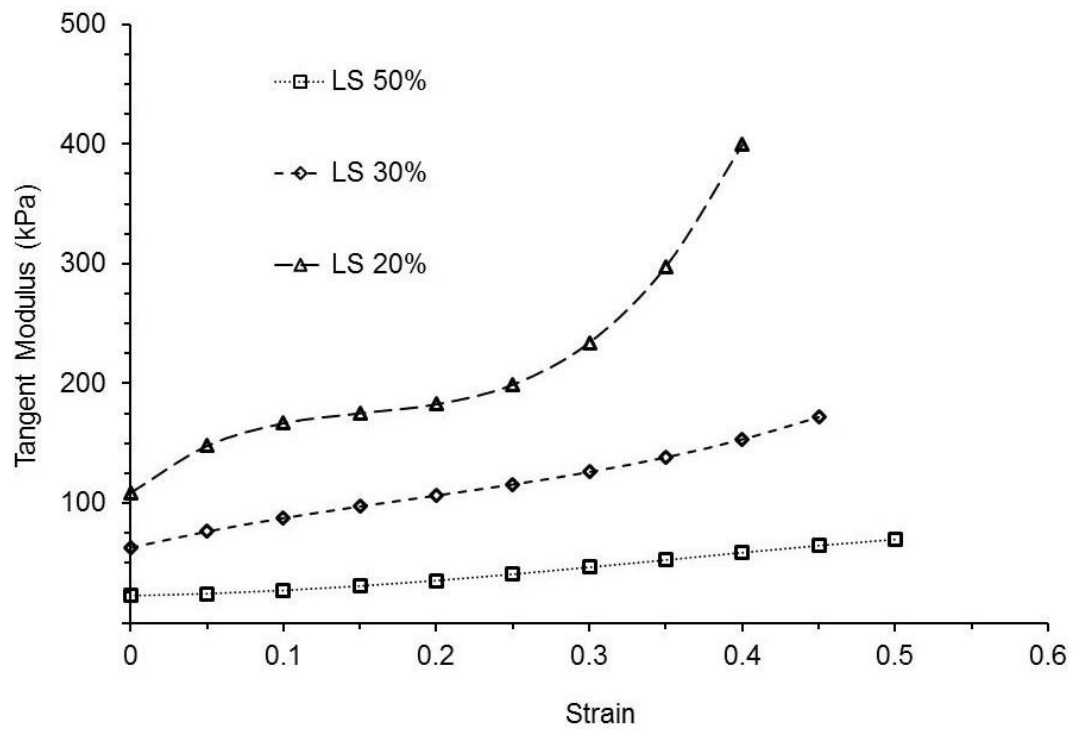


Figure 7.17: Average tangent modulus of pig liver simulants.

The tangent modulus of pig liver (average of four samples) and pig liver simulants are plotted against strain in Figure 7.18a which suggests that elasticity (or tangent modulus) of LS 50% simulant has closest match with elasticity of pig liver. Although it should be noted that there is a substantial divergence in tangent modulus at lower strain (<0.25) (Figure 7.18b).

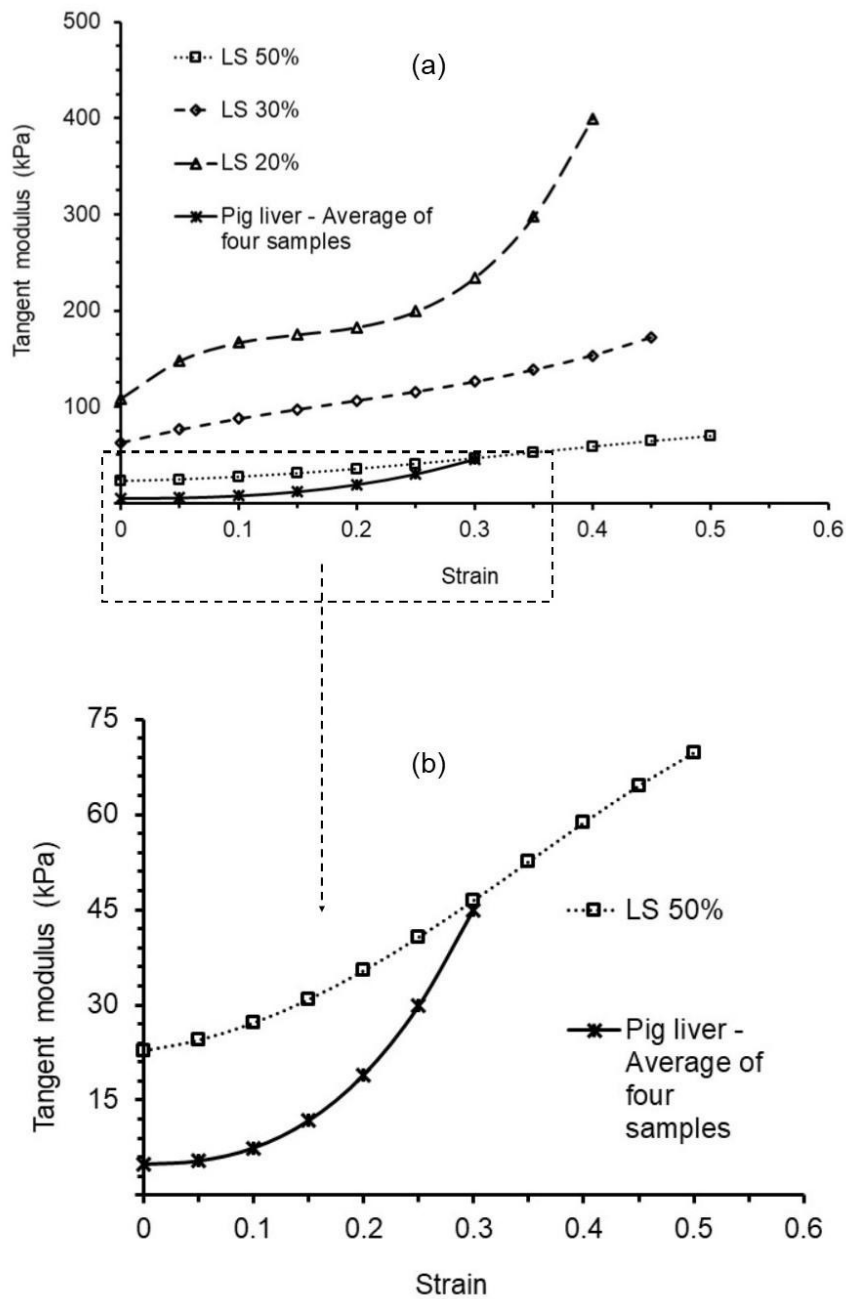


Figure 7.18: Average tangent modulus of actual pig liver and equivalent pig liver silicone simulants.

Pig kidney samples:

Average force against displacement curves for five kidney samples (average force applied for 3 compression tests on each pig kidney) are plotted in Figure 7.19. Average stresses were calculated for individual kidney samples and thereafter average stresses (Figure 7.20) as well as tangent modulus (Figure 7.21) [calculated from a moving average of the raw data (10 data points)] were plotted against strain for the five pig kidney samples as explained for the pig

liver samples. The trends in stress and tangent modulus with strain for pig kidney are similar to those noted above for pig liver.

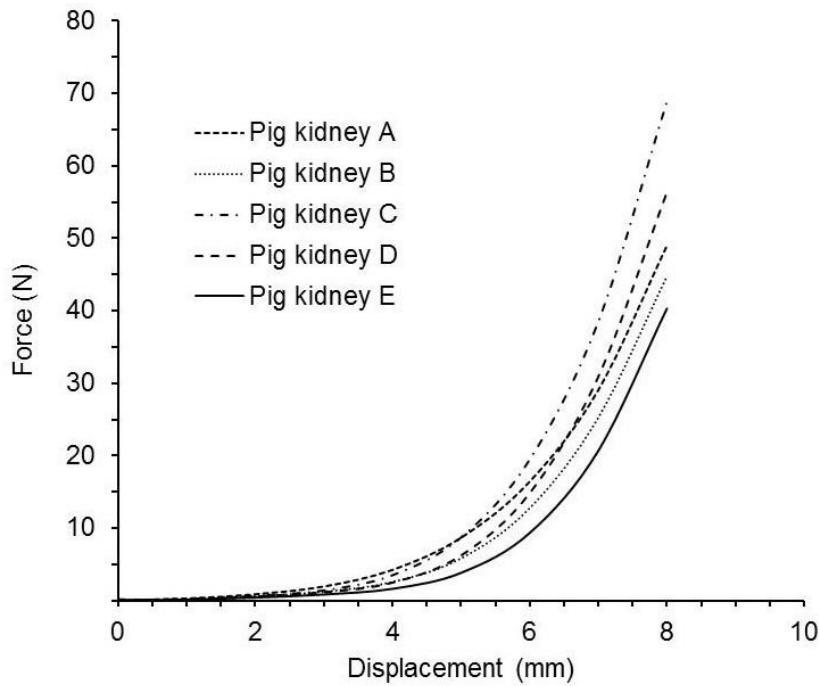


Figure 7.19: Average force vs displacement for pig kidney samples.

The average thicknesses of pig kidney samples and equivalent simulants are shown in Table 7.3. Thickness was used for the calculation of strain values.

Table 7.3: Thickness of pig kidney samples and equivalent simulants.

Real pig kidney		Pig kidney simulant	
Pig kidney samples	Thickness (mm)	Pro Gel 10 softener concentration (% v/v)	Thickness (mm)
A	17±2	30	19±3
B	20±3	40	19±1
C	20±1	50	19±2
D	20±1	60	19±2
E	18±1	70	19±4

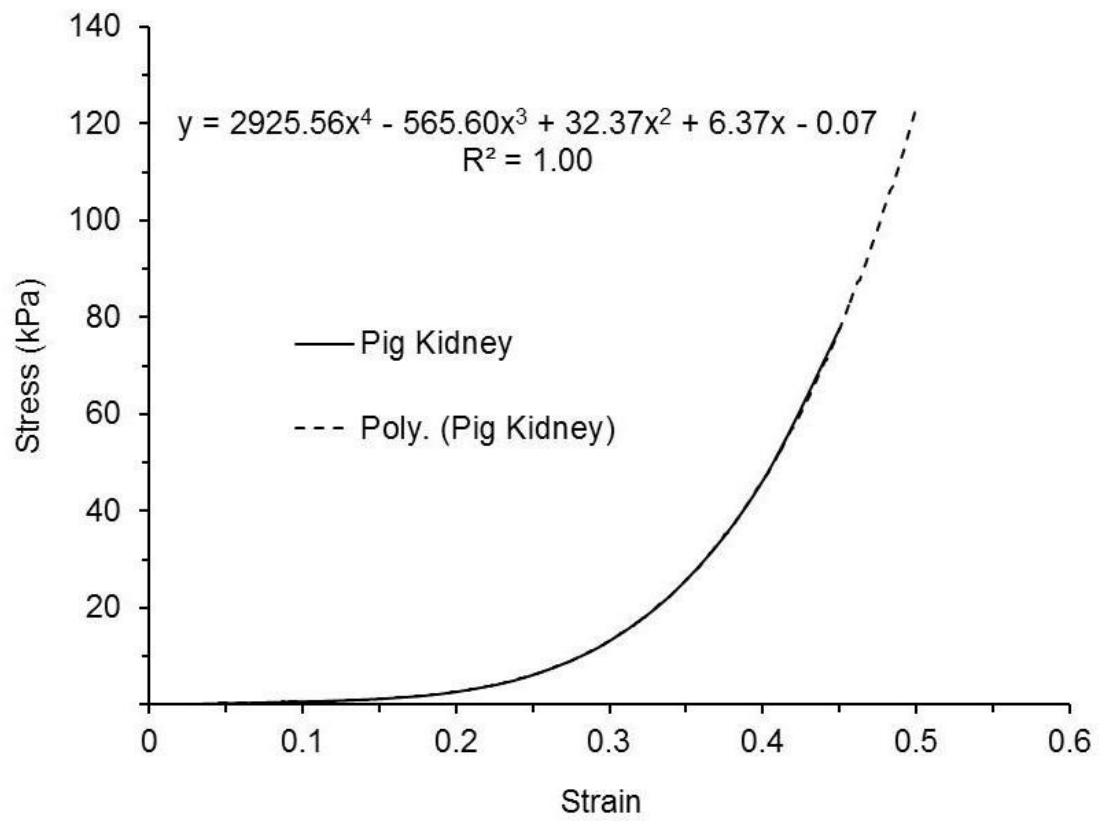


Figure 7.20: Average stress vs strain for pig kidney samples.

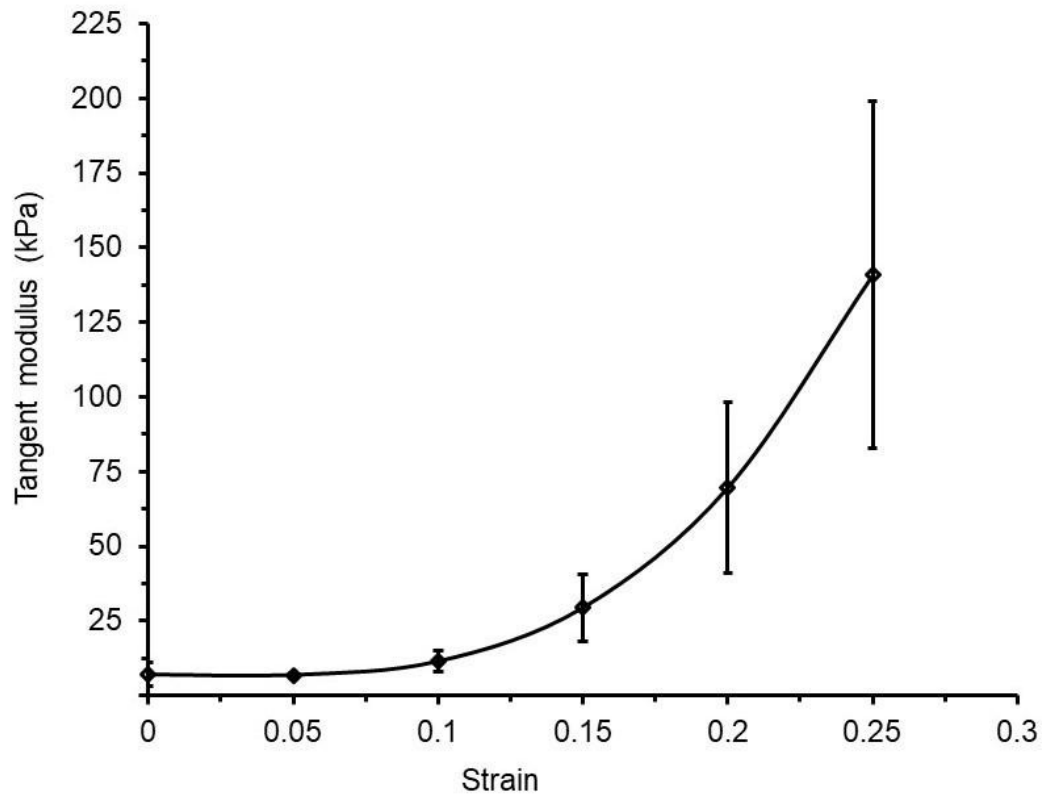


Figure 7.21: Average tangent modulus vs strain for pig kidney samples.

Pig kidney simulants:

Pig kidney simulants were fabricated from 30-70% v/v consistencies of the Pro Gel 10 softener (Chapter 4). These concentrations are referred to in the abbreviated forms as 30-70% for pig kidney simulants (KS) in this chapter. For example, 'KS 30% - Average force' in Figure 7.22.

Average force against displacement, stress vs strain and tangent modulus vs strain curves for pig kidney simulants are plotted in Figure 7.22, Figure 7.23 and Figure 7.24, respectively. The tangent modulus of pig kidney (average of five pig kidney samples) is also plotted for comparison with the simulants in Figure 7.24.

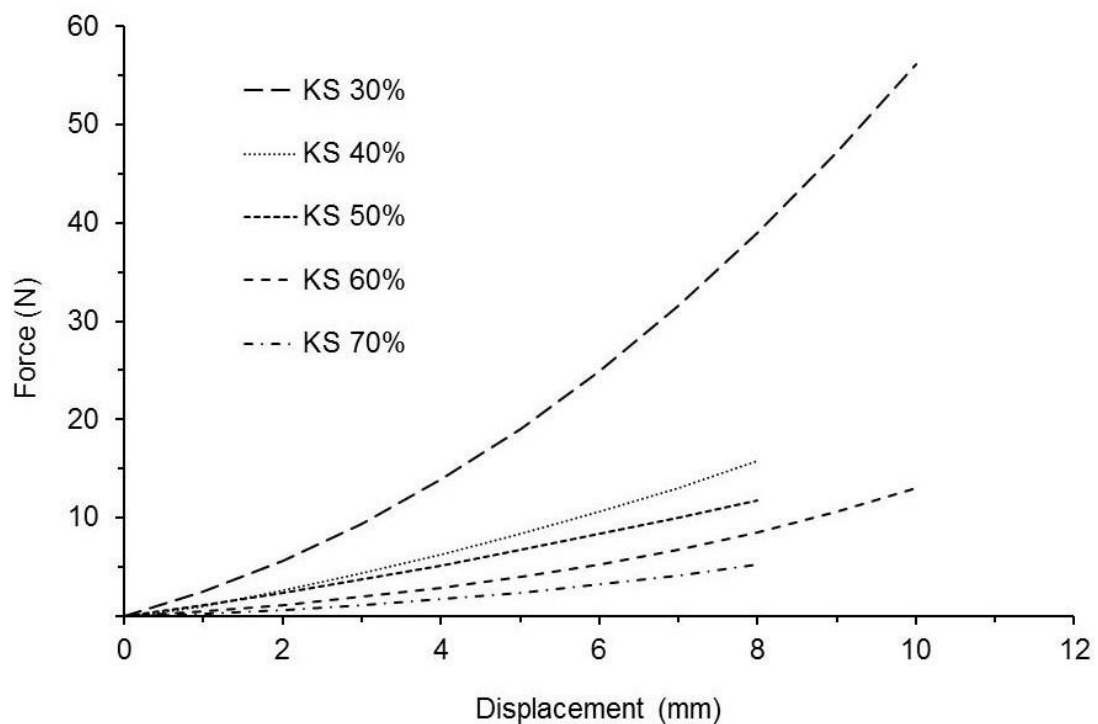


Figure 7.22: Average force vs displacement for pig kidney simulants.

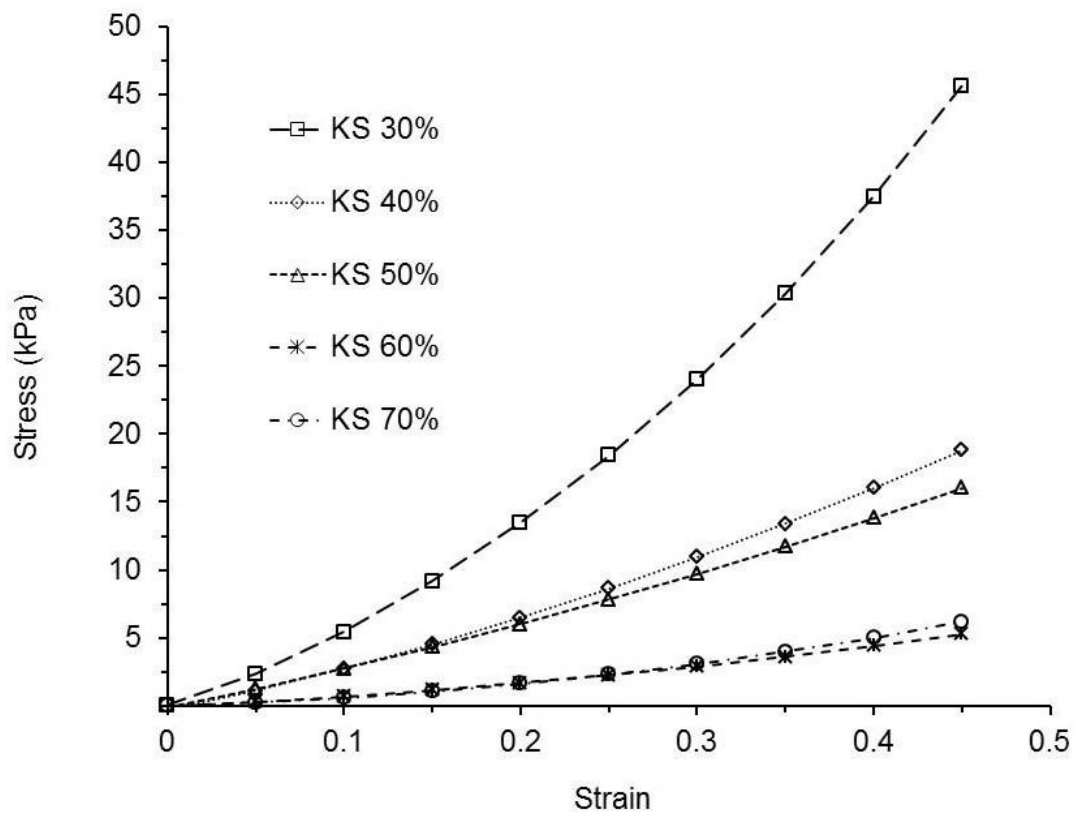


Figure 7.23: Average stress vs strain for pig kidney simulants.

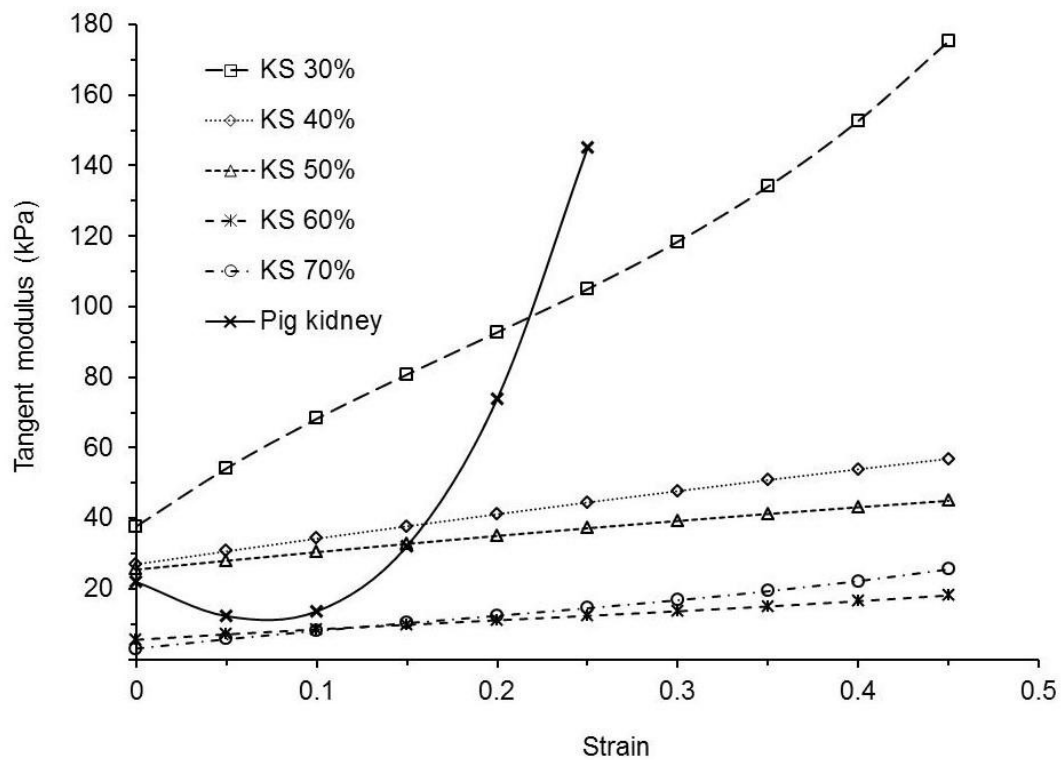


Figure 7.24: Average tangent modulus vs strain for actual pig kidney and pig kidney simulants.

The values of tangent modulus of the simulants made from 50 to 70 % weight softener were found to give the closest match to the tangent modulus of the pig kidney up to a strain of ~ 0.15 . However, simulants made of softener concentration greater than 50 % weight were found to have a sticky surface which poses a challenge when handling by hand.

It was not possible to obtain samples of pig stomach, spleen and pieces of bowel which would have allowed the assessment of their tangent modulus and in turn permit comparison with stomach and bowel simulants in a similar way to that described earlier for solid simulants. As a result, the evaluation of elastic properties and density of hollow simulant organs was undertaken as part of a survey of surgeons on the biomechanical properties (dimensions, pliability and density) of liver, kidney, spleen, stomach and bowel simulants.

7.2.3 Survey of biomechanical properties of simulant organs

The opinions of five surgeons (A to E) for solid and hollow simulant organs are summarised in Tables 7.4 and 7.5, respectively.

Table 7.4: Opinions of surgeons for solid simulant organs.

Simulant Organ	Pro Gel 10 softener concentration (% v/v)	Participating surgeons				
		A	B	C	D	E
Liver	20					
	30					
	50	✓	✓	✓	✓	✓
Kidney	30				✓	
	50	✓	✓	✓		✓
	70					
Spleen	30		✓			
	50	✓		✓	✓	✓
	70					

It is evident from Table 7.4 that solid simulant organs (liver, kidney and spleen) made with 50% weight softener concentration in the silicone gel were

considered the closest match to the biomechanical properties of the human organs by the surgeons.

Table 7.5: Opinions of five surgeons for hollow simulant organs.

Surgeon	Stomach		Bowel (% weight of wallpaper paste)			
	Mixture A (50 ml water + air)	Mixture B (200 ml water + air)	0	2.5	5	7.5
A	✓		✓	✓		
B	✓			✓		
C	✓		✓		✓	
D	✓		✓	✓		
E	✓		✓	✓		

The stomach simulant with 50 ml water and air (mixture A) was judged the closest match for the human stomach (Table 7.5). The bowel simulants filled with 0% and 2.5% weight wallpaper paste were suggested by four out of five surgeons as near matches with the biomechanical properties of the human bowel.

Taking density, elastic modulus, surface properties and the opinions of surgeons therefore into consideration, 50 % weight concentration of softener mixed with silicone gel was considered suitable for the fabrication of the liver, spleen, and kidney simulants to be used in the abdominal simulator. Based purely on the surgeon survey, the stomach simulant organ contained a mixture of 50ml water and air, and the bowel simulant contained 2.5% weight wallpaper paste.

7.3 In-house abdominal simulator

Pig liver, simulant human liver, and simulant human bowel pieces were evaluated for the defined typical 'movements' within the 'right angled shape' test-rig (Section 4.4, Chapter 4). Surface pressures applied by the fingertips of

the operator using the thin film pressure sensor were recorded and are reported in this section.

Pig liver:

Surface pressures for 'moving and squashing' and 'lifting' of pig liver are shown in Figure 7.25 and Figure 7.26, respectively.

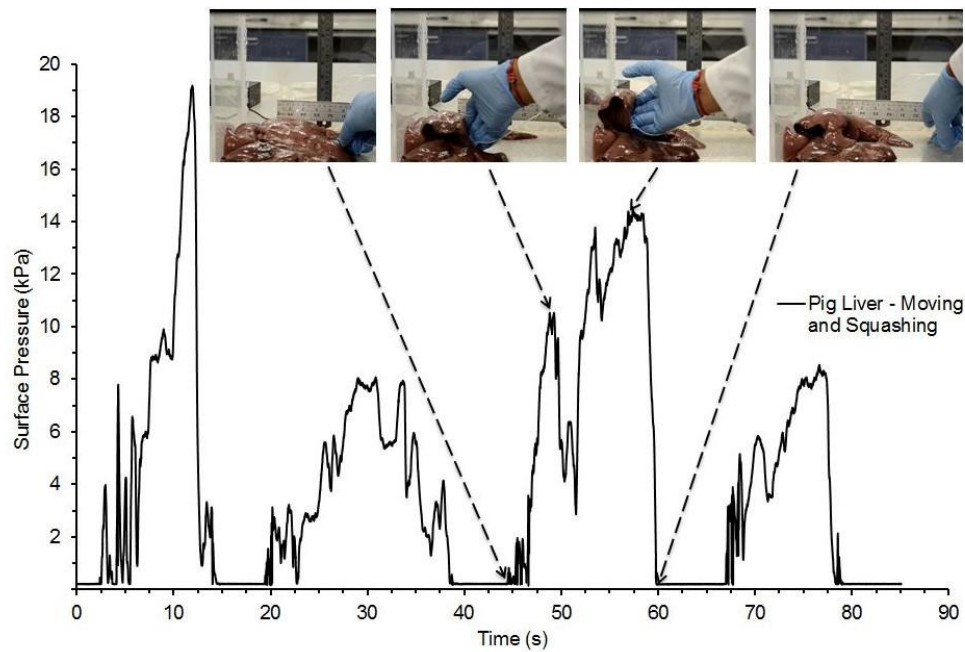


Figure 7.25: Moving and squashing of pig liver inside the test-rig.

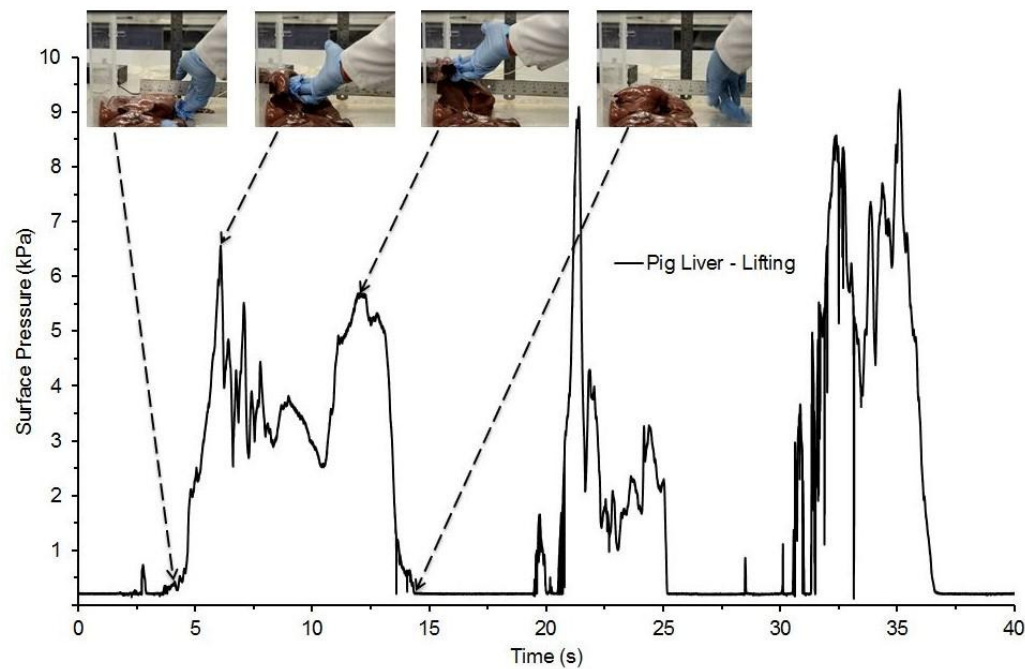


Figure 7.26: Lifting of pig liver inside the test-rig.

The surface pressure was approximately 30% higher during the 'squashing' phase compared to the 'moving' phase (2nd and 3rd stills, respectively, shown in Figure 7.25). The surface pressure required for 'lifting' of pig liver was less than half (Figure 7.26) that recorded during 'moving and squashing' (Figure 7.25). The surface pressure relaxation phenomenon (explained in Chapter 4.5.6) was observed during lifting of liver in Figure 7.26 (from 6s to 10s).

The pig liver simulant was not assessed within the rest-rig.

Simulant human liver:

Surface pressures for 'lifting' of simulant human liver are shown in Figure 7.27 and as expected surface pressure increases during lifting. The surface pressure relaxation (explained in Chapter 4.5.6) was noted (between 2nd and 3rd stills in Figure 7.27) when simulant human liver was retracted against the wall of the test-rig between 80s and 90s. Similarly, the surface pressure dropped from ~25kPa to ~20kPa between 53s and 61s (Figure 7.27). Retraction events of the simulant human liver of Figure 7.27 can be considered as 'clean' events (explained in Chapter 4.5.6).

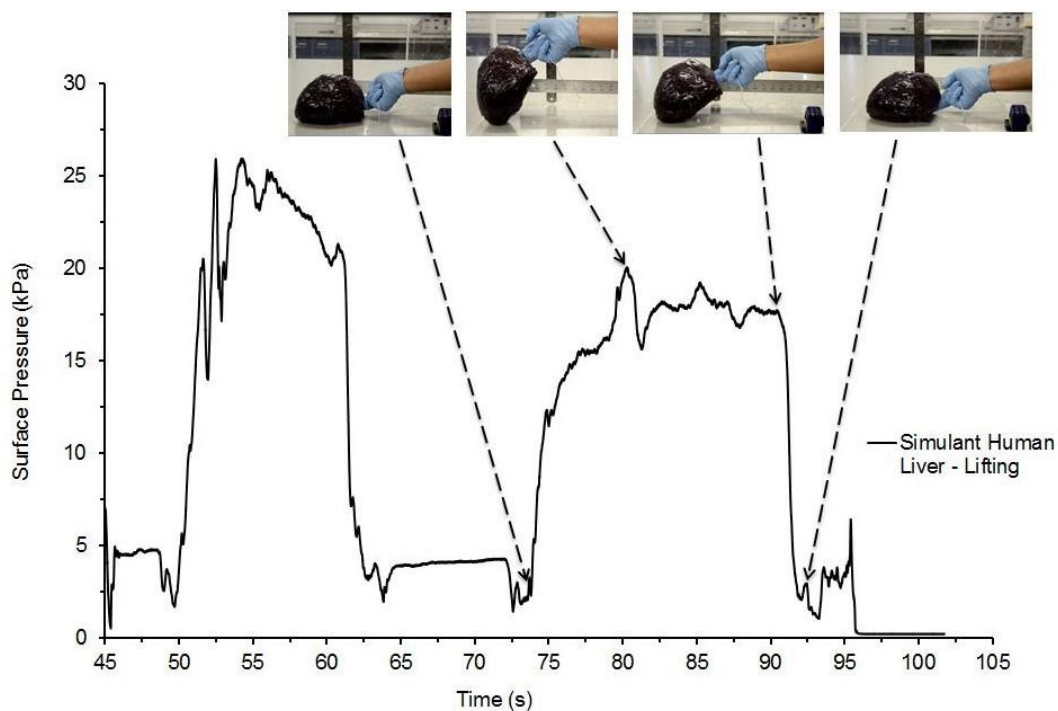


Figure 7.27: Lifting of simulant human liver inside the test-rig.

Simulant human bowel pieces:

Surface pressures for 'moving and squashing' of simulant human bowel pieces are shown in Figure 7.28.

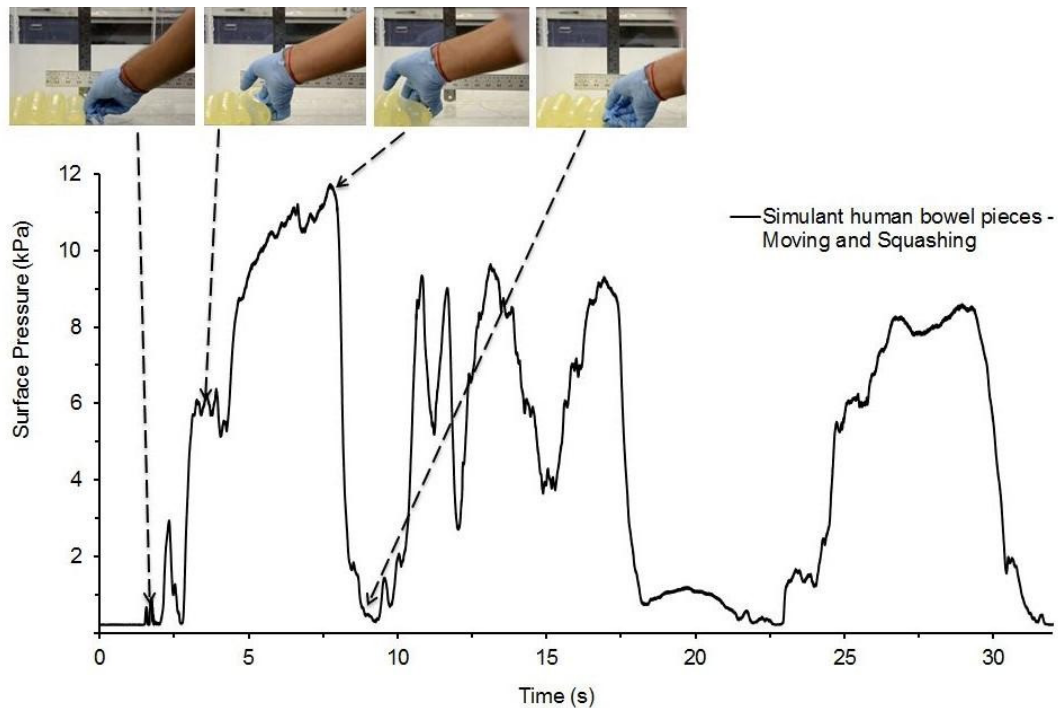


Figure 7.28: Moving and squashing of simulant human bowel pieces inside the test-rig.

The surface pressure was approximately double during the 'squashing' phase as expected compared to the 'moving' phase (3rd and 2nd stills, respectively, shown in Figure 7.28). The surface pressure for moving and squashing of simulant human liver was more than double (~25kPa) compared to simulant human bowel pieces (~12kPa). This is due to the solid and hollow nature of the simulant (and in turn human) organs.

7.4 In-vivo measurement of surface pressures

The in-vivo pilot study was designed to quantify typical surface pressures applied to key abdominal organs during abdominal surgery. The choice of Open Cholecystectomy (OC) and Hand Assisted Laparoscopic Surgery (HALS) has allowed repeatable access to key abdominal organs. It has permitted recording of typical retraction manoeuvres for several times by placing the pressure sensor between the organ and the flexor surface of the dominant hand of the participating surgeon. Typical surface pressure versus time data were acquired for each retraction event.

7.4.1 Open abdominal surgery

The liver, bowel and stomach were retracted during open abdominal surgery and surface pressure measured for each organ is described in this section.

Liver:

Retraction events for the liver (patient 3) with the direction of retraction are shown in Figure 7.29. The maximum surface pressure applied was in order of 20 kPa. Single retraction and clearly identifiable peak (48-68s) with selected stills extracted from the video footage and properties (T_{hold} , P_{max} , P_{end} and P_{rms}) considered for data analysis are shown in Figure 7.30.

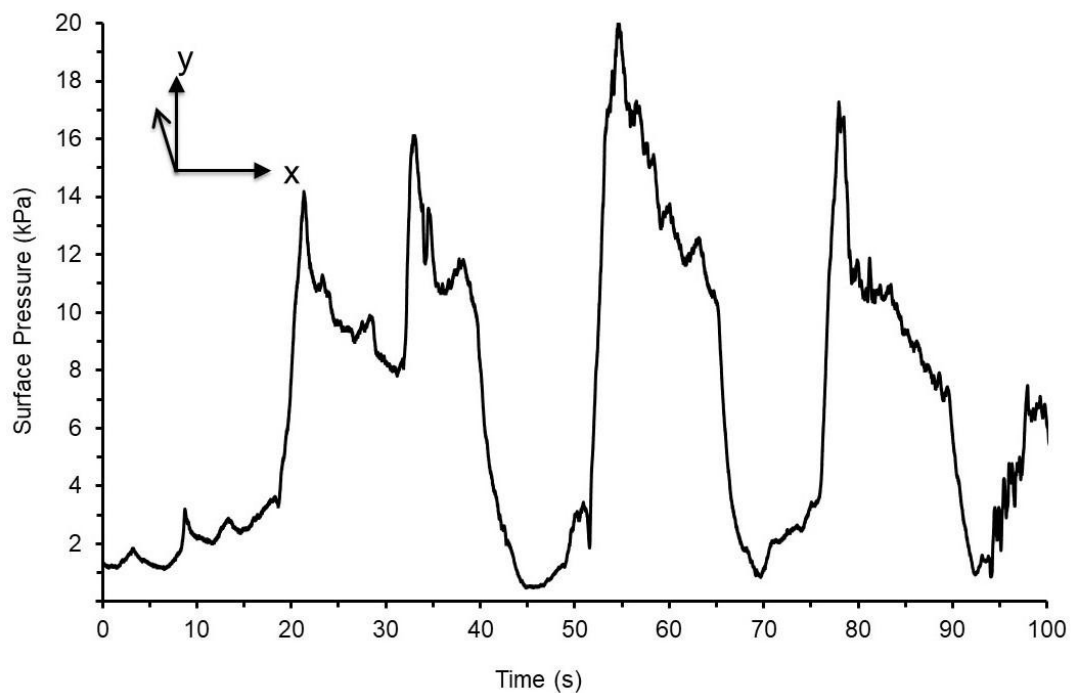


Figure 7.29: Retraction events for the liver for patient 3 undergoing open abdominal surgery. Inserts show direction of liver retraction in the coronal plane.

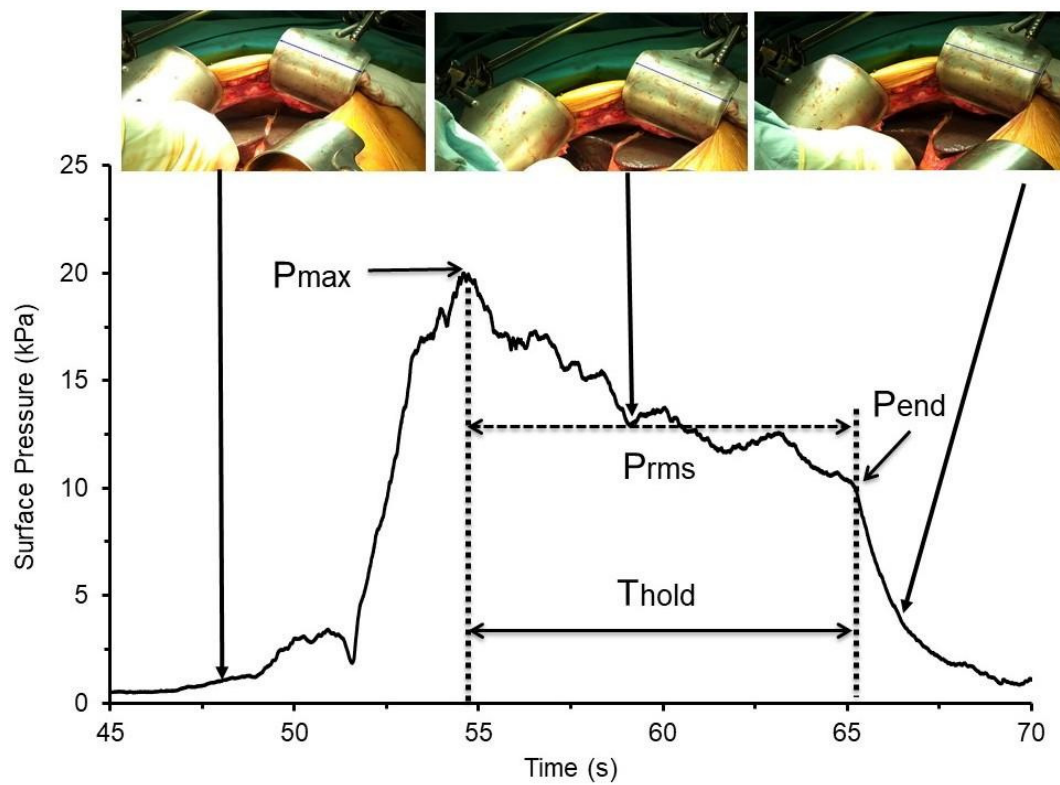


Figure 7.30: Clean retraction event for the liver for patient 3 undergoing open abdominal surgery (second event of Figure 7.29). Selected stills from the video footage are included. Properties extracted for data analysis are also indicated.

Bowel:

Retraction events for the bowel (patient 3) with the direction of retraction and selected stills extracted from the video footage are shown in Figure 7.31. The maximum surface pressure applied was in order of 10 kPa.

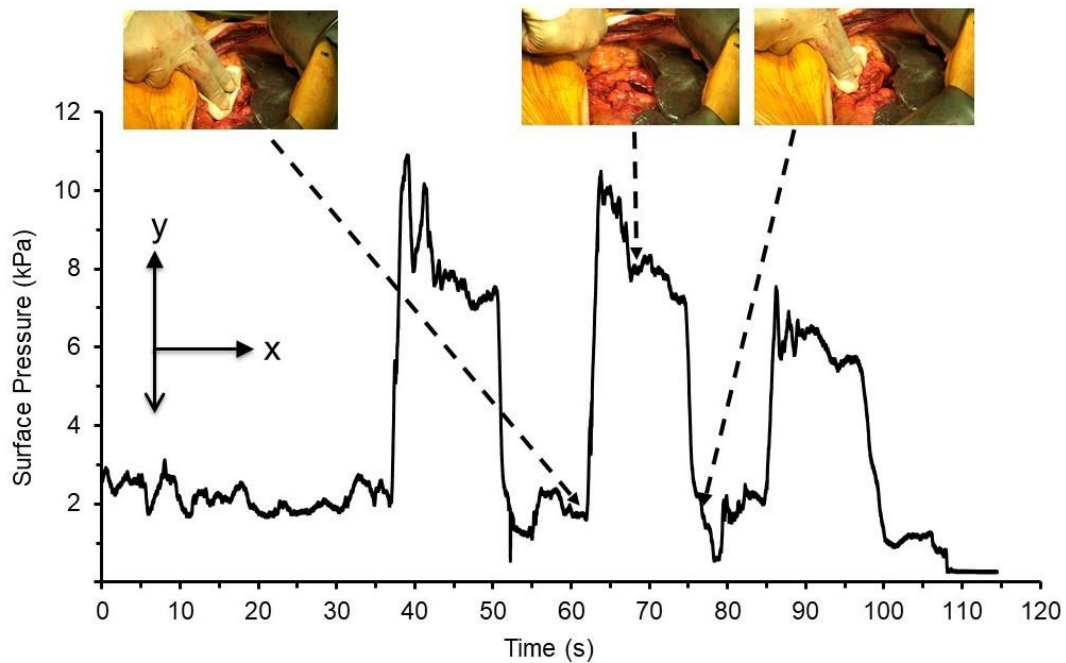


Figure 7.31: Retraction events for the bowel for patient 3 undergoing open abdominal surgery. Inserts show direction of bowel retraction in the coronal plane. Selected stills from the video footage are included for second retraction event (62-78s).

The bowel was also retracted using a metal retractor (part of the Omnitract™ retractor system) for patient 3 (Figure 7.32). The degree of surface pressure applied was in order of 20 kPa (Figure 7.32) which is double than applied by fingertips of surgeon (Figure 7.31). Due to the low number of bowel retraction events using the metal retractor they were not considered for data analysis.

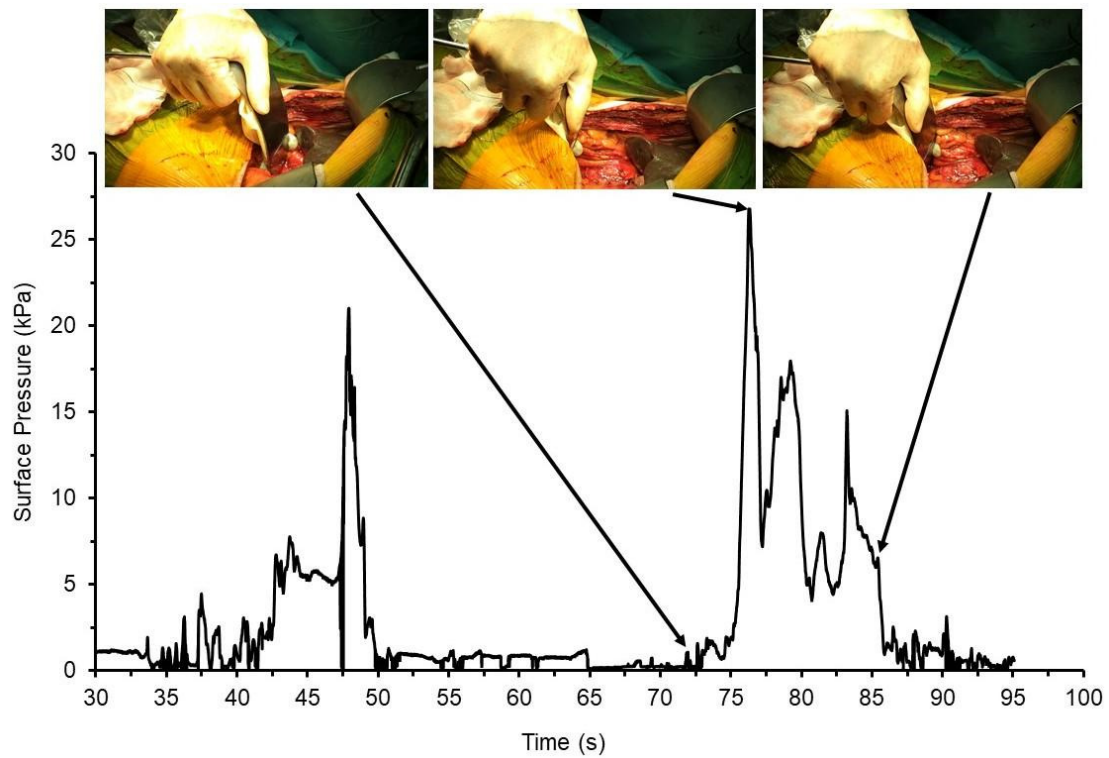


Figure 7.32: Retraction of the bowel using a metal retractor for patient 3.
Selected stills from video footage are shown.

Stomach:

Retraction events for the stomach (patient 10) with the direction of retraction and selected stills extracted from the video footage are shown in Figure 7.33. The maximum surface pressure applied was in order of 5 kPa. Double or multiple retraction peak from 26 to 40s in Figure 7.33 was considered as 'unclean' retraction event.

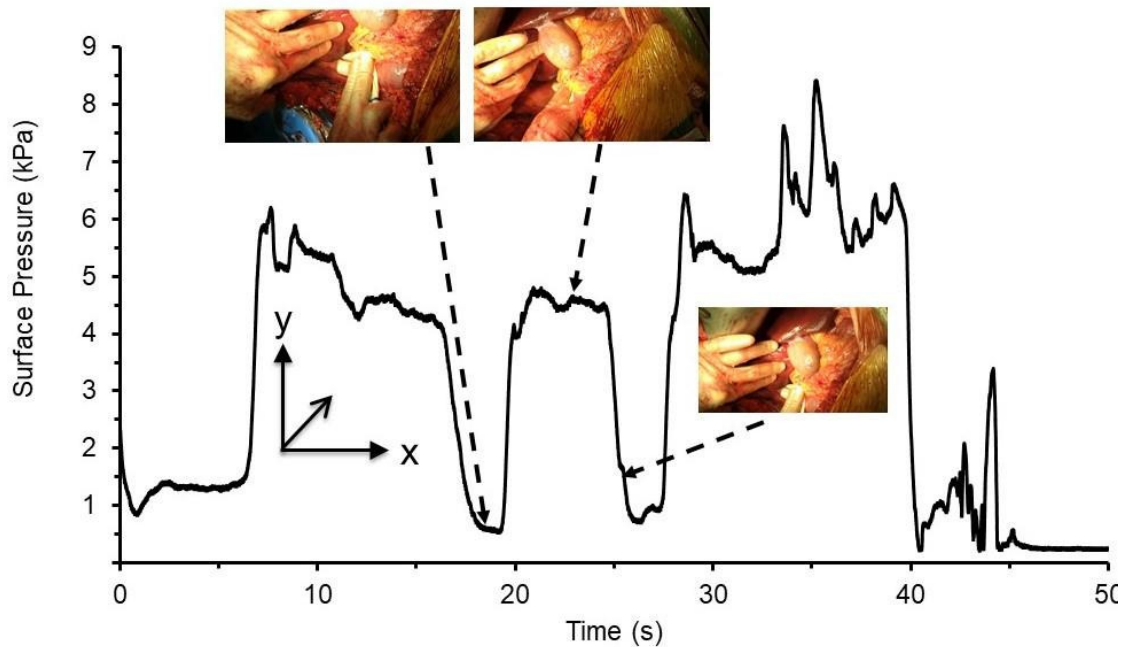


Figure 7.33: Retraction events for the stomach for patient 10 undergoing open abdominal surgery. Inserts show direction of stomach retraction in the coronal plane. Selected stills from the video footage are included for second retraction event (19-26s).

7.4.2 Hand assisted laparoscopic surgery

The liver, bowel, kidney, spleen and stomach were retracted during HALS and surface pressure measured for each organ is described in this section. Video footages were recorded using the endoscope during HALS procedures.

Liver:

The liver was retracted by the fingertips of the dominant hand of the surgeon. The direction of liver retraction in HALS procedures is identical to that used in open abdominal surgery. Unclean (patient 4) and clean (patient 8) retraction events for the liver are shown by way of example in Figure 7.34 and Figure 7.35, respectively. The degree of surface pressure applied for retraction of liver by the fingertips of the surgeon was in order of 15 kPa.

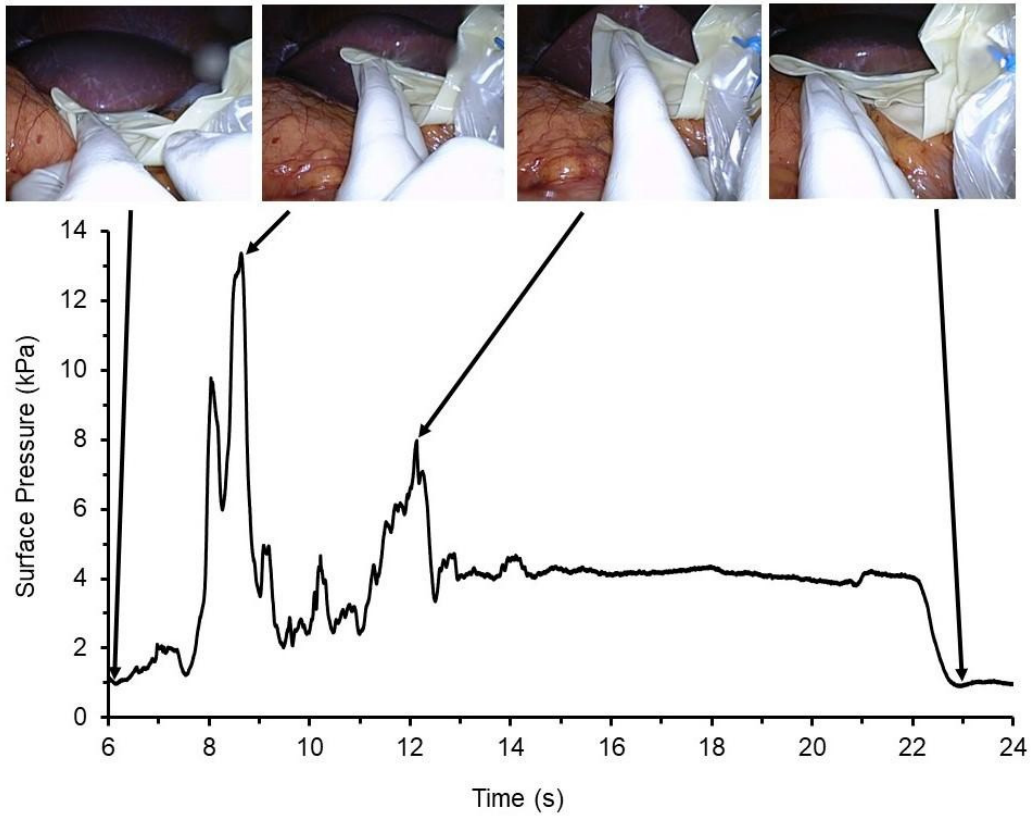


Figure 7.34: Unclean retraction event of liver for patient 4 during HALS. Selected stills from the video footage are included.

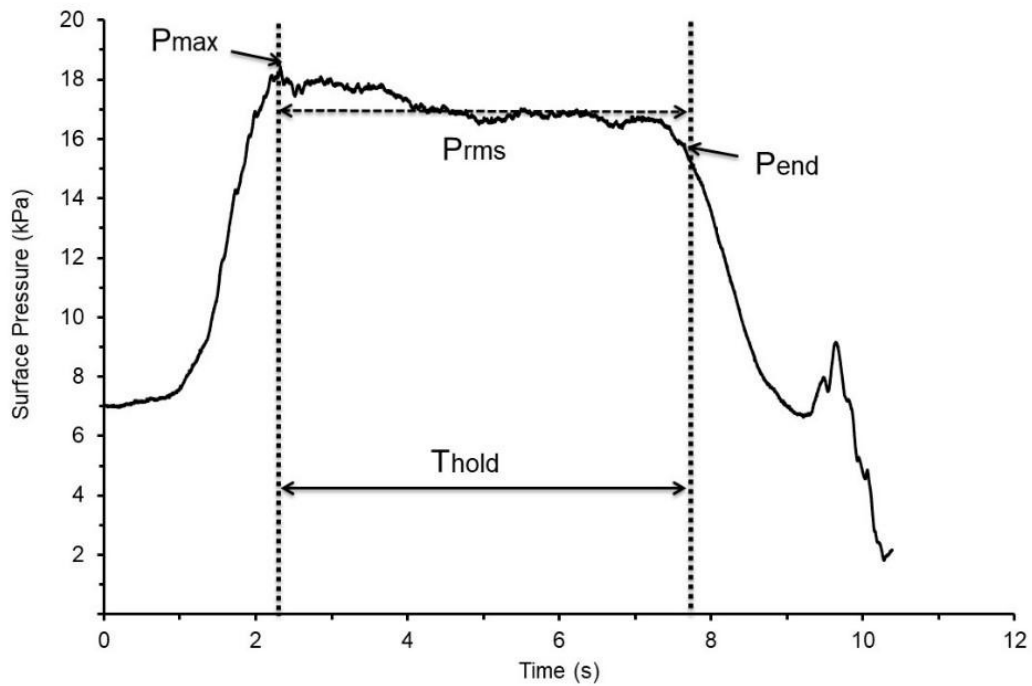


Figure 7.35: Clean retraction event of liver for patient 8 during HALS. Properties extracted for data analysis are indicated.

The liver was also retracted by metal retractor (PretzelFlex™, part of the Endoflex™ retractor, Figure 7.36) and laparoscopic grasper (Figure 7.37). The release of applied surface pressure by the PretzelFlex™ retractor (Figure 7.36) was not recorded on the data logging software due to a coordination issue between the laptop operator and the operating surgeon. The degree of surface pressure applied by metal retractors was in order of 20 kPa which is in ballpark with the surface pressure exerted by the fingertips of surgeon (Figure 7.34). Due to the low number of liver retraction events by metal retractor they were not considered for data analysis.

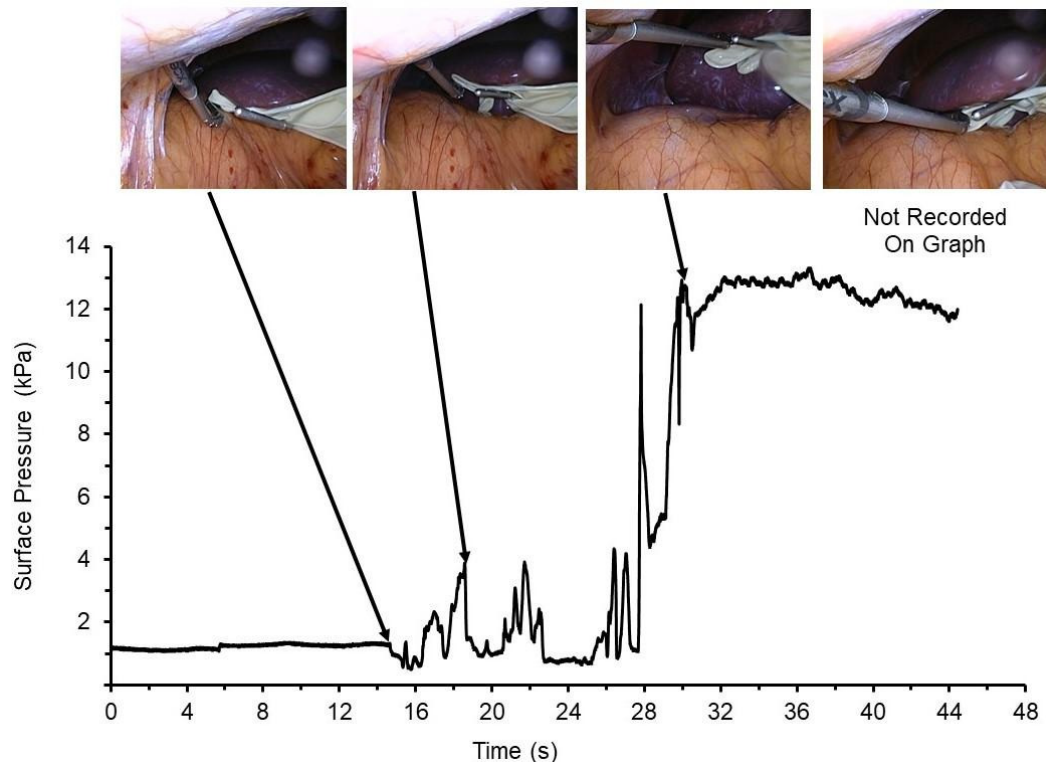


Figure 7.36: Retraction of the liver using a PretzelFlex™ retractor for patient 4. Selected stills from the video footage are included.

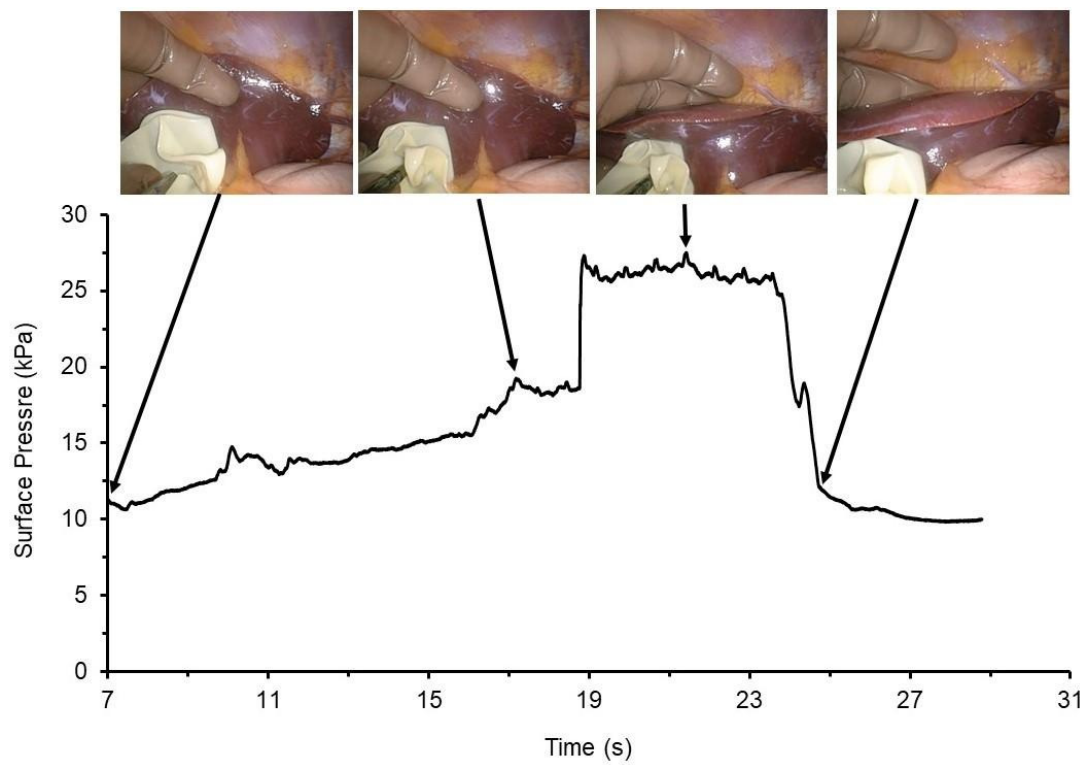


Figure 7.37: Retraction of the liver using a laparoscopic grasper for patient 5. Selected stills from the video footage are included.

Bowel:

Retraction event for the bowel (patient 5) is shown in Figure 7.38 by way of example with the selected stills extracted from the video footage and direction of bowel retraction. The degree of surface pressure applied for retraction of bowel was in order of 15 kPa.

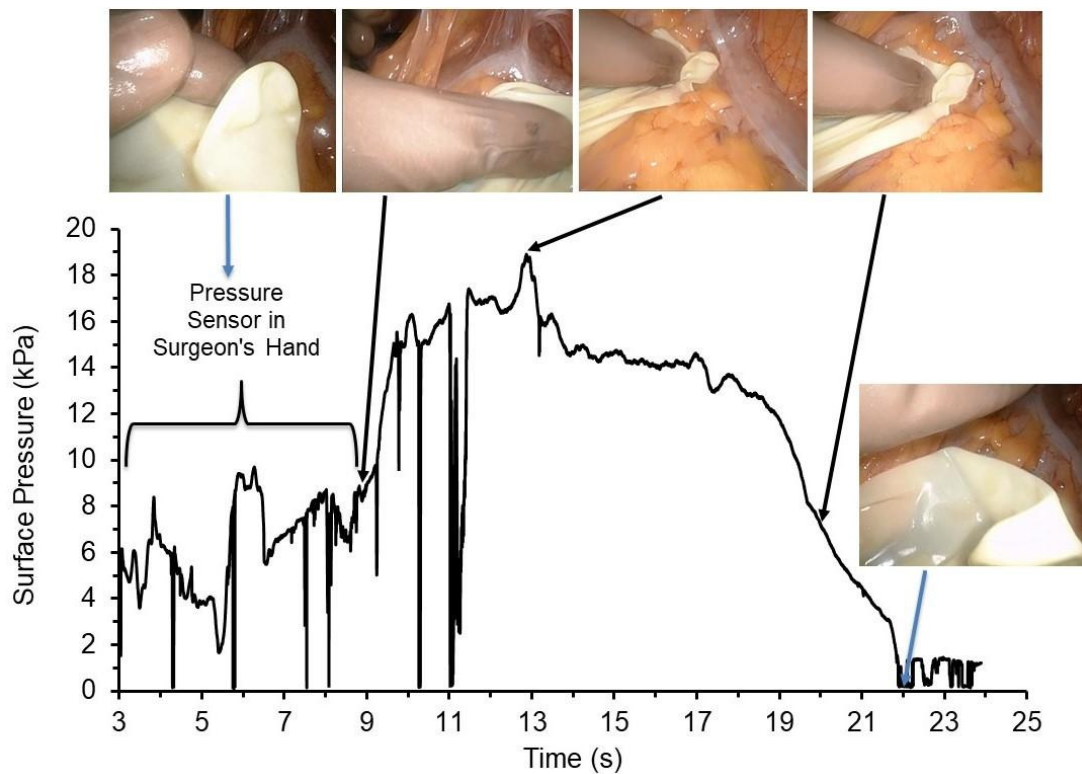


Figure 7.38: Retraction event for the bowel (patient 5) undergoing HALS. Selected stills from the video footage are also included. Inserts show direction of bowel retraction in the coronal plane.

Kidney:

Retraction events for the kidney are shown in Figure 7.39 (with the direction of retraction for patient 7) and Figure 7.40 (patient 6) by way of examples. Video footage was not obtained for patient 7 and, hence, selected stills obtained from video footage of a retraction event of patient 6 are shown in Figure 7.40. The degree of surface pressures applied for retraction of kidney was in order of 30 kPa for patient 7 and 10 kPa for patient 6.

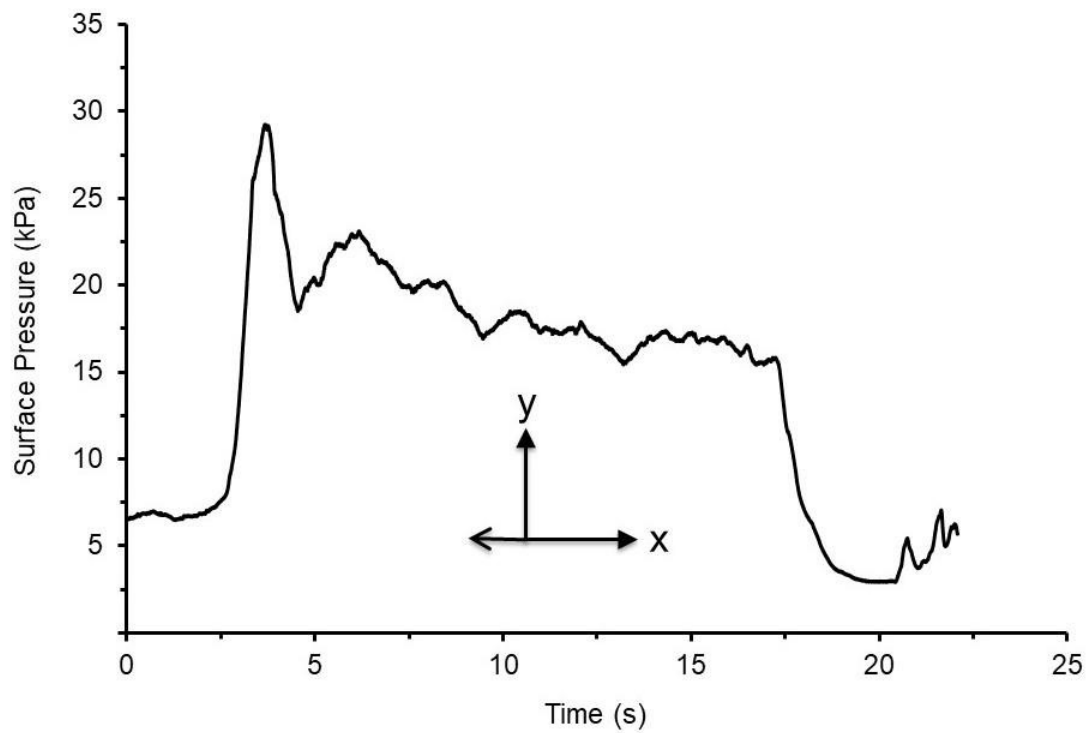


Figure 7.39: Retraction event for the kidney (patient 7) undergoing HALS. Insert shows direction of kidney retraction in the coronal plane.

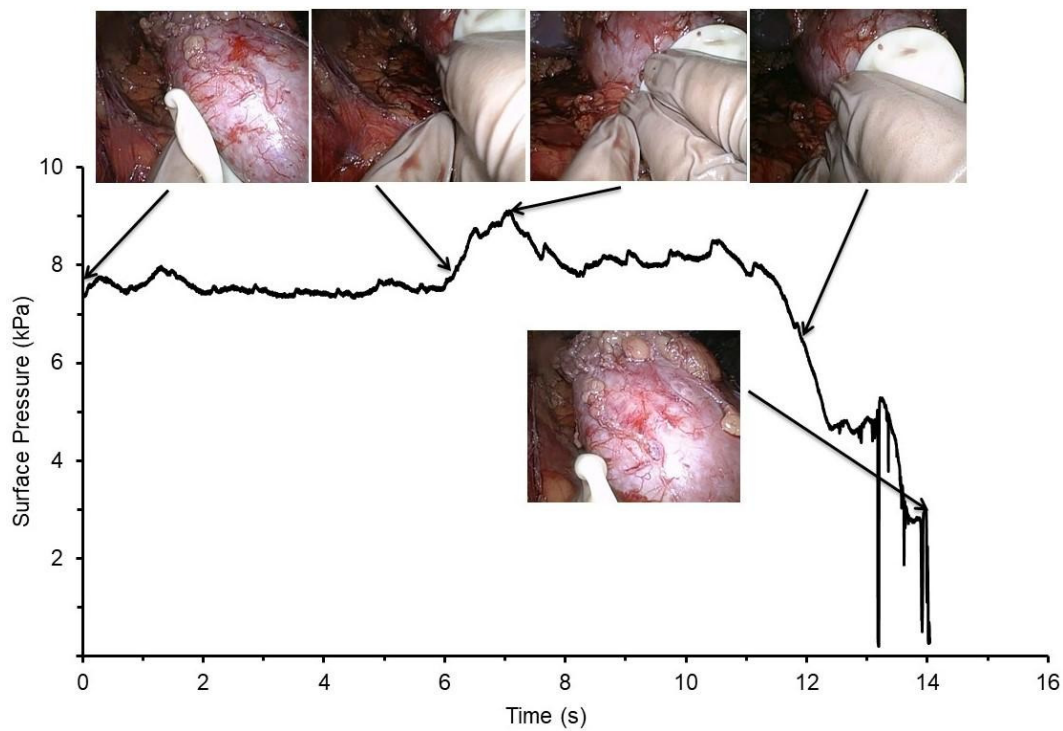


Figure 7.40: Retraction event for the kidney (patient 6) undergoing HALS. Selected stills from the video footage are included.

Spleen:

Retraction event for the spleen for patient 5 is shown in Figure 7.41 with the direction of retraction and stills extracted from video footage. The degree of surface pressure applied for retraction of spleen was in order of 15 kPa.

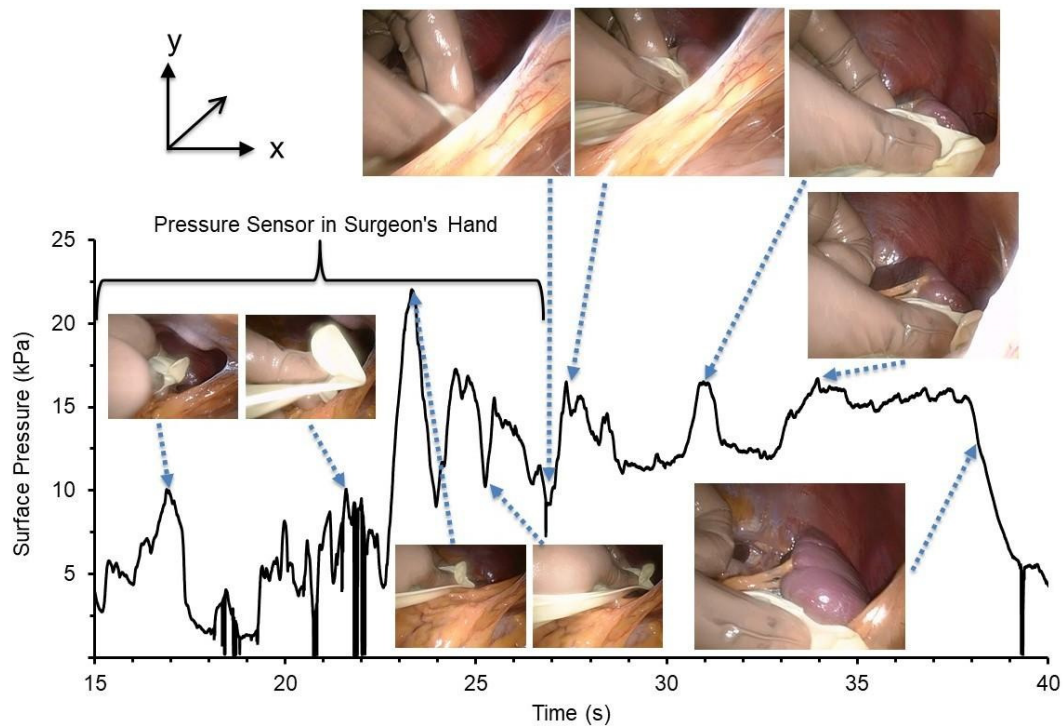


Figure 7.41: Retraction event for the spleen (patient 5) undergoing HALS. Selected stills from the video footage are included. Insert shows direction of spleen retraction in the coronal plane.

Stomach:

Retraction event for the stomach for patient 5 is shown in Figure 7.42. The degree of surface pressure applied for retraction of stomach was in order of 5 kPa.

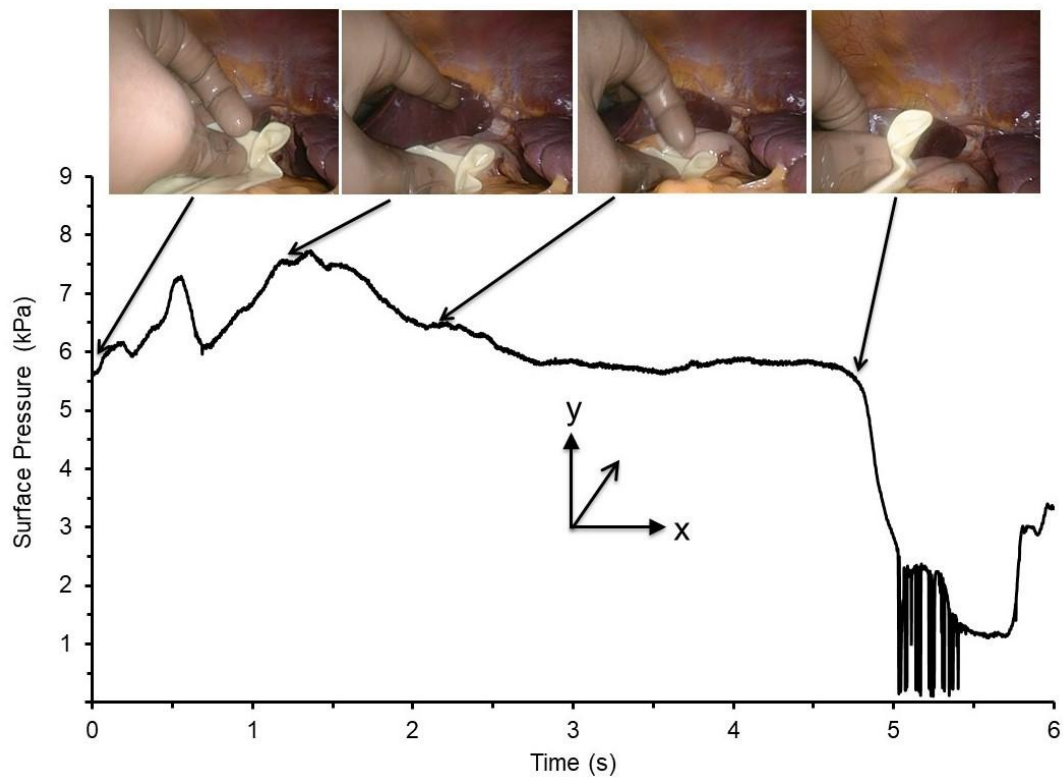


Figure 7.42: Retraction event for the stomach (patient 5) undergoing HALS. Properties extracted for data analysis and selected stills from the video footage are included.

Tissues and blood vessels surrounding key abdominal organs:

Retraction events for the abdominal aorta, omentum, inferior vena cava (IVC), and duodenum are shown in Figure 7.43. Video footage was not recorded for retractions of surrounding tissues and blood vessels and, hence, associated still images are not shown. The directions of retractions were not considered in this pilot study. Retraction events were also not considered for data analysis due to small sample size. However, the degree of surface pressures applied can be considered during the development of prototype expansion mechanisms. The degree of surface pressures applied for the retraction of the abdominal aorta was in order of 15 kPa, 10 kPa for omentum and IVC and 5 kPa for the duodenum.

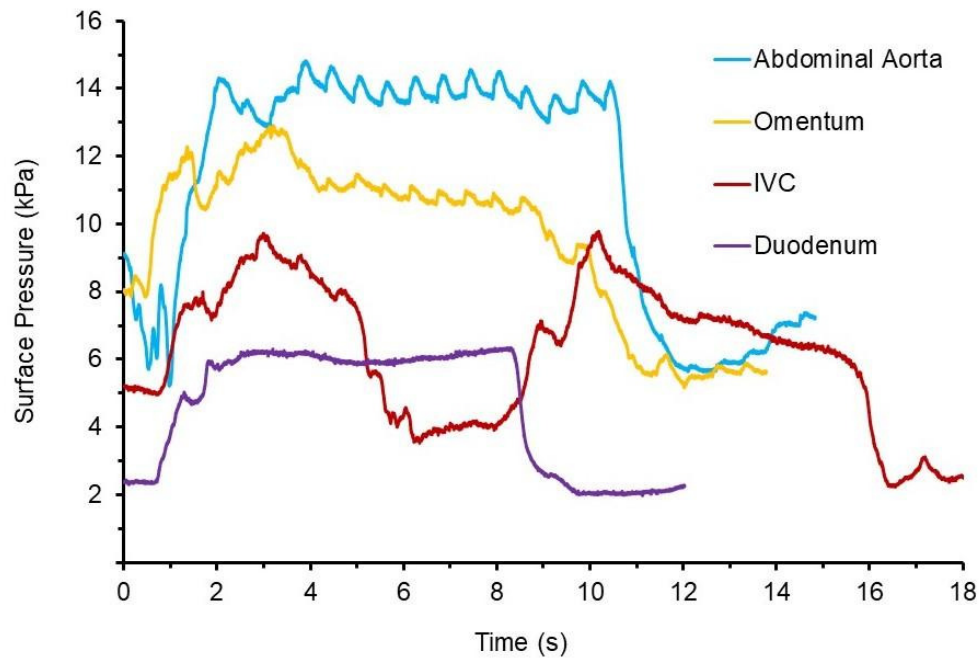


Figure 7.43: Retraction events for the abdominal aorta and omentum for patient 7 and IVC and duodenum for patient 8.

7.4.3 Data analysis

An average maximum surface pressure for each organ was determined from the measured maximum values in all retraction events and all patients for each of the open abdominal surgery and HALS procedures. The average maximum surface pressures and the range of maximum surface pressures, determined from the total number of retractions per organ, are shown in Table 7.6.

Table 7.6: In-vivo measurement of surface pressures applied to abdominal organs. (OC = open cholecystectomy; HALS = hand-assisted laparoscopic surgery; N/R = not retracted)

Abdominal organ	Liver	Bowel	Stomach	Spleen	Kidney
Number of retractions (OC)	31	21	6	N/R	N/R
Average maximum surface pressure (OC) (kPa)	15.3 ± 10.1	13 ± 4.7	6.60 ± 0.19	N/R	N/R
Range of maximum surface pressure (OC) (P_{\max}) (kPa)	1 - 41	6.3 - 21.5	3.4 - 10.2	N/R	N/R
Number of 'clean' events (OC)	14	14	3	N/R	N/R
Number of retractions (HALS)	4	15	2	5	9
Average maximum surface pressure (HALS) (kPa)	15.2 ± 2.8	12.7 ± 4.3	14.7 ± 7	12.9 ± 6.7	17.1 ± 9.6
Range of maximum surface pressure (HALS) (P_{\max}) (kPa)	11.5 - 18.4	6 - 20.0	7.7 - 21.7	6.9 - 24.4	9.1 - 37
Number of 'clean' events (HALS)	2	11	1	3	9

The typical range of maximum surface pressures applied during a single retraction episode for all organs and procedures was $1 < P_{\max} < 41$ kPa. The average value of $\langle P_{\max} \rangle$ for all organs and procedures was 14 ± 7.5 kPa.

The average P_{\max} values for all ('clean' and 'unclean') events are compared with the average P_{\max} and average P_{rms} values, with associated standard deviations, for each organ and procedure type are shown in Figure 7.44. The associated average T_{hold} data for the clean events are shown in Figure 7.45.

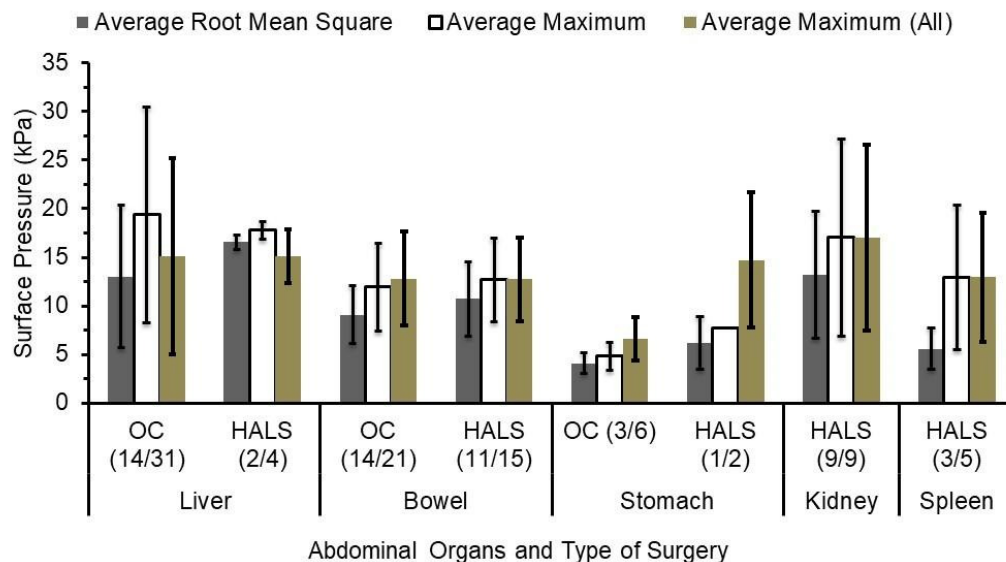


Figure 7.44: Average root mean square and maximum surface pressure ('clean' events), and average maximum surface pressure (all events) applied to key abdominal organs. OC = Open Cholecystectomy; HALS = Hand Assisted Laparoscopic Surgery. Numbers in parentheses are ratio of clean to total retraction events

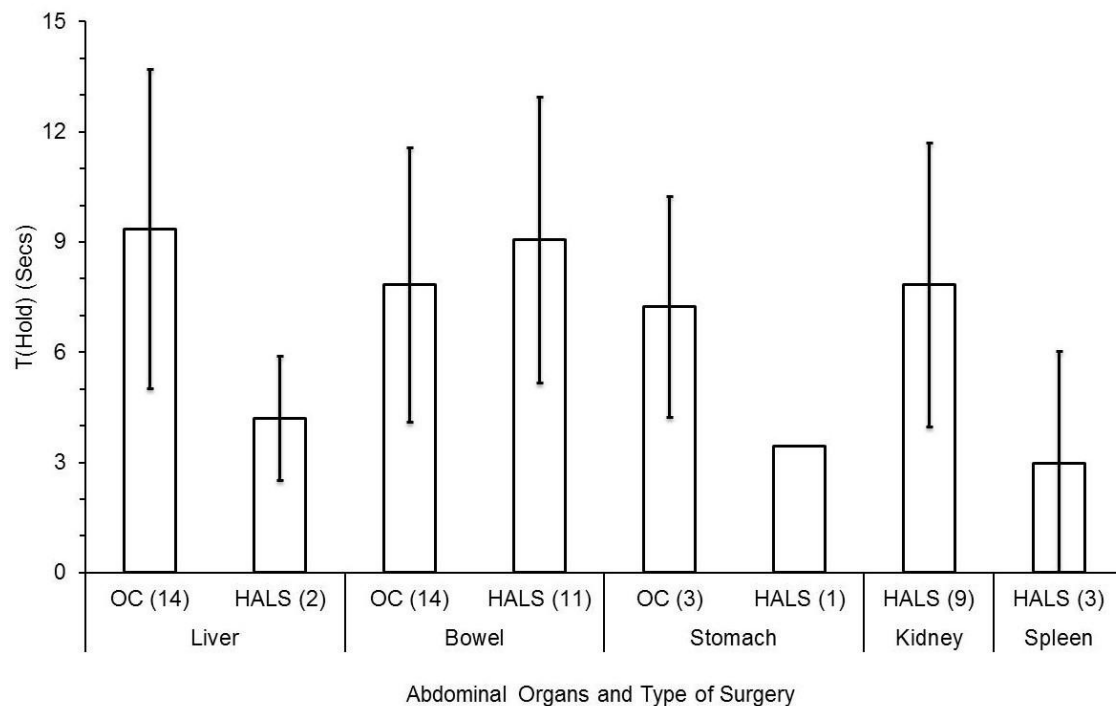


Figure 7.45: Average hold time for pressure applied to key abdominal organs ('clean' events). OC = Open Cholecystectomy; HALS = Hand Assisted Laparoscopic Surgery. Numbers in parentheses are number of clean retractions.

For 'clean' events, the data typically show decay in the applied surface pressure during the 'hold' period for each retraction event (e.g. Figures 7.29 and 7.30). The surface pressure relaxation resulted in lower average P_{rms} values compared to the average P_{max} values (Figure 7.44): $\langle P_{rms} \rangle / \langle P_{max} \rangle = 80 \pm 8\%$ over an average hold time of $\langle T_{hold} \rangle = 7 \pm 2$ seconds for all clean events for all organs and procedures.

The largest and smallest decreases in surface pressure occurred for the liver-OC ($\langle P_{rms} \rangle / \langle P_{max} \rangle = 67\%$) and liver-HALS ($\langle P_{rms} \rangle / \langle P_{max} \rangle = 93\%$) organ-procedure combinations, respectively, and these corresponded to the longest and second shortest average hold times ($\langle T_{hold} \rangle = 9 \pm 4$ and 4 ± 2 seconds), respectively. The shortest average hold time of 3 seconds occurred for the spleen-HALS combination, for which only one 'clean' events were recorded.

In order to compare the surface pressure relaxation between organ-procedure combinations the pressure drop per unit time normalised by the maximum

pressure, $\left[\frac{\Delta P}{T_{Hold}} \right] / P_{max}$ where $\Delta P = P_{end} - P_{max}$ and $T_{Hold} = T_{finish} - T_{start}$,

was determined from the Liver-OC, Bowel-OC, Bowel-HALS and Kidney-HALS data. The surface pressure relaxation phenomenon was not considered for the Liver-HALS, Stomach-OC, Stomach-HALS and Spleen-HALS data due to small number of clean retraction events. Figure 7.46 shows a clear trend of

reducing magnitude of $\left[\frac{\Delta P}{T_{Hold}} \right] / P_{max}$ with increasing T_{hold} for the Liver-OC data, corresponding to a reduction in the rate of surface pressure relaxation the longer the retraction event persists for. This trend is also evident in the Bowel-OC, Bowel-HALS and Kidney-HALS data (Figure 7.47). From the slopes of the least squares best fit lines to the data there is a suggestion that the rate of surface pressure relaxation is a factor of ~2-3 lower in the HALS procedures than the OC procedures, although the very low r^2 correlation coefficients for the HALS data in particular must be noted.

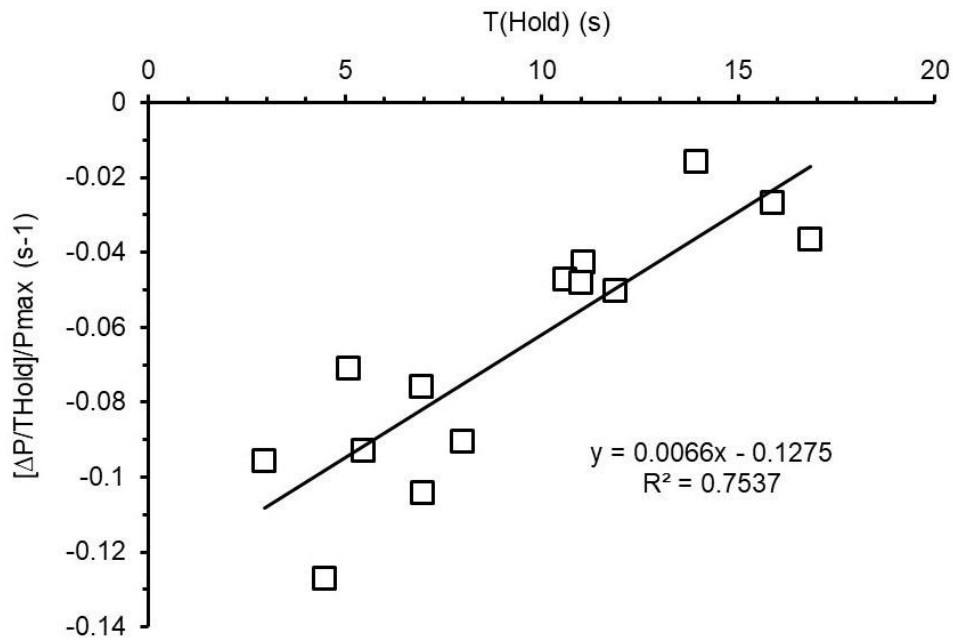


Figure 7.46: Surface pressure relaxation: $[\Delta P/T_{\text{Hold}}]/P_{\text{max}}$ vs T_{Hold} for the Liver-OC. OC = Open Cholecystectomy.

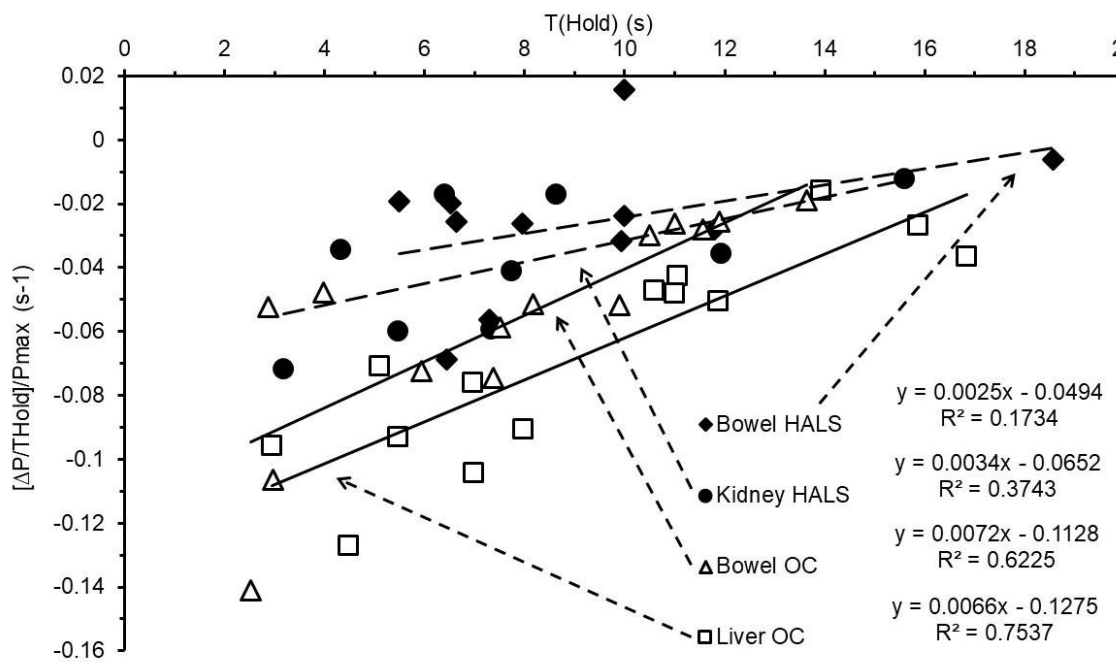


Figure 7.47: Surface pressure relaxation: $[\Delta P/T_{\text{Hold}}]/P_{\text{max}}$ vs T_{Hold} for the liver (OC – empty squares), bowel (OC – empty triangles), bowel (HALS – filled diamonds, and kidney (HALS – filled circles). OC = Open Cholecystectomy. HALS = Hand Assisted Laparoscopic Surgery.

7.5 Calculation of organ retraction distances

The organ retraction events were captured in a number of videos from which still images showing organ retraction movements have been extracted, processed and analysed to calculate the retraction distances in the plane of the images.

7.5.1 Open abdominal surgery

Quantification of liver retraction distance during open abdominal surgery (OC) is explained in this section. The second liver retraction event for patient 3 (Figure 7.29) is considered by way of example. The coordinate axes (X_1 - X_2), stationary points (1-4) and identifying marks (spot 5 and 6) are shown in Figure 7.48. The retraction distances were obtained for both the identifying marks (spot 5 and 6) for each of the sequence of images (Figure 7.49) extracted from the corresponding video footage. The image at 23 seconds was not considered for the calculation of retraction distance due to the loss of identifying mark (spot 6).

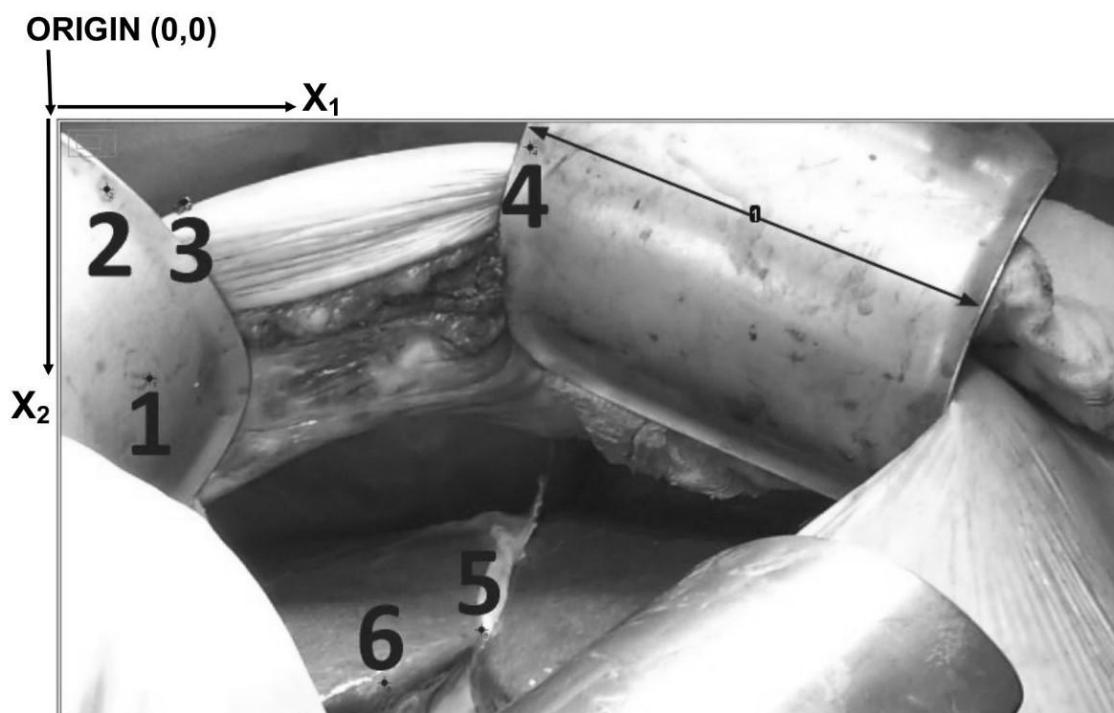


Figure 7.48: Coordinate axes, known distance of retractor (7 cm), stationary points (1-4) and identifying marks (spot 5 and 6) for Image at 1 sec.

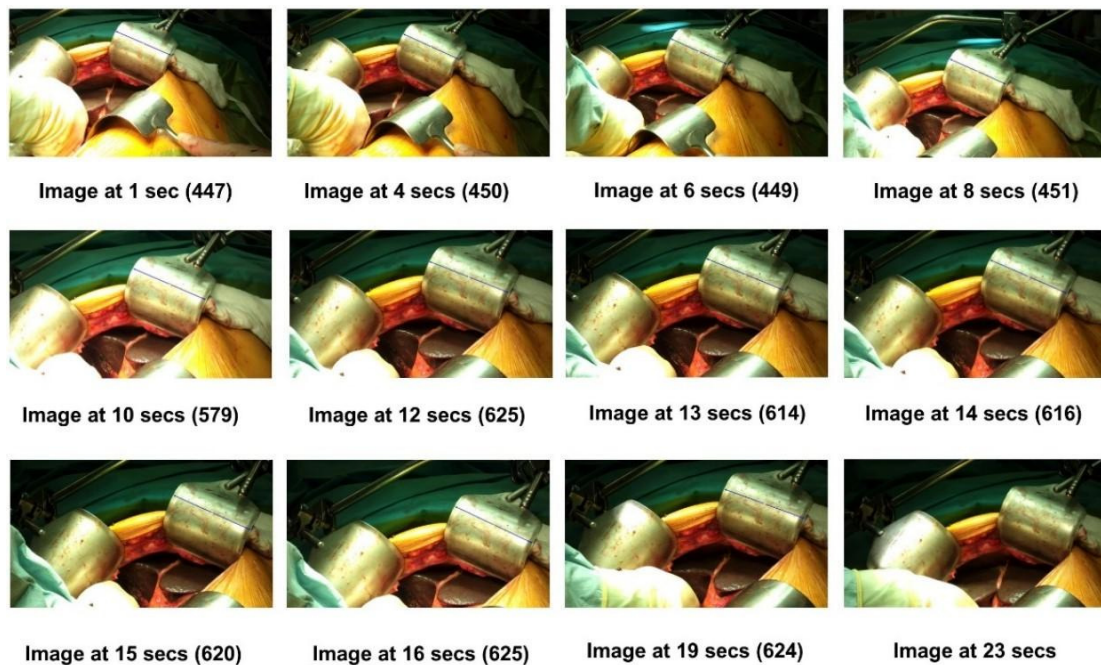


Figure 7.49: Sequence of images extracted from the video footage of the second liver retraction event for patient 3. Numbers in parentheses are pixel values of calibrated part of known distance (7 cm) of retractor.

The image analysis of the sequence of images is outlined below.

- X1 and X2 coordinates (in pixels) were obtained using ImageJ software(225) for stationary points (points 1-4, Figure 7.48) and identifying marks (spot 5 and 6, Figure 7.48) for each image shown in Figure 7.49 (except for 'Image at 23 secs').
- The distances along the x_1 and x_2 directions for both the identifying marks relative to each of the four stationary points were calculated by subtracting the respective stationary point coordinate from the respective identifying mark coordinate value for each image.
- For each image the measured distances were converted from pixels to centimetres using the measured (pixels) and known (cm) dimension of the retractor. This mitigated against apparent changes in distance due to movement of the hand-held camera between images.
- Retraction distances for both identifying marks in each image were obtained by subtracting the respective distance obtained before retraction ('Image at 1 sec') from the same distance in the image under consideration.

- The retraction distances ΔX_1 and ΔX_2 along the x_1 and x_2 directions, respectively, for each identifying mark quoted in Table 7.7 are the average of the retraction distances determined from each of the four stationary points.
- The overall retraction distance in the plane of the image was calculated using Pythagoras' equation ($\Delta X = \sqrt{(\Delta X_1)^2 + (\Delta X_2)^2}$) and is also reported in Table 7.7 for both the identifying marks (spot 5 & 6).

The retraction distances ΔX_1 and ΔX_2 along the x_1 and x_2 directions for the two identifying marks (spot 5 and 6) are plotted along with the applied surface pressure vs time data for the second liver retraction event of patient 3 in Figure 7.50. Figure 7.51 shows the same surface pressure vs time data overlaid with retraction distance in the image plane (ΔX) extracted from the image analysis of the video footage for this event. Selected stills before, during and after retraction are also presented in Figure 7.51. There is a clear correlation between surface pressure and retraction distance.

Table 7.7: Retraction distances extracted from video footage for the second liver retraction event for patient 3.

Time at images extracted (secs)	Retraction distance (ΔX_1) (cm)		Retraction distance (ΔX_2) (cm)		Retraction distance (ΔX) in plane of image (cm)	
	Spot 5	Spot 6	Spot 5	Spot 6	Spot 5	Spot 6
1	0.00 \pm 0.00	0.00 \pm 0.00	0.00 \pm 0.00	0.00 \pm 0.00	0.00	0.00
4	-0.15 \pm 0.15	-0.40 \pm 0.15	0.32 \pm 0.04	0.06 \pm 0.04	0.35	0.40
6	-0.26 \pm 0.17	-0.15 \pm 0.17	-1.50 \pm 0.15	-3.28 \pm 0.15	1.52	3.28
8	0.77 \pm 0.14	0.79 \pm 0.14	-2.00 \pm 0.25	-3.96 \pm 0.25	2.14	4.04
10	-0.50 \pm 0.94	-0.06 \pm 0.94	-3.86 \pm 0.41	-5.64 \pm 0.55	3.89	5.64
12	-1.25 \pm 1.28	0.76 \pm 1.28	-4.30 \pm 0.55	-5.98 \pm 0.55	4.48	6.03
13	-1.02 \pm 1.21	0.52 \pm 1.21	-4.17 \pm 0.54	-5.77 \pm 0.54	4.29	5.79
14	-1.08 \pm 1.24	0.57 \pm 1.24	-4.15 \pm 0.57	-5.76 \pm 0.57	4.29	5.78
15	-1.55 \pm 1.29	-0.96 \pm 1.29	-4.27 \pm 0.57	-5.91 \pm 0.58	4.54	5.99
16	-1.66 \pm 1.28	-1.19 \pm 1.28	-4.38 \pm 0.58	-5.99 \pm 0.60	4.69	6.11
19	-1.49 \pm 1.30	-0.77 \pm 1.30	-4.38 \pm 0.60	-4.78 \pm 0.60	3.73	4.84

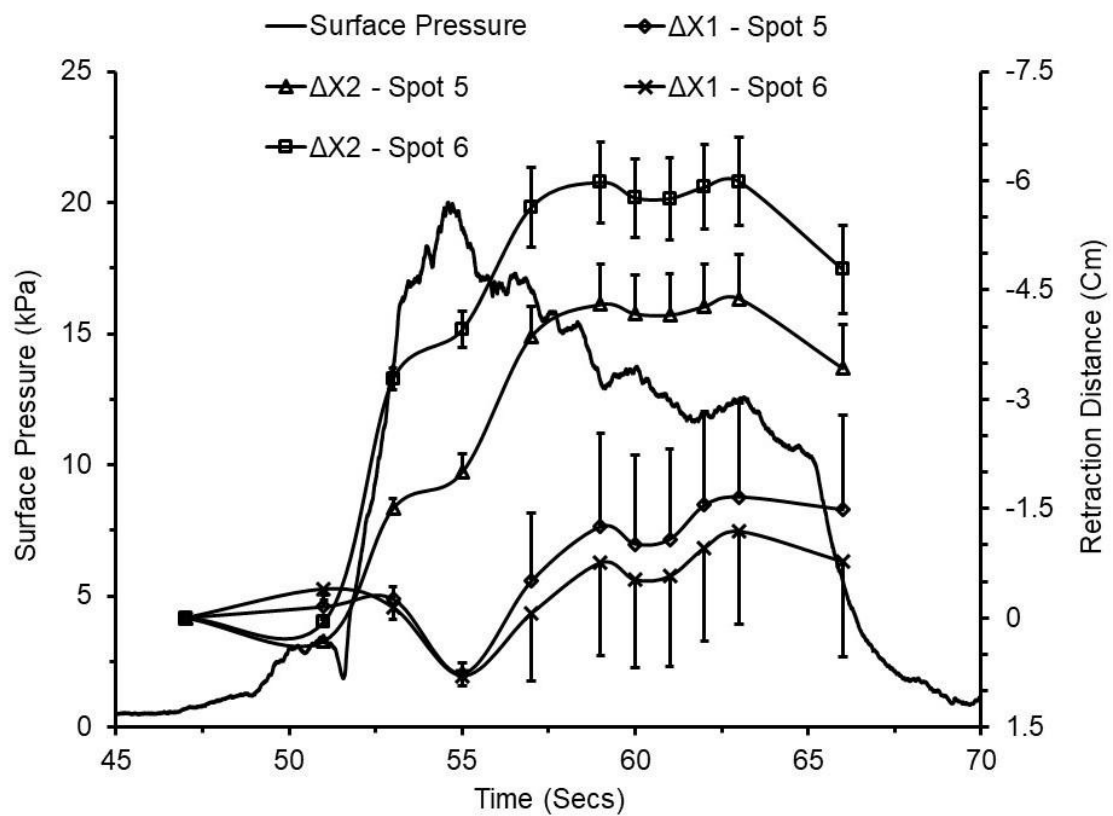


Figure 7.50: Retraction distances (ΔX_1 and ΔX_2) compared against applied surface pressure in the second liver retraction event for patient 3.

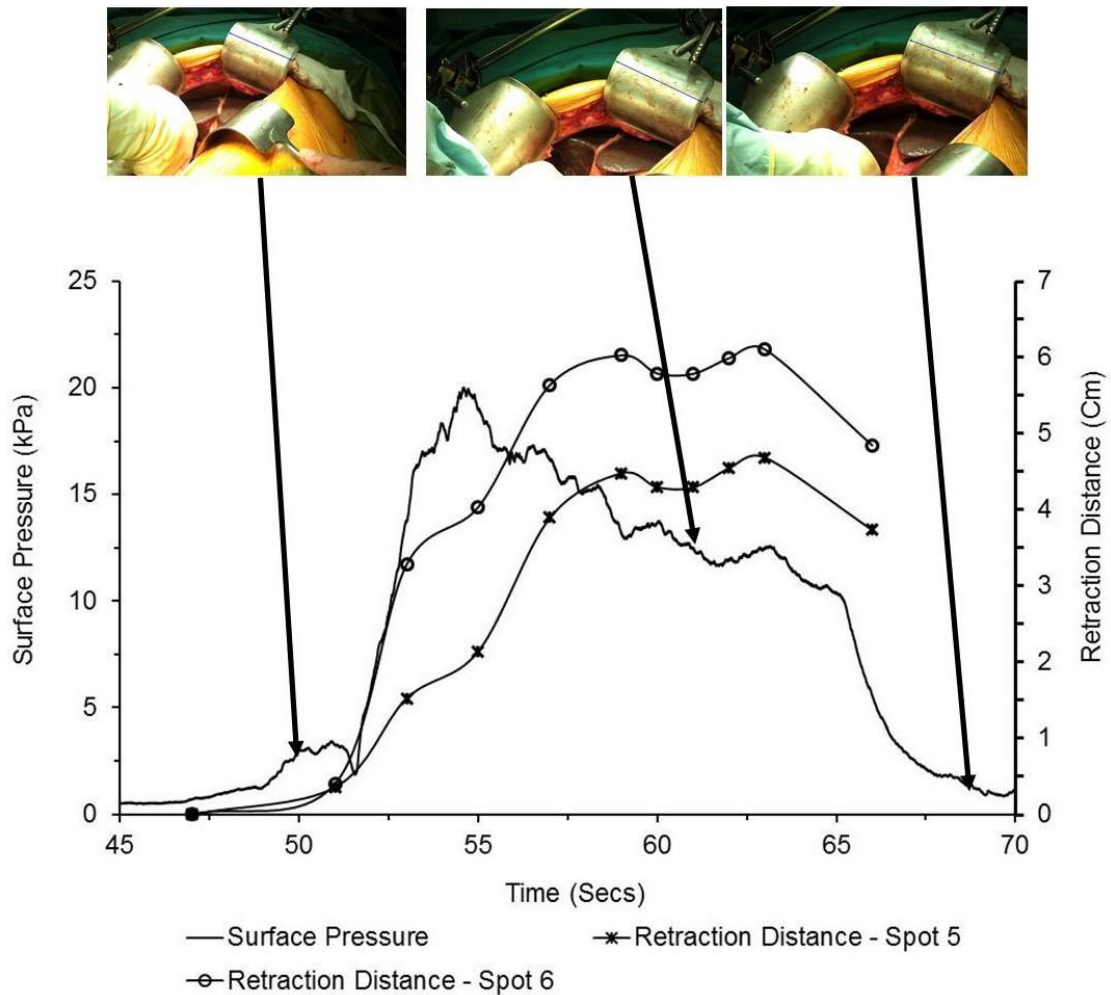


Figure 7.51: Correlation between surface pressure and retraction distance (ΔX) in the plane of the image for the second retraction event of the liver for patient 3 during OC. Selected stills from the video footage are also included.

7.5.2 Hand assisted laparoscopic surgery

Quantification of retraction distances for the bowel, kidney, stomach and spleen during HALS are summarised in this section.

The coordinate axes (X1-X2), stationary points (1-4) and identifying marks (spot 5 and 6) are shown for retraction of bowel (Figure 7.52), kidney (Figure 7.53), stomach (Figure 7.54) and spleen (Figure 7.55).

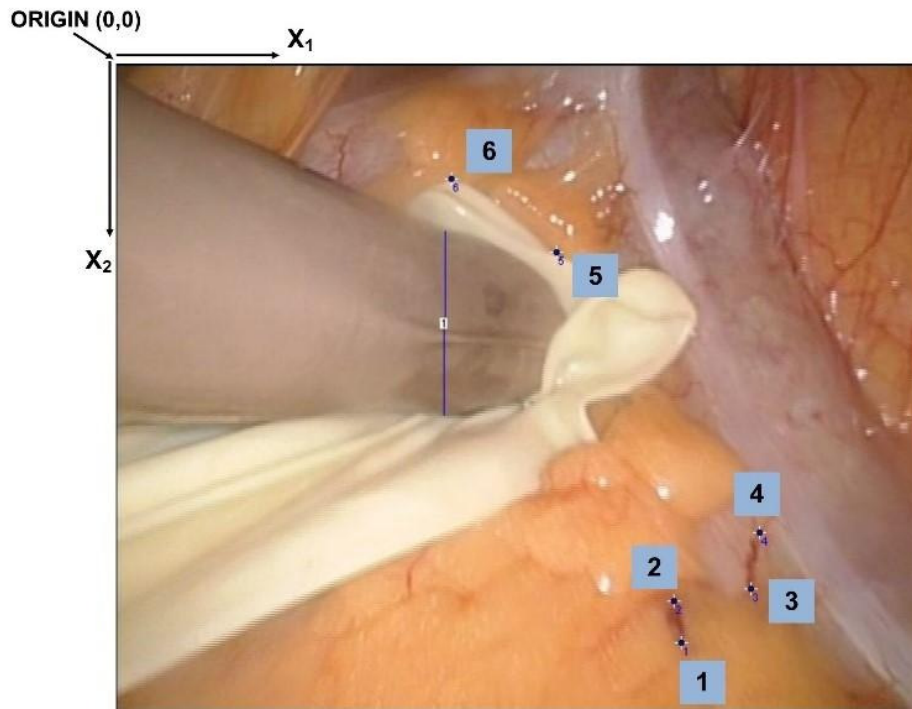


Figure 7.52: Coordinate axes, known width of thumb of surgeon (2 cm), stationary points (1-4) and identifying marks (spot 5 and 6) for Image at 9 secs for retraction of bowel for patient 5.

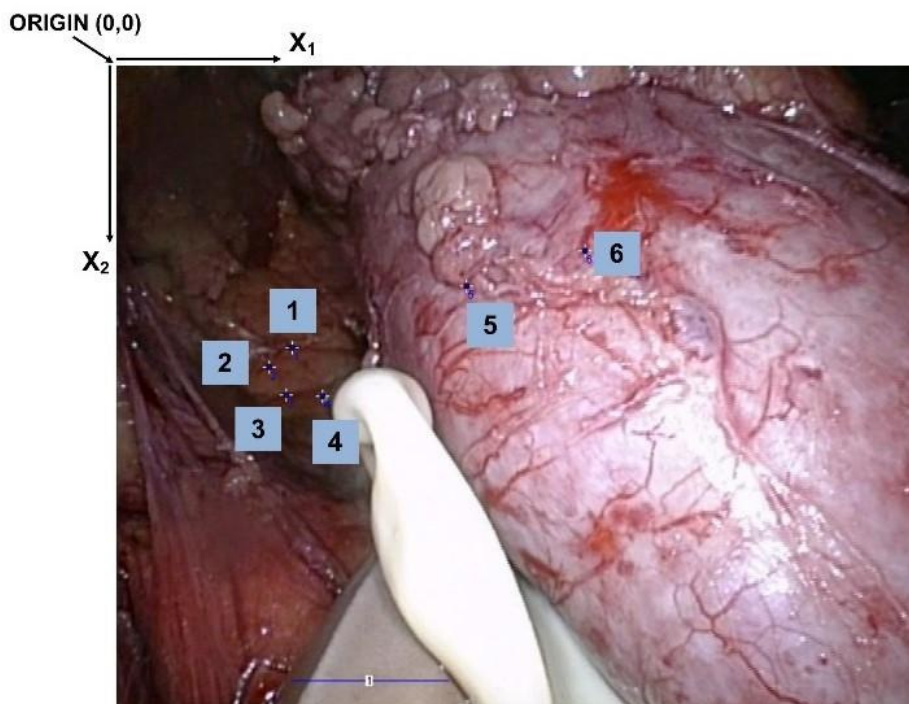


Figure 7.53: Coordinate axes, known width of fingertips of surgeon (2 cm), stationary points (1-4) and identifying marks (spot 5 and 6) for Image at 0 sec for retraction of kidney for patient 6.

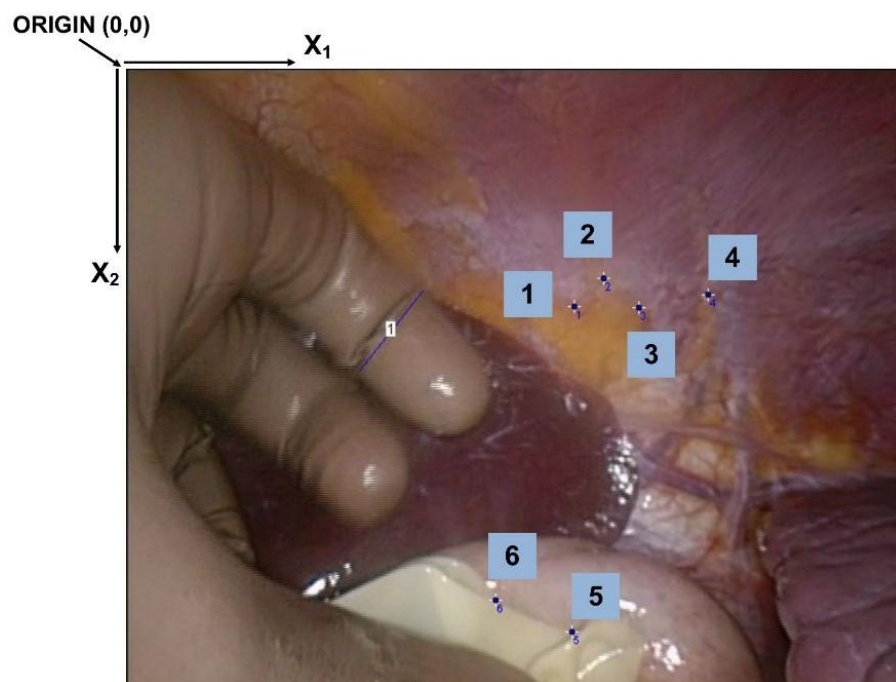


Figure 7.54: Coordinate axes, known width of fingertips of surgeon (2 cm), stationary points (1-4) and identifying marks (spot 5 and 6) for Image at 0 sec for retraction of stomach for patient 5.

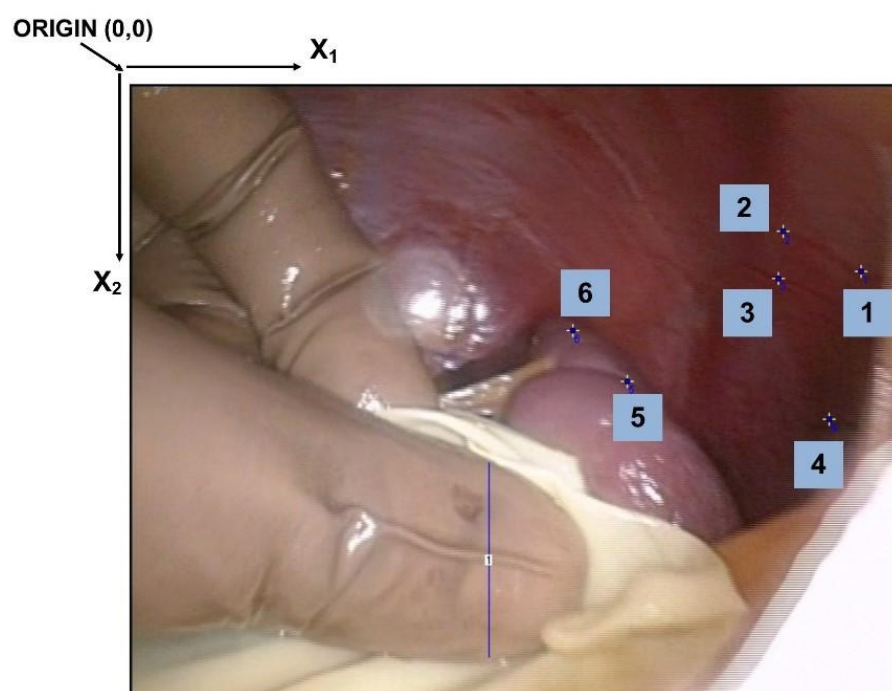


Figure 7.55: Coordinate axes, known width of thumb of surgeon (2 cm), stationary points (1-4) and identifying marks (spot 5 and 6) for Image at 29 secs for retraction of spleen for patient 5.

The surface pressure vs time data for retractions of the bowel (patient 5), kidney (patient 6), stomach (patient 5), and spleen (patient 5), overlaid with retraction distances (in the image plane) vs time data extracted from the image analysis of the corresponding video footages for these events are depicted in Figure 7.56, Figure 7.57, Figure 7.58 and Figure 7.59, respectively. Selected stills before, during and after retraction are also presented.

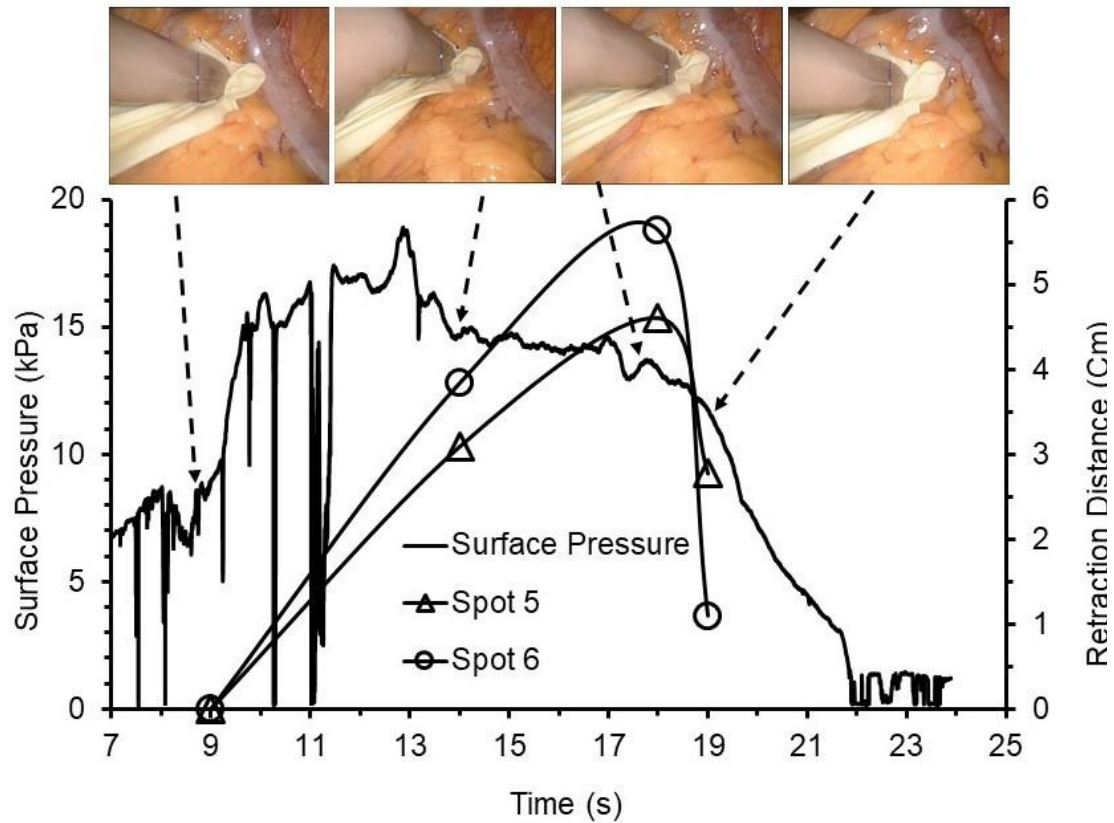


Figure 7.56: Correlation between surface pressure and retraction distance for the second retraction event of the bowel for patient 5 during HALS. Selected stills used for calculation of retraction distance are also included.

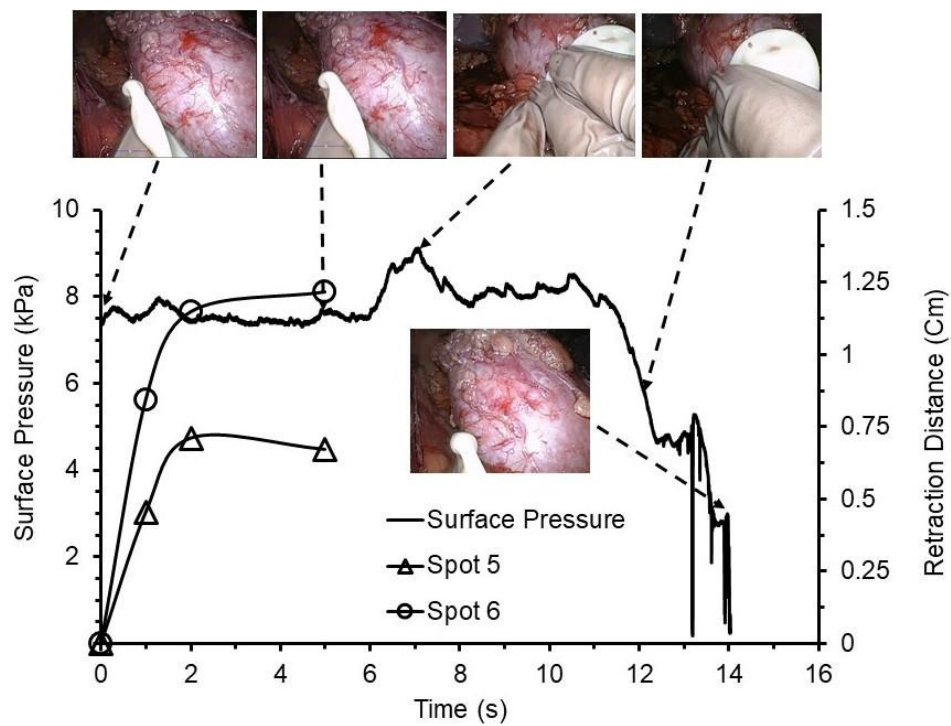


Figure 7.57: Correlation between surface pressure and retraction distance for the kidney for patient 6 during HALS. Selected stills used for calculation of retraction distance and additional stills from the video footage are also included.

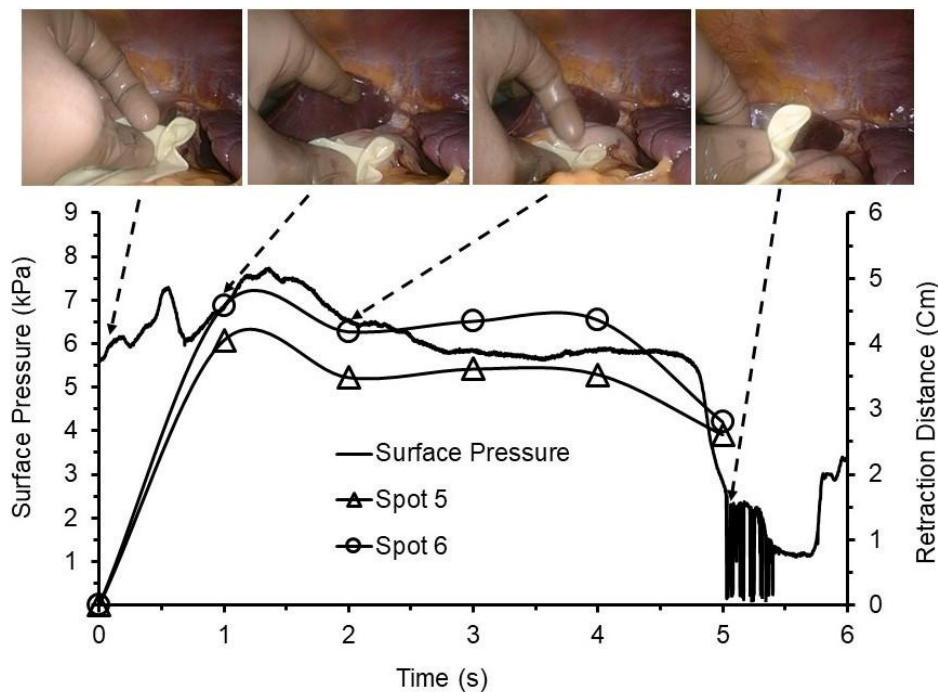


Figure 7.58: Correlation between surface pressure and retraction distance for the stomach for patient 5 during HALS. Selected stills used for calculation of retraction distance are also included.

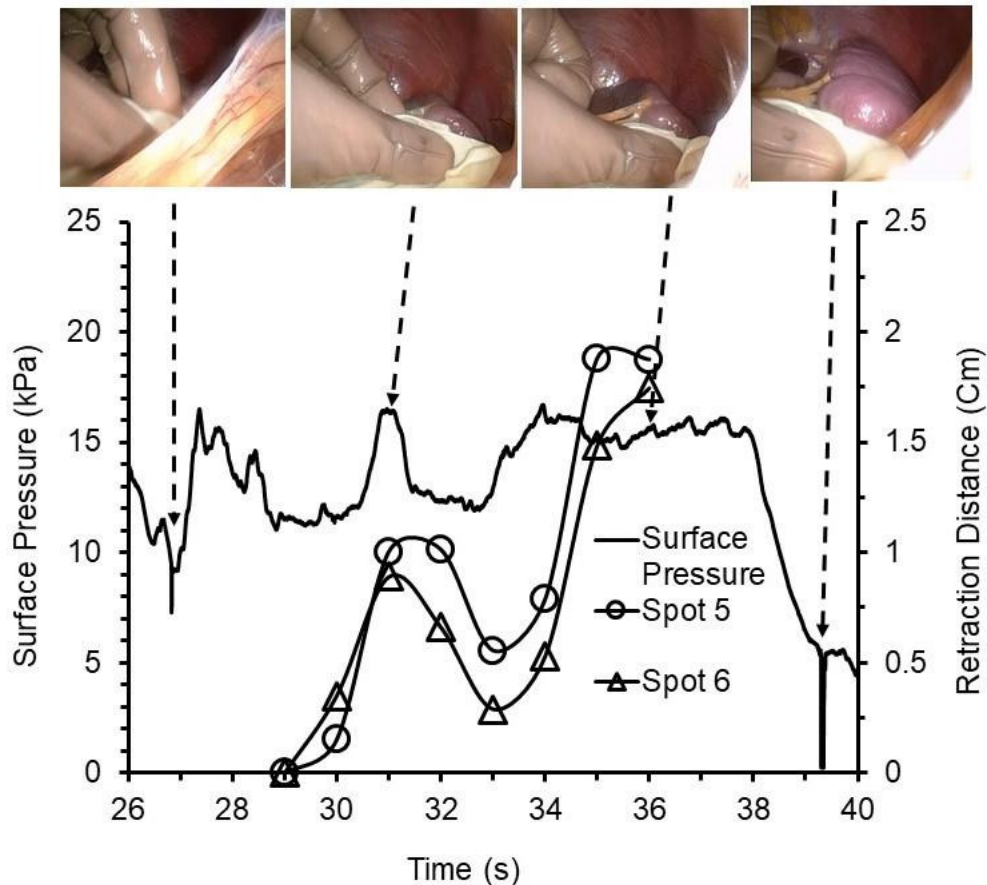


Figure 7.59: Correlation between surface pressure and retraction distance for the spleen for patient 5 during HALS. Selected stills from the video footage are also included.

Based on the liver, bowel and stomach data, the measured retraction distance appears to be correlated with the measured applied surface pressure.

Retraction distances calculated for the kidney and spleen are less than the liver, bowel, and stomach due to combinations of reasons outline below:

- Organ retracted out of the range of the endoscope (i.e. loss of retraction movements in the video footages),
- Fingertips/thumb of surgeon (considered for the calibration of image) not fully visible in subsequent images,
- Disappearing of stationary points, and
- Disappearing of identifying marks.

7.5.3 Degree of organ retraction distance

The maximum retraction distances for the key abdominal organs during OC and HALS are summarised in Figure 7.60.

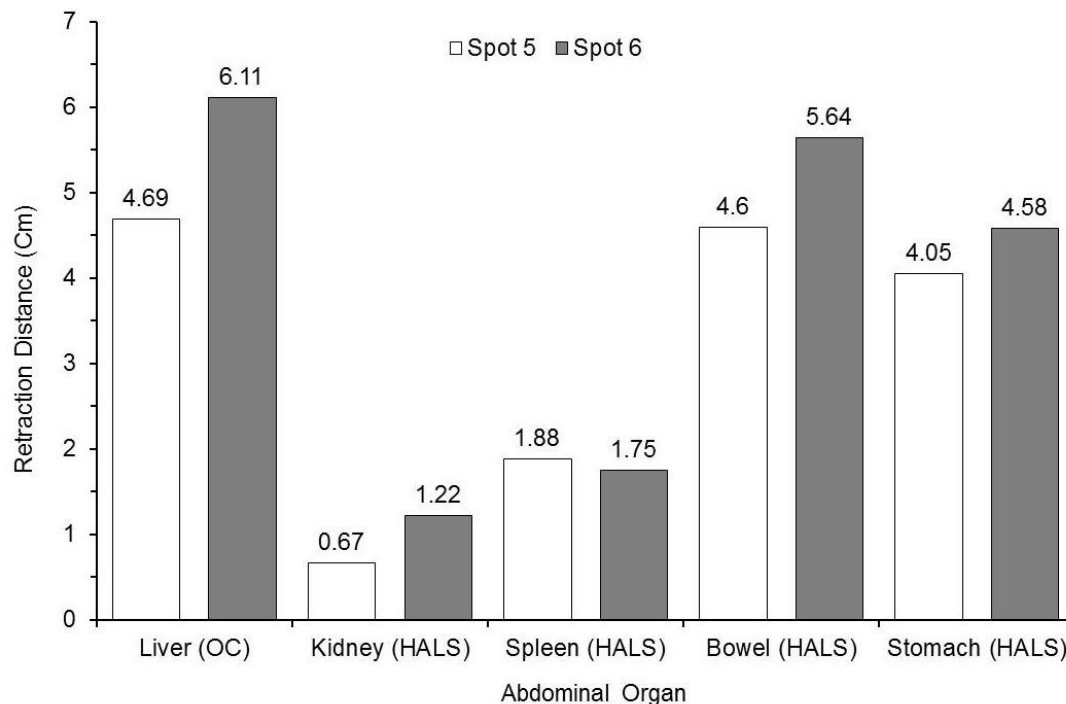


Figure 7.60: Retraction distances of key abdominal organs. OC = Open Cholecystectomy. HALS = Hand Assisted Laparoscopic Surgery.

7.6 Comparison of in-vivo and in-vitro surface pressures

Surface pressures applied for defined typical 'movements' of pig liver, simulant human liver, and simulant human bowel pieces inside the in-house test rig are compared in this section with the surface pressures applied for typical retraction movements of liver and bowel during OC and HALS.

Liver:

Surface pressures applied for 'moving and squashing' of pig liver, 'lifting' of pig liver, and 'lifting' of simulant liver (50% v/v of Pro Gel 10 softener) are compared in Figure 7.61 with surface pressures applied for the lifting of human liver by the fingertips of the surgeon during OC and HALS as well as by metal retractor during HALS. Detailed analysis of the responses is clearly difficult. However, the maximum surface pressure applied to pig, simulant human and human liver is of the order of 20 kPa. More generally, the in-house simulator is found to produce surface responses for in-vitro manipulation of simulant and pig liver broadly consistent with the in-vivo responses for human liver.

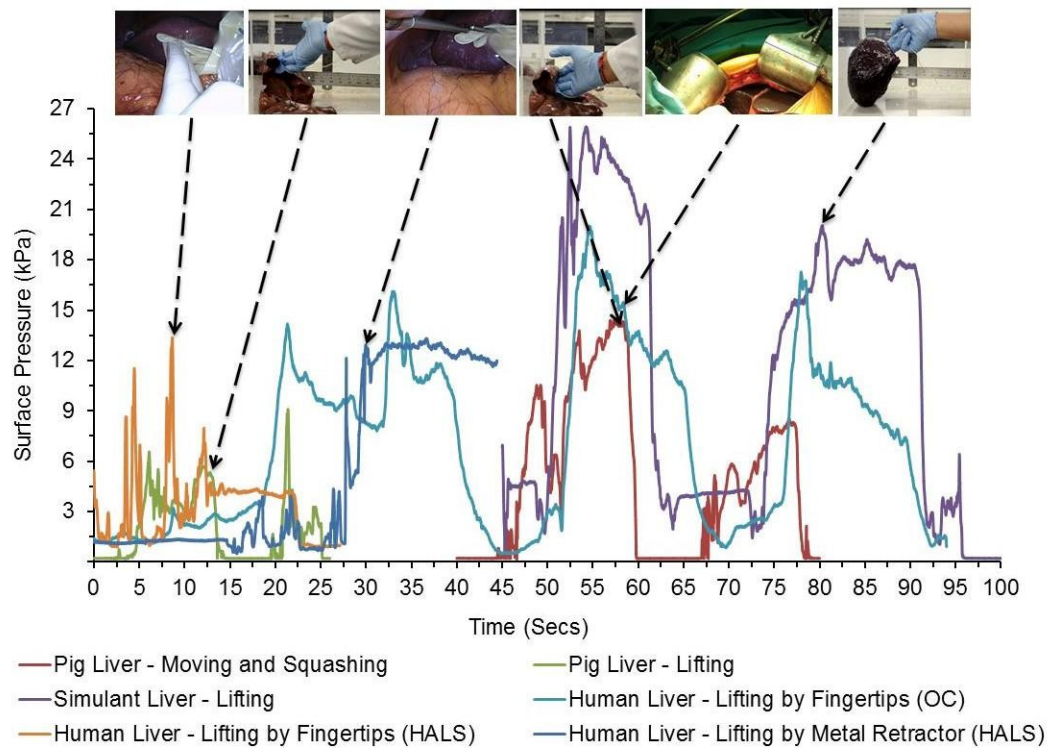


Figure 7.61: Surface pressures applied to retract pig (in-vitro), simulant human liver (in-vitro), and human liver (in-vivo). OC = Open Cholecystectomy. HALS = Hand Assisted Laparoscopic Surgery.

Bowel:

Surface pressures for 'moving and squashing' of simulant human bowel pieces are compared in Figure 7.62 with surface pressures applied for typical retraction movements of human bowel by the fingertips of the surgeon during OC and HALS as well as by a metal retractor during OC. The maximum surface pressure applied by fingertips to simulant bowel pieces (test-rig, in-vitro) and to human bowel (OC, in-vivo) is ~10 kPa. The in-vivo surface pressures applied to the human bowel with a metal retractor during OC and by the fingertips of the surgeon during HALS tend to be a little higher than those applied by fingertips to the simulant and human bowel during the OC procedure. Nevertheless, the bowel comparison study again provides appropriate validation of the in-house simulator and simulant organ material/property assessment.

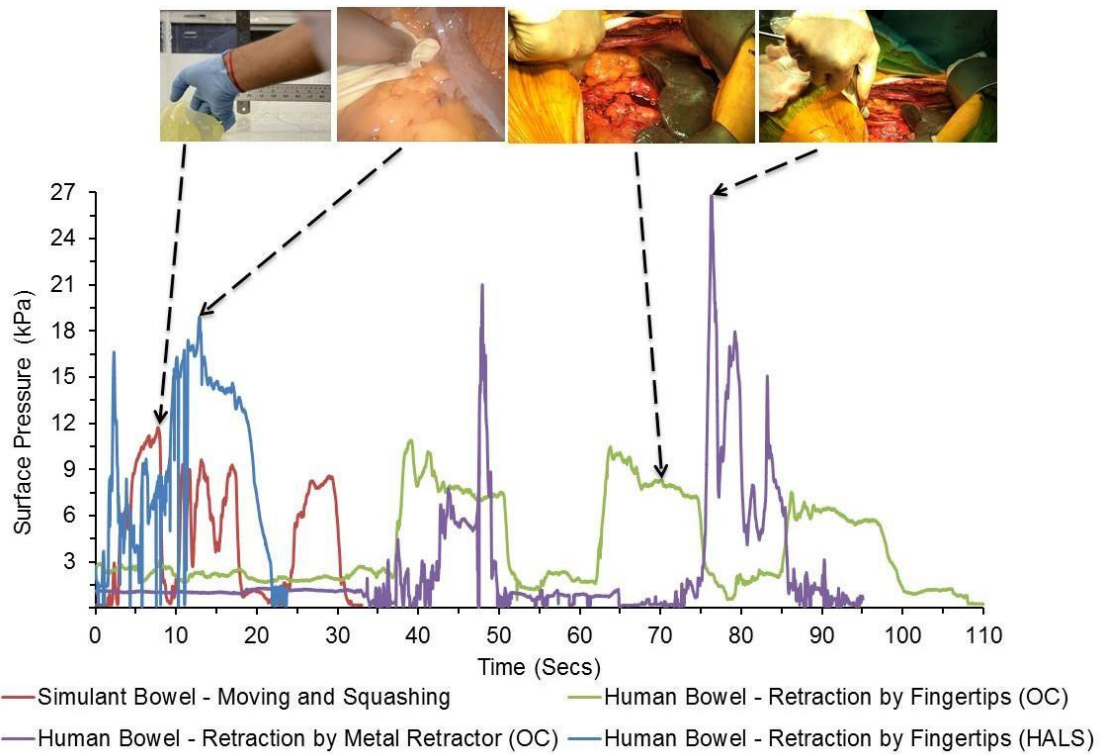


Figure 7.62: Surface pressures applied to retract pig (in-vitro), simulant human liver (in-vitro), and human liver (in-vivo). OC = Open Cholecystectomy. HALS = Hand Assisted Laparoscopic Surgery.

7.7 Summary

The solid and hollow simulant organs were fabricated and assessed to evaluate the density and elasticity since they are the important biomechanical properties to determine the degree of surface pressure required for the retraction of human abdominal organs within the abdominal cavity. The in-house test rig was utilised for in-vitro assessments of simulants and pig organs to validate the test rig and to identify the degree of surface pressure exerted by the operator on the solid and hollow simulant organs.

In summary a novel in-vivo pressure sensing experiment has been carried out to study hand-tissue surface pressures generated during abdominal surgery, including hand assisted laparoscopic procedures, in humans. The surface pressures applied to retract abdominal organs are typically 1-41 kPa, the average maximum surface pressure for all organs and procedures is 14 ± 3 kPa, and surface pressure relaxation during the retraction 'hold' period has been observed. There is a tendency for higher surface pressures and lower rate of surface pressure relaxation in HALS procedures compared to open surgery.

Surface pressures also tend to be higher in the retraction of solid organs than for hollow organs. The increased surface pressure has been shown to correlate with retraction distance for retraction of the liver in open surgery, and the bowel and stomach in HALS procedures. Comparison of surface pressure responses of simulant liver, simulant bowel and pig liver, measured in-vitro using the developed in-house simulator, with the in-vivo responses for human liver and human bowel demonstrate the in-house simulator and simulant organs provide suitable responses and, therefore validate the simulator for future use.

8 Results 2 - Finite element (FE) modelling of a solid wall cylinder

The outputs of the FE modelling of a solid wall cylinder (without and with end pieces) displaying uniform linear elastic isotropic or orthotropic material properties are described in this section.

8.1 Isotropic material properties

Uniform linear elastic isotropic material properties were simulated using finite and infinite BCs. Solid wall cylinders (300mm length, 1mm wall thickness and 40mm outer diameter) without end pieces were simulated for uniaxial compression and tension loading conditions. While, solid wall cylinders with end pieces were simulated for uniaxial compression loading condition. The applied axial compressive and tension forces were $\pm 1 \times 10^6$ N. Equatorial radial deformation (ERD) vs axial deformation (AD) are plotted for solid wall cylinder without end pieces in Figure 8.1 and with end pieces in Figure 8.2 and, stills extracted for pictorial demonstration of ERD (left) and AD (right) are also shown.

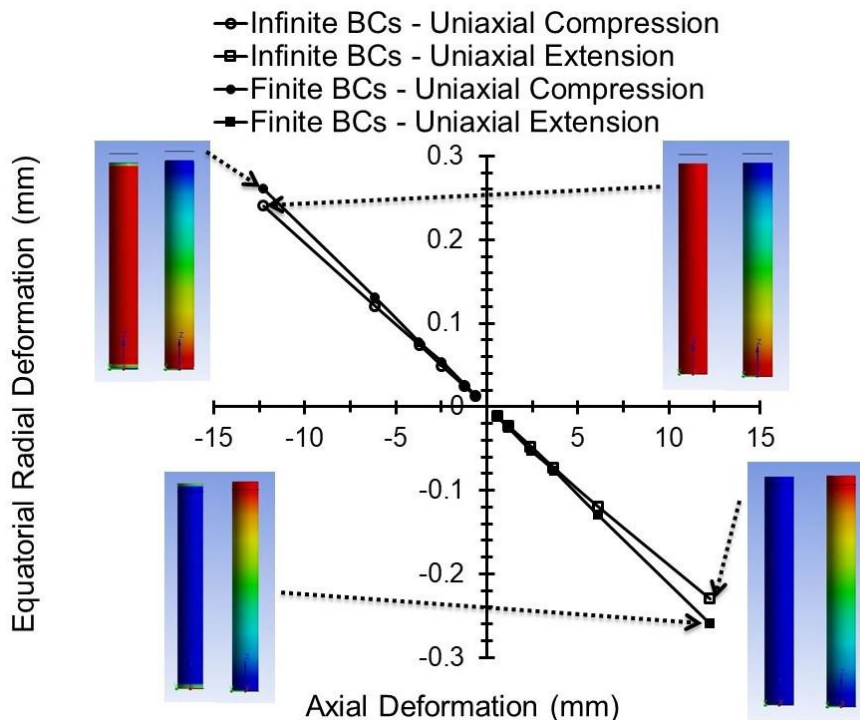


Figure 8.1: Equatorial radial deformation vs axial deformation of a solid wall cylinder with isotropic material properties employing finite and infinite BCs. Stills of ERD (left) and AD (right) are also shown.

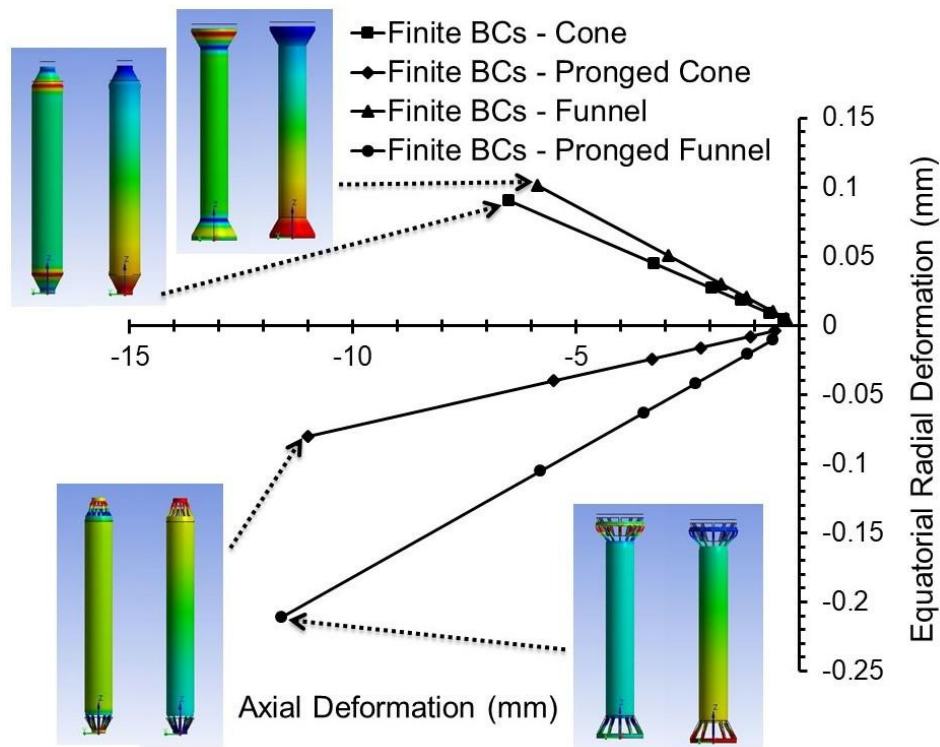


Figure 8.2: Equatorial radial deformation vs axial deformation of a cylinder with isotropic material properties and end pieces under uniaxial compressive force. Stills of ERD (left) and AD (right) are also shown.

It is evident from Figures 8.1 and 8.2 that the uniform linear elastic isotropic material properties do not produce a large equatorial radial deformation of the solid wall cylinder for small axial deformation essential for the expansion mechanism required in this project. The FE modelling methodology employed to study the impact of isotropic material properties on the solid wall of cylinder with and without end pieces produces the expected results based on the input Young's modulus and Poisson's ratio (Table 5.1, Chapter 5) and outer diameter, wall thickness and length of solid wall cylinder. For example, uniaxial extension of solid wall cylinder (employing finite and infinite BCs) in Figure 8.1 shows 12.2mm and -0.24mm of axial and radial deformation (due to axial-circumferential plane deformation dominates over axial-radial deformation), respectively validating the FE modelling.

8.2 Orthotropic material properties

Parametric studies of a solid wall cylinder with and without end pieces were carried out using orthotropic material properties and the results are described in this section.

8.2.1 Parametric study 1 of solid wall cylinder with end pieces

The parametric study 1 of solid wall cylinder with pronged cone end pieces was carried out using the finite BCs and uniaxial compression mechanism in accordance with the protocol defined for 'parametric study 1' in Table 5.3, Chapter 5.

8.2.1.1 Simulation of standard properties

The set of orthotropic material properties specified in Table 5.3, Chapter 5, geometrical parameters defined in Chapter 5.3.1, and pronged cone end pieces at both ends were considered as the 'standard' configuration.

8.2.1.1.1 Orthotropic material properties

Young's moduli (E_r , E_θ and E_z), in-plane Poisson's ratio ($\nu_{\theta z}$) and shear moduli ($G_{r\theta}$, $G_{\theta z}$ and G_r) were varied during parametric study of orthotropic material properties. Young's moduli and shear moduli were reduced to two and four orders of magnitude from the 'standard' configuration outlined in Table 5.3, Chapter 5. For instance, E_θ was varied from 2×10^8 Pa to 2×10^6 Pa and 2×10^4 Pa ($\nu_{\theta z}$ were recalculated to maintain the symmetric compliance matrix). $\nu_{\theta z}$ was simulated for zero, positive (+0.5, +1, +2, +5 and +10) and negative (-0.5, -1, -2, -5, -10) values. ERD vs AD, ERD vs axial compressive force and ERD vs axial strain were plotted to describe results of parametric studies of orthotropic properties.

Young's modulus:

Results of parametric studies of E_r (Figure 8.3 and Figure 8.4), E_θ (Figures 8.5-8.7) and E_z (Figure 8.8 and Figure 8.9) are outlined below. Stills showing ERD are also included in Figure 8.3, Figure 8.5 and Figure 8.8.

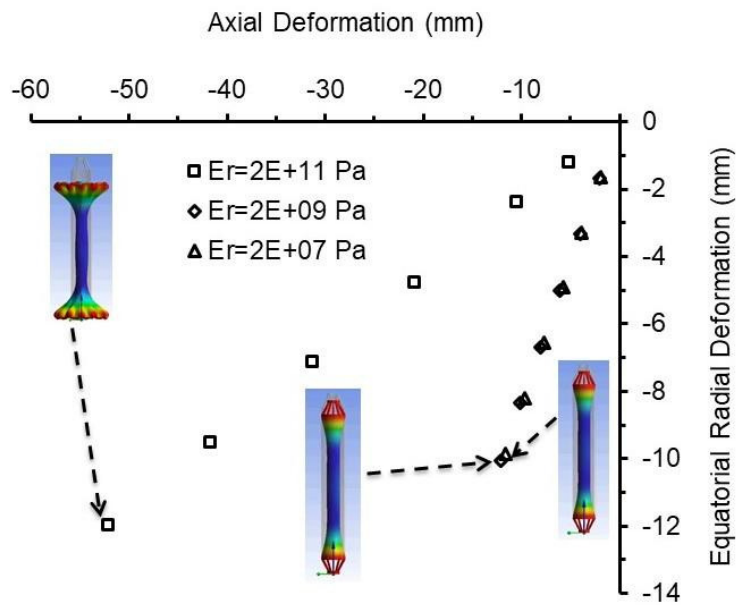


Figure 8.3: ERD vs AD for parametric study of E_r (parametric study 1 of cylinder with pronged cone end pieces and in-plane negative Poisson's ratio). Stills of ERD are also shown.

The variations in the 'standard' value of E_r from 2×10^{11} Pa to 2×10^9 Pa and 2×10^7 Pa did not promote the out-of-plane bending (for a large equatorial deformation at small axial deformation) of solid wall cylinder; in fact, solid wall of a cylinder has narrowed under uniaxial compression (Figure 8.3). The degree of axial compressive force required when $E_r = 2 \times 10^9$ Pa and 2×10^7 Pa is approximately three and five orders of magnitude less than the 'standard' value ($E_r = 2 \times 10^{11}$ Pa) (Figure 8.4).

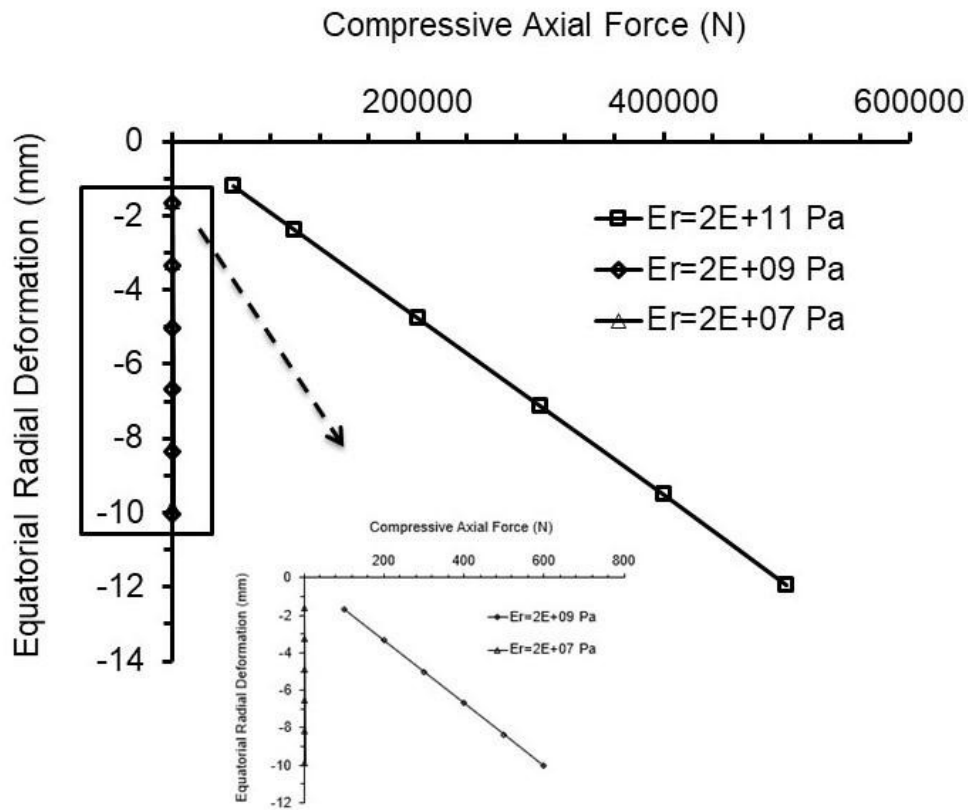


Figure 8.4: ERD vs compressive axial force for parametric study of E_r (parametric study 1 of cylinder with pronged cone end pieces and in-plane negative Poisson's ratio).

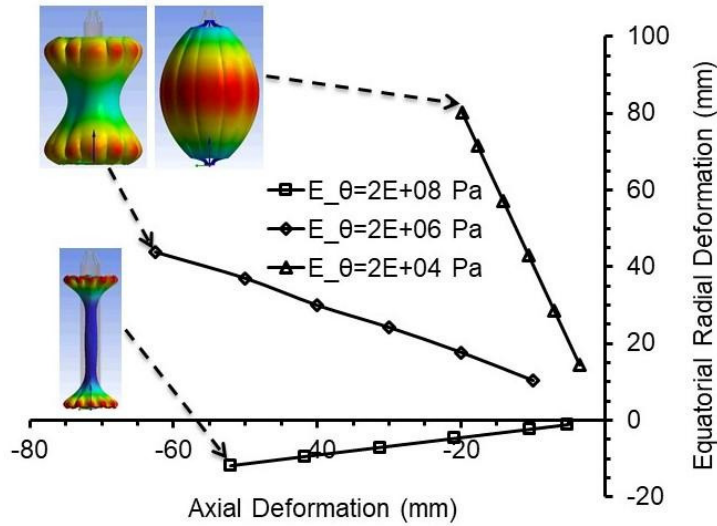


Figure 8.5: ERD vs AD for parametric study of E_θ (parametric study 1 of cylinder with pronged cone end pieces and in-plane negative Poisson's ratio). Stills of ERD are also shown.

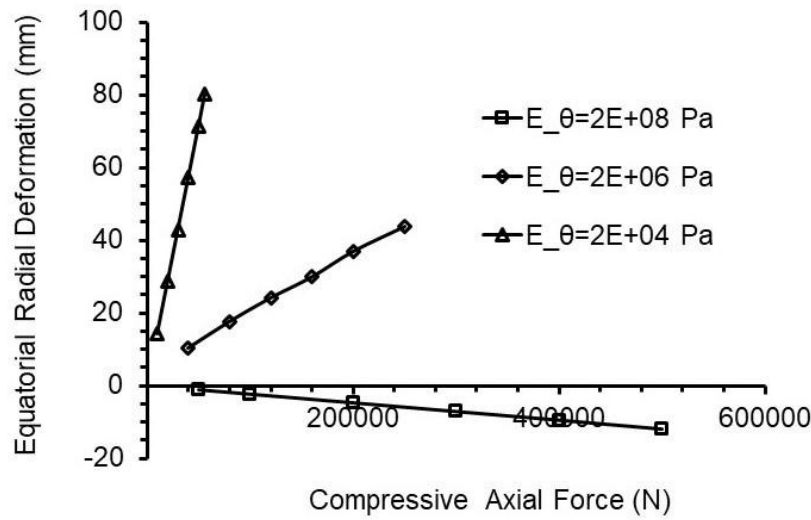


Figure 8.6: ERD vs compressive axial force for parametric study of E_θ (parametric study 1 of cylinder with pronged cone end pieces and in-plane negative Poisson's ratio).

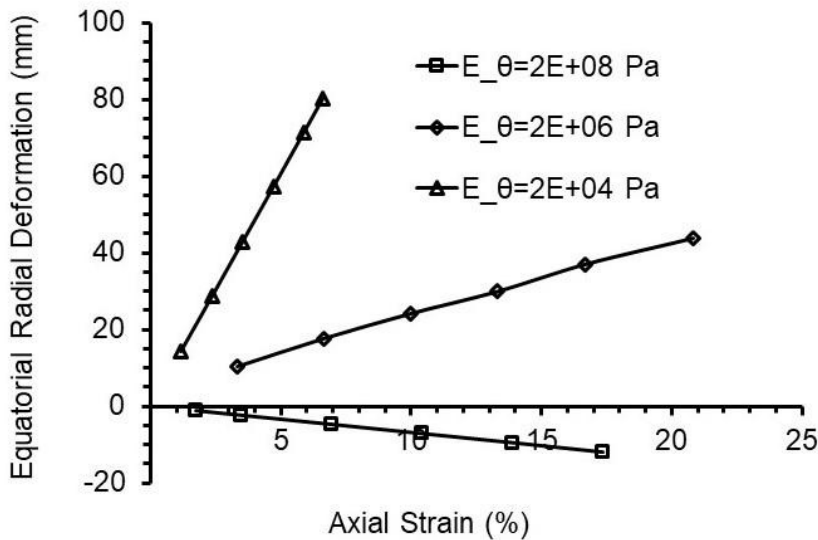


Figure 8.7: ERD vs axial strain for parametric study of E_θ (parametric study 1 of cylinder with pronged cone end pieces and in-plane negative Poisson's ratio).

An equatorial narrowing occurs for $E_\theta = 2 \times 10^8$ Pa, a transition occurs around $E_\theta = 2 \times 10^6$ Pa (where the equator is wider than the undeformed values, but still narrower than at the ends), and when $E_\theta = 2 \times 10^4$ Pa the cylinder adopts the shape of a prolate spheroid (Figure 8.5). The degree of axial compressive force required for $E_\theta = 2 \times 10^4$ Pa (~ 56100 N) is approximately one order of magnitude

less than for the $E_\theta=2 \times 10^6$ Pa (250,000N) and $E_\theta=2 \times 10^8$ Pa (500,000N) (Figure 8.6). A large equatorial radial deformation of the solid wall cylinder (~ 80 mm) for small axial strain ($\sim 7\%$) was obtained when E_θ was 2×10^4 Pa (Figure 8.7).

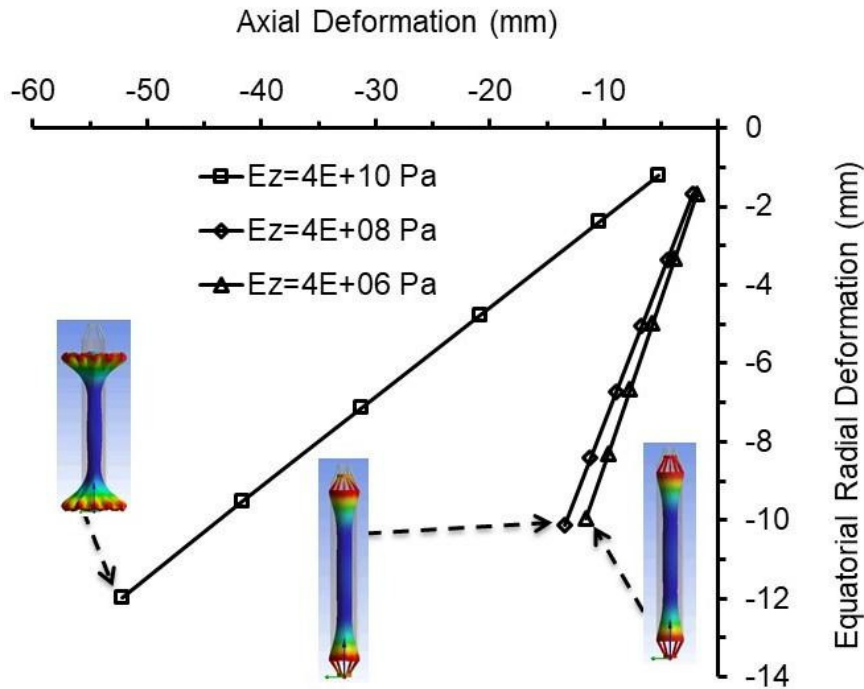


Figure 8.8: ERD vs AD for parametric study of E_z (parametric study 1 of cylinder with pronged cone end pieces and in-plane negative Poisson's ratio). Stills of ERD are also shown.

The variations in the 'standard' value of E_z from 4×10^{10} Pa to 4×10^8 Pa and 4×10^6 Pa did not promote the out-of-plane bending (for a large equatorial deformation at small axial deformation) of solid wall cylinder (Figure 8.8). The degree of axial compressive force required when $E_z=4 \times 10^8$ Pa and 4×10^6 Pa is approximately three and four orders of magnitude less than the 'standard' value ($E_r=4 \times 10^{10}$ Pa) (Figure 8.9).

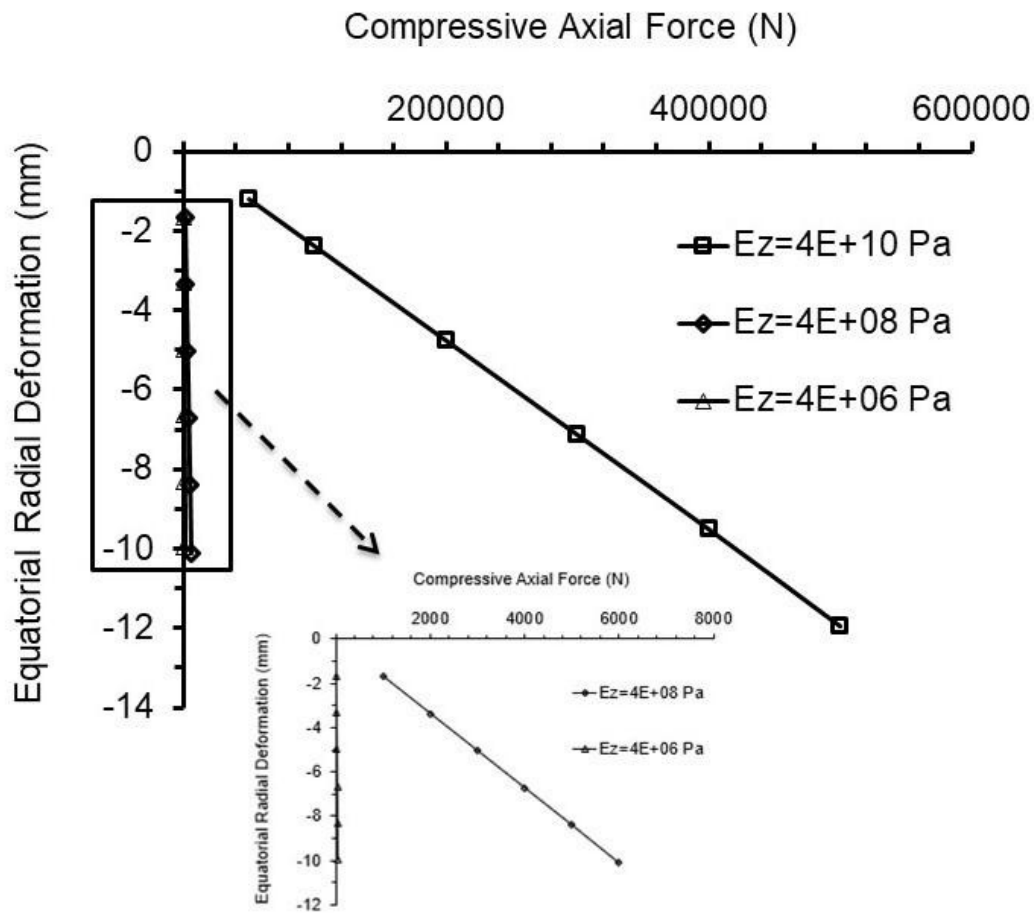


Figure 8.9: ERD vs compressive axial force for parametric study of E_z (parametric study 1 of cylinder with pronged cone end pieces and in-plane negative Poisson's ratio).

Summary:

The parametric study of Young's modulus has indicated that E_θ is critical to obtain a large equatorial deformation of solid wall cylinder with pronged cone end pieces at low axial deformation.

Shear moduli:

Results of parametric studies of $G_{r\theta}$ (Figure 8.10 and Figure 8.11), $G_{\theta z}$ (Figure 8.12 and Figure 8.13) and G_{rz} (Figure 8.14 and Figure 8.15) are outlined below. Stills showing ERD are also included in Figure 8.10, Figure 8.12 and Figure 8.14.

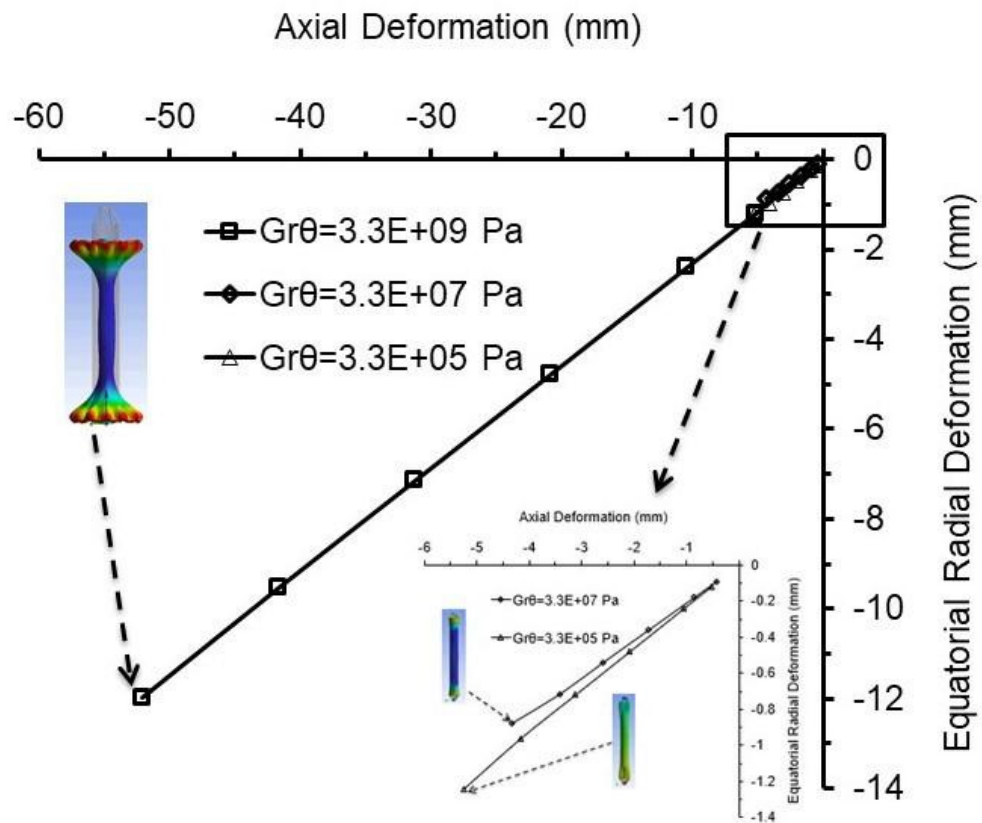


Figure 8.10: ERD vs AD for parametric study of Gr_θ (parametric study 1 of cylinder with pronged cone end pieces and in-plane negative Poisson's ratio). Stills of ERD are also shown.

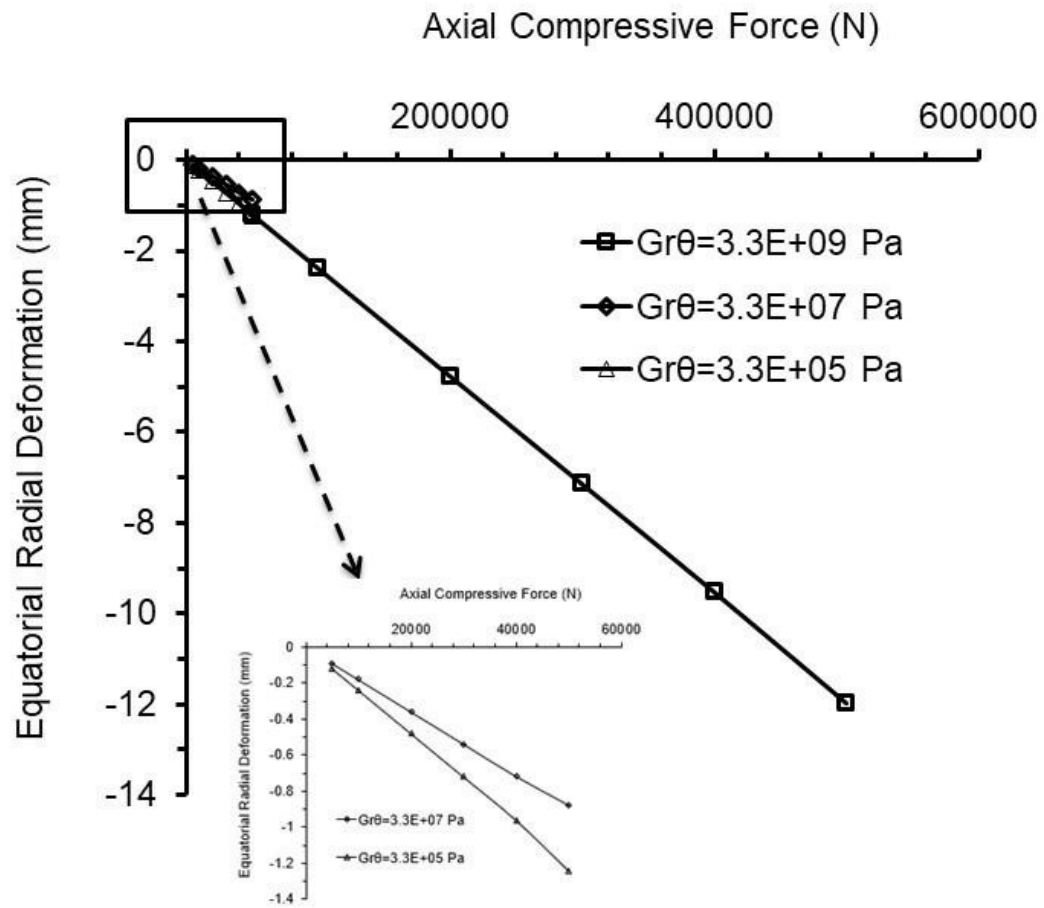


Figure 8.11: ERD vs compressive axial force for parametric study of $G_{r\theta}$ (parametric study 1 of cylinder with pronged cone end pieces and in-plane negative Poisson's ratio).

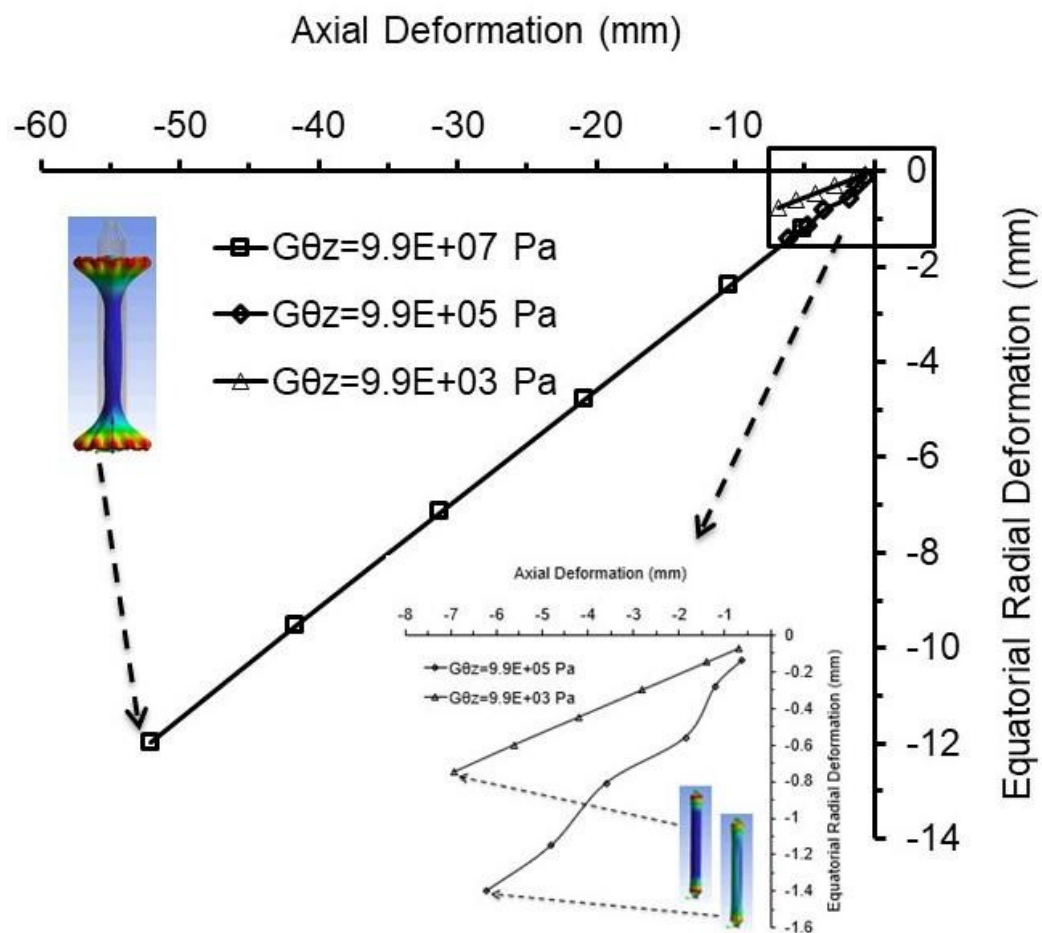


Figure 8.12: ERD vs AD for parametric study of $G_{\theta z}$ (parametric study 1 of cylinder with pronged cone end pieces and in-plane negative Poisson's ratio). Stills of ERD are also shown.

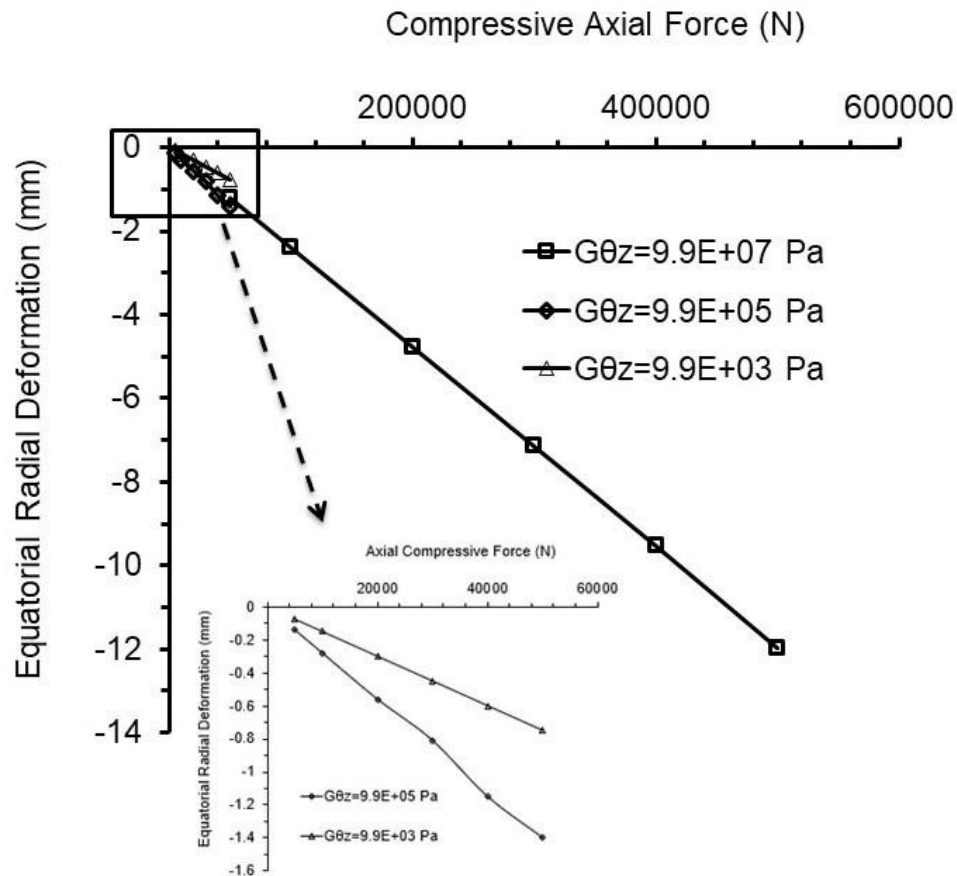


Figure 8.13: ERD vs compressive axial force for parametric study of $G_{\theta z}$ (parametric study 1 of cylinder with pronged cone end pieces and in-plane negative Poisson's ratio).

The variations (reductions of two and four orders of magnitude than the 'standard' values of $G_{r\theta}$, $G_{\theta z}$ and G_{rz} as shown in Table 5.4, Chapter 5) did not trigger the out-of-plane bending (required for a large equatorial deformation at small axial deformation) of solid wall cylinder (Figure 8.10, Figure 8.12 and Figure 8.14). The degree of axial compressive force required when shear moduli ($G_{r\theta}$, $G_{\theta z}$ and G_{rz}) reduced by two and four orders of magnitude than the 'standard' values is approximately one order of magnitude less than the 'standard' values (Figure 8.11, Figure 8.13 and Figure 8.15). The parametric study of shear moduli (Figures 8.10-8.15) is suggested that they don't facilitate the shape change of solid wall of cylinder with pronged cone end pieces.

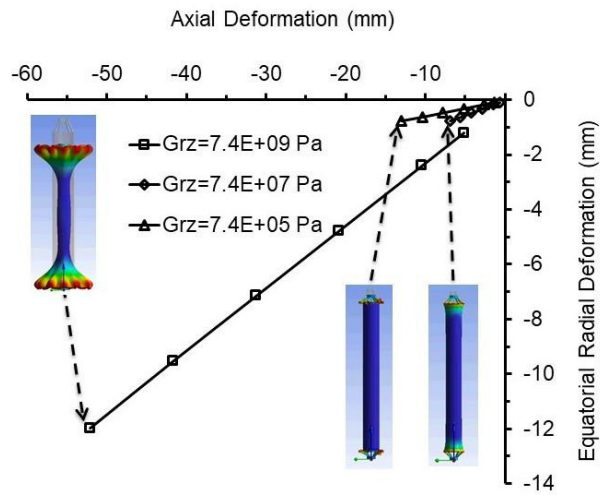


Figure 8.14: ERD vs AD for parametric study of G_{rz} (parametric study 1 of cylinder with pronged cone end pieces and in-plane negative Poisson's ratio). Stills of ERD are also shown.

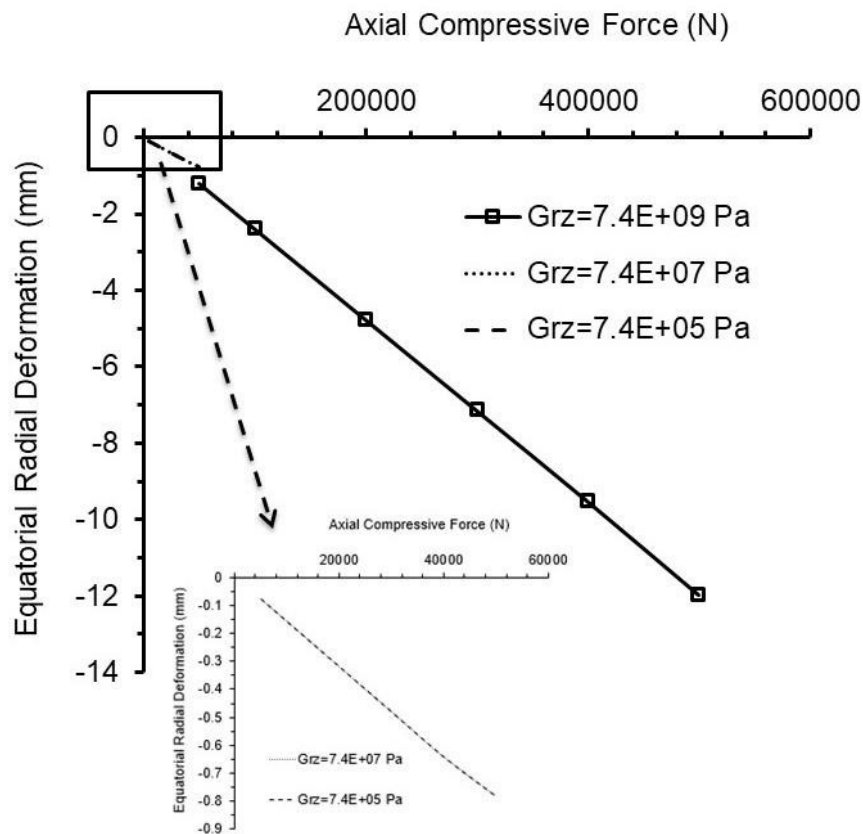


Figure 8.15: ERD vs compressive axial force for parametric study of G_{rz} (parametric study 1 of cylinder with pronged cone end pieces and in-plane negative Poisson's ratio).

In-plane Poisson's ratios:

Results of parametric studies of in-plane Poisson's ratios are described in Figure 8.16 (ERD vs AD) and Figure 8.17 (ERD vs compressive axial force). Stills showing ERD are also shown in Figure 8.16. The different values of the in-plane Poisson's ratios (negative, zero and positive) did not cause the out-of-plane bending (required for a large equatorial deformation at small axial deformation) of solid wall cylinder for the 'standard' configurations (Figure 8.16 and Figure 8.17).

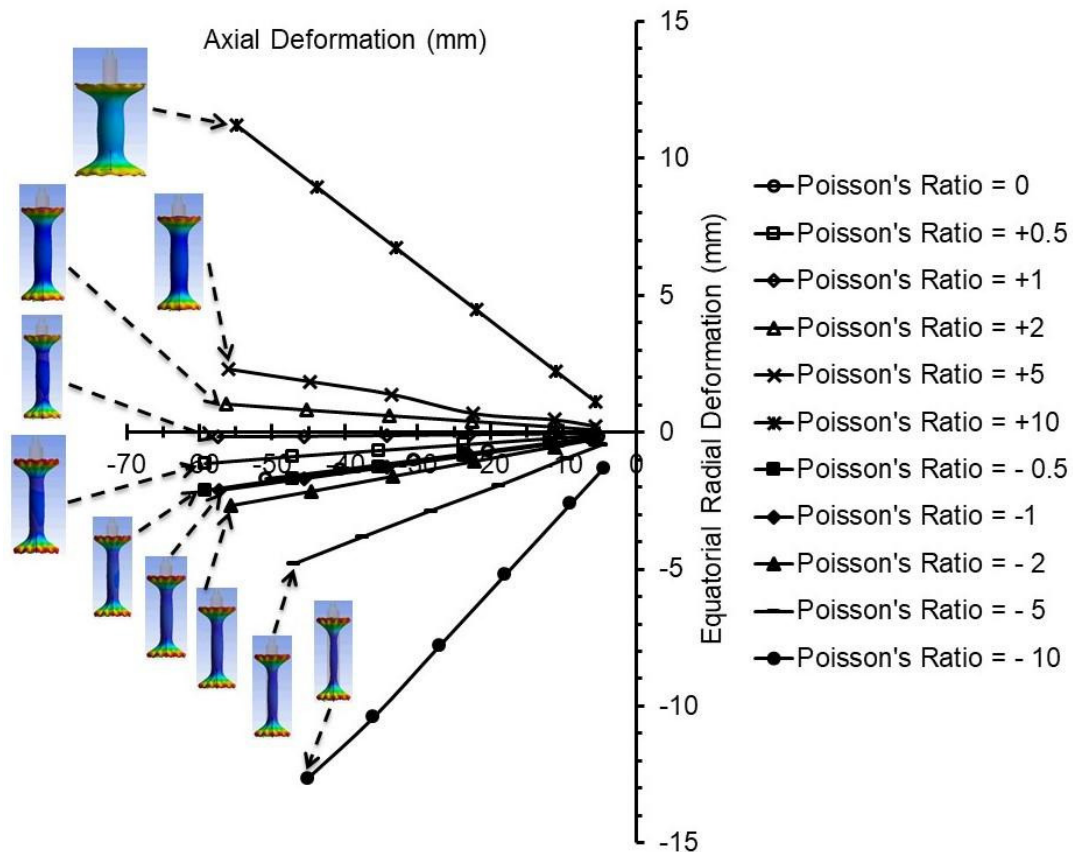


Figure 8.16: ERD vs AD for parametric study of in-plane Poisson's ratios (parametric study 1 of cylinder with pronged cone end pieces and in-plane negative Poisson's ratio). Stills of ERD are also shown.

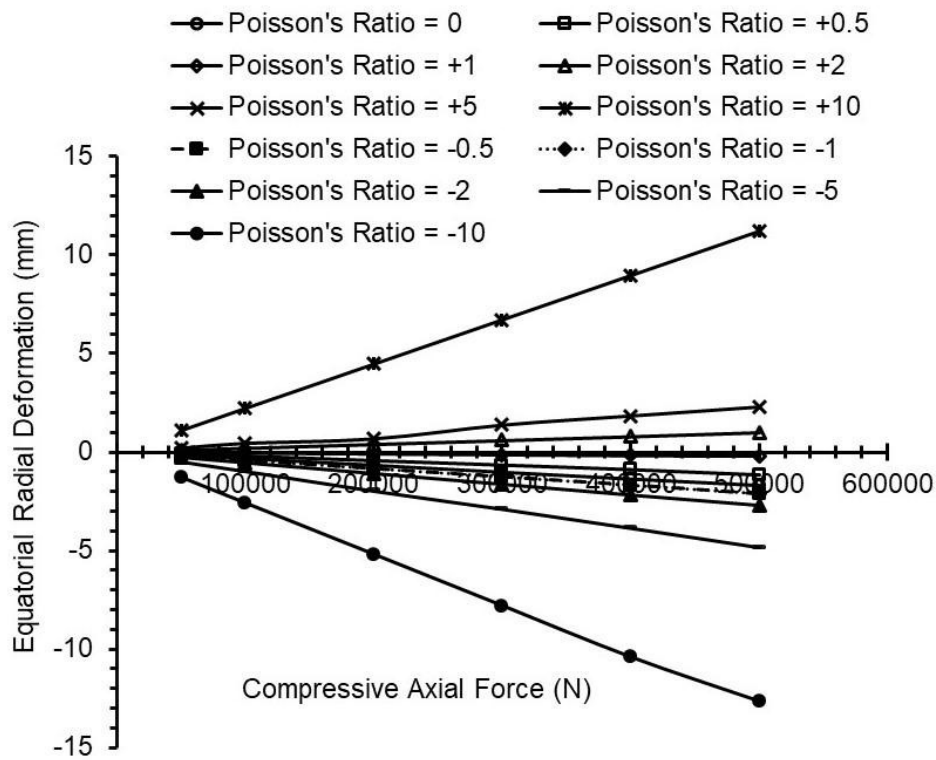


Figure 8.17: ERD vs compressive axial force for parametric study of in-plane Poisson's ratios (parametric study 1 of cylinder with pronged cone end pieces and in-plane negative Poisson's ratio).

8.2.1.1.2 Geometric parameters

The geometrical parameters were varied to study their impact on the deformation of the solid wall cylinder with pronged cone end pieces. The maximum axial compressive forces (applied incrementally to obtain the ERD and AD) are given in Table 8.1 for the different geometrical parameters.

Table 8.1: Maximum axial compressive force applied during parametric study of geometrical parameters (parametric study 1 of cylinder with pronged cone end pieces and negative in-plane Poisson's ratio).

Geometrical parameters		Axial Compressive force (N)
Outer diameter (D) (mm)	20	3×10^5
	30	5×10^5
	40	5×10^5
Length (L) (mm)	150	5×10^5
	200	5×10^5
	300	5×10^5
Wall thickness (T) (mm)	1	9×10^4
	2.5	5×10^5
	5	5×10^5
Young's modulus of end pieces (Pa)	= Structural steel	5×10^5
	> Structural steel (2×10^{13})	5×10^5
	< Structural steel (2×10^9)	1×10^5
Types of end pieces	Cone	5×10^5
	Pronged cone	5×10^5
	Funnel	5×10^5
	Pronged funnel	1×10^5

ERD vs AD were plotted for variation of the outer diameter (Figure 8.18), length (Figure 8.19), and wall thickness (Figure 8.20) of the cylinder as well as for the Young's modulus of the pronged cone end pieces (Figure 8.21) and different

types of end pieces (Figure 8.22). Stills showing ERD (left) and AD (right) are included in Figures 8.18-8.22.

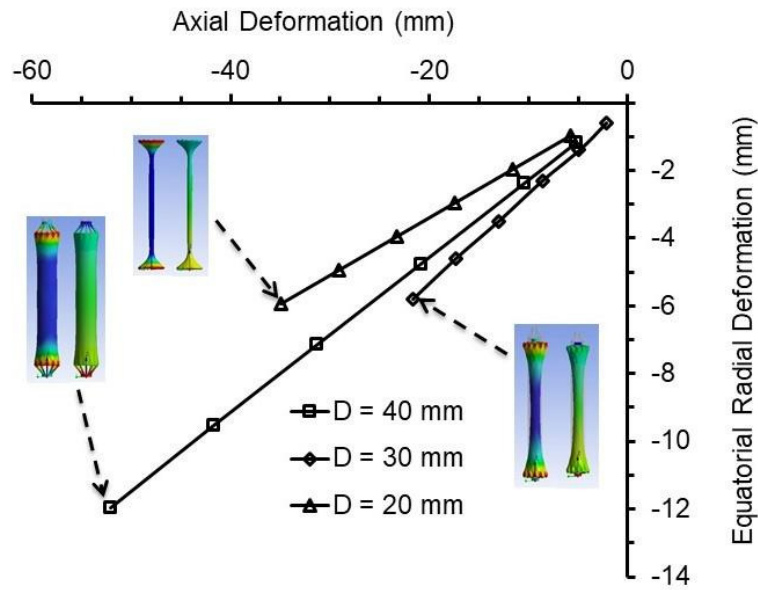


Figure 8.18: Parametric study of outer diameter of cylinder using 'standard' properties (parametric study 1 of cylinder with pronged cone end pieces and in-plane negative Poisson's ratio). Stills of ERD (left) and AD (right) are also shown.

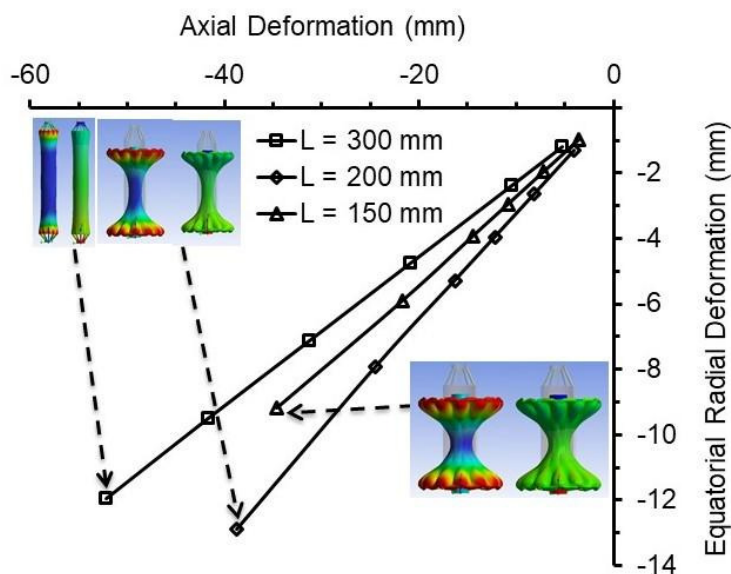


Figure 8.19: Parametric study of length of cylinder using 'standard' properties (parametric study 1 of cylinder with pronged cone end pieces and in-plane negative Poisson's ratio). Stills of ERD (left) and AD (right) are also shown.

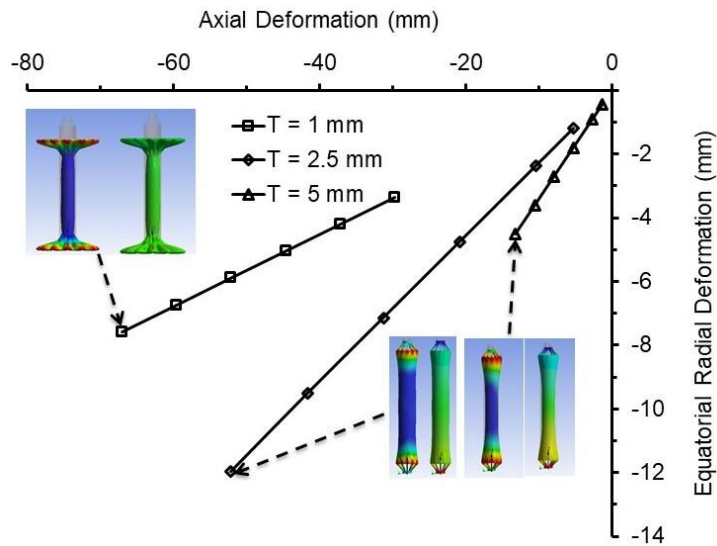


Figure 8.20: Parametric study of wall thickness of cylinder using 'standard' properties (parametric study 1 of cylinder with pronged cone end pieces and with in-plane negative Poisson's ratio). Stills of ERD (left) and AD (right) are also shown.

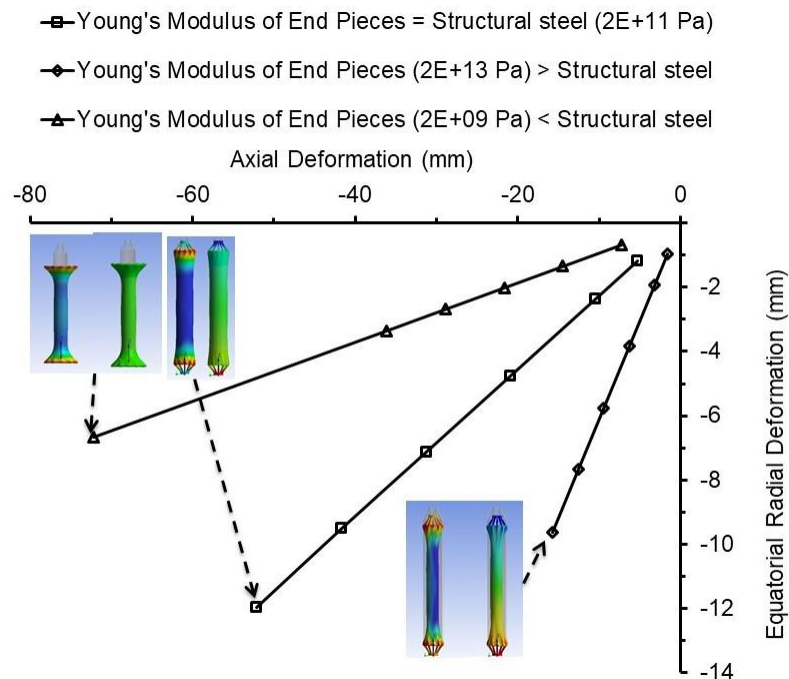


Figure 8.21: Parametric study of Young's modulus of pronged cone end pieces using 'standard' properties (parametric study 1 of cylinder with pronged cone end pieces and with in-plane negative Poisson's ratio). Stills of ERD (left) and AD (right) are also shown.

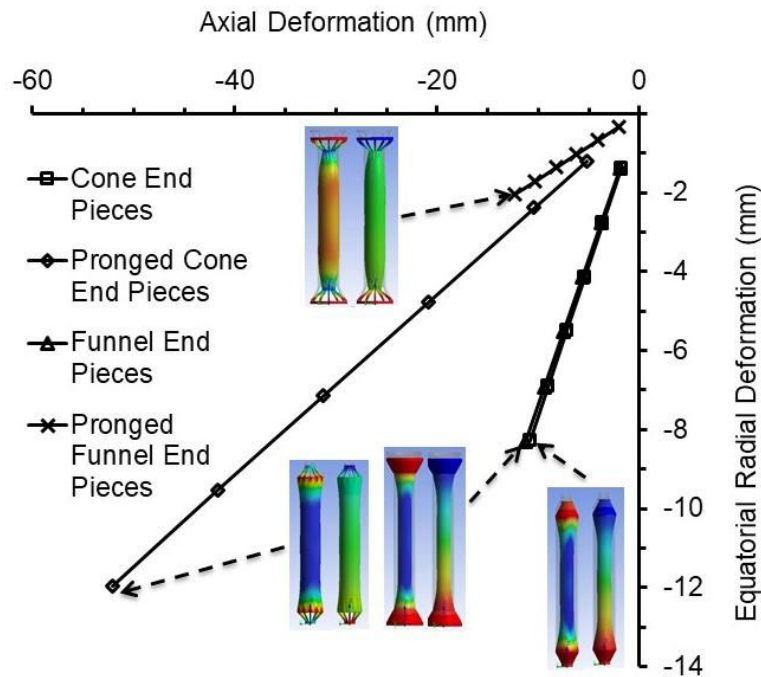


Figure 8.22: Parametric study of different types of end pieces using 'standard' properties (parametric study 1 of cylinder with pronged cone end pieces and with in-plane negative Poisson's ratio). Stills of ERD (left) and AD (right) are also shown.

The parametric study of geometrical parameters using 'standard' properties (Table 5.3, Chapter 5) suggests that they do not promote the out-of-plane bending of a solid wall of cylinder (a large equatorial radial deformation) in presence of the pronged cone end pieces at both ends of cylinder (Figure 8.18-8.22).

8.2.1.2 Simulation of shape change properties

Orthotropic material properties required for a large equatorial radial deformation of solid wall of a cylinder assembled with pronged cone end pieces for small axial strain (Figure 8.5) are considered as 'shape change' properties and are depicted in Table 8.2. In-plane Poisson's ratio (negative, zero and positive values) is the only orthotropic constant evaluated using 'shape change' properties since it may be essential criteria along with the E_θ (Table 8.2) for a large equatorial deformation of solid wall of a cylinder.

Table 8.2: 'Shape change' properties for parametric study 1 of solid wall cylinder with pronged cone end pieces.

Orthotropic Material Properties	Geometrical Parameters
$E_r = 2 \times 10^{11} \text{ Pa}$	Outer Diameter (D) = 40mm
$E_\theta = 2 \times 10^4 \text{ Pa}$	Length (L) = 300mm
$E_z = 4 \times 10^{10} \text{ Pa}$	Wall thickness (T) = 2.5mm
$\nu_{\theta r} = 3 \times 10^{-8}$	Young's modulus of end pieces = $2 \times 10^{11} \text{ Pa}$
$\nu_{\theta z} = -0.0005$	End Pieces = Pronged cone at both ends
$\nu_{zr} = 0.06$	
$G_{r\theta} = 3.3 \times 10^8 \text{ Pa}$	
$G_{\theta z} = 1.0 \times 10^7 \text{ Pa}$	
$G_{rz} = 7.4 \times 10^{10} \text{ Pa}$	

8.2.1.2.1 Orthotropic material properties

Parametric studies of in-plane Poisson's ratios were carried out using 'shape change' properties (Table 8.2). $\nu_{\theta r}$ was recalculated to maintain symmetric matrix compliance when $\nu_{\theta z}$ were varied (from -10 to -0.5, 0 and +0.5 to +10). The remaining orthotropic constants were not changed. Results are described in Figure 8.23 (ERD vs AD) and Figure 8.24 (ERD vs compressive axial force). Stills showing ERD are also shown in Figure 8.23. A large equatorial deformation (~80mm) for the small axial deformation (~20mm) was obtained approximately for the same value of axial compressive force for each value of the in-plane Poisson's ratio (-10 to -0.5, 0 and +0.5 to +10) considered during parametric study (Figure 8.23 and Figure 8.24).

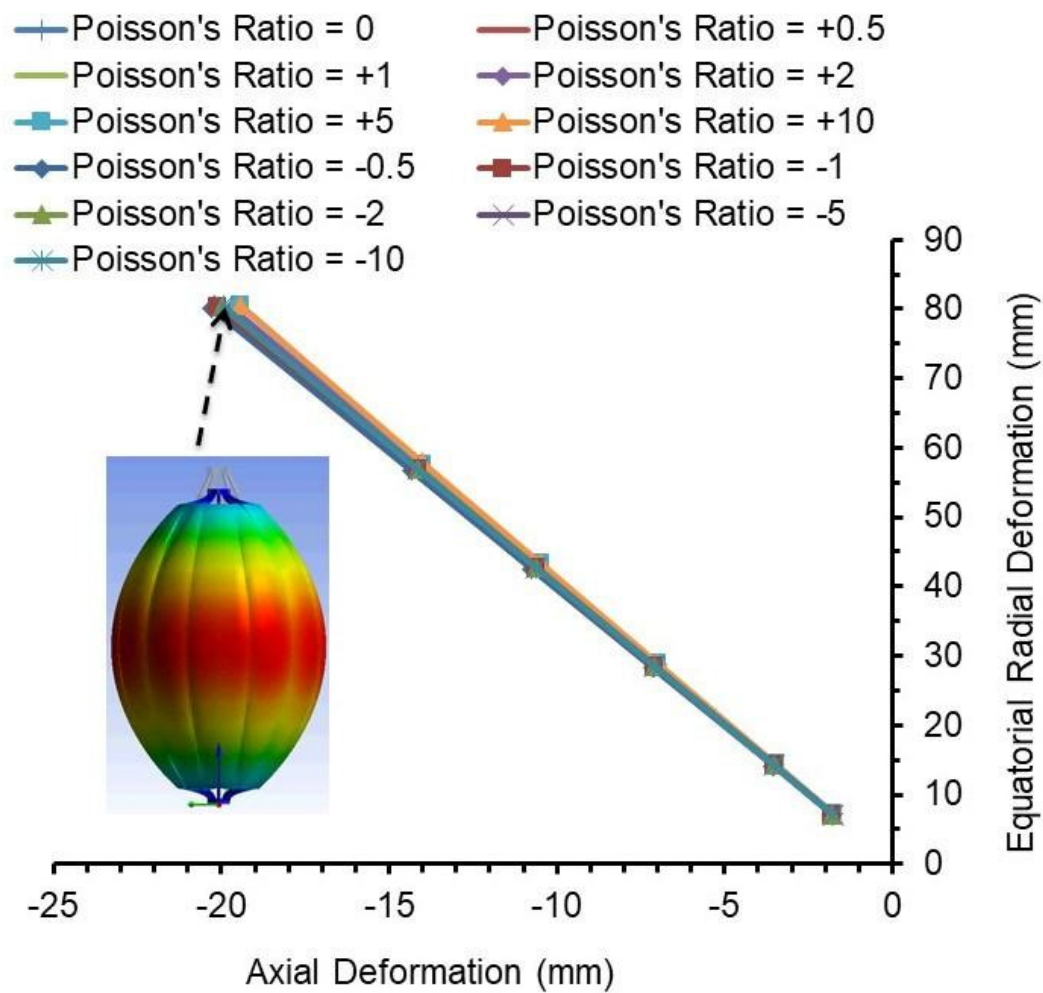


Figure 8.23: ERD vs AD for parametric study of in-plane Poisson's ratios using 'shape change' properties (parametric study 1 of cylinder with pronged cone end pieces and in-plane negative Poisson's ratio). Still of ERD are also shown.

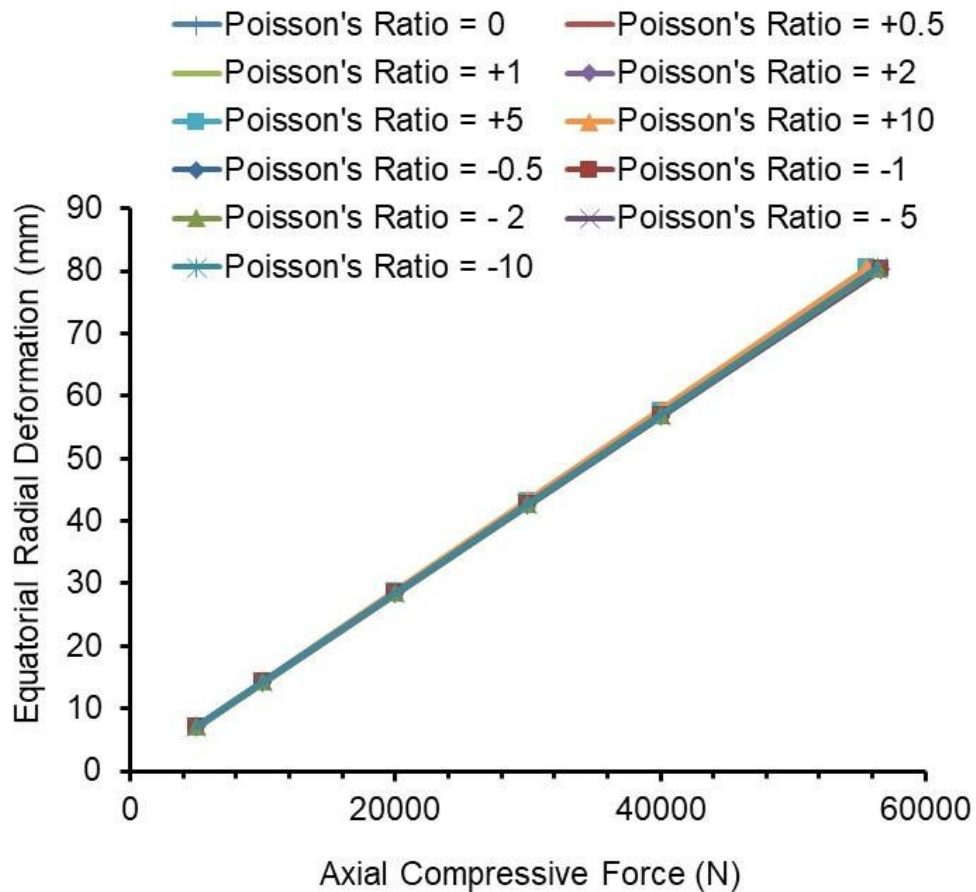


Figure 8.24: ERD vs axial compressive force for parametric study of in-plane Poisson's ratios using 'shape change' properties (parametric study 1 of cylinder with pronged cone end pieces and in-plane negative Poisson's ratio).

8.2.1.2.2 Geometric parameters

The geometrical parameters except the type of end pieces (Table 8.2) were varied to study their impact on the deformation of a solid wall of cylinder with 'shape change' properties.

Outer diameter:

ERD vs AD (Figure 8.25), ERD vs axial compressive force (Figure 8.26), ERD vs axial strain (Figure 8.27) were plotted for the different outer diameters of cylinder. Stills of ERD for the different outer diameters are shown in Figure 8.25. The different outer diameters of cylinder do not significantly affect the large equatorial radial deformation of the solid wall cylinder at low strain (Figure 8.25 and Figure 8.27). However, the 20mm outer diameter cylinder (would be of the

expansion mechanism required for the laparoscopic device), for example, requires 20% more axial compressive force than the 40mm outer diameter cylinder (Figure 8.26).

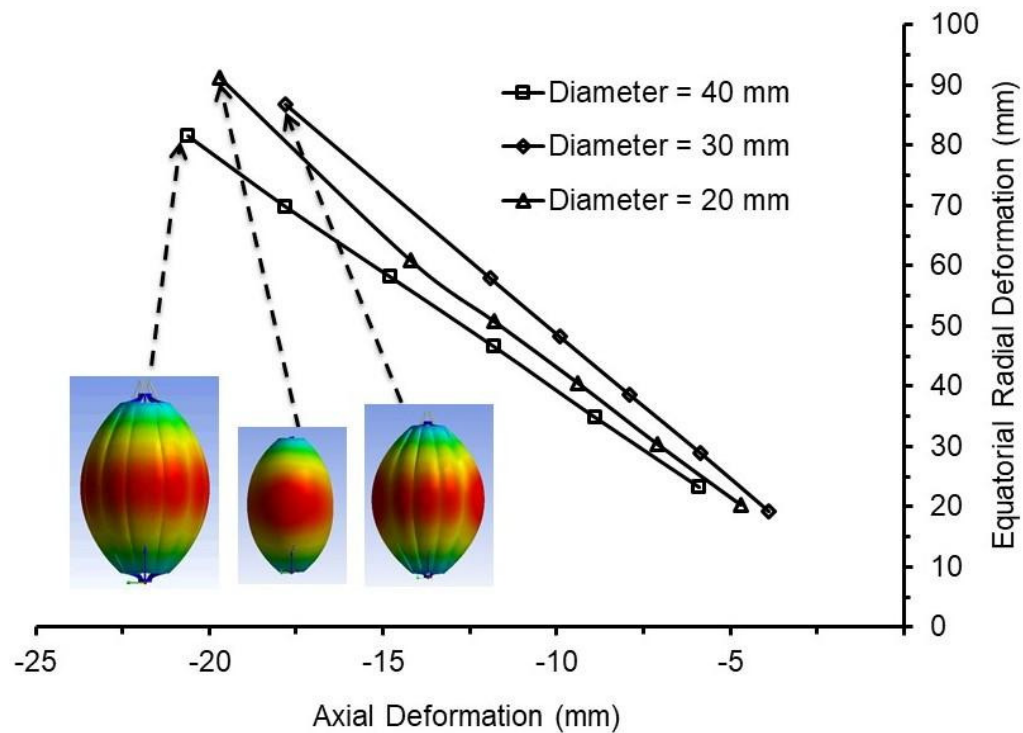


Figure 8.25: Parametric study of outer diameter of cylinder using 'shape change' properties (ERD vs AD) (parametric study 1 of cylinder with pronged cone end pieces and in-plane negative Poisson's ratio). Stills of ERD are also shown.

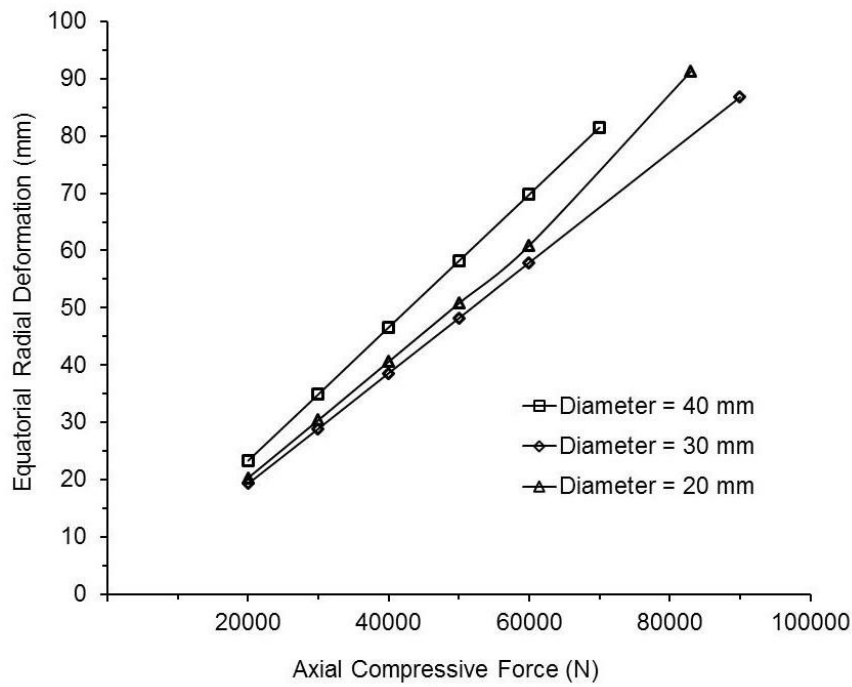


Figure 8.26: Parametric study of outer diameter of cylinder using 'shape change' properties (ERD vs axial compressive force) (parametric study 1 of cylinder with pronged cone end pieces and in-plane negative Poisson's ratio).

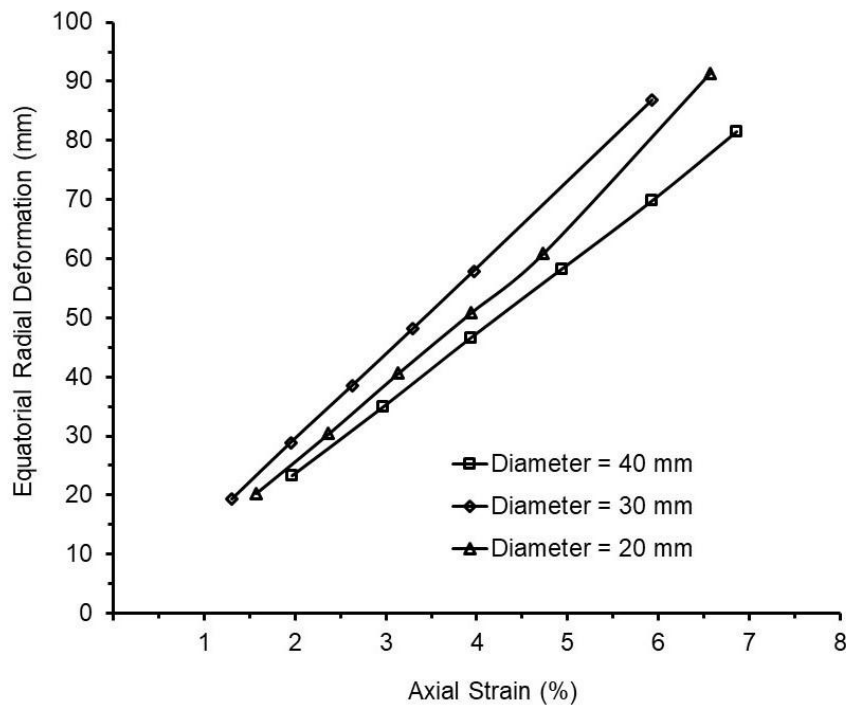


Figure 8.27: Parametric study of outer diameter of cylinder using 'shape change' properties (ERD vs axial strain) (parametric study 1 of cylinder with pronged cone end pieces and in-plane negative Poisson's ratio).

Length of cylinder:

ERD vs AD (Figure 8.28), ERD vs axial compressive force (Figure 8.29) and ERD vs axial strain (Figure 8.30) are plotted for the different lengths of cylinder. Stills of ERD are shown in Figure 8.28 for the different lengths of solid wall cylinder. The higher equatorial radial deformation was obtained for the lowest compressive axial deformation ($\sim 20\text{mm}$) and axial compressive force ($\sim 70000\text{N}$) for longer cylinders (i.e. 300mm vs 200mm and 150mm length of cylinder) (Figures 8.28 and 8.29).

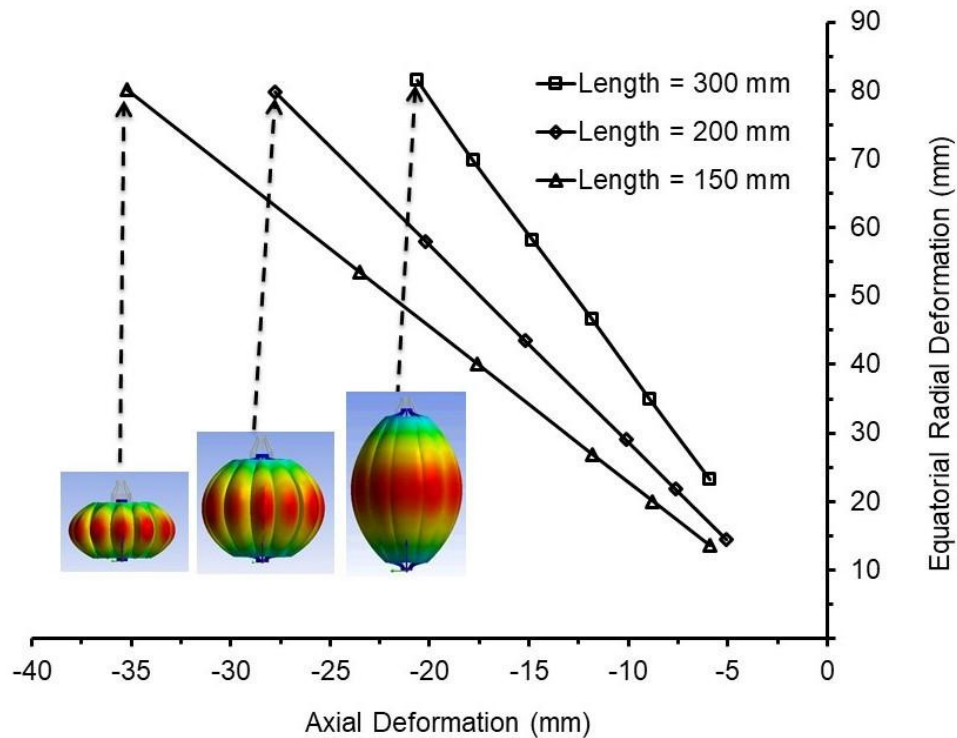


Figure 8.28: Parametric study of length of cylinder using 'shape change' properties (ERD vs AD) (parametric study 1 of cylinder with pronged cone end pieces and in-plane negative Poisson's ratio). Stills of ERD are also shown.

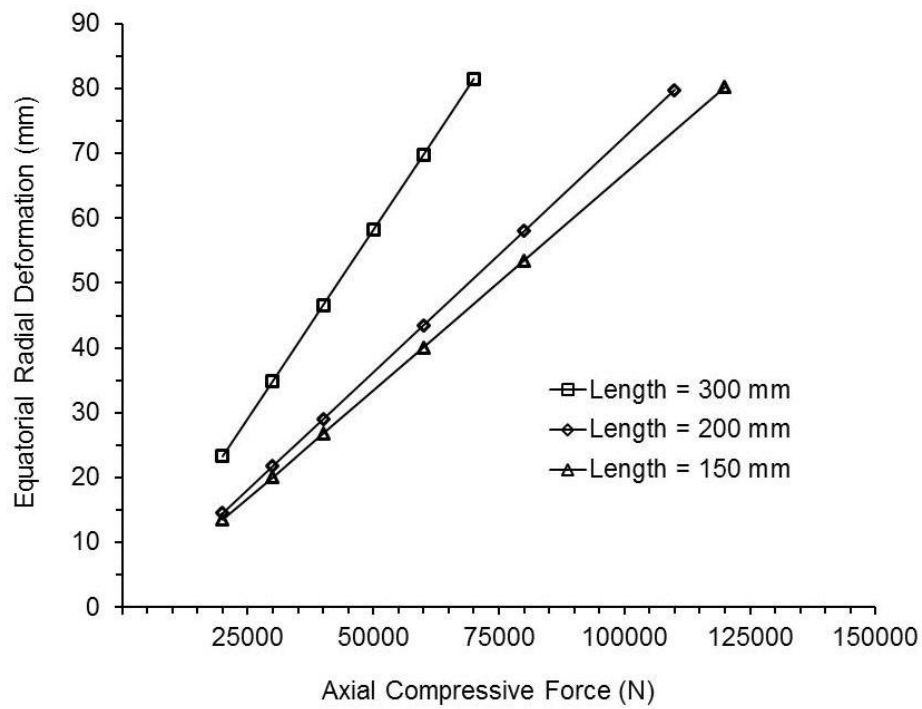


Figure 8.29: Parametric study of length of cylinder using 'shape change' properties (ERD vs axial compressive force) (parametric study 1 of cylinder with pronged cone end pieces and in-plane negative Poisson's ratio).

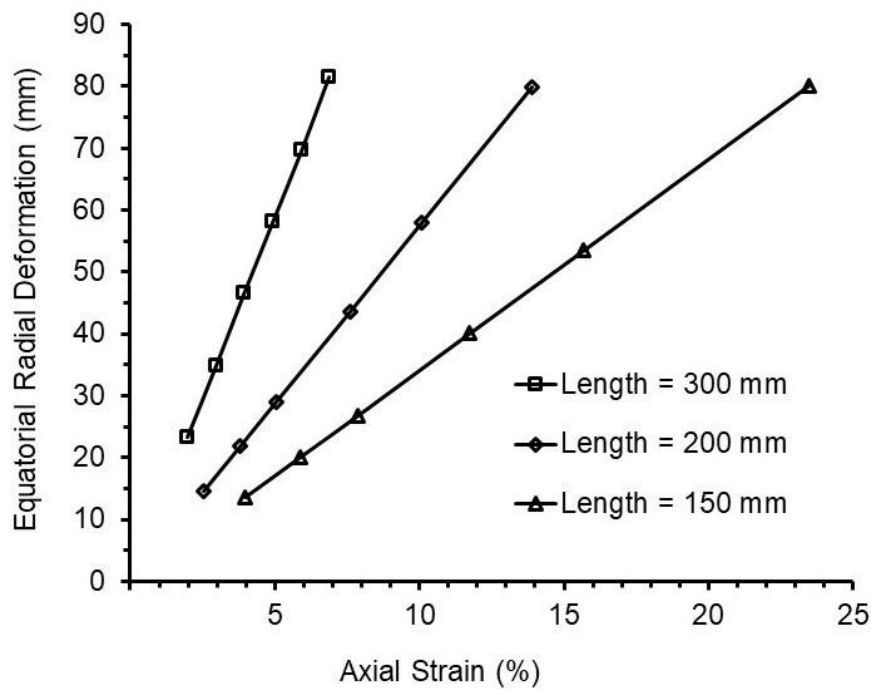


Figure 8.30: Parametric study of length of cylinder using 'shape change' properties (ERD vs axial strain) (parametric study 1 of cylinder with pronged cone end pieces and in-plane negative Poisson's ratio).

Wall thickness of cylinder:

ERD vs compressive axial deformation (Figure 8.31), ERD vs axial compressive force (Figure 8.32) and ERD vs axial strain (Figure 8.33) are plotted for the different wall thicknesses of cylinder. Changes in wall thickness of the solid wall cylinder do not affect the degree of equatorial radial deformation of solid wall cylinder and axial strain as shown in Figure 8.31 and Figure 8.33, respectively. However, axial compressive force, for example, was ten times for 5mm wall thickness compared to 2.5mm wall thickness for the solid wall cylinder (Figure 8.32).

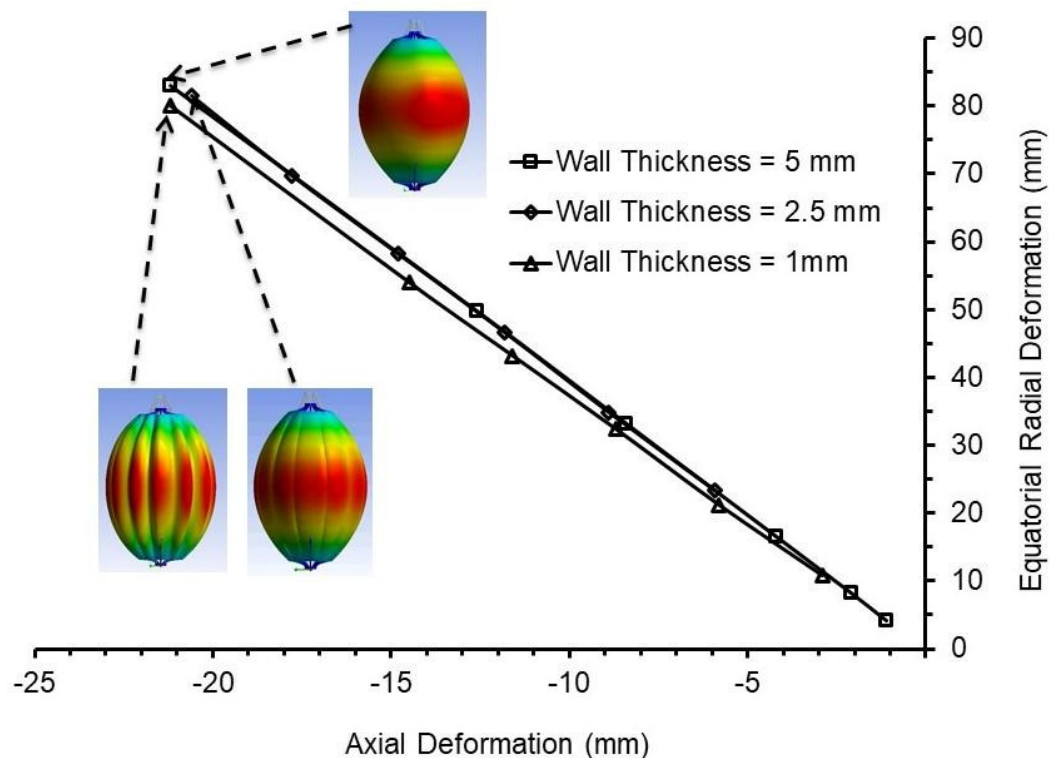


Figure 8.31: Parametric study of wall thickness of cylinder using 'shape change' properties (ERD vs AD) (parametric study 1 of cylinder with pronged cone end pieces and in-plane negative Poisson's ratio). Stills of ERD are also shown.

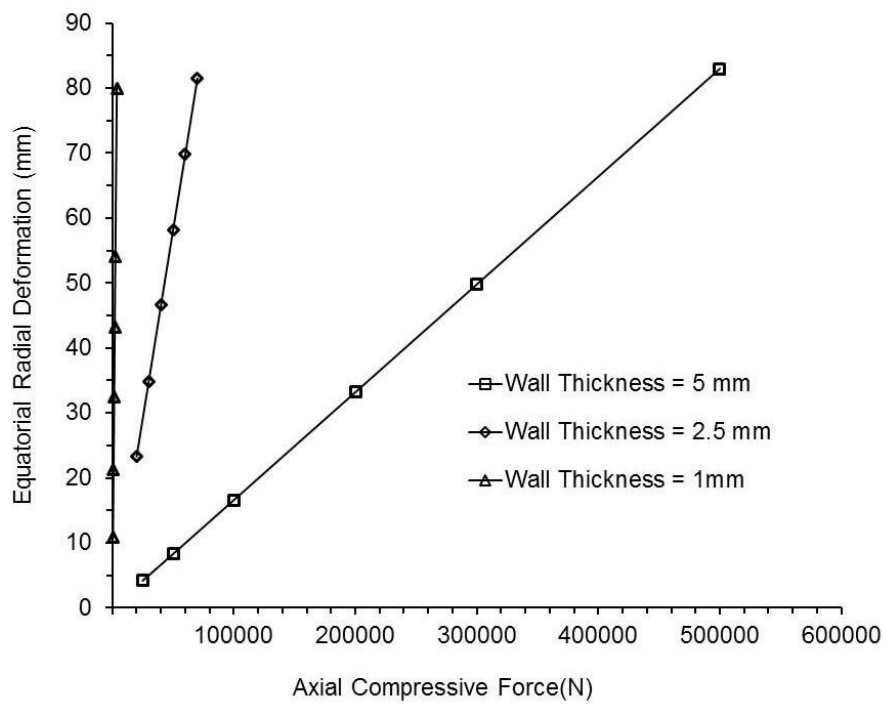


Figure 8.32: Parametric study of wall thickness of cylinder using 'shape change' properties (ERD vs axial compressive force) (parametric study 1 of cylinder with pronged cone end pieces and in-plane negative Poisson's ratio).

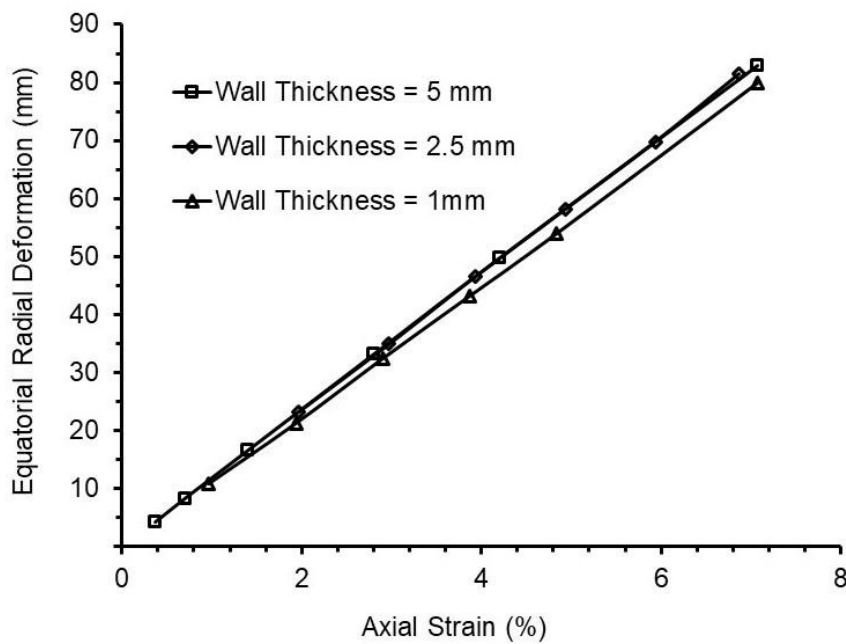


Figure 8.33: Parametric study of wall thickness of cylinder using 'shape change' properties (ERD vs axial strain) (parametric study 1 of cylinder with pronged cone end pieces and in-plane negative Poisson's ratio).

Young's modulus of pronged cone end pieces:

ERD vs compressive axial deformation (Figure 8.34), ERD vs axial compressive force (Figure 8.35) and ERD vs axial strain (Figure 8.36) are plotted for the different Young's modulus of end piece material assembled on the solid wall cylinder. They had significant impact on the deformation of the solid wall cylinder when simulated using 'shape change' properties (Figure 8.34), for example, pronged cone end pieces at both the ends of solid wall cylinder were distorted disproportionately in case of Young's modulus of pronged cone end pieces two order of magnitude less than the structural steel.

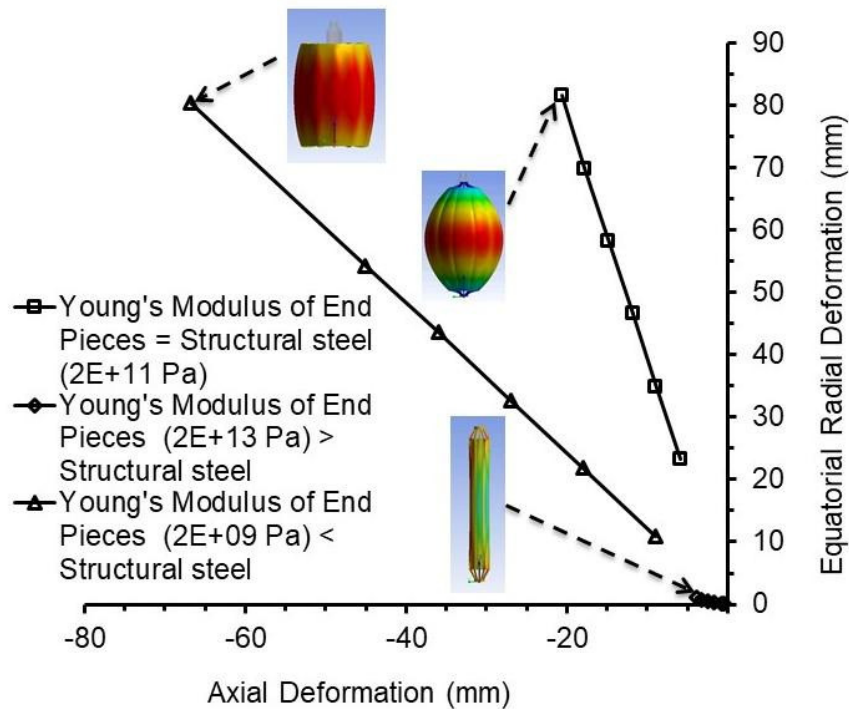


Figure 8.34: Parametric study of Young's modulus of pronged cone end pieces using 'shape change' properties (ERD vs AD) (parametric study 1 of cylinder with pronged cone end pieces and in-plane negative Poisson's ratio). Stills of ERD are also shown.

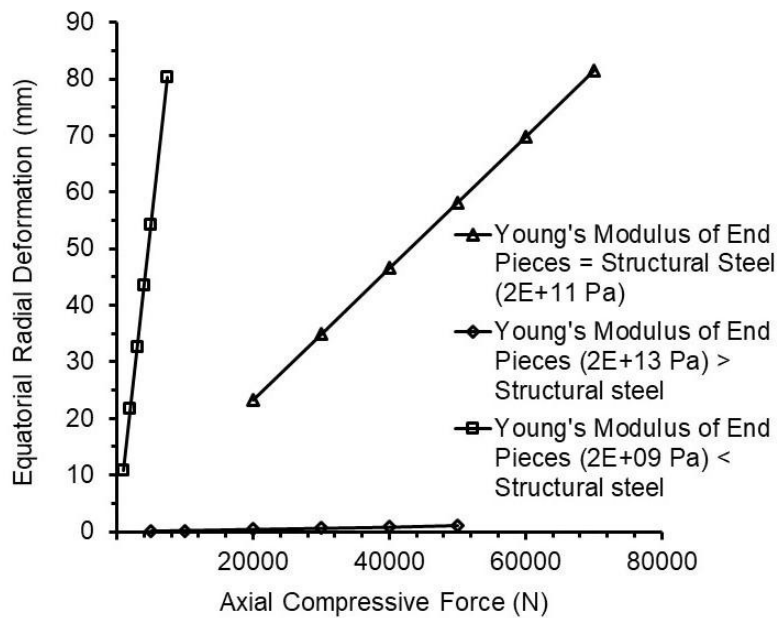


Figure 8.35: Parametric study of Young's modulus of pronged cone end pieces using 'shape change' properties (ERD vs axial compressive force) (parametric study 1 of cylinder with pronged cone end pieces and in-plane negative Poisson's ratio).

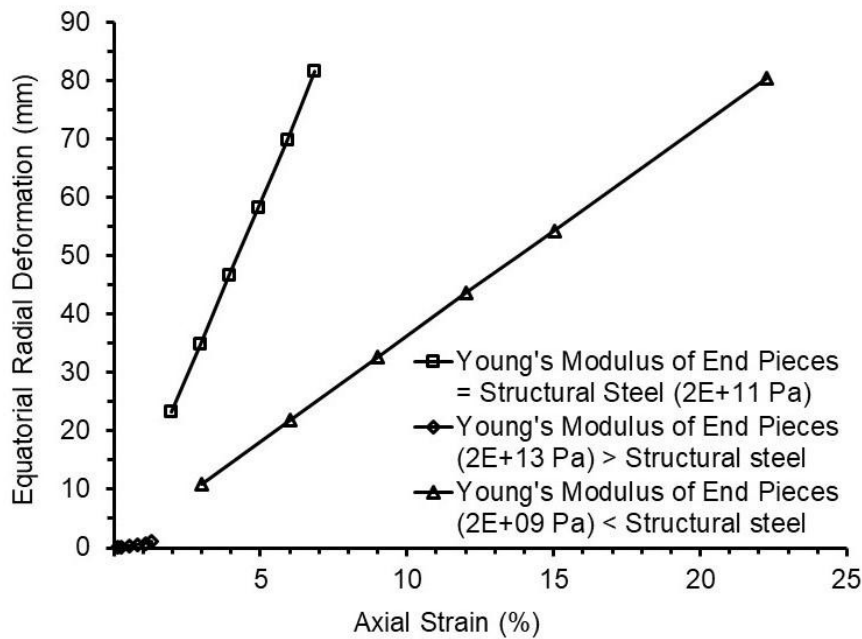


Figure 8.36: Parametric study of Young's modulus of pronged cone end pieces using 'shape change' properties (ERD vs axial strain) (parametric study 1 of cylinder with pronged cone end pieces and in-plane negative Poisson's ratio).

8.2.1.3 Summary

The outcomes of parametric study 1 suggested that E_θ is a critical orthotropic material property (or E_z/E_θ) to obtain a large equatorial deformation of solid wall cylinder with pronged cone end pieces at the low axial deformation. Geometrical parameters (except the Young's modulus of pronged cone end pieces) do not significantly affect the degree of equatorial deformation. These outcomes were considered during the parametric study 2.

8.2.2 Parametric study 2 of solid wall cylinder with end pieces

In-plane negative Poisson's ratios were simulated for uniaxial compression of a solid wall cylinder consisting of pronged cone end pieces at both ends. The parametric study was carried out using finite BCs in accordance with the protocol defined for 'parametric study 2' (Table 5.4, Chapter 5).

8.2.2.1 Simulation of standard properties

The set of orthotropic material properties specified in Table 5.4 (Chapter 5), geometrical parameters defined in Chapter 5.3.1, and pronged cone end pieces at both ends were considered as the 'standard' configuration.

Orthotropic material properties:

When E_θ varied from 1.98×10^8 Pa to 1.98×10^3 Pa; $\nu_{\theta z}$ and $\nu_{z\theta}$ (in-plane), and $\nu_{\theta r}$ (out-of-plane) were recalculated to maintain the symmetric compliance matrix and reciprocal Poisson's ratio relationships (Table 8.3). ν_{rz} and E_z were constant values of 0.03033 and 2.02×10^{10} Pa, respectively during parametric study of E_θ (not shown in Table 8.3). Shear moduli were also derived with respect to the change in the in-plane negative Poisson's ratios (Table 8.3).

Table 8.3: Calculation of orthotropic constants corresponding to the change in E_θ during parametric study 2 of cylinder with pronged cone end pieces (in-plane negative Poisson's ratio).

E_θ (Pa)	$\nu_{\theta z}$	$\nu_{z\theta}$	$\nu_{\theta r}$	$G_{r\theta}$ (Pa)	$G_{\theta z}$ (Pa)	G_{rz} (Pa)
1.98×10^8	-0.098	-10.1	2.9×10^{-4}	3.3×10^9	9.9×10^7	7.4×10^9
1.98×10^7	-0.031	-31.9	2.9×10^{-5}	1.6×10^9	9.9×10^7	1.1×10^{10}
1.98×10^6	-0.0098	-101.1	2.9×10^{-6}	7.6×10^8	9.9×10^7	1.6×10^{10}
1.98×10^5	-0.0031	-320.9	2.9×10^{-7}	3.5×10^8	9.9×10^7	2.7×10^{10}
1.98×10^4	-0.00098	-1013.5	2.9×10^{-8}	1.6×10^8	1×10^7	3.3×10^{10}
1.98×10^3	-0.00031	-3180.6	2.9×10^{-9}	7.7×10^7	1×10^8	4.9×10^{10}

The maximum axial compressive force applied was 7×10^4 N (force applied incrementally to obtain the ERD and AD). ERD vs AD and ERD vs axial strain are plotted (Figure 8.37 and Figure 8.38). Selected stills showing ERD (left) and AD (right) are included in Figure 8.37.

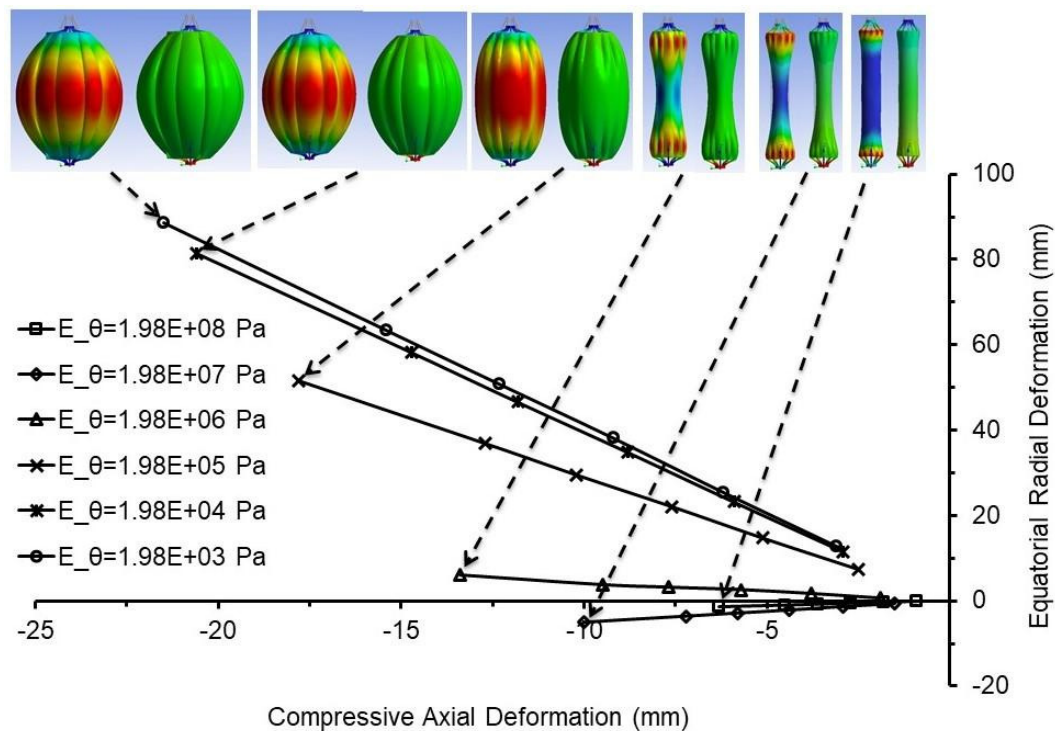


Figure 8.37: ERD vs compressive axial deformation for parametric study of E_θ (parametric study 2 of cylinder with pronged cone end pieces and in-plane negative Poisson's ratio). Stills of ERD (left) and AD (right) are also shown.

An equatorial narrowing occurs for $E_\theta=1.98 \times 10^8$ Pa and $E_\theta=1.98 \times 10^7$ Pa, a transition occurs around $E_\theta=1.98 \times 10^6$ Pa (where the equator is wider than the undeformed values, but still narrower than at the ends), and when $E_\theta=1.98 \times 10^5$ - 1.98×10^3 Pa the cylinder adopts the shape of a prolate spheroid (Figure 8.37). A large equatorial radial deformation of the solid wall cylinder (~ 80 mm) for small axial strain ($\sim 7\%$) was obtained when E_θ was 1.98×10^4 Pa and 1.98×10^3 Pa (Figure 8.38).

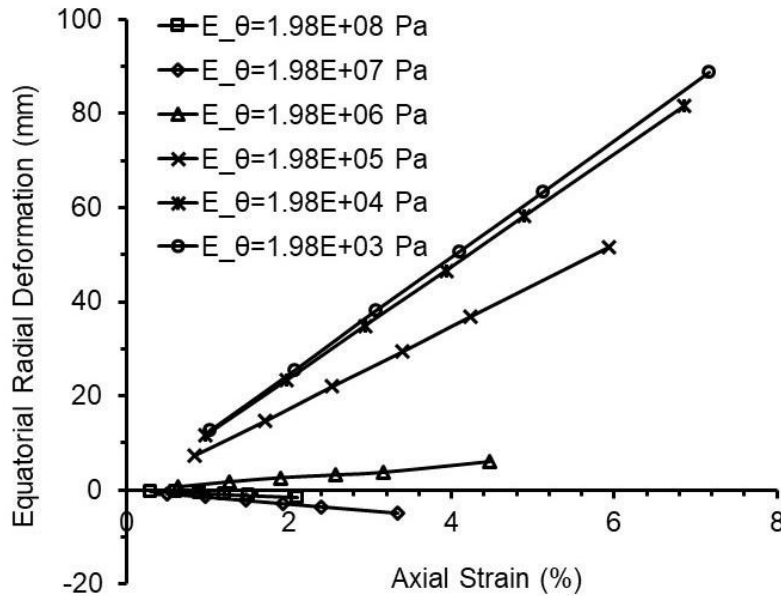


Figure 8.38: ERD vs axial strain for parametric study of E_θ (parametric study 2 of cylinder with pronged cone end pieces and in-plane negative Poisson's ratio).

Geometrical parameters:

The results of parametric study of geometrical parameters carried out using 'standard' configuration (Table 5.4, Chapter 5) were nearly identical to the results outlined for the parametric study of geometrical parameters performed using the 'standard' set of material properties outlined in Table 5.3, Chapter 5 and hence, they are not described here.

8.2.2.2 Simulation of shape change properties

Orthotropic material properties required for a large equatorial radial deformation of solid wall cylinder assembled with pronged cone end pieces are considered as 'shape change' properties (Table 8.4).

Table 8.4: 'Shape change' properties to carry out parametric study of cylinder with pronged cone end pieces.

Orthotropic Material Properties	Geometrical Parameters
$E_r = 2 \times 10^{11} \text{ Pa}$	Outer Diameter (D) = 40mm
$E_\theta = 1.98 \times 10^5 \text{ Pa}$	Length (L) = 300mm
$E_z = 2.02 \times 10^{10} \text{ Pa}$	Wall thickness (T) = 2.5mm
$\nu_{\theta r} = 2.9 \times 10^{-7}$	Young's modulus of end pieces = $2 \times 10^{11} \text{ Pa}$
$\nu_{\theta z} = -0.0031$	End Pieces = Pronged cone at both ends
$\nu_{zr} = 0.03033$	
$G_{r\theta} = 3.5 \times 10^8 \text{ Pa}$	
$G_{\theta z} = 1.0 \times 10^7 \text{ Pa}$	
$G_{rz} = 2.7 \times 10^{10} \text{ Pa}$	

The magnitude of in-plane negative Poisson's ratio required for large equatorial radial deformation of solid wall cylinder was found during parametric study of set of 'standard' properties (Table 8.3 and Figure 8.37). Additionally, in-plane negative Poisson's ratios ($\nu_{\theta z}$ and $\nu_{z\theta}$) are related with E_θ and E_z due to symmetric matrix compliance. Hence, in-plane negative Poisson's ratio was not varied for 'shape change' properties to maintain the set of nine orthotropic constants outlined in Table 5.4, Chapter 5. The results of parametric study of geometrical parameters carried out using 'shape change' configuration (Table 8.4) were nearly identical to the results outlined for the parametric study of geometrical parameters performed using the 'shape change' material properties outlined in Table 8.2 and hence, they are not described here.

8.2.3 Parametric study 2 of solid wall cylinder without end pieces

In-plane positive and negative Poisson's ratios were simulated for uniaxial compression and tension mechanism, respectively during parametric study 2 of solid wall cylinder without end pieces. It was carried out using finite BCs in accordance with the protocol defined for 'parametric study 2' (Table 5.4, Chapter 5).

8.2.3.1 Uniaxial compression mechanism

In-plane positive Poisson's ratios were simulated for uniaxial compression mechanism and results are described in this section.

8.2.3.1.1 Simulation of standard properties

A set of orthotropic material properties specified in Table 5.4 (Chapter 5) and geometrical parameters defined in Chapter 5.3.1 were considered as the 'standard' configuration.

Orthotropic material properties:

When E_θ varied from 1.98×10^8 Pa to 1.98×10^3 Pa; $\nu_{\theta z}$ and $\nu_{z\theta}$ (in-plane), and $\nu_{\theta r}$ (out-of-plane) were recalculated to maintain the symmetric compliance matrix and reciprocal Poisson's ratio relationships (Table 8.5). ν_{rz} and E_z were constant values of 0.03033 and 2.02×10^{10} Pa, respectively during parametric study of E_θ (not shown in Table 8.5). Shear moduli were also derived with respect to the change in the in-plane positive Poisson's ratios (Table 8.5).

Table 8.5: Calculation of orthotropic constants corresponding to the parametric study of E_θ (parametric study 2 of cylinder without end pieces and with in-plane positive Poisson's ratio).

E_θ (Pa)	$\nu_{\theta z}$	$\nu_{z\theta}$	$\nu_{\theta r}$	$G_{r\theta}$ (Pa)	$G_{\theta z}$ (Pa)	G_{rz} (Pa)
1.98×10^8	0.098	10.1	2.9×10^{-4}	2.5×10^8	2.2×10^9	1.5×10^{10}
1.98×10^7	0.031	31.9	2.9×10^{-5}	1.1×10^9	2.8×10^8	2.2×10^{10}
1.98×10^6	0.0098	101.1	2.9×10^{-6}	5.2×10^8	2.9×10^8	3.2×10^{10}
1.98×10^5	0.0031	319.5	2.9×10^{-7}	2.5×10^8	2.9×10^8	4.7×10^{10}
1.98×10^4	0.00098	1012.0	2.9×10^{-8}	1.1×10^8	2.9×10^8	6.9×10^{10}
1.98×10^3	0.00031	3192.8	2.9×10^{-9}	5.3×10^7	3.0×10^8	1.0×10^{11}

ERD vs AD with stills from the simulation movies, ERD vs axial compressive force and ERD vs compressive axial strain are plotted (Figures 8.39-8.41). The magnitude of axial compressive force required for a large equatorial radial deformation was increased when E_θ reduced from 1.98×10^8 Pa to 1.98×10^3 Pa (Figure 8.40). A large radial deformation in the equatorial region of solid wall of cylinder (~ 80 mm) for the small compressive axial deformation (≤ 25 mm) and

strain ($<10\%$) was found when E_θ was $\leq 1.98 \times 10^7$ Pa in Figure 8.40 and Figure 8.41, respectively.

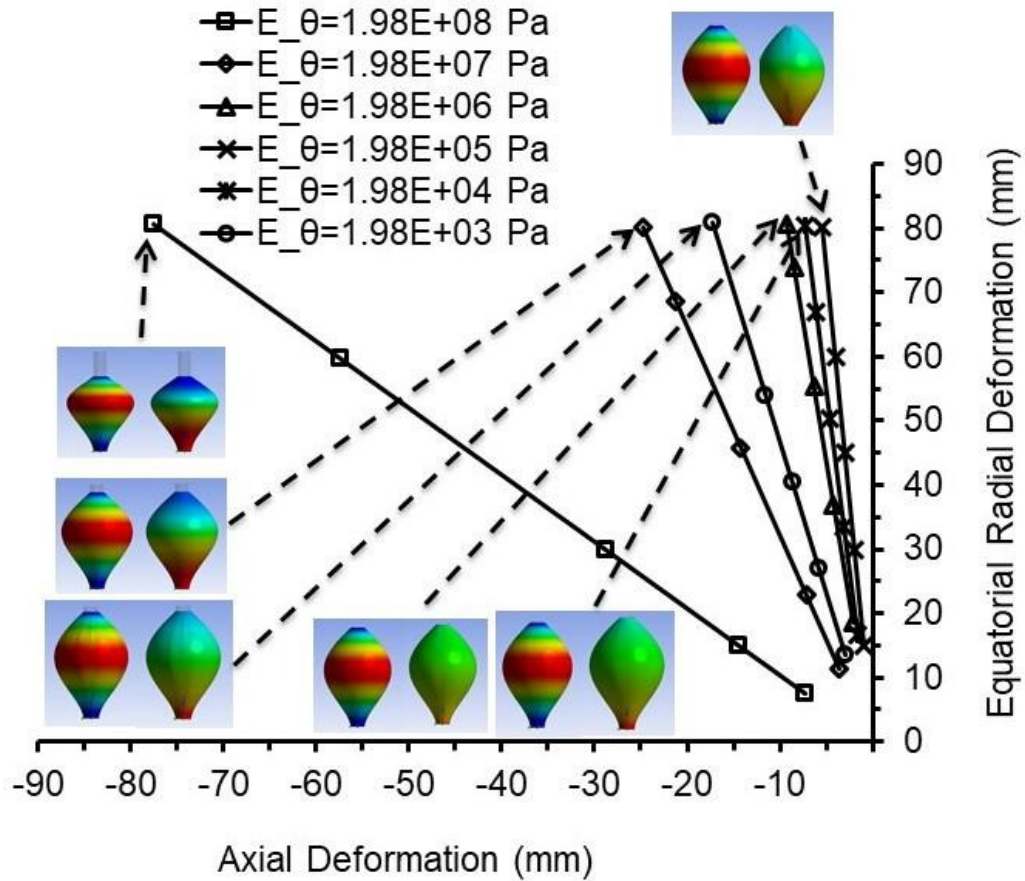


Figure 8.39: ERD vs AD for parametric study of E_θ (parametric study 2 of cylinder without end pieces and with in-plane positive Poisson's ratio). Stills of ERD (left) and AD (right) are also shown.

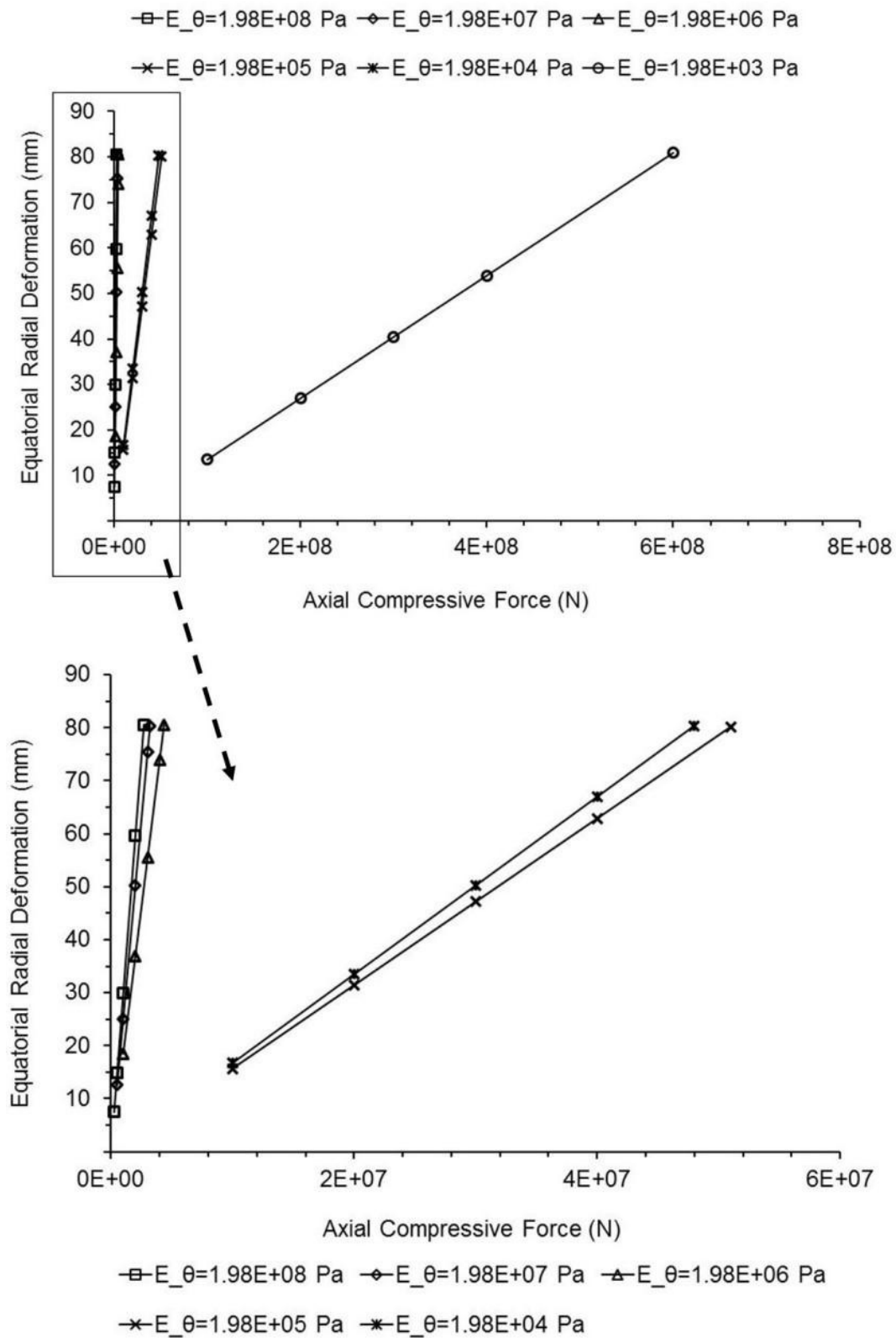


Figure 8.40: ERD vs axial compressive force for parametric study of E_θ (parametric study 2 of cylinder without end pieces and with in-plane positive Poisson's ratio).

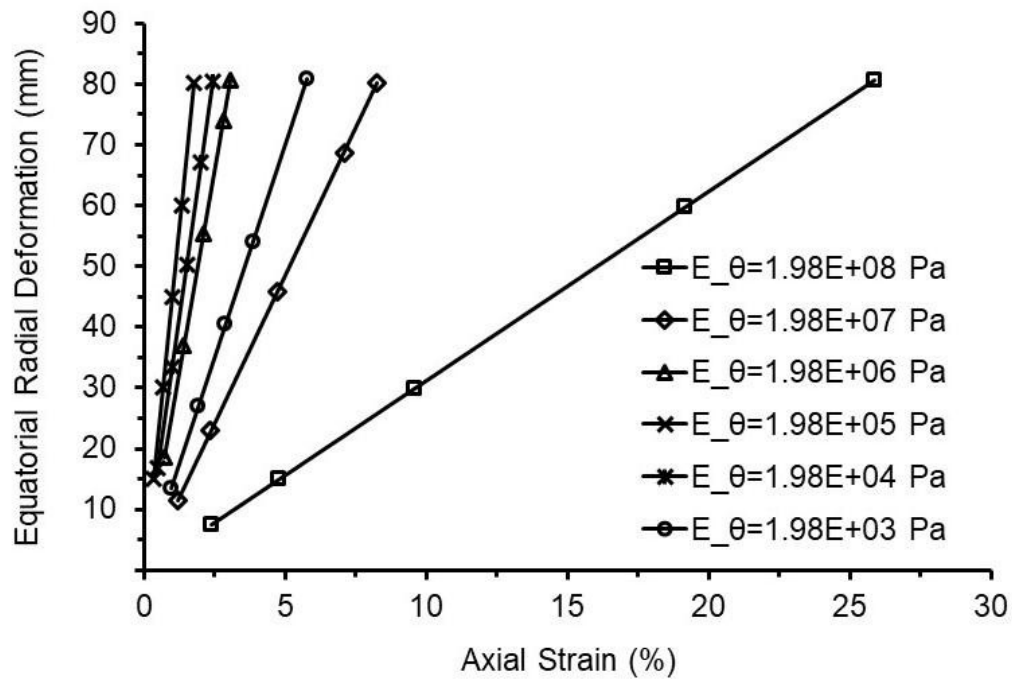


Figure 8.41: ERD vs axial strain for parametric study of E_θ (parametric study 2 of cylinder without end pieces and with in-plane positive Poisson's ratio).

Geometric parameters:

Geometrical parameters of 'standard' set of properties did not have significant impact on the equatorial deformation of solid wall cylinder with pronged cone end pieces and hence, they were not simulated using 'standard' properties for solid wall cylinder without end pieces (in-plane positive Poisson's ratio).

8.2.3.1.2 Simulation of shape change properties

Orthotropic material properties required to achieve a large equatorial radial deformation of solid wall cylinder (no end pieces) for uniaxial compression mechanism are considered as 'shape change' properties (Table 8.6).

Table 8.6: 'Shape change' properties for parametric study 2 of solid wall cylinder without end pieces and with in-plane positive Poisson's ratio.

Orthotropic Material Properties	Geometrical Parameters
$E_r = 2 \times 10^{11} \text{ Pa}$	Outer Diameter (D) = 40mm
$E_\theta = 1.98 \times 10^6 \text{ Pa}$	Length (L) = 300mm
$E_z = 2.02 \times 10^{10} \text{ Pa}$	Wall thickness (T) = 2.5mm
$\nu_{\theta r} = 2.9 \times 10^{-6}$	
$\nu_{\theta z} = 0.0098$	
$\nu_{zr} = 0.03033$	
$G_{r\theta} = 5.2 \times 10^8 \text{ Pa}$	
$G_{\theta z} = 2.9 \times 10^8 \text{ Pa}$	
$G_{rz} = 3.2 \times 10^{10} \text{ Pa}$	

The magnitude of in-plane positive Poisson's ratio requires for large equatorial radial deformation of solid wall cylinder (Table 8.5 and Figure 8.39) was found during parametric study of set of 'standard' properties. Hence, in-plane positive Poisson's ratio was not varied for 'shape change' properties. A large equatorial radial deformation ($\sim 80\text{mm}$) for small axial strains ($\leq 10\%$) were obtained when $E_\theta \leq 1.98 \times 10^7 \text{ Pa}$ (Figure 8.39). Hence, the geometrical parameters were evaluated for $E_\theta = 1.98 \times 10^6 \text{ Pa}$ as way of example and results are outlined below.

Outer diameter, length and wall thickness of solid wall cylinder:

ERD vs AD (Figures 8.42, 8.45, and 8.48), ERD vs axial compressive force (Figures 8.43, 8.46, and 8.49) and ERD vs axial strain (Figure 8.44, 8.47, and 8.50) were plotted for the different outer diameters, lengths and wall thicknesses of solid wall cylinder.

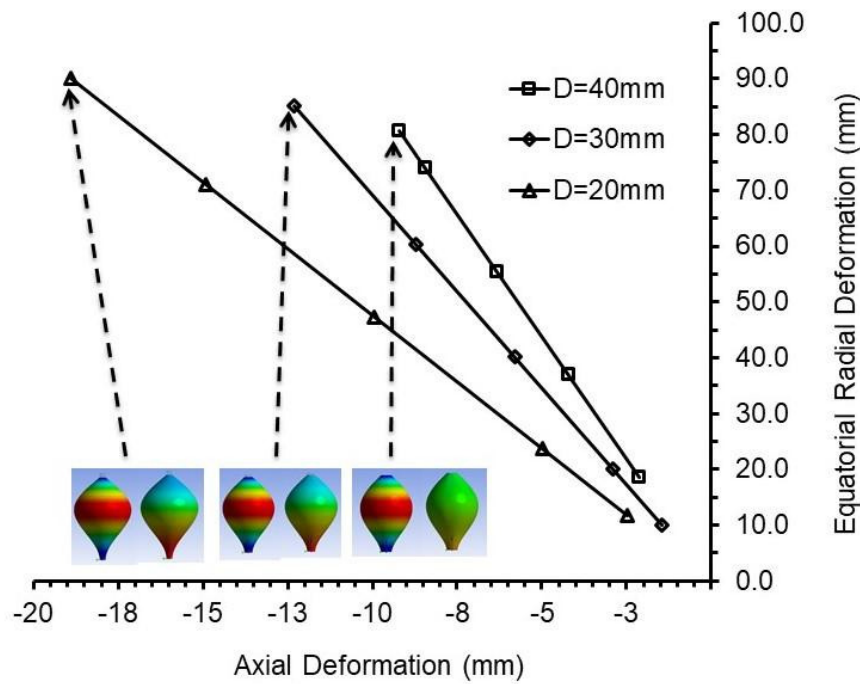


Figure 8.42: Parametric study of outer diameter of cylinder for uniaxial compression mechanism (ERD vs compressive axial deformation) (parametric study 2 of cylinder without end pieces and with in-plane positive Poisson's ratio). Stills of ERD (left) and AD (right) are also shown.

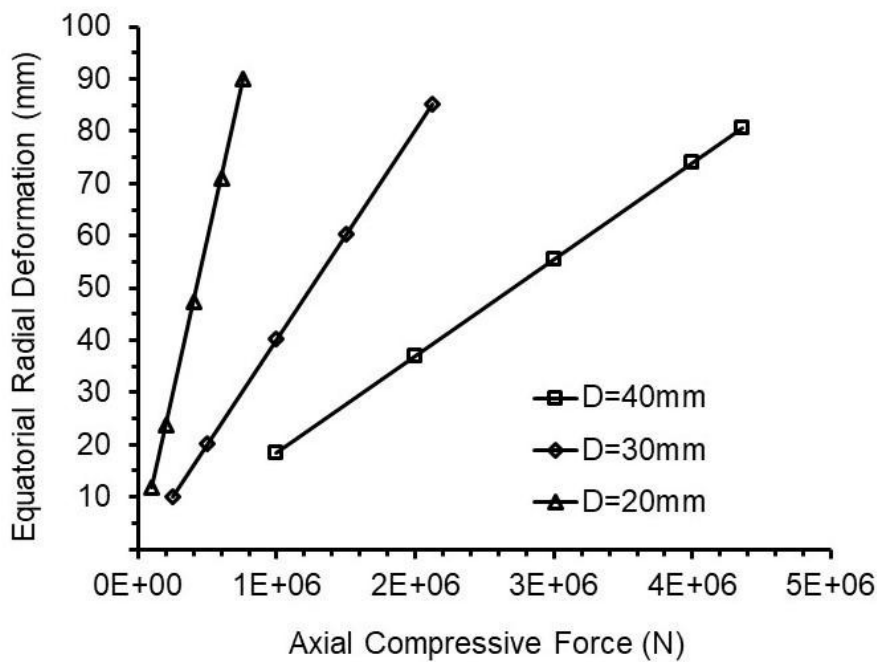


Figure 8.43: Parametric study of outer diameter of cylinder for uniaxial compression mechanism (ERD vs axial compressive force) (parametric study 2 of cylinder without end pieces and with in-plane positive Poisson's ratio).

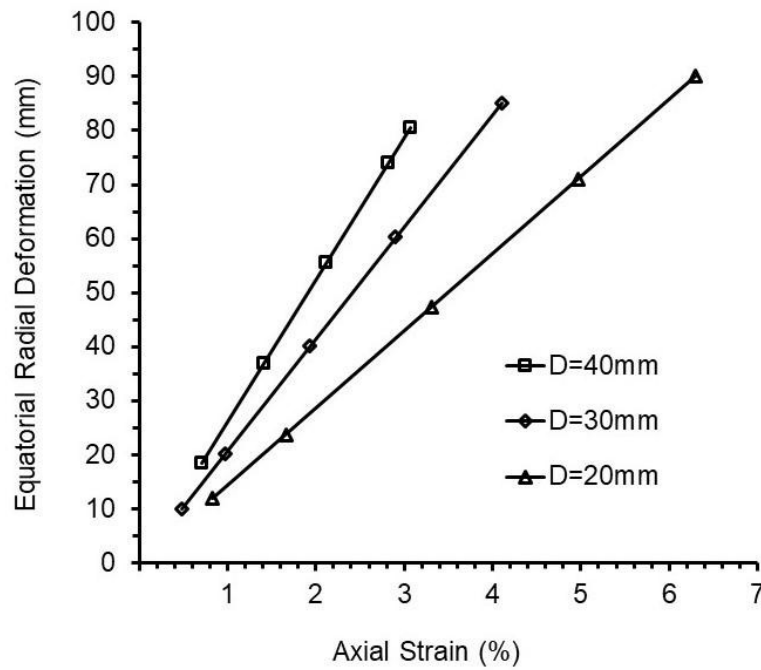


Figure 8.44: Parametric study of outer diameter of cylinder for uniaxial compression mechanism (ERD vs axial strain) (parametric study 2 of cylinder without end pieces and with in-plane positive Poisson's ratio).

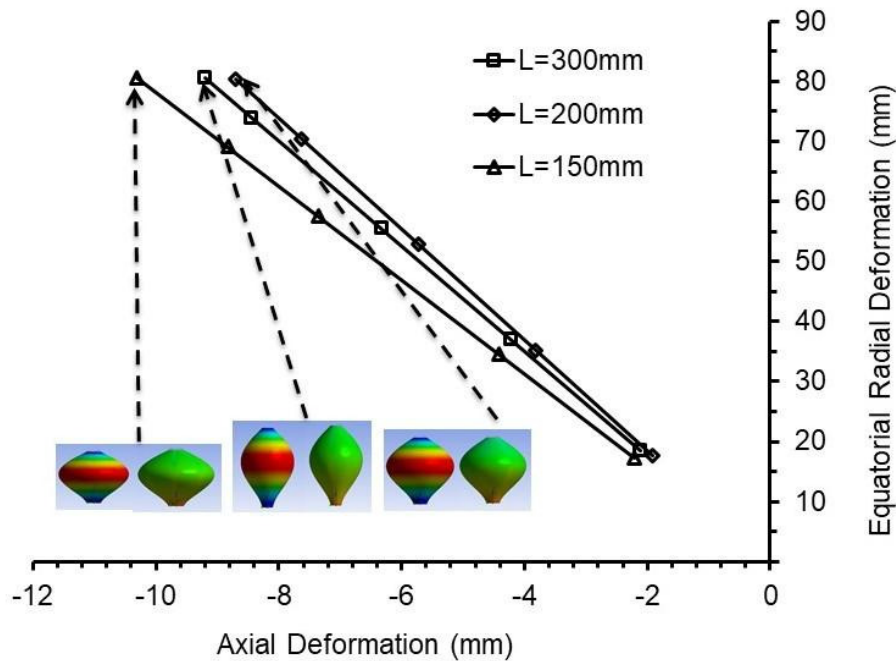


Figure 8.45: Parametric study of length of cylinder for uniaxial compression mechanism (ERD vs compressive axial deformation) (parametric study 2 of cylinder without end pieces and with in-plane positive Poisson's ratio). Stills of ERD (left) and AD (right) are also shown.

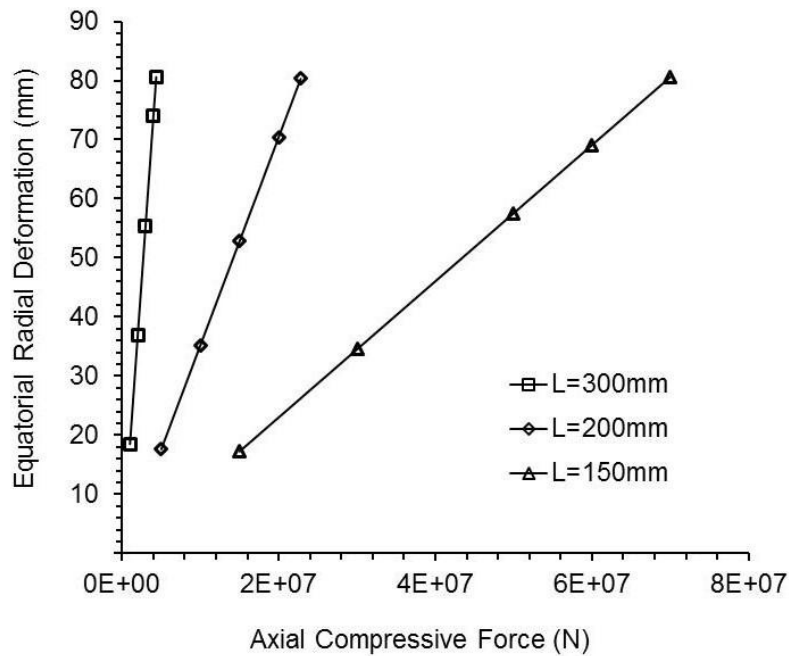


Figure 8.46: Parametric study of length of cylinder for uniaxial compression mechanism (ERD vs axial compressive force) (parametric study 2 of cylinder without end pieces and with in-plane positive Poisson's ratio).

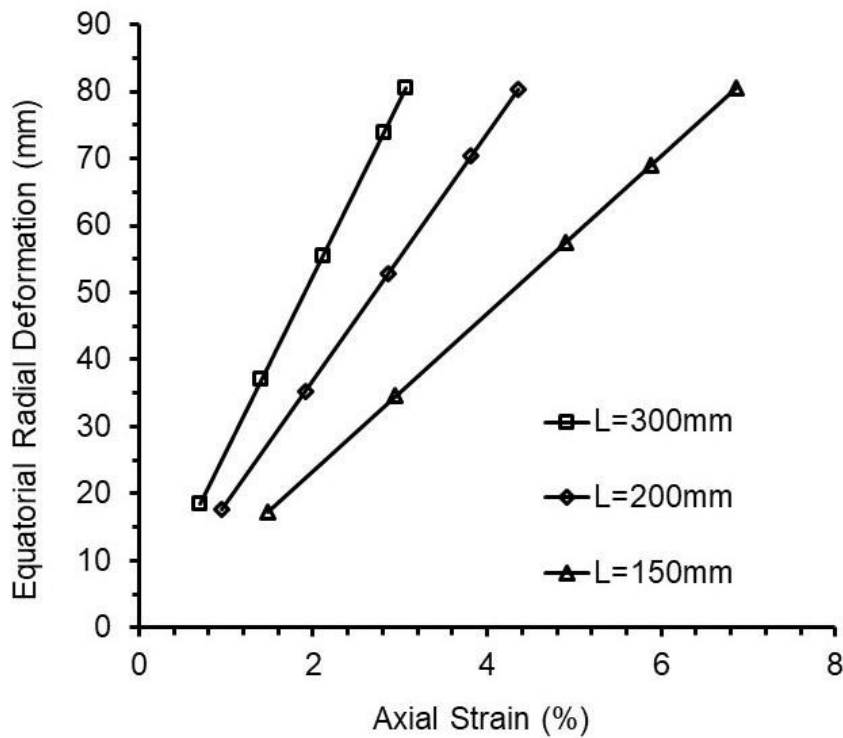


Figure 8.47: Parametric study of length of cylinder for uniaxial compression mechanism (ERD vs axial strain) (parametric study 2 of cylinder without end pieces and with in-plane positive Poisson's ratio).

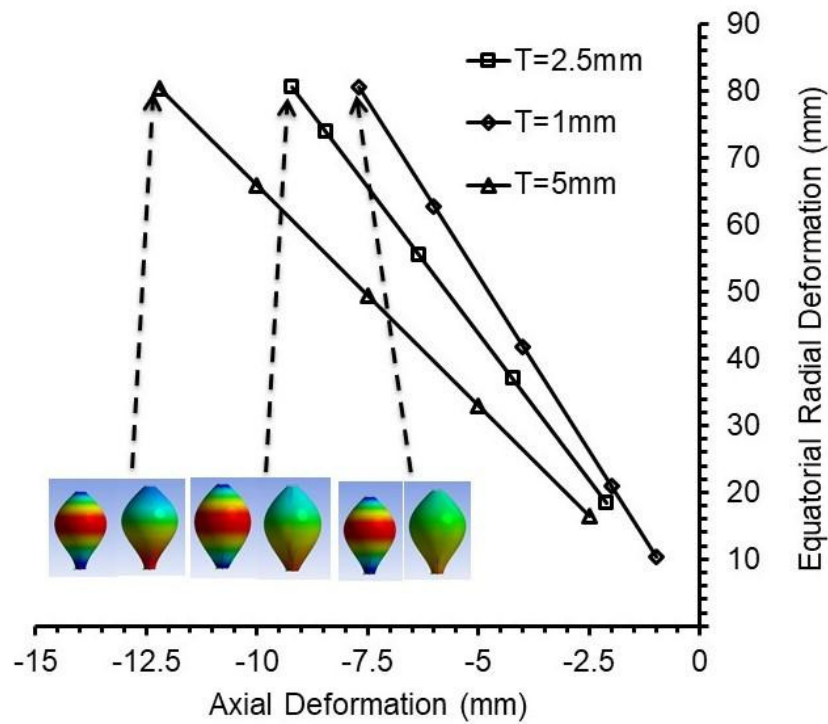


Figure 8.48: Parametric study of wall thickness of cylinder for uniaxial compression mechanism (ERD vs AD) (parametric study 2 of cylinder without end pieces and with in-plane positive Poisson's ratio). Stills of ERD (left) and AD (right) are also shown.

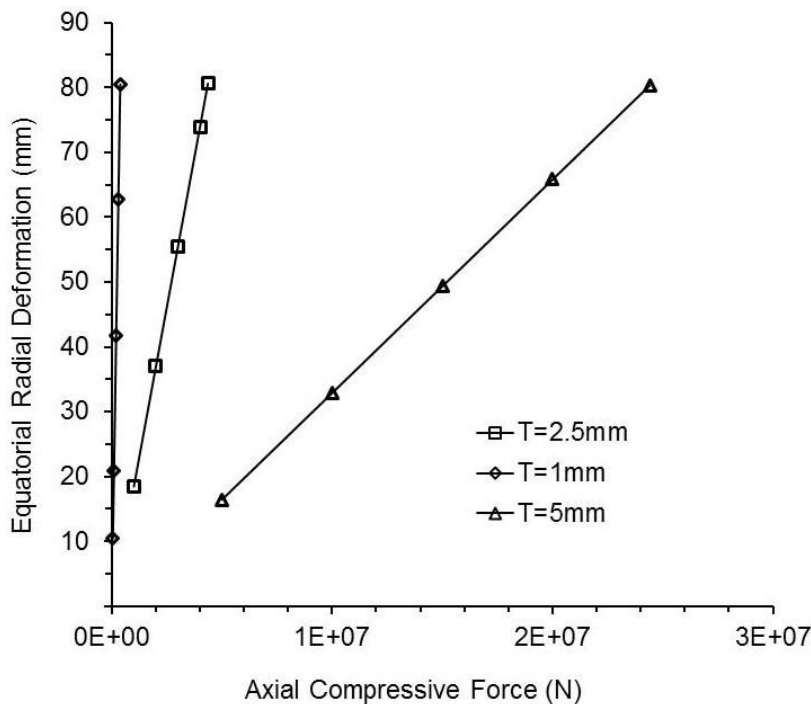


Figure 8.49: Parametric study of wall thickness of cylinder for uniaxial compression mechanism (ERD vs axial compressive force) (parametric study 2 of cylinder without end pieces and with in-plane positive Poisson's ratio).

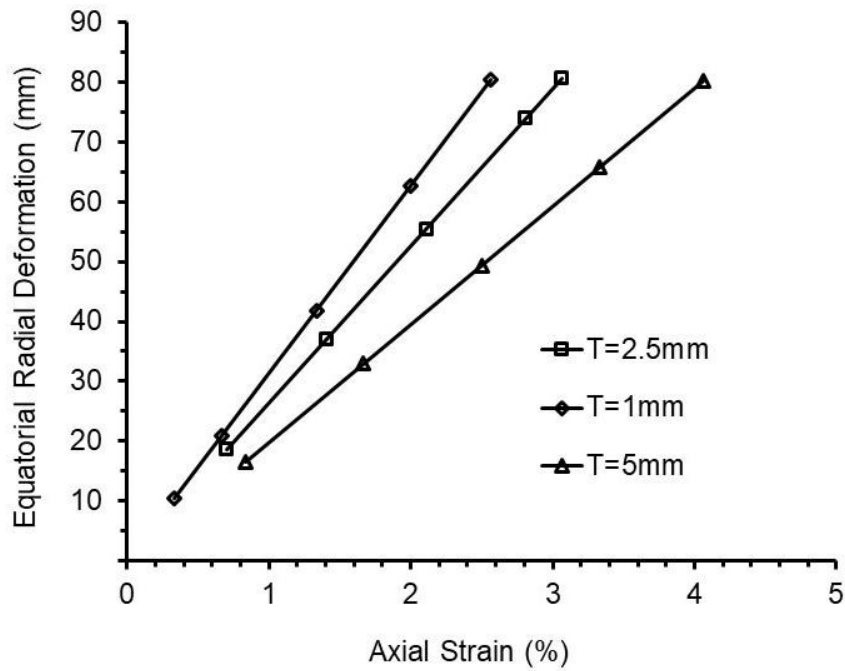


Figure 8.50: Parametric study of wall thickness of cylinder for uniaxial compression mechanism (ERD vs axial strain) (parametric study 2 of cylinder without end pieces and with in-plane positive Poisson's ratio).

The degree of equatorial radial deformation and axial strain were not significantly affected by the different outer diameters (Figure 8.42 and Figure 8.44), lengths (Figure 8.45 and Figure 8.47), and wall thicknesses (Figure 8.48 and Figure 8.50) of solid wall cylinder.

Axial compressive forces however required for a larger outer diameter (>20mm), shorter length (<300mm), and thicker wall of solid wall cylinder (>2.5mm) were significantly higher. For example, axial compressive force required for 40mm outer diameter was approximately six times more than 20mm outer diameter (Figure 8.43). Similarly, axial compressive forces were 16 times higher for 150mm length of cylinder compare to 300mm length of cylinder (Figure 8.46).

8.2.3.2 Uniaxial tension mechanism

In-plane negative Poisson's ratio was simulated for uniaxial tension mechanism and results are described in this section.

8.2.3.2.1 Simulation of standard properties

A set of orthotropic material properties specified in Table 5.4 (Chapter 5) and geometrical parameters defined in Chapter 5.3.1 were considered as the 'standard' configuration.

Orthotropic material properties:

When E_θ was varied from 2×10^8 Pa to 2×10^3 Pa; $\nu_{\theta z}$ and $\nu_{z\theta}$ (in-plane) and $\nu_{\theta r}$ (out-of-plane), recalculated to maintain the symmetric compliance matrix and reciprocal Poisson's ratio relationships (Table 8.7). ν_{rz} and E_z were constant values of 0.03033 and 2.02×10^{10} Pa, respectively during parametric study of E_θ (not shown in Table 8.7). Shear moduli were also derived with respect to the change in the in-plane negative Poisson's ratios (Table 8.7).

Table 8.7: Calculation of orthotropic constants corresponding to the change in E_θ during parametric study 2 of cylinder without end pieces (in-plane negative Poisson's ratio).

E_θ (Pa)	$\nu_{\theta z}$	$\nu_{z\theta}$	$\nu_{\theta r}$	$G_{r\theta}$ (Pa)	$G_{\theta z}$ (Pa)	G_{rz} (Pa)
1.98×10^8	-0.098	-10.1	2.9×10^{-4}	3.3×10^9	9.9×10^7	7.4×10^9
1.98×10^7	-0.031	-31.9	2.9×10^{-5}	1.6×10^9	9.9×10^7	1.1×10^{10}
1.98×10^6	-0.0098	-101.1	2.9×10^{-6}	7.6×10^8	9.9×10^7	1.6×10^{10}
1.98×10^5	-0.0031	-320.9	2.9×10^{-7}	3.5×10^8	9.9×10^7	2.7×10^{10}
1.98×10^4	-0.00098	-1013.5	2.9×10^{-8}	1.6×10^8	1×10^7	3.3×10^{10}
1.98×10^3	-0.00031	-3180.6	2.9×10^{-9}	7.7×10^7	1×10^8	4.9×10^{10}

ERD vs AD (tensile axial deformation) with stills from the simulation movies, ERD vs tensile axial force and ERD vs axial strain graphs are plotted (Figure 8.51-8.53). A large radial deformation in the equatorial region of solid wall of cylinder (~ 80 mm) for the small tensile axial deformation (≤ 28 mm) and strain ($< 10\%$) was noted when E_θ was $\leq 1.98 \times 10^7$ Pa in Figure 8.51 and Figure 8.53, respectively.

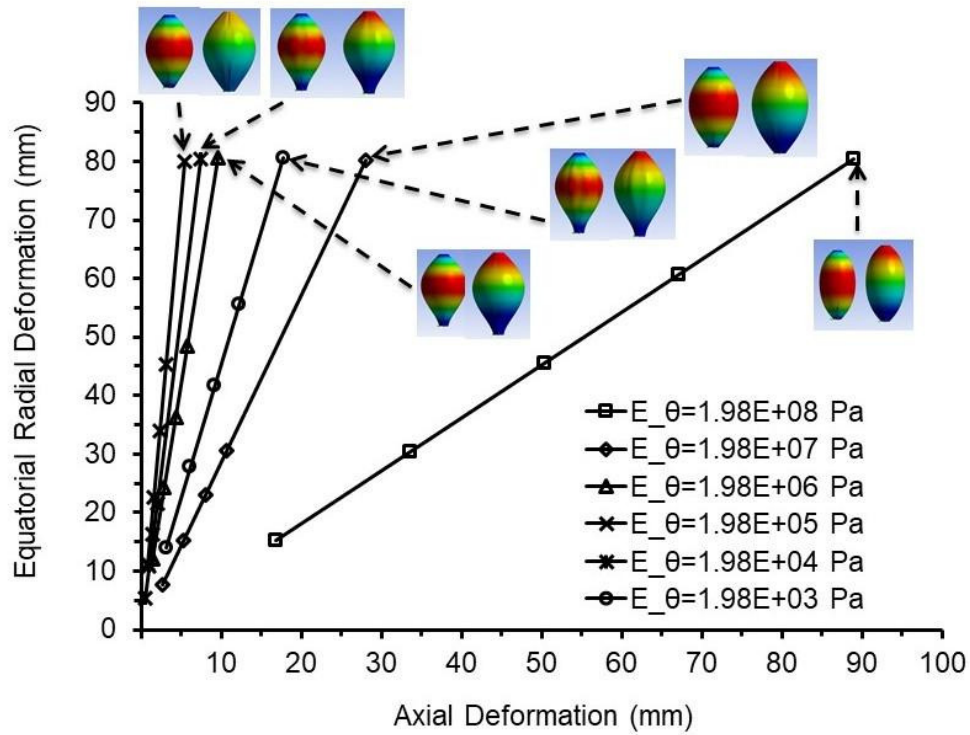


Figure 8.51: ERD vs AD for parametric study of E_θ (parametric study 2 of cylinder without end pieces and with in-plane negative Poisson's ratio). Stills of ERD (left) and AD (right) are also shown.

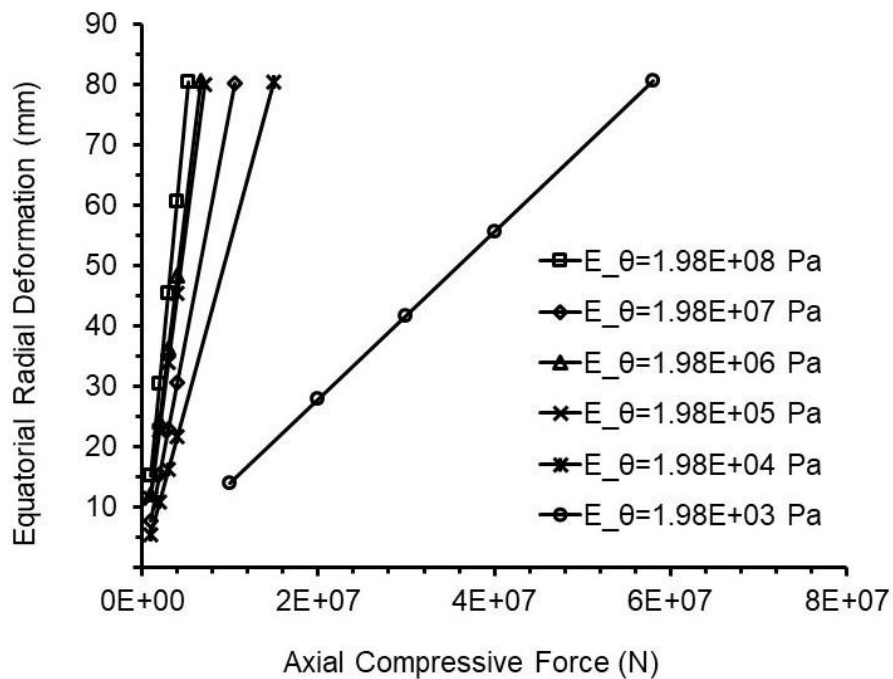


Figure 8.52: ERD vs axial tensile force for parametric study of E_θ (parametric study 2 of cylinder without end pieces and with in-plane negative Poisson's ratio).

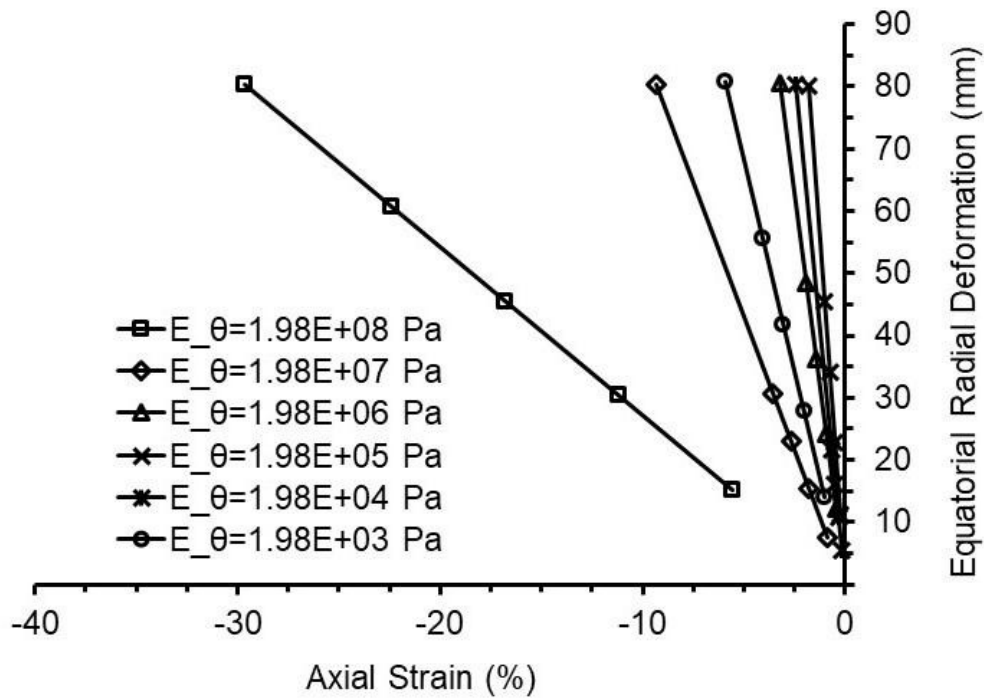


Figure 8.53: ERD vs axial strain for parametric study of E_θ (parametric study 2 of cylinder without end pieces and with in-plane negative Poisson's ratio).

Geometric parameters:

Geometrical parameters of 'standard' set of properties did not have significant impact on the deformation of solid wall cylinder with pronged cone end pieces and hence, they were not simulated using 'standard' properties for solid wall cylinder without end pieces (in-plane negative Poisson's ratio).

8.2.3.2.2 Simulation of shape change properties

Orthotropic material properties required to achieve a large equatorial radial deformation of solid wall cylinder (no end pieces) for uniaxial tension mechanism are considered as 'shape change' properties (Table 8.8).

Table 8.8: 'Shape change' properties to carry out parametric study 2 of solid wall cylinder without end pieces and with in-plane negative Poisson's ratio.

Orthotropic Material Properties	Geometrical Parameters
$E_r = 2 \times 10^{11} \text{ Pa}$	Outer Diameter (D) = 40mm
$E_\theta = 1.98 \times 10^6 \text{ Pa}$	Length (L) = 300mm
$E_z = 2.02 \times 10^{10} \text{ Pa}$	Wall thickness (T) = 2.5mm
$\nu_{\theta r} = 2.9 \times 10^{-6}$	
$\nu_{\theta z} = -0.0098$	
$\nu_{zr} = 0.03033$	
$G_{r\theta} = 7.6 \times 10^8 \text{ Pa}$	
$G_{\theta z} = 9.9 \times 10^7 \text{ Pa}$	
$G_{rz} = 1.6 \times 10^{10} \text{ Pa}$	

The magnitude of in-plane negative Poisson's ratio requires for large equatorial radial deformation of solid wall cylinder was identified during parametric study of set of 'standard' properties (Table 8.7 and Figure 8.51). Hence, the parametric study for in-plane negative Poisson's ratio was not carried out using 'shape change' properties. A large equatorial radial deformation (~80mm) for small axial strains ($\leq 10\%$) were obtained when $E_\theta \leq 1.98 \times 10^7 \text{ Pa}$ (Figure 8.51). Hence, the geometrical parameters were evaluated for $E_\theta = 1.98 \times 10^6 \text{ Pa}$ as way of example and results are outlined below.

Outer diameter, length and wall thickness of cylinder:

ERD vs AD (tensile axial deformation) (Figures 8.54, 8.57 and 8.60), ERD vs tensile axial force (Figures 8.55, 8.58 and 8.61), ERD vs axial strain (Figures 8.56, 8.59 and 8.62) were plotted for different outer diameters, lengths and wall thicknesses of solid wall cylinder.

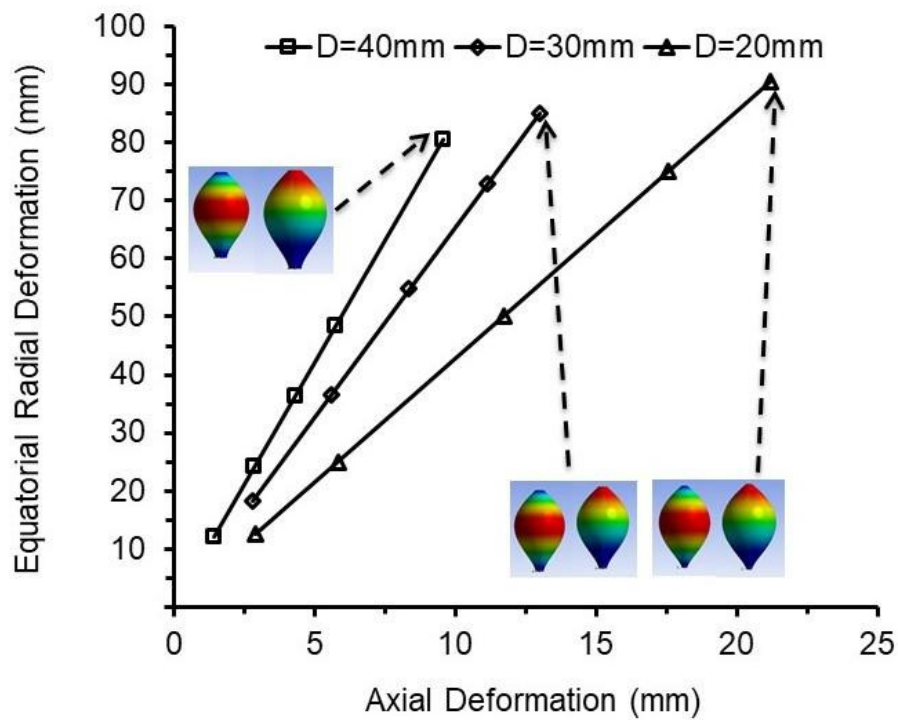


Figure 8.54: Parametric study of outer diameter of cylinder for uniaxial tension mechanism (ERD vs AD) (parametric study 2 of cylinder without end pieces and with in-plane negative Poisson's ratio). Stills of ERD and AD are also shown.

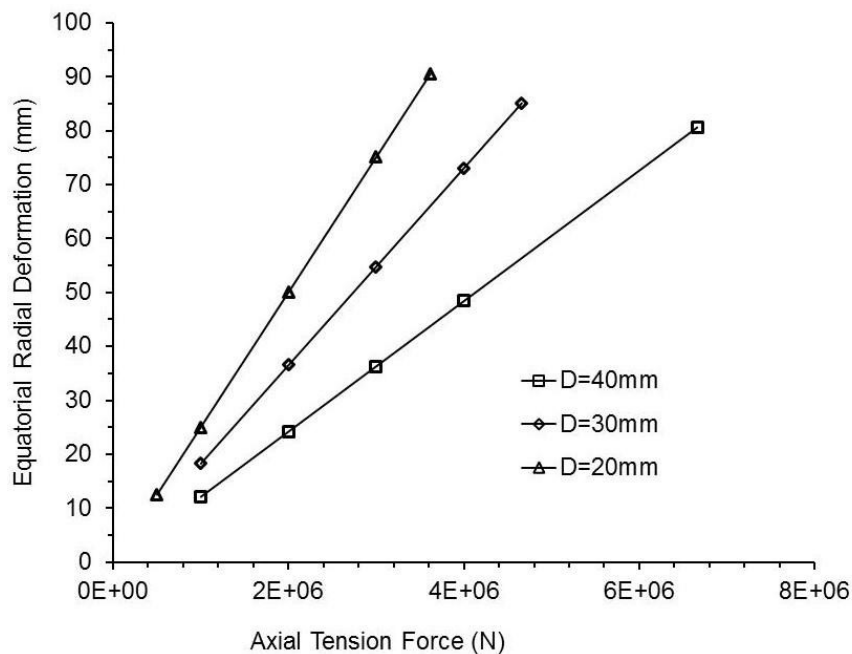


Figure 8.55: Parametric study of outer diameter of cylinder for uniaxial tension mechanism (ERD vs axial tensile force) (parametric study 2 of cylinder without end pieces and with in-plane negative Poisson's ratio).

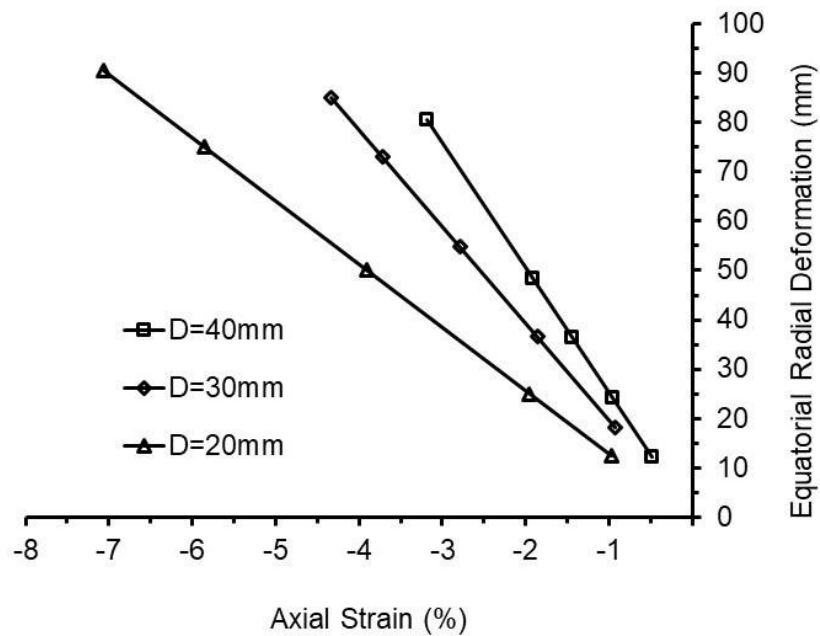


Figure 8.56: Parametric study of outer diameter of cylinder for uniaxial tension mechanism (ERD vs axial strain) (parametric study 2 of cylinder without end pieces and with in-plane negative Poisson's ratio).

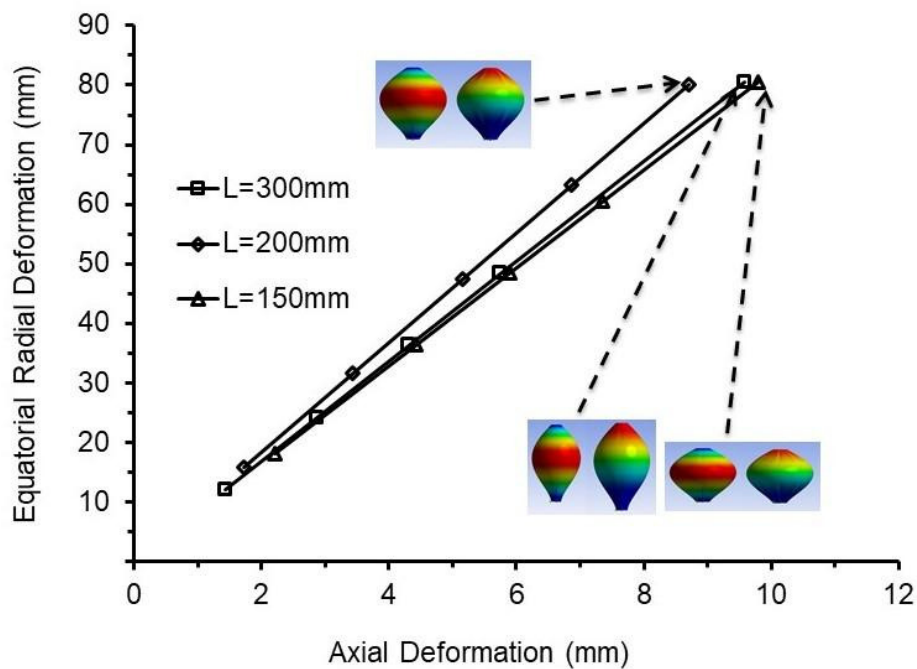


Figure 8.57: Parametric study of length of cylinder for uniaxial tension mechanism (ERD vs AD) (parametric study 2 of cylinder without end pieces and with in-plane negative Poisson's ratio). Stills of ERD and AD are also shown.

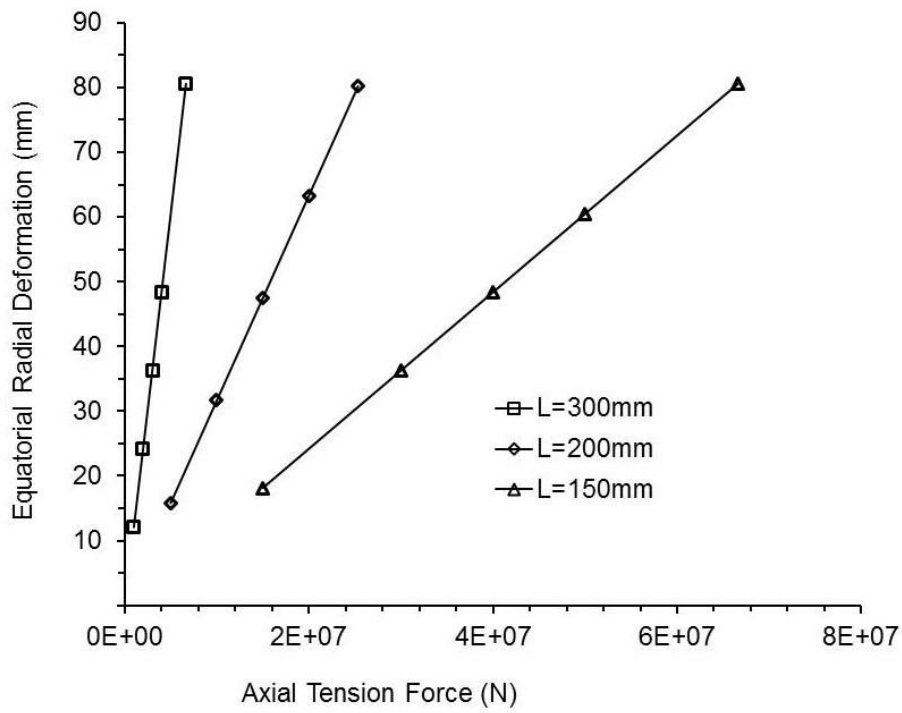


Figure 8.58: Parametric study of length of cylinder for uniaxial tension mechanism (ERD vs axial tension force) (parametric study 2 of cylinder without end pieces and with in-plane negative Poisson's ratio).

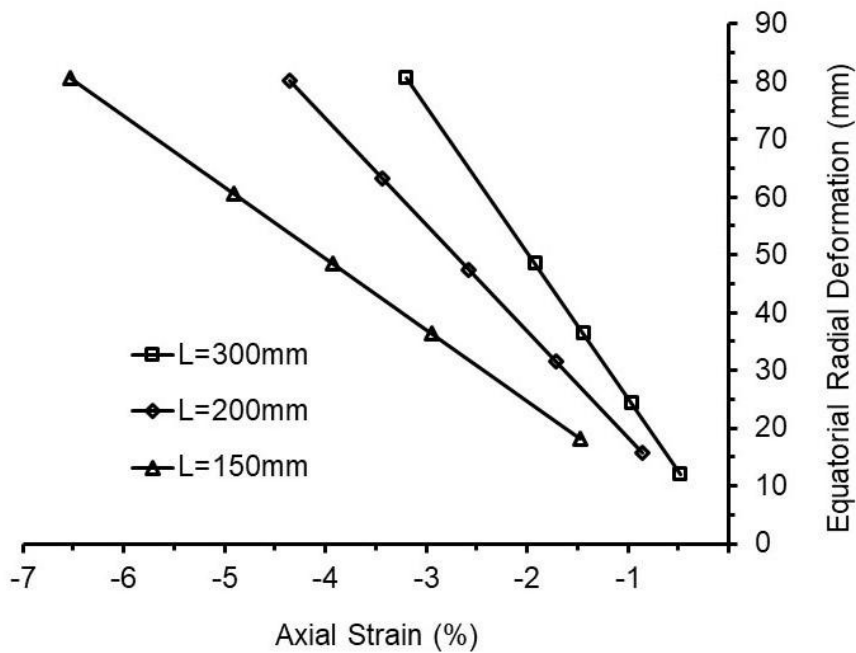


Figure 8.59: Parametric study of length of cylinder for uniaxial tension mechanism (ERD vs axial strain) (parametric study 2 of cylinder without end pieces and with in-plane negative Poisson's ratio).

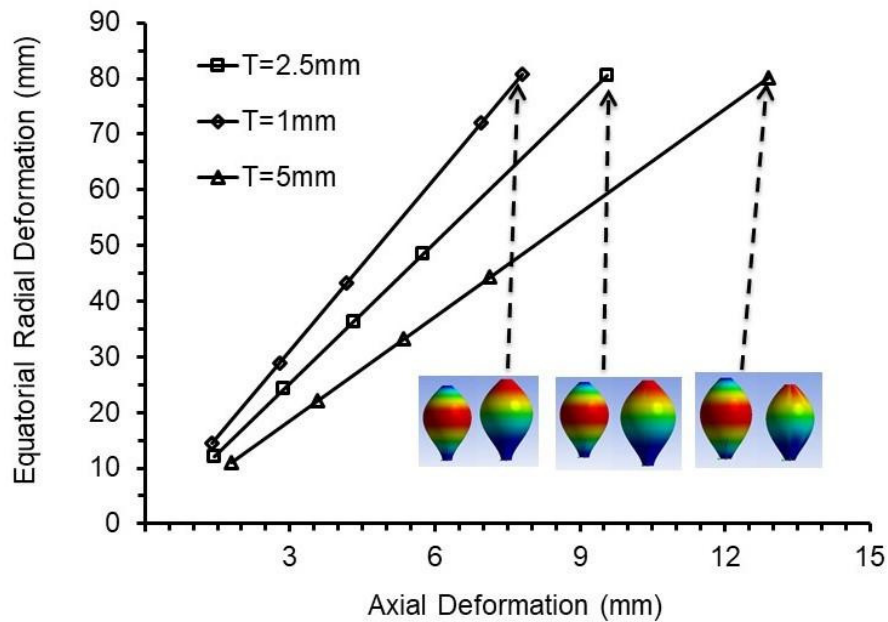


Figure 8.60: Parametric study of wall thickness of cylinder for uniaxial tension mechanism (ERD vs AD) (parametric study 2 of cylinder without end pieces and with in-plane negative Poisson's ratio). Stills of ERD and AD are also shown.

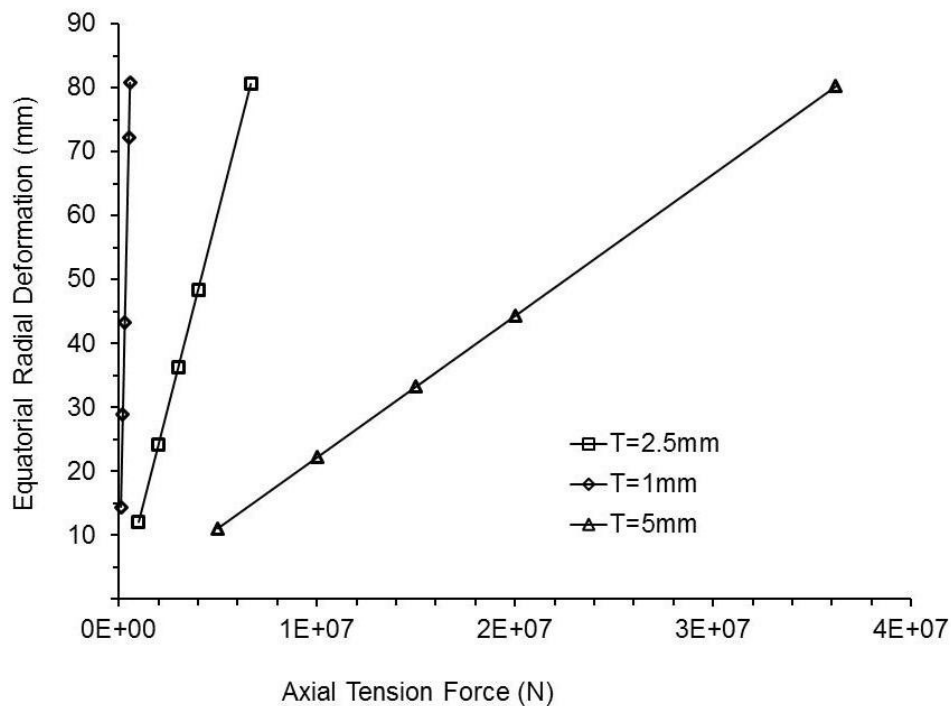


Figure 8.61: Parametric study of wall thickness of cylinder for uniaxial tension mechanism (ERD vs tensile axial force) (parametric study 2 of cylinder without end pieces and with in-plane negative Poisson's ratio).

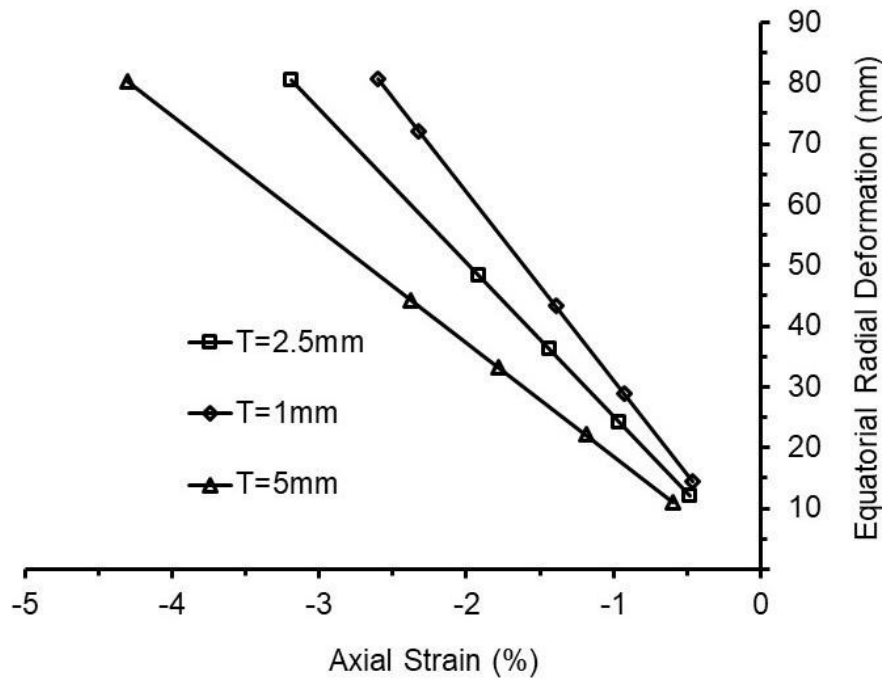


Figure 8.62: Parametric study of wall thickness of cylinder for uniaxial tension mechanism (ERD vs axial strain) (parametric study 2 of cylinder without end pieces and with in-plane negative Poisson's ratio).

The degree of equatorial radial deformation and tensile axial strain were not significantly affected by the different outer diameters (Figure 8.54 and Figure 8.56), lengths (Figure 8.57 and Figure 8.59), and wall thicknesses (Figure 8.60 and Figure 8.62) of solid wall cylinder. However, tensile axial forces were significantly higher for the larger outer diameters ($>20\text{mm}$), shorter length ($<300\text{mm}$), and thicker wall of solid wall cylinder ($>2.5\text{mm}$). For example, tensile axial force required for 40mm outer diameter was twice than 20mm outer diameter (Figure 8.55). Similarly, tensile axial forces were 10 times higher for 150mm length of cylinder compare to 300mm length of cylinder (Figure 8.58).

8.3 Summary

The results of the FE modelling of solid wall cylinder with and without end pieces carried out for the linear elastic (isotropic and orthotropic) material properties were described in this chapter. The results of the parametric study 1 suggested that E_θ (or E_z/E_θ) is the critical parameter amongst the orthotropic material properties to achieve a large equatorial deformation of a solid wall cylinder with pronged cone end pieces. The results of the parametric study 2

suggested that in-plane orthotropic material properties – Poisson's ratios ($\nu_{\theta z}$ and $\nu_{z\theta}$) and E_θ (or E_z/E_θ) related by compliance matrix symmetry – are critical parameters amongst the orthotropic material properties to achieve a large equatorial deformation of a solid wall cylinder with and without end pieces. The magnitudes of in-plane Poisson's ratios (positive and negative) essential for the large equatorial deformation at low axial deformation (or strain) were identified during the parametric study 2 of solid wall cylinder with and without end pieces and are outlined below:

- $\nu_{\theta z} \leq -320.9$ for solid wall cylinder with pronged cone end pieces (uniaxial compression mechanism),
- $\nu_{\theta z} < -10$ for solid wall cylinder without end pieces (uniaxial tension mechanism) and
- $\nu_{\theta z} > +10$ for solid wall cylinder without end pieces (uniaxial compression mechanism).

Moreover, geometric parameters of solid wall cylinder with and without end pieces were optimised. The results of the parametric studies will be discussed in the Chapter 10.

9 Results 3 - Cellular mesh cylinders, Fabrication, Characterisation, and in-vitro and in-vivo assessments of prototypes

In-silico models of cellular mesh cylinders were designed and simulated, and the results are presented in this chapter. The results of the fabrication, mechanical characterisation and in-vitro evaluation of promising prototypes are subsequently reported. Additionally, in-vivo and in-vitro assessments of doughnut shape inflatable prototypes are described.

9.1 Cellular mesh cylinders

Cellular mesh cylinders were designed and simulated for validation of outputs of the FE modelling of the solid wall cylinder (Chapter 8) and to predict the expansion behaviours of cellular mesh cylinders fabricated using laser cutting and 3D printing technology. The 'CAD-FE' parts of the 'CAD-FE-Experimental approach' is simultaneously demonstrated for promising prototypes in the absence of surrounding materials. The 'Experimental' part of the 'CAD-FE-Experimental approach' is demonstrated in Sections 9.2 and 9.3 of this chapter for promising prototypes. FE predictions of laser cut and 3D printed cellular mesh cylinders are then compared with the experimental outputs in Section 9.3.

9.1.1 Validation of outputs of FE modelling of a solid wall cylinder

Cylinders consisting of auxetic and conventional hexagonal honeycombs (Tables 6.5, Chapter 6) were designed and simulated to predict the expansion capabilities and validate the outputs of the FE modelling of solid wall cylinders described in Chapter 8.

9.1.1.1 Auxetic and conventional honeycomb mesh cylinders without end pieces

Cylinders consisting of auxetic (Auxetic 1-4 models of Table 6.5, Chapter 6) and conventional (Conventional 1-5 models of Table 6.5, Chapter 6) honeycomb meshes were designed with effective mechanical properties to match the target mechanical properties (to achieve large equatorial radial deformation at small axial strain) of the solid wall cylinder. They were subsequently simulated in

Ansys software (version 17.1). Pictorial representations of auxetic and conventional honeycomb meshes and length of end pieces at both ends of cylinder are shown in Table 9.1 and 9.2, respectively.

Table 9.1: Segments of auxetic honeycombs from CAD models and length of end pieces.

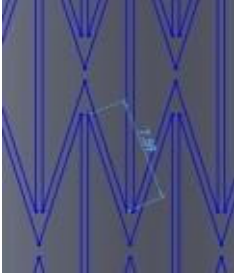
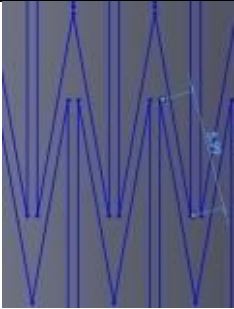
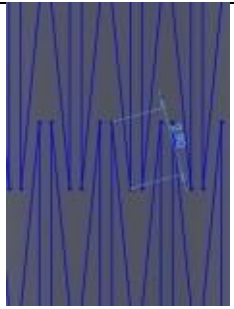
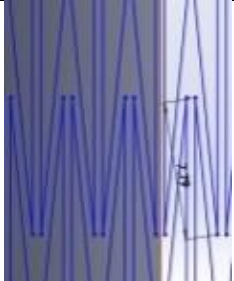
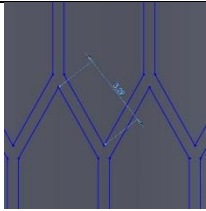
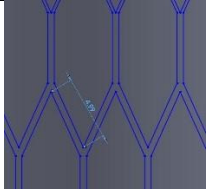

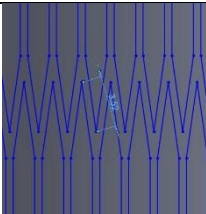
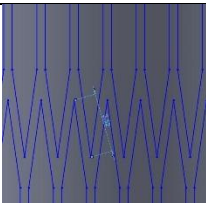
Model Name	Segment	Length of end pieces at both ends of cylinder (mm)
Auxetic 1		70.0
Auxetic 2		58.7
Auxetic 3		40.4
Auxetic 4		52.1

Table 9.2: Segments of conventional honeycombs from CAD models and length of end pieces.

Model Name	Segment	Length of end pieces at both ends of cylinder (mm)
Conventional 1		25
Conventional 2		25
Conventional 3		25
Conventional 4		25
Conventional 5		25

ERD vs AD for auxetic (Figure 9.1) and conventional (Figure 9.2) honeycomb meshes were plotted to demonstrate the expansion capabilities of the cellular mesh cylinders. Radial (left) and axial (right) deformation stills are shown as inserts for each cylinder in Figures 9.1 and 9.2.

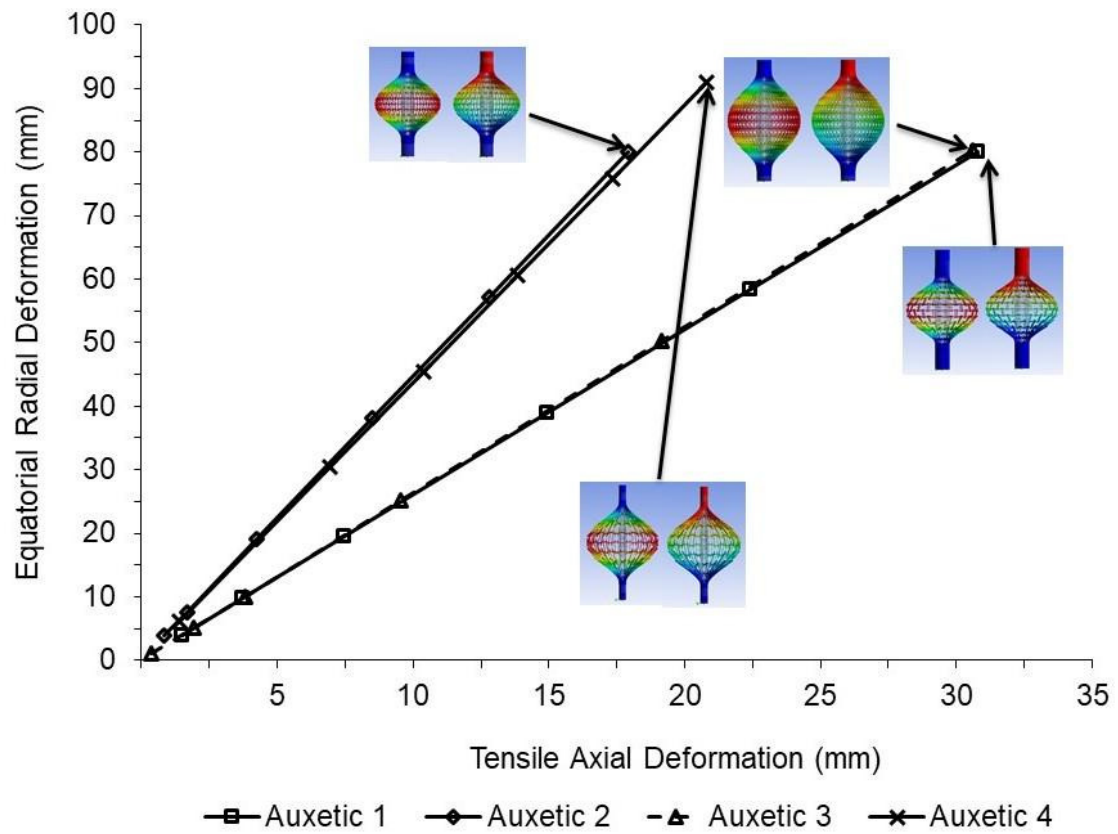


Figure 9.1: FE predictions of auxetic honeycomb mesh models (ERD vs Tensile axial deformation). Stills of ERD (left) and AD (right) are also shown.

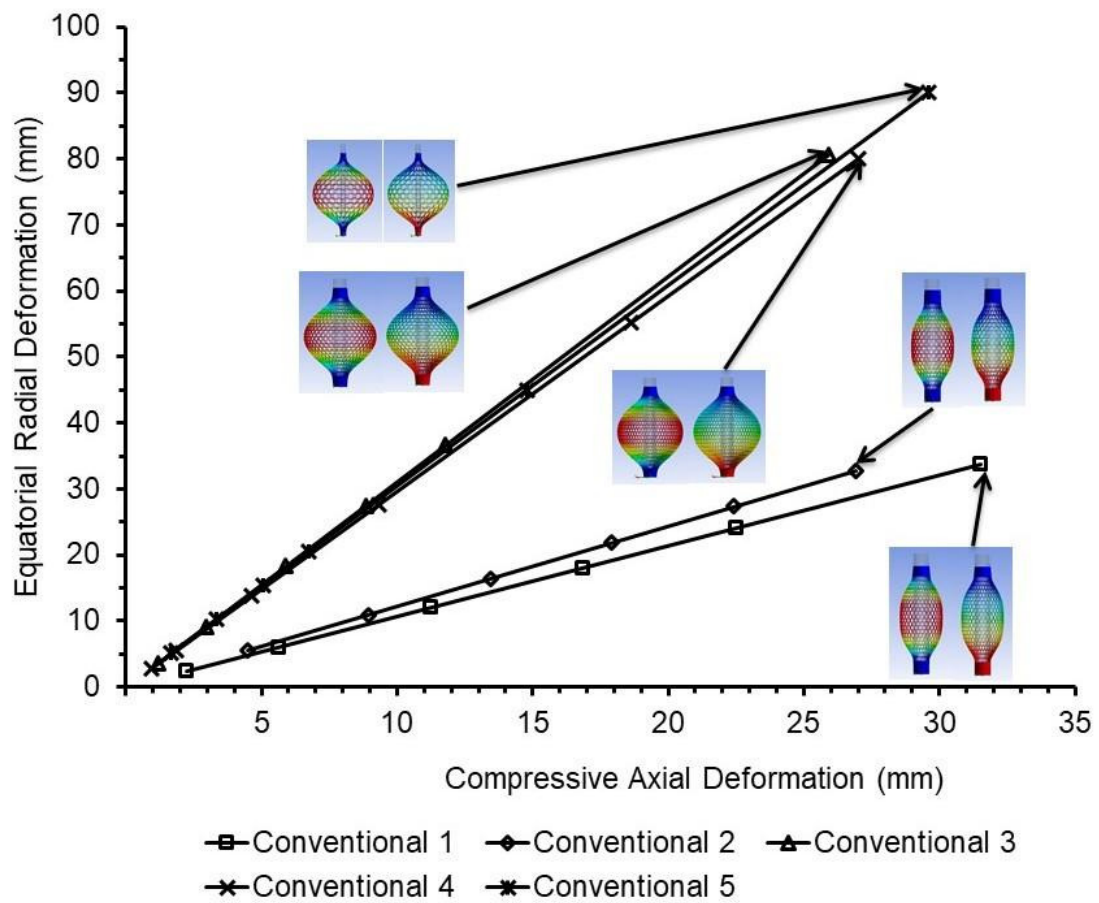


Figure 9.2: FE predictions of conventional honeycomb mesh models (ERD vs Compressive axial deformation). Stills of ERD (left) and AD (right) are also shown.

ERD vs axial tension force and ERD vs axial compressive force were plotted for auxetic and conventional honeycomb meshes in Figures 9.3 and Figure 9.4, respectively.

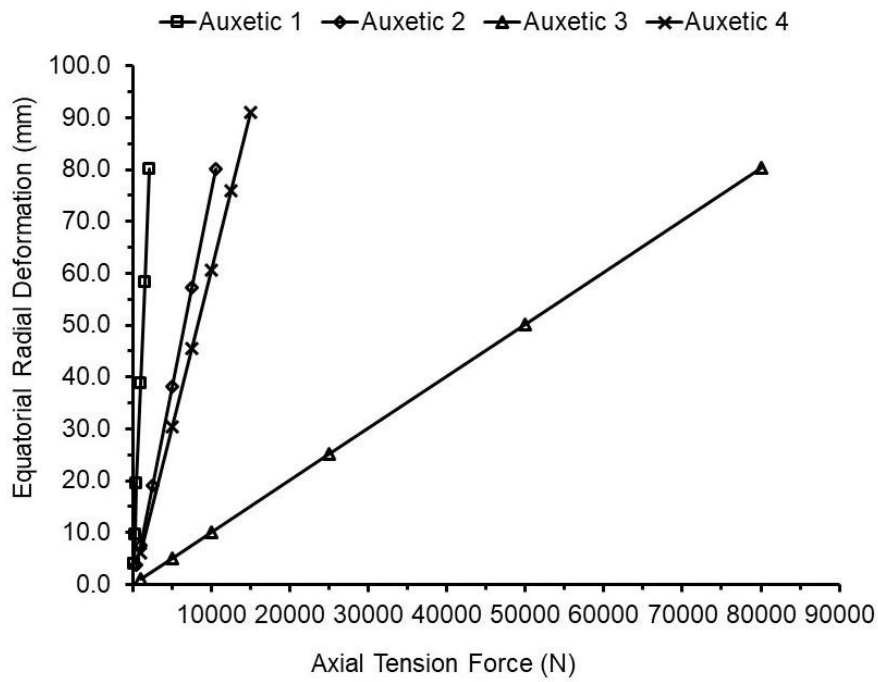


Figure 9.3: FE predictions of auxetic honeycomb mesh models (ERD vs Axial tension force).

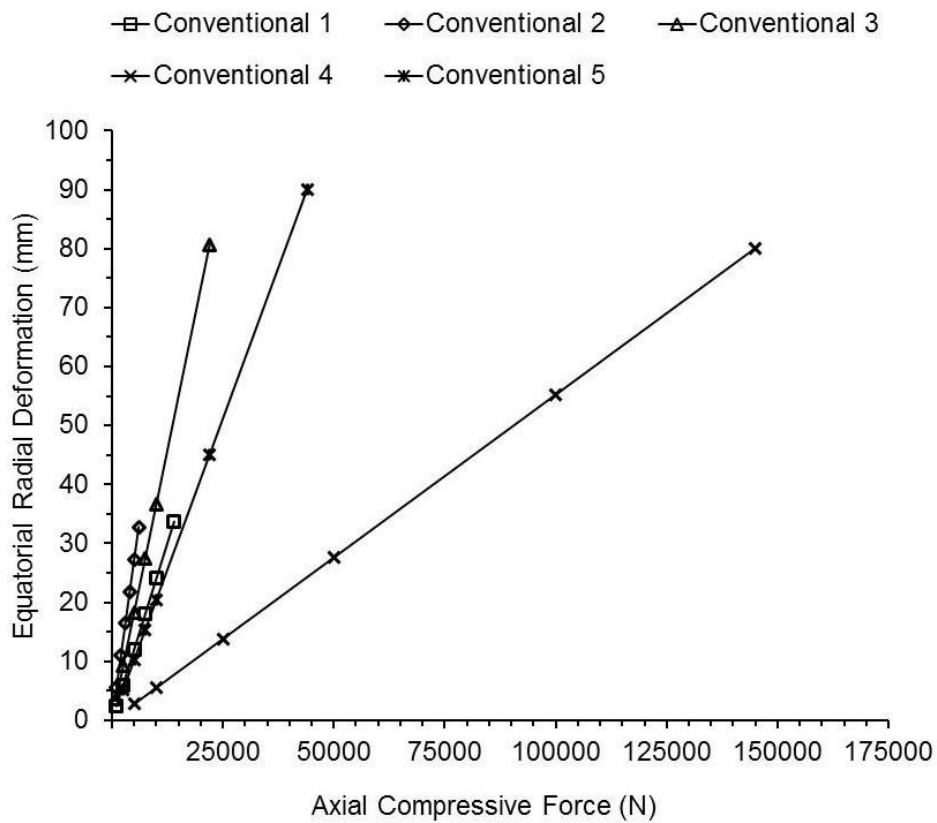


Figure 9.4: FE predictions of conventional honeycomb mesh models (ERD vs axial compressive force).

The axial tension and compressive forces shown in Figure 9.3 and Figure 9.4, respectively are extremely high for surgical purposes and are due to the models employing elastic constants based on structural steel.

ERD vs axial strain for auxetic and conventional honeycomb meshes were plotted in Figure 9.5 and 9.6, respectively. The large equatorial radial deformations were obtained for small axial tension and compressive strains (approximately 10% or less) (Figures 9.5 and 9.6).

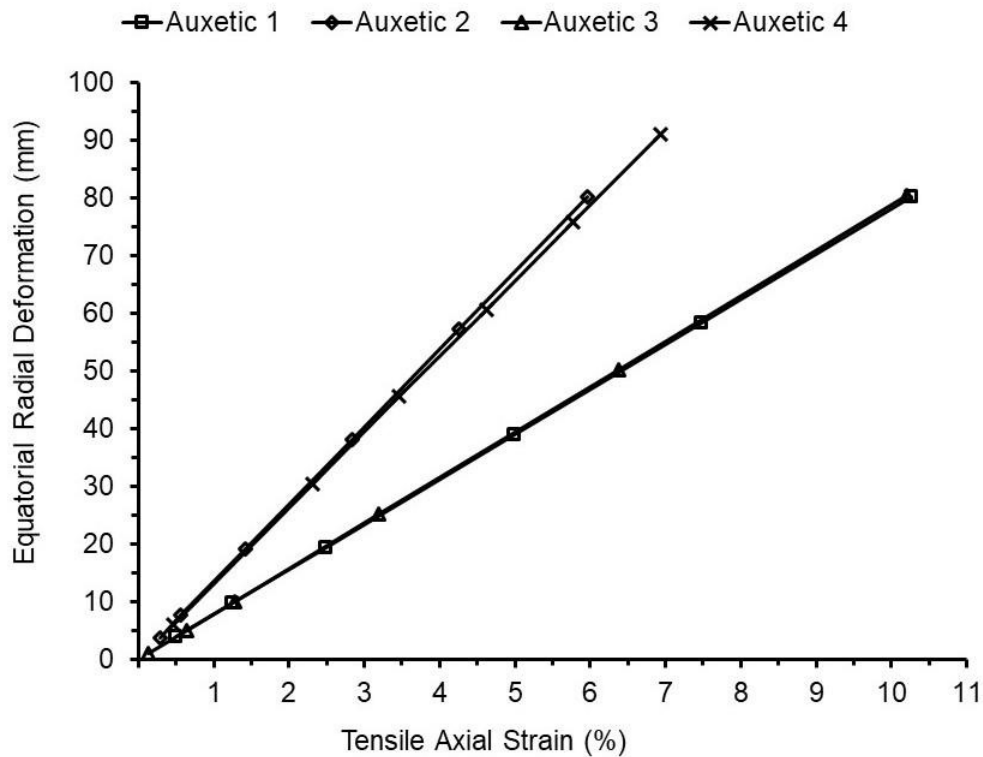


Figure 9.5: FE predictions of auxetic honeycomb mesh models (ERD vs Tensile axial strain).

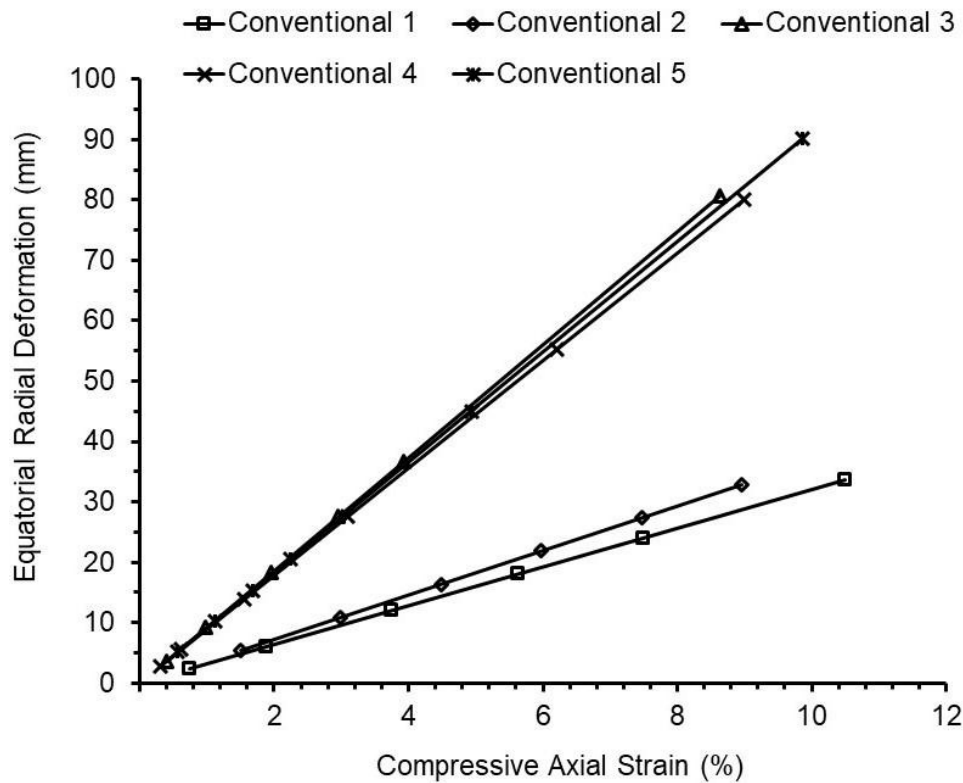


Figure 9.6: FE predictions of conventional honeycomb mesh models (ERD vs Compressive axial strain).

9.1.1.2 Auxetic honeycomb cylinders with pronged cone end pieces

Cylinders consisting of auxetic honeycomb meshes (Auxetic 5-7 models of Table 6.5, Chapter 6) were designed in SolidWorks (version 2015) with effective mechanical properties to match the target mechanical properties of the solid wall cylinder with pronged cone end pieces obtained during parametric study 2 (Chapter 8.2.2). Fillets were used to round sharp edges of the diagonal ribs of auxetic honeycombs prior to simulating expansion capabilities of the Auxetic 5-7 models in Ansys software (version 17.1). ERD vs AD, ERD vs axial compressive force and ERD vs axial strain (Figures 9.7-9.9) were plotted. Radial (left) and axial (right) deformation stills are shown in the inserts to Figure 9.7.

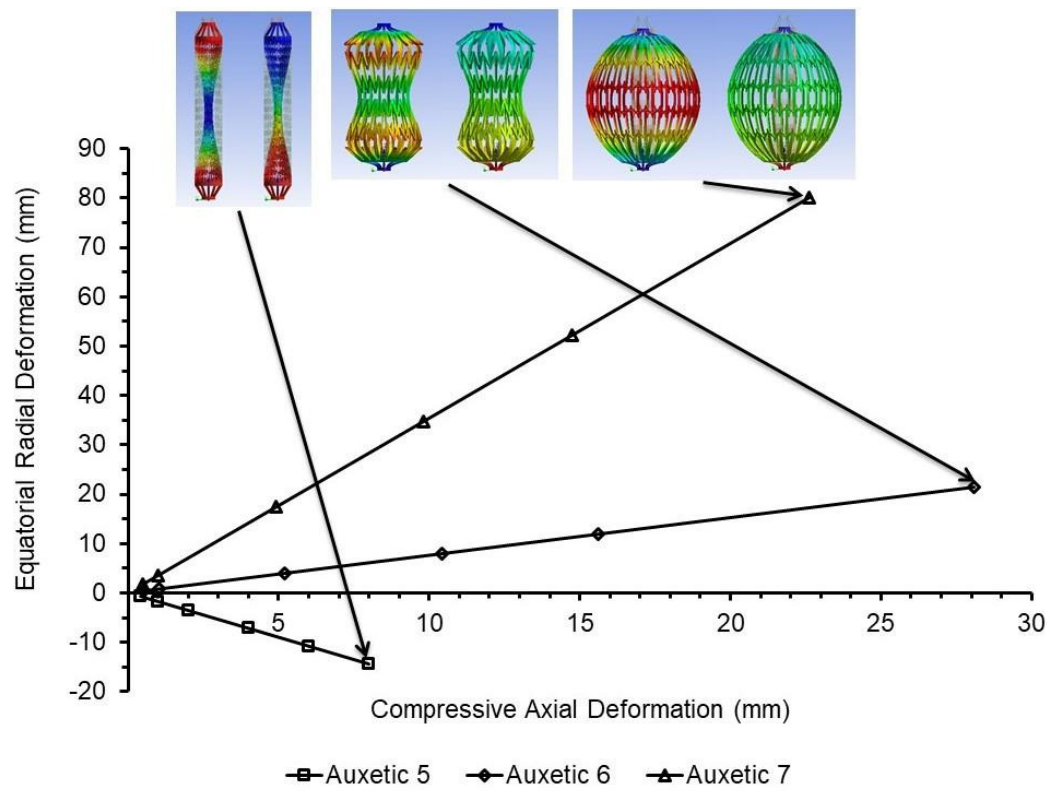


Figure 9.7: FE predictions of auxetic honeycomb mesh models with pronged cone end pieces (ERD vs Compressive axial deformation). Stills of ERD (left) and AD (right) are also shown.

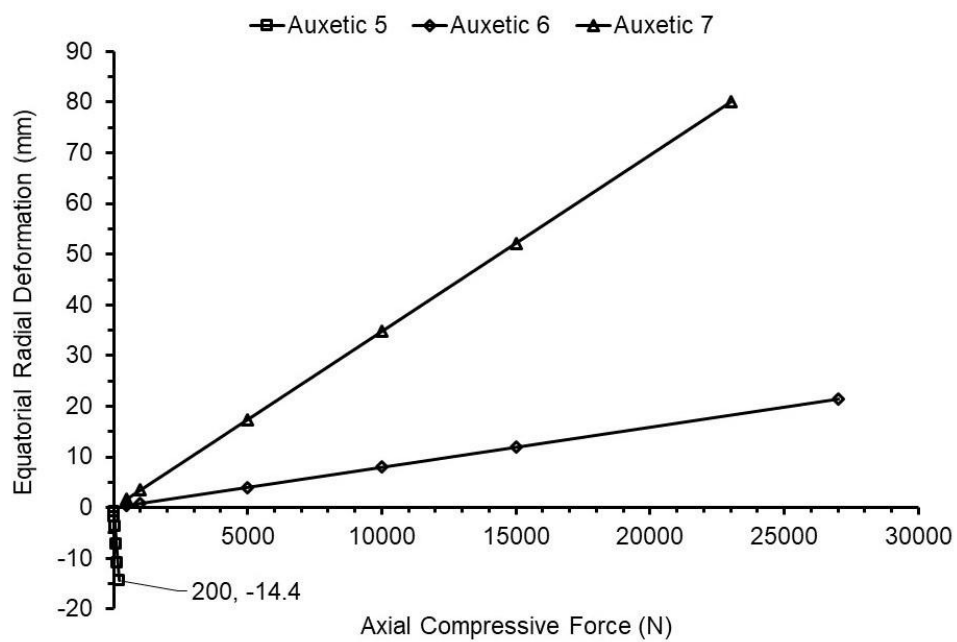


Figure 9.8: FE predictions of auxetic honeycomb mesh models with pronged cone end pieces (ERD vs Axial compressive force).

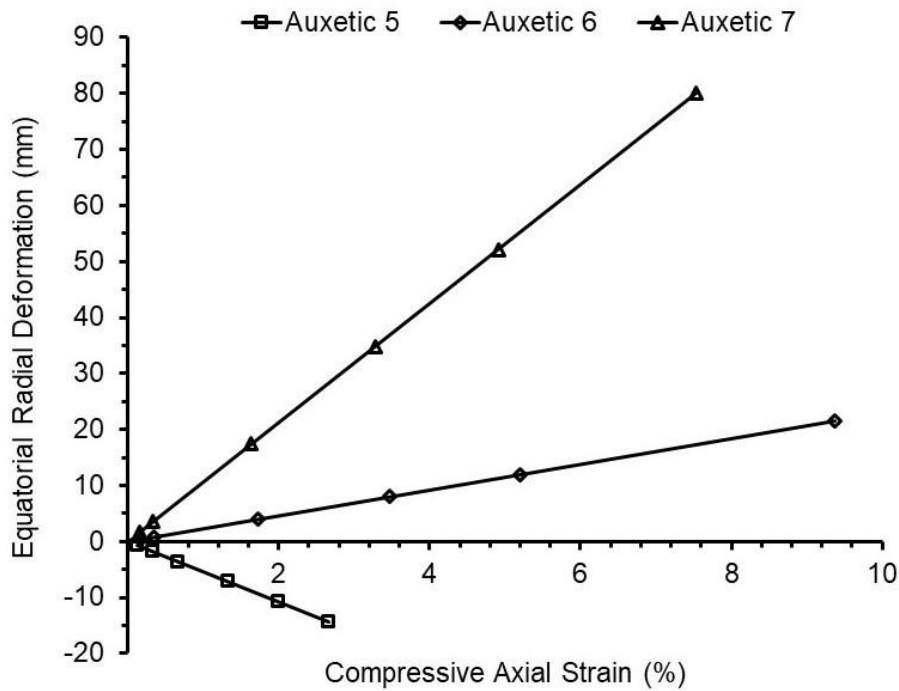


Figure 9.9: FE predictions of auxetic honeycomb mesh models with pronged cone end pieces (ERD vs Compressive axial strain).

The Auxetic 7 model clearly demonstrates the large equatorial radial deformation for small axial deformation compared to the Auxetic 6 (shows deformation in the equatorial region but less than the deformation at both ends) and Auxetic 5 (gets thinner in the equatorial region) models (Figure 9.7). The large equatorial radial deformation (approximately 80mm) for the Auxetic 7 model was obtained for small axial compressive strain (<10%) (Figure 9.9).

9.1.1.3 Validation

The results of the FE modelling of the solid wall cylinder with and without end pieces (Chapters 8.2.2 and 8.3.3) indicated the target mechanical properties (E_z/E_θ and $\nu_{z\theta}$) to achieve a large equatorial radial deformation for the small axial deformation (or strain). The cellular meshes were then derived for the target $\nu_{z\theta}$ in the Table 6.5, Chapter 6. These cellular meshes were subsequently designed and simulated to obtain ERD, AD, axial tension and compressive forces and axial tension and compressive strain values. The ERD vs AD (Figures 9.1, 9.2, and 9.7) and ERD vs axial strain (Figures 9.5, 9.6, and 9.9) plots qualitatively validate the outputs of the FE modelling of solid wall cylinder with and without end pieces (Figures 8.37-38, Chapter 8.2.2; Figures 8.39-41, Chapter 8.2.3; and Figures 8.51-53, Chapter 8.2.3).

9.1.2 FE predictions of laser cut and 3D printed cellular mesh cylinders

Cylinders consisting of auxetic and conventional hexagonal honeycombs (Tables 6.6, Chapter 6) were laser cut and 3D printed. The Auxetic 8 (laser cut), Conventional 8 (laser cut), Conventional 10 (laser cut), and Conventional 12 (3D printed) models were simulated to predict the expansion capabilities of the experimental cylinders in this section. FE predictions in the forms of ERD vs AD (Figures 9.10), ERD vs axial tension and compressive force (Figure 9.11) and ERD vs axial strain (Figures 9.12) are plotted. Radial (left) and axial (right) deformation stills are shown as inserts in Figure 9.10. They will be compared with the experimental data in Sections 9.3 and 9.4.3.

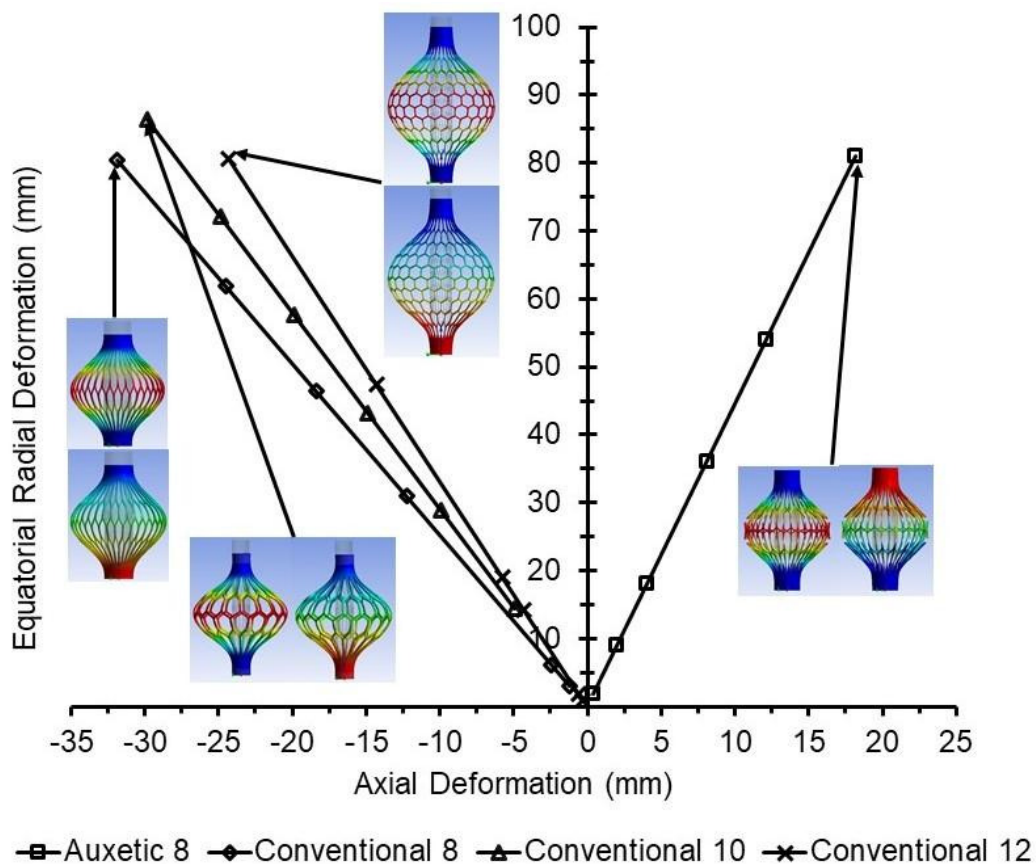


Figure 9.10: FE predictions of laser cut and 3D printed auxetic and conventional honeycomb mesh models (ERD vs AD). Stills of ERD (left) and AD (right) are shown. Tensile and compressive axial deformation applied for cellular models consisting of auxetic and conventional honeycomb meshes, respectively.

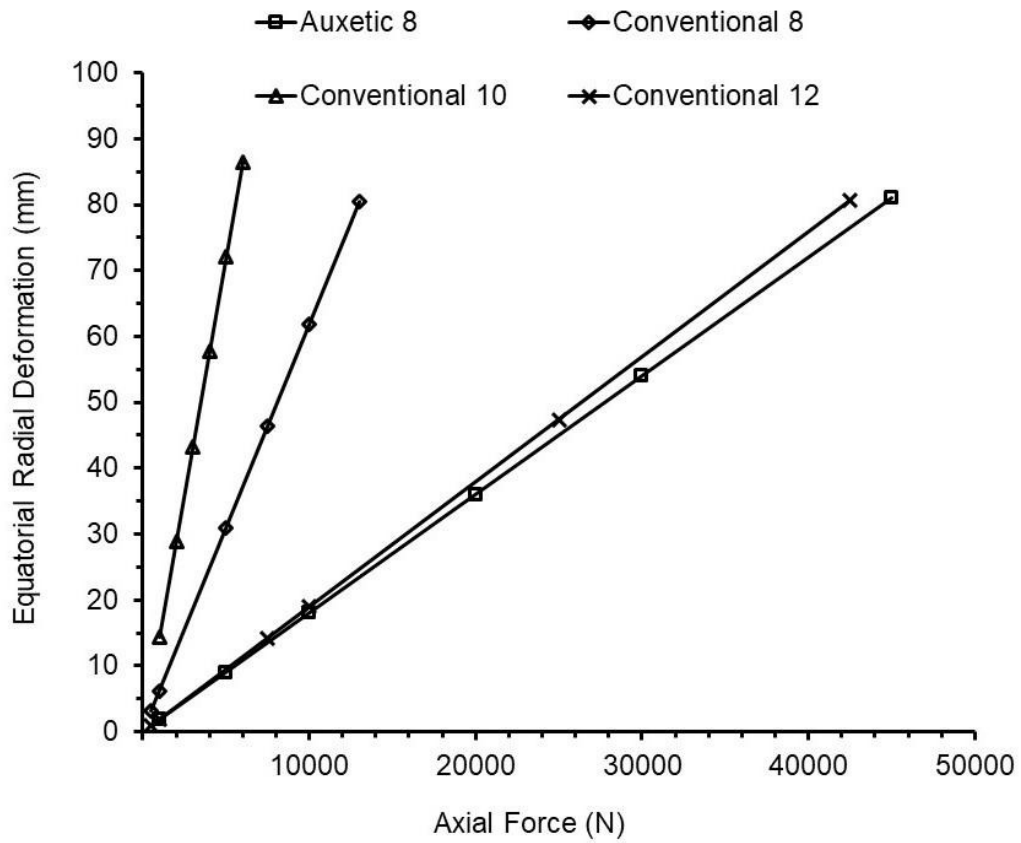


Figure 9.11: FE predictions of laser cut and 3D printed auxetic and conventional honeycomb mesh models (ERD vs Axial force). Axial tensile force for Auxetic 8 model and axial compressive force for Conventional 8, Conventional 10 and Conventional 12 cylinders.

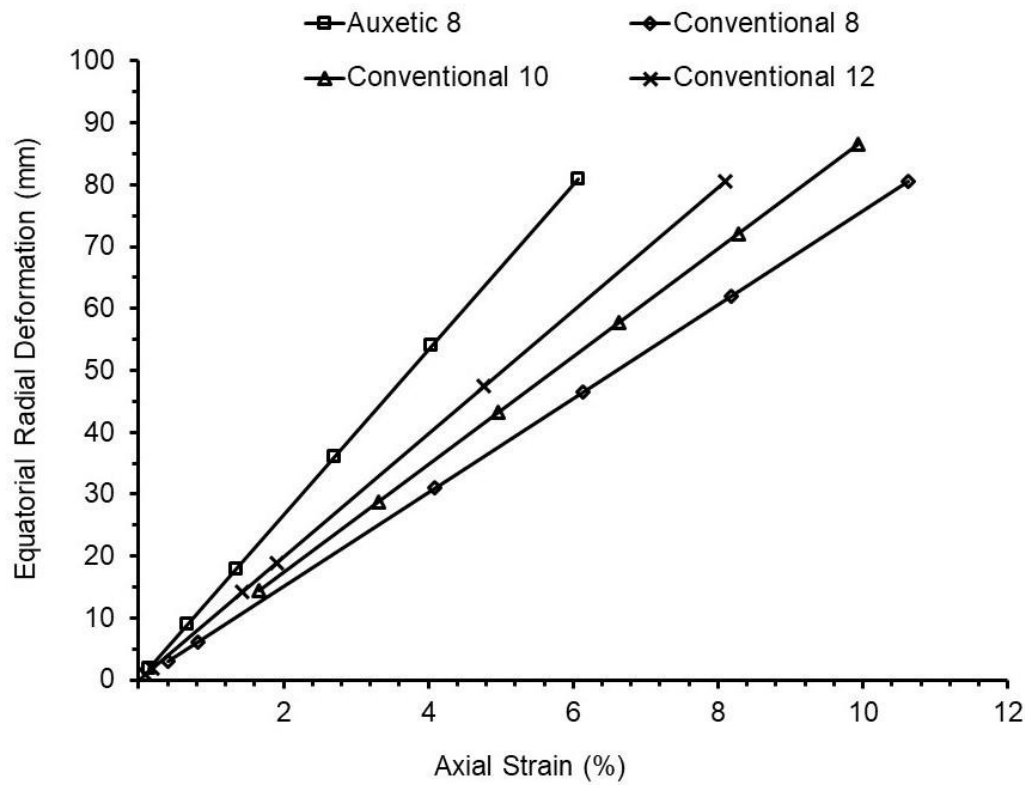


Figure 9.12: FE predictions of laser cut and 3D printed auxetic and conventional honeycomb mesh models (ERD vs Axial strain). Axial tensile strain for Auxetic 8 model and axial compressive strain for Conventional 8, Conventional 10 and Conventional 12 cylinders.

9.1.3 Relationships between global, RVE and cellular mesh parameters

Relationships of mechanical properties with the global, RVE and cellular mesh parameters are established in this section for the fixed global parameters (40mm outer diameter, 2.5mm wall thickness and 300mm length of cylinder). The different aspect ratios (h/l) of the cellular meshes (conventional and auxetic hexagonal honeycombs) are considered to achieve the target mechanical properties (Young's moduli, shear moduli and Poisson's ratios) graphically for the specified α .

Cellular mesh parameters as way of example were graphically obtained for the different RVE and aspect ratios (h/l) of the cellular meshes and fixed global parameters. Additionally, 20mm outer diameter is considered to obtain cellular mesh parameters for the different RVE and aspect ratios (h/l) which would be outer diameter for the proposed laparoscopic device.

Auxetic honeycomb cylinders:

The FE modelling of solid wall cylinder consisting of in-plane negative Poisson's ratio has suggested target mechanical properties (E_z/E_θ and $\nu_{z\theta}$) for cylinders with pronged cone end pieces (for uniaxial compression mechanism) and without end pieces (uniaxial tension mechanism) to achieve large equatorial deformation for small axial displacement (Chapter 8). The target mechanical properties for cylinders with pronged cone end pieces and without end pieces are obtained graphically for specified α by varying aspect ratios (h/l) of the auxetic honeycombs ($h/l=2, 4, 10$ and 40) in this section and their relationship with cellular mesh parameter (α) is established by plotting E_z/E_θ and $\nu_{z\theta}$ against α (Figure 9.13).

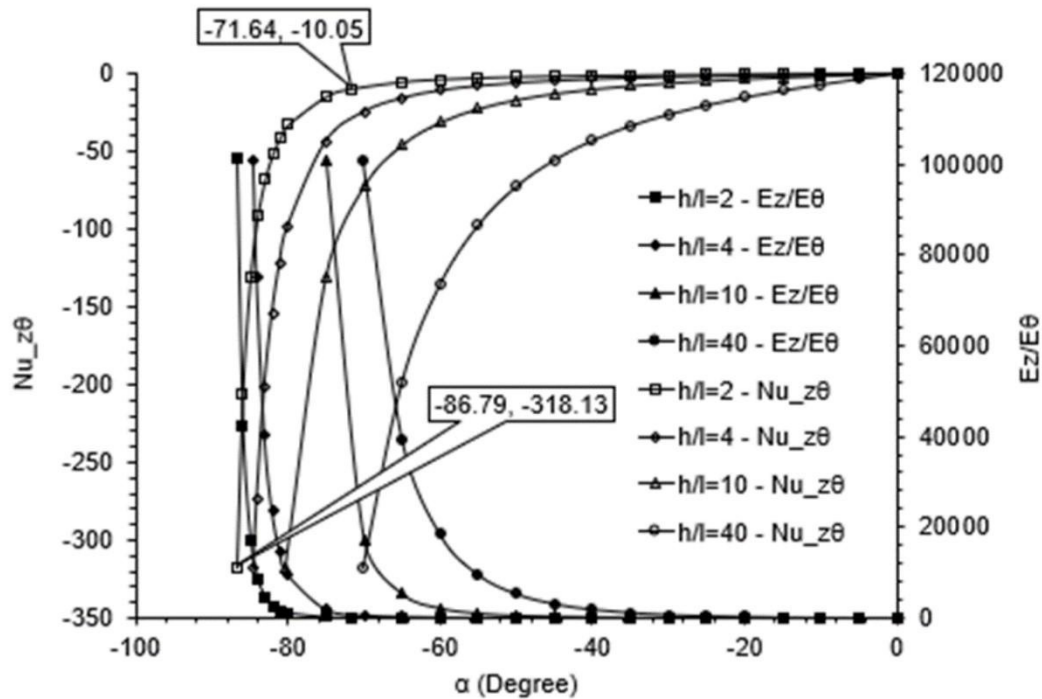


Figure 9.13: Relationship of the mechanical properties (E_z/E_θ and $\nu_{z\theta}$) with the cellular mesh parameter (α) for the different aspect ratios (h/l) of auxetic honeycombs.

Auxetic honeycomb cylinders with pronged cone end pieces (uniaxial compression mechanism) and without end pieces (uniaxial tension mechanism) can be designed for $-90 \leq \alpha \leq -86.79$ ($h/l=2$) and $-90 \leq \alpha \leq -71.64$ ($h/l=2$) (Figure 9.13), respectively for the specified global and RVE parameters presenting the

infinite possibilities to design cellular cylinders that can achieve the large equatorial deformation for small axial deformation.

As way of example, auxetic honeycomb mesh parameters were graphically obtained for the fixed global parameters of cylinder (40mm and 20mm outer diameter, 2.5mm wall thickness and 250mm length), RVEs ($N_v = 6$), t_h (2.5mm) and t_l (2mm). The target α (revealed from Figure 9.13) was obtained by varying N_c (RVE) for the different aspect ratios and is then plotted against N_c/N_v and $v_{z\theta}$ (Figure 9.14).

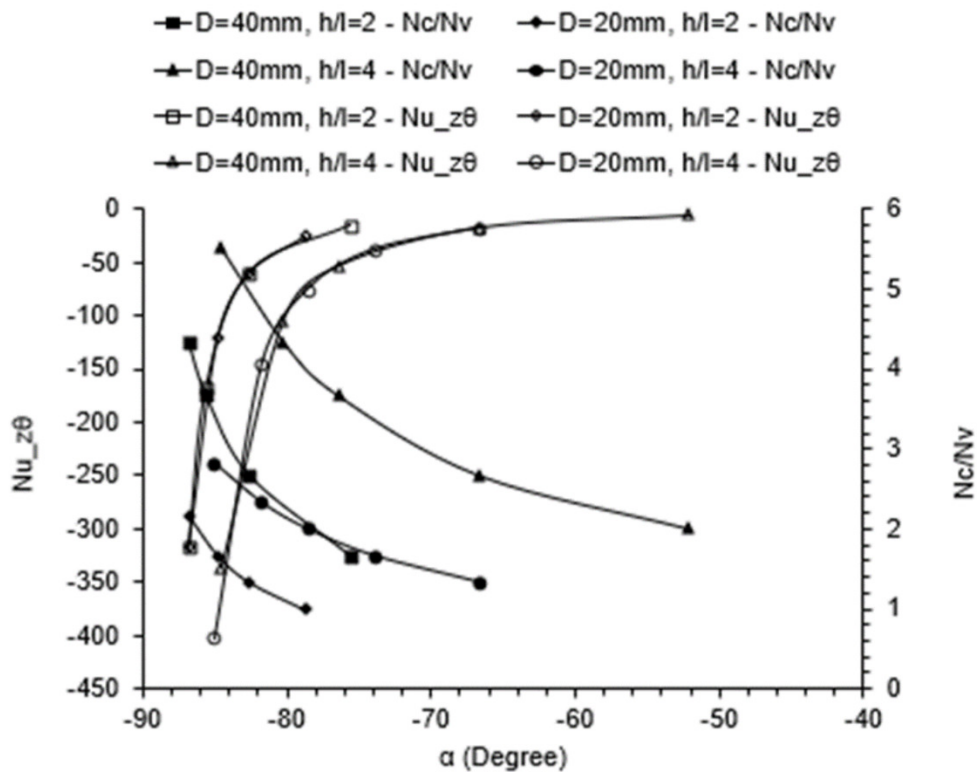


Figure 9.14: Relationship of the mechanical property ($v_{z\theta}$) and RVE (N_c/N_v) with the cellular mesh parameter (α) for the different aspect ratios (h/l) of auxetic honeycombs and outer diameters of the cylinder.

Target α was obtained for outer diameters (40mm and 20mm) of cylinder and aspect ratios ($h/l=2$, $h/l=4$) of auxetic honeycombs (Figure 9.14) which in turn meets the target mechanical properties – as shown in Figure 9.13 – required for the large equatorial deformation for small axial deformation for cylinder with pronged cone end pieces and without end pieces. Outer diameter of cylinder (global parameter) does not affect the cellular parameter (α), which is valid for

different aspect ratio of auxetic honeycombs (Figure 9.14). However, outer diameter of cylinder does impact the RVEs (N_c/N_v) as expected, for instance, the number of RVEs (N_c/N_v) required for 20mm outer diameter is half compared to 40mm outer diameter irrespective of aspect ratios of auxetic honeycombs (Figure 9.14).

The relationship of RVEs with the auxetic honeycomb mesh parameters can be obtained by plotting W and t/l against N_c/N_v (Figure 9.15 and Figure 9.16, respectively).

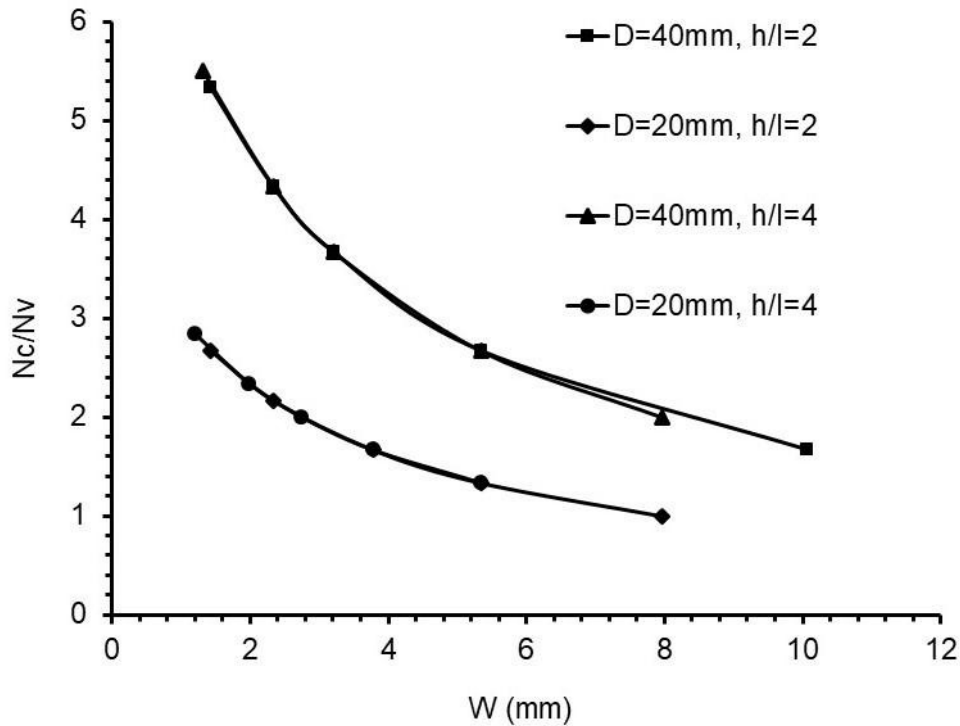


Figure 9.15: Relationship of RVE (N_c/N_v) with the cellular mesh parameter (W) for the different aspect ratios (h/l) of auxetic honeycombs and outer diameters of the cylinder.

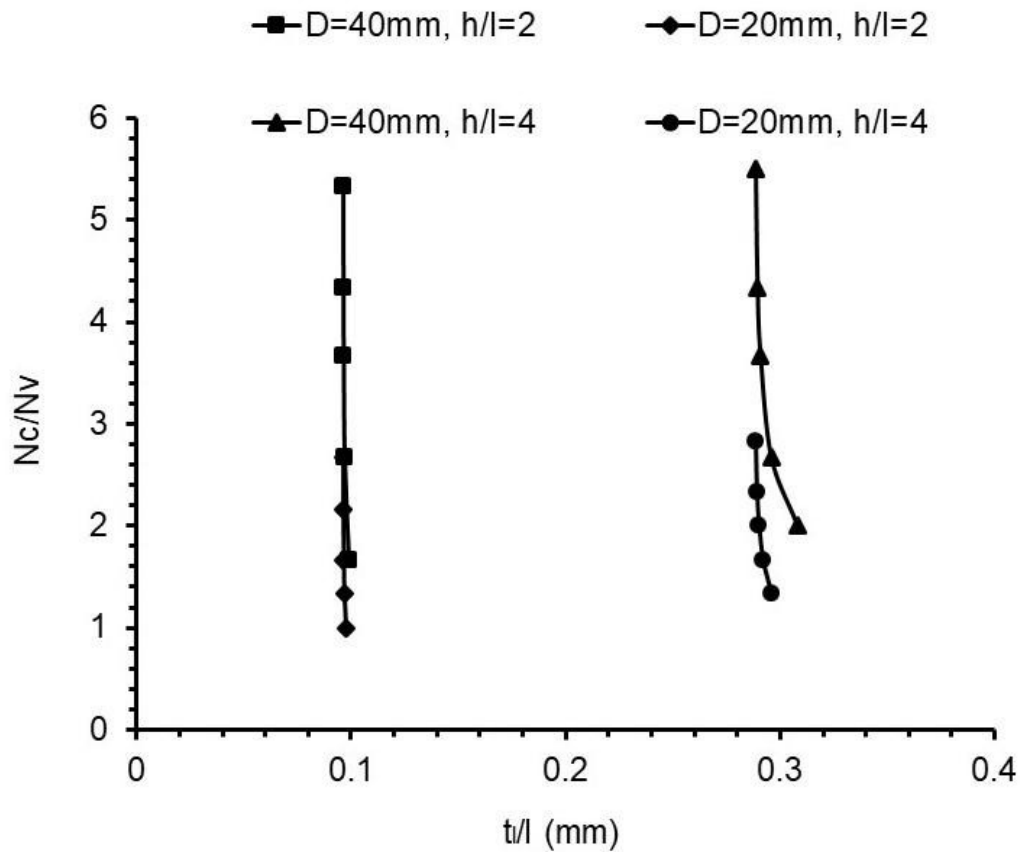


Figure 9.16: Relationship of RVE (N_c/N_v) with the cellular mesh parameter (t/l) for the different aspect ratios (h/l) of auxetic honeycombs and outer diameters of the cylinder.

Cellular (auxetic) mesh parameter (W) substantially decreases with the increase in the RVEs (N_c/N_v) irrespective of outer diameters of cylinder and aspect ratios of auxetic honeycombs which would be useful trend to consider during laser cutting (fabrication method) of auxetic cylinders. Cellular (auxetic honeycomb) mesh parameter (t/l) marginally decreases with the increase in the RVEs (N_c/N_v) (Figure 9.16). When aspect ratios changed from $h/l=2$ to $h/l=4$, t/l was increased from ~ 0.1 to ~ 0.3 which is essential to consider to ensure cellular meshes obey the flexure model of Gibson and Ashby⁽¹¹³⁾ (Figure 9.16). The outer diameter of the cylinder (20mm and 40mm) does not affect t/l .

Conventional honeycomb cylinders:

The FE modelling of solid wall cylinder consisting of in-plane positive Poisson's ratio has suggested target mechanical properties (E_z/E_θ and $\nu_{z\theta}$) for cylinder without end pieces (uniaxial compression mechanism) to achieve large

equatorial deformation for small axial displacement (Chapter 8). The target mechanical properties are obtained graphically for specified α by varying aspect ratios (h/l) of the conventional honeycombs ($h/l=1, 0.33$ and 0.033) in this section and relationship of target mechanical properties with cellular mesh parameter (α) is established by plotting E_z/E_θ and $\nu_{z\theta}$ against α (Figure 9.17).

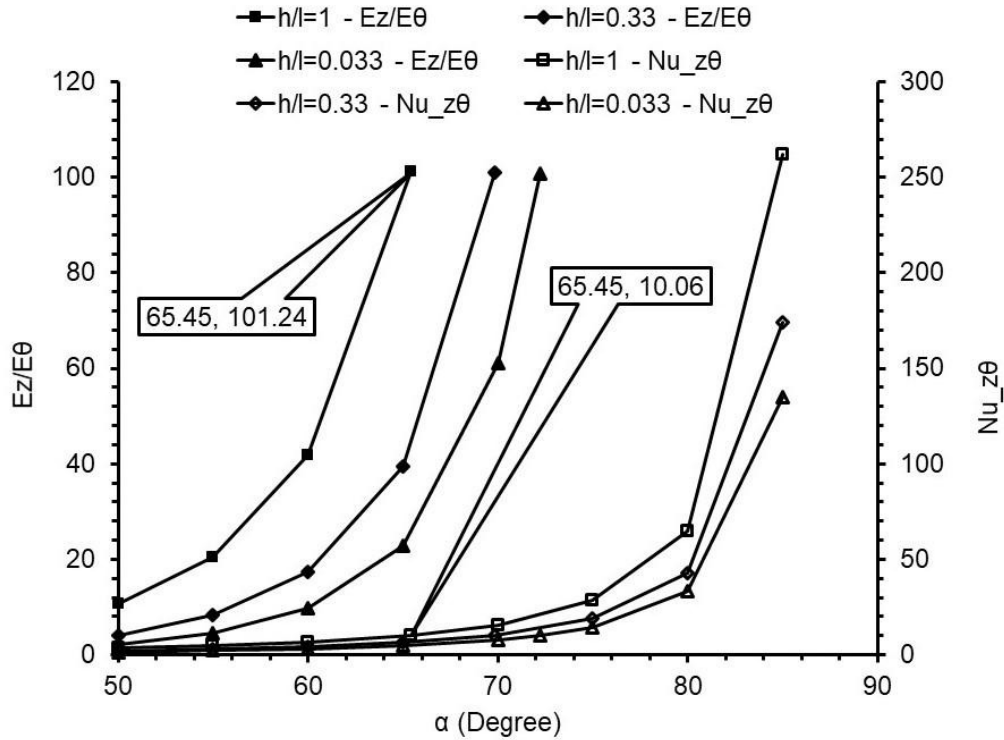


Figure 9.17: Relationship of the mechanical properties (E_z/E_θ and $\nu_{z\theta}$) with the cellular mesh parameter (α) for the different aspect ratios (h/l) of conventional honeycombs.

Conventional honeycomb cylinders without end pieces (uniaxial compression mechanism) can be designed for $65.5 \leq \alpha \leq 90$ ($h/l=1$), $69.8 \leq \alpha \leq 90$ ($h/l=0.33$) and $72.2 \leq \alpha \leq 90$ ($h/l=0.033$) (Figure 9.17) for the specified global and RVE parameters presenting the infinite possibilities to design cellular cylinders that can achieve the large equatorial deformation for small axial deformation.

As way of example, conventional honeycomb mesh parameters were graphically obtained for the fixed global parameters of cylinder (40mm and 20mm outer diameter, 2.5mm wall thickness and 250mm length), RVEs ($N_v = 6$), t_h (2.5mm) and t_l (2mm). The target α (revealed from Figure 9.17) was

obtained by varying N_c (RVE) for the different aspect ratios and is then plotted against N_c/N_v and v_{z0} (Figure 9.18).

Target α was graphically obtained for different outer diameters of cylinder and aspect ratios of conventional honeycombs (Figure 9.18) which in turn meets the target mechanical properties – as shown in Figure 9.17 – required for the large equatorial deformation for small axial deformation. Outer diameter of cylinder, a key global parameter, does not affect the cellular parameter (α) (Figure 9.18). However, the number of RVEs (N_c/N_v) required for 20mm outer diameter is half as expected compared to 40mm outer diameter (Figure 9.18).

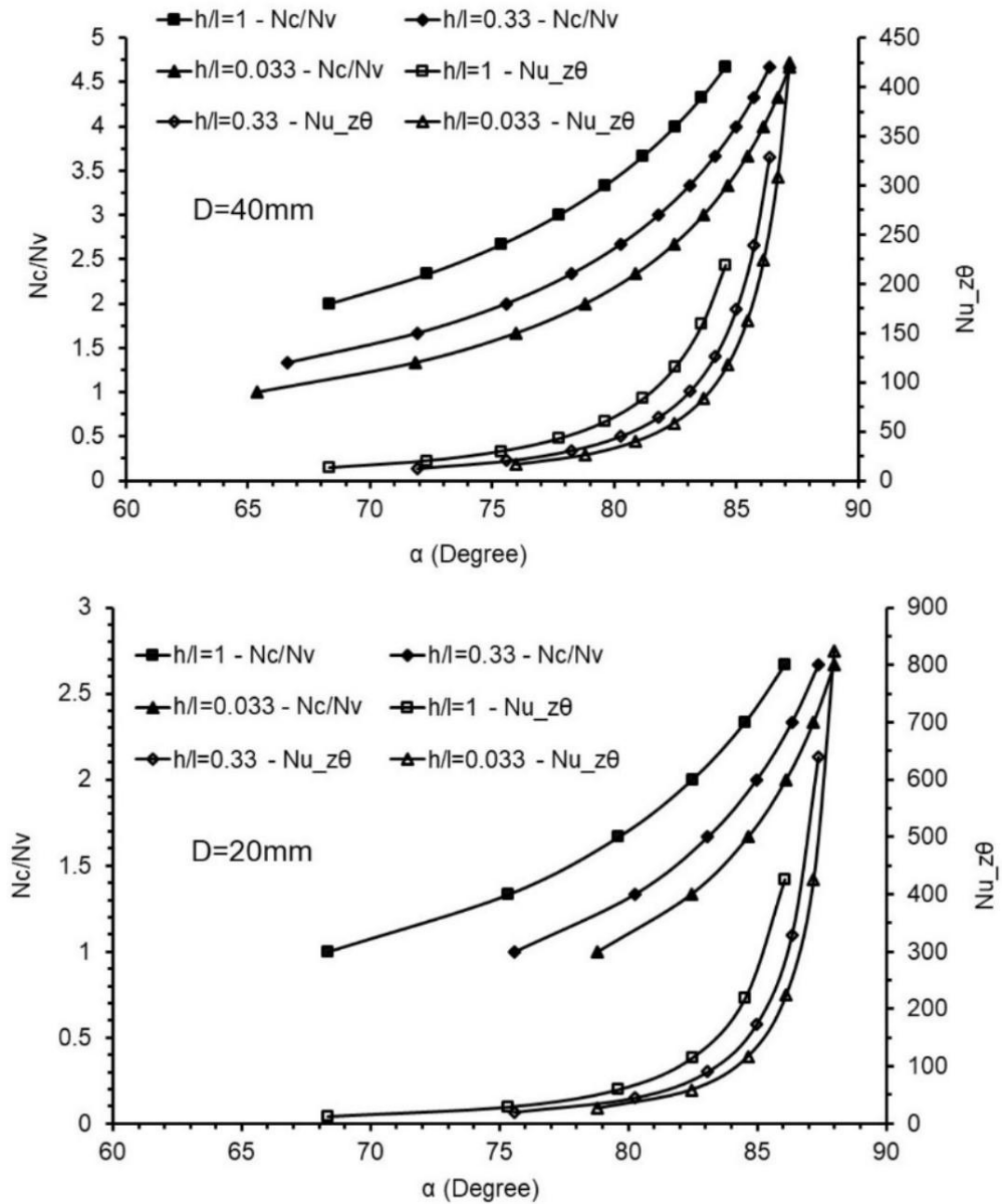


Figure 9.18: Relationship of the mechanical property ($\nu_{z\theta}$) and RVE (N_c/N_v) with the cellular mesh parameter (α) for the different aspect ratios (h/l) of conventional honeycombs and outer diameters of the cylinder.

The relationship of RVEs with the conventional honeycomb mesh parameter was obtained by plotting t_l/l against N_c/N_v for different aspect ratios (Figure 9.19). Cellular (conventional honeycomb) mesh parameter (t_l/l) marginally increases with the increase in the RVEs (N_c/N_v) (Figure 9.19) for different aspect ratios. When the aspect ratio (from $h/l=1$ to $h/l=0.033$) and t_l ($t_l = 2\text{mm}$ to

$t_l=0.5\text{mm}$) decreases, t_l/l decreases (Figure 9.19) which is essential for ensuring cellular meshes obey flexure model of Gibson and Ashby⁽¹¹³⁾.

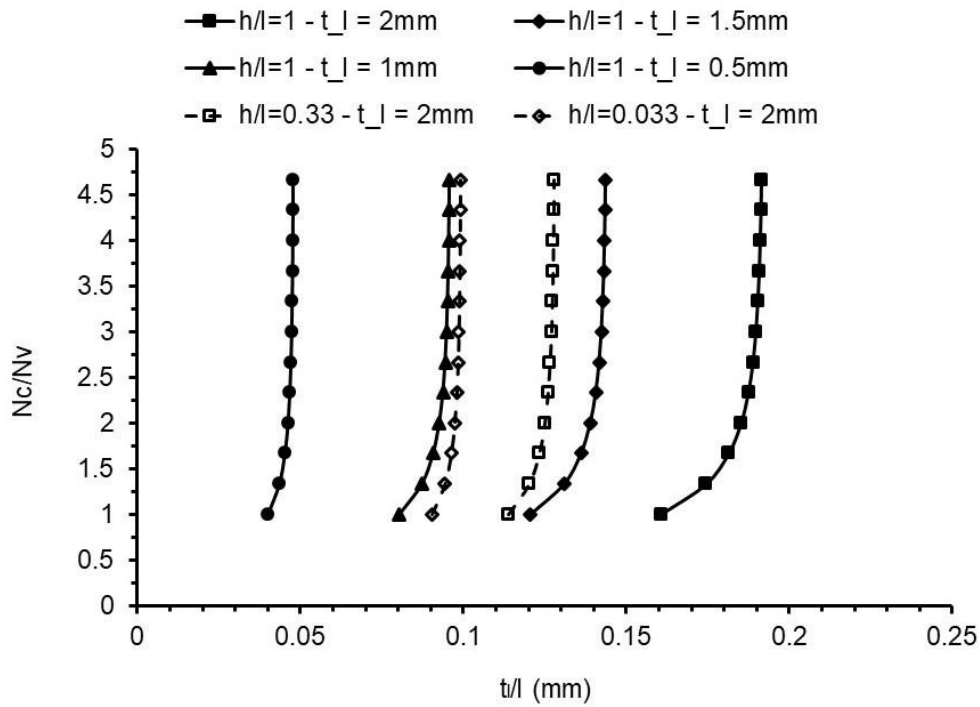


Figure 9.19: Relationship of RVE (N_c/N_v) with the cellular mesh parameter (t_l/l) for the different aspect ratios (h/l) and t_l of conventional honeycombs.

Summary:

Relationships of mechanical properties with the global, RVE and cellular mesh parameters were obtained graphically for different aspect ratios of auxetic and conventional honeycombs. The infinite possibilities to design cellular cylinders using conventional and auxetic honeycombs that can achieve the large equatorial deformation for small axial deformation were identified. Additionally, the impact of the relationship between RVE and cellular mesh parameters was explained for the design and fabrication of cellular cylinders.

9.2 Fabrication of cellular mesh cylinders

Cellular mesh cylinders were fabricated using 3D printing and laser cutting equipment. Additionally, cylinders consisting of beams/strips were laser cut. They are collectively referred as ‘expansion mechanisms’.

Laser cut cellular mesh cylinders:

The Auxetic 8-9 and Conventional 6-9 models (Table 6.6, Chapter 6) were laser cut from PVC tubes and are displayed in Figure 9.20. Fillets were introduced to round off sharp edges of the diagonal ribs of auxetic honeycombs (Auxetic 8-9 models) prior to the laser cutting process. The Conventional 10-11 models (Table 6.6, Chapter 6) were laser cut from PP tubes and are shown in Figure 9.21. Pictures displayed in Figures 9.20-22 were taken after initial application of axial compressive force by hand.

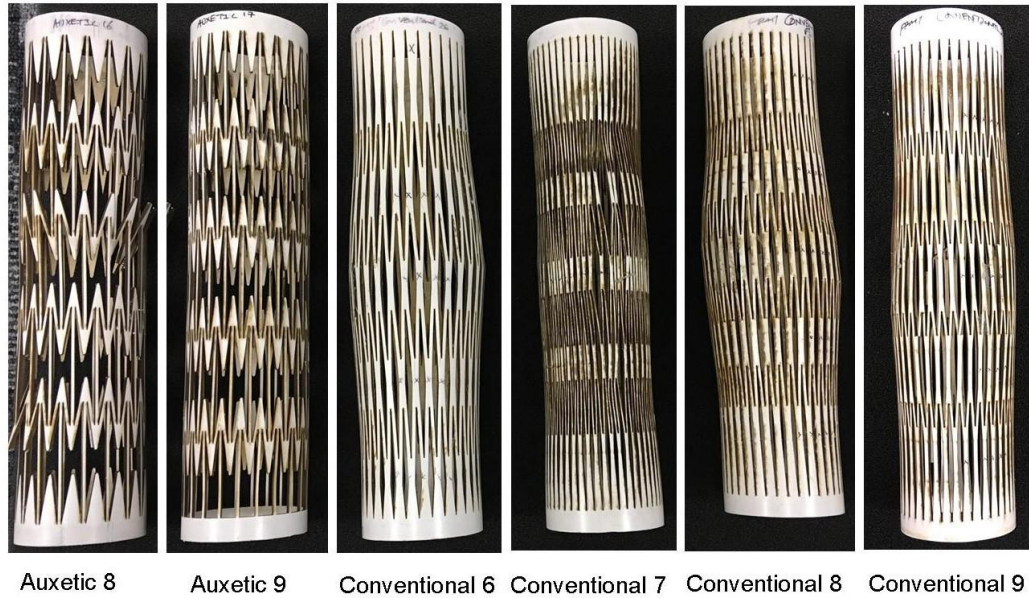
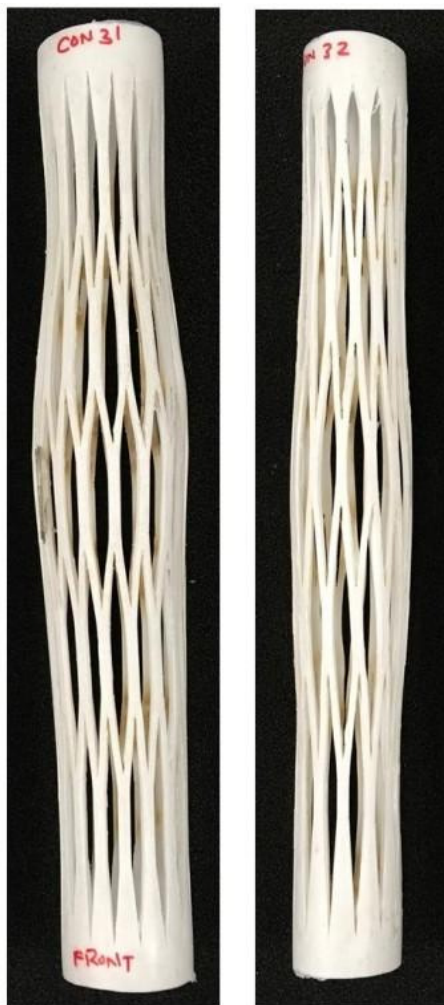


Figure 9.20: Laser cut PVC cellular mesh tubes.



Conventional 10 Conventional 11

Figure 9.21: Laser cut PP cellular mesh tube.

Laser cut cylinders consisting of beams/strips:

Beam 1 and Beam 2 cylinders (Table 6.7, Chapter 6) were laser cut from PP tubes and are presented in Figure 9.22.



Beam 1

Beam 2

Figure 9.22: Laser cut PP cylinders consisting of beams/strips.

3D printed cellular mesh cylinders:

The Conventional 12 cylinder (Table 6.7, Chapter 6) was 3D printed using DurusWhite™ material and is presented in Figure 9.23.

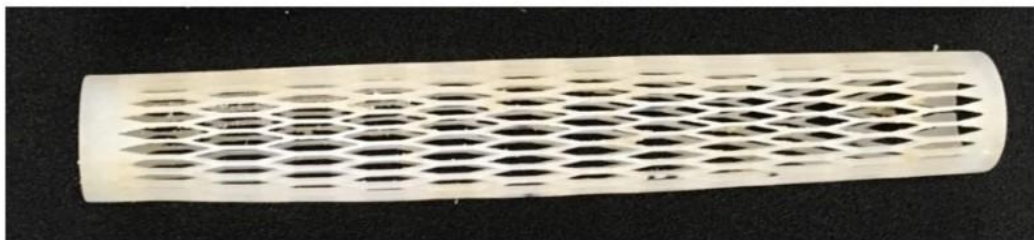


Figure 9.23: 3D printed cellular mesh cylinder.

Summary:

The expansion mechanisms were fabricated using laser cut and 3D printed techniques. The laser cut PVC and PP tubes were characterised in the Instron machine, as reported in the next section.

9.3 Characterisation of experimental expansion mechanisms

The expansion mechanisms were characterised in the absence of a surrounding material using the Instron machine and the results are described in this section. Additionally, the equatorial deformation of the Conventional 8 and Beam 2 cylinders were determined, and correlated with the applied axial deformation, from selected stills of the corresponding video footage using the ImageJ(225) image analysis software. Finally, the experimental expansion mechanism data are compared with the FE predictions (reported in Chapter 9.1.2) in this section.

9.3.1 Mechanical characterisation

The Auxetic 8 cylinder was subjected to uniaxial tension while the Conventional 6-9 and Beam 1-2 cylinders were uniaxially compressed in the Instron machine. The Conventional 12 (3D printed model) was brittle and hence not characterised mechanically. Axial force vs axial displacement and stress vs strain are plotted for the expansion mechanisms.

Axial force, axial deformation and tangent stiffness:

The axial compressive and tension forces are plotted against the corresponding displacement values (Figure 9.24). Stills extracted from video footage (at maximum axial deformation) are also presented in Figure 9.24. The expansion mechanisms show significant equatorial radial expansion (Figure 9.24) except for the Auxetic 8 cylinder which can be attributed to the issue of some of the cells coming out of the axial-circumferential plane. The Beam 1 cylinder was compressed axially for 20mm instead of 50mm due to the onset of plastic deformation of the beam strips (Figure 9.24).

The axial compressive or tension force required for activating the expansion mechanisms is initially high at small axial deformation and decreases as the axial deformation increases (Figure 9.24). This phenomenon gives a negative value of slope (called tangent stiffness) beyond the proportional limit of axial force vs axial displacement, corresponding to negative stiffness. The negative stiffness arises due to out-of-plane buckling of the cylinder wall and not due to any in-plane flexing, stretching or hinging of the mesh ribs.

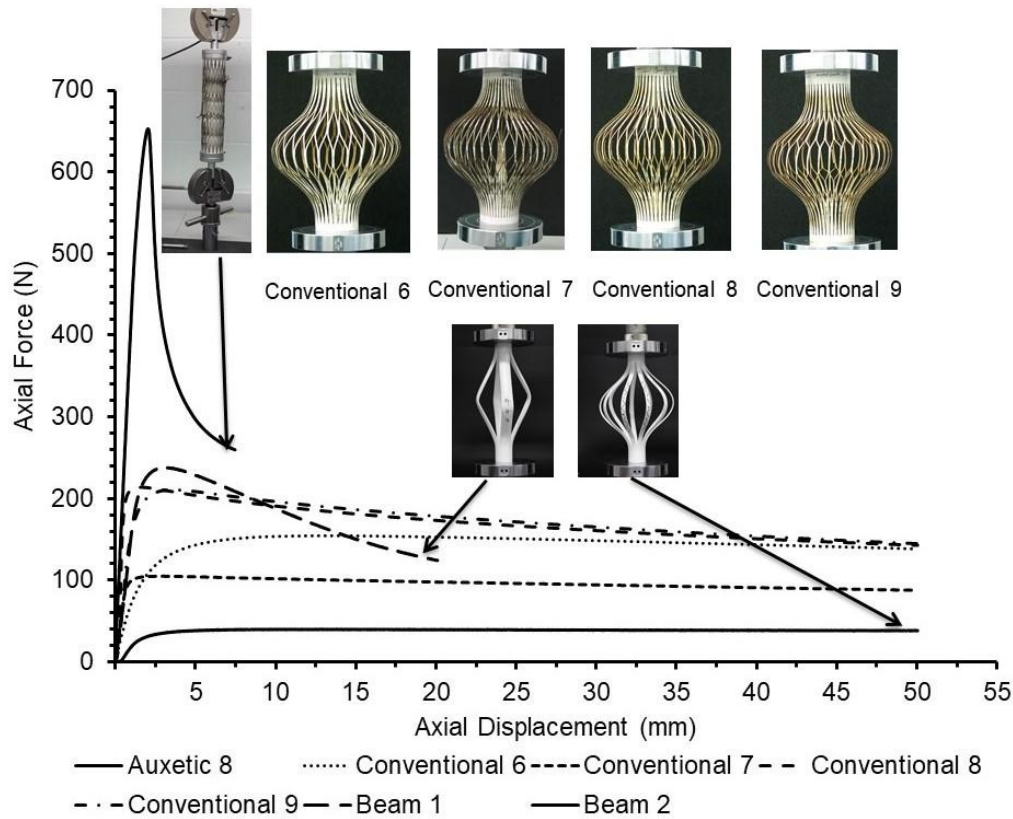


Figure 9.24: Axial force vs axial displacement curves of the expansion mechanisms. Axial tension force applied to the Auxetic 8 cylinder and axial compression forces applied to the Conventional 6-9 and Beam 1-2 cylinders. Stills showing expansion profiles are shown.

The axial force vs axial displacement responses of expansion mechanisms (Figure 9.24) are non-linear and hence, a polynomial fit to the entire displacement curve of the expansion mechanisms yielded low R^2 values (<0.70). Consequently, displacement-dependent stiffness curve was generated by considering adjacent data points of the force vs displacement curve, corresponding to the tangent stiffness. Tangent stiffness vs axial displacement curve was then plotted and shown in Figure 9.25 as split curves to show positive (Figure 9.25a) and negative (Figure 9.25b) tangent stiffness phenomenon.

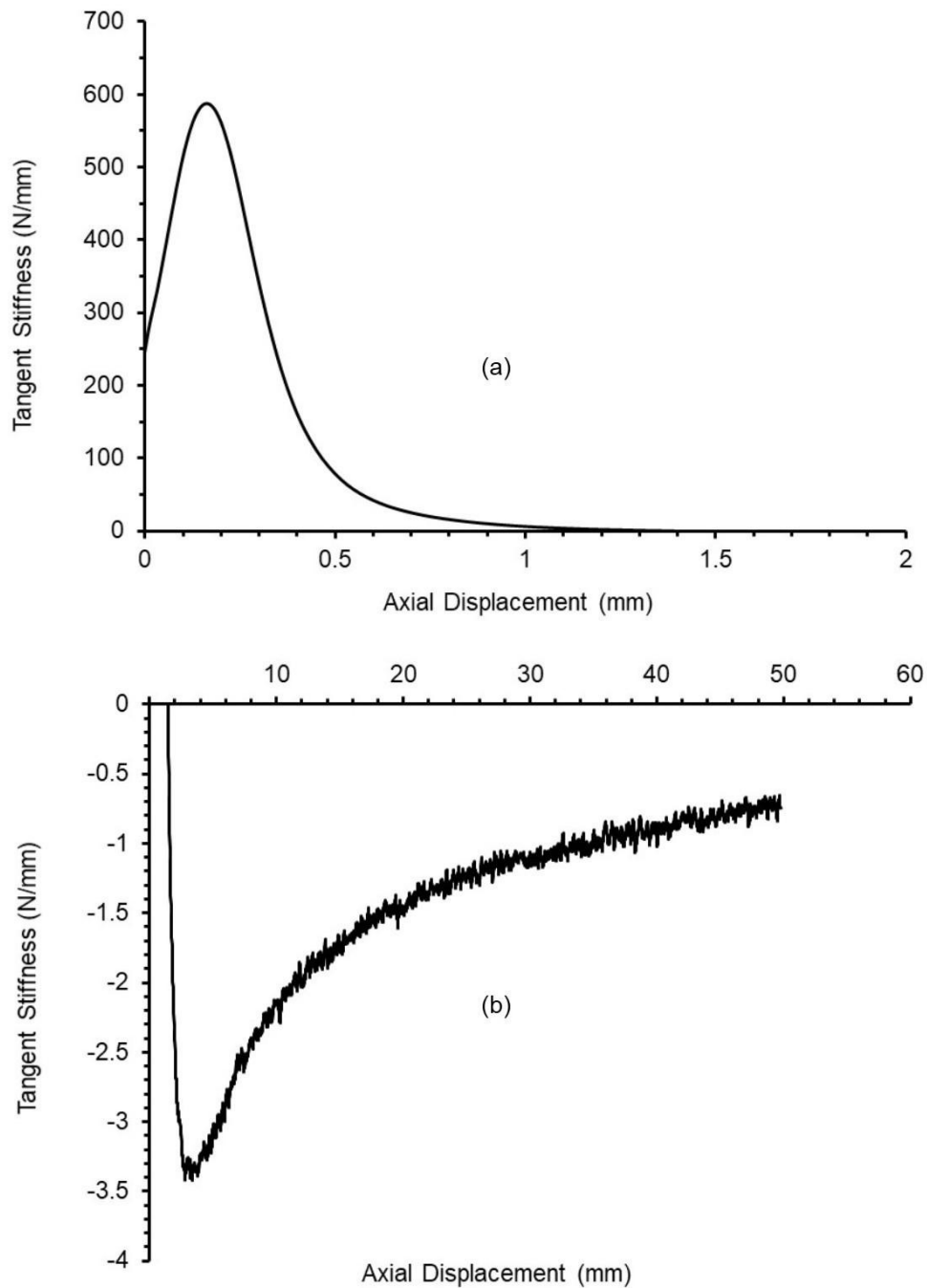


Figure 9.25: Tangent stiffness vs axial displacement curve of the Conventional 8 model characterised in the absence of a surrounding material.

Similarly, tangent stiffness curves of the other expansion mechanisms were obtained by considering adjacent data points of the corresponding force vs displacement curves and plotted against axial displacement to demonstrate positive (Figure 9.26a) and negative (Figure 9.26b) tangent stiffness phenomenon.

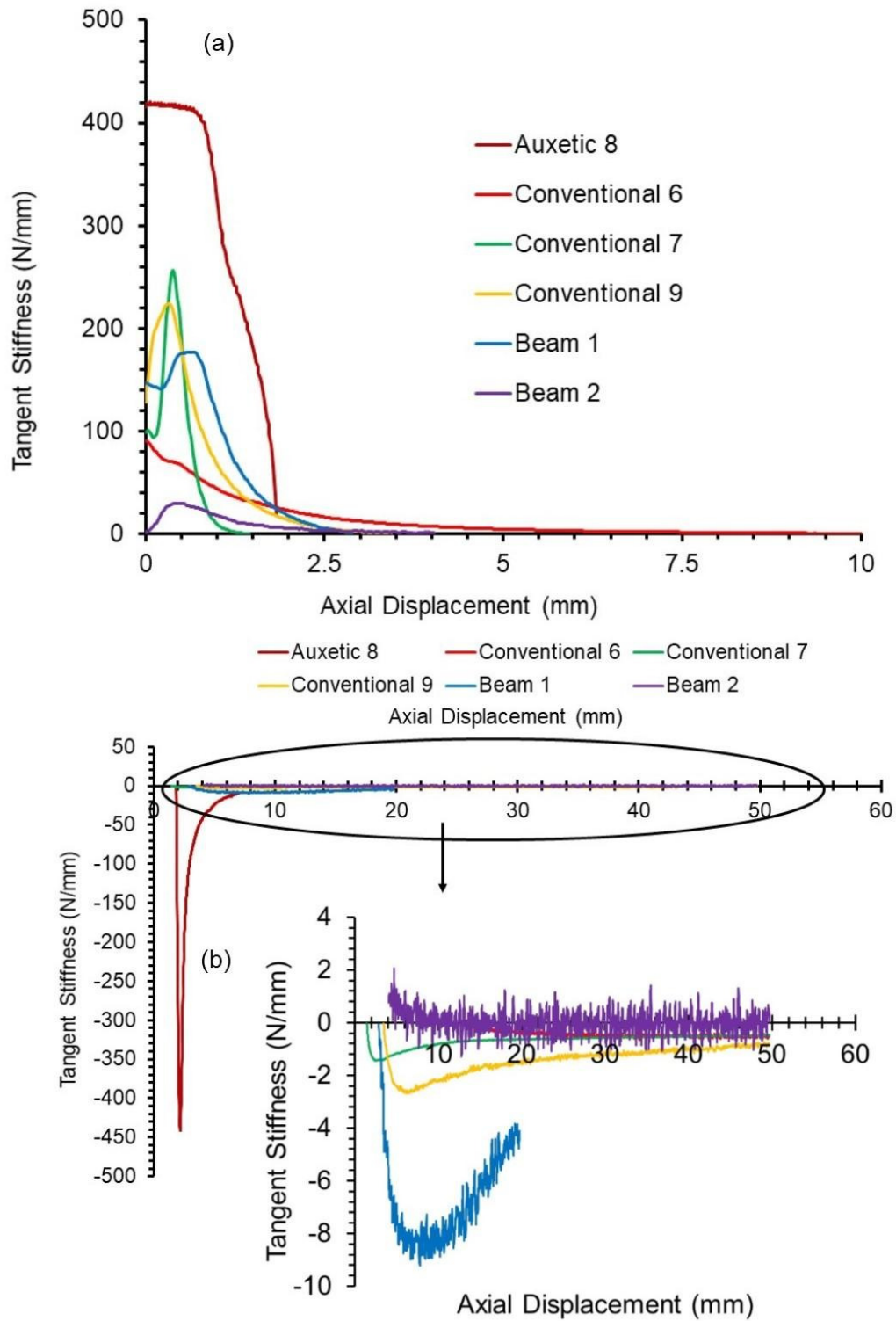


Figure 9.26: Tangent stiffness vs axial displacement curves of the expansion mechanisms.

Stress, strain and tangent modulus:

The axial forces applied to the expansion mechanisms were divided by the cross-sectional area ($\pi \cdot D \cdot T$) of the cylinder wall to obtain axial stresses. Axial

strains were obtained by dividing the axial displacement with the original length of cylinder. Axial stress vs axial strain was then plotted.

The axial compressive and tensile stresses required for activating the expansion mechanisms are initially high at small axial strain and decrease as the axial strain increases (Figure 9.27). This phenomenon gives a negative value of slope (called tangent modulus) beyond the proportional limit of axial stress vs axial strain, corresponding to negative modulus. The negative modulus, like negative stiffness, is due to out-of-plane buckling of the cylinder wall and not due to any in-plane flexing, stretching or hinging of the mesh ribs. Tangent modulus values for the expansion mechanisms unlike tangent stiffness are not reported in detail.

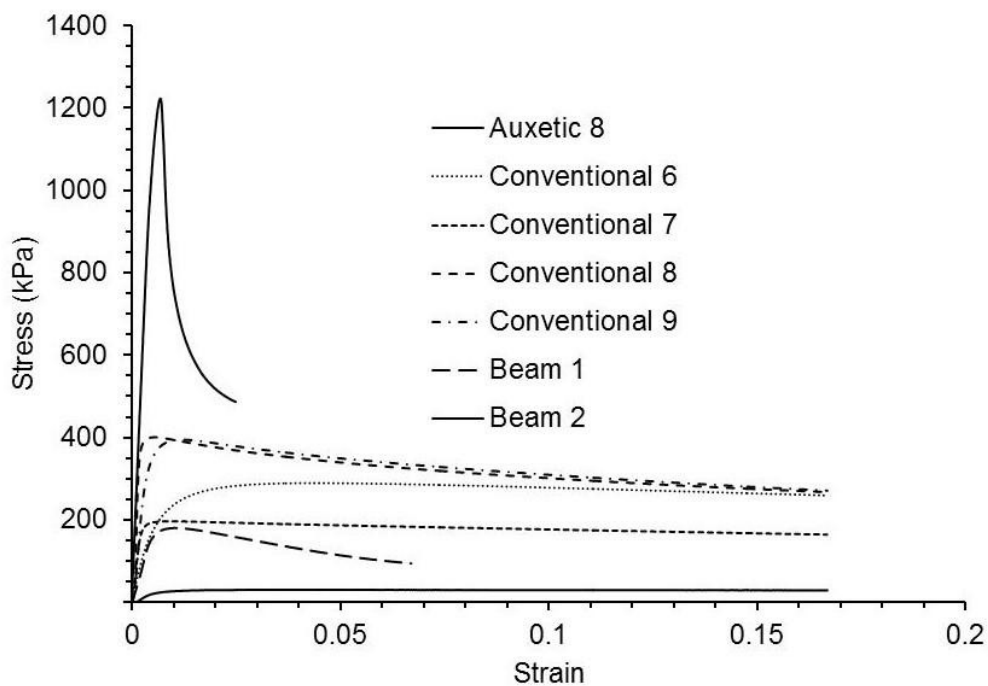


Figure 9.27: Stress vs strain curves of the expansion mechanisms.

Tensile stress and strain for the Auxetic 8 cylinder, and compressive stress and strain for the Conventional 6-9 and Beam 1-2 cylinders.

9.3.2 Calculation of equatorial deformations

Video footage of the mechanical testing of the expansion mechanisms was recorded. Image analyses of selected stills extracted from the video footage were carried out to calculate equatorial deformations for the expansion mechanisms.

Cellular mesh models:

The detailed image analysis of stills extracted from the video footage of the mechanical characterisation of the Conventional 8 cylinder is reported here by way of example. Stills at 0sec, 60secs, 120secs, 180secs, 240secs, and 304secs were extracted from the video footage and individually processed to measure the change in length and equatorial diameter of the cylinder. Length and diameter of the cylinder were measured three times (unit = pixel) when each individual image was imported into the ImageJ⁽²²⁵⁾ software, and average values were determined (Figure 9.28).

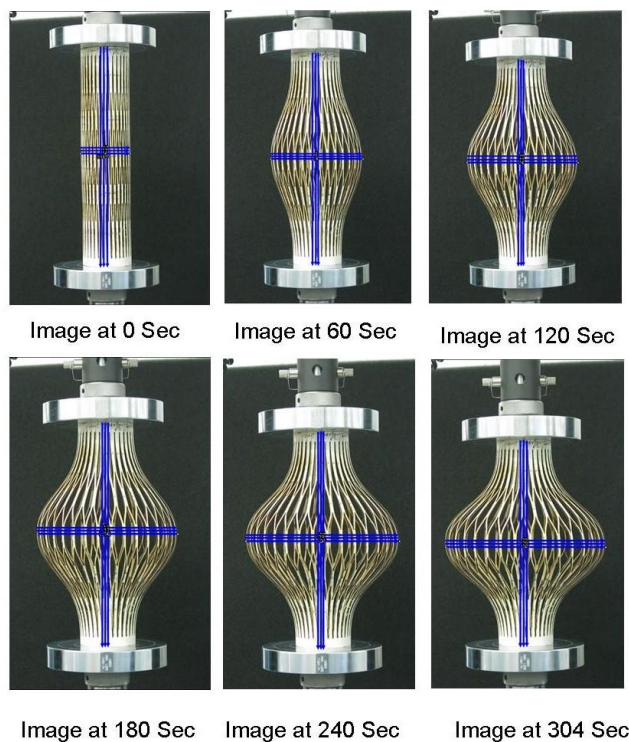


Figure 9.28: Image analysis of selected stills extracted from the video footage of the mechanical characterization of the Conventional 8 cylinder.

The image at 0 sec was calibrated in 'pixels' using length and outer diameter at equatorial region of cylinder ('known dimensions'). These pixel values of the image at 0 sec were multiplied with the 'known dimensions (300mm length and 68mm outer diameter)' to obtain two 'calibration factors'. Pixel values of length and diameter of selected stills were however converted into 'mm' using the 'calibration factor' obtained from the length of the cylinder. Equatorial radial deformation (ERD), axial deformation, and total equatorial deformation were

then obtained. ERD vs AD (Figure 9.29) and axial compressive force and total equatorial deformation vs axial deformation (Figure 9.30) are plotted. Error bars in Figure 9.29 represent standard deviation of the three measurements of length and equatorial diameter of the cylinder during image analysis.

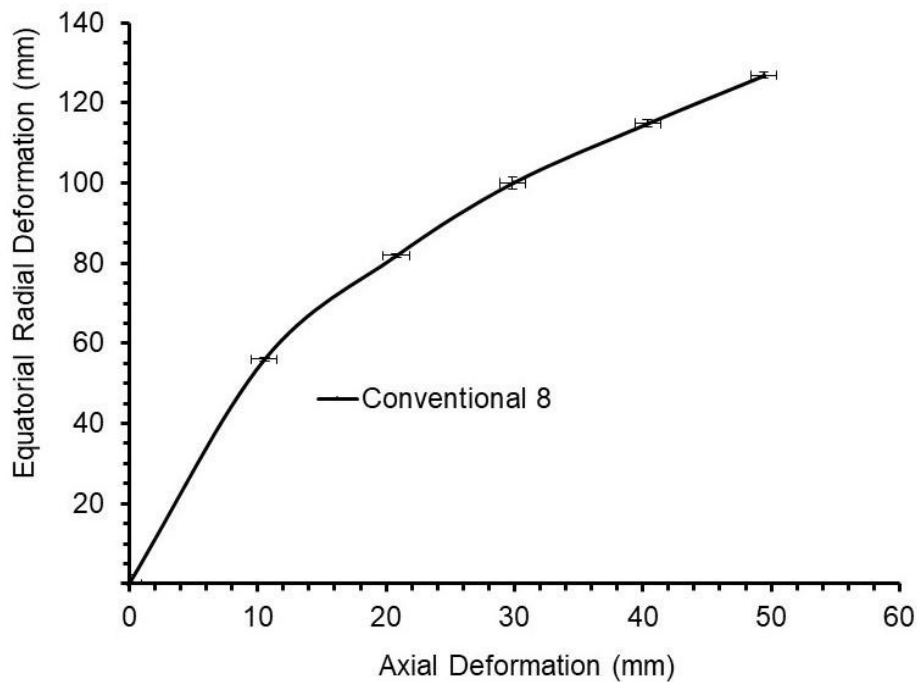


Figure 9.29: Equatorial radial deformation vs axial deformation curve for the Conventional 8 cylinder.

Large equatorial radial deformation (~125mm in Figure 9.29) is obtained at relatively small axial deformation (~50mm) for the Conventional 8 cylinder. Total equatorial deformation of ~200mm at ~50mm axial deformation (~16% axial strain) in Figure 9.30 achieves the degree of expansion (in order of 200mm) envisaged for the proposed laparoscopic device. Total equatorial deformation continues to increase with the increase in axial deformation and axial compressive force; however, there was approximately 25% of reduction in the axial compressive force applied between 10mm (~200N) and 50mm (~150N) of axial deformation of cylinder and with the increase from 100mm to 180mm of total equatorial deformation (Figure 9.30).

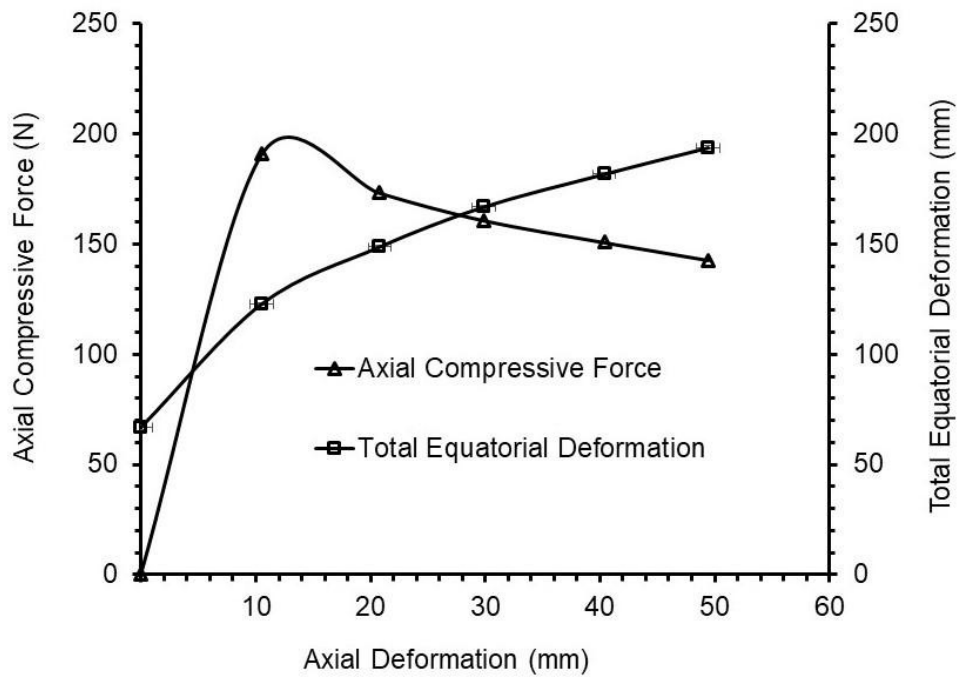


Figure 9.30: Axial compressive force and total equatorial deformation vs axial deformation curves showing the expansion capability of the Conventional 8 cylinder.

Similarly, selected stills from the video footage recorded during testing of the Conventional 6, 7, and 9 cylinders were analysed using the ImageJ⁽²²⁵⁾ software. Axial compressive force and total equatorial deformation vs axial deformation plots are shown in Figure 9.31 (Conventional 6), Figure 9.32 (Conventional 7) and Figure 9.33 (Conventional 9). Selected stills are also shown in Figures 9.31-9.33.

Total equatorial deformation of ~200mm at ~50mm axial deformation (~16% axial strain) in Figures 9.31-9.33 achieve the degree of expansion (in order of 200mm) envisaged for the proposed laparoscopic device. The degree axial compressive forces are in order of 200N for Conventional 6 and 9 models (Figure 9.31 and Figure 9.33, respectively) and 100 N for Conventional 7 model in Figure 9.32. Selective stills shown in Figures 9.31-33 demonstrate the expansion capabilities of Conventional 6, 7, and 9 models in the absence of surrounding materials.

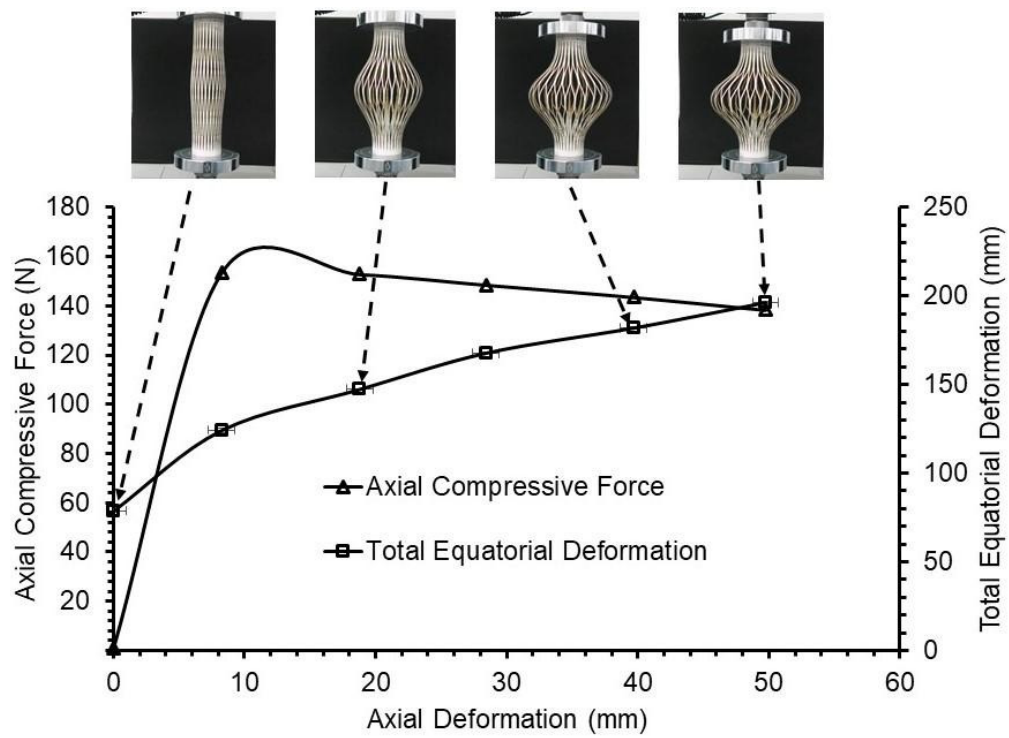


Figure 9.31: Axial compressive force and total equatorial deformation vs axial deformation curves showing the expansion capability of the Conventional 6 cylinder. Selective stills are also included.

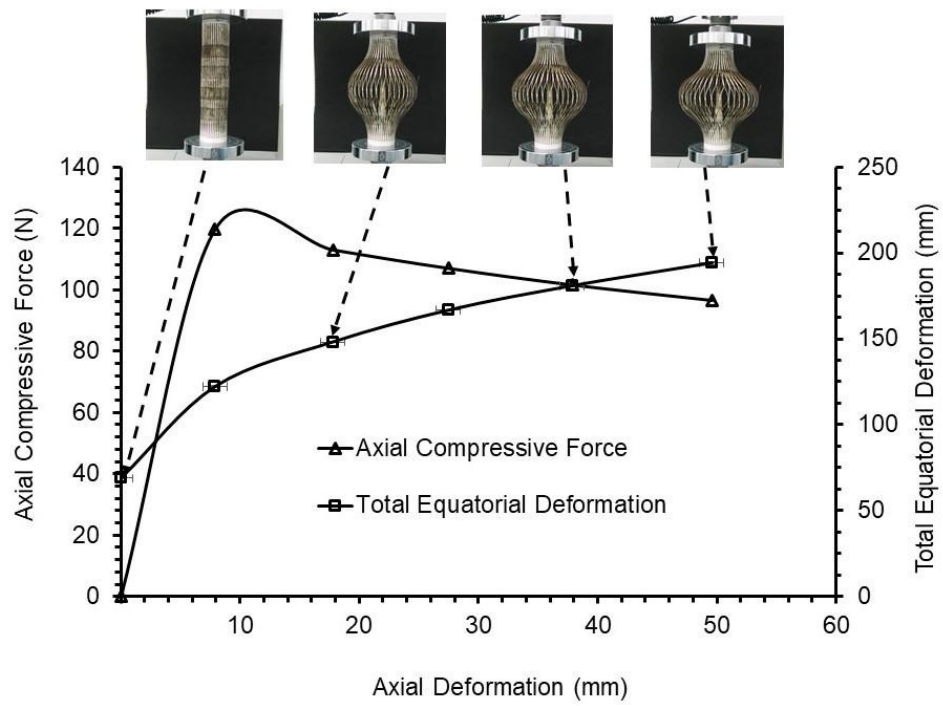


Figure 9.32: Axial compressive force and total equatorial deformation vs axial deformation curves showing the expansion capability of the Conventional 7 cylinder. Selective stills are also included.

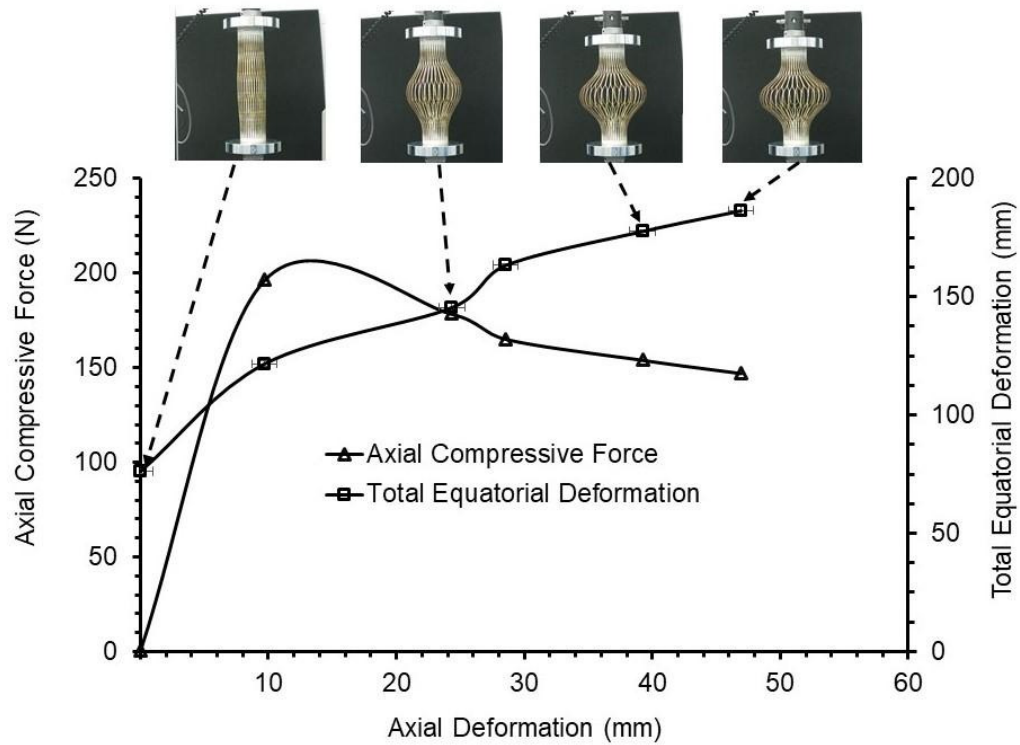


Figure 9.33: Axial compressive force and total equatorial deformation vs axial deformation curves showing the expansion capability of the Conventional 9 cylinder. Selective stills are also included.

Beam 1 and Beam 2 models:

Selected stills from the video footages recorded during testing of the Beam 1 and Beam 2 cylinders were analysed using the ImageJ⁽²²⁵⁾ software. ERD vs AD with selected stills and axial compressive force and total equatorial deformation vs axial deformation are plotted for Beam 2 model in Figure 9.34 and Figure 9.35, respectively. Likewise, axial compressive force and total equatorial deformation vs axial deformation plot for Beam 1 cylinder with the selected stills is depicted in Figure 9.36.

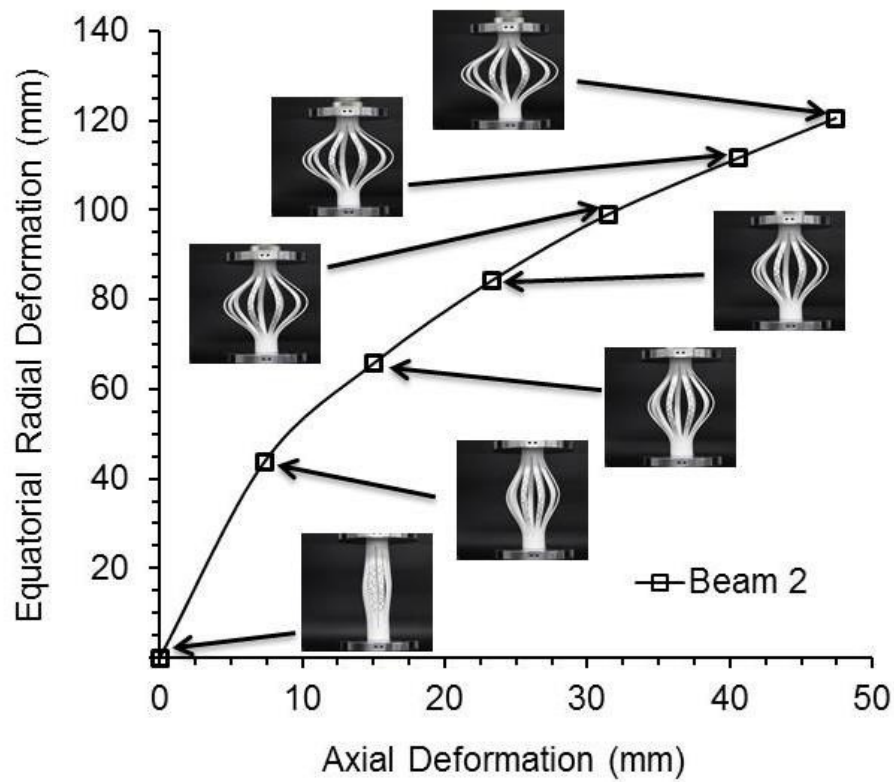


Figure 9.34: Equatorial deformation vs axial deformation curve for the Beam 2 cylinder.

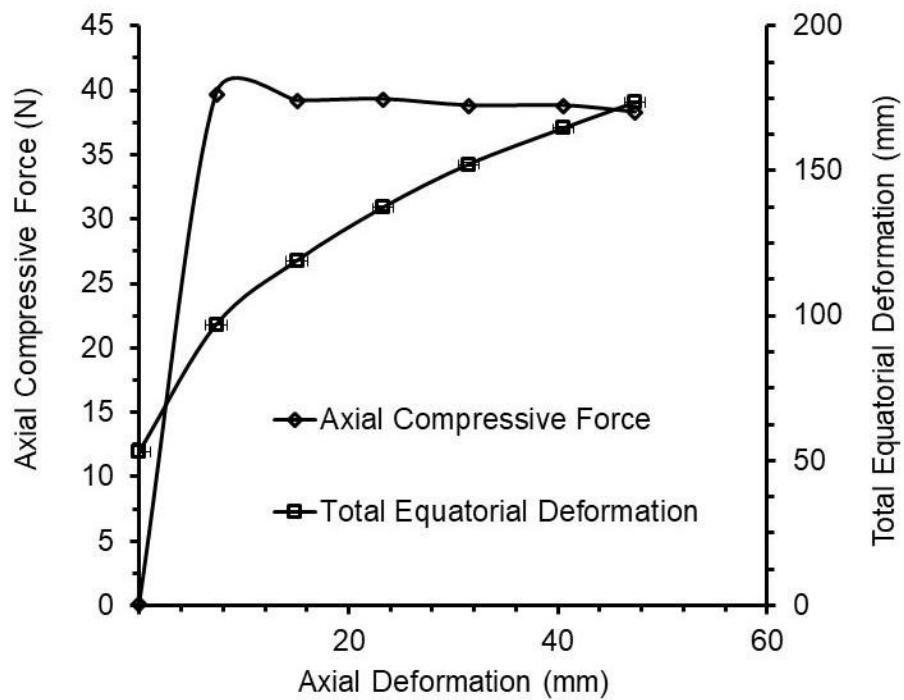


Figure 9.35: Axial compressive force and total equatorial deformation vs axial deformation curves showing the expansion capability of the Beam 2 cylinder.

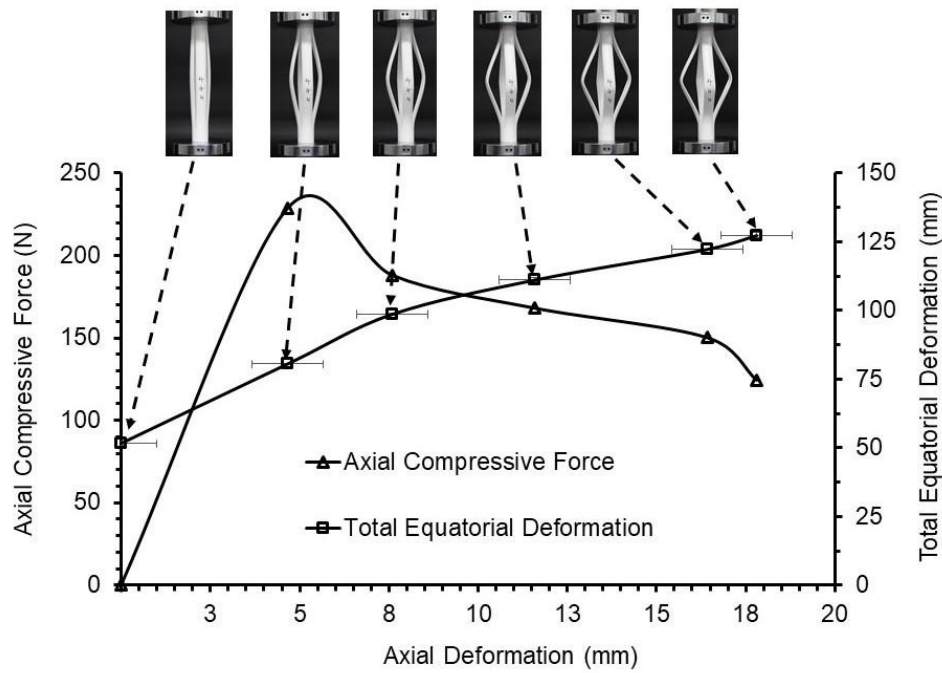


Figure 9.36: Axial compressive force and total equatorial deformation vs axial deformation curves showing the expansion capability of the Beam 1 cylinder. Selective stills are also included.

Large equatorial radial deformation (~120mm in Figure 9.34) is obtained at relatively small axial deformation (~50mm) for the Beam 2 cylinder. Total equatorial deformation of ~165mm at ~50mm axial deformation (~16% axial strain) in Figure 9.35 achieve the degree of expansion (in order of 200mm) envisaged for the proposed laparoscopic device. The total equatorial deformation for Beam 1 model is ~125mm in Figure 9.36 at ~18mm axial deformation (~6% axial strain) which would not be sufficient for the proposed laparoscopic device. The maximum axial compressive force required to activate the expansion of Beam 2 cylinder is ~40N (Figure 9.35); whereas, it is in order of 200N for Beam 1 model (Figure 9.36). The expansion capabilities of the Conventional 8 cylinder in the absence of surrounding materials will be compared in Chapter 9.4 with its ability to retract simulant organs and foam blocks and create space within the test rig mounted on the Instron machine.

9.3.3 Comparison of Experimentations and FE predictions

FE predictions of ERD and AD of the laser cut and 3D printed cellular mesh cylinders were described in Section 9.1.2 and are compared with the experimental outcomes of expansion mechanisms in this section. ERD and AD

obtained from the experimentation (Instron test without surrounding material) and FE prediction (transient structural analysis) for the Conventional 8 cylinder are compared in Figure 9.37 by way of example.

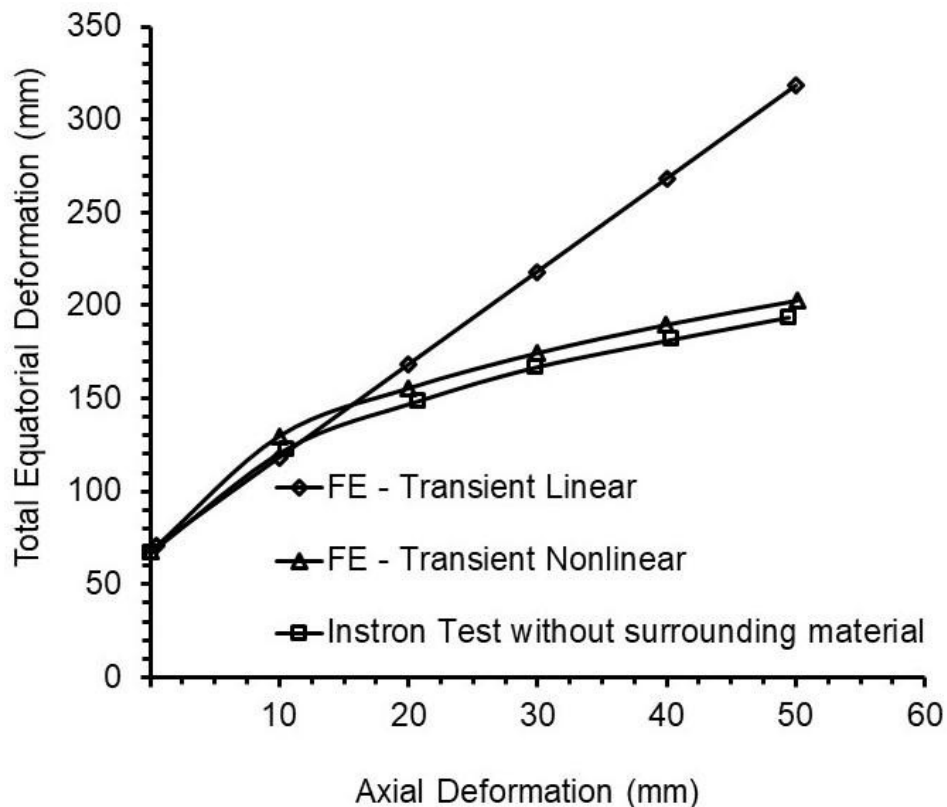


Figure 9.37: ERD vs AD curves obtained from experimental and FE approaches for the Conventional 8 cylinder.

The experimental and FE ERD vs AD data are in good agreement (Figure 9.37).

Summary:

Promising expansion mechanisms have been characterised from mechanical testing. Equatorial deformations have been determined from selected stills extracted from video footage recorded during the mechanical tests and compared with FE predictions. Candidate expansion mechanisms will be evaluated in-vitro within the test rig mounted on the Instron machine in the next section.

9.4 In-vitro assessments of expansion mechanisms

In-vitro assessment was carried out to evaluate the organ retraction and space creation functions of the promising expansion mechanisms within the test rig

mounted on the Instron machine. The Instron data was used to quantify the expansion capabilities. Video footage and surface pressures exerted on surrounding foam blocks and simulant organs were simultaneously recorded to quantify the degree of space created and/or organ retracted within the test rig and the surface pressure exerted. In-vitro assessments of Conventional 6-9, Conventional 10-11, and Beam 2 cylinders were carried out and the results are presented in this section.

9.4.1 Assessments using foam blocks

In-vitro assessment of the promising expansion mechanisms using foam blocks are briefly summarised in this section. The detailed data analysis involving image analysis of the selected stills extracted from the video footage to calculate ERD and the synchronisations of mechanical characterisation data, video footage, and surface pressures exerted by the prototypes are described in section 9.4.2 for the assessments of simulant organs.

Surface pressures exerted by the Conventional 6-11, and Beam 2 cylinders on the foam blocks within the test rig mounted on the Instron machine are summarised in Figure 9.38. Stills showing the maximum axial deformation (at 50mm) of expansion mechanisms are also shown in Figure 9.38. The Beam 1 cylinder required high axial load (~250 N in Figure 9.24, Section 9.3.1) during mechanical characterisation, making it practically not possible to deploy by human hand compared to the other expansion mechanisms assessed. The Auxetic 8 cylinder did not show promising expansion in during mechanical characterisation in the absence of any surrounding materials (Figure 9.24, Section 9.3.1). The Beam 1 and Auxetic 8 cylinders were therefore not assessed in-vitro within the test rig mounted on the Instron machine.

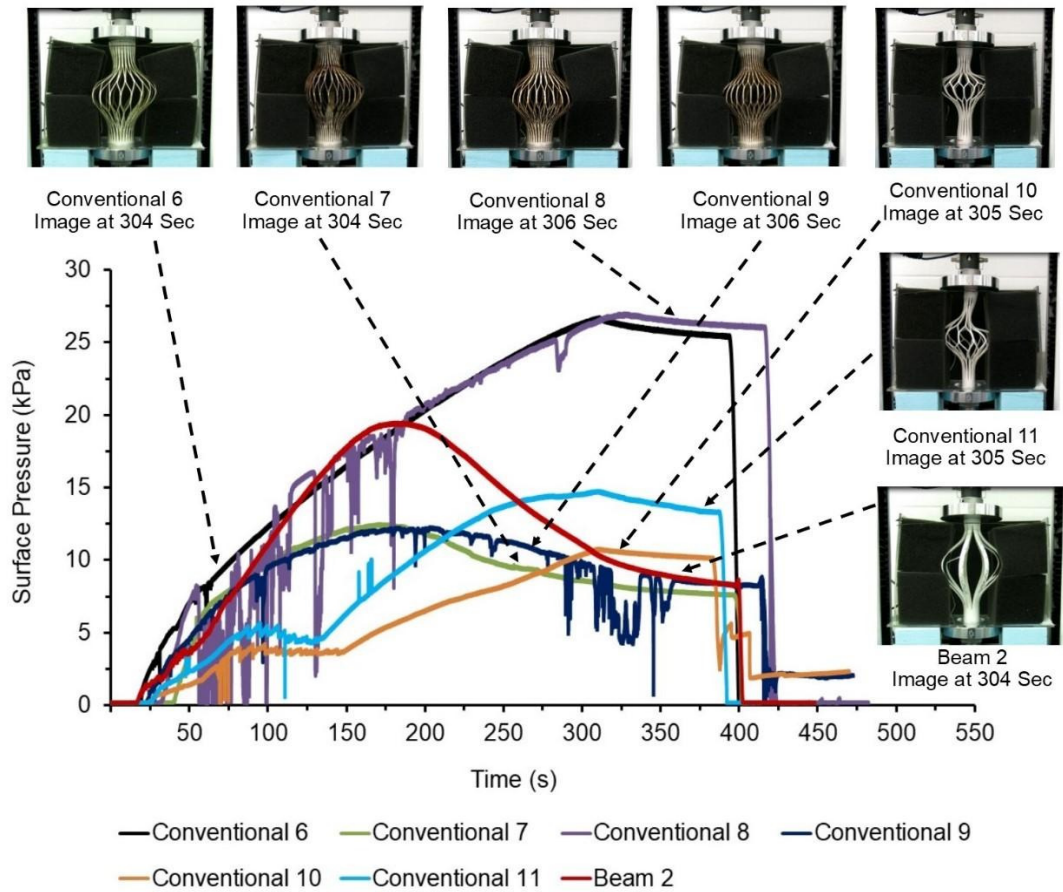


Figure 9.38: Surface pressure exerted by expansion mechanisms on surrounding foam blocks within the test rig during in-vitro assessment. Stills showing maximum axial deformation are included.

The maximum surface pressure exerted on the foam blocks was in order of 25 kPa by the Conventional 6 and Conventional 8 cylinders, 20 kPa for the Beam 2 cylinder; and 10-15 kPa for the Conventional 7-9-10-11 cylinders. Foam blocks were kept retracted within the test rig for ~1 min 30s after the completion of the Instron test (to 50mm axial deformation) by the Conventional 6-7, Conventional 10-11 and Beam 2 cylinders (~1 min 50s for Conventional 8-9 cylinders) and, hence, there is a decay in the surface pressure exerted on the foam blocks (Figure 9.38). The in-plane thickness of vertical ribs (t_h) and diagonal ribs (t_l) of conventional honeycomb units of Conventional 7 and Conventional 9 cylinders (2.5mm and 1.5mm, respectively) are less than t_h and t_l of Conventional 6 and Conventional 8 cylinders (Table 6.6, Chapter 6). Additionally, axial to circumferential stiffness ratio (E_z/E_θ) of Conventional 7 cylinder is higher than Conventional 6-8-9 cylinders (Table 6.6, Chapter 6) making it more compliant. Hence, Conventional 7 cylinder has exerted approximately half the surface

pressure (~ 12.5 kPa) on the foam blocks than applied by the Conventional 6 and Conventional 8 cylinders (~ 27 kPa). Conventional 9 cylinder has also exerted half the surface pressure (~ 12.5 kPa) on the foam blocks than Conventional 6 and Conventional 8 cylinders due to thin vertical and diagonal ribs. Similarly, Beam 2 cylinder was compliant than Beam 1 cylinder owing to high number of thin beams/strips allowing foam blocks to push it into undeployed state (still shown for Beam 2 cylinder in Figure 9.38) in the constrained environment of test rig causing substantial drop in the applied surface pressure from 180 secs (Figure 9.38).

By way of example, the sequence of selected stills extracted from the video footage recorded during assessment of the Conventional 8 cylinder are shown in Figure 9.39. It demonstrates the ability of the Conventional 8 cylinder to retract the foam blocks and create the space within the test rig.

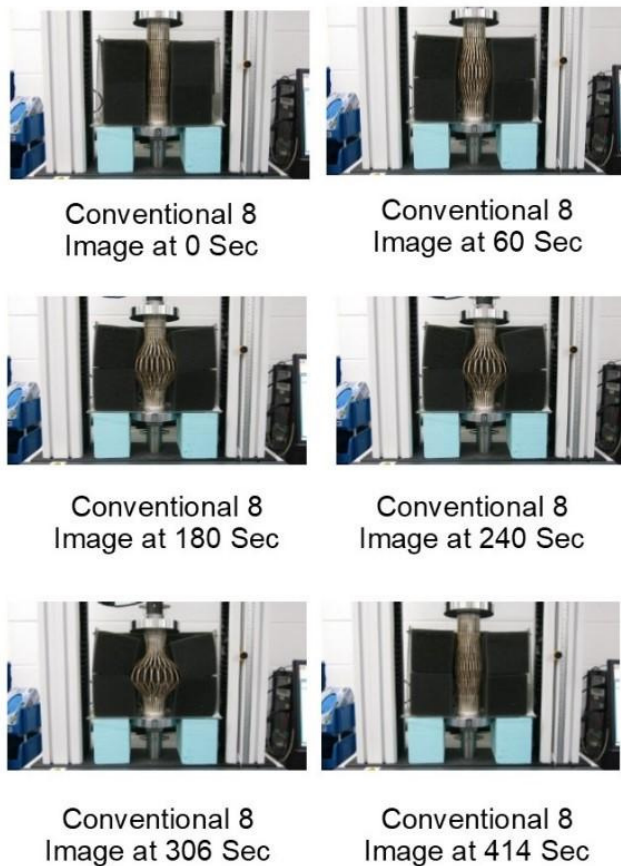


Figure 9.39: Retraction of surrounding foam blocks within the test rig mounted on the Instron machine by the Conventional 8 cylinder.

The axial compressive force required for the deployment of the expansion mechanisms within the test rig are plotted against axial deformation in Figure 9.40.

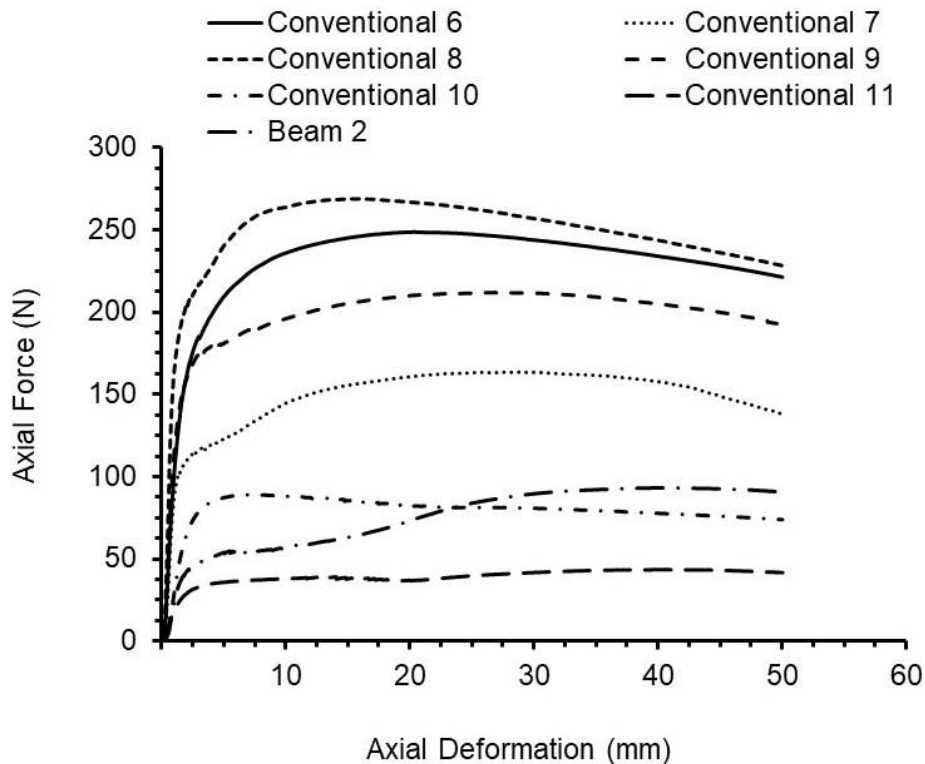


Figure 9.40: Axial force vs axial deformation data for the expansion mechanisms surrounded by foam blocks within the test rig.

The maximum axial compressive force was >200 N for the Conventional 6, 8 and 9 cylinders, ~150 N for the Conventional 7 cylinder, and 50-100 N for the Conventional 10-11 and Beam 2 cylinders (Figure 9.40).

9.4.2 Assessments using simulant organs

In-vitro assessment of the candidate expansion mechanisms was carried out using the simulants of key human abdominal organs (liver, bowel, kidney, stomach, and spleen) within the test rig mounted on the Instron machine. Video footage and surface pressure exerted by the expansion mechanisms on the simulant organs were recorded. The Conventional 8 cylinder is, by way of example, assessed using individual as well as combinations of simulant human abdominal organs within the test rig mounted on the Instron machine and

reported in section 9.4.2.1. In-vitro assessment of other expansion mechanism is briefly summarised in section 9.4.2.2.

9.4.2.1 Conventional 8 cylinder

Individual organs such as bowel, kidney and spleen present on the right and left-hand sides of the Conventional 8 cylinder within the test rig were retracted against blue colour support material. (Liver)-(Bowel & Kidney) and (Stomach & Spleen)-(Bowel) combinations of simulant organs were positioned on the (right)-(left) hand sides of the Conventional 8 cylinder within the test rig. Data obtained from the mechanical characterisations, video footage and surface pressure exerted by the expanding Conventional 8 cylinder were analysed, synchronised and presented in this section.

9.4.2.1.1 Surface pressure

The surface pressure exerted on the individual and combinations of simulant organs by the Conventional 8 cylinder is shown in Figure 9.41. Properties described for data analysis such as P_{max} , T_{hold} , P_{end} , and P_{rms} (defined in Chapter 4) are also shown by way of example for retraction of the kidney simulant.

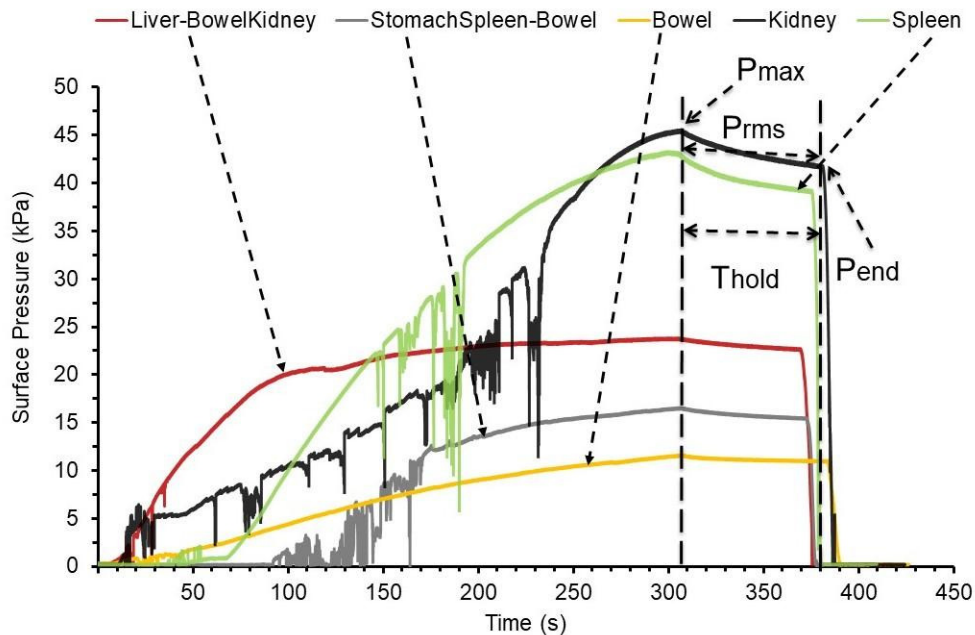


Figure 9.41: Surface pressure exerted on simulant organs by the Conventional 8 cylinder within the test rig vs time. Properties extracted for data analysis are also indicated for the retraction of the kidney simulant.

The maximum surface pressure exerted is lowest on the bowel and combination of (Stomach & Spleen)-(Bowel) (10-15 kPa), highest for the kidney and spleen (40 kPa), and intermediate for the combination of (Liver)-(Bowel & Kidney) (~20 kPa). The decrease in surface pressure during T_{hold} for all individual and combinations of simulant organs shows pressure relaxation as per the natural organs reported in Chapter 7.

9.4.2.1.2 Mechanical characterisation

Axial compressive force vs axial deformation, tangent stiffness vs axial deformation and axial stress vs axial strain are plotted to describe the mechanical characteristics of the Conventional 8 cylinder during the in-vitro assessment.

Axial force, axial deformation and tangent stiffness:

Axial compressive force vs axial deformation curves of the Conventional 8 cylinder characterised during retraction of individual and combinations of simulant organs within the test rig are shown in Figure 9.42. Axial compressive forces for the retraction of individual simulant organs such as bowel, kidney, and spleen predominantly increase as the axial deformation increases (Figure 9.42). In contrast, the data show ~25% reduction in the axial compressive force between 10mm and 50mm of the axial deformation for the Conventional 8 cylinder in the absence of surrounding simulant organs (Figure 9.24, Section 9.3.1). The axial compressive force remained approximately constant for the retraction of combinations of simulant organs such as (Liver)-(Bowel & Kidney) (slight drop of 191N to 186N between 25mm and 50mm of axial deformation) and (Stomach & Spleen)-(Bowel) between 10mm and 50mm of the axial deformation for the Conventional 8 cylinder (Figure 9.42).

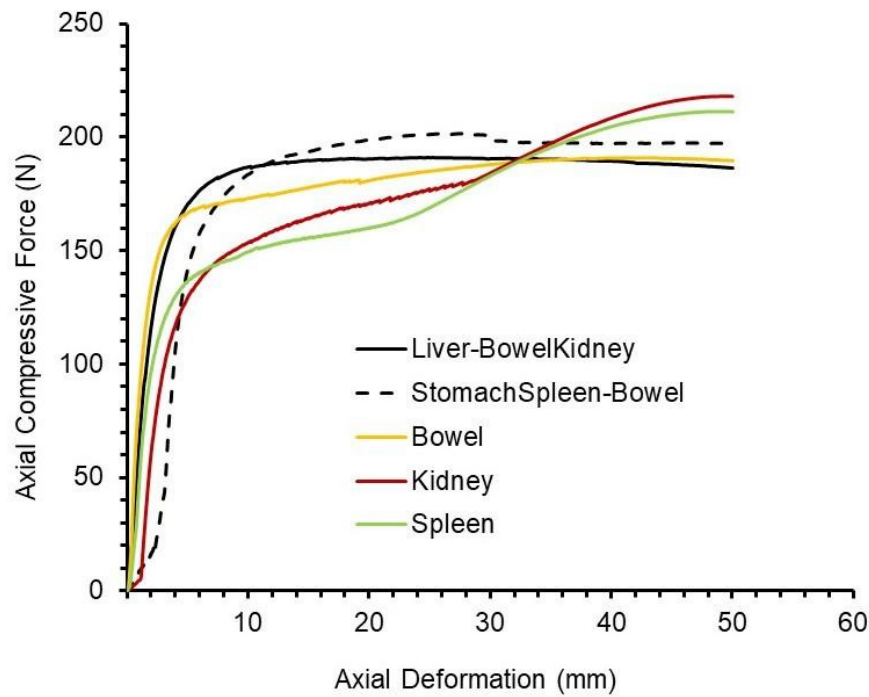


Figure 9.42: Axial compressive force vs axial deformation curves of the Conventional 8 cylinder surrounded by individual and combinations of simulant organs.

The adjacent data points of the axial compressive force vs axial displacement curve of the Conventional 8 cylinder, characterised during retraction of the combination of (Liver)-(Bowel & Kidney) within the test rig, were considered to obtain tangent stiffness. It was divided into two curves to show distinct positive (Figure 9.43a) and fluctuated positive-negative-positive phases (Figure 9.43b).

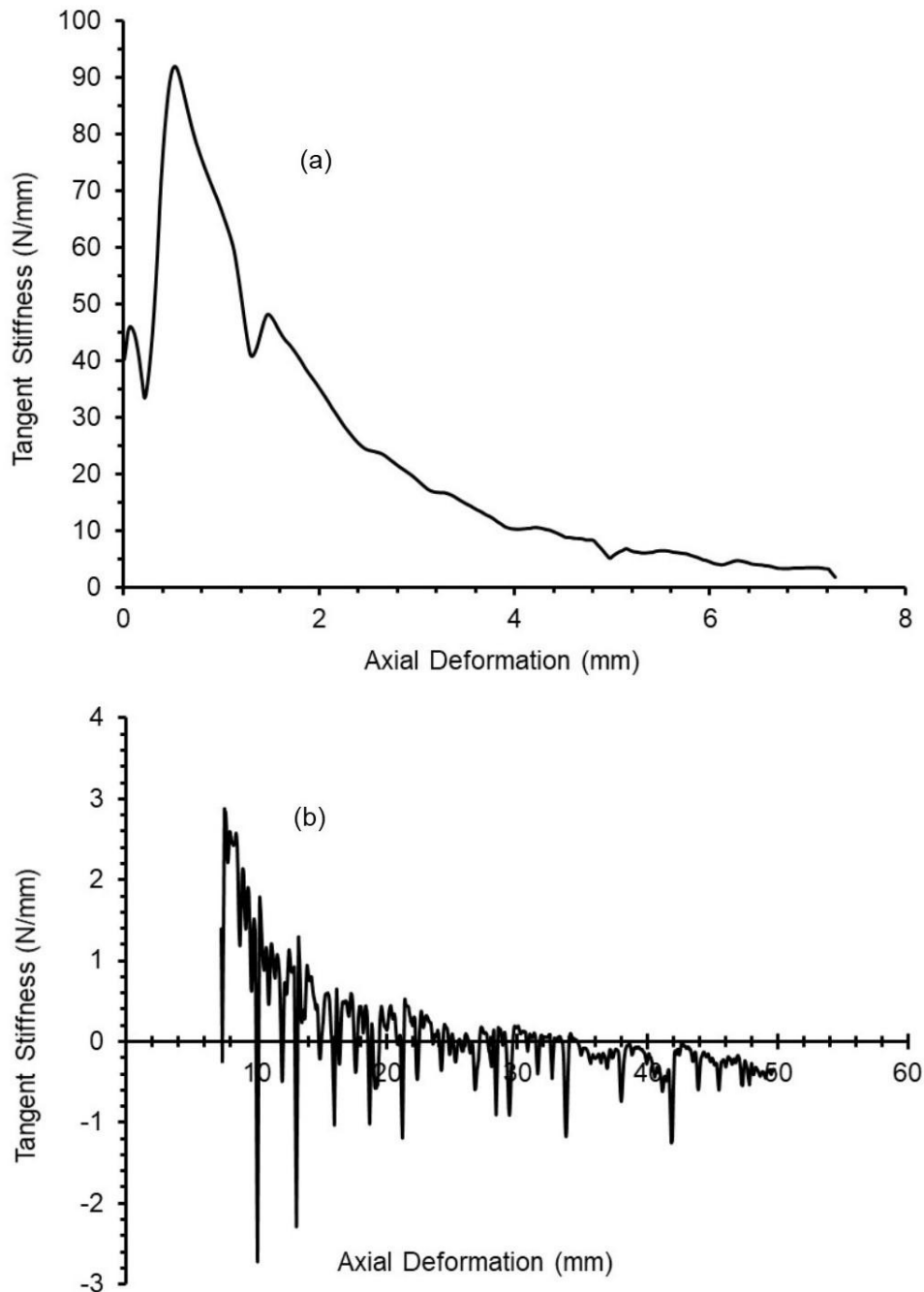


Figure 9.43: Tangent stiffness vs axial displacement curves of the Conventional 8 cylinder surrounded by a combination of (Liver)-(Bowel & Kidney) simulants.

Similarly, tangent stiffness were obtained from the adjacent data points of the corresponding axial compressive force vs axial displacement curves for the retractions of the combination of (Stomach & Spleen)-(Bowel) simulants and individual simulant organs such as the bowel, kidney, and spleen. The corresponding tangent stiffness vs axial displacement curves were divided into

two curves to show distinct positive (Figure 9.44a) and fluctuated positive-negative-positive phases (Figure 9.44b).

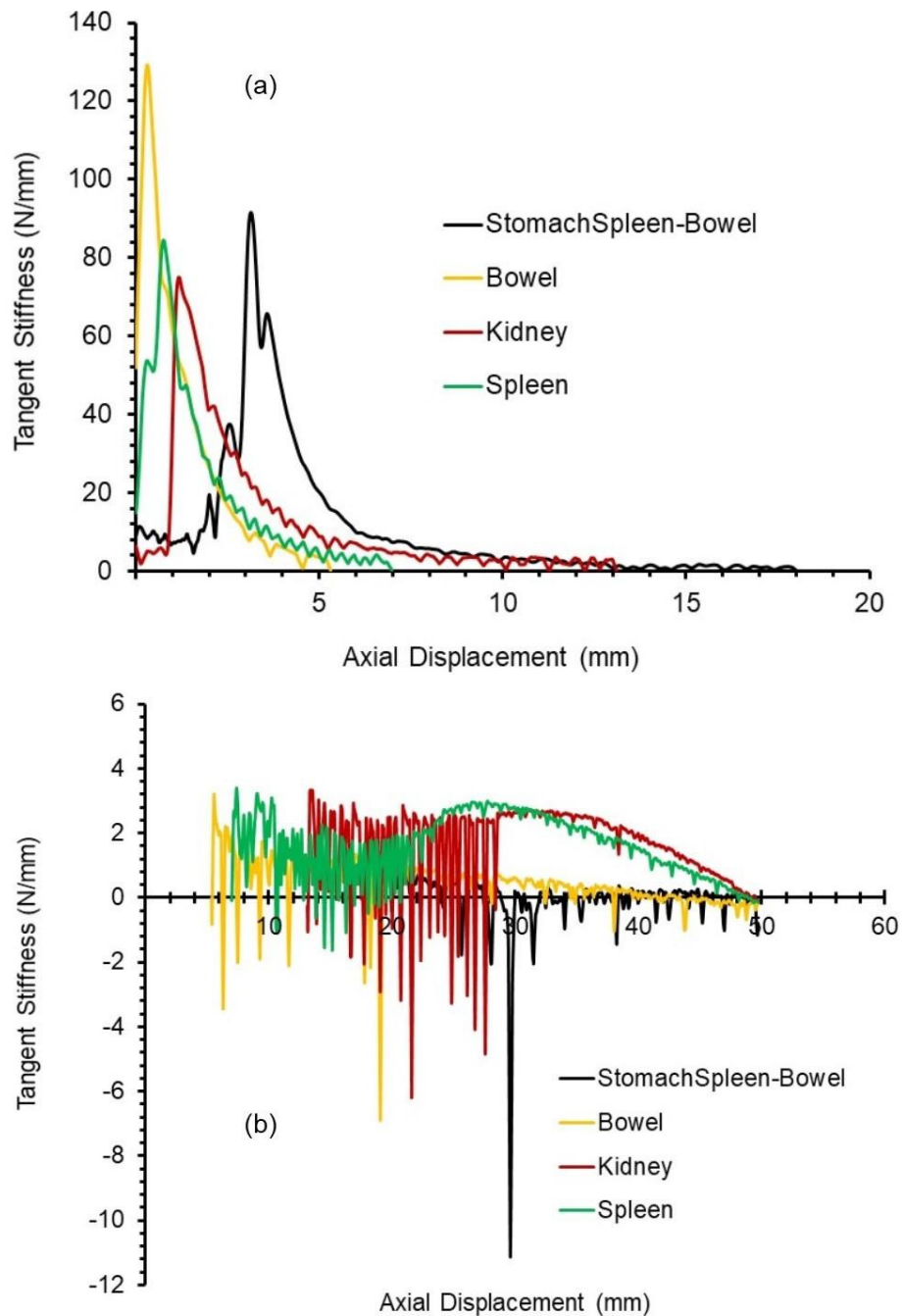


Figure 9.44: Tangent stiffness vs axial displacement curves of the Conventional 8 cylinder surrounded by individual and combinations of simulant organs.

Axial stress and axial strain:

Axial stress vs axial strain curves were obtained from the corresponding axial compressive force vs axial deformation curves of the Conventional 8 cylinder

characterised during the retraction of individual and combinations of simulant organs within the test rig (Figure 9.45).

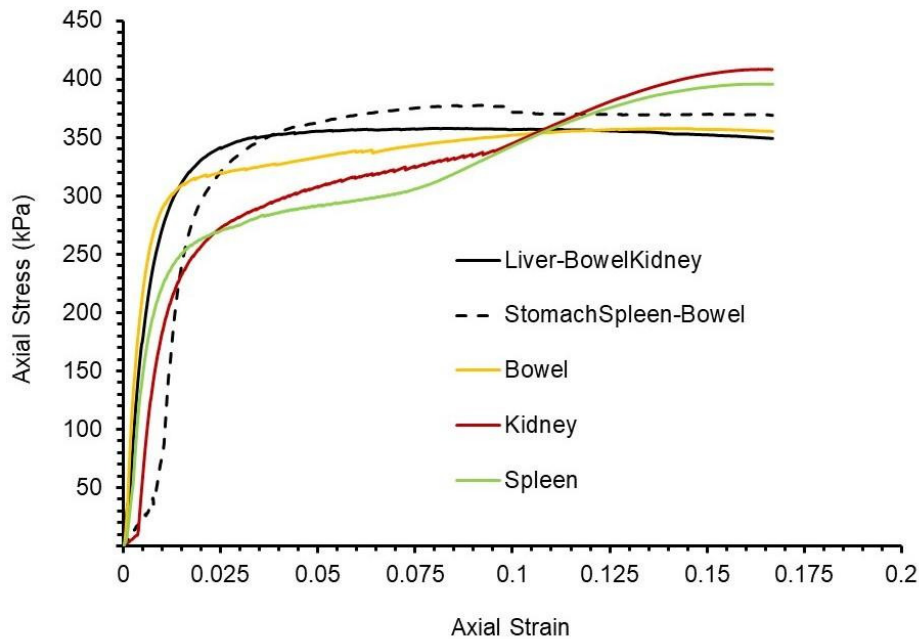


Figure 9.45: Axial compressive stress vs axial strain curves of the Conventional 8 cylinder surrounded by individual and combinations of simulant organs.

Summary:

The mechanical characteristics of the Conventional 8 cylinder during in-vitro assessment were obtained during retraction of the individual and combinations of the simulant organs within the test rig mounted on the Instron machine. Axial compressive force obtained for the Conventional 8 cylinder is synchronised with the axial deformation and equatorial radial deformation in the next section.

9.4.2.1.3 Synchronisations of data obtained during in-vitro assessment

There was approximately five seconds interval kept between starting of data logging on the laptop associated with the pressure sensor and turning the camera on for the recording of video footage. This 5s interval was required to get a 'flat line' response on the data logging software prior to the start of video recording. A five seconds interval was also ensured between starting of the camera and the Instron machine to ensure synchronisations of data collected during in-vitro assessments. Simulant organs were kept retracted within the test

rig for 1 min 30s after the completion of the Instron test (to 50mm axial deformation). Five seconds interval was again maintained between stopping of the Instron machine, camera, and data logging on the pressure measurement software. Data collected during retraction of the individual and combinations of the simulant organs within the test rig by the Conventional 8 cylinder are synchronised and reported here.

Data obtained during the in-vitro assessments of the combination of (Liver)-(Bowel & Kidney) are synchronised and described in detail by way of example. The detailed image analysis of stills extracted from the video footage of in-vitro assessment of the Conventional 8 cylinder is also reported by way of example. Stills at 6secs, 60secs, 180secs, 295secs, 340secs, 370secs, and 374secs were extracted from the video footage and individually processed according to the methodology described in section 9.3.1 for the calculation of equatorial deformation in the absence of surrounding material. Selected stills analysed are shown in Figure 9.46.

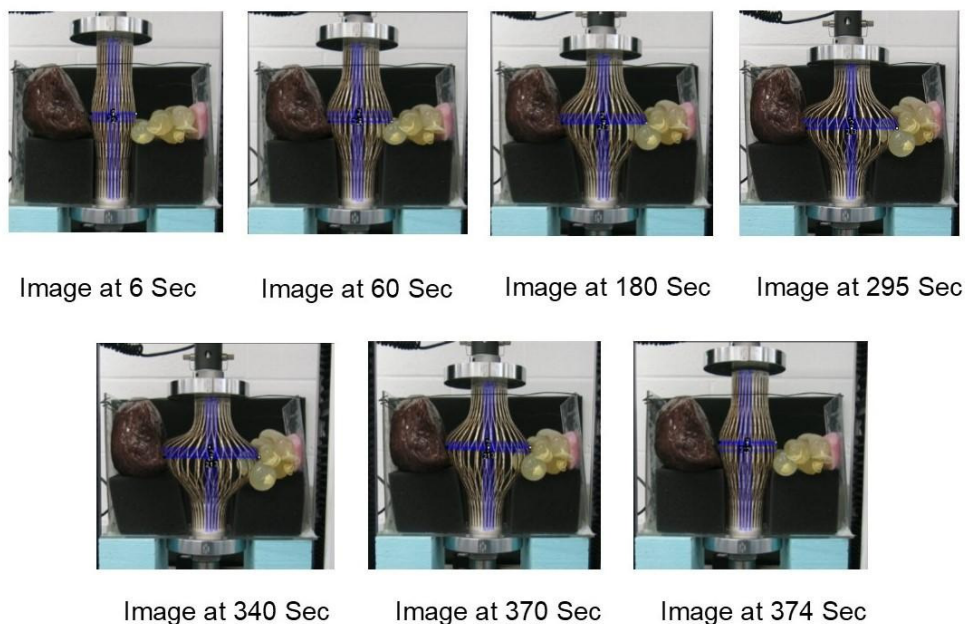


Figure 9.46: Image analysis of selected stills extracted from the video footage recorded during the retraction of the combination of (Liver)-(Bowel & Kidney) simulants by the Conventional 8 cylinder.

ERD and AD were calculated using the stills at 6secs, 60secs, 180secs, and 295secs (Figure 9.46) and are plotted in Figure 9.47.

Similarly, ERD and AD data obtained during in-vitro assessment of the combination of (Stomach & Spleen)-(Bowel) and individual bowel, kidney and spleen simulant organs are also plotted in Figure 9.47. Error bars in Figure 9.47 represent standard deviation of three measurements of the length and equatorial diameter of the cylinder during image analysis. ERD at ~50mm of AD in Figure 9.47 is ~100mm for the combination of (Liver)-(Bowel & Kidney), ~85mm for the kidney and spleen, and ~70mm for the bowel and the combination of (Stomach & Spleen)-(Bowel), respectively. These ERD values are less than the ERD obtained (~120mm) during the mechanical characterisation of the Conventional 8 cylinder in the absence of surrounding materials (Figure 9.29). This can be attributed to a combination of the presence of simulant organs within the test rig restricting the visibility of the equatorial edges of the deployed Conventional 8 cylinder during image analysis of the selected stills, as shown in Figure 9.46, and the constrained environment in the tests with surrounding material.

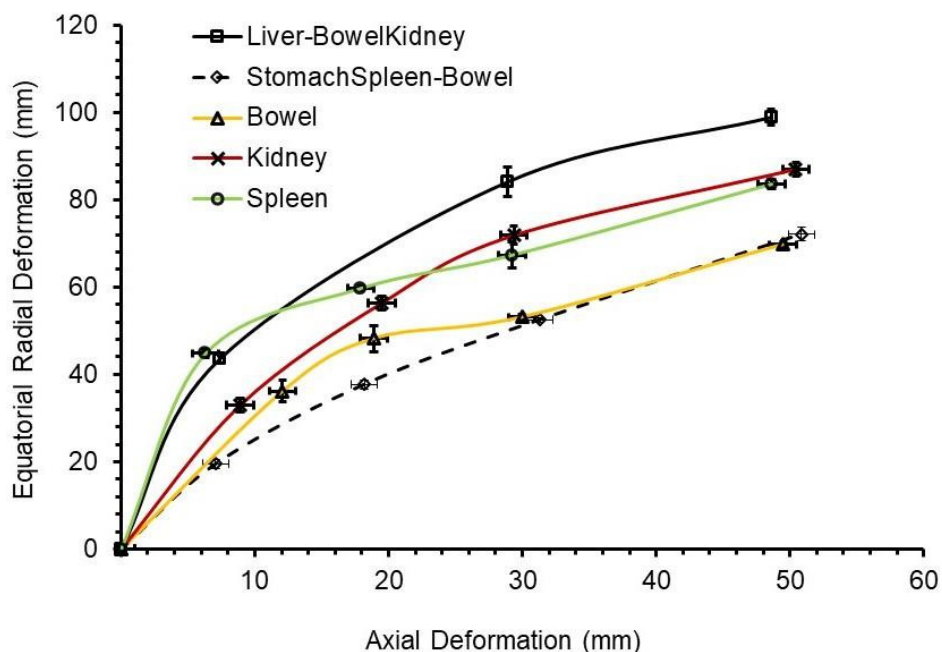


Figure 9.47: ERD vs AD curves obtained for retraction of individual and combinations of the simulant organs present within the test rig during in-vitro assessment of the Conventional 8 cylinder.

When the outer diameter (68mm) of the Conventional 8 cylinder is considered, the total equatorial deformations for retractions of individual and combinations

of the simulant organs are in the ballpark of the requirement for the expansion mechanisms developed in this project for the proposed laparoscopic device application.

Surface pressures exerted on the combinations of simulants of (Liver)-(Bowel & Kidney) and (Stomach & Spleen)-(Bowel) as well as individual bowel, kidney, and spleen simulant organs are synchronised with the total equatorial deformations obtained via image analysis of stills extracted from the corresponding video footage and are shown in Figures 9.48-52. Selected stills are also included in Figures 9.48-52 to demonstrate the deployment of the Conventional 8 cylinder within the test rig.

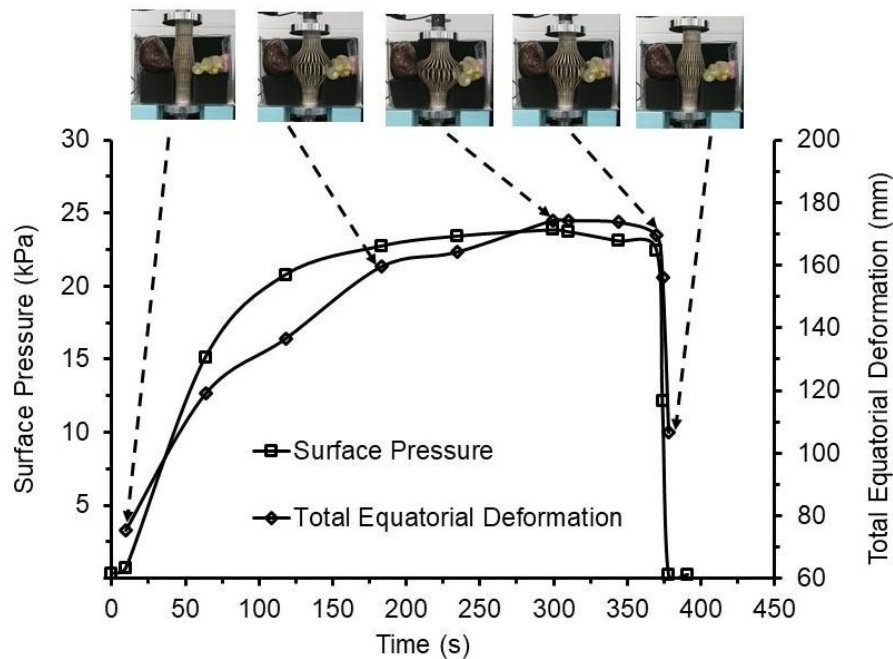


Figure 9.48: Surface pressure and total equatorial deformation vs time for retraction of the (Liver)-(Bowel & Kidney) simulant combination by the Conventional 8 cylinder. Selected stills are also included.

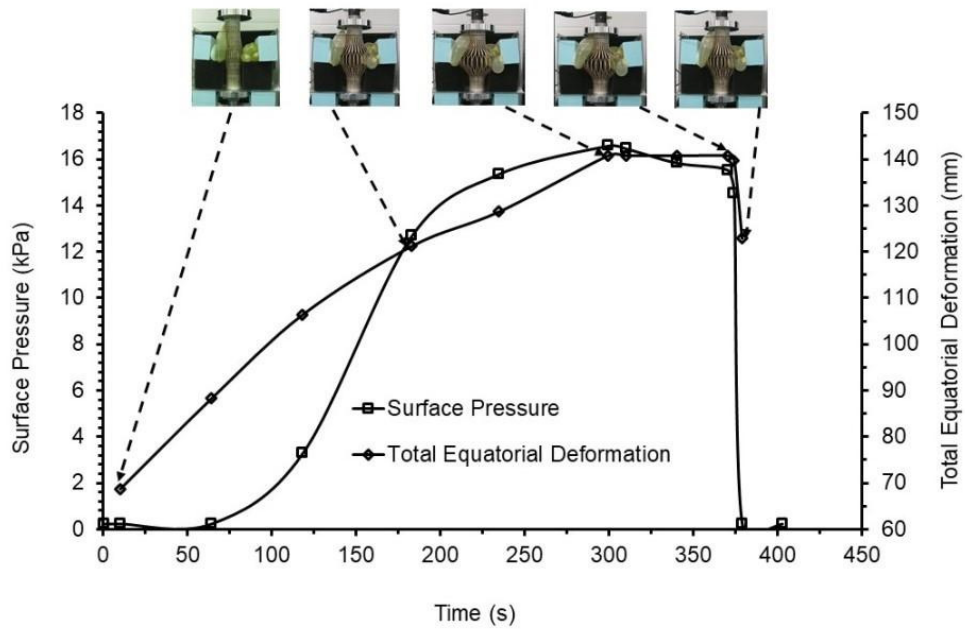


Figure 9.49: Surface pressure and total equatorial deformation vs time for retraction of the (Stomach & Spleen)-(Bowel) simulant combination by the Conventional 8 cylinder. Selected stills are also included.

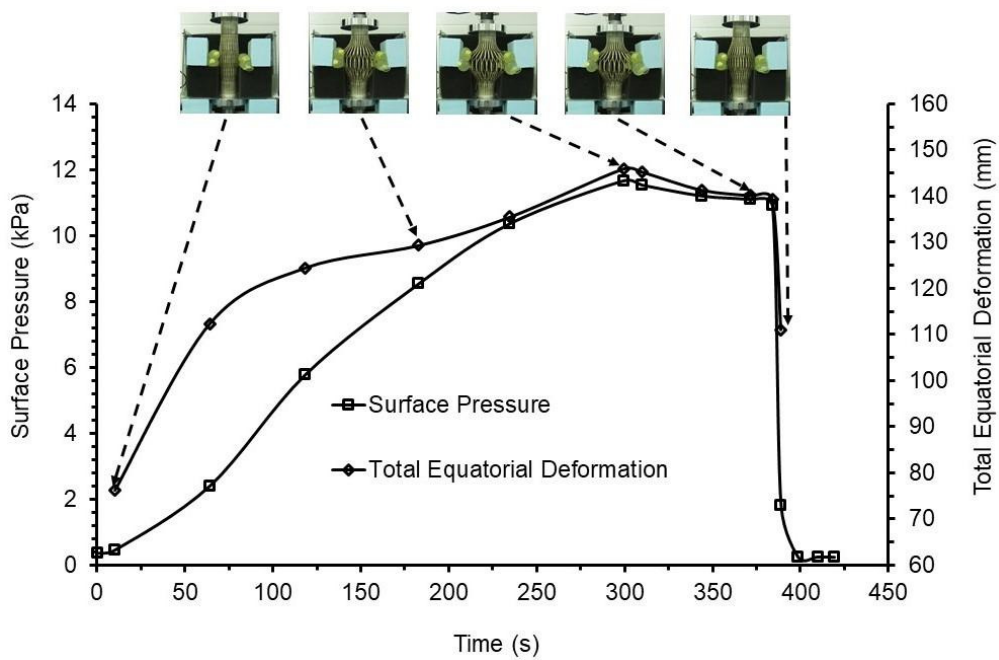


Figure 9.50: Surface pressure and total equatorial deformation vs time for retraction of bowel simulants by the Conventional 8 cylinder. Selected stills are also included.

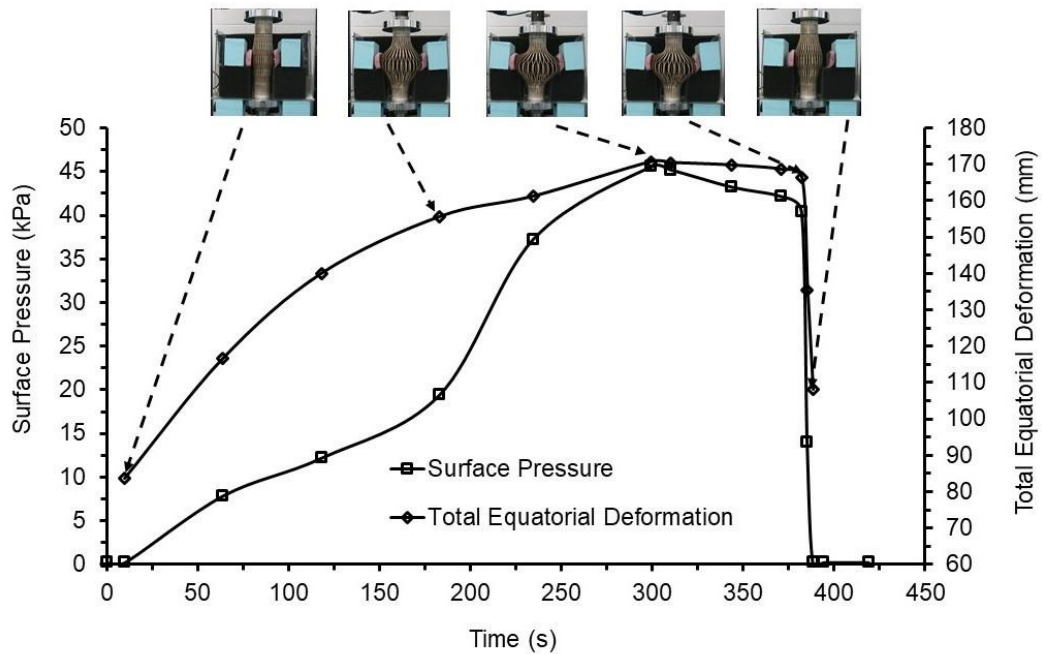


Figure 9.51: Surface pressure and total equatorial deformation vs time for retraction of kidney simulants by the Conventional 8 cylinder. Selected stills are also included.

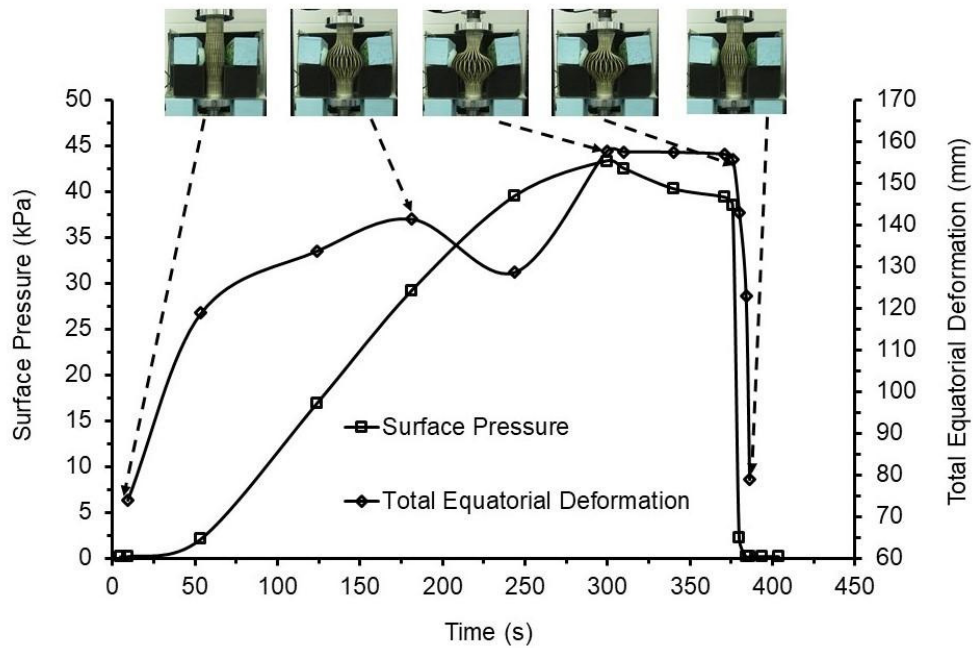


Figure 9.52: Surface pressure and total equatorial deformation vs time for retraction of spleen simulants by the Conventional 8 cylinder. Selected stills are also included.

The surface pressure exerted on the simulant organs and total equatorial deformation were both increased due to the deployment of the Conventional 8

cylinder within the test rig mounted on the Instron machine (Figures 9.48-52). The sequence of the selected stills shown with Figures 9.48-9.52 reveals the retraction movements of simulant organs within the test rig and confirms the organ (simulant) retraction and space creation (within the test rig) capabilities of the Conventional 8 cylinder.

Surface pressure drop was observed for the retraction of key human abdominal organs during in-vivo pilot study (Chapter 7). Simulant organs were therefore maintained in the retracted state within the test rig for an additional ~1 min 20 secs (~305 secs to ~385 secs in Figures 9.48-52) at the end of the Instron test to investigate whether surface pressure drops for simulant organs within the test rig, and the capability of the expansion mechanism for maintaining the space created within the test rig, an essential feature of the proposed laparoscopic device. This duration is called T_{hold} and decay in surface pressure was calculated as root mean square surface pressure (P_{rms}) between P_{max} and P_{min} (according to the methodology described in Chapter 4). The maximum surface pressure (P_{max}) and RMS pressure for T_{hold} (~1 min 20 secs) are shown in Figure 9.53 for the retraction of the individual and combinations of simulant organs within the test rig. There was a marginal decay in the surface pressure (P_{rms}) from the maximum surface pressure exerted by the Conventional 8 model (Figure 9.53) at the end of the Instron test.

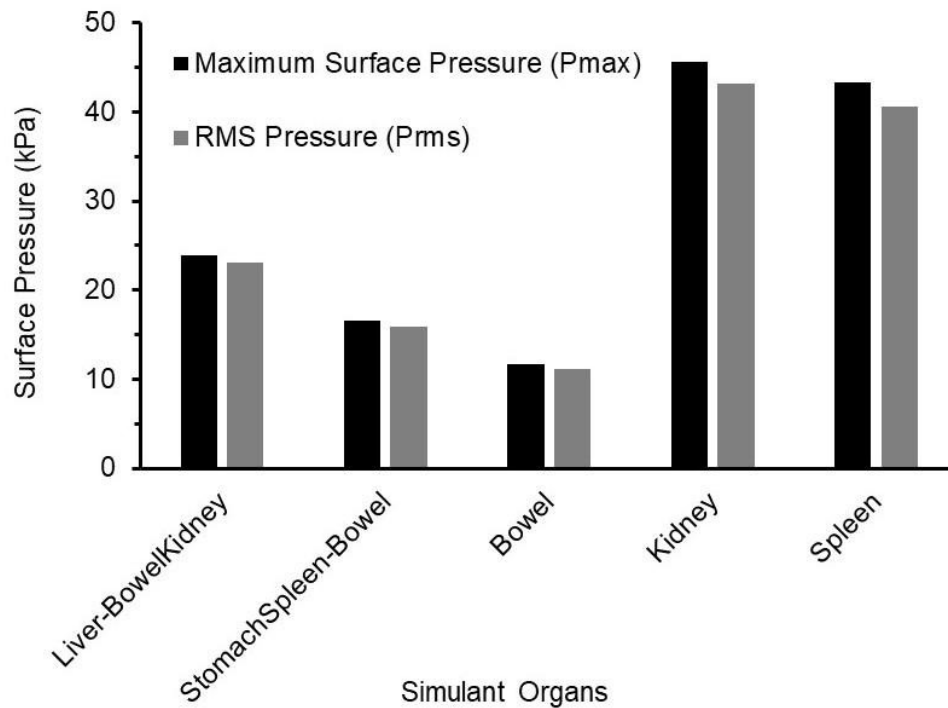


Figure 9.53: Maximum surface pressure (P_{max}) and root mean square surface pressure (P_{rms}) for the retraction of the simulant organs by the Conventional 8 cylinder.

Summary:

The results of the in-vitro assessment of the Conventional 8 cylinder were described in this section. Surface pressures exerted on the individual and combinations of simulant organs due to the deployment of the Conventional 8 cylinder were compared. Axial compressive forces required to deploy the Conventional 8 cylinder within the test rig were synchronised with the axial deformations and total equatorial deformations. Finally, surface pressures were synchronised with the total equatorial deformations obtained using the stills extracted from the corresponding video footages. Total equatorial deformations for the retraction of the simulant organs within the test rig are in the ballpark for the degree of expansion (in order of 200mm) envisaged for the proposed laparoscopic device. Other expansion mechanisms were likewise assessed within the test rig consisting of simulant organs during in-vitro assessment and are described in the next section.

9.4.2.2 Other expansion mechanisms

Individual bowel, kidney and spleen organs present on the right and left-hand sides of the Conventional 10 and Beam 2 cylinders within the abdominal simulator were retracted against support material. (Stomach & Spleen)-(Bowel) combinations of simulant organs were positioned on the right-left hand sides of the Conventional 10 cylinder within the test rig and retracted. Data obtained from the mechanical characterisations, video footage, and surface pressures exerted by Conventional 10 and Beam 2 cylinders were analysed, synchronised, and are presented in this section.

9.4.2.2.1 Surface pressure

Surface pressures exerted on the individual and combinations of simulant organs by the Conventional 10 and Beam 2 cylinders are shown in Figure 9.54. Selected stills are included in Figure 9.56 to demonstrate the expansion capabilities of the Conventional 10 and Beam 2 cylinders. The maximum surface pressure exerted by the Beam 2 cylinder is in order of 20 kPa and 10 kPa for the kidney and bowel simulants, respectively. The maximum surface pressure exerted by the Conventional 10 cylinder is in order of 30 kPa, 20 kPa, and 10 kPa for the spleen, kidney and combination of (Stomach & Spleen)-(Bowel) simulant organs. The degree of maximum surface pressure exerted on individual and combinations of the simulant organs by the Conventional 10 cylinder (Figure 9.54) is less than the Conventional 8 cylinder (Figure 9.41). This can be due to different outer diameter (41mm vs 68mm), nature of the polymer cylinders are made of (PP vs PVC) and total equatorial deformation (in order of 100mm) for the Conventional 10 cylinder within the test rig lower than required (in order of 200mm) for the proposed laparoscopic device.

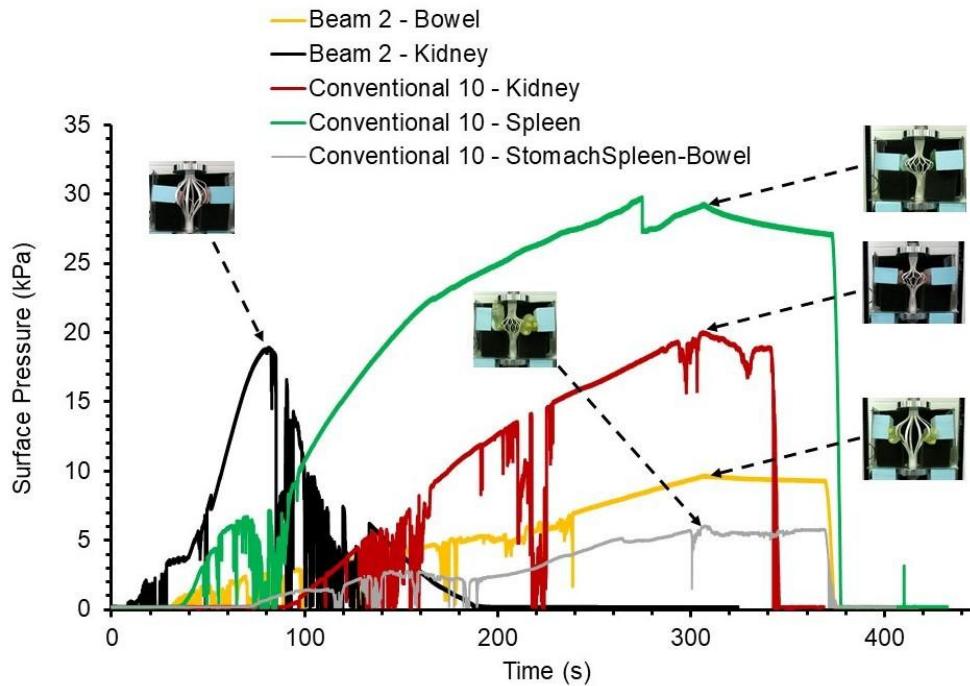


Figure 9.54: Surface pressure exerted on the simulant organs by the Conventional 10 and Beam 2 cylinders within the test rig. Selected stills are also indicated.

9.4.2.2.2 Mechanical characterisation

Axial compressive force vs axial deformation, tangent stiffness vs axial deformation and axial stress vs axial strain are plotted to describe the mechanical characteristics of the Conventional 10 and Beam 2 cylinders.

Axial force, axial deformation and tangent stiffness:

Axial compressive force vs axial deformation curves of the Conventional 10 and Beam 2 cylinders characterised during retraction of individual and combinations of simulant organs within the test rig are shown in Figure 9.55. The maximum axial compressive forces required for the retraction of bowel and combination of (stomach & spleen)-(bowel) simulant organs are in order of 60N (Figure 9.55). Maximum axial compressive forces required for the retraction of individual kidney and spleen simulant organs are ~80N, ~33% (higher than bowel and combination of (stomach & spleen)-(bowel) simulant organs (Figure 9.55).

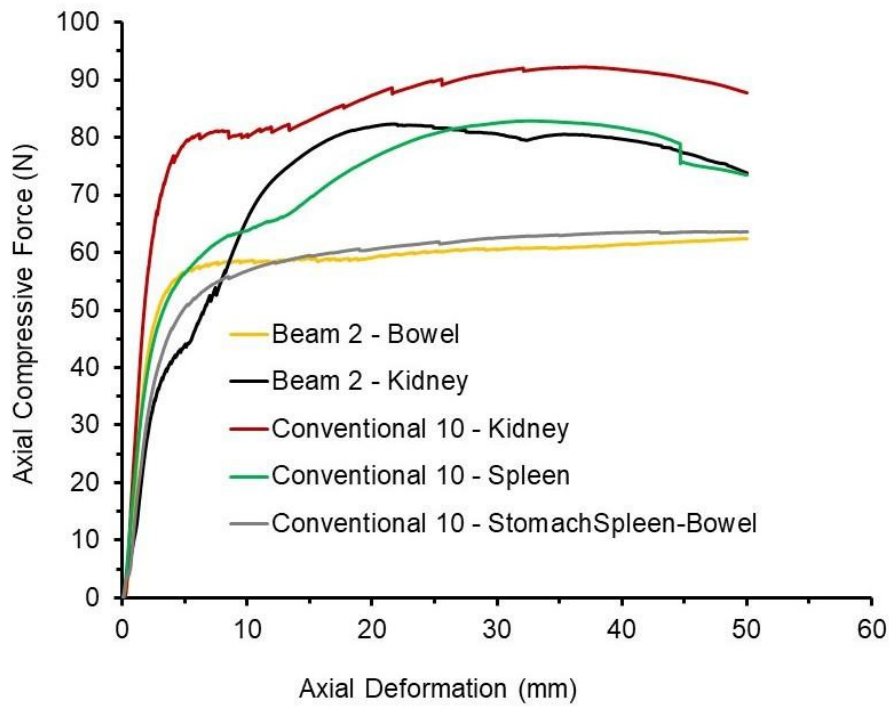


Figure 9.55: Axial compressive force vs axial deformation curves of the Conventional 10 and Beam 2 cylinders for the retraction of surrounding individual and combinations of simulant organs.

Tangent stiffness values were obtained for the Conventional 10 and Beam 2 cylinders according to the methodology described for the Conventional 8 cylinder in section 9.4.2.1.2. Tangent stiffness vs axial deformation curve were divided into two curves to show distinct positive (Figure 9.56a) and fluctuated positive-negative-positive phases (Figure 9.56b).

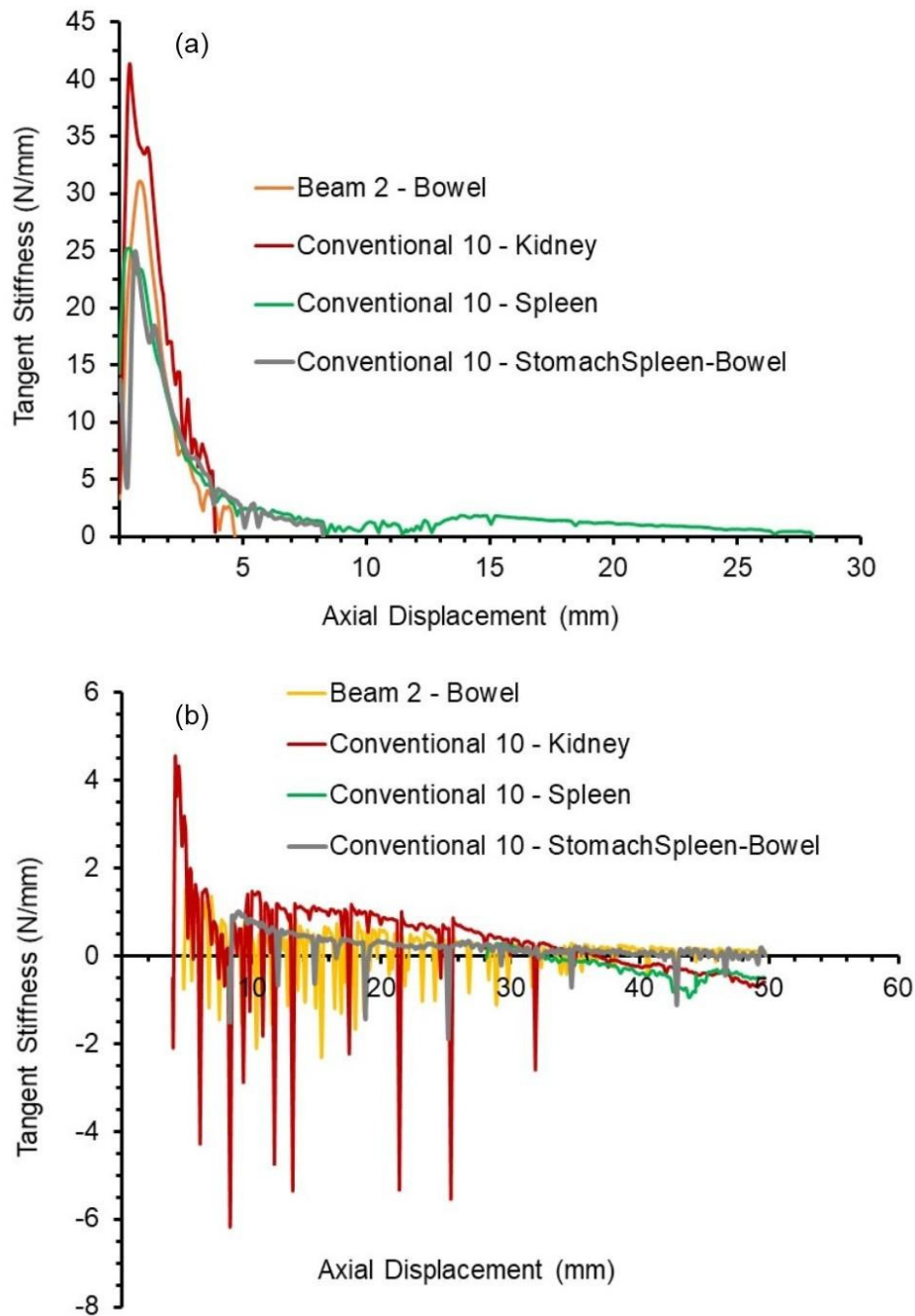


Figure 9.56: Tangent stiffness vs axial displacement curves of the Conventional 10 and Beam 2 cylinders for the retraction of surrounding combination and individual simulant organs.

Axial stress and axial strain:

Axial stress vs axial strain curves were obtained from the corresponding axial compressive force vs axial deformation curves of the Conventional 10 and Beam 2 cylinders (Figure 9.57).

The maximum axial compressive stress is in order of 180kPa for the cylinder-simulant organ combinations of Beam 2-Bowel and Conventional 10-(Stomach & Spleen)-(Bowel), whereas in order of 250kPa for the Conventional 10-Kidney and Conventional 10-Spleen (Figure 9.57).

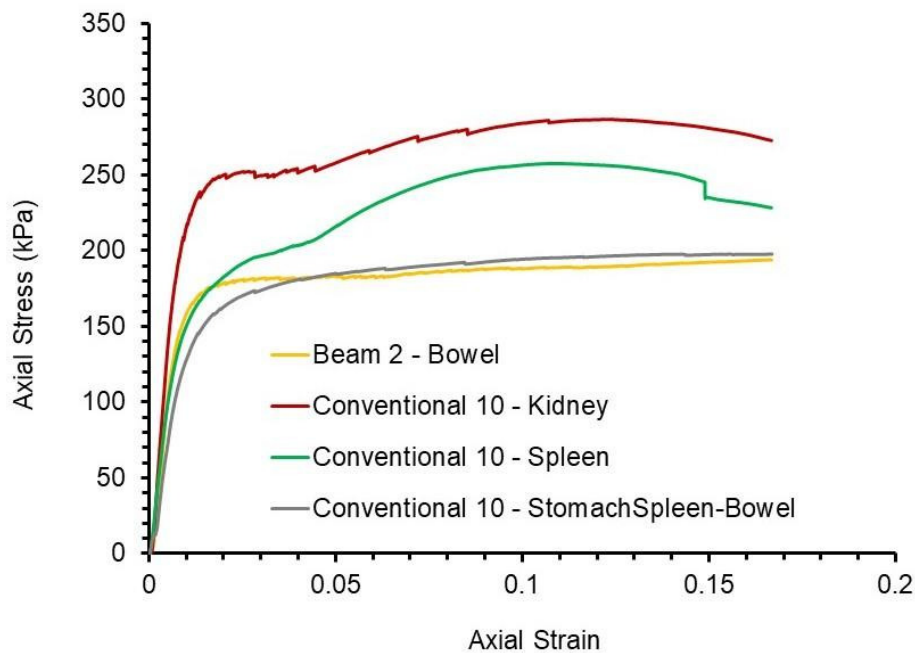


Figure 9.57: Axial stress vs axial strain curves of the Conventional 10 and Beam 2 cylinders for the retraction of the individual and combinations of simulant organs.

The maximum axial compressive stress (Figure 9.57) is approximately 50% [Beam 2-Bowel and Conventional 10-(Stomach & Spleen)-(Bowel)], 50% (Conventional 10-Spleen) and 50% (Conventional 10-Kidney) less than reported for the Conventional 8-Bowel and Conventional 8-(Stomach & Spleen)-(Bowel) (~350 kPa), Conventional 8-Spleen and Conventional 8-Kidney, respectively in Figure 9.45.

Summary:

During in-vitro assessment, the mechanical characteristics of the Conventional 10 and Beam 2 cylinders were obtained during retraction of the individual and combinations of the simulant organs within the in-house abdominal simulator. Axial compressive force obtained for the Conventional 10 and Beam 2 cylinders is synchronised with the axial deformation and equatorial radial deformation in the next section.

9.4.2.2.3 Synchronisations of data obtained during in-vitro assessment

Data collected during the retraction of individual bowel, kidney and spleen simulant organs and the combination of (Stomach & Spleen)-(Bowel) within the test rig by the Conventional 10 and Beam 2 cylinders is synchronised and reported in this section.

ERD and AD were calculated using the selected stills extracted from the corresponding video footage, and ERD vs AD curves are plotted in Figure 9.58. Error bars in Figure 9.58 represent standard deviation of three measurements of the length and equatorial diameter of the cylinder during image analysis. Maximum equatorial radial deformations for the retraction of the bowel simulant organ by the Beam 2 cylinder and retractions of the kidney, spleen, and (Stomach & Spleen)-(Bowel) by the Conventional 10 cylinder are in order of 100mm and 50mm, respectively (Figure 9.58). The expansion capacity of cellular meshes of the Conventional 10 cylinder is responsible for the lower equatorial deformation during retractions of individual and combinations of the simulant organs compared to the Beam 2 (Figure 9.58) and Conventional 8 (Figure 9.47) cylinders.

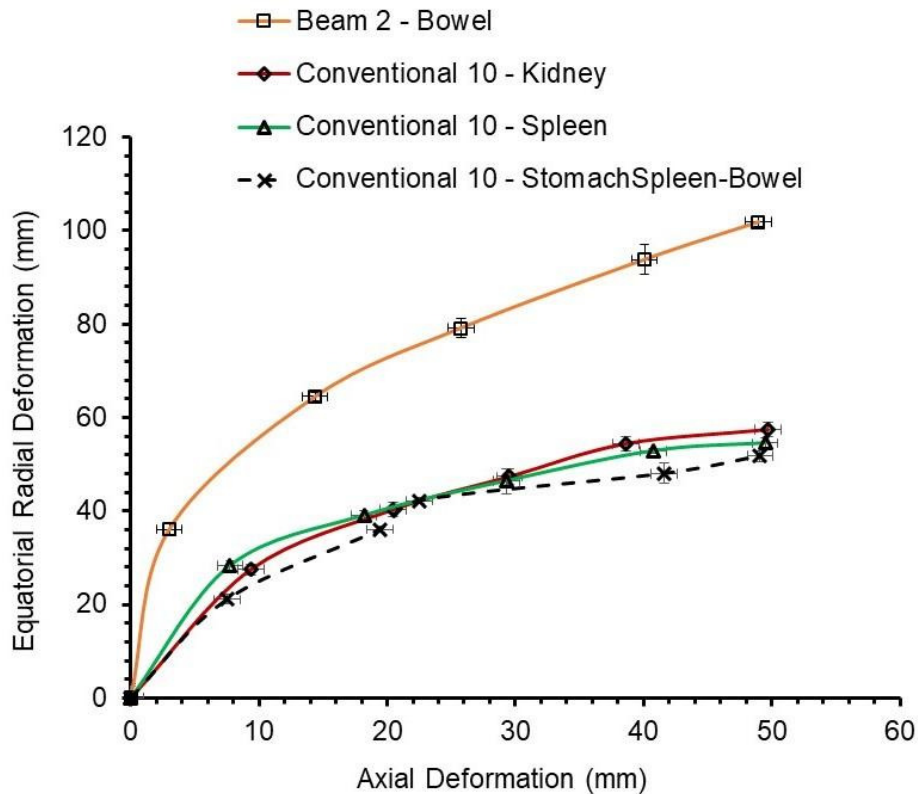


Figure 9.58: ERD vs AD curves for the retractions of the individual and combinations of the simulant organs obtained during in-vitro assessment of the Conventional 10 and Beam 2 cylinders.

When the outer diameter (41mm) of the Beam 2 and Conventional 10 cylinders is considered, the total equatorial deformations for retractions of individual and combinations of the simulant organs are in the ballpark of the requirement for the expansion mechanisms developed in this project for the proposed laparoscopic device application.

Surface pressure exerted on individual and the combination of simulant organs by the Beam 2 and Conventional 8 cylinders is synchronised with the total equatorial deformation obtained via image analysis of stills extracted from the corresponding video footages and shown in Figures 9.59-62. Selected stills are also included in the Figures 9.59-62 to demonstrate the deployment of the Conventional 10 and Beam 2 cylinders within the test rig.

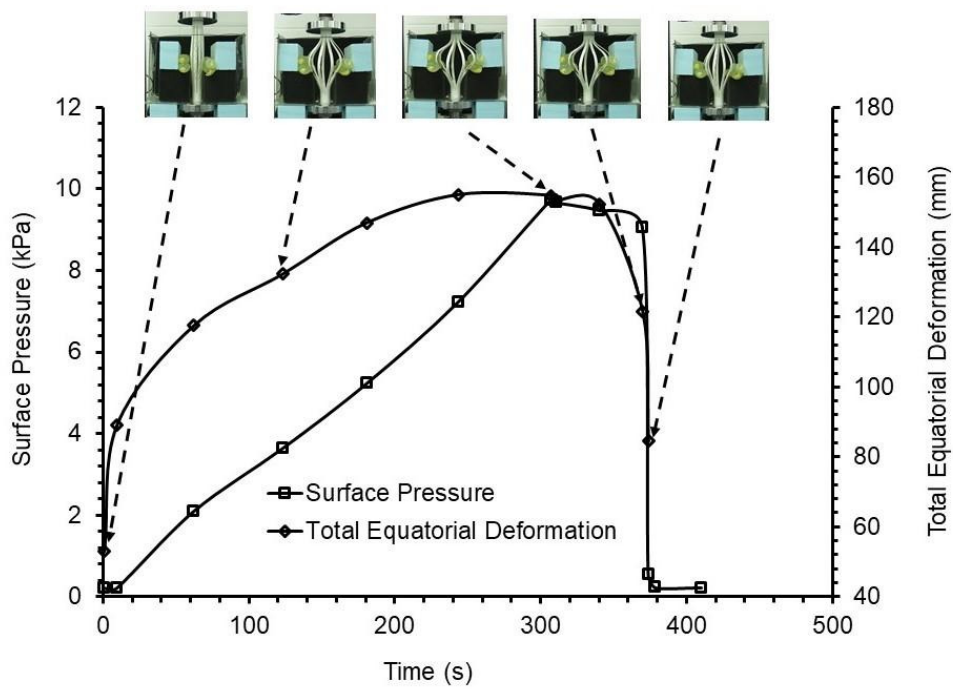


Figure 9.59: Surface pressure and total equatorial deformation vs time for retraction of bowel simulants by the Beam 2 cylinder. Selected stills are also included.

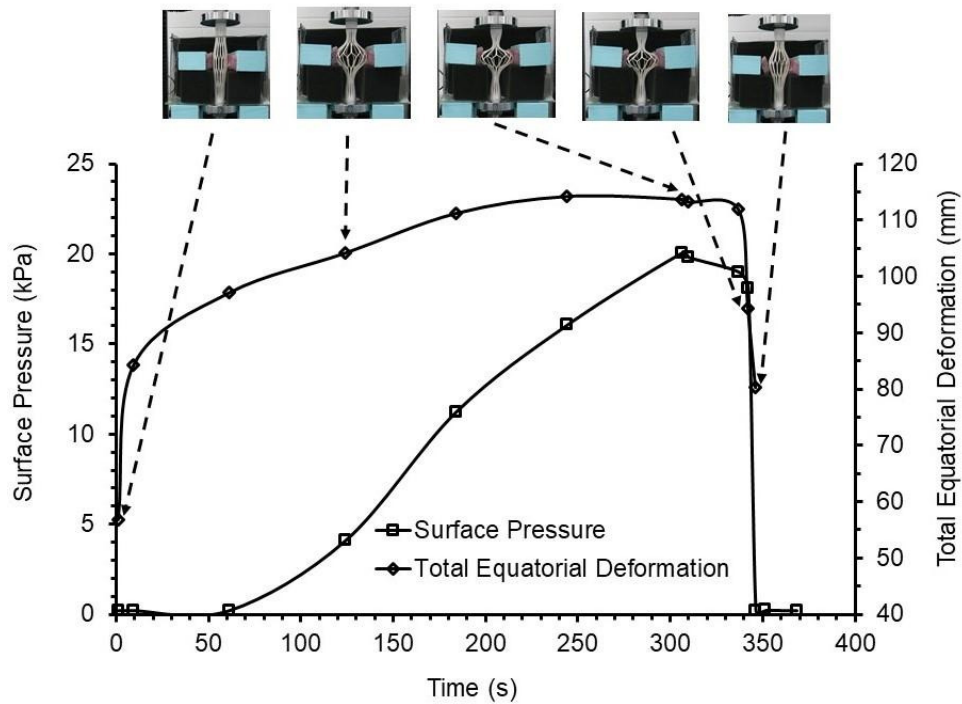


Figure 9.60: Surface pressure and total equatorial deformation vs time for retraction of kidney simulants by the Conventional 10 cylinder. Selected stills are also included.

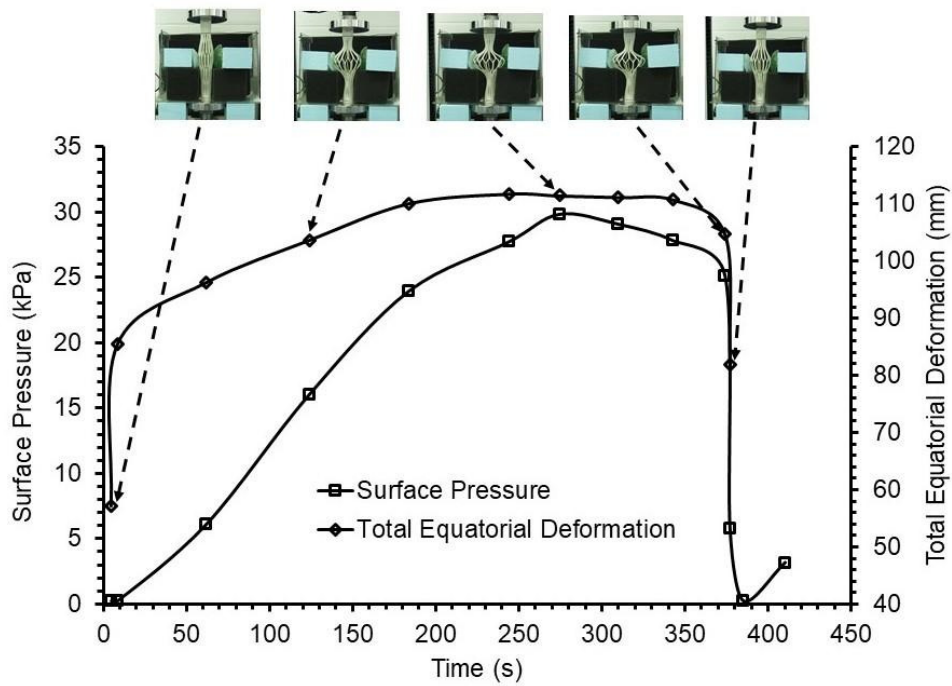


Figure 9.61: Surface pressure and total equatorial deformation vs time for retraction of spleen simulants by the Conventional 10 cylinder. Selected stills are also included.

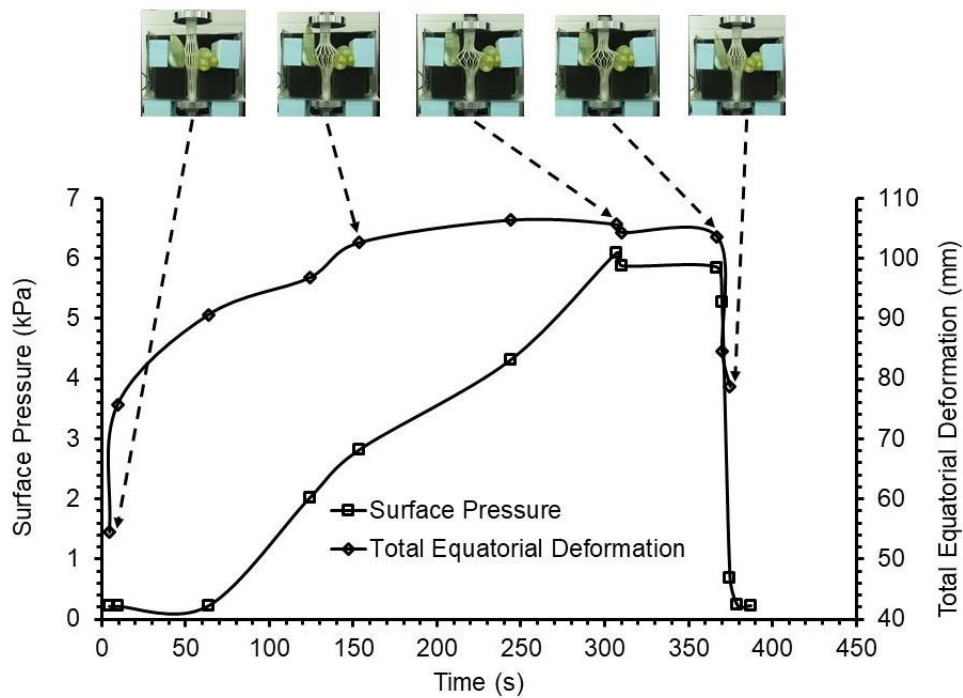


Figure 9.62: Surface pressure and total equatorial deformation vs time for retraction of the combination of (Stomach & Spleen)-(Bowel) simulants by the Conventional 10 cylinder. Selected stills are also included.

Surface pressures exerted on the simulant organs and total equatorial deformation were increased due to the deployment of the Beam 2 and

Conventional 10 cylinders within the abdominal simulator (Figures 9.59-62). The sequence of the selected stills shown with Figures 9.59-9.62 reveals the retraction movements of simulant organs within the test rig and confirms the organ (simulant) retraction and space creation (within the test rig) capabilities of the Beam 2 and Conventional 10 cylinders.

Summary:

The results of the in-vitro assessment of the Beam 2 and Conventional 10 cylinders were described in this section. Surface pressures exerted on the individual and combinations of simulant organs due to the deployment of the Beam 2 and Conventional 10 cylinders were compared. Axial compressive forces required to deploy the Conventional 10 model within the test rig and surface pressures exerted on the individual and combination of simulant organs were synchronised with the total equatorial deformations.

Experimental results are compared with FE predictions in the next section.

9.4.3 Experimentations vs FE predictions

Total equatorial deformation vs AD for the Conventional 8 cylinder is plotted to compare the FE predictions with the characterisation without surrounding material and within the test rig surrounded by foam blocks and simulant organs (Figure 9.63). Total equatorial deformation vs AD for the Conventional 10 cylinder is plotted to compare the FE predictions with the assessment within the test rig surrounded by foam blocks and simulant organs (Figure 9.64).

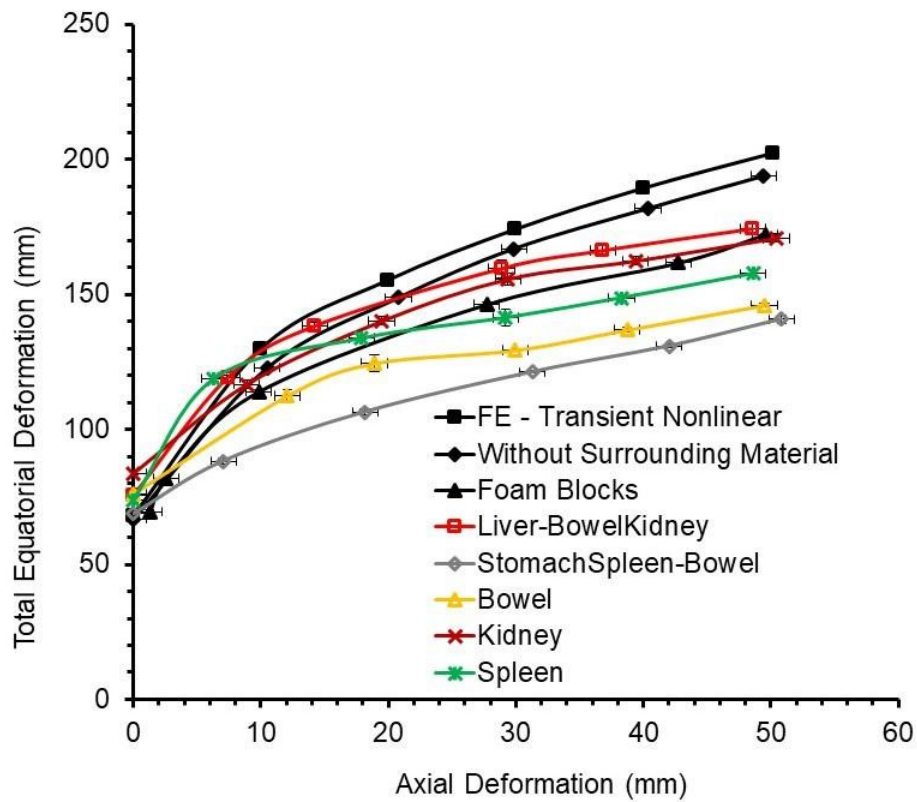


Figure 9.63: Total equatorial deformation vs AD curves obtained from the FE modelling and experimental approaches for the Conventional 8 cylinder.

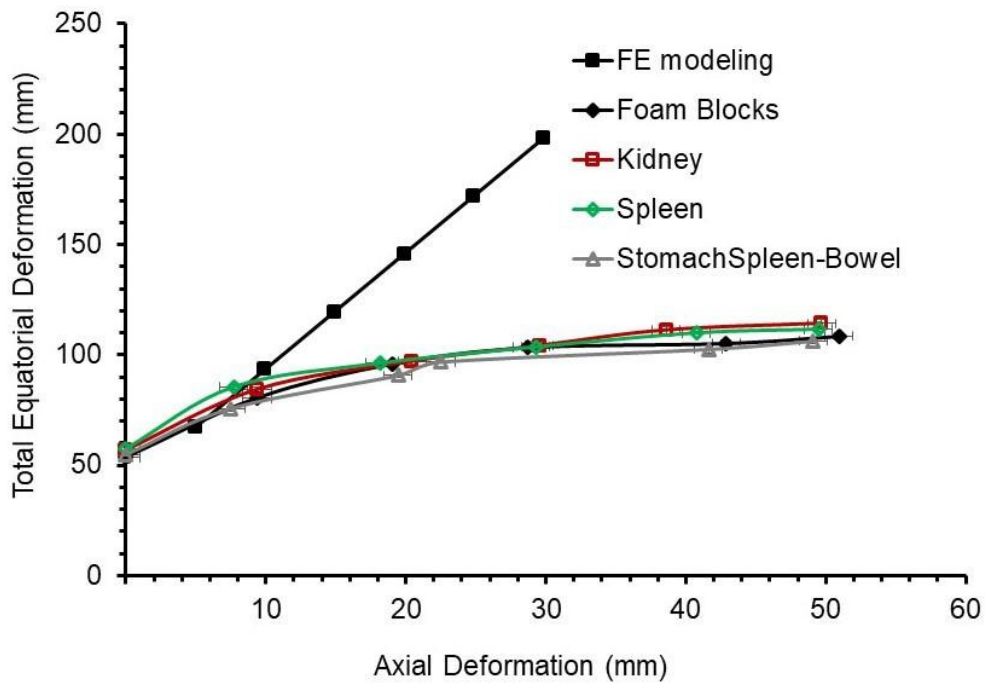


Figure 9.64: Total equatorial deformation vs AD curves obtained from the FE modelling and experimental approaches for the Conventional 10 cylinder.

The experimental and FE data of the Conventional 8 cylinder in Figure 9.63 are in good agreement. However, total equatorial deformations diverge significantly from the FE prediction beyond 10mm of AD for the Conventional 10 cylinder (Figure 9.64). The poor agreement is due to linear elastic behaviour considered for the mesh rib material in the FE modelling which would not account for changes in the stiffness of the deformed cellular mesh material in reality.

The maximum axial compressive forces of ~14000N and 6000N (Conventional 8 and 10 cylinder, respectively) in the FE prediction (Figure 9.11) are two orders of magnitude higher than ~200N and ~80N (Conventional 8 and 10 cylinder, respectively) reported experimentally in Figure 9.17 (Conventional 8 cylinder characterised in absence of the surrounding materials), in Figure 9.40 (foam blocks), and in Figure 9.42 and Figure 9.55 (Conventional 8 and 10 cylinders for simulant organs, respectively). This is attributed to the FE model employing structural steel mechanical properties and, therefore, a Young's modulus for the mesh ribs two orders higher than the polymer used in the experimental cylinder.

9.4.4 Surface pressure for the retraction of human and simulant abdominal organs

Surface pressures applied by the fingertips of surgeons for the retraction of liver, bowel, kidney, stomach and spleen within the human abdominal cavity during OC and HALS (in-vivo pilot study, Chapter 7) are compared in this section with surface pressures exerted by the Conventional 8 and 10 cylinders during retractions of simulant organs within the test rig mounted on the Instron machine (in-vitro assessment, sections 9.4.1 and 9.4.2). The comparison between the retraction distances calculated using selected stills extracted from the video footages obtained during in-vivo pilot study (Chapter 7) and total equatorial deformations obtained for the promising expansion mechanisms during experimental work in this chapter (Mechanical characterisation and in-vitro assessment) have not been done due to the difficulties encountered in measuring retraction distances during surgery.

Surface pressures measured for the retractions of liver, bowel, kidney, stomach, and spleen during OC and HALS are compared with the surface pressures exerted by the Conventional 8 and 10 cylinders on the corresponding simulant

organs in Figures 9.65-69. Selected stills included in Figures 9.65-69 demonstrate the retractions of simulant and human organs when the maximum surface pressure is applied by the expansion mechanisms and the fingertips of surgeons and metal retractors, respectively.

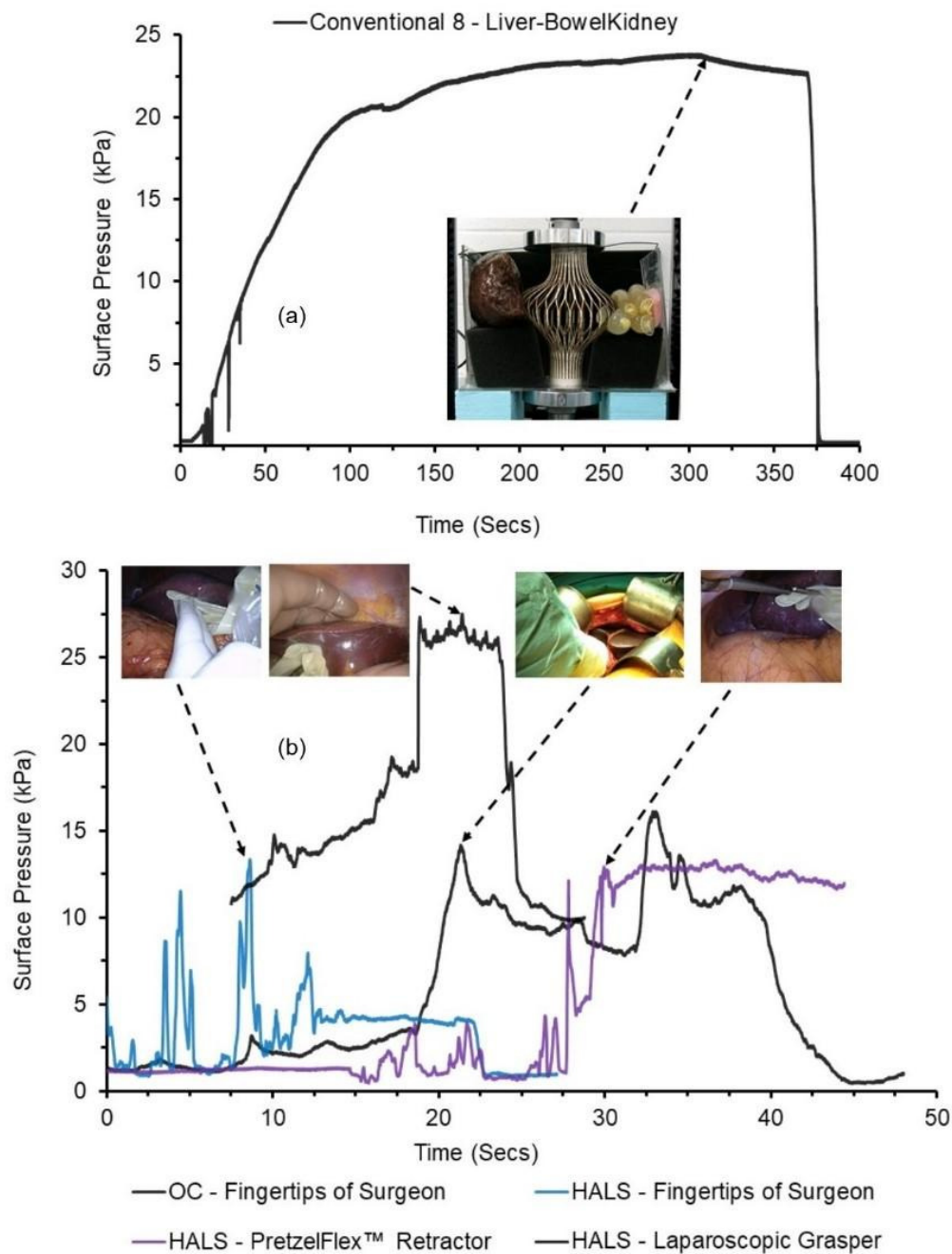


Figure 9.65: Surface pressure applied (a) on the combination of Liver-BowelKidney simulants within the test rig (in-vitro) by the Conventional 8 cylinder and (b) on the human liver during OC and HALS (in-vivo) by the fingertips of the surgeon and metal retractors. Selected stills are also included in (a) and (b).

The surface pressure exerted on the liver simulant (part of the combination of Liver-BowelKidney simulants) during in-vitro assessment is in order of 20kPa and in the ballpark of the surface pressures applied by the fingertips of surgeons and metal retractors during OC and HALS (Figure 9.65).

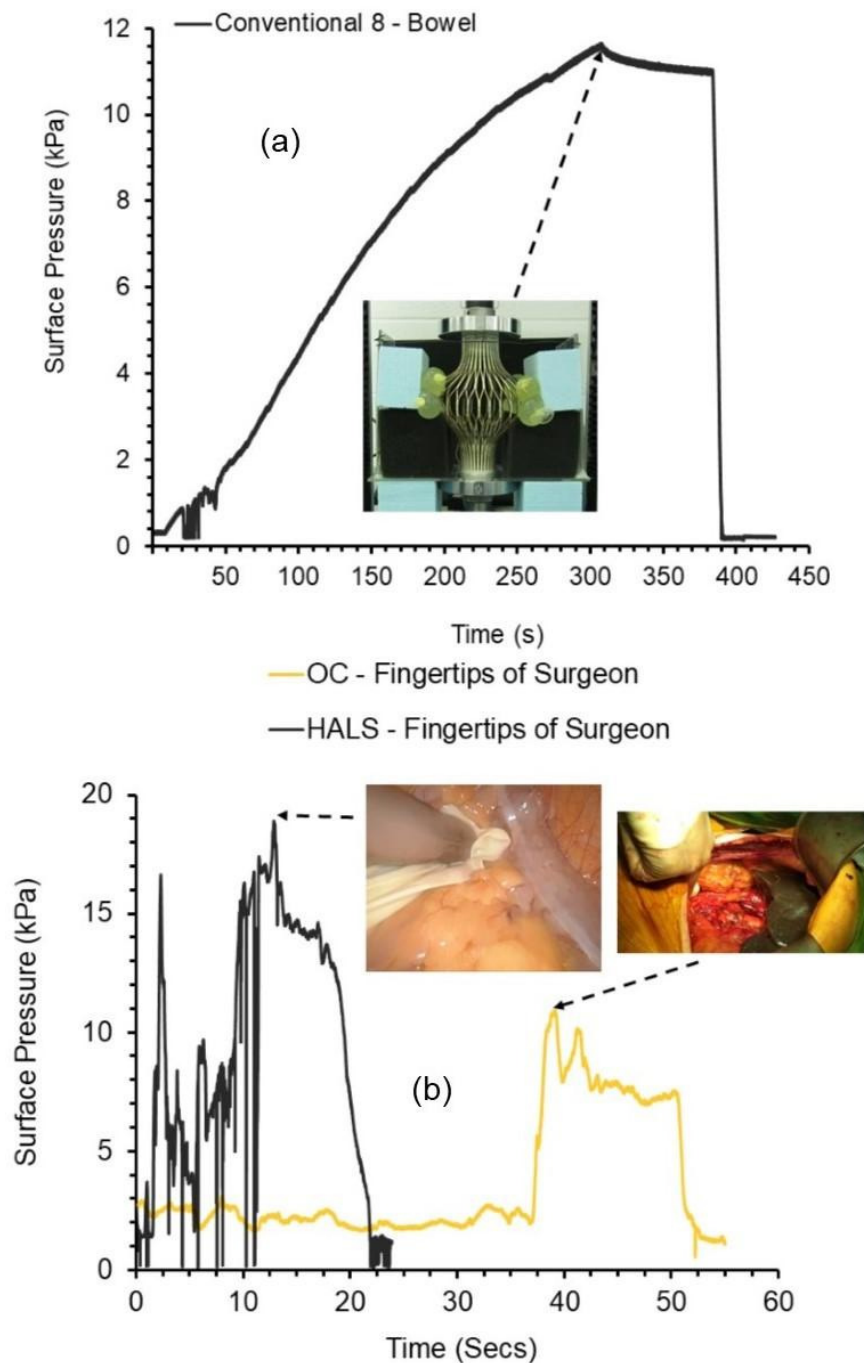


Figure 9.66: Surface pressure applied (a) on the bowel simulants within the test rig (in-vitro) by the Conventional 8 cylinder and (b) on the human bowel during OC and HALS (in-vivo) by the fingertips of the surgeon. Selected stills are also included in (a) and (b).

The surface pressure exerted on the bowel simulants by the Conventional 8 cylinder during in-vitro assessment is in order of 10kPa and in the ballpark with the surface pressure applied by the fingertips of the surgeon during OC (Figure 9.66). The surface pressure applied by the fingertips of the surgeon during HALS (~19kPa) is ~50% higher than the surface pressure exerted by the Conventional 8 cylinder during in-vitro assessment (~13kPa), which can be attributed to the difficulty in retracting human bowel during hand assisted laparoscopic surgery (Figure 9.66).

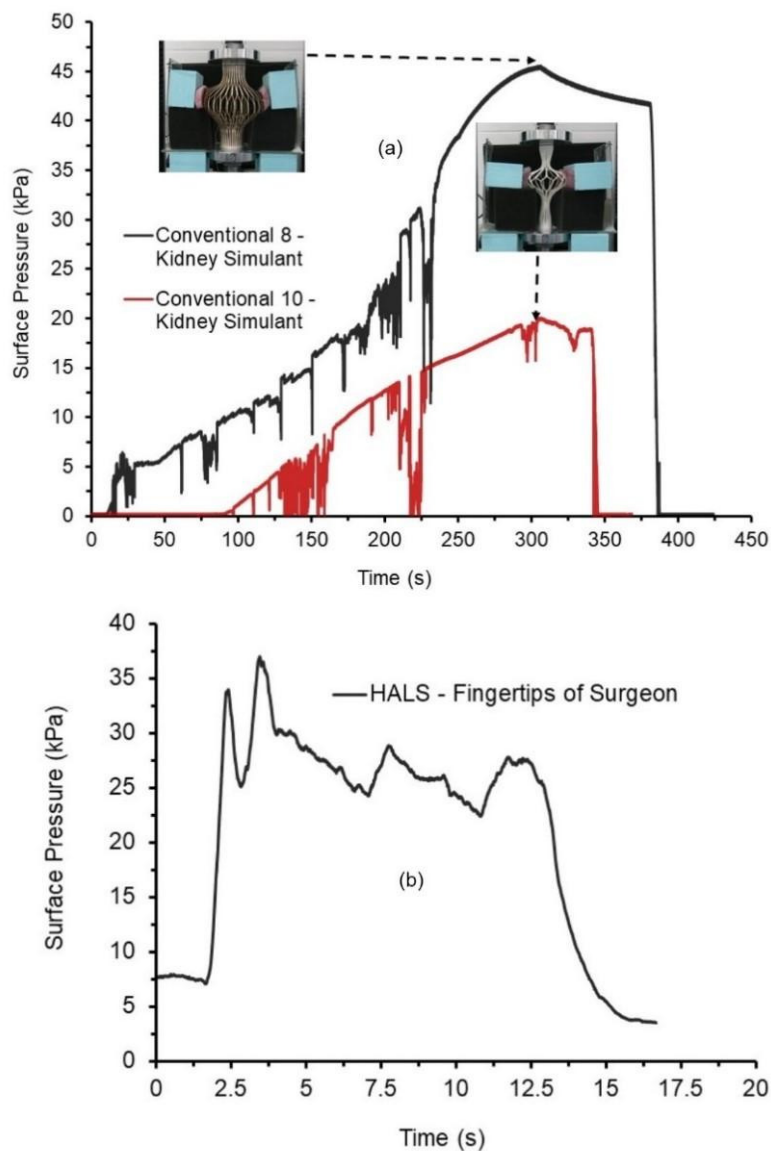


Figure 9.67: Surface pressure applied (a) on the kidney simulants within the test rig (in-vitro) by the Conventional 8 and 10 cylinders and (b) on the human kidney during HALS (in-vivo) by the fingertips of the surgeon. Selected stills are also included in (a).

The surface pressure exerted on the kidney simulants by the Conventional 8 cylinder during in-vitro assessment is in order of 45kPa and in the ballpark with surface pressure applied by the fingertips of the surgeon (~37kPa) during HALS (Figure 9.67). On the contrary, the surface pressure applied by the Conventional 10 cylinder during in-vitro assessment is approximately half (~20kPa) compared to the surface pressure applied by the fingertips of the surgeon. The difference between the surface pressure exerted by the Conventional 8 and 10 cylinder (Figure 9.67a) should primarily be due to the large (in order of 200mm) total equatorial deformation obtained for the Conventional 8 model against small (in order of 100mm) for the Conventional 10 model (owing to the longer and shorter diagonal ribs of the cellular meshes, respectively) for the fixed axial deformation (50mm) within the test rig mounted on the Instron machine. The secondary reason may be the difference in the outer diameter of the Conventional 8 (68mm) and the Conventional 10 (41mm) cylinder which affected the placing of blue support material (vertically and horizontally, respectively in Figure 9.67a). This in turn allowed the squashing of kidney simulant predominantly against walls of the test rig for the Conventional 8 cylinder in contrast to the squashing predominantly against more compliant support material for the Conventional 10 cylinder.

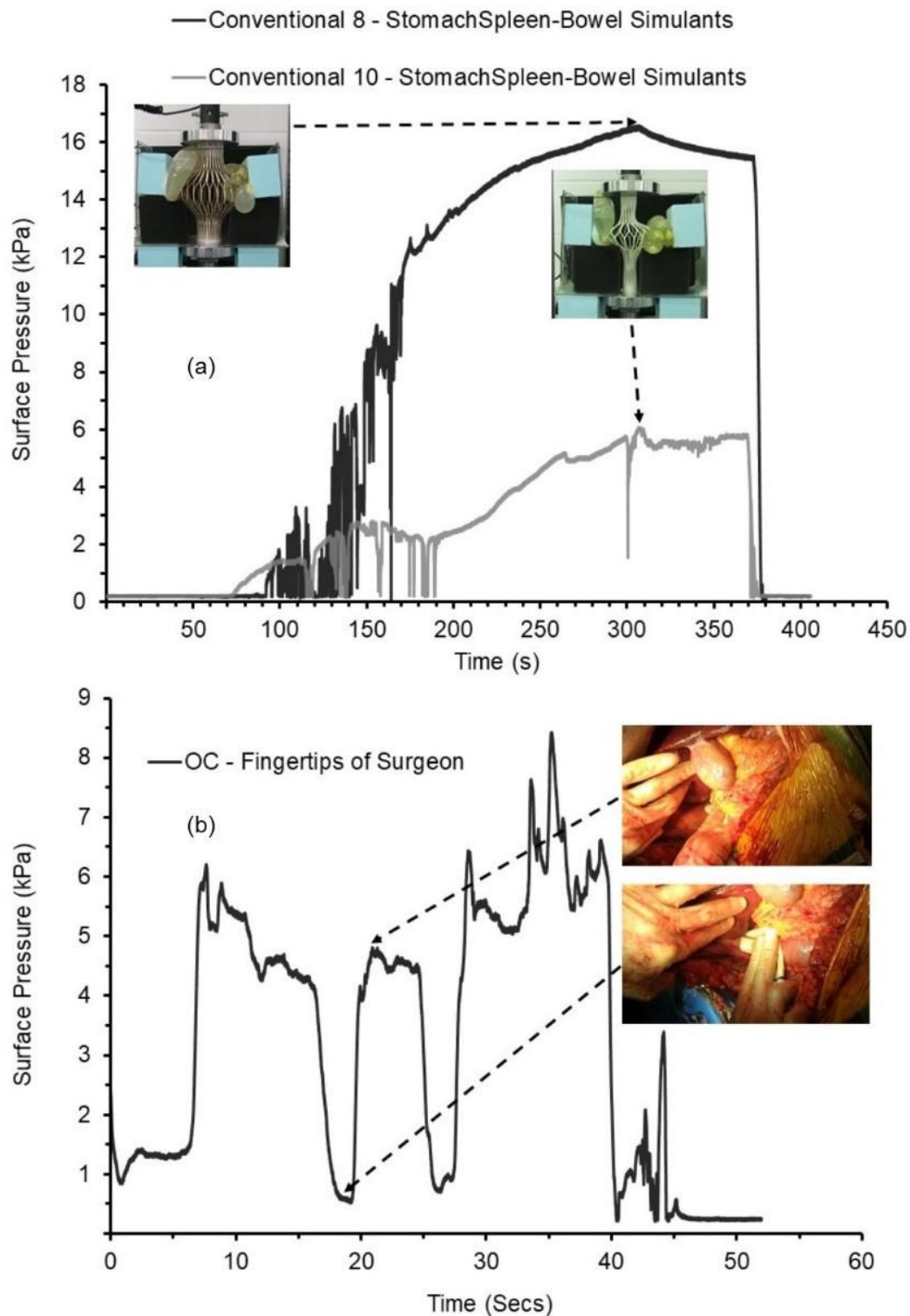


Figure 9.68: Surface pressure applied (a) on the combination of StomachSpleen-Bowel simulants within the test rig (in-vitro) by the Conventional 8 and 10 cylinders and (b) on the human stomach during HALS (in-vivo) by the fingertips of surgeon. Selected stills are also included in (a) and (b).

Surface pressure exerted (~ 5 kPa) by the Conventional 10 cylinder on the stomach simulant (part of the combination of StomachSpleen-Bowel simulants) is in excellent agreement with that applied by the fingertips of the surgeon during OC (Figure 9.68b), whereas the Conventional 8 cylinder exerts 3 times the surface pressure (Figure 9.68a).

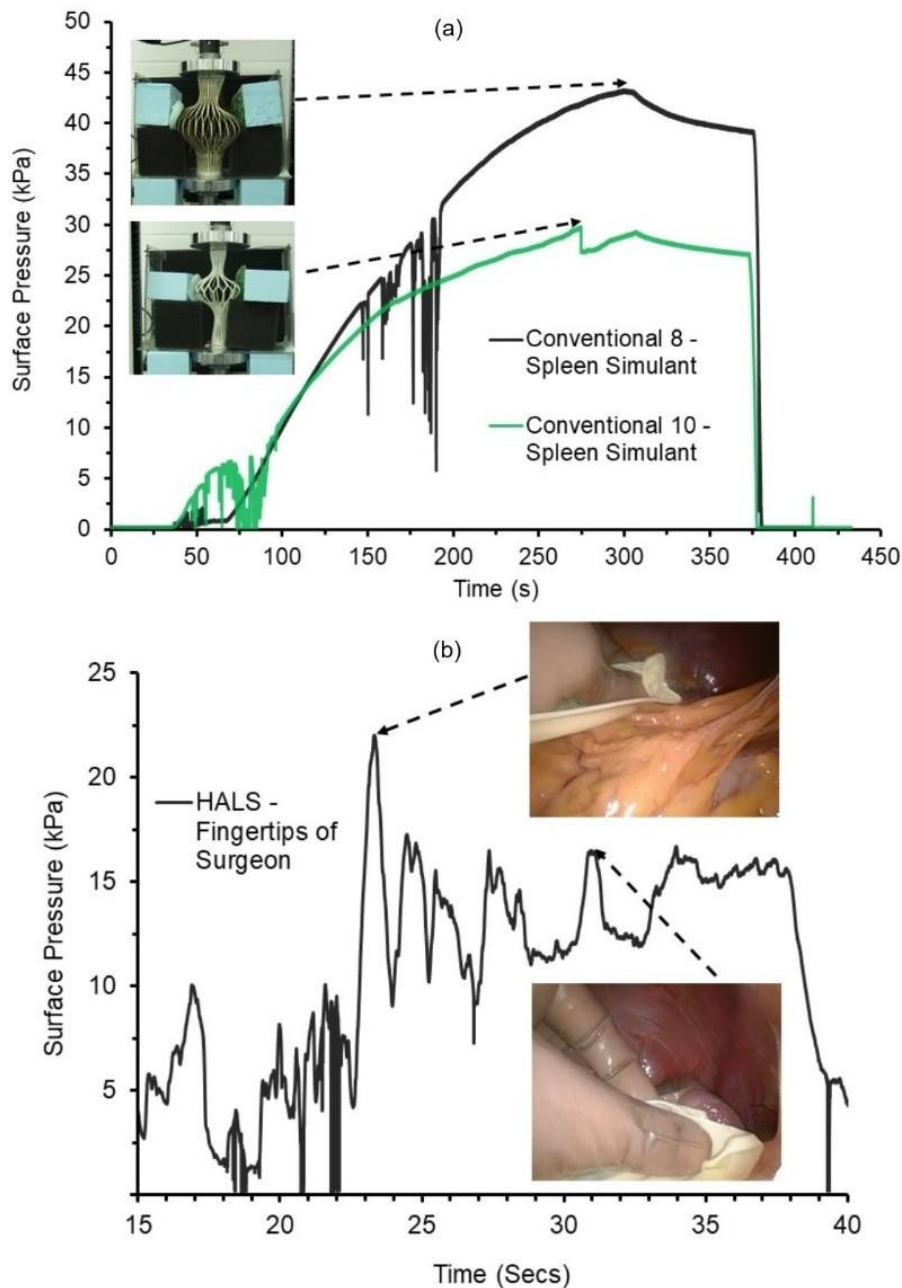


Figure 9.69: Surface pressure applied (a) on the spleen simulants within the test rig (in-vitro) by the Conventional 8 and 10 cylinders and (b) on the human spleen during HALS (in-vivo) by the fingertips of the surgeon. Selected stills are also included in (a) and (b).

Surface pressure exerted (~30 kPa) by the Conventional 10 cylinder on the spleen simulant is 50% higher than that applied by the fingertips of the surgeon during HALS (Figure 9.69b), whereas the Conventional 8 cylinder exerts 2 times the surface pressure (Figure 9.69a).

Summary:

The surface pressures applied by the fingertips of surgeons and metal retractors during OC and HALS (in-vivo) have been quantitatively compared with the surface pressure exerted on the individual and combinations of simulant organs (in-vitro) by the expansion mechanisms. Surface pressures exerted on the hollow (stomach and bowel) and solid (liver, spleen and kidney) organs by the Conventional 10 and Conventional 8 cylinders are in ballpark to surface pressures applied by fingertips of surgeons during OC and HALS.

9.4.5 Summary of in-vitro assessment of expansion mechanisms

The promising expansion mechanisms were evaluated within the test rig mounted on the Instron machine (in-vitro set up) using foam blocks and simulant organs. The degree of axial compressive force required to deploy the expansion mechanisms (without surrounding materials and within the test rig consisting of simulant organs), the surface pressure exerted during the retraction of the foam blocks and simulant organs within the test rig by the expansion mechanisms and the total equatorial deformation for the expansion mechanisms were major outcomes.

The axial compressive forces and surface pressures are correlated with the total equatorial deformation. The gradual increase in the axial compressive forces during the deployment of the expansion mechanisms within the test rig gradually increase the total equatorial deformation (i.e. space creation) and the surface pressure exerted on the simulant organs. The degree of surface pressure reported for the retraction of simulant organs during in-vitro assessment of promising expansion mechanisms is broadly in agreement with the degree of surface pressure measured for the corresponding human abdominal organs during the in-vivo pilot study.

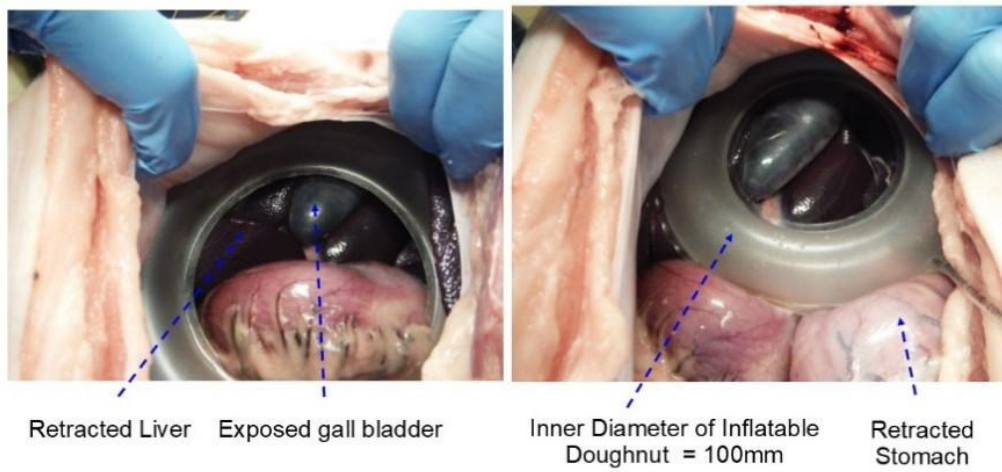
The FE modelling predictions of the total equatorial deformation of the Conventional 8 and Conventional 10 cylinders are in good agreement with the total equatorial deformation of laser cut models without surrounding materials and within the test rig at low axial deformations (<20mm). The order of total equatorial deformation (~200mm for the Conventional 8 and ~100mm for the Conventional 10 cylinders) without surrounding materials as well as for the retraction of the simulant organs within the test rig are in the ballpark of the retraction distances reported for human abdominal organs (Chapter 7) and the degree of expansion (in order of 200mm) envisaged for the proposed laparoscopic device.

9.5 In-vivo and in-vitro assessments of Doughnut shape inflatable prototypes

The doughnut shape inflatable prototypes were assessed within the pig abdomen (in-vivo) and inside the test rig (in-vitro) to evaluate expansion capabilities and the results are described in this section.

In-vivo:

Selected stills captured during the in-vivo assessment of the inflatable doughnut shape prototypes within the pig abdomen are shown in Figure 9.70 for the retraction of the pig liver and bowel.



Retraction of Pig Liver



Retraction of Pig Bowel

Figure 9.70: Retraction of pig liver and bowel by the doughnut shape inflatable prototypes.

Surface pressures exerted by the fingertips of the surgeon on the pig liver, bowel and abdomen are plotted in Figure 9.71.

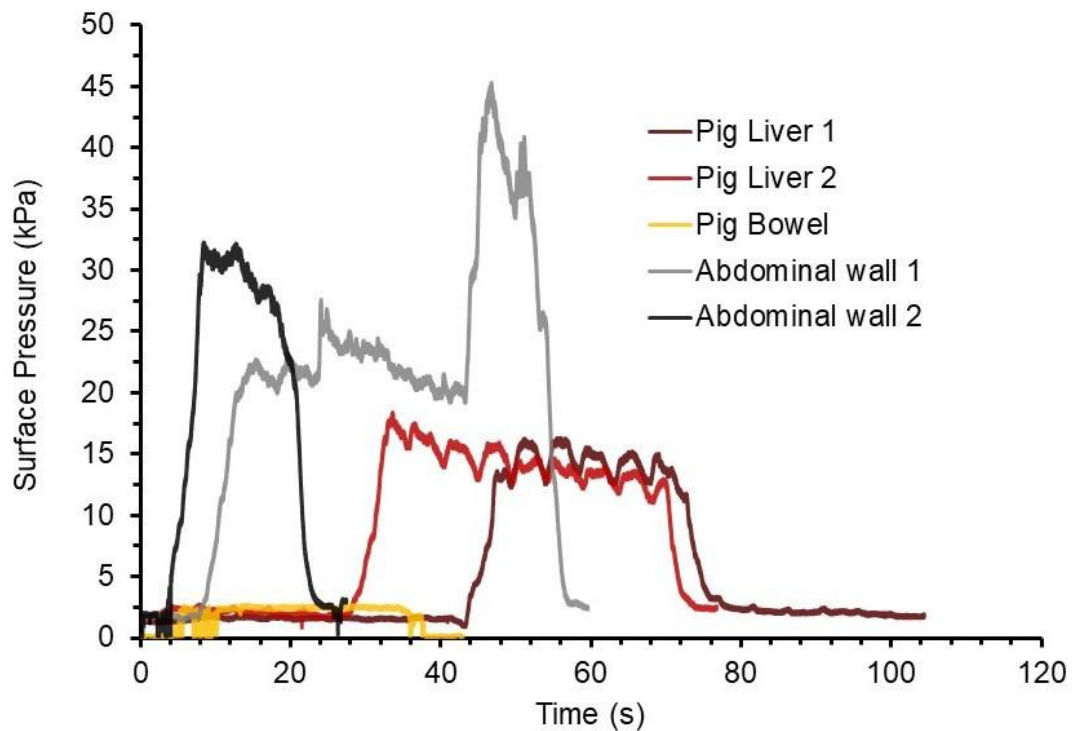


Figure 9.71: Surface pressure exerted by the fingertips of the surgeon on the pig liver, bowel and abdominal wall.

Surface pressure applied for retraction of the pig liver, bowel and abdomen is in order of 15kPa, 3kPa and 40kPa, respectively (Figure 9.71). Surface pressure exerted on pig liver and bowel (Figure 9.71) is in the ballpark of the surface pressure applied on the human liver and bowel by the fingertips of the surgeon during the in-vivo pilot study (Figures 7.29 and 7.31, Chapter 7.4.1).

In-vitro:

Sequences of the selected stills extracted from the video footage of the retraction of the pig liver and simulant bowel and liver during the in-vitro assessment of the inflatable doughnut shape prototype (inner diameter = 100mm) within the test rig are shown in Figure 9.72-74.

The doughnut shape prototype when inflated does not show retraction of pig liver and simulant bowel and liver (Figure 9.72-74). It does not have the axial strength to deploy within the test rig and inside the pig abdomen. Additionally, it does not have cellular structures and hence, do not permit insertion of surgical instruments. There is also a risk of bursting of the inflated prototype during the in-vivo and in-vitro assessments.



Image at 0 Sec



Image at 10 Sec

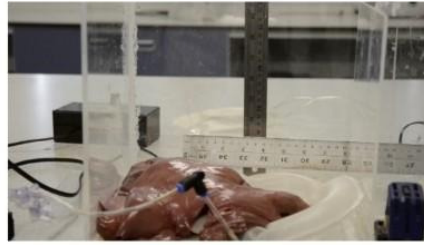


Image at 15 Sec



Image at 25 Sec

Figure 9.72: Retraction of pig liver during the in-vitro assessment of the inflatable doughnut shape prototypes.

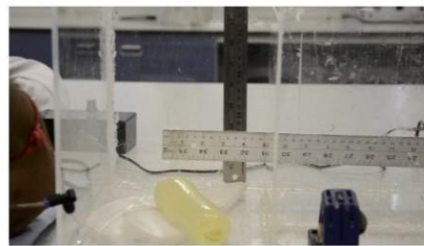


Image at 0 Sec



Image at 30 Sec

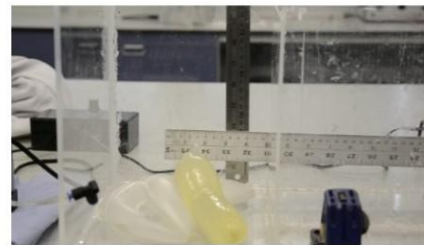


Image at 60 Sec

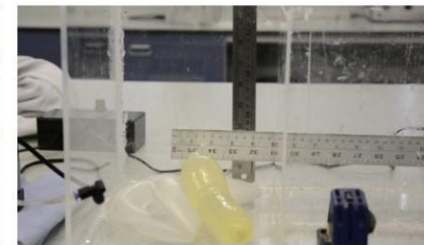


Image at 90 Sec

Figure 9.73: Retraction of the bowel simulant during the in-vitro assessment of the inflatable doughnut shape prototypes.

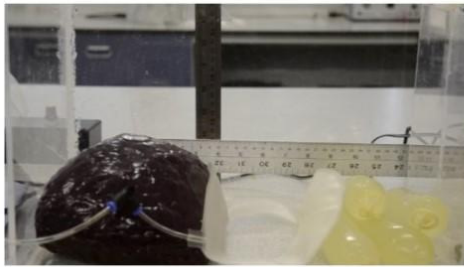


Image at 0 Sec

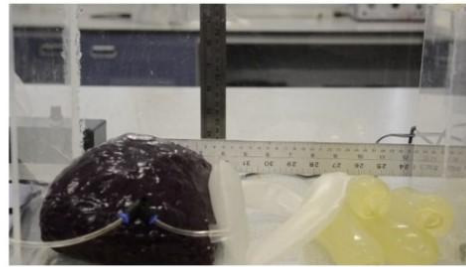


Image at 30 Sec

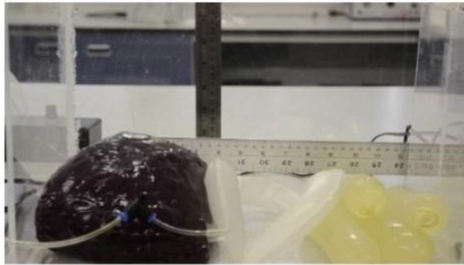


Image at 60 Sec

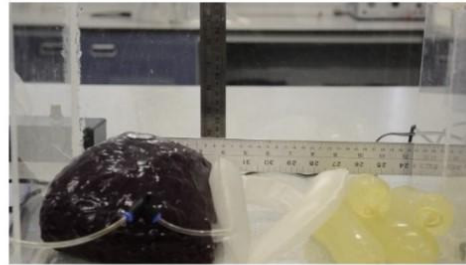


Image at 90 Sec

Figure 9.74: Retraction of the liver simulant during the in-vitro assessment of the inflatable doughnut shape prototypes.

Summary:

The doughnut shape inflatable prototypes were assessed in-vivo (within pig abdomen) and in-vitro (within the test rig) to evaluate their expansion capabilities. The expansion capability of the doughnut shape inflatable prototypes is compared with the expansion mechanisms developed in this project in the next section.

9.6 Novel expansion mechanisms

The novel expansion mechanisms are developed in this PhD project in addition to the inflatable doughnut shape prototypes developed by the industry sponsors. They are ranked into two categories based on – (a) FE predictions of the candidate cellular cylinders and (b) experimental outputs (mechanical characterisation and in-vitro assessment) of the promising cellular cylinders by considering the essential features of the expansion mechanisms outlined below:

- large total equatorial deformation for small (tensile or compressive) axial deformation (or strains) without surrounding materials (Sections 9.1 and 9.3) and inside the test rigs consisting of simulant organs (Section 9.4.2),

- deployability and expansion capabilities in surrounding without material or simulant organs (Sections 9.1 and 9.3) and inside the test rigs consisting of simulant organs (Sections 9.4.2 and 9.5),
- scaffold-like cellular and semi-rigid structure to support the retraction of the simulant organs and space creation functions within the test rig (Section 9.4.2), and
- the degree of surface pressure applied on the simulant organs by the promising expansion mechanisms when deployed inside the test rigs (Sections 9.4.2.1.1 and 9.4.2.2.1).

The candidate expansion mechanisms are ranked by plotting the axial deformation (Figure 9.75a) and axial force (Figure 9.75b) (compressive and tensile) predicted during FE modeling against the total equatorial deformation. The outer diameter and wall thickness of Auxetic 3, Auxetic 7 and Conventional 4 cylinders (Figure 9.75) are 40mm and 2.5mm, respectively. Whereas, the outer diameter and wall thickness of Auxetic 4 and Conventional 5 cylinders are 20mm and 2.5mm, respectively.

The total equatorial deformation of Auxetic 3 cylinder for the applied axial force and axial deformation is greater than Auxetic 7 and Conventional 4 cylinders (Figure 9.75). Although the axial deformation for Auxetic 7 cylinder (31mm) to achieve ~200mm of total equatorial deformation is higher than Conventional 4 cylinder (23mm), the required axial force (~80000N) is half that of the Conventional 4 cylinder (~150000N) (Figure 9.75). The axial deformation required to achieve ~200mm of total equatorial deformation for the Auxetic 4 cylinder (20mm) is approximately 50% less than the Conventional 5 cylinder (~30mm) (Figure 9.75a). Additionally, the axial tensile force required to deploy in free space for the Auxetic 4 cylinder (~15000N) is three times less than the Conventional 5 cylinder (~45000N) (Figure 9.75b).

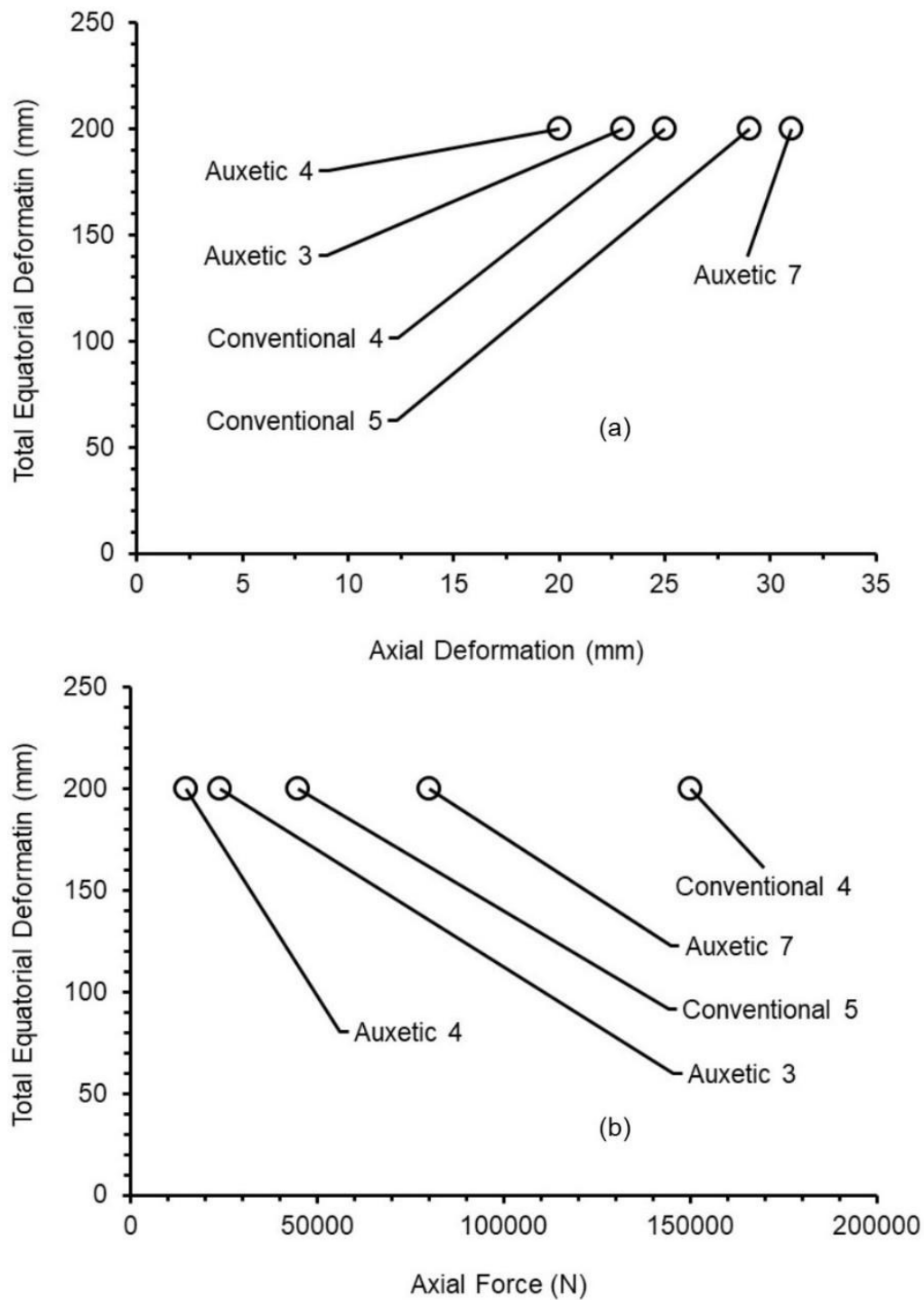


Figure 9.75: Ranking of the expansion mechanisms according to (a) axial deformation and (b) axial force predicted during FE modeling. Axial compressive and tensile deformation and force for the cellular cylinders consisting of conventional and auxetic hexagonal honeycombs, respectively.

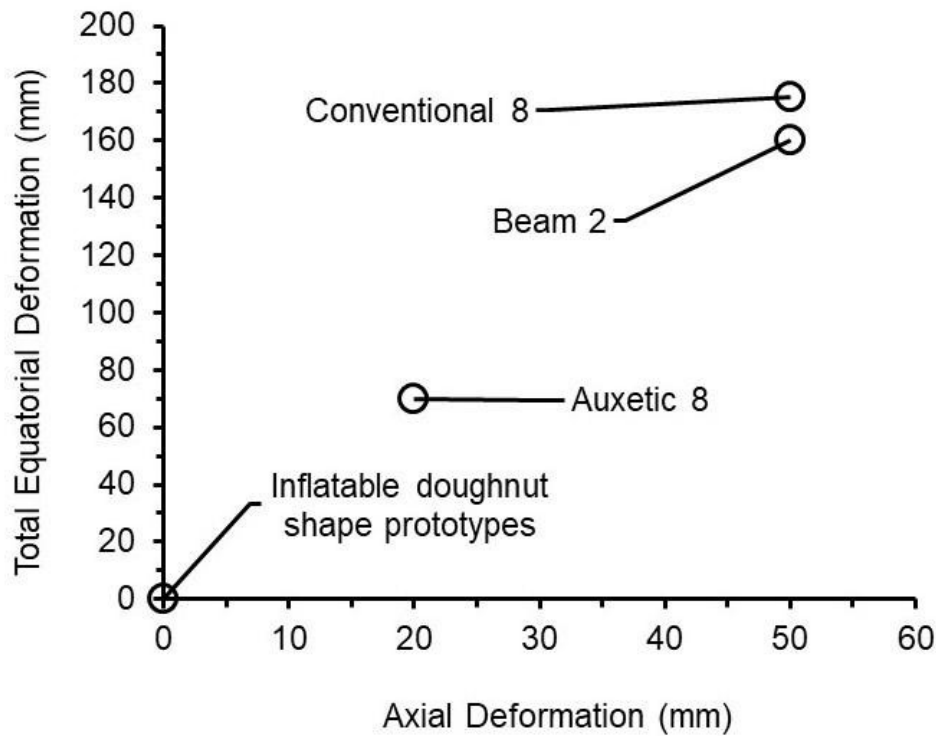


Figure 9.76: Ranking of the promising expansion mechanisms according to the experimental outputs.

To rank the promising expansion mechanisms assessed during the experimental stages (mechanical characterisation in case of Auxetic 8 cylinder and in-vitro assessment), the total equatorial deformation is plotted against the axial deformation in Figure 9.76. The inflatable doughnut shape prototype is ranked lowest in Figure 9.76 since they do not have sufficient strength to enable them to deploy within the test rig. The Auxetic 8 cylinder is also ranked very low compared to the Beam 2 and Conventional 8 cylinders since it did not show significant equatorial deformation during mechanical characterisation without surrounding materials. Despite the total equatorial deformation for Beam 2 and Conventional 8 cylinders being in the ballpark of the expansion (in order of 200mm) required for the proposed laparoscopic device, the Conventional 8 cylinder should be preferred over the Beam 2 cylinder due to former's cellular and scaffold-like structure promoting the retraction of simulant organs and space creation functions within the test rig.

9.7 Summary

Expansion mechanisms were designed, simulated, fabricated, characterised and assessed (in-vivo and in-vitro) in this chapter. Novel expansion mechanisms were ranked according to the outputs of FE modelling and experimental work. Results described in this chapter are discussed in Chapter 10.

10 Discussion

The results outlined in Chapters 7-9 are discussed in this chapter for overarching explanations of phases (outlined below) of the development of the prototype expansion mechanisms for space creation and organ retraction functions during abdominal surgery.

- Development of in-house abdominal simulator.
- In-vivo measurement of surface pressures and organ retraction distances.
- FE modeling of solid wall cylinder to identify the mechanical properties required to achieve a large equatorial deformation for small axial deformation (or strain).
- Computer-aided-designing of cellular meshes for the expansion mechanisms.
- Fabrication of candidate expansion mechanisms.
- Mechanical characterisation of expansion mechanisms without surrounding materials.
- In-vitro assessment of promising prototype expansion mechanisms.

10.1 Development of in-house abdominal simulator

The results of the development (fabrication and assessment) of simulant organs and utilisation of the in-house abdominal simulator for in-vitro assessment of simulant and pig organs are discussed in this section.

10.1.1 Fabrications and assessment of simulant organs

Simulant organs of human liver, kidney, spleen, bowel and stomach essential for the development of the in-house abdominal simulator were fabricated. The ballpark physical dimensions of human simulant organs (such as liver, kidney and spleen) and pig liver simulants were obtained via fabricating them within the respective moulds (Figures 7.1-7.4). The J-shape stomach simulant were obtained by RF welding of PU sheets (Figure 7.5).

Density of simulant organs:

The different consistencies of Pro Gel 10 softener (% v/v) and wall paper paste (% w/v) were used during fabrication of solid simulants (liver, kidney and

spleen) and hollow simulant (bowel), respectively to achieve the required biomechanical properties (density and elasticity). The density of solid simulants was in good agreement with the density of the human liver, kidney and spleen, with the largest discrepancy noted at 60% and 70% of Pro Gel 10 softener (Figure 7.7).

Elasticity of pig liver and simulants:

Elasticity of pig simulant organs (liver and kidney) were evaluated by comparing the tangent modulus obtained via in-vitro mechanical indentation tests with that to actual pig liver and kidney.

The stress-strain responses of the Area 4 of right and Area 1 of left lobes of the actual pig liver A are non-linear and have shown significant degree of variability at higher strain (Figure 7.9). These variations could be due to the difference in the thickness of right ($20 \pm 1.3\text{mm}$) and left lobe ($16 \pm 1.2\text{mm}$) and sample geometry effects (i.e. irregular physical dimensions or contours). Overall, the non-linear responses of actual pig liver A (and of actual pig Livers B-D) (Figure 7.12) are consistent with the non-linear nature of pig and human liver^(18,105,229–232). Rosen et al.⁽²²⁹⁾ have reported the non-linear behaviour (stress-strain curves for the first and fifth loading cycles) of pig liver tissues for the compression tests carried out during post-mortem (ex-corpus) using the Universal testing machine. The difference of two orders of magnitude in the applied stress – $\sim 100\text{ kPa}$ reported by Rosen et al.⁽²²⁹⁾ vs $\sim 1\text{ kPa}$ in Figure 7.12 at 30% strain – can be due to the nature of pig liver sample (ex-corpus vs in-vitro) and size of the indenter (7mm diameter right circular cylinders vs 35mm diameter circular indenter). The average tangent modulus of pig liver samples of 20 kPa at 20% strain (Figure 7.14) is compared with the elastic modulus (the mean gradient of stress-strain curves) of 600 kPa at 20% strain reported in Carter et al.⁽³⁵⁾ Discrepancy between the two studies may be attributable to in-vitro (this work) vs in-vivo⁽³⁵⁾ testing, size of indenter [diameter of 35mm (this work) vs 4.5mm⁽³⁵⁾] and displacement rate [30mm/min or 0.5mm/s (this work) vs 1mm/s⁽³⁵⁾].

The force-displacement responses of the pig liver simulants, similar to the actual pig liver A (Figure 7.8), are non-linear and have varied significantly for

displacement >1.5mm (Figure 7.15) due to the difference in the thickness of right and left lobes and irregular contours of pig liver simulants. The force vs displacement (Figure 7.15), stress vs strain (Figure 7.16) and tangent modulus vs strain (Figure 7.17) curves of the pig liver simulants suggested that 50% v/v consistency of Pro Gel 10 softener makes simulant organs less stiff than 20% and 30% v/v consistencies. The tangent modulus of 50% v/v pig liver simulant at 20% strain (~30 kPa) is in ballpark with the actual pig liver (~20 kPa) (Figure 7.18).

The stress-strain responses (and elastic/tangent modulus) of intra-abdominal organs of living humans have not frequently reported in literature due to ethical constraints. However, the stress-strain responses (~25 kPa at 10% strain) and elastic modulus (~270 kPa at 10% strain) of only right lobe (25mm thickness) of healthy human liver of five patients measured during open surgery (in-vivo) using hand-held compliance probe were reported.⁽³⁵⁾ The mechanical responses (stress and elastic modulus) of healthy human liver are compared with those of actual pig liver [stress and tangent modulus were ~0.5 kPa (Figure 7.12) and ~5 kPa (Figure 7.14) at 10% strain, respectively] and 50% v/v pig liver simulant [stress and tangent modulus were ~2.5 kPa (Figure 7.16) and ~25 kPa (Figure 7.17) at 10% strain, respectively]. Discrepancy between two studies may be attributable to in-vitro (this work) vs in-vivo⁽³⁵⁾ testing, size of indenter [diameter of 35mm (this work) vs 4.5mm⁽³⁵⁾], indentation rate [30mm/min or 0.5mm/s (this work) vs 3-4mm/s⁽³⁵⁾], indentation depth [10mm (this work) vs 5mm⁽³⁵⁾] and area of liver [right and left lobes of liver (this work) vs only right lobe⁽³⁵⁾].

Elasticity Pig kidney and simulants:

The force-displacement and stress-strain responses of the actual pig kidney samples are non-linear (Figures 7.19-7.20) similar to the actual pig liver (Figures 7.8-7.9). These responses are consistent with the non-linear nature of pig and human kidney^(229,232,233). Tamura et al.⁽²³²⁾ have reported the non-linear behaviour of rectangular pig kidney specimens (20×20×10mm) for the in-vitro compression tests carried out at 0.5mm/s indentation rate using the universal testing machine. The difference of one order of magnitude in the applied stress – ~150 kPa reported by Tamura et al.⁽²³²⁾ vs ~15 kPa in Figure 7.20 at 30%

strain – can be due to the nature of specimens of the pig kidney (rectangular pieces vs whole organ).

The force-displacement responses of the pig kidney simulants like the actual pig kidney in Figure 7.19, are non-linear and have varied significantly for displacement >2mm for KS 30-60% in Figure 7.22 due to irregular contours of pig kidney simulants. The average force, average stress and average tangent modulus values for pig kidney simulants at lower displacements and strains (Figures 7.22-24) suggested that 60 %v/v and 70 %v/v consistencies of Pro Gel 10 softener makes simulant less stiff than other consistencies (30-50 %v/v). The tangent modulus of 50% v/v pig kidney simulant is in excellent agreement with the actual pig kidney (~25 kPa at 15% strain) (Figure 7.24). The tangent modulus of the pig kidney simulants made from 60 %v/v and 70 % v/v Pro Gel 10 softener were also found to give the closest match to the tangent modulus of the actual pig kidney up to a strain of ~0.1. However, simulants made of softener concentration greater than 50 % v/v were found to have a sticky surface which poses a challenge when handling by hand.

The slight discrepancies in the tangent modulus vs strain data between pig liver (Figure 7.17) and pig kidney (Figure 7.24) simulants having same softener concentrations (e.g. 30% and 50% curves in both figures) are attributable to sample geometry/dimensions. The fixed sample size (cubes/cuboid or rectangular) should be considered for the compression tests instead of indentation tests to avoid such discrepancies.⁽²³²⁾

According to the tangent modulus vs strain curves for the pig liver (Figure 7.17) and pig kidney simulants (Figure 7.24) and opinions of surgeons on the physical dimensions, density and pliability of solid simulants obtained during survey of biomechanical properties (Table 7.4), it is concluded that solid simulant organs fabricated using 50 %v/v of Pro Gel 10 softener closely match the biomechanical properties of the corresponding human abdominal organs and should be considered for the in-vitro assessment of the promising expansion mechanisms within the test rig.

10.1.2 In-house abdominal simulator (in-vitro test rig)

Surface pressure was applied by the fingertips of the operator using the thin film pressure sensor during the predefined typical 'movements' of the pig liver, human liver simulant and simulant human bowel pieces within the 'right angled shape' test-rig (Figures 7.25-7.28).

The range of maximum surface pressures required for the 'moving and squashing' (8-19 kPa in Figure 7.25) and 'lifting' (3-9 kPa in Figure 7.26) of the actual pig liver; 'lifting' (20-25 kPa in Figure 7.27) of human liver simulant and 'moving and squashing' (8-11 kPa in Figure 7.28) of simulant human bowel pieces within the test rig (in-house abdominal simulator) fall within the range (1-41 kPa) of maximum surface pressures (Table 7.6) reported for the typical retraction movements of human liver and bowel during OC and HALS (Figures 7.61-7.62).

The surface pressure responses generated within the test rig validate the development of the in-house abdominal simulator (test rig and simulant organs). The in-house abdominal simulator was developed to evaluate the organ retraction and space creation functions of the promising expansion mechanisms at the later stages of this PhD.

10.2 In-vivo measurement of organ surface pressures and retraction distances

Results of in-vivo measurement of surface pressures and retraction distances applied to key abdominal organs during abdominal surgery (OC and HALS) are discussed in this section.

Surface pressure:

The in-vivo study was designed to quantify typical surface pressures applied to organs and surrounding tissues by the hand of the surgeon and metal retractors carrying out standard manoeuvres during abdominal surgery. The choice of open abdominal surgery and hand assisted laparoscopic nephrectomy allowed repeatable access to key abdominal organs and, therefore, repeating typical retraction manoeuvres of the liver, bowel, stomach, spleen and kidney readily

whilst placing the pressure sensor between the organ and the flexor surface of the dominant hand of the operator.

To the best of our knowledge, this is the first time a study has electronically measured surface pressures typically applied on human abdominal organs during open and laparoscopic surgery. Carter et al⁽³⁵⁾ and Nava et al⁽¹⁰⁵⁾ have reported in-vivo indentation tests on six human livers to characterise liver mechanical properties during MIS and open abdominal surgery, respectively. Sterile hand-held compliance probe and aspiration devices were employed to study liver tissues, but no surface pressures were measured. Barrie et al. 2016⁽¹⁰⁶⁾ have obtained the grasping force for the major abdominal organs using a fenestrated grasper for an in-vivo porcine model. In the in-vivo study reported in Chapters 5 and 7, a broad flat pressure sensor was deployed between the operator's fingers and the organ during a manoeuvre specifically to mimic typical organ retraction carried out with currently employed retractors intraoperatively at the MFT. For example, the liver was retracted superiorly in the coronal (x-y) plane before the excursion was stopped by compression/squashing of the liver against the diaphragm and rib cage. This is typical of liver retraction to gain access to the gall bladder during open and laparoscopic cholecystectomy and other surgical procedures in the sub-hepatic region.

Assuming full contact of the pressure sensor with the organ during retraction, the recorded pressure can be converted to applied force by multiplication of the pressure with the sensor cross-sectional area ($= 6.25 \times 10^{-4} \text{ m}^2$). In this case the values of $\langle P_{\text{rms}} \rangle = 9 \pm 3 \text{ kPa}$ and $\langle P_{\text{max}} \rangle = 12 \pm 5 \text{ kPa}$ for the Bowel-OC combination (Figure 7.44), for example, correspond to average rms and maximum forces of $\langle F_{\text{rms}} \rangle = 6 \pm 2 \text{ N}$ and $\langle F_{\text{max}} \rangle = 7 \pm 3 \text{ N}$, respectively. Similarly, for the Bowel-HALS combination $\langle P_{\text{rms}} \rangle = 11 \pm 4 \text{ kPa}$ and $\langle P_{\text{max}} \rangle = 13 \pm 4 \text{ kPa}$ correspond to $\langle F_{\text{rms}} \rangle = 7 \pm 2 \text{ N}$ and $\langle F_{\text{max}} \rangle = 8 \pm 3 \text{ N}$, respectively. For comparison, Barrie et al. 2016⁽¹⁰⁶⁾ reported $\langle F_{\text{rms}} \rangle = 13.7 \pm 5.4 \text{ N}$ and $\langle F_{\text{max}} \rangle = 20.5 \pm 7.2 \text{ N}$ using a fenestrated grasper to manipulate the small bowel in an in-vivo porcine model⁽¹⁰⁶⁾.

The surface pressure relaxation phenomenon associated with the hand-tissue interaction observed in this in-vivo study on human abdominal organs (Figure 7.30 and Figure 7.35) was also found in the tool-tissue interaction of the in-vivo fenestrated grasper study of pig abdominal organs⁽¹⁰⁶⁾, and is known to be a feature of the biomechanical properties of soft tissues under an applied surface pressure.⁽²²⁹⁾ Barrie et al. 2016⁽¹⁰⁶⁾ attributed the force relaxation phenomenon in their work to a combination of a maximum force to lift the organ initially and subsequent tissue response and grasper handle applied pressure. Similarly, I believe in the work I report the initial applied pressure is higher to initiate movement of the organ (the dynamic retraction phase), followed by a static retraction phase where the organ is held in one place. The surface pressure in this static retraction phase is less, since the organ is in a state of rest, and decreases due to a combination of tissue relaxation and pressure applied by the surgeon fingertips.

The suggestion of a lower rate of surface pressure relaxation in the HALS procedures compared to the OC procedures (Figure 7.47) possibly indicates the surface pressure relaxation is affected by external constraints: the more constrained abdominal environment in the HALS procedure providing some degree of mitigation against surface pressure relaxation. This may have implications in the design of organ retractors and other surgical implements used in laparoscopic surgery.

Caution should be applied in drawing firm conclusions between organ type and open versus hand assisted laparoscopic surgery given the relatively low number of retractions studied in this pilot study. The average maximum and rms surface pressures applied to the solid organs (liver and kidney) were both higher in comparison to the hollow organs (bowel and stomach) for both types of procedure – Figure 7.4. With the exception of $\langle P_{\max} \rangle$ for the liver-OC case, which has a large associated standard deviation, there is a slight tendency for higher average maximum and rms surface pressures applied in HALS than in open surgery, again consistent with the more constrained abdominal environment in HALS.

Retraction distance:

Due to logistical and infection control imperatives in the operating theatre to position the camera, and movements of the operators' hands and organ retraction out of the line of sight of the camera lens and behind the abdominal wall, full tracking of abdominal organ retraction in a controlled frame of reference relative to the defined human coordinate system (Figure 2.9) was not possible in this study. Consequently, a fully quantitative measurement of retraction distances and directions has not been undertaken. Nevertheless, a direct correlation has been established between the organ retraction distance data extracted from image analysis and the surface pressure data measured using the pressure sensor for retraction of the liver in OC (Figure 7.51) and bowel, kidney, stomach and spleen in HALS (Figure 7.56-59). The degrees of organ retraction distances (Figure 7.60) are ~ 60mm, ~50mm, ~20mm and ~10mm for the retraction of liver (OC) and bowel (HALS), stomach (HALS), spleen (HALS) and kidney (HALS), respectively. It is estimated by the participating surgeons that ~30-40mm of distance organs retracted was not captured due to movements of organs out of the range of the hand-held camera/endoscope. Hence, total retraction distance of abdominal organs (solid and hollow) in the plane of image is in the range of ~40-100mm. This range of retraction distance would be (~80-200mm diameter of sphere) required for the proposed expansion mechanisms in the fully deployed state and, in fact, considered as target value of deformation of solid wall cylinder during FE modeling. A more detailed study employing fixed cameras at appropriate locations is now merited for a fully quantitative assessment of surface pressure and retraction distance relationships for specific organs and procedures.

Importance of in-vivo measurement of surface pressures and retraction distances:

While the degree of surface pressure used to retract tissues and organs is subjective and learnt through experience of surgical craftsmanship, in the current era of increasing technology in surgery, methods of objective assessment of surface pressures in real time could be of immense value in improving outcomes and decreasing morbidity in the form of traction injuries. This includes robotic surgery and mechanised tissue manipulation which employ force sensing and feedback. The approach reported in this work could

be used to develop databases of typical surface pressures (or forces) and retraction distances for specific organs and procedures, against which applied forces and distances can be monitored. This will improve control and accuracy for improved dexterity, and mitigate against both excessive forces causing trauma and tissue damage, and insufficient forces in grasping devices leading to slippage.⁽²³⁴⁾ Well-defined objective retraction surface pressure parameters could be of value in the training of surgeons in all disciplines of surgery. Accurate definition of these surface pressures may be, and especially of value in laparoscopic surgery. For example, surface pressure data can be incorporated within the software of advanced laparoscopic simulators to improve haptic feedback during simulated laparoscopic surgery which is becoming increasingly sophisticated. In addition, quantified surface pressures and organ retraction distances for key abdominal organs will be key inputs for the design and development of organ retraction and space creation devices for use during laparoscopic surgery.

10.3 FE modelling of a solid wall cylinder

Results of the FE modelling of a solid wall cylinder with pronged cone and without end pieces displaying uniform linear elastic isotropic and orthotropic material properties are discussed in this section.

Isotropic material properties:

Results of uniform linear elastic isotropic material properties (without end pieces in Figures 8.1, Chapter 8) suggested (as expected) that the magnitude of the Poisson's ratio (0.3) was not sufficient to achieve the large equatorial deformation of a solid wall of cylinder for small axial strain. When the different types of end pieces (assembled at both ends of a solid wall of cylinder) simulated using isotropic material properties, they did not induce out-of-plane bending of solid wall of cylinder to achieve the large equatorial deformation against our expectation at low strain ($\leq 4\%$) (Figure 8.2, Chapter 8). Hence, uniform orthotropic material properties were subsequently simulated during parametric studies 1 and 2 using finite BCs.

Parametric study 1:

The parametric study 1 for solid wall cylinder was carried out using the set of orthotropic material properties (Table 5.3, Chapter 5) (defined as ‘standard’ set of properties), geometrical parameters defined in Chapter 5.3.1, and pronged cone end pieces at both ends under the uniaxial compression mechanism. Young’s moduli (E_r , E_θ and E_z), shear moduli ($G_{r\theta}$, $G_{\theta z}$ and G_r) and in-plane Poisson’s ratio ($\nu_{\theta z}$) (negative) of orthotropic material properties (Table 5.3, Chapter 5) were varied during parametric study 1 and results were shown in Figures 8.3-8.9 (Chapter 8), Figures 8.10-8.15 (Chapter 8) and Figures 8.16-17 (Chapter 8), respectively. The geometrical parameters were subsequently varied using the set of orthotropic material properties (Table 5.3, Chapter 5) and results were displayed in Figures 8.18-8.22, Chapter 8.

Except the parametric study of E_θ (Figure 8.5, Chapter 8), variations in other orthotropic material properties as well as geometric parameters did not affect the equatorial deformation of solid wall cylinder. When E_θ was reduced to 2×10^4 Pa from the ‘standard’ value of 2×10^8 Pa (without changing the remaining orthotropic properties except $\nu_{\theta z}$ to maintain the symmetric matrix compliance), a solid wall of cylinder has shown the large equatorial deformation (the shape of a prolate spheroid) for the small axial deformation (Figure 8.5, Chapter 8). This is because E_z/E_θ has increased to 2×10^6 Pa from 2×10^2 Pa making the solid wall of cylinder extremely compliant which in turn allowed the pronged cone end pieces at the both ends to induce the out-of-plane bending of solid wall of cylinder when uniaxially compressed along its cylindrical axis (E_z). The difference of one order of magnitude in the required axial compressive force to achieve the large equatorial deformation was indicative of compliant solid wall when E_θ was 2×10^4 Pa than $E_\theta = 2 \times 10^6$ Pa and 2×10^8 Pa (Figure 8.6, Chapter 8).

The impact of varying E_θ suggested that in-plane properties would be crucial from the set of orthotropic material properties to achieve the large equatorial deformation for the small axial deformation (or strain) when solid wall of cylinder was uniaxially compressed along its cylindrical axis. Hence, in-plane Poisson’s ratio ($\nu_{\theta z}$) was the only parameter from the set of orthotropic material properties varied during the simulation of ‘shape change’ properties (Table 8.2, Chapter 8). Variations in $\nu_{\theta z}$ did not affect the large equatorial deformation of solid wall of cylinder which was not expected (Figures 8.23-8.24, Chapter 8). It is therefore

concluded that $v_{\theta z}$ did not impact the deformation of solid wall of cylinder with pronged cone end pieces when simulated using the 'shape change' properties.

As expected, parametric studies of geometric parameters (outer diameter, length and wall thickness of cylinder, and Young's modulus of pronged cone end pieces) carried out using the 'shape change' properties did impact the degree of equatorial deformation. The required equatorial radial deformation (90mm) for 20mm outer diameter is greater than 40mm outer diameter (80mm) of cylinder to achieve the target value of 200mm diameter of sphere for the proposed expansion mechanisms when fully deployed, and hence, it required 20% more axial compressive force than the 40mm outer diameter of cylinder (Figure 8.26, Chapter 8). The length of solid wall cylinder when simulated using the 'shape change' properties (Table 8.2, Chapter 8) had significant impact on the degree of equatorial deformation (Figure 8.28, Chapter 8) and axial compressive force (Figure 8.29, Chapter 8). The ratio of outer diameter (fixed at 40mm for 'shape change' properties) to length of solid wall cylinder (D/L) is half (0.13) for 300mm length than for 150mm length of cylinder (0.26) which should be the reason for achieving the target value of equatorial deformation (80mm) for the approximately half the axial deformation in case of 300mm length than 150mm length of cylinder (~19mm vs ~36mm) (Figure 8.28, Chapter 8). It is suggested that the impact of the length of solid wall cylinder should be investigated for 20mm of outer diameter of cylinder ($D/L=20/300=0.067$) during further development of the expansion mechanisms to optimise the D/L ratio. The parametric study of wall thickness of cylinder (Figures 8.31-8.32, Chapter 8) suggested that the axial compressive force required for 5mm of wall thickness was significantly higher than 1mm of wall thickness which will affect the amount of force required for the deployment of the expansion mechanisms from cylinder to sphere. Wall thickness of cylinder is therefore critical along with the length of cylinder. The parametric study of Young's modulus of pronged cone end pieces suggested that there was a significant deformation of the pronged end piece as the Young's modulus of material of end pieces decreases (Figure 8.34, Chapter 8). Linear elastic model employed in this PhD may therefore not be sufficient to evaluate the impact of the Young's modulus of pronged cone end pieces.

It is concluded from the parametric study 1 that E_θ is a critical orthotropic material property (or E_z/E_θ) to obtain a large equatorial deformation of solid wall cylinder with pronged cone end pieces. It is also suggested that presence of pronged cone end pieces at the both ends of solid wall cylinder might have neutralised the impact of in-plane negative Poisson's ratio. The parametric study 2 was further employed in accordance with the symmetric compliance matrix condition and the reciprocal Poisson's ratio relationship in hexagonal honeycombs deforming by flexure in light of the eventual cellular nature of the expansion mechanism.

Parametric study 2:

The parametric study 2 for solid wall cylinder was carried out using the set of orthotropic material properties (Table 5.4, Chapter 5) (defined as 'standard' set of properties), geometrical parameters defined in Chapter 5.3.1, and pronged cone end pieces at both ends under the uniaxial compression mechanism (Chapter 8.2.2) as well as without end pieces under the uniaxial compression (Chapter 8.2.3.1) and tension mechanisms (Chapter 8.2.3.2).

Solid wall cylinder with pronged cone end pieces:

E_θ was the only parameter varied (incrementally from 1.98×10^8 Pa to 1.98×10^3 Pa) to maintain the two conditions – symmetric compliance matrix condition and the reciprocal Poisson's ratio relationships – during parametric study 2 of solid wall cylinder with pronged cone end pieces (Table 8.3, Chapter 8). The solid wall of cylinder adopted the shape of a prolate spheroid when E_θ was 1.98×10^5 Pa, 1.98×10^4 Pa and 1.98×10^3 Pa (Figure 8.37, Chapter 8). This is as explained during parametric study 1, due to the significant increase in E_z/E_θ from 1.02×10^2 Pa for $E_\theta = 1.98 \times 10^8$ Pa to 1.02×10^5 Pa, 1.02×10^6 Pa and 1.02×10^7 Pa, respectively making the solid wall of cylinder extremely compliant which in turn allowed the pronged cone end pieces at the both ends to induce the out-of-plane bending of solid wall of cylinder when uniaxially compressed along its cylindrical axis (E_z). The magnitude of in-plane negative Poisson's ratio required for large equatorial radial deformation of solid wall cylinder was found during parametric study of set of 'standard' properties (Table 8.3, Chapter 8) ('shape change' from cylinder to prolate spheroid obtained when E_θ was 1.98×10^5 Pa)

due to the symmetric compliance matrix condition and the reciprocal Poisson's ratio relationships employed in the parametric study 2. Additionally, shear moduli can't be varied using the 'shape change' properties (Table 8.4, Chapter 8) due to two conditions (outlined above) employed for the parametric study 2.

Solid wall cylinder without end pieces:

E_θ was the only parameter varied (incrementally from 1.98×10^8 Pa to 1.98×10^3 Pa) to maintain the two conditions – symmetric compliance matrix condition and the reciprocal Poisson's ratio relationships – during the parametric study 2 of solid wall cylinder without end pieces under uniaxial compression (Table 8.5, Chapter 8) and tension (Table 8.7, Chapter 8) mechanisms.

The large equatorial deformation of a solid wall of cylinder for the small axial deformation (or strain) was obtained when $E_\theta \leq 1.98 \times 10^7$ Pa [Figure 8.39 in case of uniaxial compression mechanism (in-plane positive Poisson's ratio) and Figure 8.51 in case of uniaxial tension mechanism (in-plane negative Poisson's ratio), Chapter 8]. This should be due to combinations of two factors – a) an increase/decrease in the magnitude of the in-plane positive/negative Poisson's ratios (commonly known to govern the transverse deformation) and b) an increase in ratio of E_z/E_θ from 1.02×10^2 Pa (for $E_\theta = 1.98 \times 10^8$ Pa) to 1.02×10^3 Pa (for $E_\theta = 1.98 \times 10^7$ Pa) and so on. Due to the symmetric compliance matrix condition and the reciprocal Poisson's ratio relationships employed in the parametric study 2 of solid wall cylinder without end pieces, the remaining orthotropic constants were not varied. The parametric studies of geometrical parameters of solid wall cylinder without end pieces were carried out using the 'shape change' properties [Table 8.6 in case of uniaxial compression mechanism (in-plane positive Poisson's ratio) and Table 8.8 in case of uniaxial tension mechanism (in-plane negative Poisson's ratio), Chapter 8]. The outcomes depicted in Figures 8.42-8.50 [in case of uniaxial compression mechanism (in-plane positive Poisson's ratio)] and Figures 8.54-8.62 [in case of uniaxial tension mechanism (in-plane negative Poisson's ratio)], Chapter 8 were approximately similar to that outlined for a solid wall cylinder with pronged cone end pieces for parametric study 1.

Importance of parametric studies of solid wall cylinder:

The in-plane Poisson's ratios ($\nu_{\theta z}$ and $\nu_{z\theta}$) and E_{θ} (or E_z/E_{θ}) related by compliance matrix symmetry and the magnitudes of in-plane Poisson's ratios (positive and negative) were identified as key orthotropic material properties to achieve a large equatorial deformation of a solid wall cylinder with and without end pieces. These effective mechanical properties required for shape change were subsequently utilised to achieve the hexagonal honeycomb meshes assumed to deform by flexure of the honeycomb ribs, previously developed by Gibson and Ashby.⁽¹¹³⁾

10.4 Designing cellular mesh cylinders

Results of the designing of cellular (hexagonal auxetic and non-auxetic honeycombs) mesh cylinders (in-silico models) are discussed in this section. They were developed for the validation of outputs of the FE modelling of the solid wall cylinder (Chapter 8) and to predict the expansion behaviours of cylinders fabricated using laser cutting and 3D printing technology.

10.4.1 Validation of outputs of FE modeling of a solid wall cylinder

Auxetic honeycomb mesh models without end pieces (Auxetic 1-4 models, Table 6.5, Chapter 6), Auxetic honeycomb mesh models with pronged cone end pieces (Auxetic 5-7 models, Table 6.5, Chapter 6) and Conventional honeycomb mesh models (Conventional 1-5 models, Table 6.5, Chapter 6) were designed and simulated without surrounding materials. These steps have demonstrated the 'CAD-FE' parts of the 'CAD-FE-Experimental approach'.

FE predictions of Auxetic 1-4 and Conventional 1-5 models were depicted as ERD vs tensile and compressive AD (Figure 9.1-9.2, Chapter 9), ERD vs axial tensile and compressive force (Figure 9.3-9.4, Chapter 9) and ERD vs axial tensile and compressive strain (Figure 9.5-9.6, Chapter 9). The large equatorial deformations (~80mm) were obtained for the Auxetic 1-4 models for the small tensile AD (Figure 9.1, Chapter 9) or tensile axial strain ($\leq 10\%$) (Figure 9.5, Chapter 9) and for the Conventional 3-5 models for the small compressive AD (Figure 9.2, Chapter 9) or compressive axial strain ($\leq 10\%$) (Figure 9.6, Chapter 9) which have qualitatively validated the outputs of FE modeling of a solid wall cylinder. The large equatorial deformations (~80mm) were not achieved by the

Conventional 1 and 2 models due to the high aspect ratio of vertical to diagonal ribs ($h/l=2$) and magnitude of the in-plane positive Poisson's ratio (+10), respectively.

Tensile AD and the maximum axial tensile force required to achieve a large equatorial deformation ($\sim 80\text{mm}$) was approximately 50% higher ($\sim 30\text{mm}$ vs $\sim 20\text{mm}$) and five times ($\sim 80000\text{N}$ vs $\sim 16000\text{N}$) for Auxetic 3 model than Auxetic 4 model, respectively which could be due to the bigger outer diameter (40mm vs 20mm) and higher numbers of N_v (12 vs 8) (Figure 9.3, Chapter 9). The maximum axial tensile force required to achieve a large equatorial deformation ($\sim 80\text{mm}$) was minimum for Auxetic 1 model ($\sim 2500\text{N}$) than Auxetic 2 ($\sim 10000\text{N}$) and Auxetic 3 (80000N) models (Figure 9.3, Chapter 9) because of least numbers of N_c (Table 6.5, Chapter 6). The maximum axial compressive force required to achieve a large equatorial deformation ($\sim 80\text{mm}$) was approximately three times (150000N vs 50000N) for Conventional 4 model than Conventional 5 due to the bigger outer diameter (40mm vs 20mm) and higher numbers of N_v ($N_v = 12$ vs 8 in Table 6.5, Chapter 6) (Figure 9.4, Chapter 9). Conventional 4 model required approximately twice the axial force ($\sim 150000\text{N}$ vs $\sim 80000\text{N}$) than Auxetic 3 model to achieve the large equatorial deformation ($\sim 80\text{mm}$) (Figures 9.3-9.4, Chapter 9) which can be attributed to the higher numbers of N_c ($N_c = 64$ vs 49 in Table 6.5, Chapter 6) and double value of t/l ($t/l = 0.0955$ vs 0.0482 in Table 6.5, Chapter 6). The axial tension and compressive forces shown in Figure 9.3 and Figure 9.4, Chapter 9, respectively are extremely high for surgical purposes and are due to the models employing elastic constants based on structural steel.

FE predictions of Auxetic 5-7 models (assembled with the pronged cone end pieces) were shown as ERD vs axial compressive AD (Figure 9.7, Chapter 9), ERD vs axial compressive force (Figure 9.8, Chapter 9) and ERD vs axial compressive strain (Figure 9.9, Chapter 9) which have qualitatively validated the outputs of FE modeling of a solid wall cylinder. The effective material properties for 'shape change' of solid wall cylinder with pronged cone end pieces were identified as $\nu_{\theta z} \leq -320.9$ and E_{θ} (or $E_z/E_{\theta} = 1.98 \times 10^5 \text{ Pa}$ (or 1.02×10^5) in Table 8.3 and Figure 8.37 (Chapter 8.2.2.1). However, it must be noted that Auxetic 7 model has $\nu_{\theta z} = -216.2$ and $E_z/E_{\theta} = 4.76 \times 10^4$ and it has

shown large equatorial deformation (~80mm) for small axial compressive deformation (Figure 9.7, Chapter 9). The large equatorial deformation of Auxetic 7 model for small axial deformation was obtained due to conversion of axisymmetric load into bending load by the pronged cone end pieces assembled at both ends of cylinder (causing out-of-plane bending of wall of cylinder) and converts cylinder into sphere when fully deployed. This effect is shown in Figure 3.15, Chapter 3 for the deployment of the origami folded paper into sphere by simple application of the axisymmetric compressive load (cylinder to ball mechanism).⁽¹⁶⁴⁾ This phenomenon was investigated based on the double curvature effect of auxetic honeycombs predicted in the flat sheet (Figure 3.13, Chapter 3).^(5,161,162)

10.4.2 FE predictions of cellular mesh cylinders

FE predictions of Auxetic 8 (laser cut), Conventional 8 (laser cut), Conventional 10 (laser cut), and Conventional 12 (3D printed) cylinders in the forms of ERD vs AD (Figures 9.10, Chapter 9), ERD vs axial tension and compressive force (Figure 9.11, Chapter 9) and ERD vs axial strain (Figures 9.12, Chapter 9) were carried out to predict the expansion capabilities of the experimental cylinders (laser cut and 3D printed).

The large equatorial deformation (~80mm) for Auxetic 8 cylinder obtained for the small tensile AD (~18mm in Figure 9.10, Chapter 9) or tensile axial strain (~6% in Figure 9.12, Chapter 9) was approximately half as compare to the compressive AD (~33mm in Figure 9.10, Chapter 9) or tensile axial strain (~11% in Figure 9.12, Chapter 9) for the Conventional 8 cylinder (outer diameter is 68mm for both cylinders). However, the axial tensile force for Auxetic 8 cylinder was 3.5 times than axial compressive force for Conventional 8 cylinder (~46000N vs ~13000N in Figure 9.11, Chapter 9). This could be attributed to nature of deploying mechanisms (tension vs compression), α [acute (-80.8°) vs extremely acute (88.2°) which would require higher axial force to initiate the bending of diagonal rib before stretching and/or flexing mechanisms start dominating], and number of N_c ($N_c = 18$ vs 36 in Table 6.6, Chapter 6).

Although the large equatorial deformation was achieved for approximately equal axial deformations for Conventional 10 (outer diameter is 41mm) and Conventional 12 (outer diameter is 40mm) cylinders, the axial compressive force required to deploy the Conventional 12 cylinder is approximately eleven times (44000N vs 4000N in Figure 9.10, Chapter 9) than Conventional 10 cylinder. It could be due to higher numbers of RVEs for Conventional 12 than Conventional 10 cylinder ($N_c = 24$ vs 16 and $N_v = 6$ vs 3 in Table 6.6, Chapter 6).

Possibilities of designing expansion mechanisms:

Designing of the cellular mesh cylinders/in-silico models (with and without end pieces) using auxetic and non-auxetic honeycomb meshes were assessed through relationships between mechanical properties, global, RVE and cellular mesh parameters. These relationships are outlined below:

- Relationship of the mechanical properties (E_z/E_θ and $\nu_{z\theta}$) with the cellular mesh parameter (α) for the different aspect ratios (h/l) of auxetic and conventional honeycombs (Figures 9.13 and 9.17, Chapter 9)
- Relationship of the mechanical property ($\nu_{z\theta}$) and RVE (N_c/N_v) with the cellular mesh parameter (α) for the different aspect ratios (h/l) of auxetic and conventional honeycombs and outer diameters of the cylinder (Figures 9.14 and 9.18, Chapter 9)
- Relationship of RVE (N_c/N_v) with the cellular mesh parameter (W) and (t/l) for the different aspect ratios (h/l) of auxetic honeycombs and outer diameters of the cylinder in Figures 9.15 (W) and 9.16 (t/l), respectively, Chapter 9)
- Relationship of RVE (N_c/N_v) with the cellular mesh parameter (t/l) for the different aspect ratios (h/l) and t_l of conventional honeycombs (Figure 9.19, Chapter 9).

These relationships as explained in Chapter 9 present 'n' number of opportunities to design cellular mesh cylinders. However, cellular meshes should be designed considering following aspects of development of the expansion mechanisms.

- Deformation mechanisms of cellular meshes such as flexure model of Gibson and Ashby⁽¹¹³⁾ considered in this PhD.
- Impact of t_h , t_l , N_c and W during fabrication (laser cutting process) process which in turn affect the semi-rigid nature of prototype structures essential for the retraction of the simulant organs and actual abdominal organs of pig and human.
- Impact of t_h and t_l on the selection of wall thickness of cylinder (T) – $t_l \leq T$ is essential for the validity of the flexure model of Gibson and Ashby⁽¹¹³⁾ considered in this PhD. t_l of the laser cut cylinders (Table 6.6, Chapter 6), for example, were kept less than T (2.5mm) to ensure flexing of the diagonal ribs during deploying of the expansion mechanisms.
- Types of materials of cylinder sourced from suppliers [metal (structural steel, mild steel, etc.), metal alloys (nitinol), and biocompatible plastics.].
- Deploying mechanisms within the in-house abdominal simulator or pig abdomen (axial compression and tension).
- Different aspect ratios (h/l) of the honeycomb meshes lead to change in E_θ (Equation 3.44, Chapter 3) and in turn affect the E_z/E_θ . E_z/E_θ is related with the $\nu_{z\theta}$ due to the symmetric matrix compliance condition. This makes the material properties highly anisotropic. The high order of $\nu_{z\theta}$ lead to high number of N_c making cylinder wall extremely compliant (Conventional 7 cylinder, Tables 6.5 and 6.6, Chapter 6). Hence, the trade-off between the extremely compliant and semi-rigid nature of cellular wall should be maintained to ensure the retraction of organs and to prevent expansion mechanisms reverting to undeployed state during surgical procedures.

10.5 Fabrication of expansion mechanisms

Candidate cellular mesh cylinders were laser cut and 3D printed (Figures 9.20-23) and were referred as the 'expansion mechanisms'. Conventional 6-11 and Beam 1-2 cylinders were deployed immediately after the laser cutting process by the human hand without any surrounding materials to evaluate their expansion capabilities before subjecting them to the mechanical characterisation using the Instron machine. Auxetic 8-9 and Conventional 12 cylinders were unable to deploy by the human hand due to the quantity of axial

load required and brittle nature of 3D printed sample, respectively. Plastic deformation was observed after the initial deployment of the Conventional 6-11 and Beam 1-2 cylinders (Figures 9.20-22, Chapter 9) which should be due to the material properties (PVC and PP corresponding to 68mm and 41mm outer diameters of cylinders, respectively) of cylinders sourced for fabrication of the expansion mechanisms.

Auxetic honeycomb cylinders with or without pronged cone end pieces consisting of thin vertical and diagonal ribs (due to high number of N_c required to achieve the order of magnitude of v_{z0} obtained during the parametric studies of solid wall cylinder with and without end pieces) can be fabricated using the StarCut Tube machines developed by the Rofin(235). Although there is a doubt that such auxetic honeycomb cylinders would retract the simulant or actual abdominal organs in fully deployed conditions. Conventional honeycomb cylinders should be designed and fabricated using higher number of N_v than considered in this project. Beam models should be developed using the metal strips.

In a nutshell, laser cut cylinders (made up of PP and PVC) were deformed into sphere compared to 3D printed cylinder and hence, laser cutting technique should be considered in future for the fabrication of the expansion mechanisms.

10.6 Characterisation of experimental cylinders

The expansion mechanisms were subjected to uniaxial tension (Auxetic 8) and compression (Conventional 6-9 and Beam 1-2 cylinders) mechanisms using the Instron machine in the absence of a surrounding material to determine their mechanical behaviours and were then compared with the FE modeling results.

The mechanical responses of the expansion mechanisms were non-linear, but the degree of non-linearity have varied, for instance, Auxetic cylinder vs Conventional cylinders and cellular cylinders vs Beam cylinders (Figure 9.24, Chapter 9). The axial compressive or tension force required for activating the cellular expansion mechanisms was initially high at small axial deformation due the acute angles of the diagonal ribs. Forces decreased as the axial deformation increased giving a negative value of slope (called tangent stiffness), corresponding to negative stiffness which arise due to out-of-plane

buckling of the cylinder wall and not due to any in-plane flexing, stretching or hinging of the mesh ribs.

Tangent stiffness values were positive at the small axial deformation (linear phase) and negative for the large axial displacement (non-linear phase) (Figures 9.25-26, Chapter 9). Like axial forces, axial stresses applied on the expansion mechanisms were non-linear giving the negative value of slope (called tangent modulus) beyond the proportional limit of axial stress vs axial strain (Figure 9.27, Chapter 9), corresponding to negative modulus.

Selected stills from the video footages recorded during mechanical characterisation of the cellular and Beam 1-2 cylinders were analysed using the ImageJ⁽²²⁵⁾ software to obtain the ERD, AD and total equatorial deformation. Total equatorial deformation of ~200mm at ~50mm axial deformation (~16% axial strain) in Figures 9.30-9.33, Chapter 9 achieve the degree of expansion (in order of 200mm) envisaged for the proposed laparoscopic device, and hence, they were regarded as promising expansion mechanisms to be evaluated in-vitro for their organ retraction and space creation functions within the in-house abdominal simulator. There was approximately 20-25% of reduction in the axial compressive force applied between 10mm and 50mm of axial deformation of Conventional 6-9 cylinders (Figures 9.30-9.33, Chapter 9) due to the cylinders utilising the energy (due to plastic deformation) stored from the initial application of force for the axial deformation beyond 10mm. Total equatorial deformation of ~165mm at ~50mm axial deformation (~16% axial strain) in Figure 9.35, Chapter 9 for Beam 1 cylinder is greater than ~125mm in Figure 9.36 at ~18mm axial deformation (~6% axial strain) for Beam 2 cylinder in Figure 9.36, Chapter 9. Hence, Beam 2 cylinder with the higher number of vertical strips should be considered as promising expansion mechanism and evaluated in-vitro along with the cellular cylinders.

ERD and AD obtained from the experimentation and FE prediction for the Conventional 8 cylinder are in good agreement (Figure 9.37, Chapter 9).

The mechanical responses of the promising expansion mechanisms were subsequently evaluated in-vitro within the test rig mounted on the Instron

machine for their organs retraction and space creation functions and results are discussed in the next section.

10.7 In-vitro assessment of expansion mechanisms

In-vitro assessment of Conventional 6-9, Conventional 10-11, and Beam 2 cylinders was carried out using foam blocks within the test rig mounted on the Instron machine. The degree of surface pressure exerted by the cellular and beam cylinders on the foam blocks, and axial compressive force required for the deployment of the expansion mechanisms within the test rig were obtained – Figure 9.38 and Figure 9.40, Chapter 9, respectively. The sequence of selected stills extracted from the video footage recorded during assessment of the Conventional 8 cylinder (Figure 9.39, Chapter 9) has demonstrated its ability to retract foam blocks and create space inside the test rig. Conventional 8 cylinder was selected for in-vitro assessment using simulant organs owing to the semi-rigid nature of cellular meshes.

Assessment of Conventional 8 cylinder:

Individual simulant organs such as bowel, kidney and spleen and (Liver)-(Bowel & Kidney) and (Stomach & Spleen)-(Bowel) combinations of simulant organs were retracted within the test rig by the Conventional 8 cylinder. The degree of maximum surface pressure exerted on simulant organs by the Conventional 8 cylinder (Figure 9.41, Chapter 9) is in good agreement with that of reported for the natural organs during in-vivo pilot study (Figure 7.29 for Liver-OC, Figures 7.31-32 for bowel-OC, Figure 7.33 for stomach-OC, Figures 7.34-37 for liver-HALS, Figure 7.38 for bowel-HALS, Figures 7.39-40 for kidney-HALS, Figure 7.41 for spleen-HALS and Figure 7.42 for stomach-HALS). The surface pressure relaxation (calculated as P_{rms}) phenomenon for simulant organs during T_{hold} also correlated with that of natural organs (Figure 7.30 for liver-OC and Figure 7.35 for liver-HALS). The degree of P_{max} and surface pressure relaxation (P_{rms}) validate the simulant organs and use of test rig during in-vitro assessment of the promising expansion mechanisms.

The mechanical characteristics of the Conventional 8 cylinder during in-vitro assessment were obtained (and plotted as axial compressive force vs axial deformation, tangent stiffness vs axial deformation and axial stress vs axial

strain) for the retraction of the individual and combinations of the simulant organs. The degree of axial force required for the deployment of the Conventional 8 cylinder without surrounding materials (Figure 9.24, Chapter 9) and within the test rig consisting of individual and combinations of simulant organs (Figure 9.42, Chapter 9) are in ballpark ($\sim 200\text{N}$). The maximum value of tangent stiffness noted for 0-10mm of axial deformation was $\sim 550\text{ N/mm}$ for the deployment of cylinder without surrounding materials (Figure 9.25, Chapter 9) against $\sim 130\text{ N/mm}$ for the deployment of cylinder within the test rig consisting of individual and combinations of simulant organs (Figure 9.44, Chapter 9). This could be attributed to the presence of surrounding materials (simulant organs) exerting force back onto the expanding structures within the more constrained environment of test rig. The positive tangent stiffness immediately turned negative (at $\sim 1.5\text{mm}$ of axial deformation) in the case of cylinder without surrounding materials and remained negative for the remaining duration of the mechanical test (Figure 9.25, Chapter 9). In contrast, the positive tangent stiffness turned negative at $\sim 10\text{mm}$ of axial deformation in the case of cylinder surrounded by simulant organs within the test rig and oscillated between positive and negative values for the remaining duration (15-50mm) of the mechanical test (Figure 9.44, Chapter 9).

The image analysis of stills extracted from the video footages recorded during in-vitro assessment of the Conventional 8 cylinder within the test rig consisting of the individual and combinations of simulant organs were carried out to obtain ERD and AD. ERD vs AD curves for retractions of individual and combinations of simulant organs were depicted in Figure 9.47, Chapter 9 to demonstrate the degree of space created within the test rig when the Conventional 8 cylinder deployed by uniaxial compression mechanism using the Instron machine. ERD values of the Conventional 8 cylinder reported in Figure 9.47, Chapter 9 for retractions of individual and combinations of simulant organs are less than the ERD obtained ($\sim 120\text{mm}$) during the mechanical characterisation of the Conventional 8 cylinder in the absence of surrounding material (Figure 9.29, Chapter 9). This trend could be attributed to the difficulty encountered in the complete tracking of the deformation in the equatorial region of the cylinder during the image analysis of stills due to the nature of organ (solid vs hollow).

Further explanations are given below for the individual and combinations of organs in this regard.

- (Liver)-(Bowel & Kidney) (~100mm): It was relatively easy to track equatorial deformation on the side of liver simulant within the test rig. Since edges of the deformed cylinder in the equatorial region were behind the squashed bowel simulant (on the side of bowel simulant within the test rig), there was a substantial loss of distance during image analysis of stills. Hence, ERD (~100mm) was less compared to ERD obtained in the absence of surrounding material.
- Kidney and spleen (~85mm): Acrylic wall of the in-house abdominal simulator on the side of liver simulant was bended outward due to the physical dimension and weight of liver simulant (~1.5 kg) and by the virtue of in direct contact with acrylic wall. This has allowed higher amount of equatorial deformation of cylinder (~100mm for 50mm of AD) within the test rig when compared with kidney and spleen simulants (~85mm for 50mm of AD) due to presence of blue support material between the simulant organ and acrylic wall of simulator.
 - The phenomenon of bending of acrylic wall of in-house abdominal simulator when cylinder is fully deployed can be linked with the possibility of the expansion mechanisms lifting the human/pig abdominal wall (compliant than acrylic wall) in addition to the retraction of abdominal organs, reducing/eliminating the need for CO₂ insufflation during surgical procedures.
- Bowel and combination of (Stomach & Spleen)-(Bowel) (~70mm): Edges of the deformed cylinder in the equatorial region on the both sides were behind the squashed bowel in case of individual bowel and were behind the stomach and bowel in case of combinations of (Stomach & Spleen)-(Bowel). Hence, it was not possible to track the complete equatorial deformation during image analysis of stills.

Surface pressures exerted on the individual and combinations of simulant organs were synchronised with the total equatorial deformations obtained via image analysis of stills (Figures 9.48-52, Chapter 9). Selective stills were included to demonstrate the simultaneous process of deployment of the

Conventional 8 cylinder and retraction movements of simulant organs within the test rig which in turn has demonstrated the organ (simulant) retraction and space creation (within the test rig) capabilities of the Conventional 8 cylinder. There was a marginal drop in the maximum surface pressure exerted by the Conventional 8 cylinder during the retractions of individual and combination of simulant organs (Figure 9.53, Chapter 9).

Total equatorial deformations for the retraction of the simulant organs within the test rig are in the right ballpark for the degree of expansion (in the range of 80-200mm) envisaged for the proposed laparoscopic device.

Assessment of Conventional 10 and Beam 2 cylinders:

Individual simulant organs such as bowel and kidney and (Stomach & Spleen)-(Bowel) combination of simulant organs were retracted within the test rig by the Conventional 10 and Beam 2 cylinders. The degree of maximum surface pressures exerted on bowel and kidney simulants by the Conventional 10 and Beam 2 cylinders (Figure 9.54, Chapter 9) are in reasonable agreement with that of reported for the natural organs during in-vivo pilot study (Figures 7.31-32 for bowel-OC, Figure 7.38 for bowel-HALS and Figures 7.39-40 for kidney-HALS, Chapter 7). The degree of maximum surface pressure exerted on (Stomach & Spleen)-(Bowel) combination of simulant organs is in reasonable agreement with that of reported for the natural organs during in-vivo pilot study (Figure 7.33 for stomach-OC, Figure 7.41 for spleen-HALS and Figure 7.42 for stomach-HALS, Chapter 7).

The mechanical characteristics of the Conventional 10 and Beam 2 cylinders during in-vitro assessment were obtained (and plotted as axial compressive force vs axial deformation, tangent stiffness vs axial deformation and axial stress vs axial strain) for the retraction of the individual and combinations of the simulant organs. The axial compressive force required for the deployment of the Beam 2 cylinder without surrounding materials (Figure 9.24, Chapter 9) is ~40N, and within the test rig consisting of bowel and kidney simulant organs is ~55N and ~80N, respectively (Figure 9.55, Chapter 9). Tangent stiffness values of Beam 2 and Conventional 10 cylinders have followed similar trends (positive values ranging from 20-40 N/mm at low axial deformations and oscillating

between negative and positive stiffness at higher axial deformation – Figure 9.56, Chapter 9) to that explained for Conventional 8 cylinder for individual and combinations of simulant organs within the test rig.

ERD vs AD curves for retractions of individual and combinations of simulant organs were depicted in Figure 9.58, Chapter 9 to demonstrate the degree of space created within the test rig when the Conventional 10 and Beam 2 cylinders deployed by uniaxial compression mechanism using the Instron machine. The expansion capacity of cellular meshes of the Conventional 10 cylinder is responsible for the lower equatorial deformation (~50mm) during retractions of individual and combinations of the simulant organs compared to the Beam 2 (Figure 9.58) and Conventional 8 (Figure 9.47) cylinders. It can also be attributed to the nature of the materials of cylinder (PP vs PVC) when compared with the Conventional 8 cylinder.

Surface pressures exerted by the Beam 2 and Conventional 10 cylinders on the individual and combinations of simulant organs were synchronised with the total equatorial deformations obtained via image analysis of stills (Figures 9.59-62, Chapter 9). Selective stills were included to demonstrate – a) the simultaneous process of the deployment of the Beam 2 and Conventional 10 cylinders and b) retraction movements of simulant organs within the test rig – which in turn has demonstrated the organ (simulant) retraction and space creation (within the test rig) capabilities of the Beam 2 and Conventional 10 cylinders.

The surface pressures applied by the fingertips of surgeons and metal retractors during OC and HALS (in-vivo) have been quantitatively compared with the surface pressure exerted on the individual and combinations of simulant organs (in-vitro) by the expansion mechanisms in Figures 9.65-69, Chapter 9. The order of total equatorial deformation (~200mm for the Conventional 8 cylinder) for the retraction of the simulant organs within the test rig was in the good agreement with the retraction distances reported for human abdominal organs (Chapter 7) and the degree of expansion (in order of 200mm) envisaged for the proposed laparoscopic device.

Doughnut shape inflatable prototype structure:

The doughnut shape inflatable prototypes were assessed within the pig abdomen (in-vivo) and inside the test rig (in-vitro) to evaluate expansion capabilities (Figures 9.70, 9.72-74). They did not show significant deformation when inflated due to passing of pressurised air and were unable to retract simulant organs within the test rig. They lacked semi-rigid structure and cellular apertures like expansion mechanisms developed in this PhD.

10.8 Summary

Results obtained in the different phases of the development of the novel expansion mechanisms for space creation and organ retraction functions during abdominal surgery were discussed in this chapter. The conclusion, novelties of the expansion mechanisms and recommendations for future work are outlined in the next chapter.

11 Conclusion, Novelties and Recommendations for Future work

11.1 Conclusion

Novel expansion mechanisms were developed for the organ retraction and space creation during open and laparoscopic abdominal surgery.

A detailed literature review of salient aspects of the human abdominal environment, existing surgical devices for organ retraction, elasticity theory, beam theory, and auxetic materials has been undertaken. An in-house abdominal simulator has been developed as an in-vitro test rig to evaluate the space creation and organ retraction functions of novel expanding prototype structures.

During the in-vivo study involving human participants, the surface pressures applied by fingertips of participating surgeons and metal retractors to retract key abdominal organs during open and hand-assisted laparoscopic abdominal procedures have been measured for 12 patients using a pressure sensor kit. The degree of surface pressures applied for typical retraction movements of key abdominal organs and the space created inside the abdominal cavity were the major outcomes. The working space quantified during in-vivo study was considered as the target expansion in the fully deployed state of the proposed device during the design and development of prototype structures.

A fundamental finite element (FE) modelling study and parametric investigations of the influence of the mechanical properties (including negative and positive Poisson's ratios) on the expansion behaviour of cylindrical structures with and without end pieces has been undertaken. The effective mechanical properties required for a large equatorial deformation at the small axial deformation (or strain) were identified for solid wall cylinder with (pronged cone) and without end pieces, and were considered as target properties during computer-aided-designing of cellular meshes. Additionally, deploying cylinders comprising of beams or strips were considered as candidate expansion mechanisms. CAD models were simulated to predict the expansion capabilities of promising prototype structures.

The candidate expansion mechanisms have been laser cut and 3D printed using cylindrical tubes. The laser cut tubes were consequently characterised using the Instron mechanical compression and tension testing to quantify the degree of expansion without surrounding materials. During in-vitro assessment, a test rig was mounted on the Instron machine and the degree of surface pressure exerted for the retraction of the foam blocks and simulant organs was recorded using pressure sensor kit. In-vitro assessment events were simultaneously recorded, and still images were extracted from the video footages to quantify the degree of space created inside the test rig (i.e. total equatorial deformation). Retraction movements of simulant organs within the test rig were correlated with the surface pressures exerted by the expansion mechanisms. The range of surface pressure exerted on the simulant organs (in-vitro) by expansion mechanisms (5-45 kPa) and on key abdominal organs (in-vivo) by fingertips of participating surgeons (3-41 kPa) is matched.

Innovative expansion mechanisms for the further development of the LaparOsphere™ device were simulated, designed, fabricated, characterised, and evaluated in-vitro for their space creation and organ retraction capabilities.

11.2 Novelties

The research in this project is original and novelties are outlined below.

- The degrees of surface pressure and organ retraction distance quantified for typical retraction movements of key abdominal organs during an open and laparoscopic abdominal surgery are original contributions to the existing knowledge in the surgical field.
- The methodology of the fabrication of human liver simulants using patient CT scan data and silicone gel material is appearing to be new.
- The FE modelling of solid wall cylinder with and without end pieces carried out to identify the effective mechanical properties required for a large equatorial deformation of solid wall cylinder for small axial deformation (or strain) is novel and reported for the first time in the field of medical engineering. The 'shape change' mechanical properties and geometrical parameters identified during parametric studies of solid wall cylinder were subsequently used as target mechanical properties and

global parameters to derive cellular meshes (auxetic and conventional hexagonal honeycombs) for the computer-aided-designing of the expansion mechanisms (in-silico models).

- The methodology developed for the derivation of cellular meshes for cylinder is unique and the designing of in-silico models of the expansion mechanisms using auxetic and conventional hexagonal honeycombs and beam or strips are first of its kind. Cellular mesh cylinders were subsequently used to predict the expansion capabilities of candidate expansion mechanisms.
- The use of 2D laser cutting kit in combination with the rotary attachment to fabricate the expansion mechanisms is a new in-house approach.
- The range of surface pressure (1-41 kPa) and the degree of organ retraction distance (indicates ~200mm diameter of sphere) quantified during in-vivo are in ballpark with the range of surface pressure (5-45 kPa) and the degree of total equatorial deformation (indicates ~170mm diameter of sphere) quantified during in-vitro assessment of the expansion mechanisms.
- The expansion mechanisms designed and developed for the further development of the LaparOsphere™ are innovative and reported for the first time.

Key attributes of the novel expansion mechanisms (including in-silico models) are summarised below.

Innovative mechanical features:

- Large expansion capability in response to the extremely small activation force and strain (axial strain $\leq 17\%$).
- Shape change function from cylinder to sphere.
- A mechanism enabling combined space creation and organ retraction functions in one device.
- Cellular, hollow, and semi-rigid deployable structure that would not damage the delicate tissues.
- Retractable and repeatable deployability function for repositioning within the abdominal cavity.

- Expansion mechanisms are deployed by uniaxial compression. Cellular mesh cylinder can also be encapsulated in the flexible double wall structure and deployed by passing the sterilised liquid (saline) or gas (medical grade CO₂).
- Cellular meshes were developed for (including in-silico models) the broad range of outer diameter of cylinder (20mm – 68mm). This feature permits the use of novel expansion mechanisms for open, hand assisted laparoscopic, and complete laparoscopic abdominal procedures.
- Negative stiffness phenomenon means large equatorial deformation can be achieved for less axial compressive or tensile force.
- Expansion mechanisms can be further optimised by varying the wall thickness and length of the cylinder without significantly compromising the expansion capabilities for small activation strain.
- The mechanical properties of expansion mechanisms are transferable for different biocompatible materials such as plastic and metal alloys currently used for the development of medical technology. Nitinol alloy, for example, is widely used for development of cardiac stent.

Benefits to surgeons and patients during and after surgical procedures:

- It would generate clear working space essential for abdominal surgical procedures.
- The large omnidirectional expansion capabilities of the prototype structures have potentials to eliminate the use of CO₂ insufflation and/or abdominal wall lifting techniques currently used during laparoscopic surgery to inflate the abdominal wall. Therefore, patient side effects associated with these techniques can significantly be reduced. It may also eliminate the need for multiple gas tight access ports. It would allow use of suction without deflation of abdominal wall and further promotes the use of thermal cutting systems.
- It would increase the visibility and access to the target surgical sites for the surgeon due to its combined space creation and organ retraction functions inside the abdominal cavity as well as possibility of inflating abdominal wall. This would reduce the number of injuries to tissues

and/or surrounding organs which can lead to quick recovery. It would allow use laparoscopic surgery for older and higher risk patients and longer operations due to reduced need of converting to the open abdominal surgery.

- Cellular nature (multiple holes) will give the surgeon access to the surgical field, facilitate the insertion of laparoscope and other surgical devices, and allow removal of diseased or unwarranted tissues and/or organs such as extraction of gall bladder during open and laparoscopic cholecystectomy.
- Semi-rigid cellular scaffold of expansion mechanisms would continuously maintain clear working space by preventing tissues and/or bulky organs such as human liver to cause the collapse of device in to the undeployed state. This should reduce interruptions throughout surgical procedures.
- The benefits explained above would either limit the role of or eliminate the need for assistant surgeon or surgeons during abdominal surgical procedures. This scenario would further promote better coordination during complex abdominal surgical procedures amongst participating surgeons.

Benefits to the healthcare delivery systems and economy:

- Advantages of novel prototype expansion mechanisms would decrease surgical hours by speeding up surgical procedures. This in turn would free up surgeon's time and may also reduce postoperative engagement of surgeon.
- It would reduce the number of hours of paramedics required for each abdominal surgery.
- The prototype device provides the possibility to increase the number of elected procedures that are carried out on a day case basis.
- A reduction or elimination of patients' side effects has a direct benefit on the recovery time of the patient, thus enabling them to return to normal activity quicker.
- Overall, it can significantly reduce the cost of healthcare delivery and bolster the economy.

11.3 Recommendations for future works

The recommendations for future works are categorised based on outputs of the experimental work (reported in Chapters 7-9) in the different phases of the development of prototype structures and outlined below.

In-vivo measurement of surface pressures and organ retraction distances:

While a novel in-vivo pressure sensing experiment is a first of its kind study, it provides a glimpse of potential utility of obtaining objective surface pressures for retracting abdominal organs. The scope of this pilot study can be broadened by increasing number of participating patients and surgeons, varying experience of surgeon from junior to consultant surgeons having few to several years of experience of carrying out open and laparoscopic abdominal surgery, and selecting other abdominal surgeries such as laparoscopic hernia repair, adrenalectomy, appendectomy, etc. During my 3 months of secondment at the 'Research Office' of the MFT, I have worked on the 'study closure' activities of the multisite clinical trial called MiNESS (Midland and North of England Stillbirth Study). The identical clinical study was carried out in Auckland, New Zealand at the pilot scale. Our pilot study can be scaled up like MiNESS to develop a broader range of surface pressure applied on abdominal organs and tissues which would then be valuable during the further development of the expansion mechanisms for clinical trials in pigs.

There are significant opportunities with modern biomedical technology to design a newer generation of instruments both for open and laparoscopic surgery having improved space creation and organ retraction functions with a potential for real time feedback on applied surface pressures. Data gathered from in-vivo pilot study in this PhD on the surface pressures exerted during organ retraction and the extent of organ retraction, in our opinion can contribute to the design and development of such instruments.

Additionally, precise surface pressure limits for key human organs and tissues should be incorporated into existing surgical simulators used in surgical training and simulation to develop newer generation surgical and especially laparoscopic simulators for surgical training. It will ultimately lead to augmented surgical skills and instrumental feedback required to undertake complex

laparoscopic surgery. It may enable the manufacture of safer retractors with feedback sensors indicating excessive retraction forces and reducing surgical morbidity in the form of traction injuries.

Well-defined objective retraction surface pressure parameters could be of value in the training of surgeons in all disciplines of surgery. Accurate definition of these surface pressures may be especially of value in laparoscopic surgery. For example, surface pressure data can be incorporated within the software of advanced laparoscopic simulators to improve haptic feedback during simulated laparoscopic surgery which is becoming increasingly sophisticated.

The solid simulant organs (spleen and kidney) and hollow simulant organs (bowel and stomach) can be developed using CT scan data of healthy patients. They can subsequently be used to develop next generation surgical simulator for an accurate force feedback.

Finite element modelling of expansion mechanisms:

A finite element (FE) modelling of solid wall of cylinder should be carried out to incorporate the nonlinear response of system due to the change in the stiffness of elements during large transverse deformation. Nitinol alloy can be used to fabricate the expansion mechanisms and hence, the FE modelling can be studied for superelastic or shape memory behaviour of solid wall of cylinder. Moreover, the deformation of solid wall and cellular cylinder should be studied in the constrained environment to evaluate the impact of 'contact nonlinearity' on the expansion capabilities.

Design and fabrication of cellular mesh cylinders:

The recommendations for the design and fabrication phases of the prototype development are outlined below.

- Further optimisations of uniform cellular meshes.
- Consideration of the gradient cellular (honeycombs) meshes.
- Fundamental investigation of the use of cellular meshes other than honeycombs.

- In-silico models of honeycomb meshes can be deployed into the hemisphere (half-sphere) shape via uniaxial compression and tension mechanisms.
- Use of nitinol tube during fabrication of prototype structures for the shape memory and superelasticity responses to ensure removal through laparoscopic ports which are generally 15-25mm in diameter.
- Biocompatible plastics can also be evaluated as candidate material in addition to the nitinol.

Mechanical characterisation and in-vitro assessment of the expansion mechanisms:

The recommendations for the mechanical characterisation and in-vitro assessment phases of the prototype development are listed below.

- Auxetic cylinders should be further characterised for uniaxial tension and compression (pronged cone end pieces at both ends of cellular cylinder) mechanisms.
- In-vitro test rig should be converted into the closed chamber (except top end to permit the in-vitro assessment using the Instron machine) and place the simulant organs surrounding the expansion mechanism which should allow evaluation of the retraction capabilities in omni directions.
- In-vivo evaluation of organ retraction and space creation capabilities of the expansion mechanisms inside the abdominal cavity of pigs. In this case, hand held instrument should be used to activate/deploy the expansion mechanism instead of the Instron machine.

12 References

1. Bayless TM, Diehl A. Advanced Therapy in Gastroenterology and Liver Disease [Internet]. 5th ed. Hamilton, London: B. C. Decker Inc; 2005. (Pmph USA Ltd Series). Available from: <https://books.google.co.uk/books?id=XR-Jsxx0qRwC>
2. Tjandra JJ, Clunie JAG, Kaye HA, Smith AJ. Textbook of Surgery [Internet]. 3rd ed. Massachusetts, Oxford, Carlton: Blackwell Publishing; 2006. 1-30 p. Available from: <http://onlinelibrary.wiley.com/doi/10.1002/9780470757819.fmatter/pdf>
3. Dulucq J-L. Tips and Techniques in Laparoscopic Surgery. 1st ed. Berlin, Heidelberg, New York: Springer-Verlag Berlin Heidelberg; 2005.
4. Corden J, Augustine T. UK Patent No. 2495522B. Newport, South Wales: UK Intellectual Property Office. GB2495522B, 2013.
5. Evans KE. The design of doubly curved sandwich panels with honeycomb cores. Compos Struct [Internet]. 1991;17(2):95–111. Available from: <http://www.sciencedirect.com/science/article/pii/0263822391900646>
6. Sanami M., Alderson A. UK Patent No. 2496167A. Newport, South Wales: UK Intellectual Property Office. GB2496167, 2013.
7. Gray H. Anatomy of the Human Body. 40th ed. Susan Standring, editor. 2008.
8. Song C, Alijani A, Frank T, Hanna G, Cuschieri A. Elasticity of the living abdominal wall in laparoscopic surgery. J Biomech [Internet]. 2006 Jan [cited 2012 Jul 24];39(3):587–91. Available from: <http://www.ncbi.nlm.nih.gov/pubmed/16389099>
9. Yao S, Li J, Liu F, Pei L. Significance of measurements of herniary area and volume and abdominal cavity volume in the treatment of incisional hernia: application of CT 3D reconstruction in 17 cases. Comput Aided Surg [Internet]. 2012 Jan [cited 2012 Jul 24];17(1):40–5. Available from: <http://www.ncbi.nlm.nih.gov/pubmed/22145789>
10. WebMD. Image Collection: Human Anatomy. [Internet]. 2016 [cited 2017 May 27]. Available from: <http://www.webmd.com/digestive-disorders/picture-of-the-intestines#1>
11. Fung YC. Biomechanics: Mechanical Properties of Living Tissues [Internet]. 2nd ed. New York: Springer-Verlag New York; 2010. Available from: <http://books.google.co.uk/books?id=zo2McgAACAAJ>
12. Basdogan C. Dynamic Material Properties of Human and Animal Livers. In: Payan Y, editor. Soft Tissue Biomechanical Modeling for Computer Assisted Surgery [Internet]. Berlin, Heidelberg: Springer Berlin Heidelberg; 2012. p. 229–41. Available from: http://dx.doi.org/10.1007/8415_2012_122
13. Brown JD. In-Vivo and Postmortem Biomechanics of Abdominal Organs Under Compressive Loads: Experimental Approach in a Laparoscopic Surgery Setup (Doctoral thesis) [Internet]. 2003. Available from: <http://brl.ee.washington.edu/eprints/id/eprint/161%0A>
14. Chatelin S, Oudry J, Périchon N, Sandrin L, Allemann P, Soler L, et al. In vivo liver tissue mechanical properties by Transient Elastography: comparison with Dynamic Mechanical Analysis. Biorheology [Internet]. 2011 Jan [cited 2012 Jul 16];48(2):75–88. Available

from: <http://www.ncbi.nlm.nih.gov/pubmed/21811013>

15. Egorov VI, Schastlivtsev I V, Prut E V, Baranov AO, Turusov RA. Mechanical properties of the human gastrointestinal tract. *J Biomech* [Internet]. 2002 Oct;35(10):1417–25. Available from: <http://www.ncbi.nlm.nih.gov/pubmed/12231288>
16. Cox AJ. Variations in Size of the Human stomach. *Cal West Med*. 1945;63(6):267–8.
17. Molina DK, DiMaio VJM. Normal organ weights in men: part II-the brain, lungs, liver, spleen, and kidneys. *Am J Forensic Med Pathol*. 2012 Dec;33(4):368–72.
18. Saraf H, Ramesh KT, Lennon AM, Merkle AC, Roberts JC. Mechanical properties of soft human tissues under dynamic loading. *J Biomech* [Internet]. 2007 Jan [cited 2012 Jul 26];40(9):1960–7. Available from: <http://www.ncbi.nlm.nih.gov/pubmed/17125775>
19. Wells, PNT, Liang H-D. Medical ultrasound: imaging of soft tissue strain and elasticity. *J R Soc Interface* [Internet]. 2011 Nov 7 [cited 2012 Jul 13];8(64):1521–49. Available from: <http://www.ncbi.nlm.nih.gov/pubmed/21680780>
20. Gupta M, Sodhi L, Yadav TD. Morphology of liver. *Indian J Surg* [Internet]. 2008 Feb;70(1):3–7. Available from: <http://www.pubmedcentral.nih.gov/articlerender.fcgi?artid=3452600&tool=pmcentrez&rendertype=abstract>
21. Yu HC, You H, Lee H, Jin Z-W, Moon J II, Cho BH. Estimation of standard liver volume for liver transplantation in the Korean population. *Liver transplantation official Publ Am Assoc Study Liver Dis Int Liver Transplant Soc* [Internet]. 2004 Jun [cited 2012 Sep 12];10(6):779–83. Available from: <http://www.ncbi.nlm.nih.gov/pubmed/15162473>
22. Karlo C, Reiner CS, Stolzmann P, Breitenstein S, Marincek B, Weishaupt D, et al. CT- and MRI-based volumetry of resected liver specimen: comparison to intraoperative volume and weight measurements and calculation of conversion factors. *Eur J Radiol* [Internet]. 2010 Jul [cited 2012 Jul 19];75(1):e107-11. Available from: <http://www.ncbi.nlm.nih.gov/pubmed/19782490>
23. Muller SA, Pianka F, Schobinger M, Mehrabi A, Fonouni H, Radeleff B, et al. Computer-based liver volumetry in the liver perfusion simulator. *J Surg Res*. 2011 Nov;171(1):87–93.
24. Geraghty EM, Boone JM, McGahan JP, Jain K. Normal organ volume assessment from abdominal CT. *Abdom Imaging* [Internet]. 2004 [cited 2012 Jul 16];29(4):482–90. Available from: <http://www.ncbi.nlm.nih.gov/pubmed/15024516>
25. Henderson JM, Heymsfield SB, Horowitz J, Kutner MH. Measurement of liver and spleen volume by computed tomography. Assessment of reproducibility and changes found following a selective distal splenorenal shunt. *Radiology* [Internet]. 1981;141(2):525–7. Available from: <http://www.scopus.com/inward/record.url?eid=2-s2.0-0019787481&partnerID=40&md5=7989aa4a73d0598ea2abdc5b4f24fa1>
26. Urata K, Kawasaki S, Matsunami H, Hashikura Y, Ikegami T, Ishizone S, et al. Calculation of child and adult standard liver volume for liver transplantation. *Hepatology* [Internet]. 1995;21(5):1317–21. Available from: <http://dx.doi.org/10.1002/hep.1840210515>
27. Heinemann A, Wischhusen F, Püschel K, Rogiers X. Standard liver volume in the Caucasian population. *Liver Transpl Surg* [Internet]. 1999 Sep;5(5):366–8. Available

from: <http://www.ncbi.nlm.nih.gov/pubmed/10477836>

28. Yu HC, You H, Lee H, Jin Z-W, Moon JI, Cho BH. Estimation of standard liver volume for liver transplantation in the Korean population. *Liver Transplant* [Internet]. 2004;10(6):779–83. Available from: <http://www.scopus.com/inward/record.url?eid=2-s2.0-2942717008&partnerID=40&md5=6a232e49f99406678162d0e2f040e0e8>
29. Ferraioli G, Tinelli C, Zicchetti M, Abov E, Poma G, Di Gregorio M, et al. Reproducibility of real-time shear wave elastography in the evaluation of liver elasticity. *Eur J Radiol* [Internet]. 2012 Jun 27 [cited 2012 Jul 11];10–4. Available from: <http://www.ncbi.nlm.nih.gov/pubmed/22749107>
30. Son CY, Kim SU, Han WK, Choi GH, Park H, Yang SC, et al. Normal liver elasticity values using acoustic radiation force impulse imaging: a prospective study in healthy living liver and kidney donors. *J Gastroenterol Hepatol* [Internet]. 2012 Jan [cited 2012 Jul 10];27(1):130–6. Available from: <http://www.ncbi.nlm.nih.gov/pubmed/21679249>
31. Roulot D, Czernichow S, Le Clésiau H, Costes J-L, Vergnaud A-C, Beaugrand M. Liver stiffness values in apparently healthy subjects: influence of gender and metabolic syndrome. *J Hepatol* [Internet]. 2008 Apr [cited 2012 Jul 19];48(4):606–13. Available from: <http://www.ncbi.nlm.nih.gov/pubmed/18222014>
32. Kumar M, Sharma P, Garg H, Kumar R, Bhatia V, Sarin SK. Transient elastographic evaluation in adult subjects without overt liver disease: influence of alanine aminotransferase levels. *J Gastroenterol Hepatol* [Internet]. 2011 Aug [cited 2012 Sep 13];26(8):1318–25. Available from: <http://www.ncbi.nlm.nih.gov/pubmed/21443658>
33. Huwart L, Salameh N, ter Beek L, Vicaute E, Peeters F, Sinkus R, et al. MR elastography of liver fibrosis: preliminary results comparing spin-echo and echo-planar imaging. *Eur Radiol* [Internet]. 2008 Nov [cited 2012 Jul 13];18(11):2535–41. Available from: <http://www.ncbi.nlm.nih.gov/pubmed/18504591>
34. Pop M, Davidson SRH, Gertner M, Jewett MAS, Sherar MD, Kolios MC. A Theoretical Model for RF Ablation of Kidney Tissue and Its Experimental Validation. In: Bello F, Cotin S, editors. *Biomedical Simulation: 5th International Symposium, ISBMS 2010, Phoenix, AZ, USA, January 23-24, 2010 Proceedings*. Berlin, Heidelberg: Springer; 2010. p. 119–29.
35. Carter FJ, Frank TG, Davies PJ, McLean D, Cuschieri A. Measurements and modelling of the compliance of human and porcine organs. *Med Image Anal* [Internet]. 2001 Dec;5(4):231–6. Available from: <http://www.ncbi.nlm.nih.gov/pubmed/11731303>
36. Kang K-Y, Lee YJ, Park SC, Yang CW, Kim Y-S, Moon IS, et al. A comparative study of methods of estimating kidney length in kidney transplantation donors. *Nephrol Dial Transplant* [Internet]. 2007 Aug [cited 2013 Sep 22];22(8):2322–7. Available from: <http://www.ncbi.nlm.nih.gov/pubmed/17452412>
37. Kadioglu A. Renal measurements, including length, parenchymal thickness, and medullary pyramid thickness, in healthy children: what are the normative ultrasound values? *AJR Am J Roentgenol* [Internet]. 2010 Feb [cited 2013 Sep 22];194(2):509–15. Available from: <http://www.ncbi.nlm.nih.gov/pubmed/20093617>
38. Shin HS, Chung BH, Lee SE, Kim WJ, Ha H II, Yang CW. Measurement of kidney volume with multi-detector computed tomography scanning in young Korean. *Yonsei Med J* [Internet]. 2009 Apr 30 [cited 2013 Sep 22];50(2):262–5. Available from:

39. Bakker J, Olree M, Kaatee R, De Lange EE, Moons KG, Beutler JJ, et al. Renal volume measurements: accuracy and repeatability of US compared with that of MR imaging. *Radiology* [Internet]. 1999 Jun;211(3):623–8. Available from: <http://www.ncbi.nlm.nih.gov/pubmed/10352583>
40. Gandy SJ, Armoogum K, Nicholas RS, McLeay TB, Houston JG. A clinical MRI investigation of the relationship between kidney volume measurements and renal function in patients with renovascular disease. *Br J Radiol* [Internet]. 2007 Jan [cited 2013 Sep 22];80(949):12–20. Available from: <http://www.ncbi.nlm.nih.gov/pubmed/17267472>
41. Moorthy HK, Venugopal P. Measurement of renal dimensions in vivo: A critical appraisal. *Indian J Urol* [Internet]. 2011 Apr [cited 2013 Sep 22];27(2):169–75. Available from: <http://www.pubmedcentral.nih.gov/articlerender.fcgi?artid=3142824&tool=pmcentrez&rendertype=abstract>
42. Walter F. *Medical Physiology: A Cellular And Molecular Approach*. Elsevier/Saunders; 2004.
43. Singh D, Bansal YS, Sreenivas M. Weights of human organs at autopsy in Chandigarh zone of north-west India. *J Indian Acad Forensic Med*. 2004;26(3):971–3.
44. De La Grandmaison GL, Clairand I, Durigon M. Organ weight in 684 adult autopsies: new tables for a Caucasoid population. *Forensic Sci Int* [Internet]. 2001 Jun 15;119(2):149–54. Available from: <http://www.ncbi.nlm.nih.gov/pubmed/11376980>
45. Duck FA. *Physical Properties of Tissue, A Comprehensive Reference Book*. Harcourt, Brace Jovanovich, London; 1990.
46. Warner L, Yin M, Glaser KJ, Woollard JA, Carrascal CA, Korsmo MJ, et al. Noninvasive In vivo assessment of renal tissue elasticity during graded renal ischemia using MR elastography. *Invest Radiol*. 2011 Aug;46(8):509–14.
47. Gennisson J, Grenier N, Hubrecht R, Couzy L, Delmas Y, Derieppe M, et al. Multiwave technology introducing shear wave elastography of the kidney : Pre-clinical study on a kidney fibrosis model and clinical feasibility study on 49 human renal transplants . In: 2010 IEEE International Ultrasonics Symposium Proceedings. 2010. p. 1356–9.
48. Grenier N, Gennisson J-L, Cornelis F, Le Bras Y, Couzi L. Renal ultrasound elastography. *Diagn Interv Imaging* [Internet]. 2013 May [cited 2013 Sep 22];94(5):545–50. Available from: <http://www.ncbi.nlm.nih.gov/pubmed/23567180>
49. Gennisson J-L, Grenier N, Combe C, Tanter M. Supersonic shear wave elastography of in vivo pig kidney: influence of blood pressure, urinary pressure and tissue anisotropy. *Ultrasound Med Biol*. 2012 Sep;38(9):1559–67.
50. Fenchel S, Boll DT, Fleiter TR, Brambs H-J, Merkle EM. Multislice helical CT of the pancreas and spleen. *Eur J Radiol*. 2003 Mar;45 Suppl 1:S59-72.
51. Wegener, O H, Fassel, R; Welger D. *Full body computed tomography*. [Internet]. Berlin: Blackwell Wissenschafts-Verlag GmbH; 1992. 357-66 p. Available from:

52. Rodrigues AJ, Rodrigues CJ, Germano MA, Rasera I, Cerri GG. Sonographic assessment of normal spleen volume. *Clin Anat* [Internet]. 1995;8(4):252–5. Available from: <http://dx.doi.org/10.1002/ca.980080403>
53. Siddiqui, M.A. & Ali AHA. Assessment of normal spleen size. *Int J Pharma Bio Sci* [Internet]. 2015;6(3):(B) 46-57. Available from: http://www.ijpbs.net/cms/php/upload/4355_pdf.pdf
54. Ehimwenma O, Tagbo MT. Determination of normal dimension of the spleen by ultrasound in an endemic tropical environment. *Niger Med J*. 2011 Jul;52(3):198–203.
55. Hosey RG, Mattacola CG, Kriss V, Armsey T, Quarles JD, Jagger J. Ultrasound assessment of spleen size in collegiate athletes. Vol. 40, *British Journal of Sports Medicine*. 2006. p. 251–4.
56. Prassopoulos P, Daskalogiannaki M, Raissaki M, Hatjidakis A, Gourtsoyiannis N. Determination of normal splenic volume on computed tomography in relation to age, gender and body habitus. *Eur Radiol*. 1997;7(2):246–8.
57. Harris A, Kamishima T, Hao HY, Kato F, Omatsu T, Onodera Y, et al. Splenic volume measurements on computed tomography utilizing automatically contouring software and its relationship with age, gender, and anthropometric parameters. *Eur J Radiol* [Internet]. 2010 Jul [cited 2013 Sep 22];75(1):e97-101. Available from: <http://www.ncbi.nlm.nih.gov/pubmed/19775843>
58. Kaneko J, Sugawara Y, Matsui Y, Ohkubo T MM. Normal splenic volume in adults by computed tomography. *Hepatogastroenterology*. 2002;49(48):1726–7.
59. Tanna JA, Patel PN, Kalele SD. Relation between Organ Weights and Body Weight in Adult Population of Bhavnagar Region- A Post-Mortem Study Exclusion Criteria. *J Indian Acad Forensic Med*. 2011;33(1):971–3.
60. Reddy KSN. *The Essentials of Forensic Medicine and Toxicology* [Internet]. 28th ed. K. Suguna Devi; 1994. Available from: <http://books.google.co.uk/books?id=SHvdtgAACAAJ>
61. Kohli A, Aggrawal NK. Normal organ Weights in Indian Adults. 2006.
62. Stingl J., Báča V., Cech P., Kovanda J., Kovandová H., Mandys V., Rejmontová J. SB. Morphology and some biomechanical properties of human liver and spleen. *Surg Radiol Anat* [Internet]. 2002 Dec [cited 2012 Jul 16];24(5):285–9. Available from: <http://www.ncbi.nlm.nih.gov/pubmed/12497218>
63. Cools L, Osteaux M, Divano L, Jeanmart L. Prediction of splenic volume by a simple CT measurement: a statistical study. *J Comput Assist Tomogr*. 1983 Jun;7(3):426–30.
64. Karlo CA, Stolzmann P, Do RK, Alkadhi H. Computed tomography of the spleen: how to interpret the hypodense lesion. *Insights Imaging* [Internet]. 2013;4(1):65–76. Available from: <http://link.springer.com/10.1007/s13244-012-0202-z>
65. Mannelli L, Godfrey E, Joubert I, Patterson AJ, Graves MJ, Gallagher FA, et al. MR elastography: Spleen stiffness measurements in healthy volunteers--preliminary experience. *AJR Am J Roentgenol*. 2010 Aug;195(2):387–92.

66. Bensamoun SF, Robert L, Leclerc GE, Debernard L, Charleux F. Stiffness imaging of the kidney and adjacent abdominal tissues measured simultaneously using magnetic resonance elastography. *Clin Imaging* [Internet]. 2011;35(4):284–7. Available from: <http://dx.doi.org/10.1016/j.clinimag.2010.07.009>
67. Geliebter A, Melton PM, McCray RS, Gallagher DR, Gage D, Hashim SA. Gastric capacity, gastric emptying, and test-meal intake in normal and bulimic women. *Am J Clin Nutr*. 1992 Oct;56(4):656–61.
68. Ross JM. *Post mortem appearances*. 4th ed. London: Oxford; 1939.
69. Reed B. *Lectures to general practitioners on the diseases of the stomach and intestines: With an Account*. Miami: Book on Demand, Miami; 1904.
70. Baraki, YM, Traverso, P, Elariny, HA, Fang Y. Preoperative prediction of stomach weight to be removed in laparoscopic sleeve gastrectomy procedure. *Surg Technol Int* [Internet]. 2010;(20):167–71. Available from: <http://www.ncbi.nlm.nih.gov/pubmed/21082564>
71. Lim Y-J, Deo D, Singh TP, Jones DB, De S. In situ measurement and modeling of biomechanical response of human cadaveric soft tissues for physics-based surgical simulation. *Surg Endosc* [Internet]. 2009 Jun [cited 2013 Mar 8];23(6):1298–307. Available from: <http://www.pubmedcentral.nih.gov/articlerender.fcgi?artid=2693244&tool=pmcentrez&rendertype=abstract>
72. Cummings JH. *The Large Intestine in Nutrition and Disease* [Internet]. Danone JHCI, editor. Bruxelles; 1997. 21 p. Available from: http://www.angelfire.com/folk/cusp/images/large_intestine.pdf
73. Cummings J.H., Banwell J.G., Segal I., Coleman N., Englyst H.N., Macfarlane GT. The amount and composition of large bowel contents in man. *Gastroenterol* 98(5 PART) [Internet]. 1990;(2):408. Available from: <https://eurekimag.com/research/033/716/033716308.php#close>
74. Kavanagh BD, Pan CC, Dawson LA, Das SK, Li XA, Ten Haken RK, et al. Radiation Dose-Volume Effects in the Stomach and Small Bowel. *Int J Radiat Oncol Biol Phys*. 2010;76(3 SUPPL.):101–7.
75. *Abdominal X-ray - System and anatomy* [Internet]. 2017. Available from: http://www.radiologymasterclass.co.uk/tutorials/abdo/abdomen_x-ray/anatomy_system_bowel_gas
76. Johnson LA, Rodansky ES, Sauder KL, Horowitz JC, Mih JD, Tschumperlin DJ, et al. Matrix stiffness corresponding to strictured bowel induces a fibrogenic response in human colonic fibroblasts. *Inflamm Bowel Dis*. 2013 Apr;19(5):891–903.
77. Medscape. *Organ procurement* [Internet]. 2003 [cited 2017 Jun 5]. Available from: http://www.medscape.com/content/2003/00/44/98/449855/449855_fig.html
78. Danny AS, Harry LA, Sunny LF, Lee SC, Michele FM. *Laparoscopic Cholecystectomy: Media Gallery*. [Internet]. 2016 [cited 2017 Jun 5]. Available from: <http://emedicine.medscape.com/article/1582292-overview#showall>
79. Anthony N. Kalloo, Jacques Marescaux RZ. *Natural Orifice Transluminal Endoscopic*

80. Kitajima T, Kaido T, Lida T, Seo S, Taura K, Fujimoto Y, et al. Short-term outcomes of laparoscopy-assisted hybrid living donor hepatectomy: a comparison with the conventional open procedure. *Surg Endosc* [Internet]. 2017;1–10. Available from: <http://dx.doi.org/10.1007/s00464-017-5575-0>
81. MacFadyen JBV, Arregui M, Eubanks S, Olsen DO, Peters JH, Soper NJ, et al. *Laparoscopic Surgery of the Abdomen* [Internet]. 1st ed. New York: Springer-Verlag New York; 2004. 87-97 p. Available from: <http://www.springer.com/medicine/surgery/book/978-0-387-98468-1>
82. Gall Bladder removal procedures
<http://www.nhs.uk/conditions/laparoscopiccholecystectomy/pages/introduction.aspx> [accessed on 18/09/2014].
83. Demographics of Cholecystectomy
<http://www.surgery.com/procedure/cholecystectomy/demographics> [accessed on 18/09/2014].
84. Kruschinski D. The pneumoperitoneum – a continuing mistake in laparoscopy? 2005;1–16.
85. Otsuka Y, Katagiri T, Ishii J, Maeda T, Kubota Y, Tamura A, et al. Gas embolism in laparoscopic hepatectomy: what is the optimal pneumoperitoneal pressure for laparoscopic major hepatectomy? *J Hepatobiliary Pancreat Sci* [Internet]. 2012 Sep 22 [cited 2012 Dec 10];10–3. Available from: <http://www.ncbi.nlm.nih.gov/pubmed/23001192>
86. Steve W. Waxman MD HNW. Complications of Laparoscopic and Robotic Urologic Surgery [Internet]. Ghavamian R, editor. Springer New York; 2010. 3-6 p. Available from: http://link.springer.com/chapter/10.1007/978-1-60761-676-4_1?LI=true
87. Kaplan JR, Lee Z, Eun DD, Reese AC. Complications of Minimally Invasive Surgery and Their Management. *Curr Urol Rep* [Internet]. 2016;17(6):47. Available from: <http://dx.doi.org/10.1007/s11934-016-0602-6>
88. Törnqvist B, Waage A, Zheng Z, Ye W, Nilsson M. Severity of Acute Cholecystitis and Risk of Iatrogenic Bile Duct Injury During Cholecystectomy, a Population-Based Case--Control Study. *World J Surg* [Internet]. 2016;40(5):1060–7. Available from: <http://dx.doi.org/10.1007/s00268-015-3365-1>
89. Browne IL, Dixon E. Delayed jejunal perforation after laparoscopic cholecystectomy. *J Surg Case Reports* [Internet]. 2016;2016(2):rjw017. Available from: <http://dx.doi.org/10.1093/jscr/rjw017>
90. Vittorio Paolucci BS. *Gasless Laparoscopy in General Surgery and Gynecology* [Internet]. Stuttgart - New York: Thieme Medical Publishers; 1996. Available from: <https://www.amazon.co.uk/d/cka/Gasless-Laparoscopy-General-Surgery-Gynecology-Diagnosis-Procedures/0865776040>
91. Viani M, Poggi R, Pinto A, Fusai G, Andreani S, Marvotti R. Gasless laparoscopic gastrotomy. *J Laparoendosc Surg*. 1995 Aug;5(4):245–9.
92. Kruczynski D, Schäffer U, Knapstein P. Gasless laparoscopy with conventional surgical

- instruments. *Gynaecol Endosc.* 1996;5(277–81).
93. Gutt CN, Daume JM, Linker R, Paolucci V. VarioLift retraction system for laparoscopy without pneumoperitoneum. *Minim Invasive Ther Allied Technol* [Internet]. 1998;7(3):241–5. Available from: <http://dx.doi.org/10.3109/13645709809152857>
 94. Alijani A, Cuschieri A. Abdominal Wall Lift Systems in Laparoscopic Surgery: Gasless and Low-pressure Systems. *Semin Laparosc Surg* [Internet]. 2001;8(1):53–62. Available from: <http://dx.doi.org/10.1177/155335060100800106>
 95. Gutt CN, Daume JM, Paolucci V, Encke A. First Results of Experience with the VarioLift System. In: Hartel W, editor. *Klinik und Forschung in der Chirurgie unter dem Aspekt von Effizienz und Ökonomie: 114 Kongreß der Deutschen Gesellschaft für Chirurgie 1--5 April 1997, München* [Internet]. Berlin, Heidelberg: Springer Berlin Heidelberg; 1997. p. 1238–41. Available from: http://dx.doi.org/10.1007/978-3-642-60881-0_313
 96. Surgical Innovations. PretzelFlex™ [Internet]. UK. 2011 [cited 2017 Jun 5]. Available from: <http://www.surginno.com/pretzelflex/>
 97. Aesculap Inc. Cinch Organ Retractor System [Internet]. Center Valley, PA:Aesculap. 2011 [cited 2017 Jun 6]. Available from: <https://www.aesculapusa.com/products/surgical-instruments/laparoscopy/less-invasive-solutions>
 98. Bryant T, Robbins G. Cinch suture and method for using [Internet]. United States Patents; US20020151932 A1, 2002. Available from: <http://appft1.uspto.gov/netacgi/nph-Parser?Sect1=PTO1&Sect2=HITOFF&d=PG01&p=1&u=/netahtml/PTO/srchnum.html&r=1&f=G&l=50&s1=20020151932.PGNR>.
 99. FreeHold Surgical. Hands-Free Intracorporeal Retractors. New Hope, PA: FreeHold Surgical. 2016.
 100. Corden J. LaporOsphere™ Innovation Binder (Private Communication). Manchester; 2010.
 101. Brown JD, Rosen J, Chang L, Sinanan MN, Hannaford B. Quantifying surgeon grasping mechanics in laparoscopy using the Blue DRAGON system. *Stud Health Technol Inform* [Internet]. 2004 Jan;98:34–6. Available from: <http://www.ncbi.nlm.nih.gov/pubmed/15544237>
 102. Moradi Dalvand M, Shirinzadeh B, Nahavandi S, Karimirad F, Smith J. Force Measurement Capability for Robotic Assisted Minimally Invasive Surgery Systems. *Int Conf Intell Autom Robot.* 2013;l:419–424, Best Paper Award.
 103. Matsumoto S, Ooshima R, Kobayashi K, Kawabe N, Shiraishi T, Mizuno Y, et al. A tactile sensor for laparoscopic cholecystectomy. *Surg Endosc.* 1997;11:939–41.
 104. Fakhry M, Bello F, Hanna GB. Real time cancer prediction based on objective tissue compliance measurement in endoscopic surgery. *Ann Surg* [Internet]. 2014 Feb [cited 2015 Feb 19];259(2):369–73. Available from: <http://www.scopus.com/inward/record.url?eid=2-s2.0-84892909907&partnerID=tZ0tx3y1>
 105. Nava A, Mazza E, Furrer M, Villiger P, Reinhart WH. In vivo mechanical characterization

- of human liver. *Med Image Anal* [Internet]. 2008 Apr [cited 2012 Mar 5];12(2):203–16. Available from: <http://www.ncbi.nlm.nih.gov/pubmed/18171633>
106. Barrie J, Jayne DG, Neville A, Hunter L, Hood AJ, Culmer PR. Real-Time Measurement of the Tool-Tissue Interaction in Minimally Invasive Abdominal Surgery: The First Step to Developing the Next Generation of Smart Laparoscopic Instruments. *Surg Innov* [Internet]. 2016; Available from: <http://sri.sagepub.com/cgi/doi/10.1177/1553350616646475>
 107. Ugural AC; Fenster SK. *Advanced Mechanics of Materials and Applied Elasticity*. Fifth Edit. Pearson Education; 2012. 65-97 p.
 108. Craig R. R. Jr. *Mechanics of Materials*. Third Edit. John Wiley & Sons, Inc.; 2011. 22-82 p.
 109. Sanami M, Alderson A, Alderson KL, McDonald SA, Mottershead B, Withers PJ. The production and characterization of topologically and mechanically gradient open-cell thermoplastic foams. *Smart Mater Struct* [Internet]. 2014;23(5):55016. Available from: <http://stacks.iop.org/0964-1726/23/i=5/a=055016?key=crossref.4bfbf3257bcc872534be765e0177065d>
 110. Horgan CO. Recent developments concerning Saint-Venant's principle: An update. *Am Soc Mech Eng*. 1989;(1973).
 111. Lakes RS, Lee T, Bersie A, Wang YC. Extreme damping in composite materials with negative-stiffness inclusions. *Nature* [Internet]. 2001 Mar 29;410(6828):565–7. Available from: <http://dx.doi.org/10.1038/35069035>
 112. Kashdan L, Seepersad CC, Haberman M, Wilson PS. Design, fabrication, and evaluation of negative stiffness elements using SLS. *Rapid Prototyp J* [Internet]. 2012;18(3):194–200. Available from: <https://doi.org/10.1108/13552541211218108>
 113. Gibson LJ, Ashby MF. *Cellular solids: structure and properties*. London: Pergamon press; 1988. 69-119 p.
 114. Yap HW, Lakes RS, Carpick RW. Mechanical instabilities of individual multiwalled carbon nanotubes under cyclic axial compression. *Nano Lett*. 2007;7(5):1149–54.
 115. Correa DM, Seepersad CC, Haberman MR. Mechanical design of negative stiffness honeycomb materials. *Integr Mater Manuf Innov* [Internet]. 2015;4(1):10. Available from: <http://dx.doi.org/10.1186/s40192-015-0038-8>
 116. Love AEH. *A Treatise on the Mathematical Theory of Elasticity* [Internet]. 4th ed. New York: Dover Publications; 1944. 96 p. Available from: <https://ia700404.us.archive.org/15/items/atreatiseonmath01lovegoog/atreatiseonmath01lovegoog.pdf>
 117. Masters IG, Evans KE. Models for the elastic deformation of honeycombs. *Compos Struct*. 1997;35(1996):403–22.
 118. Raymond J. Roark WCY. *Formulas of stress and strain*. 5th Edi. London: MacGraw-Hill; 1976. 96 p.
 119. Kelsey S., Gellatly R.A. CBW. *Aircraft Engineering*. 1958. 294 p.
 120. Gibson LJ, Ashby MF, Schajer GS, Robertson CI. The Mechanics of Two-Dimensional Cellular Materials. *Proc R Soc A Math Phys Eng Sci* [Internet]. 1982 Jul 8 [cited 2013 Sep

- 23];382(1782):25–42. Available from:
<http://rspa.royalsocietypublishing.org/cgi/doi/10.1098/rspa.1982.0087>
121. Gibson LJ, Ashby MF. The Mechanics of Three-Dimensional Cellular Materials. *Proc R Soc A Math Phys Eng Sci* [Internet]. 1982 Jul 8 [cited 2013 Sep 23];382(1782):43–59. Available from: <http://rspa.royalsocietypublishing.org/cgi/doi/10.1098/rspa.1982.0088>
 122. Lakes RS. Foam Structures with a Negative Poisson's Ratio. *Science* (80-). 1987;235(4792):1038–40.
 123. Caddock B, Evans KE. Microporous materials with negative Poisson's ratios. I. Microstructure and mechanical properties. *J Phys D Appl Phys*. 1989;22(12):1877–82.
 124. Evans K CB. Microporous materials with negative Poisson's ratios. II. Mechanisms and interpretation. *J Phys D Appl Phys*. 1989;22:1883–7.
 125. Evans K., Nkansah M., Hutchinson I. RS. Molecular network design. *Nature*. 1991;353(6340):124–8.
 126. Greaves GN, Greer AL, Lakes RS, Rouxel T. Poisson's ratio and modern materials. *Nat Mater*. 2011;10(12):986–986.
 127. Veronda DR, Westmann RA. Mechanical characterization of skin-finite deformations. *J Biomech*. 1970;3(1):111–24.
 128. Lees C, Vincent JF V, Hillerton JE. Poisson's ratio in skin. *Biomed Mater Eng* [Internet]. 1991;1(1):19–23. Available from: <http://www.scopus.com/inward/record.url?eid=2-s2.0-0026361008&partnerID=40&md5=8c4822085716912022b6f32b2bdef978>
 129. Soman P, Lee JW, Phadke A, Varghese S, Chen S. Spatial tuning of negative and positive Poisson's ratio in a multi-layer scaffold. *Acta Biomater* [Internet]. 2012;8(7):2587–94. Available from: <http://dx.doi.org/10.1016/j.actbio.2012.03.035>
 130. Timmins LH, Wu Q, Yeh AT, Moore JE, Greenwald SE. Structural inhomogeneity and fiber orientation in the inner arterial media. *Am J Physiol Heart Circ Physiol*. 2010;298(5):H1537–45.
 131. Gatt R, Vella Wood M, Gatt A, Zarb F, Formosa C, Azzopardi KM, et al. Negative Poisson's ratios in tendons: An unexpected mechanical response. *Acta Biomater* [Internet]. 2015;24:201–8. Available from: <http://www.sciencedirect.com/science/article/pii/S1742706115002871>
 132. Wang N. Stem cell mechanics: auxetic nuclei. *Nat Mater* [Internet]. 2014;13(6):540–2. Available from: <http://www.ncbi.nlm.nih.gov/pubmed/24845989>
 133. Chen X, Brodland GW. Mechanical determinants of epithelium thickness in early-stage embryos. *J Mech Behav Biomed Mater* [Internet]. 2009;2(5):494–501. Available from: <http://dx.doi.org/10.1016/j.jmbbm.2008.12.004>
 134. Williams JL, Lewis JL. Properties and an anisotropic model of cancellous bone from the proximal tibial epiphysis. *J Biomech Eng* [Internet]. 104(1):50–6. Available from: <http://www.scopus.com/inward/record.url?eid=2-s2.0-0020093354&partnerID=40&md5=a77fc1121185218bff52146080ea86e2>
 135. Wilgeroth JM. On the behaviour of porcine skeletal muscle tissue under shock compression. 2012.

136. Yeganeh-Haeri A, Weidner D, Parise J. Elasticity of Alpha-Cristobalite: A Silicon Dioxide with a Negative Poisson's Ratio. *Science*. 1992;257(5070):650–2.
137. Kimizuka H, Ogata S, Shibutani Y. High-Pressure Elasticity and Auxetic Property of α -Cristobalite. *Mater Trans*. 2005;46(6):1161–6.
138. Garber A. Pyrolytic materials for thermal protection systems. *Aerosp Eng*. 1963;22:126–37.
139. Gunton DJ, Saunders GA. The Young's modulus and Poisson's ratio of arsenic, antimony and bismuth. *J Mater Sci* [Internet]. 1972;7(9):1061–8. Available from: <http://dx.doi.org/10.1007/BF00550070>
140. Li Y. The anisotropic behavior of Poisson's ratio, Young's modulus, and shear modulus in hexagonal materials. *Phys status solidi* [Internet]. 1976;38(1):171–5. Available from: <http://dx.doi.org/10.1002/pssa.2210380119>
141. Jiang J-W, Park HS. Negative poisson's ratio in single-layer black phosphorus. *Nat Commun* [Internet]. 2014 Aug 18;5. Available from: <http://dx.doi.org/10.1038/ncomms5727>
142. Baughman RH, Shacklette JM, Zakhidov AA, Stafstrom S. Negative Poisson's ratios as a common feature of cubic metals. *Nature* [Internet]. 1998 Mar 26;392(6674):362–5. Available from: <http://dx.doi.org/10.1038/32842>
143. Peura M, Grotkopp I, Lemke H, Vikkula A, Laine J, Müller M, et al. Negative poisson ratio of crystalline cellulose in kraft cooked Norway spruce. *Biomacromolecules*. 2006;7(5):1521–8.
144. Barthelat F, Tang H, Zavattieri PD, Li CM, Espinosa HD. On the mechanics of mother-of-pearl: A key feature in the material hierarchical structure. *J Mech Phys Solids*. 2007;55(2):306–37.
145. Lakes R. Foam structures with a negative Poisson's ratio. *Sci Mag*. 1987;238:551.
146. Alderson KL, Evans KE. The fabrication of microporous polyethylene having a negative Poisson's ratio. *Polymer (Guildf)*. 1992;33(20):4435–8.
147. Alderson A, Alderson KL, Chirima G, Ravirala N, Zied KM. The in-plane linear elastic constants and out-of-plane bending of 3-coordinated ligament and cylinder-ligament honeycombs. *Compos Sci Technol* [Internet]. 2010;70(7):1034–41. Available from: <http://dx.doi.org/10.1016/j.compscitech.2009.07.010>
148. Boldrin L, Hummel S, Scarpa F, Di Maio D, Lira C, Ruzzene M, et al. Dynamic behaviour of auxetic gradient composite hexagonal honeycombs. *Compos Struct* [Internet]. 2016;149:114–24. Available from: <http://dx.doi.org/10.1016/j.compstruct.2016.03.044>
149. Lira C, Scarpa F. Transverse shear stiffness of thickness gradient honeycombs. *Compos Sci Technol*. 2010;70(6):930–6.
150. Scarpa F. Auxetic and kirigami systems in multiphysics and EMC applications. *EPE 2014 - Proc 2014 Int Conf Expo Electr Power Eng*. 2014;(Epe):25–33.
151. Alderson KL, Alderson A, Smart G, Simkins VR, Davies PJ. Auxetic polypropylene fibres: Part 1 - Manufacture and characterisation. *Plast Rubber Compos* [Internet]. 2002;31(8):344–9. Available from:

152. Sloan MR, Wright JR, Evans KE. The helical auxetic yarn – A novel structure for composites and textiles; geometry, manufacture and mechanical properties. *Mech Mater* [Internet]. 2011 Sep [cited 2012 Dec 3];43(9):476–86. Available from: <http://linkinghub.elsevier.com/retrieve/pii/S0167663611000913>
153. Alderson K, Alderson A, Anand S, Simkins V, Nazare S, Ravirala N. Auxetic warp knit textile structures. *Phys Status Solidi Basic Res* [Internet]. 2012;249(7):1322–9. Available from: <http://www.scopus.com/inward/record.url?eid=2-s2.0-84863524957&partnerID=40&md5=1e7ec95c8e4424d12c2dfae7d61c4458>
154. Hong H, Zhengyue W, Su L. Development of auxetic fabrics using flat knitting technology. *Text Res J* [Internet]. 2011;81(14):1493–502. Available from: <http://journals.sagepub.com/doi/10.1177/0040517511404594>
155. Yanping L, Hong H, Lam JKC, Su L. Negative Poisson's Ratio Weft-knitted Fabrics. *Text Res J* [Internet]. 2010;80(9):856–63. Available from: <http://trj.sagepub.com/cgi/doi/10.1177/0040517509349788>
156. Harkati EH, Bezazi A, Scarpa F, Alderson K, Alderson A. Modelling the influence of the orientation and fibre reinforcement on the Negative Poisson's ratio in composite laminates. *Phys Status Solidi Basic Res*. 2007;244(3):883–92.
157. Choi J. LR. Nonlinear properties of polymer cellular materials with a negative Poisson's ratio. *J Mater Sci*. 1992;27:4678–84.
158. Prawoto Y. Seeing auxetic materials from the mechanics point of view: A structural review on the negative Poisson's ratio. *Comput Mater Sci* [Internet]. 2012 Jun [cited 2013 Oct 8];58:140–53. Available from: <http://linkinghub.elsevier.com/retrieve/pii/S092702561200078X>
159. Choi, JB and Lakes RS. Fracture Toughness of Re-entrant Foam Materials with a Negative Poisson's Ratio: Experiment and Analysis. *Int J Fract*, 1996. 1996;80:73–83.
160. Lakes, RS and Lowe A. "Negative Poisson's ratio foam as seat cushion material." *Cell Polym*. 2000;19:157–67.
161. Evans KE. Tailoring the Negative Poisson's Ratio. *Chem Ind*. 1990;20:654–7.
162. Alderson A, Alderson KL. Auxetic materials. *Proc Inst Mech Eng Part G J Aerosp Eng* [Internet]. 2007 Jan 1 [cited 2014 Aug 11];221(4):565–75. Available from: <http://pig.sagepub.com/lookup/doi/10.1243/09544100JAERO185>
163. Alderson KL, Alderson A, Smart G, Simkins VR, Davies PJ. Auxetic polypropylene fibres: Part 1 - Manufacture and characterisation. *Plast Rubber Compos* [Internet]. 31(8):344–9. Available from: <http://www.ingentaconnect.com/content/maney/prc/2002/00000031/00000008/art00003>
164. Shumakov Y. Origami Magic Ball [Internet]. YouTube. 2012 [cited 2017 Jun 13]. Available from: <https://www.youtube.com/watch?v=VgXwSdJNks8>
165. Liu Y, Hu H. A review on auxetic structures and polymeric materials. *Sci Res Essays*. 2010;5(10):1052–63.

166. Kaminakis NT, Drosopoulos GA, Stavroulakis GE. Design and verification of auxetic microstructures using topology optimization and homogenization. *Arch Appl Mech* [Internet]. 2014;85(9):1289–306. Available from: <http://link.springer.com/10.1007/s00419-014-0970-7>
167. Grima JN, Gatt R, Alderson A, Evans KE. On the potential of connected stars as auxetic systems. *Mol Simul* [Internet]. 2005 Nov [cited 2013 Oct 10];31(13):925–35. Available from: <http://www.tandfonline.com/doi/abs/10.1080/08927020500401139>
168. Theocaris PS, Stavroulakis GE, Panagiotopoulos PD. Negative Poisson's ratios in composites with star-shaped inclusions: a numerical homogenization approach. *Arch Appl Mech* [Internet]. 1997;67(4):274–86. Available from: <http://link.springer.com/10.1007/s004190050117>
169. Smith C., Grima J., Evans K. A novel mechanism for generating auxetic behaviour in reticulated foams: missing rib foam model. *Acta Mater* [Internet]. 2000 Nov;48(17):4349–56. Available from: <http://linkinghub.elsevier.com/retrieve/pii/S135964540000269X>
170. Gaspar N, Ren X, Smith C, Grima J, Evans K. Novel honeycombs with auxetic behaviour. *Acta Mater* [Internet]. 2005 May [cited 2013 Oct 11];53(8):2439–45. Available from: <http://linkinghub.elsevier.com/retrieve/pii/S1359645405000820>
171. Friis EA, Lakes RS, Park JB. Negative Poisson's ratio polymeric and metallic foams. *J Mater Sci* [Internet]. 1988 Dec;23(12):4406–14. Available from: <http://link.springer.com/10.1007/BF00551939>
172. Lakes RS, Witt R. Making and characterizing negative Poisson's ratio materials. *Int J Mech Eng Educ* [Internet]. 2002 Jan 1;30(1):50–8. Available from: <http://dx.doi.org/10.7227/IJMEE.30.1.5>
173. Lorato A, Innocenti P, Scarpa F, Alderson A, Alderson KL, Zied KM, et al. The transverse elastic properties of chiral honeycombs. *Compos Sci Technol* [Internet]. 2010 Jul [cited 2013 Oct 9];70(7):1057–63. Available from: <http://linkinghub.elsevier.com/retrieve/pii/S0266353809002802>
174. Grima JN, Gatt R, Alderson A, Evans KE. On the auxetic properties of “rotating rectangles” with different connectivity. *J Phys Soc Japan* [Internet]. 2005;74(10):2866–7. Available from: <http://www.scopus.com/inward/record.url?eid=2-s2.0-27144484986&partnerID=40&md5=85f8c85850613c8b2e3fa9f2555af679>
175. Prall D, Lakes RS. Properties of a chiral honeycomb with a poisson's ratio of - 1. *Int J Mech Sci*. 1997;39(3):305–14.
176. Alderson A, Alderson KL, Attard D, Evans KE, Gatt R, Grima JN, et al. Elastic constants of 3-, 4- and 6-connected chiral and anti-chiral honeycombs subject to uniaxial in-plane loading. *Compos Sci Technol* [Internet]. 2010 Jul [cited 2013 Oct 9];70(7):1042–8. Available from: <http://linkinghub.elsevier.com/retrieve/pii/S0266353809002814>
177. Alderson A, Alderson KL, Chirima G, Ravirala N, Zied KM. The in-plane linear elastic constants and out-of-plane bending of 3-coordinated ligament and cylinder-ligament honeycombs. *Compos Sci Technol* [Internet]. 2010 Jul [cited 2013 Oct 9];70(7):1034–41. Available from: <http://linkinghub.elsevier.com/retrieve/pii/S0266353809002826>
178. William Jacob Spenner Dolla. Rotational expansion auxetic structures. 2014.

179. Gaspar N. A granular material with a negative Poisson's ratio. *Mech Mater* [Internet]. 2010 Jul [cited 2013 Oct 11];42(7):673–7. Available from: <http://linkinghub.elsevier.com/retrieve/pii/S0167663610000554>
180. Ravirala N, Alderson A, Alderson KL. Interlocking hexagons model for auxetic behaviour. *J Mater Sci* [Internet]. 2007;42(17):7433–45. Available from: <http://www.scopus.com/inward/record.url?eid=2-s2.0-34547246274&partnerID=40&md5=e501094506dd7dcf18fec6d05f3444c9>
181. Alderson A. *Smart Solutions from Auxetic Materials*. Society of Chemistry and Industry. 2011;
182. Moyers RE. Dilator for opening the lumen of a tubular organ [Internet]. US 5108413 A, 1992. Available from: <https://encrypted.google.com/patents/US5108413>
183. Chludzinski M, Hammill E. Expanded UHMWPE for guiding catheter liners and other lubricious coatings [Internet]. United States Patents; US 6837890 B1, 2005. Available from: <https://www.google.com/patents/US6837890>
184. Alderson A, Alderson K. Expanding materials and applications: exploiting auxetic textiles. *Tech Text Int*. 2005;(14):29–34.
185. Ugbolue SC, Kim YK, Warner SB, Fan Q, Yang C-L, Feng Y, et al. Formation and Performance of Auxetic Textiles. 2008;(November):1–10.
186. Miller W, Hook PBB, Smith CWW, Wang X, Evans KEE. The manufacture and characterisation of a novel, low modulus, negative Poisson's ratio composite. *Compos Sci Technol* [Internet]. 2009;69(5):651–5. Available from: <http://search.ebscohost.com/login.aspx?direct=true&db=eoah&AN=18068324&site=ehost-live%5Cnhttp://linkinghub.elsevier.com/retrieve/pii/S026635380800523X>
187. Alderson A, Rasburn J, Evans KE. Mass transport properties of auxetic (negative Poisson's ratio) foams. *Phys status solidi* [Internet]. 2007 Mar 1;244(3):817–27. Available from: <http://dx.doi.org/10.1002/pssb.200572701>
188. Alderson A, Rasburn J, Ameer-Beg S, Mullarkey PG, Perrie W, Evans KE. An Auxetic Filter: A Tuneable Filter Displaying Enhanced Size Selectivity or Defouling Properties. *Ind Eng Chem Res* [Internet]. 2000;39:654–65. Available from: <http://dx.doi.org/10.1021/ie990572w%5Cnhttp://pubs.acs.org/doi/abs/10.1021/ie990572w%5Cnhttp://pubs.acs.org/doi/full/10.1021/ie990572w%5Cnhttp://pubs.acs.org/doi/pdf/10.1021/ie990572w>
189. Alderson A, Davies PJ, Williams MR, Evans KE, Alderson KL, Grima JN. Modelling of the mechanical and mass transport properties of auxetic molecular sieves: an idealised organic (polymeric honeycomb) host–guest system. *Mol Simul*. 2005;31(13):897–905.
190. Choi JB, Lakes RS. Design of a fastener based on negative Poisson's ratio foam. *Cell Polym*. 1991;10(3):205–12.
191. Simkins VR, Alderson A, Davies PJ, Alderson KL. Single fibre pullout tests on auxetic polymeric fibres. *J Mater Sci*. 2005;40(16):4355–64.
192. Budden GDD. *Elastomer Composition*. 2012.
193. Lenoble, BLJ; Mallen, EF; Robson, S; Budden G. *Pressure Material*. 2012.

194. Darwish SMH, Aslam MU. Auxetic Cellular Structures for Custom Made Orthopedic Implants using Additive Manufacturing. *Int J Eng Adv Technol*. 2014;4(2):10–5.
195. Alderson KL, Pickles AP, Neale PJ, Evans KE. Auxetic polyethylene: The effect of a negative poisson's ratio on hardness. *Acta Metall Mater*. 1994;42(7):2261–6.
196. Carolin Koerner F, Heintl, Peter N, Robert Friedrich Singer E. Auxetic Material. US Patent; US 2011/0282452 A1, 2011.
197. Abdelaal O, Darwish S. Analysis, Fabrication and a Biomedical Application of Auxetic Cellular Structures. *Int J Eng Innov Technol* [Internet]. 2012;2(3):218–23. Available from: http://ijeit.com/vol 2/Issue 3/IJEIT1412201209_40.pdf
198. Scarpa F. Auxetic materials for bioprostheses. *IEEE Signal Process Mag*. 2008;25(5).
199. Baker CE. Auxetic Spinal Implants: Consideration of Negative Poisson's Ratio in the Design of an Artificial Intervertebral Disc. Master's Thesis. 2011.
200. Anthony Sabatino. Auxetic prosthetic implant. US 20140058517 A1, 2014.
201. Park KO, Park JC, Choi JB, Lee SJ, Choi HH, Kim JK. Polyurethane foam with a negative poisson's ratio for diabetic shoes [Internet]. Vols. 288–289, *Key Engineering Materials*. 2005. p. 677–80. Available from: <http://www.scopus.com/inward/record.url?eid=2-s2.0-34147170268&partnerID=40&md5=cb27954369442f02c335ed31ec573c80>
202. Park KO, Choi JB, Park J-C, Park DJ, Kim JK. An improvement in shock absorbing behavior of polyurethane foam with a negative poisson effect [Internet]. Vols. 342–343, *Key Engineering Materials*. 2007. p. 845–8. Available from: <http://www.scopus.com/inward/record.url?eid=2-s2.0-34147156832&partnerID=40&md5=65804216e242db0a93b64deb01ca74e3>
203. J. H. Shadduck. Ophthalmic devices, methods of use and methods of fabrication. US Patent; 21139, 2005.
204. Forgacs G, Sun W. Biofabrication: Micro- and Nano-fabrication, Printing, Patterning and Assemblies [Internet]. Elsevier Science; 2013. (Micro and Nano Technologies). Available from: <https://books.google.co.uk/books?id=3kSXVx6uT1QC>
205. Fozdar DY, Soman P, Lee JW, Han L-H, Chen S. Three-Dimensional Polymer Constructs Exhibiting a Tunable Negative Poisson's Ratio. *Adv Funct Mater* [Internet]. 2011;21(14):2712–20. Available from: <http://www.pubmedcentral.nih.gov/articlerender.fcgi?artid=3155506&tool=pmcentrez&rendertype=abstract>
206. Zhang W, Soman P, Meggs K, Qu X, Chen S. Tuning the Poisson's Ratio of Biomaterials for Investigating Cellular Response. *Adv Funct Mater*. 2013;23(25):3226–3232.
207. Soman P, Chen S, Fozdar D. Micro-structured biomaterials and fabrication methods therefor. US Patent; US20130344601A1, 2013.
208. Ali MN, Rehman IU. An Auxetic structure configured as oesophageal stent with potential to be used for palliative treatment of oesophageal cancer; development and in vitro mechanical analysis. *J Mater Sci Mater Med* [Internet]. 2011;22(11):2573–81. Available from: <http://link.springer.com/10.1007/s10856-011-4436-y>
209. Mizzi L, Attard D, Casha A, Grima JN, Gatt R. On the suitability of hexagonal

- honeycombs as stent geometries. *Phys Status Solidi* [Internet]. 2014 Feb [cited 2014 Nov 13];251(2):328–37. Available from: <http://doi.wiley.com/10.1002/pssb.201384255>
210. Dolla WJS, Fricke BA, Becker BR. Structural and drug diffusion models of conventional and auxetic drug-eluting stents. *J Med Devices, Trans ASME* [Internet]. 2007;1(1):47–55. Available from: <http://www.scopus.com/inward/record.url?eid=2-s2.0-44649172416&partnerID=40&md5=d1296b219a426cc167ce7aed49ba7239>
 211. Lim D, Cho S-K, Park W-P, Kristensson A, Ko J-Y, Al-Hassani STS, et al. Suggestion of Potential Stent Design Parameters to Reduce Restenosis Risk driven by Foreshortening or Dogboning due to Non-uniform Balloon-Stent Expansion. *Ann Biomed Eng* [Internet]. 2008;36(7):1118–29. Available from: <http://link.springer.com/10.1007/s10439-008-9504-1>
 212. Rosenfield K, Schainfeld R, Pieczek A, Haley L, Isner JM. Restenosis of endovascular stents from stent compression. *J Am Coll Cardiol* [Internet]. 1997;29(2):328–38. Available from: <http://www.ncbi.nlm.nih.gov/pubmed/9014985>
 213. Zheng-Dong, Ma; Yuayuan L. Auxetic Stents. US Patent; US 2011/0029063 A1, 2011.
 214. Abunassar Chand. Stent having optimized expansion ratio. USA; US 2011/0295356 A1, 2011.
 215. Rudy H. Auxetic tubular lines. US Patent; US 2006/0129227 A1, 2006.
 216. Dolla WJS, Fricke BA, Becker BR. Structural and Drug Diffusion Models of Conventional and Auxetic Drug-Eluting Stents. *J Med Device* [Internet]. 2007;1(1):47–55. Available from: <http://medicaldevices.asmedigitalcollection.asme.org/article.aspx?articleid=1451274>
 217. Ali MN, Busfield JJC, Rehman IU. Auxetic oesophageal stents: structure and mechanical properties. *J Mater Sci Mater Med* [Internet]. 2014;25(2):527–53. Available from: <http://link.springer.com/10.1007/s10856-013-5067-2>
 218. Yasuda H, Yang J. Reentrant Origami-Based Metamaterials with Negative Poisson's Ratio and Bistability. *Phys Rev Lett* [Internet]. 2015;114(18):185502. Available from: <http://link.aps.org/doi/10.1103/PhysRevLett.114.185502>
 219. Kuribayashi K. A novel foldable stent graft. University of Oxford; 2004.
 220. Smooth-on. Shore Hardness Scale [Internet]. 2017 [cited 2012 Nov 15]. Available from: <https://www.smooth-on.com/page/durometer-shore-hardness-scale/>
 221. Daniels AU. Silicone breast implant materials. *Swiss Med Wkly* [Internet]. 2012 Jan [cited 2013 Oct 21];142(July):w13614. Available from: <http://www.ncbi.nlm.nih.gov/pubmed/22826101>
 222. EngineeringToolBox. Young's Modulus - Tensile Modulus or Modulus of Elasticity - for steel, glass, wood and other common materials. [Internet]. [cited 2013 Mar 18]. Available from: https://www.engineeringtoolbox.com/young-modulus-d_417.html
 223. Treloar L.R.G. The elasticity and related properties of rubbers. *Reports Prog Phys* [Internet]. 1973;36:755–826. Available from: http://femtoscopia.phys.uniroma1.it/scopigno/static/TEACHING/Termodinamica_2011/treolar.pdf

224. Reckitt Benckiser. Durex Thin Feel Condoms [Internet]. 2017 [cited 2017 Jun 14]. Available from: <https://www.durex.co.uk/en-gb/p/durex-thin-feel-condoms-12-pack#tabdetails>
225. ImageJ - Image Processing and Analysis in Java <http://imagej.nih.gov/ij/download.html>.
226. Silva MJ, Gibson LJ. The effects of non-periodic microstructure and defects on the compressive strength of two-dimensional cellular solids. *Int J Mech Sci* [Internet]. 1997;39(5):549–63. Available from: <http://www.sciencedirect.com/science/article/pii/S0020740396000653>
227. Whitty, J. P.M.; Nazare, F.; and Alderson A. Modelling the effects of density variations on the in-plane Poisson's ratios and Young's Moduli of periodic conventional and re-entrant honeycombs - Part 1: Rib thickness variations. *Cell Polym*. 2002;21(2).
228. Alkas Yonan S, Silva MB, Martins PAF, Tekkaya AE. Plastic flow and failure in single point incremental forming of PVC sheets. *Express Polym Lett*. 2014;8(5):301–11.
229. Rosen J, Brown JD, De S, Sinanan M, Hannaford B. Biomechanical properties of abdominal organs in vivo and postmortem under compression loads. *J Biomech Eng* [Internet]. 2008 Apr [cited 2012 Oct 26];130(2):21020. Available from: <http://www.ncbi.nlm.nih.gov/pubmed/18412507>
230. Tay BK, Kim J, Srinivasan M a. In vivo mechanical behavior of intra-abdominal organs. *IEEE Trans Biomed Eng* [Internet]. 2006 Nov;53(11):2129–38. Available from: <http://www.ncbi.nlm.nih.gov/pubmed/17073317>
231. Kerdok AE. Characterizing the Nonlinear Mechanical Response of Liver to Surgical Manipulation (Doctoral thesis). Harvard University; 2006.
232. Tamura A, Omori K, Miki K, Lee JB, Yang KH, King AI, et al. Mechanical Characterization of Porcine Abdominal Organs 46th Stapp Car Crash Conference. *Stapp Car Crash J*. 2002;46(November).
233. Snedeker JG, Niederer P, Schmidlin FR, Farshad M, Demetropoulos CK, Lee JB, et al. Strain-rate dependent material properties of the porcine and human kidney capsule. *J Biomech* [Internet]. 2005 May [cited 2013 Sep 23];38(5):1011–21. Available from: <http://www.ncbi.nlm.nih.gov/pubmed/15797583>
234. Trejos AL, Patel R V., Naish MD. Force sensing and its application in minimally invasive surgery and therapy: A survey. *Proc Inst Mech Eng Part C J Mech Eng Sci*. 2010;224(7):1435–54.
235. Rofin. StarCut Tube Laser Cutting Machines [Internet]. [cited 2017 Aug 15]. Available from: <https://www.rofin.com/en/products/systems-and-solutions/laser-cutting-systems/laser-cutting-machines-starcut-tube/>

Appendix A

Survey Sheet:

Aim:

Single blind study to identify simulant abdominal organs that mimic the healthy human abdominal organs.

Introduction:

My name is Dignesh Shah, PhD student at the Sheffield Hallam University, working on a project to develop novel organ retraction and space creation devices for use in laparoscopic procedures.

My supervisory team includes Prof Andrew Alderson of Sheffield Hallam University and Dr James Corden of TrusTECH. Mr. Titus Augustine has developed this concept with Dr James Corden and Prof Andrew Alderson.

This project is being undertaken in partnership with TrusTECH, the NorthWest NHS Innovation Service and is sponsored by Central Manchester University Hospitals NHS Foundation Trust (CMFT).

As part of the PhD project I am developing an in-house abdominal simulator consisting of simulants of key abdominal organs such as liver, bowel, kidney, spleen, and stomach. In-house abdominal simulator will be used as in-vitro test-rig to evaluate expansion capabilities of the prototype devices.

I have fabricated simulants of key abdominal organs using different concentrations of silicone gel and wallpaper paste. I am now seeking opinions on organs that most closely represent the density and pliability of human organs from surgeons experienced in carrying out open and laparoscopic abdominal surgeries.

I would be most grateful if you could spare 10 minutes of your time to assess simulants and fill in the accompanying data sheet. Please can you do this independently without discussing your opinions with your colleagues?

Place:

Manchester Royal Infirmary, CMFT, Manchester.

Participants/Personnel:

Open and laparoscopic abdominal surgeons

Procedure:

1. Please add your name (optional), job title and number of years' experience in abdominal surgical procedures to the data collection sheet.
2. Please manipulate the various simulant organs and tick the box indicating which simulant organ you feel most closely represents the density and pliability of healthy human organs.
3. Please provide any additional general comments you have in the comments box.

Conclusion:

The selected simulant organs by surgeons will be utilized for the further development of an in-house abdominal simulator.

DATA COLLECTION SHEET:

Surgeon x (x = 1 to 5)

Name (Optional):

Experience in years for open and/or laparoscopic abdominal surgeries:

Abdominal organs:

- I. Liver: Simulants are made up of Pro Gel 10 System (Silicone gel).

Sample No.	A	B	C
Opinion (Yes/No)			

Please tick the box indicating which simulant you feel most closely represents the density and pliability of a healthy human liver.

- II. Kidney: Simulants are made up of Pro Gel 10 System (Silicone gel).

Sample No.	A	B	C
Opinion (Yes/No)			

Please tick the box indicating which simulant you feel most closely represents the density and pliability of a healthy human kidney.

- III. Bowel: Simulants are filled with the mixture of different concentrations of wallpaper paste and water.

Sample No.	A	B	C
Opinion (Yes/No)			

Please tick the box indicating which simulant you feel most closely represents the density and pliability of a healthy human bowel.

IV. Stomach: Simulants are filled with the mixture of water and air.

Sample No.	A	B
Opinion (Yes/No)		

Please tick the box indicating which simulant you feel most closely represents the density and pliability of a healthy human stomach.

V. Spleen: Simulants are made up of Pro Gel 10 System (Silicone gel).

Sample No.	A	B
Opinion (Yes/No)		

Please tick the box indicating which simulant you feel most closely represents the density and pliability of a healthy human spleen.

Comments:

1.

2.

Appendix B

Study Protocol To Measure Surface Pressure

Title:

In-vivo measurement of surface pressures applied on human abdominal organs and tissue during open and laparoscopic surgical procedures.

Summary of proposed in-vivo pilot study:

The proposed in-vivo pilot study is summarised in Table B.1.

Table B.1: Summary of proposed in-vivo pilot study.

Title of Study	In-vivo measurement of surface pressures exerted on human abdominal organs and tissue during open and laparoscopic surgical procedures.
Principal Investigator	Mr Titus Augustine
Study Site	Manchester Royal Infirmary, Central Manchester University Hospitals NHS Foundation Trust (CMFT), Manchester, England
Duration	Four calendar months
Study Design	<p>The study is a pilot study to validate the surface pressure measurement method and to obtain initial data from a small number of basic surgical procedures. The study will involve two consultant surgeons, two surgical procedures and 10 to 12 patients.</p> <p>Name of consultant surgeons: Mr. Titus Augustine and Mr. Thomas Satyadas</p> <p>Surgical procedures: Hepatectomy, Laparoscopic Cholecystectomy, and Laparoscopic Nephrectomy</p> <p>Approx. 10-12 patients split 50:50 between open and laparoscopic procedures.</p>
Objective	The objective of this pilot study is to accurately measure the in-vivo surface pressures exerted on abdominal organs by retracting instruments and surgeon's hands during open and laparoscopic surgery using sensitive pressure sensors.
Outcomes	<ul style="list-style-type: none"> The primary outcome will be basic measurements that quantify the surface pressures exerted during open and abdominal laparoscopic procedures.

	<ul style="list-style-type: none"> • The data referred to above will be a key input into a PhD project being undertaken at Bolton University (at the Materials and Engineering Research Institute of the Sheffield Hallam University from Oct 2013), part funded by CMFT and will include: <ol style="list-style-type: none"> 1. Utilisation of the data for the design and development of the LaparOsphere™, a prototype organ retraction and space creation system for use during laparoscopic surgery 2. The design and evaluation of a prototype abdominal laparoscopic simulator • The data may also be of value: <ol style="list-style-type: none"> 3. For use within the software of advanced laparoscopic simulators to improve haptic feedback during simulated laparoscopic surgery. 4. During laparoscopic surgical training 5. In the design of more advanced pressure measurement studies (such as the comparison between different procedures or the comparison between different surgeons).
--	---

Background:

Laparoscopic Surgery, also known as Minimally Invasive Surgery (MIS), is the surgical technique of operating within body cavities through small incisions. Its use is growing significantly because of its advantages over open surgery. The advantages include; earlier recovery, reduced post-operative pain, reduced length of stay, decreased morbidity and increased cost effectiveness.

The most common laparoscopic procedures include Laparoscopic Cholecystectomy, Laparoscopic Nephrectomy, Laparoscopic Appendectomy, and Laparoscopic Hernia repair (2) (3). Laparoscopic surgery is increasingly being used in complex abdominal procedures including hepatic resections and even surgery on major vascular structures including the aorta.

Briefly, the technique involves making a number of small incisions in the abdominal wall to enable the insertion of a camera and surgical instruments. In order to create space within the abdominal cavity and for the surgeon to access the surgical field it is necessary to inflate the abdominal cavity using CO₂ gas, a process referred to as CO₂ insufflation (79) (81). This is outlined in Figure B.1.

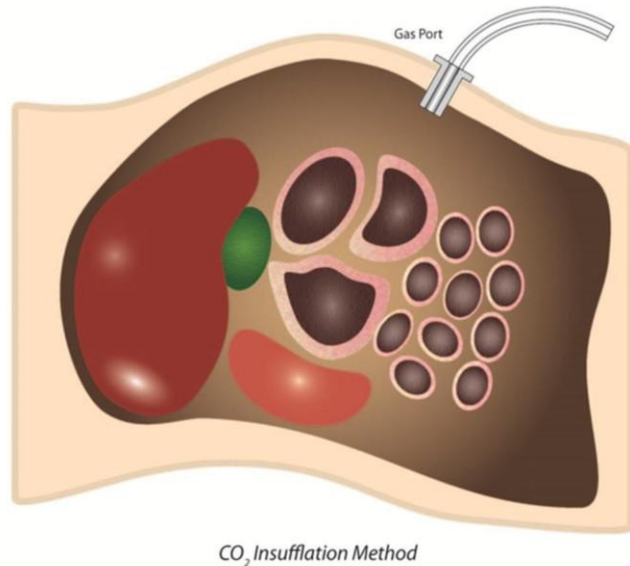


Figure B.1: CO₂ Insufflation.

There are a number of recognised problems associated with the use of CO₂ insufflation (84) (85):

8. Increased risk of hypothermia because of increased exposure to cold, dry CO₂ gas during inflation of the abdomen.
9. The need to constantly insufflate the abdominal cavity to maintain a working space. Leaks and suction causes deflation often at crucial points during surgery which leads to collapse of the working space with reduced visibility for the surgeon.
10. Raised abdominal pressure resulting in reduced heart and lung function.

Difficulties in using electrosurgical and laser based cutting and sealing instruments.

1. The increased intra-abdominal pressure due to the pneumoperitoneum can cause hemodynamic and metabolic effects such as an increase in

CO₂ absorption. This is a major disadvantage especially in neonatal and paediatric laparoscopic surgery

2. The requirement for several different components (the gas cylinder, tubing, pump, and pressure monitor) for delivery of the CO₂ and also the availability of medical grade CO₂ in some less developed markets are some of the disadvantages with use of CO₂
3. Leaks of CO₂ with deflation increases surgical time, volume of CO₂ used and could contribute to complications and therefore, can affect overall cost and outcome of surgery.

During both open and laparoscopic abdominal surgery, access to, and visibility of the surgical field is reduced due to the presence of surrounding organs and tissues. It is necessary for the surgeon to constantly retract (move) surrounding organs and tissues from the surgical field. For example, during a routine laparoscopic cholecystectomy it can be necessary for the surgeon to lift the liver in excess of 50 times to gain access to the gall bladder. This often requires an assistant surgeon, is distracting and can be time consuming. The need to constantly handle surrounding organs increases the potential of inadvertent damage or injury to these structures.

The LaparOsphere™ concept:

The LaparOsphere™ is a potential alternative to the use of CO₂ insufflation to create a pneumoperitoneum during abdominal laparoscopic procedures. It has the potential to reduce or eliminate the above described drawbacks of CO₂ insufflation. The initial concept was proposed by Mr Titus Augustine, a consultant transplant surgeon at the CMFT. The concept is now being further developed by Dignesh Shah in a PhD project at Bolton University (at the Materials and Engineering Research Institute of the Sheffield Hallam University from Oct 2013), part funded by CMFT.

The LaparOsphere™ is an expanding device that is initially inserted into the abdominal cavity in its unexpanded state. Upon inflation it takes the shape of a truncated hollow sphere with a number of access holes for surgical instruments. It creates space within the abdomen by moving the abdominal wall upwards and

by moving surrounding structures away from the surgical field. The surgeon operates within the space inside the sphere. The laparoscope and other laparoscopic instruments are inserted through holes/apertures within the surface of the sphere without affecting the inflation or structural integrity of the sphere. Surrounding organs and tissues remain outside the sphere and are retracted and protected from the surgical field. This concept is illustrated in Figure B.2.

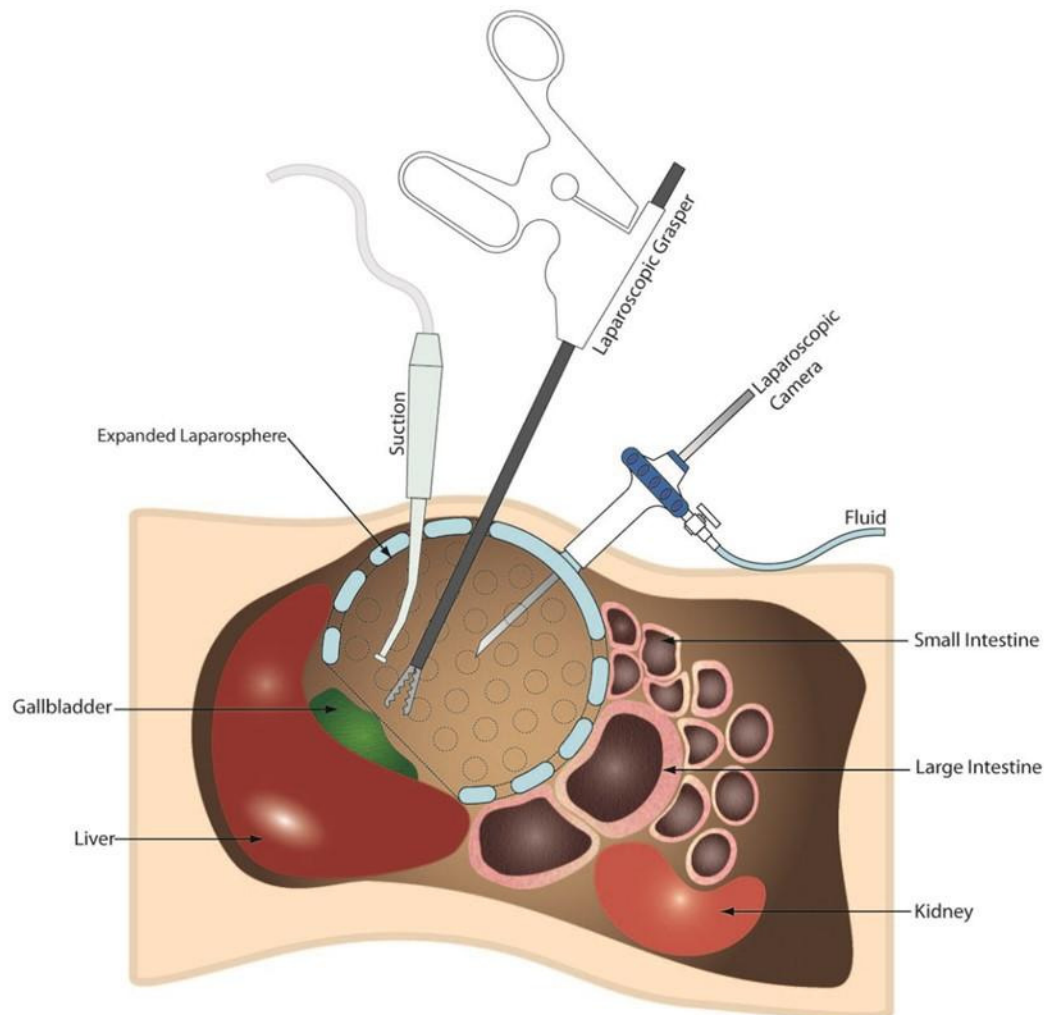


Figure B.2: The concept of the LaparOsphere™ device.

Surface pressure measurements during organ retraction:

In order to further develop the LaparOsphere™ it is necessary to understand the mechanics of organ retraction during laparoscopic surgical procedures. Specifically, it is necessary to determine the extent of organ retraction (i.e. the distances moved) and the surface pressures exerted on the main abdominal organs during retraction.

During surgery, surface pressures can be applied to single organs by the surgeon's hand, across a number of organs using metal retraction plates and to individual organs by surgical instruments. To our knowledge no studies have been undertaken to quantify the surface pressures for the organ retraction applied during surgery. We are aware of some studies that have measured the pressures and forces applied to surgical instruments by surgeons in an attempt to improve the design of surgical instruments.

The primary outcome of this study will be basic measurements that quantify the surface pressures exerted during open and abdominal laparoscopic procedures.

This data will be a key input into a PhD project being undertaken at Bolton University (at the Materials and Engineering Research Institute of the Sheffield Hallam University from Oct 2013), sponsored by CMFT and will enable:

- The design and development of a range of prototype expanding structures.
- The design and evaluation of an in-house abdominal simulator to enable in vitro testing of these structures.
- Mathematical modelling of the process of organ retraction

Outside of the PhD project, the data may also be of value:

- For use within the software of advanced laparoscopic simulators to improve haptic feedback during simulated laparoscopic surgery.
- During laparoscopic surgical training
- In the design of more advanced surgical pressure measurement studies (such as the comparison of the surface pressures exerted between different procedures or between different surgeons).

We propose to utilize flexible thin film pressure sensors placed between the surgeons hand or retracting instrument during surgery to directly measure the surface pressures applied to abdominal organs during common laparoscopic and open abdominal procedures.

Study Personnel:

1. Mr Titus Augustine

The Principal Investigator on this study will be Mr Titus Augustine, a Consultant Transplant and Endocrine Surgeon and Clinical Director of Transplantation at CMFT.

Mr Augustine has over 25 years of experience as a surgeon, 15 years of experience in laparoscopic surgery and is a Royal College of Surgery trainer for laparoscopic techniques.

Mr Augustine proposed the concept of the LaparOsphere™ as an alternative to CO₂ insufflations.

2. Mr Thomas Satyadas

Mr Thomas Satyadas will be involved in the study and will undertake some of the surgical procedures during which retraction pressures will be measured.

Mr Satyadas is a Consultant Hepatobiliary, Pancreatic and Advanced Laparoscopic Surgeon at CMFT. He has over 15 years of experience in laparoscopic abdominal surgery.

3. Dr James Corden

Dr James Corden is a Chartered Mechanical Engineer and has a PhD in medical device development. Dr Corden is the Business Development manager at TrusTECH, the NorthWest NHS Innovation Service. He is the industrial supervisor for the PhD project being undertaken at the University of Bolton (at the Materials and Engineering Research Institute of the Sheffield Hallam University from Oct 2013).

4. Mr Dignesh Shah

Mr Dignesh Shah is a PhD student at the Institute of Materials Research and Innovation (IMRI) of the University of Bolton (at the Materials and Engineering Research Institute of the Sheffield Hallam University from Oct 2013). He has a first degree in Pharmacy and an MSc in Healthcare and Medical Devices. His PhD project is funded by an EPSRC Industrial Case PhD studentship with additional sponsorship from CMFT.

5. Dr Tahir Shah

Dr Tahir Shah is Dignesh Shah's academic supervisor at Bolton University. He has general expertise in the area of materials science and the characterisation of material properties with research interests in polymer science and the application of novel polymers and processing methods across a range of industries.

Study Site:

All clinical measurements will be taken at Manchester Royal Infirmary, part of CMFT.

Study Procedures:

Patients scheduled for the following routine procedures at CMFT will be invited to participate in the study.

- a) Open liver resection
- b) Open gall bladder removal
- c) Hand assisted laparoscopic kidney removal

In addition to their routine appointment letter patients will be sent a covering letter inviting patients to participate in the study and a patient information sheet. This sheet details the background to the study and also the risks associated with the study. Upon attendance for surgery the surgeon will speak to the patient about the study and resolve any further queries they have. The surgeon will then ask the patient if they would like to participate in the study. Patients who agree to participate will be asked to sign the study consent form.

Clinical Procedures:

The main abdominal organs are outlined in the diagram in Figure B.3.

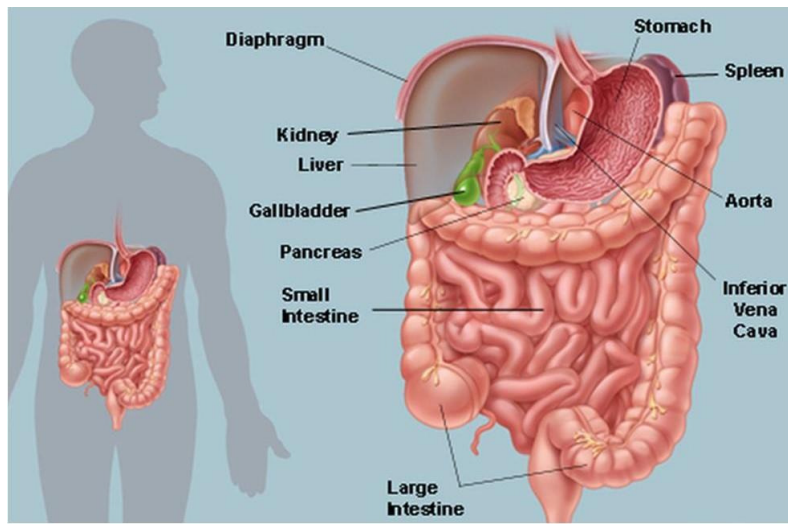


Figure B.3: Major abdominal organs. '©2016, WebMD, LLC. All rights reserved' (4)

Open Abdominal Surgery:

In open abdominal surgery an incision is generally along the midline of the abdomen. The muscle and fascia are retracted using steel retractors to expose the main abdominal organs. This is illustrated in the Figure B.4.



Figure B.4: Exposure of the abdominal cavity during open abdominal surgery.

A common abdominal procedure is gall bladder removal (cholecystectomy). The gall bladder is located below the left lobe of the liver. In order to obtain access to the gall bladder the surgeon must lift the liver in the cranial direction by approximately 5 to 10 cm and move the stomach and large bowel in the caudal direction by approximately 5 to 10 cm.

Other surgical procedures require abdominal organs to be retracted in a range of directions to access the surgical field. As this is a pilot study, we propose to concentrate on the retraction of the liver, stomach, and the bowel only. Such basic retraction is required in the majority of abdominal procedures to obtain deeper access within the abdomen and expose the gall bladder, kidneys, etc. (Figures B.5).



Figure B.5: Retraction of liver in cranial and stomach in right lateral directions during an open abdominal procedure. 'ACS Surgery 2003. © 2003 WebMD Inc. All rights reserved'. (77)

Hand Assisted Laparoscopic Surgery:

Hand assisted laparoscopic surgery (HALS) is a half-way house between open and laparoscopic procedures. A number of small incisions are made in the abdomen to enable the insertion of laparoscopic instruments. A larger incision of 3 to 5 cm is also made in the abdomen to enable the surgeon to insert their hand into the abdomen to facilitate advanced retraction and manipulation of the abdominal organs. CO2 insufflation is used in this procedure and in order to prevent CO2 leakage a “GelPort” is used to seal round the surgeons hand and the incision in the abdomen (Figure B.6). HALS is typically used during more advanced laparoscopic procedures such as laparoscopic nephrectomy. During these procedures, the bowel and spleen are typically retracted by 10 cm distally from the kidney.



Figure B.6: A GelPort used to hand assisted laparoscopic surgery.(80)

Surgical procedures during the study:

In this pilot study we propose to undertake basic surface pressure measurements at the start of a number of open abdominal procedures and at the start of a number of HALS procedures. Primarily we will be measuring the surface pressures involved in the retraction of the liver, bowel, and stomach.

The surface pressures required to retract abdominal organs will be measured using flexible thin film pressure sensors that are inserted between the

liver/bowel and the surgeon's hand. The sensors and associated wires will be enclosed within a sterile wrapper to address sterility issues.

The pressure data will be obtained at the start of the surgical procedure, once access to the abdomen has been obtained but prior to any further surgery. Obtaining the pressure measurements should take no longer than 10 minutes. Once the pressure data has been obtained the pressure sensors will be removed from the abdomen and the surgeon will be free to proceed in accordance with the procedure.

STUDY EQUIPMENT:

Study equipment

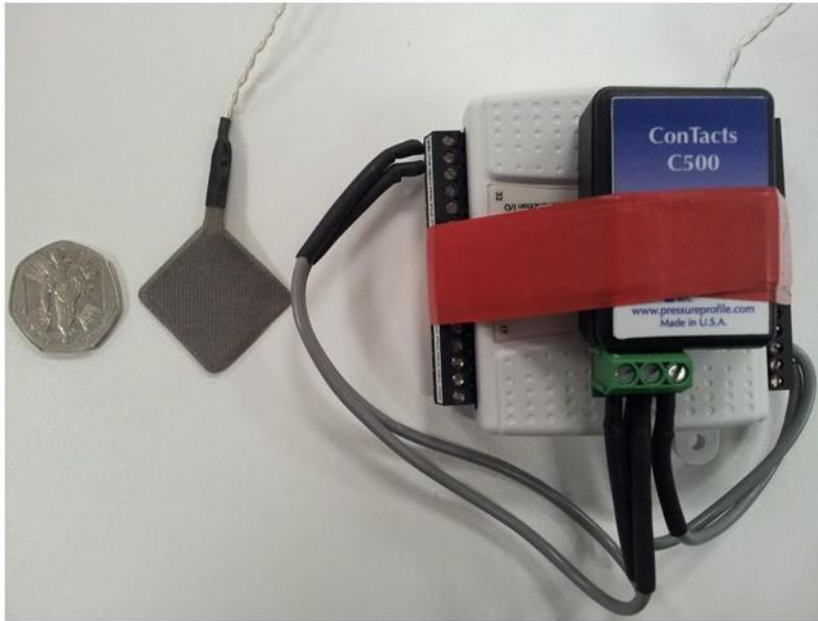
The pressure sensor is shown in Figure B.7a and described below.

- The Pressure Profile C500 Tactile Sensor is a simple, 3-wire device that provides precise and repeatable measurements of tactile force and pressure. This single element pressure sensor allows you to conveniently measure pressure at different locations.
- The sensor is a thin film flexible capacitive sensor which is encapsulated into a fabric layer.
- Application of a pressure to the sensor results in a DC analogue output with a voltage range of 0 to 4V and a current of 13mA.
- The sensor has a cable approximately 1m in length which is hardwired to an amplifier and signal conditioning unit. This connects via a USB interface to a laptop or PC with associated data logging software.
- A range of available sensors are available. We are proposing to use two sensors, one that is 10mm x 10mm square and another that is 25mm x 25 mm square. Both sensors are approx. 1mm thick.

Sterility issues

The thin film pressure sensors are not sterile.

To address this they will be covered in a sterile outer cover that completely covers the sensor and the associated cables. The cover that will be used is a sterile ultrasound probe cover. This is approximately 1.5m encapsulating the sensor in latex part (Figure B.7b) and enabling the cables to be covered entirely until the cables reach the laptop which will be placed outside of the sterile field (Figure B.7c).



(a)



(b)



(c)

Figure B.7: Components of C500 Pressure Sensor system. (a) Components of C500 Pressure Sensor System (b) Enclosure of the Pressure Sensor (c) Sterile Ultrasound Probe Cover encapsulating Pressure Sensor System.

Operating theatre setup

The operating theatre is split into a sterile field and a non-sterile field (Figure B.8). All personnel within the sterile field must be dressed in sterile gowns, gloves, facemasks etc. All equipment within the sterile field must be sterile or covered in a sterile barrier. Personnel outside of the sterile field do not have to wear sterile gowns. Equipment outside of the sterile field does not have to be sterilised.

The surgical field is the area of the body in which the operation is taking place.

For this study, the pressure sensors and cables will enter the sterile field and the surgical field. The sensors will be contained within a sterile outer layer as described above. The associated laptop and assistant who will operate the laptop will be outside of the sterile field and will not have to be sterile.

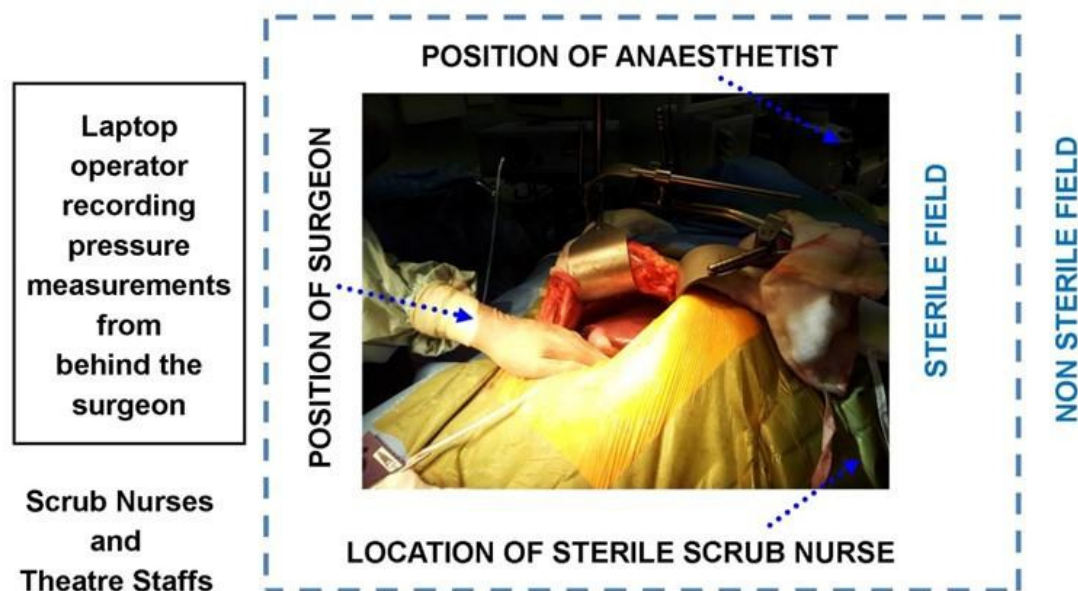


Figure B.8: Representation of sterile and non-sterile fields within an operation theatre.

SYSTEM VALIDATION:

Prior to in-vivo measurements, the pressure sensing system will be evaluated by manipulating various simulant organs within the assembly of in-house abdominal simulator.

Both surgeons involved in the in-vivo work will have the opportunity to familiarise themselves with the equipment. During this work, the surgeon will wear surgical gloves and the sensors will be contained within their sterile cover

to ensure the evaluation closely represents how the device will be used in-vivo. This will enable the exact procedure for passing the sensor into the sterile field and the interaction between the surgeon and the assistant to be practiced before any in-vivo measurements are undertaken. This will ensure that the time required to obtain these measurements during surgery is kept to a minimum.

EXPERIMENTAL PROCEDURE:

- Prior to using the pressure sensor in-vivo, the surgeon and associated theatre staff will have the opportunity to familiarise themselves with the pressure sensor and the procedure for introducing it into the sterile field and collecting data from the surgical field.
- The pressure sensing system will be set up and checked by the non-sterile assistant prior to surgery commencing.
- The pressure sensor will be inserted into its sterile cover in a suitable manner to ensure that the outer layer of the cover remains sterile and the sterile field is not compromised. This procedure will be practiced by the non-sterile assistant and the sterile scrub nurse before any surgery commences. This is similar to the method currently used for encapsulating a non-sterile ultra sound probe into its sterile cover and the scrub nurse will be familiar with this procedure.
- The surgeon will gain access to the abdomen using standard surgical procedures.
- Upon inspection of the abdominal cavity the surgeon will confirm that the patient is suitable for the pressure measurements to be undertaken and there are no underlying pathologies which make the patient unsuitable (such as significant adhesions).
- The sterile scrub nurse will hand over the pressure sensor to the surgeon when requested by the surgeon.
- The surgeon will place the pressure sensor within the abdominal cavity between the appropriate organ and their hand. They will liaise with the

non-sterile assistant to confirm that the pressure sensor is functioning correctly.

- The surgeon will retract the organ in question using standard surgical techniques. During the retraction the assistant will record the pressure data.
- The retraction will be repeated 4 or 5 times to confirm the repeatability of the measurements.
- Before concluding the pressure measurements the non-sterile assistant will confirm that the pressure data has been correctly recorded.
- The surgeon will remove the pressure sensor from the abdomen and hand back to the sterile scrub nurse.
- The surgeon will continue with the operation as planned.
- The total time required to obtain the pressure data should not add more than 10 minutes to the overall surgery time.
- During the pressure measurement procedure and the resulting surgical procedure the patient will be monitored by the surgeon and anaesthetist in accordance with standard clinical practice.
- Following surgery and during their recovery, the patient will be cared for in accordance with standard clinical practice
- No further patient follow up will be undertaken or is required.

INCLUSION CRITERIA:

- 1) Male and female patients scheduled for the following routine operations will be invited to participate in the study.
 - Open liver resection
 - Open gall bladder removal
 - Hand assisted laparoscopic kidney removal

- 2) Only patients over the age of 18 will be invited to participate in the study.

EXCLUSION CRITERIA:

1. Pregnant woman.
2. Patients who have previously undergone abdominal surgery
3. Patients admitted for emergency abdominal surgery
4. As this is a pilot study there is insufficient resource to be able to translate the patient information sheet into other languages apart from English or to provide an interpreter to explain the procedure to the patient. For this reason only patients with a good understanding of spoken and written English will be included in the study.
5. The surgeon undertaking the procedure will be able to exclude any patient that initially meets the inclusion criteria but upon further investigation prior to surgery or during surgery is no longer considered suitable.

STUDY SIZE:

A medical statistician has been consulted to determine the appropriate number of patients for this study. His view was that as this is a pilot study to validate the in-vivo pressure measurement technique and that as no comparisons are being made with the data (such as comparisons with other pressure measurement techniques, between surgeons or the outcome of patients) it was appropriate to limit the study size to 10 to 12 patients.

STUDY RISKS:

The study risks are outlined in Table B.2.

Table B.2: Study risks.

Risk	Severity	Mitigated by
Sterility of sensors	Medium	The sensor will initially be cleaned by wiping the sensor and wires with an

		<p>alcohol solution and then drying it with a sterile cloth.</p> <p>The sensor will then be enclosed in a sterile outer layer that is typically used to cover intra-operative ultra-sound probes. The procedure for this is similar to the procedure for introducing the ultrasound probe into the sterile field and will be practiced before surgery.</p> <p>The sensors are flexible fabric based sensors and do not have any sharp edged that could result in rupture of the sterile cover.</p> <p>Prior to surgery the surgeons involved will practice using the sensor to manipulate simulant organs. This will ensure that they are familiar with the handling of the sensors prior to use in-vivo.</p>
Electrical hazard	Low	<p>The pressure sensors do not receive an electrical current.</p> <p>They generate a DC voltage in the range of 0.25 to 4V when pressure is applied. The associated current output is in the region of 13mA.</p> <p>These levels are an order of magnitude below the levels required to cause pain and at least two orders of magnitude below the level that could affect the patient's heart.</p>

		<p>The pressure sensors are encapsulated in an insulating fabric layer and the wires are encapsulated in insulating plastic. The pressure sensors and wires will be further insulated by the sterile outer cover.</p>
Additional time for surgical procedure	Low	<p>The entire pressure measurement procedure should take no more than 10 minutes and will take place at the start of the surgical procedure once access to the abdomen has been obtained.</p> <p>The procedure can be stopped at any time.</p> <p>The patient will be monitored as standard by anaesthetist during surgery and postoperatively.</p> <p>Subjects undergoing an emergency surgical procedure will not be recruited to the study.</p>
Damage to organs	Low	<p>The sensors are embedded into a flexible fabric layer with no sharp edges.</p> <p>Surgeons will use surgical instruments and their hands' to apply pressure for the retraction of organs as per standard surgical operating procedure.</p>
Sensor retained in body after surgery	Low	<p>Only one sensor will be used per study. It is connected by a wire to a laptop so it will be obvious that the sensor cannot be left in the abdominal cavity. The entire assembly of sensor, wire and sterile cover</p>

		is at least 1m long so again it would be very difficult to misplace the sensor.
--	--	---

PATIENT FOLLOW UP:

Patients will be followed up as standard for the procedure and as the clinical situation dictates. No additional follow up will be required for the trial.

CONFIDENTIALITY AND DATA PROTECTION:

Patients are not identifiable from data.

It will not be possible to identify personal data such as name, address.

ADVERSE EVENTS:

The most likely adverse event arising from this study is a surgical site infection (SSI) as a result of the placement of the pressure sensor within the abdomen. Note that as the pressure sensor will be placed in a sterile cover the additional risk of an SSI due to the use of the sensor is very low.

Any patient undergoing an abdominal surgical procedure is at risk of an SSI and in the event that they experience the symptoms of infection following surgery they are likely to contact the hospital where the procedure took place, present to their local Accident and Emergency department or make an appointment with their GP. Upon presenting, they would be diagnosed and treated in accordance with standard clinical procedures associated with a suspected SSI. There is no requirement to implement additional diagnostic tests or treatments to manage an SSI specifically caused by the use of the pressure sensor and it would not be possible to identify if the SSI was caused specifically by the pressure sensor or was just a general side effect associated with the abdominal surgery.

Due to the very low risk of additional infections caused as a result of participating in the study we do not consider that any specific adverse event reporting procedures are required in addition to the standard adverse event reporting system that exists within CMFT.

DATA ANALYSIS:

We will obtain surface pressure vs time graphs that are associated with the degree of retraction of each abdominal organ from a number of patients. We will correlate this data with surface pressure data collected in the laboratory to validate that the pressure measurement system functioned correctly.

We will attempt to generate "average surface pressure curves" that represent all the data collected.

We will attempt to determine if the surface pressure data was significantly higher or lower than the average for a particular abdominal organ or for a particular patient.

We will attempt to correlate the surface pressure data with the degree of organ movement recorded in the video footage.

Appendix C
Patient Information Sheet and Patient Consent Form

Mr Titus Augustine

Consultant Transplant and Endocrine Surgeon

Manchester Royal Infirmary

Oxford Road

Manchester

M13 9WL

Add Date

Dear

Invitation to take part in a research study

As a patient who will shortly be admitted to the Manchester Royal Infirmary for an operation within your abdomen I am inviting you to participate in a research study that I am leading. This study involves the measurement of the pressures exerted by surgeon's during surgery and may lead to the development of a new surgical device that could make abdominal surgical procedures simpler and quicker.

A participant information sheet is attached to this letter that explains the research study in more detail. I would be grateful if you could read this participant information sheet before you attend for surgery and consider whether you are interested in participating in the study. If you have any queries relating to this invitation you can contact me or my colleague to discuss these on the numbers below.

Yours Sincerely

Mr Titus Augustine – Consultant Transplant and Endocrine Surgeon (0161 2763467)

Mr Thomas Satyadas – Consultant Hepatobiliary, Pancreatic and Advanced Laparoscopic Surgeon (0161 2712534)

PARTICIPANT INFORMATION SHEET

Measurement of organ retraction pressures during surgery.

Introduction to the research and invitation to take part.

As a patient who will shortly be admitted to the hospital for a surgical procedure in your abdomen you are being invited to take part in a research project.

Why have I been chosen?

The hospital is involved in a research project that may lead to the development of a new surgical device that improves a surgeon's access to the area within the abdomen in which they are operating. The new device has the potential to make abdominal surgical procedures simpler and quicker. The research is being led by Mr Titus Augustine, a consultant transplant and endocrine surgeon at the Trust. We have invited you to take part in our study as you will shortly be admitted to hospital for a surgical procedure within your abdomen as part of your planned care. Your consent to participation in the study gives us the opportunity to undertake some simple measurements during surgery and collect information which will contribute to the development of the new device.

What is the research study about?

During abdominal surgical procedures it is necessary for the surgeon to move surrounding organs and tissue away from the diseased area that they wish to focus on (the surgical field) in order to obtain good access to the surgical field and a good view of the surgical field. This process is called retraction. During conventional "open" abdominal surgery in which access to the abdomen is obtained via a large incision in the tummy a number of special instruments called retractors are used to retract organs. During "laparoscopic" or keyhole surgery in which access to the abdomen is obtained through a number of small incisions in

the tummy, organ retraction is more difficult and often requires the help of an assistant surgeon with further specialised retracting instruments.

We are in the process of developing a new surgical device which we hope will simplify the process of organ retraction, especially during laparoscopic abdominal surgery. The device has the potential to simplify surgical procedures by improving access to the surgical field resulting in a clearer view of the surgical field to the surgeon and their assistants. It may also help to reduce complications associated with surgery and perhaps reduce operating times.

As part of the process of developing the new device we need to gain an improved understanding of the retraction pressures that a surgeon exerts on the major abdominal organs (such as the liver, kidney, spleen etc) during abdominal surgery. Obtaining this information will enable us to ensure that the new device applies a similar pressure to a surgeon's hand or the instruments currently used for organ retraction. These pressures are thought to be quite low, similar to the pressures involved in stroking a dog or kneading bread mixture. Hence it is essential that the pressures are accurately known so that the pressures exerted by the new device are not excessive which could result in damage to the abdominal organs.

We are proposing to collect this information during surgical procedures using a thin pressure sensing mat that is placed between the surgeon's hand and the organ being retracted. By undertaking this procedure on a number of patients and during a variety of surgical procedures we will obtain a database of the typical pressures involved during abdominal surgery. As far as we are aware, such information has never been obtained before and is not available in the literature.

What will I have to do?

All the information that we wish to collect will be collected during your surgical procedure after you have had your anaesthetic. Hence you do not actually have to do anything before, during or after the procedure.

During surgery the electronic pressure sensing mat will be placed in your abdomen within a sterile cover. Your organs will be moved aside in the same way as usual but while we do this we will measure the pressure we use with a small sensor the size of a 50 pence piece. The pressures will be recorded and

the process will be videoed. This will take about 10 minutes. After this your operation will continue in the usual way.

Some clinical information will be recorded and will only be used for the purpose of this study. Your doctor is not being paid any additional fees for your participation in this study.

What are the benefits?

Collection of this information will result in an improved understanding of the pressures exerted by a surgeon during abdominal surgery.

This could contribute to:

- 1) The design of a new organ retraction and space creation device for use in surgery. This device has the potential to improve a surgeon's access and view during surgery, to simplify surgical procedures, to speed up surgical procedures and to reduce some of the complications associated with surgery.
- 2) The design of advanced surgical simulators to help train surgeons and to enable surgeons to practice new procedures on the simulator without the risk of harming patients.
- 3) Improved training of junior surgeons.

What are the risks?

We have undertaken a thorough risk assessment of the pressure measurement procedure. The main risks identified from this risk assessment were:

- 1) There is a very slightly increased risk of infection as it is not possible to sterilise the pressure sensors that are being used. To address this, the pressure sensors will be inserted within a sterile cover prior to being placed in your abdomen. This cover is normally used to cover ultra-sound sensors that are routinely inserted into the abdomen during surgery and that are also not sterile. There will only be an increased risk of infection if, for some reason, there was a hole in the sterile cover.
- 2) There is a very small risk of an electric current passing into your body. This could only occur if the insulation on the wires of the pressure sensor were damaged and if the sterile cover was also damaged. The pressure sensors

operate with a very low level of electrical current and there is no risk of electrocution or injury. If the same level of electric current were applied to you whilst you were awake it is unlikely that you would be able to feel it. The electrical current generated by the pressure sensor is very much lower than the current supplied to other electrical instruments that are routinely used during surgery.

What if I do not want to take part?

If you decide not to take part this will not affect your medical care. Also, if you do decide to take part and then change your mind before your scheduled operation, you are also free to withdraw from the study without giving a reason. Again, this will not affect your medical care.

What happens to the information?

The information collected during this study is kept confidential and will be used for the purpose of this study only. Should we publish any material resulting from the study in medical journals the information will be anonymous.

Who else is taking part?

Other patients attending the hospital for routine abdominal surgery are being asked to take part.

What happens at the end of the research study?

When we complete the study, we will evaluate the results. The results may be published in medical journals or presented at scientific conferences, but no participants will be identified or named.

What happens now if I decide to take part?

When you attend for your operation your surgeon will ask if you received this information sheet with your appointment letter. The surgeon will ask if you have any questions about the study and will answer any queries you have. The surgeon will then ask if you wish to take part in the study.

If you do decide to take part you will be asked to sign the consent form which will be kept with your patient notes. You will also be given a copy of this information sheet to keep.

If you do not wish to take part, your operation will be performed in accordance with the standard hospital procedures.

Declaration of commercial interests

This study does not involve any companies and the surgeons involved are not being paid to undertake this study. The research may lead to the development of a new medical device and if this is commercially successful the researchers may benefit financially from this in the future.

Complaints

If you have a concern about any aspect of this study, you should ask to speak to the researchers (Mr Titus Augustine or Mr Thomas Satyadas) who will answer your questions. If they are unable to resolve your concern or you wish to make a complaint regarding the study, please contact the PALS (Patient Advice and Liaison Service) team on 0161 276 8686 or you can email them on pals@cmft.nhs.uk

Contact name and number:

Mr Titus Augustine
Consultant Transplant and Endocrine Surgeon
Manchester Royal Infirmary
Central Manchester University Hospitals NHS Foundation Trust
Oxford Road
Manchester
M13 9WL
0161 2763467

Mr Thomas Satyadas
Consultant Hepatobiliary Surgeon and Advanced Laparoscopic Surgeon
Manchester Royal Infirmary
Central Manchester University Hospitals NHS Foundation Trust
Oxford Road
Manchester
M13 9WL
0161 2712534

Department of Surgery
Manchester Royal Infirmary
Oxford Road
Manchester
M13 9WL
0161 2763467

PATIENT CONSENT FORM

Title of Project: Measurement of Organ Retraction Forces During Surgery
Name of Researcher: Mr Titus Augustine, Consultant Transplant and Endocrine Surgeon.
Study Number: R03194

**Please
Initial box**

1. I confirm that I have read and I understand the information sheet dated 15th March 2013 (version: 1) for the above study. I have had the opportunity to consider the information, ask questions and have had these answered satisfactorily.

2. I consent to the procedure being recorded with a video camera and the video footage being used for the research project on the basis that it will not be possible to identify me from the video footage.

3. I understand that my participation is voluntary and that I am free to withdraw at any time without giving any reason, and without my medical care or legal rights being affected.

4. I understand that relevant sections of my medical notes and data collected during the study may be looked at by individuals from Central Manchester University Hospitals NHS Foundation Trust or from regulatory authorities, where it is relevant to my taking part in this research. I give permission for these individuals to have access to my records.

5. I agree to take part in the above study.

Participant's _____
Name:

Signature: _____

Date: _____

Name of Person _____
Taking consent:

Signature: _____

Date: _____

When completed: 1 for participant; 1 for researcher site file; 1 (original) to be kept in medical notes.

Appendix D

Ethical Approval of In-vivo Pilot Study



NRES Committee North West - Liverpool Central

HRA NRES Centre - Manchester
3rd Floor
Barlow House
4 Minshull Street
Manchester
M1 3DZ

Telephone: 0161 625 7818
Facsimile: 0161 625 7299

15 May 2013

Mr Titus Augustine
Consultant Transplant and Endocrine Surgeon and Clinical Director of Transplantation
Central Manchester University Hospitals NHS Foundation Trust
Manchester Royal Infirmary
Oxford Road
Manchester
M13 9WL

Dear Mr Augustine

Study title: In vivo measurement of retraction and displacement forces applied on human abdominal organs and tissues during open and laparoscopic surgical procedures.
REC reference: 13/NW/0258
IRAS project ID: 124838

Thank you for your email of 9 May, responding to the Committee's request for further information on the above research and submitting revised documentation.

The further information has been considered on behalf of the Committee by the Chair. .

We plan to publish your research summary wording for the above study on the NRES website, together with your contact details, unless you expressly withhold permission to do so. Publication will be no earlier than three months from the date of this favourable opinion letter. Should you wish to provide a substitute contact point, require further information, or wish to withhold permission to publish, please contact the Co-ordinator Mrs Carol Ebenezer, nrescommittee.northwest-liverpoolcentral@nhs.net.

Confirmation of ethical opinion

On behalf of the Committee, I am pleased to confirm a favourable ethical opinion for the above research on the basis described in the application form, protocol and supporting documentation as revised, subject to the conditions specified below.

Ethical review of research sites

NHS sites

The favourable opinion applies to all NHS sites taking part in the study, subject to management permission being obtained from the NHS/HSC R&D office prior to the start of the study (see "Conditions of the favourable opinion" below).

Conditions of the favourable opinion

The favourable opinion is subject to the following conditions being met prior to the start of the study.

Management permission or approval must be obtained from each host organisation prior to the start of the study at the site concerned.

Management permission ("R&D approval") should be sought from all NHS organisations involved in the study in accordance with NHS research governance arrangements.

Guidance on applying for NHS permission for research is available in the Integrated Research Application System or at <http://www.rdforum.nhs.uk>.

Where a NHS organisation's role in the study is limited to identifying and referring potential participants to research sites ("participant identification centre"), guidance should be sought from the R&D office on the information it requires to give permission for this activity.

For non-NHS sites, site management permission should be obtained in accordance with the procedures of the relevant host organisation.

Sponsors are not required to notify the Committee of approvals from host organisations

It is the responsibility of the sponsor to ensure that all the conditions are complied with before the start of the study or its initiation at a particular site (as applicable).

Approved documents

The final list of documents reviewed and approved by the Committee is as follows:

Document	Version	Date
Covering Letter		21 March 2013
Investigator CV	Augustine	
Investigator CV	Shah (D)	
Investigator CV	Dr Tahir Shah	
Letter of invitation to participant	1	15 March 2013
Participant Consent Form	2	09 May 2013
Participant Information Sheet	2	09 May 2013
Protocol	1	15 March 2013
REC application	3.4	20 March 2013
Response to Request for Further Information		

Statement of compliance

The Committee is constituted in accordance with the Governance Arrangements for Research Ethics Committees and complies fully with the Standard Operating Procedures for Research Ethics Committees in the UK.

After ethical review

Reporting requirements

The attached document "*After ethical review – guidance for researchers*" gives detailed guidance on reporting requirements for studies with a favourable opinion, including:

- Notifying substantial amendments
- Adding new sites and investigators
- Notification of serious breaches of the protocol
- Progress and safety reports
- Notifying the end of the study

The NRES website also provides guidance on these topics, which is updated in the light of changes in reporting requirements or procedures.

Feedback

You are invited to give your view of the service that you have received from the National Research Ethics Service and the application procedure. If you wish to make your views known please use the feedback form available on the website.

Further information is available at National Research Ethics Service website > After Review

13/NW/0258	Please quote this number on all correspondence
------------	--

We are pleased to welcome researchers and R & D staff at our NRES committee members' training days – see details at <http://www.hra.nhs.uk/hra-training/>

With the Committee's best wishes for the success of this project.

Yours sincerely


pp.

Mrs Julie Brake
Chair

Email: nrescommittee.northwest-liverpoolcentral@nhs.net

Enclosures: "After ethical review – guidance for researchers"

Copy to: *Dr. Lynne Webster*
James Cordon